Multi-Level Forensic and Functional Analysis of the 787 Main/APU Lithium Ion Battery

CORPORATE RESEARCH

PROJECT: 13CA50802

May 28, 2014

Underwriters Laboratories Inc.
333 Pfingsten Road, Northbrook, IL 60062-2096 USA
T: 847.272.8800 www.UL.com

DOCUMENT INFORMATION

Release Type	☐ Internal ☒ External (Confidential) ☐External (Public)	
UL Distribution	Corporate Research	
External Distribution	NTSB (Office of Aviation Safety)	
Date: March 28, 2014	Keywords: Lithium Ion Battery, Safety, Forensic, Cold Cycling	
Title: Multi-Level Forensic and Functional Analysis of 787 Main/APU Lithium Ion Battery		
Author(s)	Department	Email
Helena Chiang Dennis Grzic Alvin Wu	Corporate Research Power Test Laboratory Corporate Research	
Reviewer(s)	Department	Email
Mahmood Tabaddor	Corporate Research	

Project Team

Donald Champlin	Operations Engineering Manager
J. Thomas Chapin, PhD	VP Corporate Research, Corporate Fellow
Lillian Chen	Research Staff
Sunny Chi	Research Staff
Helena Chiang	Research Staff
Dennis Grzic	Operations Engineering Staff
Eric Hjelm	Project Engineer
Kenneth Keighron	Lab Technician
Julie Shih	Research Staff
Mahmood Tabaddor, PhD	Manager, Distinguished Member of Technical Staff
Carl Wang, PhD	Manager, Distinguished Member of Technical Staff
Ethan Wang	Research Staff
Alvin Wu	Research Staff
Dean Wu	Lab Assistant
Michael Wu	Lab Technician
Jerry Yen	Research Staff

KEY FINDINGS AND RECOMMENDATIONS

Introduction

As the intent of this work was to support the National Transportation Safety Board (NTSB) investigation into 787 /APU lithium ion battery failure, it was important to gather and analyze any background information that would help the design of a test plan to uncover or confirm possible root causes.

- Looking at the circumstances of the two 787 incidents in January 2013[1, 2] and the more recent 787 incident in January 2014[3], one contributing factor seems to be cold weather. Two incidents took place in Japan and one in Boston, Mass. during the winter with exposure temperatures falling below freezing during some days/nights. According to data from NTSB, the aircrafts may have been exposed to temperatures as low as -10 °C. Since the cells were not warmed up prior to any cycling, then one possibility is that the internal thermal state of the cells were at such cold conditions. Though the cited temperatures are within the operational range for the aircraft of 70 °C to -18 °C[4], it is known from published technical literature that charging of cells under cold temperatures may lead to internal faults and so it was important that the test plan include some cold temperature testing, both at the cell level and battery level.

- [redacted] part of this investigation also included trying to determine if there was a contributing factor in the battery design that would increase the chances of an internal fault in cell positions 6 and/or 5.

[1] NTSB report, Interim Factual Report, Case no.: DCA13IA037, Mar. 7, 2013.

[2] JTSB report, 航空重大インシデント調査（進捗状況), Jan. 23, 2013.

[3] http://www.cnn.com/2014/01/14/travel/787-dreamliner/

[4] Y47-1590, Battery Service Life Report, Rev. b, Thales, 2011.

For lithium-ion cells (LIC) that act as the source of primary motive power for transportation applications, exposure to the extreme conditions and climates possibly seen by ground vehicles and aircraft poses a challenge to safe and reliable performance. One key issue is the stability of the solid electrolyte interface (SEI). The SEI plays an important role in LIC, acting as a protective layer that can prevent undesired interactions between the electrolyte and electrodes. At high temperatures (typically greater than 60 ˚C), research has shown that the SEI layer degrades and changes cell impedance. Similar studies on LIC operating at low temperatures indicate that lithium plating is likely to occur especially in combination with high currents.

Also, LIC, as with other battery chemistries, requires adherence to a strict specification range for charging and discharging to ensure safety. Temperature is one critical factor that can affect the charging/discharging operating range. If a LIC is operated outside of the relevant specification region then a variety of adverse internal behaviors are possible. For example, when charging a LIC at temperatures below the low temperature specifications (cell design dependent), metallic lithium is more likely to deposit on the negative electrode surface as the ion transfer rate and kinetics energy of reactants decrease and so insertion of lithium ions into the negative electrode active material (typically carbon) slows down. In this state, the cell may become thermally unstable if the metal deposits can bridge opposite electrodes creating an internal short circuit. An internal short circuit generates localized heating under a charged state. This localized heat source may trigger electrochemical reactions of the active materials of the LIB, or may cause the separator film to locally react exposing a region where opposing electrodes can make contact[5]. These reactions are exothermic and can be self-sustaining, unless the generated heat is safely dissipated. The feedback of heat from the reactions into the remaining unreacted materials within the cell may then result in thermal runaway. For a grouping of cells, when one cell fails as described, then heat propagation may result in similar failure of adjacent cells.

To understand the failure modes of the 787 Main/APU battery, it was necessary and practical to first understand the failure modes of a single cell. Of course, the environment and usage conditions of the cell within the battery will determine the final cell behavior and so the test plan included both cell level and battery level testing. In this section, only findings that might have direct relevance to the investigation are described[6]. Details of the complete testing program can be found in the body of this report for both cell and battery level testing.

---

[5] Melting of the separator may also lead to an internal short circuit.

[6] This investigation is constrained by the number of samples provided, and their received conditions.

Cell-Level Key Findings

- FINDING 1: Destructive physical analysis (DPA) of three cells (cells 3, 5 and 6) from the surviving aircraft battery, asset 412, was conducted.[7] Prior to receipt by UL, there cells had been subjected to approximately one year of undocumented storage. All cells were at 100% state of charge (SOC).[8] Careful visual examinations of the windings removed from cell 5 and cell 6 revealed the presence of dendrites (Figure 1). Cell 6 was subjected to cell level pulse charging under 25 °C conditions. Cell 5 was simply subjected to normal constant current-constant voltage charging under standard conditions. Cell 3 was subjected to cold pulse charging under -18 °C conditions.
- RECOMMENDATIONS: New cells (with a known history) should be subjected to the cell-level pulse charging under sub-freezing[9] temperatures to determine whether failure of the cell will occur. A subset of cells should also be disassembled for anomaly detection and analysis after a pre-determined number of cycles if failed cells cannot be analyzed due to extensive damage.

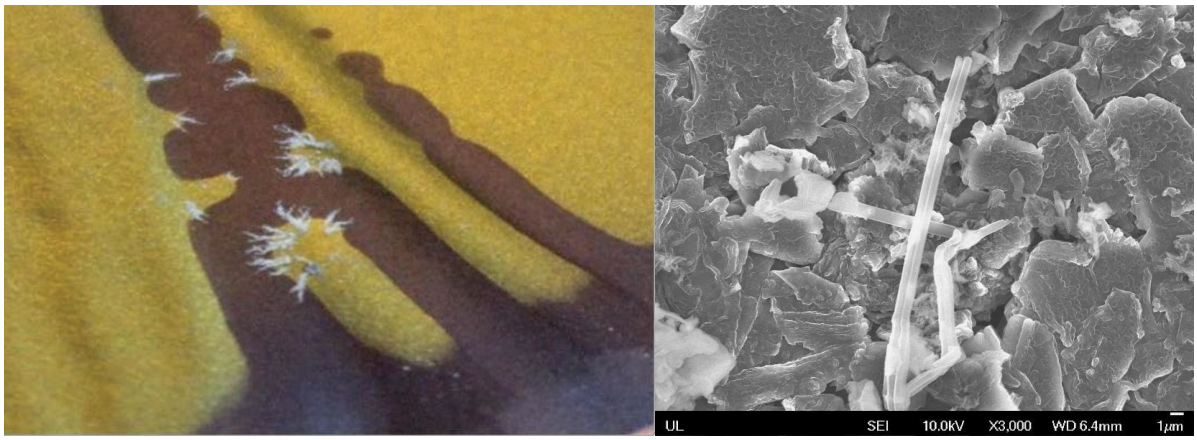

Figure 1 Photo (left) and SEM image (right) of Dendrites in Windings of Cell 5 (100% SOC) from Battery 412 (gold color shows a high charged region and the brown shows a lower charged region)

[7] Cell numbering has a battery serial number, which is followed by the location where the cell was installed. For example cell 412-3 indicates the third cell from the exterior connections on the left of two rows of cells, in battery with serial number 412.

[8] Cell level testing included subjecting cells to normal CC-CV charging mode with the target voltage set to 4.025 V. This is the standard procedure to charge LVP65 cells.

[9] The temperature that is lower than 0°C.

DISCUSSION: While the data is not conclusive about the effect of cell-level pulse charge testing under cold conditions on dendrite formation, in our opinion it is very likely that these cells contained the observed internal anomalies that may be due to operational use, storage, post-operational testing, and/or shipping prior to receipt by UL. Though it has not been established whether the dendrites contained lithium, the presence of any dendrites should be cause for concern. Also, as these cells are from battery 412, the surviving main battery of the JAL aircraft, if the anomalies were generated during usage then it might suggest that the failed battery in the Boston incident, battery 394, may have been exposed to similar conditions and also contained internal anomalies. Of course, this is not definite without knowing the complete usage history of these cells from battery 412 to ensure that no post-incident testing of the cells generated the observed internal anomalies. It is also important to note that the operational conditions, extent and frequency of the charge/discharge cycles, for the main and APU batteries are very different.

- FINDING 2: All observed dendrites occurred along a wrinkled region of the windings. Cell 3, where no dendrites were found despite the presence of wrinkles, suggests that the wrinkles are involved but not sufficient in the formation of dendrites.
- RECOMMENDATIONS: Based on current state of art in battery design and manufacturing, the presence of folds and wrinkles in the windings should be avoided.

DISCUSSION: The wrinkles may be contributing to the formation of dendrites by creating non-uniform current density distributions within the windings. This can be a direct consequence of the uneven contact between the electrodes and separator in a wrinkled region with a subsequent effect on lithium-ion transport leading to excess lithium-ion accumulation at a local site along the wrinkle. A simplified schematic of the alterations in the lithium-ion pathways due to the presence of wrinkles or folds in the windings is shown in Figure 2. The figure on the left shows a normal electrode assembly with perfectly uniform contact between layers, where lithium-ions can transit via the shortest pathway causing a uniform distribution throughout the electrode sheets. The figure on the right shows an electrode assembly with a region of poor contact between layers due to wrinkling. This introduces a region with very little to no lithium ion transfer surrounded by regions with strong charge concentration. This charge gradient is responsible, under conditions of lithium-ion transport, for initiating localized flaws or accumulation sites. Also such sites will be more problematic with pre-existing flaws.

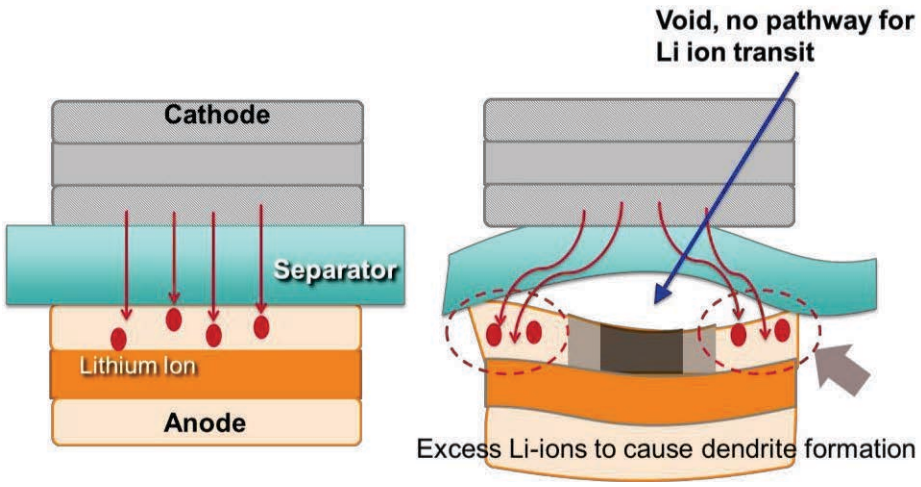

Figure 2 (left) Normal Lithium-Ion Transport and (right) Lithium-Ion Transport in Wrinkled Windings

In addition to the possibility of localized deformations of the windings being introduced during manufacturing, there are other possible causes for poor contact between electrode sheets and separator for this design. One possibility could be that welding of the current collectors on both sides of windings can lead to non-uniform stress around the edge of electrode sheets. Figure 3 shows a typical example of the welded tab to current collectors that can cause the deformation around the edge of windings. The LVP65 tab (aka collector) fingers extend approximately 60% from the top of the case.

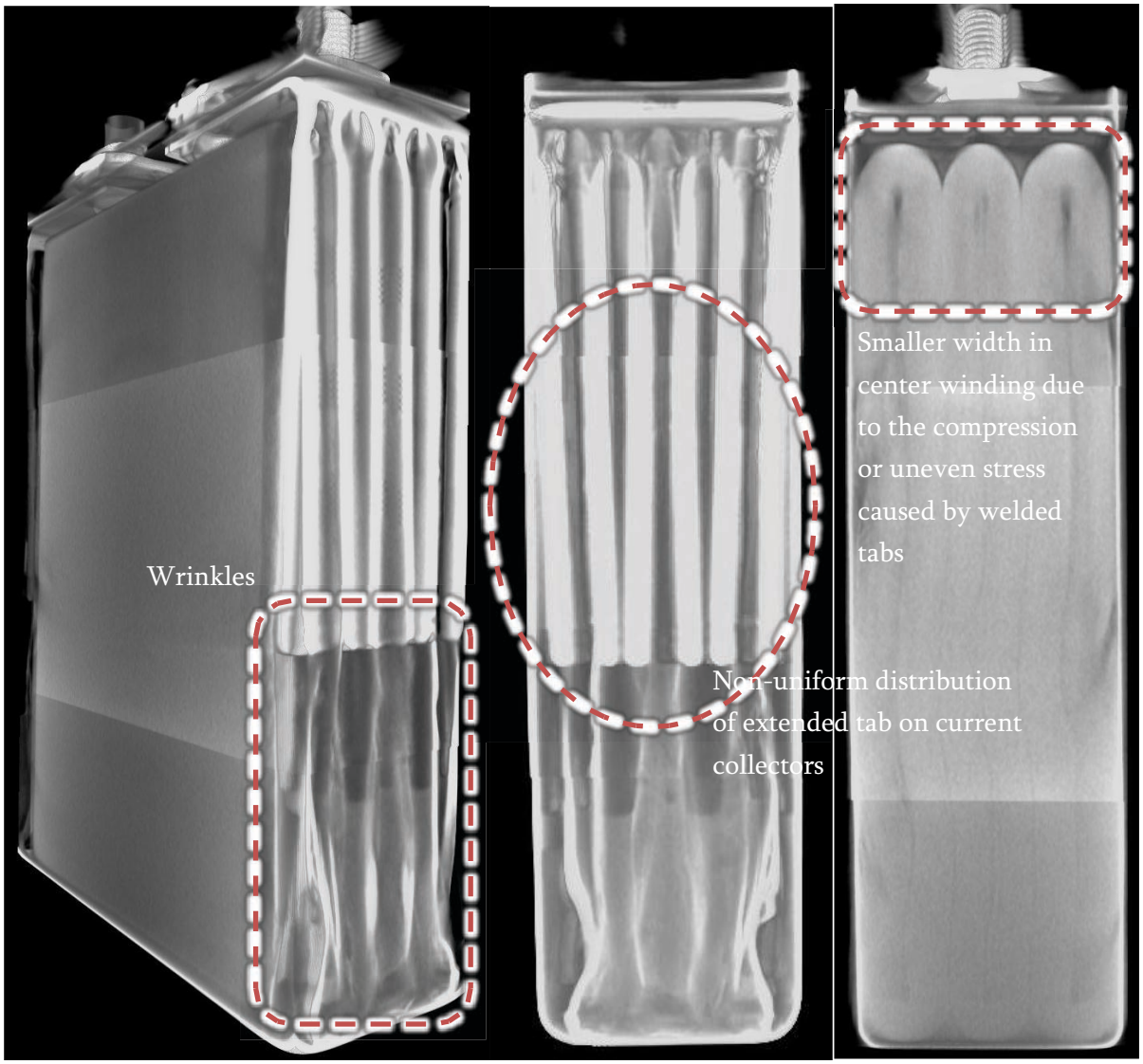

Figure 3 CT Scan of Current Collectors

Localized deformations of the windings can also be caused by vibration or shock. Finally, poor quality control of the coating or winding process can be responsible for abnormal patterns visible from a disassembled cell as an indicator of charge gradients in the electrode sheets and/or separator (Figure 4). Regardless of the source of folds and wrinkles, when a cell with wrinkled windings is subjected to charging/discharging cycles under different temperature conditions, there is a possibility for an internal fault to develop that could lead to safety issues.

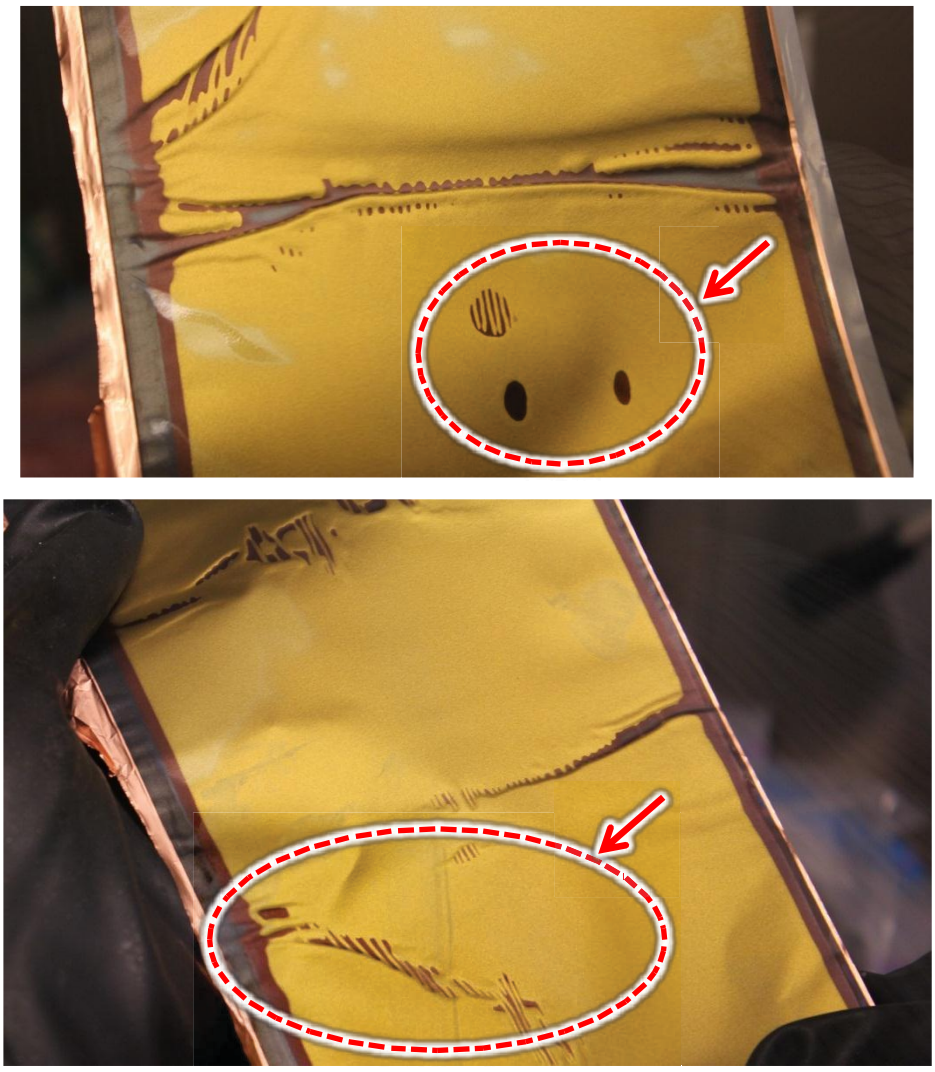

Figure 4 Abnormal Patterns created and observed on Electrode Sheets

- FINDING 3: The rate of change of the electrochemical properties of the cell changes dramatically as the temperature is lowered especially below 0 °C (Figure 5). Both non-destructive EIS measurements and electrolyte (taken from a disassembled cell) characterization show how the rate of change of key properties of the cell is affected as temperatures reach the lower operating limits for this application. As the temperature is lowered, an increasing viscosity and decreasing electrical conductivity of the electrolyte is expected as the kinetic energy of molecular ion transport can become a dominant effect. The changes in the electrolyte properties are a key contributing factor to the observed increase in the bulk material resistance from the EIS measurements.

- RECOMMENDATIONS: The use of the EIS as a non-destructive technique to characterize the internal electrochemical property changes of the cell is highly recommended. The dramatic property changes noted in the electrolyte were first detected via the EIS. Cell level testing and electrolyte characterization at low temperatures should be linked to identify a possible correlation and to ensure that the rapid changes in properties at the low temperature operating limits do not pose a safety hazard.

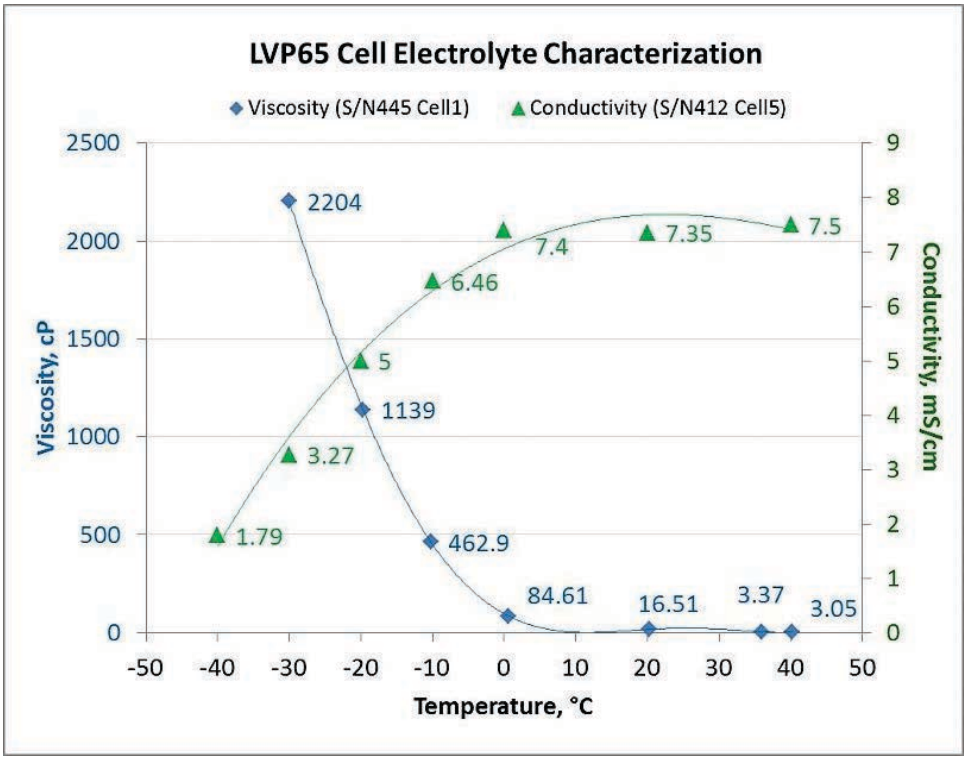

Figure 5 Electrical Conductivity and Viscosity of LVP65 Electrolyte as a function of Temperature

DISCUSSION: As the temperature of the cell is lowered, the kinetic energy of the reactants is lowered and the charge transfer resistance becomes higher, so that dendrites are more likely to be formed as the cells are charged. This change in the internal kinetics of the cell can be observed via electrochemical impedance spectroscopy (EIS) where measurements for cell 412-2 are shown in Figure 6. The EIS profiles of the LVP65 cells show a dramatic increase in bulk material resistance[10]

[10] In EIS profile, the left intersection of semi-circle to X-axis is the bulk material resistance, which is the intrinsic resistance of the bulk materials.

and charge transfer resistance[11] as the temperature is lowered, especially below freezing. The increase in bulk material resistance can lead to more Joule heat developing globally within the cell during operation. Simultaneously, more localized heat will be generated at the ion-exchange boundary layer due to the dramatic increase in the charge transfer resistance under sub-freezing temperature. The excess heating at electrode/electrolyte interface might not have direct safety concerns to the LIC but it can accelerate degradation of the SEI layer and hence to weaken its protective function[12] in the following use of the battery.

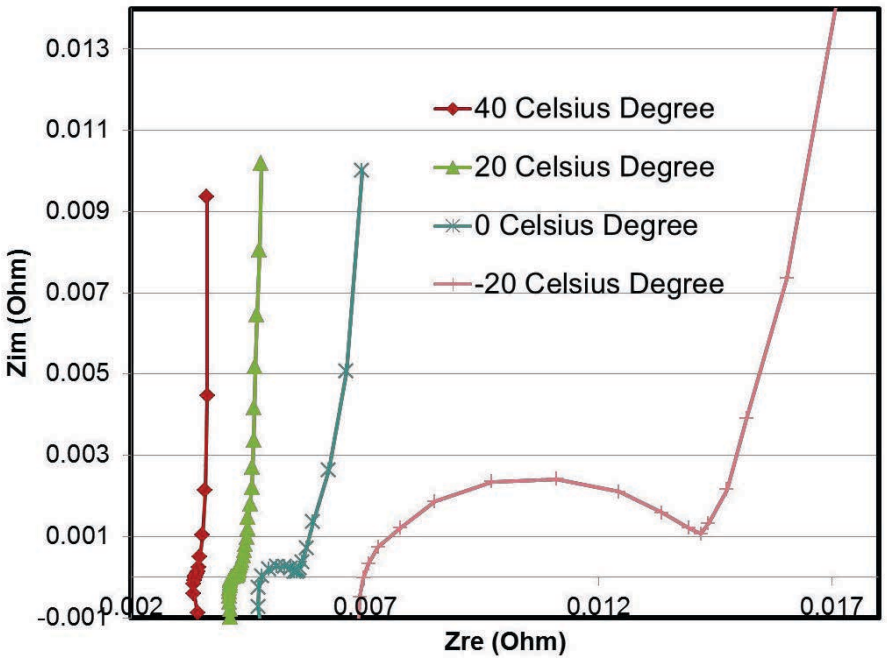

Figure 6 EIS plot for Cell 2 from Battery 412 at 0% SOC

[11] In EIS profile, the value in X-coordinate at the right intersection of semi-circle and X-axis is the sum of bulk material resistance and charge transfer resistance. That is, the diameter of the semi-circle is about the value of charge transfer resistance of the cell under that particular test condition.

[12] P. Verma et al., "A review of the features and analyses of the solid electrolyte interphase in Li-ion batteries", Electrochimica Acta 55, pp6332-6341, 2010

- FINDING 4: Self-heating of LVP65 cells under adiabatic conditions can start at 60 °C[13] which is below the upper operational temperature limit of 70 °C. This thermal stability limit was observed on cells at 0% and 100% SOC run under adiabatic conditions through Accelerating Rate Calorimetry (ARC) testing (Figure 7). As ambient conditions were raised beyond 80 °C for a fully charged cell in the ARC, the self-heating rate exceeded 0.02 °C/min.[14] At approximately 130 °C, the separator melted. In ARC testing of a fully charged cell, the cell did undergo thermal runaway and venting. As the temperature was increased, it is likely that an internal fault (internal short circuit due to melting of the separator) activated self-sustaining exothermic reactions and subsequent observed thermal runaway.
- RECOMMENDATIONS: Since the ARC testing showed that self-heating for the LVP65 begins at 60 °C which is below the current upper operational limit of 70 °C, a large sample size of cells should be studied via the ARC to determine with high confidence that the real thermal stability limits for this design are above operational limits. Active thermal management of cells during operation can also extend the operating range or provide a larger safety margin.

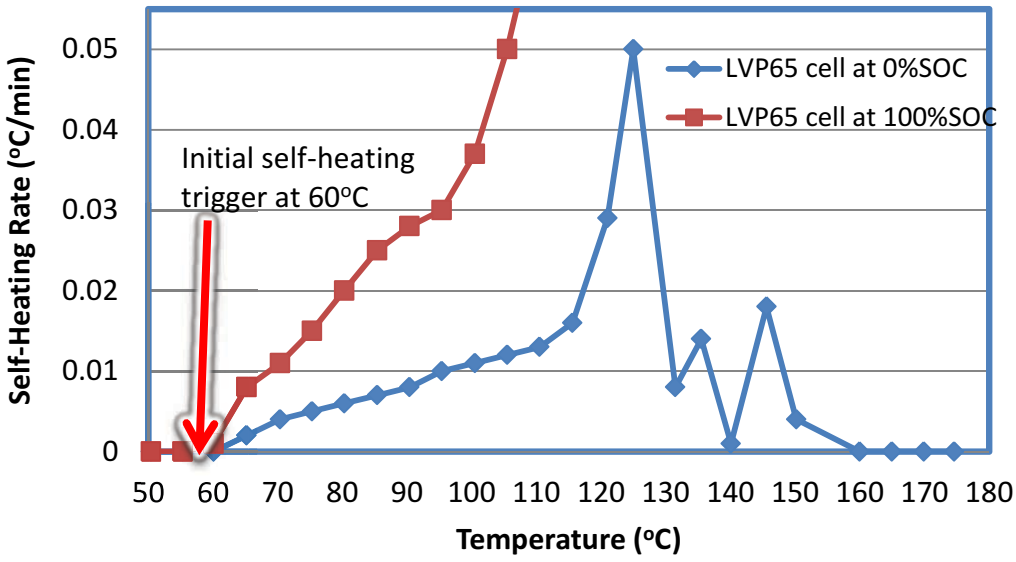

Figure 7 Self Heating Rate in LVP65 cells via ARC Thermal Abuse Test

[13] This trigger point is not a temperature at which the cell will go into thermal runaway. This self-heating trigger point is the temperature at which the SEI layer begins to break down, leading to safety concerns during subsequent charging/discharging over time.

[14] The calibrated scale of the heating rate is 0.01°C/min for a normal ARC thermal abuse test. 0.02°C/min is usually the setting of self-heating threshold to trigger the temperature tracing mode in ARC test.

DISCUSSION: The ARC is a powerful technique for characterizing the thermal stability limits of a single cell. Since the test is conducted under adiabatic conditions, it represents a worst case as any heat loss will shift thermal stability limits higher. However, it is possible that when the cell is placed within the tight confines of the battery in an environment without any active cooling or strong natural convection that the adiabatic conditions of the ARC test provide a reasonable approximation of the real thermal boundary conditions of the cell inside the battery.

- FINDING 5: At a 1C (70 A) discharge rate, the cell was found to be 95% efficient. That is, 5% of the total energy in the cell was released as heat under 70 A discharging to 2.75 V. At higher discharge rates, such as during APU start, the cells will generate an even higher fraction of their energy as heat. Thermal management can be more challenging when the cells are tightly packed within a confined battery box at higher temperatures or under adiabatic conditions possibly leading to a larger temperature increase.
- RECOMMENDATIONS: Consider active thermal management of the cells within the battery.

DISCUSSION: For example, under the 1st cycle of the simulated cell-level APU start test [redacted] cell 7 of battery 459 released over 32 kJ[15] of heat out of a total energy of 109 kJ[16]. For this test run, the energy efficiency was only 70% with 30% of the energy released as heat. The test was conducted with a single cell in a test chamber set to -18 °C.[17]

[15] Total heat released is:
Mass of Cell (2751.5 g) × Heat Capacity (1.074 $J/g \cdot$ °C) × TemperaTemperature Rise (11°C) = 32506.2 Joule≈ 32kJ.

[16] The electrical energy is 77kJ, so the total energy is 32kJ+77kJ=109kJ

[17] The lower test temperature will lead to the lowering of the discharging efficiency.

Battery Level Key Finding

- FINDING 1: During simulated APU starts on the battery, high temperatures regions were recorded at the rivet-based electrical connections located on the positive terminals of the cells during charging (Figure 8). The highest temperature reading of 125 °C was observed at the rivet on the positive terminal for cell 5. These cell-inside-battery temperature readings were much higher than the temperatures readings from the cell-only tests when subjected to the same electrical loading and ambient conditions. This certainly suggests that some aspect of the cell to battery connections is contributing to the excessive heating of cell position 5. The IR thermal image also shows that as the temperature of the rivet on the positive terminal of cell 5 increases, heat transfers to cell 6 via the copper bus tie bar (Figure 9).
- RECOMMENDATIONS: As a matter of best practices for safety, published UL safety standards almost universally disallow the use of rivets in electrical connections. Some UL safety standards allow the use of rivets but only when paired with a spring washer. The general safety concern is that through thermal cycling, rivets may become deformed and loosen, and make poor electrical connections. Mechanical electrical connections require positive pressure to be maintained safely. Subjecting the rivet (or consider alternate design) connections to a heat cycle study would be recommended.

DISCUSSION: For the cells in the battery, the same tests were conducted at the cell level. Cells 3, 5 and 7 from battery 459 were tested for APU start simulation at cell level only. The temperature reading on the rivets for these cells is shown in Figure 10 which is much lower than reading from the cells placed within the battery. Therefore, the high temperatures seen on the rivets for the cells in the battery are a consequence of the cells being placed within the battery. From the strain gauge measurements, the largest cell swelling recorded was for cell 5 within the battery. It is possible that the thermally-driven deformations and additional mechanical/torque loading due to constraints or mechanical connections within the battery generate undesired forces on the rivet. The rivets on LVP65 serve a dual purpose: sealing of the cover plate components and creating an electrical path from the electrodes to the terminals. If the rivet was not manufactured to tight tolerances (accounting for differential thermal expansion or external mechanical loadings) then loosening of the rivet is possible reducing the integrity of the electrically conductive pathways. Poor electrical connections can increase interface electrical resistance and raise temperatures through increased joule heating.

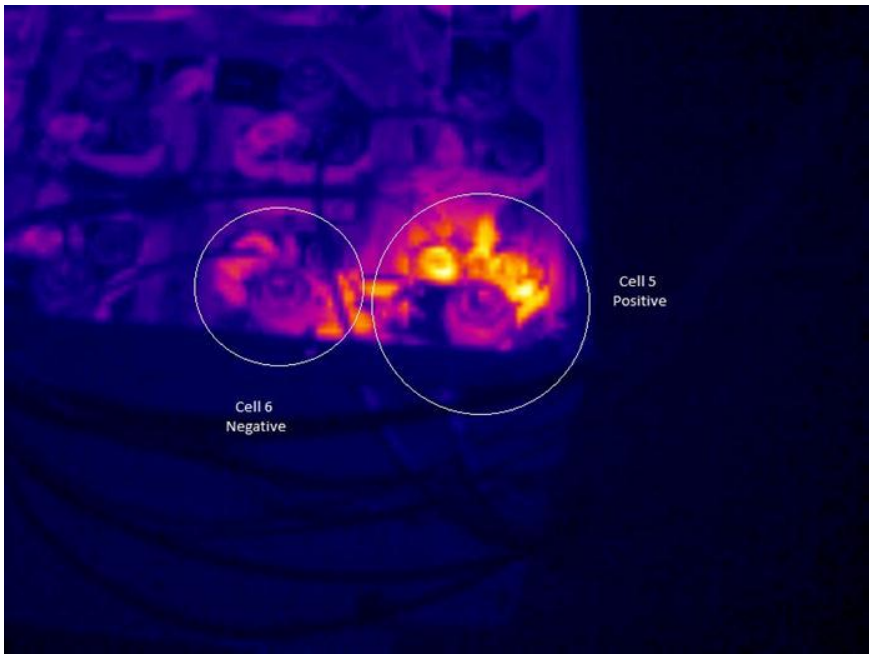

Figure 8 IR Thermal Image of Battery during simulated APU starts

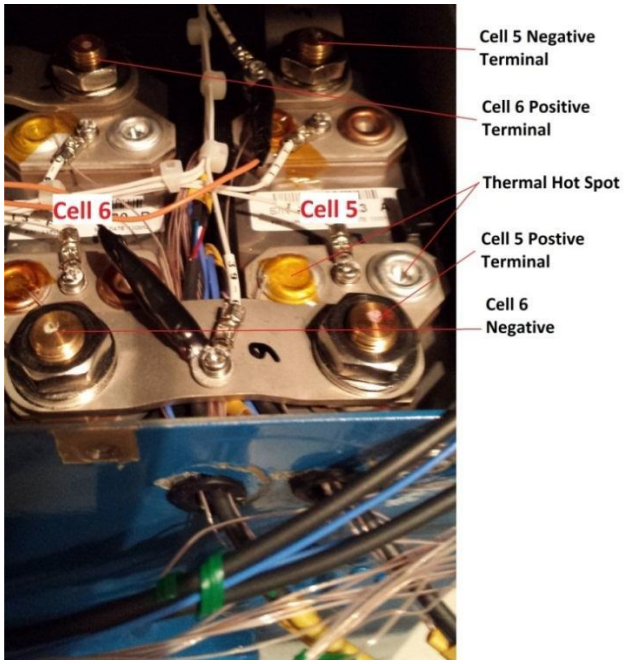

Figure 9 Picture of Cell to Cell Connections in a Battery

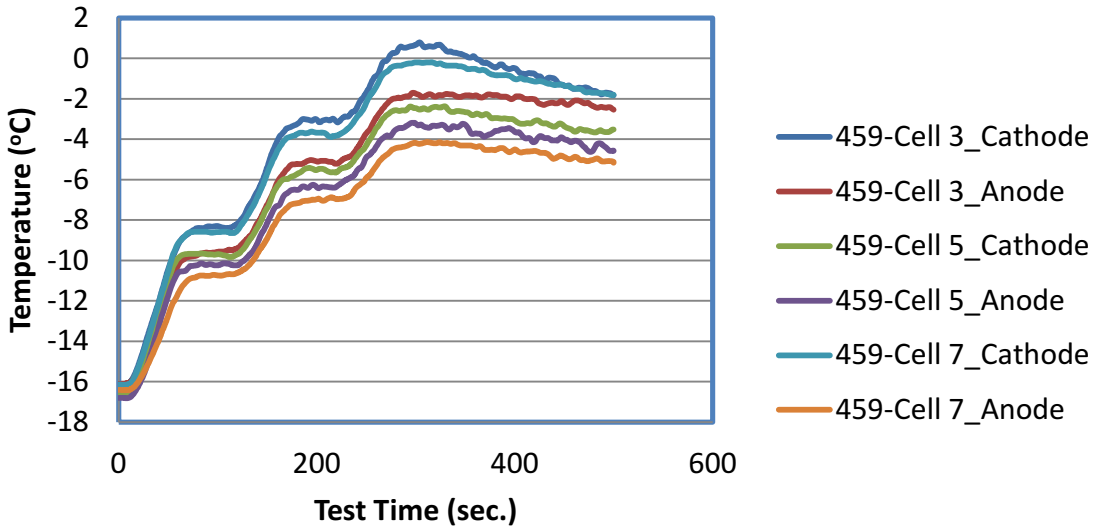

Figure 10 Temperature reading on Rivets (Cathode and Anode) during APU Start Simulation of a Single Cell Test

Examining the construction details of the rivets on the positive terminal (of a disassembled cell), Figure 11, an aluminum alloy rivet holds the following components: connection plate (copper) to terminal post, [redacted] insulation layers, cover plate (stainless steel), and the current collector. The electrical pathway is from the current collector through the rivet to the copper connection plate (or vice versa). There are two interfaces, one between the rivet and the current collector and one between the rivet and the copper connection plate. The electrical resistance at the interfaces is highly dependent upon apparent contact area which is a function of surface roughness and normal loading[18]. Any increase in the resistance at these interfaces would likely lead to high heating and the observed increase in temperature.

[18] Kogut, L. et al., "Electrical Contact Resistance Theory for Conductive Rough Surfaces", Journal of Applied Physics, Vol. 94, pp. 3153-3162, 2003.

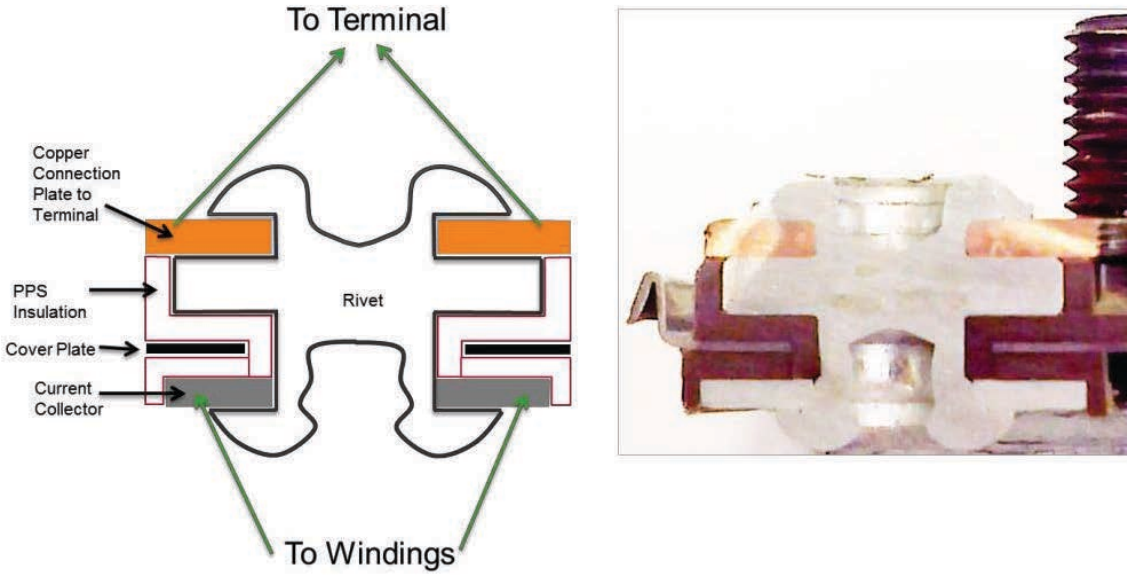

Figure 11 Positive Terminal from a Cut Cell (right) and Schematic with Labels (left)

Pre-existing gaps at these interfaces could become more problematic under the conditions of undesired constrained loading and thermally driven forces. Figure 12 shows a cross-section of one aluminum rivet on the positive terminal. Gaps are apparent at the interfaces between the rivet and the conducting elements.

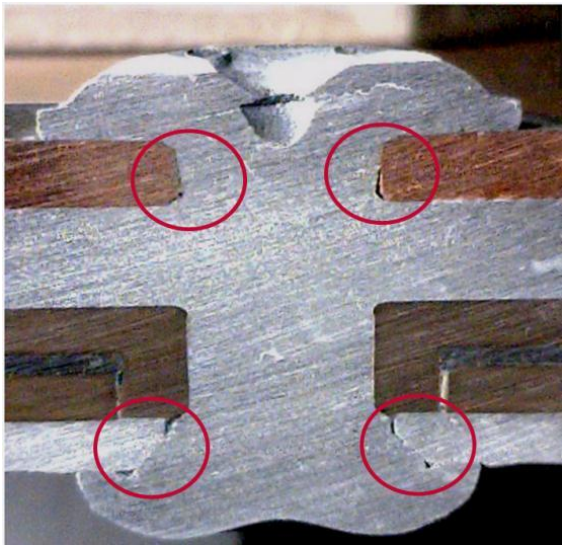

Figure 12 Gaps in the Conductive Interfaces with the Rivet (shown in circled areas)

As the cell is being heated, different materials will experience differential thermal gradients and differential deformations. Thermal gradients can lead to curvature effects while uniform temperature changes can lead to uniform deformations. The details of the mechanical constraints will dictate the final response. For this design, the rivets on the positive terminals are manufactured from an aluminum alloy, while the connection plate is copper creating a mismatch in the thermal expansion coefficients.

So the most likely scenario for the high temperatures recorded in the rivet of the cell in position 5 in the battery could be that as the cell is charged and discharged, it swells in a constrained condition that leads to forces on the positive terminal that in turn increases the electrical contact resistance of the mating surfaces between the rivet and the connection plate and/or current collectors. As the interface resistance is increased, there is an increase in joule heating at one or both interfaces creating additional thermally-driven deformations that worsen the situation. Clearly this is a consequence of the battery design (cell to cell connections, cell constraints, thermal management) and the cell design (rivet, electrical contact resistance at interfaces).[19] In addition, it has been recorded that the bus bar connecting cell 5 positive terminal to cell 6 negative terminal had the highest temperature amongst all the bus bars in the battery. Therefore, heat generated within cell 5 is transferred via the bus bar to cell 6. Now both cells can be susceptible to being the first to fail based on variations in design and assembly from battery to battery.

[19] Taheri, P. et al., "Investigating Electrical Contact Resistance Losses in Lithium-Ion Battery Assemblies for Hybrid and Electric Vehicles", Journal of Power Sources, Vol 196, pp. 6525-6533, 2011.

OTHER COMMENTS: Strengths for the LVP65 cells were also identified. By no means is this meant to be a comprehensive analysis but mainly an overview based on this single investigation and constrained by the number of samples provided. Some strengths of the cell are categorized as follows:

Design

- Compactness of materials within cell casing.
- Conservative design in energy density.[20]
- Windings construction design of jelly-roll allows for continuous production process at low cost.

Quality

- Good quality in adhesion of electrode materials on substrates.
- Performance variations between cells appear to be small.

Use Scenario

- Good efficiency in charging under room temperature (charging cells from 0% to 100% SOC required only 2.5 to 3 hours).
- APU start under room temperature generates acceptable levels of heating (6-7 °C temperature rise can be observed in single cell test).
- The slope of the open circuit voltage (OCV) profiles from the aging sorting testing for the cells was found to be highly correlated to the extent of capacity fading for the LVP65. This suggests that there are some parameters that could help estimate the state of health (SOH) of such cells during operation.

Finally, when charging a lithium-ion battery at low temperatures, there is a greater potential for cell imbalance in batteries with series connected cells. This is due to the differential capacities and rates of incorporating lithium ions in the active materials of each cell. Therefore, within an operating environment with highly variable conditions such as temperature, the thermal history will strongly affect the long-term performance and safety of the battery.

[20] Specific energy of LVP65 cell is approximately 101Wh/kg, which is about 50-60% of typical commercial Li_xCoO_2 cells.

CONTENTS

INTRODUCTION

As part of the National Transportation Safety Board (NTSB) investigation into an incident of smoke and fire reported on a Boeing 787 linked to the lithium ion battery of the auxiliary power unit in January of 2013, NTSB announced a need for a contractor with experience in "safety, environmental testing, and safety certification of lithium ion batteries to provide technical support to assist the NTSB". On September 3rd, 2014, UL LLC was awarded the contract and this report contains the details and analysis that was conducted to assist the NTSB investigation as defined by the scope of work within the contract[21].

Literature Overview

LVP65, a lithium-ion cell manufactured by GS-YUASA, was specifically designed for use in the Boeing 787 airplane. The cell is optimized to achieve high rate discharge capability and long life required for aviation application. For example, LVP65 cells can retain 89% of original capacity after 1000 cycles of full charge-discharge cycle life test at 25 °C[22]. However, it is important the temperature dependent behavior of the cell be well characterized over (and beyond) the expected operating conditions.

Use of commercial off the shelf lithium-ion battery (LIB) under elevated temperature have been described in the technical literature[23, 24] to understand safe use of high energy and high power lithium-ion battery technologies for portable cellphone and electric vehicle (EV) applications. When exposed to sufficiently high temperatures, various exothermic reactions between the electrolyte and electrodes can lead to thermal runaway[25]. However, the decomposition in the solid electrolyte

[21] Contract Award Number: NTSB-C-13-0004.

[22] J. Ueda et al., "Development of Large-sized Lithium-ion Battery for Aviation Applications", GS News Technical Report, Volume 7, No. 1, pp 14-19, 2010.

[23] S. Tobishima et al., "Lithium ion cell safety", Journal of Power Sources, Vol. 90, pp. 188–195, 2000.

[24] E. P. Roth et al., "Thermal abuse performance of high-power 18650 Li-ion cells", Journal of Power Sources, Vol. 128, pp 308–318, 2004.

[25] Q. Wang et al., "Thermal runaway caused fire and explosion of lithium ion battery", Journal of Power Sources, Vol. 208, pp. 210–224, 2012.

interface (SEI) has been found to play a key role in the initiation of these exothermic chain reactions. Hence additives that stabilize the SEI[26], improving the thermal stability of SEI, and introducing effective heat dissipation paths or internal safety mechanisms[27] that block the exothermic chain reactions demonstrate the multiple areas of active research in improving lithium ion cell safety performance. Another route for degradation of SEI under moderate temperature (ex. 50 °C-70 °C) is thermal aging which may also lead to safety issues[28]. As the typical electrolyte is electrochemically unstable under the high working voltage range in lithium-ion batteries, unintended chemical interactions between electrolyte and electrodes are highly likely to occur if there is any anomalies within the SEI layers. There are also reports to indicate that the SEI performance depends on the composition of electrolyte and the compatibility between anode material and electrolyte[29, 30]. Differential scanning calorimeter (DSC) is a very popular tool to study the interaction and compatibility between electrode materials and electrolyte[31,32]. However, the behaviors of a complete battery usually cannot be well explained through only this technique since DSC is an analytical technique limited to the component/material level. To investigate further the thermal behavior at cell level, an Accelerating Rate Calorimeter (ARC) is more useful tool. The ARC is designed to subject an entire cell to thermal abuse under simulated adiabatic condition. Hence it is well suited in establishing the thermal stability profile of a commercial lithium ion cell.

A similar study to investigate the properties of SEI and electrolyte in LIB under low temperature conditions was also published recently[33], listing charge-transfer resistance at the electrolyte/SEI

---

[26] S. Zhang, "A review on electrolyte additives for lithium-ion batteries", Journal of Power Sources, Vol. 162, pp. 1379-1394, 2006.

[27] P. G. Balakrishnan et al., "Safety mechanisms in lithium-ion batteries", Journal of Power Sources, Vol. 155, pp. 401-414, 2006.

[28] J. Vetter et al., "Ageing mechanisms in lithium-ion batteries", Journal of Power Sources, Vol. 147, pp. 269–281, 2005.

[29] M. Broussely et al., "Main aging mechanisms in Li ion batteries", Journal of Power Sources, Vol. 146, pp. 90–96, 2005.

[30] G.E. Blomgren, "Electrolytes for advanced batteries", J. Power Sources, Vol. 81–82, pp. 112–118, 1999.

[31] J. Shu et al., "Thermal reactivity of three lithiated carbonaceous materials", Ionics, Vol. 17, pp.183-188, 2011.

[32] Y. S. Park et al., "Effect of carbon coating on thermal stability of natural graphite spheres used as anode materials in lithium-ion batteries", Journal of Power Sources, Vol. 190, pp. 553-557, 2009.

[33] F. Vullum et al., "Thermal characterization of anode materials for Li-ion batteries", July 2012, http://ntnu.diva-portal.org/smash/get/diva2:566516/FULLTEXT01.pdf.

interface as the kinetic barrier for lithium-ion cells at low temperature. There are also studies that show the possibility of lithium plating likely under conditions of high currents and at low temperatures[34, 35]. Even in the region of constant current (CC) charging mode, the potential of the graphite might drop below 0 V versus Li+/Li. As a result, lithium plating and re-intercalating of the plated lithium into the graphite coexist. When the current exceeds a certain level, further increasing the current does not shorten the charging time significantly, but can induce lithium plating and increase the constant voltage (CV) charging time. Electrochemical Impedance Spectroscopy (EIS) is a powerful tool employed to investigate the behaviors of charge transfer resistance (R_{ct}) in LIB in low temperature regions.[36,37] It was found that the R_{ct} increases significantly and becomes a dominant factor as the temperature falls to below –10 °C. Based on a review of the literature, it seems that generally poor performance and safety concerns of LIB at low temperatures are associated with[38]: (1) poor electrolyte conductivity; (2) sluggish kinetics of charge transfer; (3) increased resistance of SEI; and (4) slow lithium ion diffusion through the surface layers and through the bulk of active material particles.

Generally, the published research points to the importance that the SEI plays in commercial LIB, as it not only acts as a protection layer to prevent the interactions between electrolyte and electrodes but can also introduce polarization effect during ion-exchanging[39]. Therefore, an SEI with enhanced thermal stability under elevated temperature and good permeability for lithium-ion transit under cold temperature would greatly enhance the safety performance of LIB.

---

[34] M.C. Smart et al., "Performance characteristics of lithium ion cells at low temperatures", Aerospace and Electronic Systems Magazine, IEEE (Volume:17 , Issue: 12), 2003.

[35] S.S. Zhang et al., "Study of the charging process of a LiCoO2-based Li-ion battery", Journal of Power Sources, Vol. 160, Issue 2, pp. 1349–1354, 2006.

[36] S.S. Zhang et al., "Electrochemical impedance study on the low temperature of Li-ion batteries", Electrochimica Acta, Vol. 49, Issue 7, pp. 1057–1061, 2004.

[37] S.S. Zhang et al., "The low temperature performance of Li-ion batteries", Journal of Power Sources, Vol. 115, Issue 1, pp. 137–140, 2003.

[38] Y. Ji et al., "Li-Ion Cell Operation at Low Temperatures", J. Electrochem. Soc., Volume 160, Issue 4, Pages A636-A649, 2013.

[39] C.R. Yang et al., "Impedance spectroscopic study for the initiation of passive film on carbon electrodes in lithium ion batteries", J. Appl. Electrochem., Vol. 30, pp. 29-34, 2000.

To effectively study the safety behavior of LVP65 cells, a safety window needs to be established. The safety window of a LIB can be categorized from three perspectives: design, quality and use scenarios. UL and NTSB have developed a strategy and test plan with the aid of appropriate analysis techniques to correlate potential root causes to the 787 battery accident. Figure 13 shows the key aspects that need to be considered as possible factors leading to unsafe operation of a LIB. To dig deeper into these factors, both public and proprietary information (provided by NTSB) was used to organize and develop the testing plan and subsequent analysis.

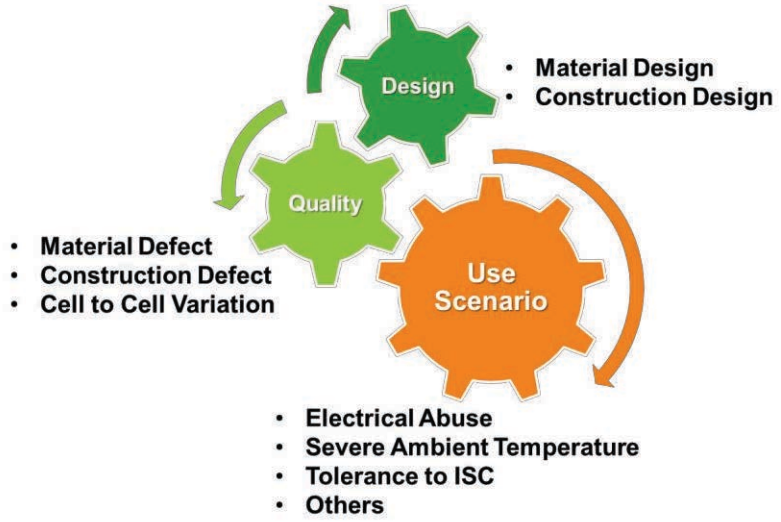

Figure 13 Key Aspects of Cell Safety Investigation

Overview of Cell Design

The design of the battery sets the foundation for the safety performance of a LIB[40]. The major challenge with LIB safety is the high energy density, exothermic reactions possible within the cell and flammability of materials[41]. The organic electrolyte used in the cell chemistry of the current generation of LIB is flammable and if heated through internal or external means in the presence of oxygen will lead to fire. In addition, polarization effect is more dominant in a large format cell as it will always be more challenging to maintain uniform current density and temperature distribution

[40] H. A. Kiehne, "Battery Technology Handbook", 2nd edition, 2003.

[41] K. E. Aifantis et al., "High Energy Density Lithium Batteries – Materials, Engineering, Applications", 2009.

throughout a big cell especially under high rate charging or discharging. It's hence important to construct a cell with appropriate current pathways internally and externally to meet the scope for the intended use scenarios. As a result, material and construction design in a LIB is the most important factor to determine its safety characteristics.

Material Design

The basis for LVP65 cell is a $LiCoO_2$/Carbon electrode design.[42] The major advantages of the material design are[43]: 1) high energy density, 2) reliability, and 3) ease of SOC estimation. However, it is also well known that $LiCoO_2$, like all battery chemistries, poses unique issues for large format battery applications due to a reduced thermal stability[44] as compared to other materials such as NMC[45] or LFP[46]. For example, $LiCoO_2$ could be less robust during an internal short-circuit (ISC) as it may be more likely to experience thermal runaway due to its reduced thermal stability.

The electrolyte design in LVP65 cell is a ternary solvent mixture EC/EMC/DMC with $LiPF_6$ lithium salt. Although $LiPF_6$-based electrolyte has been reported to be somewhat poor in thermal stability and sensitive to moisture[47], there are not many better alternatives so far as other lithium salt formulations are concerned, and other formulations may introduce disadvantages[48]. EC, EMC and DMC are mixed to form the non-aqueous organic electrolyte that acts as an ionic path between the electrodes. EMC is a useful co-solvent to extend electrolyte application range due to its low freezing point. Organic carbonate electrolytes, particularly cyclic carbonates (ex. EC), are decomposed during the first several lithium intercalations cycles into graphite to form the SEI film between the graphite

---

[42] NTSB document, "GS Yuasa Li-Ion Battery chemistry V4.pdf".

[43] NTSB document. "LI-ION BATTERIES FOR AIRCRAFT APPLICATIONS 08.pdf".

[44] J. Jiang et al., "ARC studies of the thermal stability of three different cathode materials: $LiCoO_2$; $Li[Ni_{0.1}Co_{0.8}Mn_{0.1}]O_2$; and $LiFePO_4$, in $LiPF_6$ and LiBoB EC/DEC electrolytes", Electrochemistry Communications, Vol. 6, pp. 39-43, 2004.

[45] NMC = cathode material; $Li(Ni_xMn_yCo_z)O_2$.

[46] LFP = cathode material; $LiFePO_4$.

[47] C. Campion et al., "Thermal Decomposition of LiPF6-Based Electrolytes for Lithium-Ion Batteries", Journal of Power Sources, vol. 152,pp. A2327-A2334, 2005.

[48] D. Aurbach et al., "Design of electrolyte solutions for Li and Li-ion batteries: a review", Electrochimica Acta, volume 50, issue 2-3, pp. 247-254, 2004.

anode surface and the electrolyte. The SEI film plays a crucial role that affects the capacity, cycle life, and safety in the lithium-ion rechargeable battery[49].

In addition to the solvent species and lithium salt, [redacted]

Table 1 Electrolyte composition in LVP65 cell

	Item	Specification, wt%	Freeze Point, °C	Function
1	EC	[redacted]	34 to 37	Solvent
2	EMC		-53 to -55	Solvent
3	DMC		2 to 4	Solvent
[redacted]				
7	$LiPF_6$	[redacted]		Source of Li ion

*a: PEGLST: 1,2-pentanediol sulfate ester *b: PRS: 1,3-propene sultone

[49] J. Vetter et al., "Ageing mechanisms in lithium-ion batteries", Journal of Power Sources, vol. 147, pp. 269–281, 2005.

[50] NTSB document, "L-A-1067(A)organic electrolyte.pdf".

[51] US Patent: US 2005/0130035 A1, "Nonaqueous electrolyte secondary battery", Jun. 16, 2005.

In summary, the functional additives can provide improvements in battery performance and cycle life but no specific additives seem to address thermal stability.

Construction Design

Cell construction design is also an important factor to determine the battery safety characteristics, such as heat dissipation[52, 53], potential failure mode(s) due to loss of housing integrity, and polarization effect due to the asymmetric construction[54] within cell. In this investigation, we will analyze the basic cell thermal properties and enthalpy generated under 1C discharge condition to observe the potential failure modes during thermal abuse. To some degree, polarization effects are inevitable in a large format battery like LVP65 cell. It is expected that the current density, temperature and potential distributions within the whole cell will be non-uniform during charging and discharging. However, the effect can be minimal in the short-term as polarization induced failures require many cycles to register degradation in performance or safety.

Overview of Cell Quality

One concern from some early field failures involving 18650 type LIB powering consumer products had been the introduction of foreign debris within the cell during manufacturing. Such debris can eventually lead to an internal fault that might cause thermal runaway. Therefore, manufacturers have put in great efforts to minimize such foreign debris through clean room environments and enhanced quality controls.

There are some other aspects of the LIB design that must be carefully watched during manufacturing. One example relates to how the typical LIB requires more capacity to be available at the anode with less available capacity at the cathode so that the anode will not be fully saturated with lithium-ions

---

[52] N. Omar et al., "Assessment of Performance Characteristics of Lithium-Ion Batteries for PHEV Vehicles Applications Based on a Newly Test Methodology", The 25th World Battery, Hybrid and Fuel Cell Electric Vehicle Symposium & Exhibition, Shenzhen, China, Nov. 5-9, 2010.

[53] K. Yeow et al., "3D Thermal Analysis of Li-ion Battery Cells with Various Geometries and Cooling Conditions Using Abaqus", 2012 SIMULIA Customer Conference.

[54] A. Nyman et al., "Analysis of the Polarization in a Li-Ion Battery Cell by Numerical Simulations", Journal of Power Sources, vol. 157, pp. A1236-A1246, 2010.

under fully charged condition. This is a critical factor as it is well known that lithium dendrites can form when the anode is beyond the lithium-ion saturated state[55]. As a result, the coated area of anode sheet is always slightly wider than that of cathode. From our visual inspection, the LVP65 cell also follows this important rule. However, there must also be stringent manufacturing controls on the uniformity of coating materials on electrodes as anomalies or non-uniformities could lead to safety issues.

Material Defects

As mentioned earlier, one major concern is the presence of impurities or foreign debris. One source for impurities could be internal. Impurities in raw materials or poor quality control during manufacturing processes can create a flawed cell that may not necessarily be detected by quality checks. A typical example is the recall of Dell laptop due to the flaw(s) in batteries that were caused by manufacturing defect[56]. Of course, it is also possible that flaws develop internally over time as the cell is cycled leading to impurities. As the cell is cycled numerous reactions take place and slightest imbalance can lead to localized build-up of impurities. For example, corrosion of copper current collector generally occurs under over-discharge condition to produce copper ions, which can then be deposited as metal particles after recharging. Copper will become an impurity and act as a seed for further side reactions.

Mechanical Defects

Mechanical defects can also lead to safety concerns. For example, misalignment in the electrode sheet can increase the possibility of an internal short-circuit[57]. In a large format battery, the construction integrity is more important as more polarization effect is expected. Another mechanical defect could be localized deformations of the electrode assembly. Such localized deformations can lead to uneven

[55] K. Sato et al., "A Mechanism of Lithium Storage in Disordered Carbons", Science, 264, pp. 556, 1994.

[56] "Dell Battery Danger Stems from Manufacturing Defect", Fox News, 2006 (http://www.foxnews.com/story/2006/08/17/dell-battery-danger-stems-from-manufacturing-defect)

[57] W. Cai et al., "Experimental simulation of internal short circuit in Li-ion and Li-ion-polymer cells", Journal of Power Sources, vol. 196, pp. 7779-7783, 2011.

distribution of current density[58] which, in turn, could cause local excess lithium ion deposition or plating.

Variation between Cells

When selecting cells that will be arranged into a multi-cell configuration for a battery, it is important that cell to cell variation is known and kept to a minimum. For reliability purposes, greater initial electrical imbalance amongst cells in a battery can lead to early death of the battery or cause a safety issue. Therefore, it is important to establish the baseline measurements for any grouping of cells within a battery to determine whether an imbalance exists. For a battery that has been in service, measuring electrical imbalance beyond a certain limit may suggest an internal fault within a cell or number of cells. Detailed knowledge of the usage history will be critical to any forensic analysis.

Potential Use Scenario

When a cell or battery powers a device, it is subjected to electrical loading (charging and discharging cycles) under different temperature conditions. Depending upon the particular application and quality of the cells, other conditions such as humidity and mechanical forces (such as vibration) may be impactful, too. Though a single use condition may be a contributing factor to a failure, one must consider that multiple use conditions may be a more likely contributor to failure. For this investigation, based on some knowledge regarding the usage history of the failed 787 battery, several aspects of the aircraft use scenario were considered:

1. Charging protocol and high rate discharging profile: Normal charging protocol to LVP65 cell is common CC (Constant Current)-CV (Constant Voltage) mode at 46 A/4.025 V, which was provided by NTSB[59]. The most severe discharging profile can occur when operating the APU start in the 787 aircraft. [redacted]

[58] J. M. Tarascon et al., "Issues and challenges facing rechargeable lithium batteries", Nature 414, pp. 359-367, 2001.

[59] NTSB-Boeing-UL meeting at UL Taipei office; Nov. 5-7, 2013.

[60] NTSB document; "BAT_QTPR_Y15-2536_f_Climatic.pdf".

2. Temperature range for the normal application of LVP65 cells: The battery is designed for use within the temperature range from -18 ˚C to 70 ˚C.[61]

3. Alterations to normal charging and discharging profile: The possibility that variations to the normal discharging and charging cycle of the battery may be a contributing factor.

[61] NTSB documents; "Lithium_ion_battery_for_Boeing_787.ppt".

OUTLINE OF INVESTIGATION

The work described herein and defined by the Task Area A.1 in the contract consisted of cell and battery level testing. Task Area A.1 was divided into three general categories:

- A.1.a Characterization of the Thermal and Electrochemical Properties of a Cell
- A.1.b Characterization of the Thermal and Electrochemical Properties of a Battery
- A.1.c Oscillatory Testing of a Battery

For all tasks, UL followed a systematic process consisting of baseline tests, non-destructive characterization tests and where possible, destructive characterization tests.

Baseline tests: The purpose of the baseline tests was to establish the current state of each cell and determine whether a cell or battery is suitable for further testing. If the cells were deemed suitable, then these measurements would serve as a baseline against which all future measurements can be compared to track any changes in the state of a cell as the testing proceeds all the way through to the battery-level.

Non-destructive Characterization tests: The purpose of these characterization tests was to develop an understanding of the cell or battery performance when subjected to a variety of temperature conditions and a limited number of charge/discharge cycles to avoid significant changes to the internal kinetics of the cell.

Destructive Characterization tests: The purpose of these characterization tests was to develop an understanding of the cell or battery performance when subjected to a high temperature conditions and possibly electrical loads from multiple charge/discharge cycles which could be very damaging to the cell. Some destructive testing included teardown of the cell to analyze and evaluate individual components.

Task A.1.a and Task A.1.c: Cell Level Characterization

Figure 14 shows the overall test procedure of task A.1.a. The task consisted of cell level characterization tests. After receiving battery 436, some basic visual inspections, battery level

electrical and physical measurements along with battery disassembly were carried out. Then all eight cells from the battery were removed from the battery for cell level testing: rate capacity measurements, initial discharge profile, aging sorting testing, EIS measurements before and after aging sorting testing, CT scan, heat capacity measurements, and heat flux measurements during 1C-discharging along with IR thermal imaging. All cell level tests were conducted at the UL Corporate Research battery laboratory in Taipei, Taiwan. Then the cells were re-assembled into the battery with thermocouples and strain gages added to each cell and some select parts of the battery unit. Finally, the test battery was sent to UL Power Laboratory in Melville, NY, for the completion of Task A.1.b. A similar approach was followed for the cell level tests for task A.1.c using battery 459 (Figure 15).

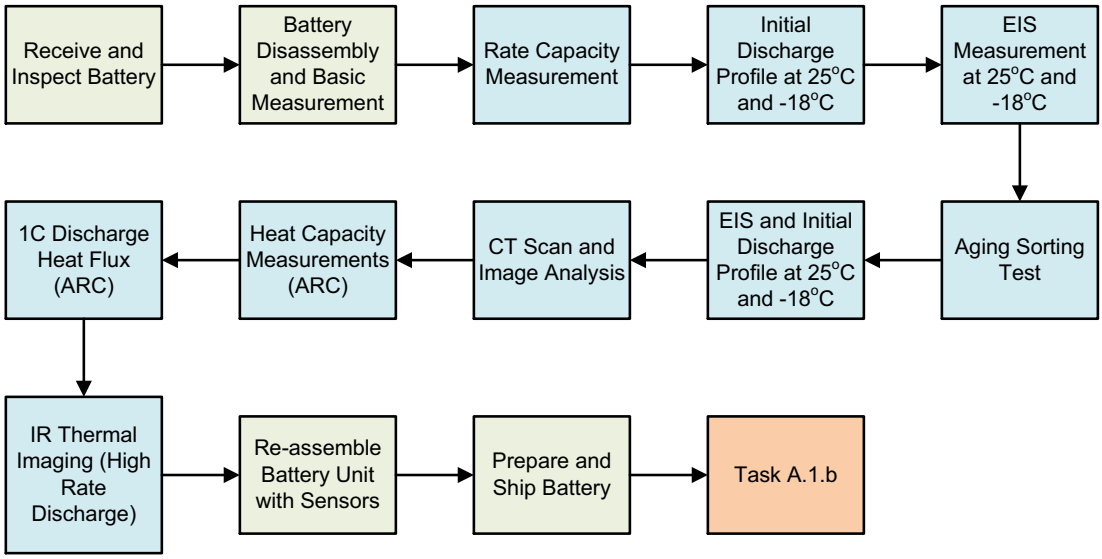

Figure 14 Cell Level Test Procedure of Task A.1.a (Battery 436)

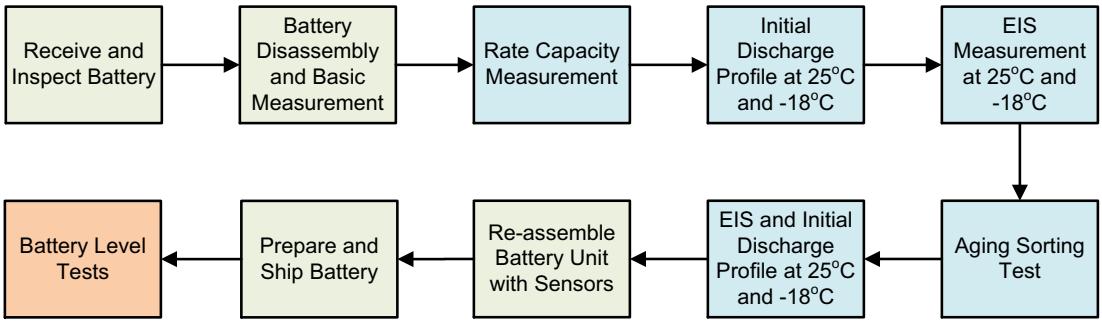

Figure 15 Cell Level Test Procedure of Task A.1.c (Battery 459)

Task A.1.b and Task A.1.c: Battery Level Characterization

Task area A.1.b required subjecting a battery to normal electrical loadings representative of what is seen during normal operations. In addition to electrical loadings, the effect of temperature was also considered.

Task area A.1.c required subjecting a battery to two types of charge/discharge duty cycles: one where there were "input charge current interruptions" (at some point during the CC-CV cycle) and another where the electrical load experiences "repetitive, short duration, charging input current interruptions". For both cases, the performance of the battery is to be examined under a variety of temperature conditions. To adequately study the effects of the charge current oscillations and the repetitive charging input current interruptions on the system it was required to also study the system without these effects. Studying the system with and without the presence of these effects will provide data which can be analyzed and compared for more meaningful results.

Temperature-Dependent Properties of LVP65

According to cell specifications of LVP65, it has been designed to operate in a wider temperature range (-18 to 70 °C) than typical Li_xCoO_2 battery designs and so the safety performance of the cell at both the low temperature and high temperature limits need to examined closely. Figure 16 shows the testing approach to investigate the temperature-dependent characteristics of LVP65 cells. The analysis relies on data generated from the EIS and ARC. The EIS technique is used to characterize the AC impedance of test samples as some of features of an EIS profile can be correlated to material

properties - such as electrolyte viscosity - and charge transfer property at passivation layers[62] or SEI. In addition, a few cells were subjected to teardown or DPA (Destructive Physical Analysis) to collect and measure electrolyte conductivity and viscosity and examine windings for any signs of anomalies.

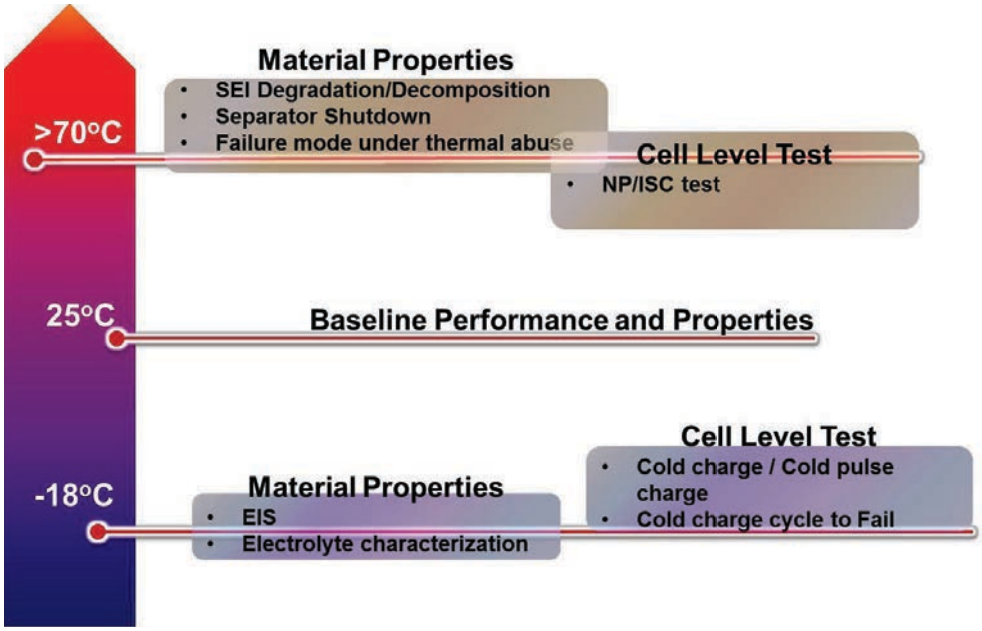

Figure 16 Testing Approach to Study Temperature-Dependency

The ARC is a powerful technique that is used to characterize the endothermic and exothermic reactions that can be self-triggered under the temperature range from room ambient to elevated temperature[63] (i.e. up to 305 ˚C maximum). Hence the technique can be used to analyze the temperature range to initiate chemical reactions (ex. decomposition of SEI, reaction between electrolyte and electrode and decomposition of electrode materials) and phase changes (ex. melting of separator layer) within electrochemical cells. This helps identify the appropriate temperature operating range for a cell. Furthermore, the cell will generally experience thermal runaway as the temperature is increased. The failure mode of the cell can also be observed to evaluate construction

[62] S. S. Zhang et al., "EIS study on the formation of solid electrolyte interface in Li-ion battery", Electrochimica Acta, Vol. 51, pp. 1636-1640, 2006.

[63] Y. Wang et al., "Accelerating rate calorimetry studies of the reactions between ionic liquids and charged lithium ion battery electrode materials", Electrochemica Acta, Vol. 52, pp. 6346-6352, 2007.

integrity. For example, a lithium-ion cell with hard metal case will usually need a vent plate to release excess pressure while thermal runaway occurs to avoid physical injury from violent explosion.

Cell DPA

To further investigate the potential risks under specific applications of LVP65 cell, such as low temperature, destructive physical analysis (DPA) was conducted for selected cells. The basic information captured from a cell DPA is summarized in Table 2. All the cells were charged to 100% SOC with standard CC-CV charging process or specialized pulse charging protocol. While asset 412 cell 5 was regarded as the controlled baseline, asset 412 cell 3 and cell 6, which displayed higher open circuit voltages due to additional pulse charging steps, were the experimental group. These cells were disassembled and examined for any internal anomalies that might raise safety concerns.

Table 2 Sample list for DPA

Sample	Description	OCV (V)	Electrolyte Characterization			Thermal analysis	Anomaly Inspection
			Viscosity	Conductivity	ICP		
#445 cell 1	Standard charge to 100% SOC	4.0199	X				
#412 cell 5	Standard charge to 100% SOC (Baseline)	4.0199		X	X	X	X
#412 cell 3	-18 °C Pulse charging	4.0807			X	X	X
#412 cell 6	25 °C Pulse charging	4.0707			X	X	x

[Note] The OCV is measured right before the cell disassembly.

The DPA plan covered two facets: one helped to characterize the materials in the cell; the other focused on defect inspection, especially the signs of lithium plating formed on the carbonaceous anode.

- Material characterization
  - Electrolyte characterization: viscosity and ionic conductivity in the temperature range (-30 to 40 °C), inorganic element analysis by Inductively coupled plasma (ICP) analysis
  - Thermal stability of cathode/anode materials
- Morphology check and defect inspection
  - Visual inspection, SEM/EDS examination

ASSETS UNDER INVESTIGATION

This section details the specifications available on the Assets.

Specifications

Three assets (batteries) and twelve additional cells were delivered to UL in three separate shipments.

Assets: #436 (Oct 22, 2013 shipped from Boeing)

#459 (Nov 4, 2013 shipped from Boeing)

#445 (Nov 4, 2013 shipped from Boeing)

Cells: #412 cell 2,3,4,5,6,7,8 (Oct 13, 2014 shipped from Carderock)

Note: #412 is surviving battery from the JAL airplane incident in Boston.

#376 cell 7 (Oct 13, 2014 shipped from Carderock)

#271 cells 1,2,7,8 (shipped from GS-Yuasa)

The key specifications[64] for the Assets are as follows:

- Nominal Voltage: 28.8 VDC
- OCV Fully Charged: 32.2 VDC +/- 0.35 VDC
- Weight: 29.3 kg (approximately)
- Number of Cells: 8
- Cell Model LVP65
- Nominal Capacity: 65 Ah (1 hour rate)
- EOL Capacity: 50 Ah (1 hour rate)
- Cell Assembly Case Material: Stainless Steel
- Battery Case Material: Aluminum

The GS Yuasa Corporation Product Safety Data Sheet (PSDS)[65] identifies each cell within the Assets as a lithium-ion rechargeable cell with the following general characteristics:

[64] Component Maintenance Manual, Thales Avionics Electric System, B3856-901, Revision 4, June 29/12.

[65] Document provided by Boeing. No date/revision date information.

- Model: LVP65-8
- Avg. Capacity: 65 Ah
- Avg. Operating Voltage: 28.8 V
- Cathode: Lithium Cobalt Oxide (active material)
  Polyvinyl Fluoride (binder)
  Graphite (conductive material)
- Anode: Carbon (active material)
  Polyvinyldene Fluoride (binder)
- Electrolyte: Organic Solvent (non-aqueous liquid)
  Lithium Salt
- Enclosure: PVC
- Precautions: Do not expose to temperatures above 50 ˚C

CELL-LEVEL TEST DESCRIPTIONS

This section will describe all testing conducted at the cell level, including physical, electrical and thermal measurements, cell charge/discharge conditioning protocols and cell DPA. Basically, all the testing can be classified into four categories: electrochemical measurements, electrical tests, thermal analysis and cell DPA.

Electrochemical Measurements

These measurements relate to cell properties at an electrochemically static state. That is, the measurement is to be made without electrical load on the test samples. Within this category, DC and 1 kHz AC resistance, open circuit voltage, EIS and aging sorting are covered.

DC Resistance and Open Circuit Voltage (OCV)

A multi-meter, Fluke 289, is used to measure the DC resistance and OCV on test sample. Measurements were taken at least three times to make sure that the readings are stable. If the reading is unstable (greater than 3% variation) then all connection points between the equipment and test sample should be checked as a possible error source. In addition, any interference from electronics in proximity of the test setup should be eliminated.

Figure 17 Hioki 3561 Milliohm-meter

1 kHz AC-Resistance

A milliohm-meter from Hioki 3561 (Figure 17) was used to measure the 1 kHz resistance of the test sample. Measurements were repeated at least three times to ensure a stable reading. If the reading is

unstable (greater than 3% variation) then all connection points between the equipment and test sample should be checked as a possible error source. In addition, any interference from other electronics in proximity of the test setup should be eliminated. The outer housing of the test sample shall be connected to ground if the noise issues still exist.

EIS (electrochemical impedance spectroscopy)

Electrochemical Impedance Spectroscopy (EIS), also known as AC Impedance Measurement or Dielectric Spectroscopy, is an electrochemical technique with applications in battery development, fuel cell development, physical electrochemistry, corrosion, biosensors, paint characterization and sensor development. The technique measures the impedance of a system over a range of electrical frequencies, and therefore the frequency response of the system, including the energy storage and dissipation properties, can be revealed.

Technical Note: A typical impedance spectra for batteries is usually shown in a Nyquist plot indicated in Figure 18.[66] The x-axis represents the real component of the complex impedance and y-axis is the imaginary component of the complex impedance. The kinetic steps include electronic conduction through the particles and ionic conduction through the electrolyte in cavities between particles. On the surface of each particle, charge transfer involves the resistance of an insulating layer and activated electron transfer resistance on the electronic/ionic conduction boundary. Ions diffuse into the bulk of particles via solid-state diffusion. Other ensuing processes, such as the formation of new crystalline structures, can also become limiting kinetic steps that can usually be observed at frequencies below 1 mHz.[67]

[66] E. Barsoukov et al., "Parametric Analysis using Impedance Spectroscopy: Relationship between Material Properties and Battery Performance", J. New Materials for Electrochem. Sys., vol. 3, pp. 301–308, 2000.

[67] E. Barsoukov et al., "Impedance spectroscopy theory, experiment, and applications", second edition, 2005.

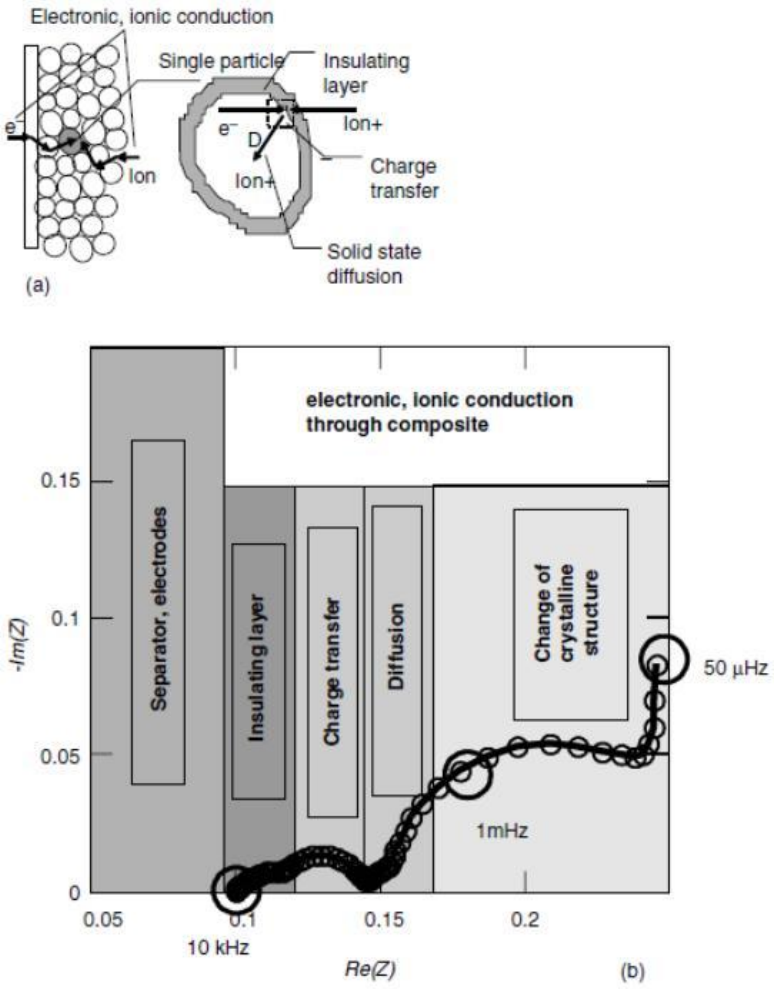

Figure 18 Kinetic Steps and Impedance Spectra typical in Batteries[68]

The kinetic steps in most cells are very similar because all cells have porous electrodes consisting of particles of energy-storing material with a conductive additive held together by a polymeric binder. Cells also include an electrolyte and a separator, which is an inert insulating component that can prevent electrical contact between anode and cathode. The EIS technique can be used as a tool not only to create a working kinetic model of the cell as a whole, but allows evaluation of the effect of each single component inside the electrochemistry unit, and a comparison between different chemistries. The EIS technique is a useful tool that can be used to characterize the aging effects

[68] E. Barsoukov et al., "Parametric Analysis using Impedance Spectroscopy: Relationship between Material Properties and Battery Performance", J. New Materials for Electrochem. Sys., vol. 3, pp. 301–308, 2000.

inside a lithium-ion cell[69] and have been studied for years as an indication to state of health (SOH) of a battery[70].

Test Methodology

EIS measurement was taken for each cell at 0% SOC as baseline. All subsequent EIS measurements were taken on cells at 100% SOC before and after being subjected to select tests such as the cold pulse charge test. As the EIS technique is very sensitive to contact resistance and since the resistance of the LVP65 cells is extremely small, the setup required very careful development and prove-in to achieve an acceptable signal to noise ratio. For the EIS setup, the main source of error typically would be high contact resistance between the electrodes of EIS and test sample. To establish a baseline, a mini-Ohm meter was used to measure cell resistance at AC 1 kHz. This serves as a potential calibration point that may be used to shift the measured EIS profile. Since the 1 kHz resistance is not necessarily exactly the same when using different EIS equipment, the difference in the AC resistance at 1 kHz between the different equipment can be used to help normalize the data.

Figure 19 details the test procedure to conduct the EIS measurements on LVP65 cells. First of all, the test sample was setup inside an environmental chamber with the terminals connected to EIS equipment (Figure 20) since some measurements were taken at temperatures other than ambient. Then there was a waiting period to ensure thermal equilibrium of the test sample. Using the Hioki 3561, measured data at 1 kHz resistance of the test sample five times checking that data variation was less than 5%. If the variation was too large, then measurement point was re-polished and the terminal of mini-Ohm meter was re-checked. In some cases, it was necessary to replace the terminal to achieve variation of less than 5%. The average of the 5 data points was set as the baseline 1 kHz AC resistance for subsequent EIS data processing.

[69] A. Wu, "Ageing Effects to the Safety Behavior of Lithium-Ion Batteries", Battery Power conference, US, 2011.

[70] A. Zenati et al., "Estimation of the SOC and the SOH of Li-ion Batteries, by combining Impedance Measurements with the Fuzzy Logic Inference", IECON 2010 - 36th Annual Conference on IEEE Industrial Electronics Society, 2010.

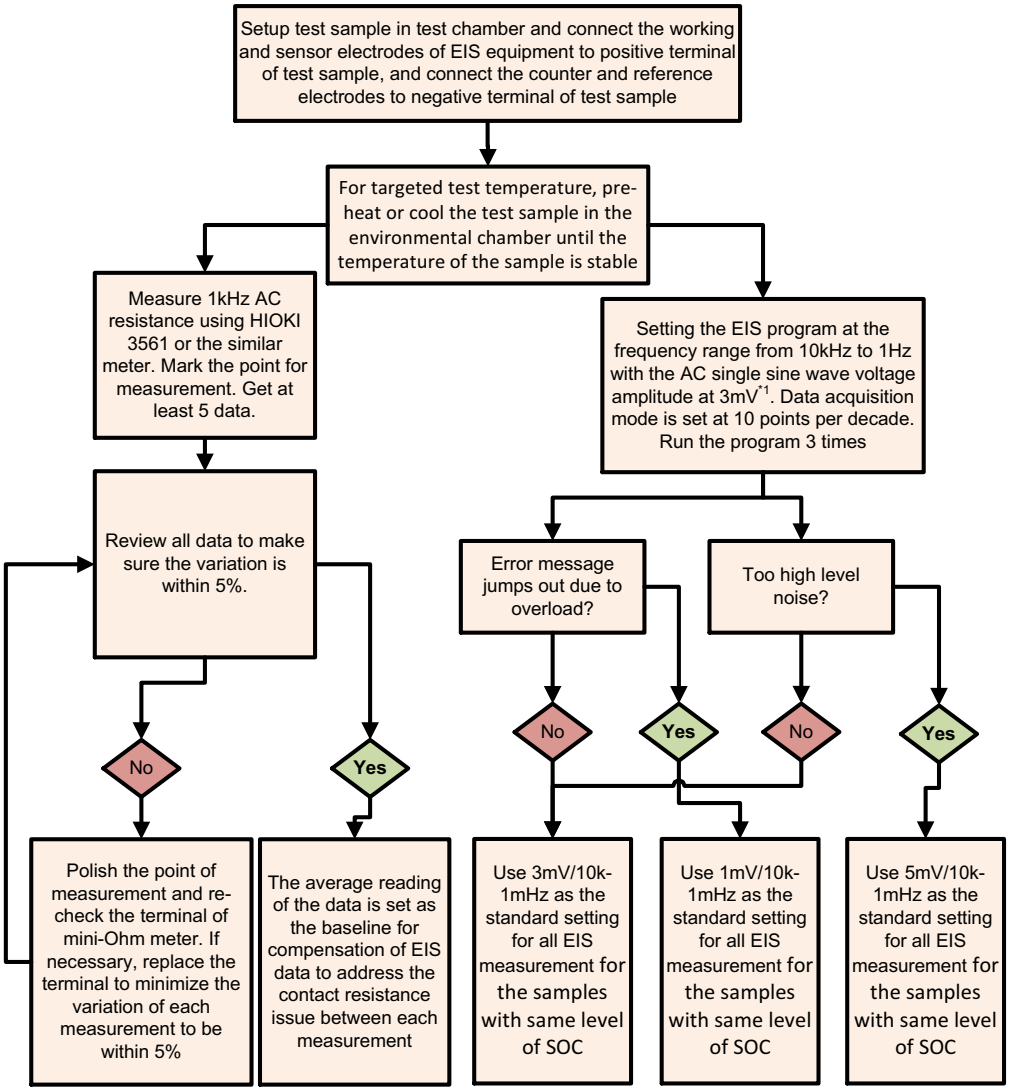

Note *1: As LVP65 has intrinsically lower resistance than normal lithium-ion cells, the setting Of AC voltage amplitude for Versastat4 and Parstat4000 shall be restricted within 1mV-5mV to avoid the damage to test equipment

Figure 19 Test Procedure for EIS measurements

Next, the EIS measurement program was set to 3 mV amplitude AC single-sine wave with a frequency sweep from 10 kHz to 1 Hz. The program was run three times. If an overload single jumped out in any of the three trial runs, the amplitude was reduced to 1 mV with a frequency range of 10 kHz – 1 mHz as the test parameter settings without changing the cell SOC. A threshold

amplitude lower than 1 mV should not be set as it will generate a high noise to signal ratio. When evaluating a battery for the first time, recommend a setting of 5 mV for the amplitude with a frequency sweep of 10 kHz – 1 mHz as a good starting setup.

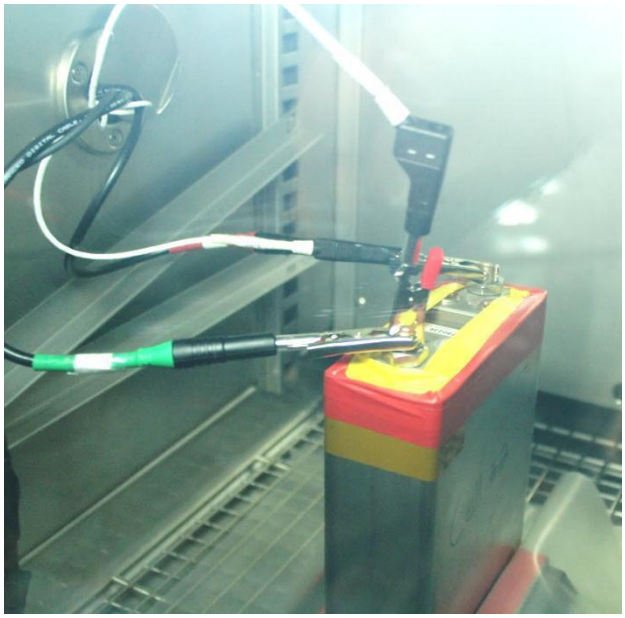

Figure 20 Cell in Environmental Chamber showing Terminals connected to EIS Equipment

Test Equipment

The test equipment used for the EIS measurements included the Versastat4 and the Parstat4000 (Figure 21) without power booster. This equipment can only be used for EIS measurements with working voltage less than 10 V.

Figure 21 Versastat 4 (Left) and Parstat 4000 (Right)

Aging Sorting Test

The main intent of this test method is to screen production by helping to identify cells with possible internal anomalies. Cells with internal anomalies may exhibit higher self-discharging rates than normal cells. As sometimes the initial state of received test samples is not known or the usage history is incomplete, the test method was used to screen and select cells for suitability in this investigation.

Technical Note: After a cell is conditioned completely, the cell OCV will generally not reach an equilibrium state due to two effects. The first effect is a consequence of the entropy of the anode and cathode not reaching a stable state within short time[71]. The second effect is the inevitable self-discharging behavior of a cell. In turn, self-discharging has several different causes[72]:

1. Internal electron leakage coming from the electrolyte partial electronic conductivity, or other internal shorts.
2. External electron leakage resulting from the poor isolating properties of the battery seals or from external finite resistance between the leads.
3. Electrode/electrolyte reactions such as anode corrosion or cathode reduction by the electrolyte or impurities.
4. Partial dissolution of the electrodes active material.
5. Electrode mechanical disintegration or isolation from current collectors.
6. Internal pressure built up and electrolyte leakage.

Test Methodology

The first step was to establish a reference SOC (0%). A cell was subjected to 70 A to 2.75 V followed by CV mode at 2.75V until the discharging current is less than 0.25 A. Half-cell voltage from anode/cathode to cell casing were also monitored and recorded. The aging portion (Figure 22) of the

[71] R. E. Williford et al., "Effects of entropy changes in anodes and cathodes on the thermal behavior of lithium ion batteries", Journal of Power Sources, vol. 189, pp. 101-107, 2009.

[72] R. Yazami et al., "Mechanism of self-discharge in graphite-lithium anode", Electrochimica Acta, vol. 47, pp. 1217-1223, 2002.

test requires subjecting the cell to 45 ˚C temperature conditions for three days in environmental chamber. The higher than room temperature setting helps shorten the testing time.

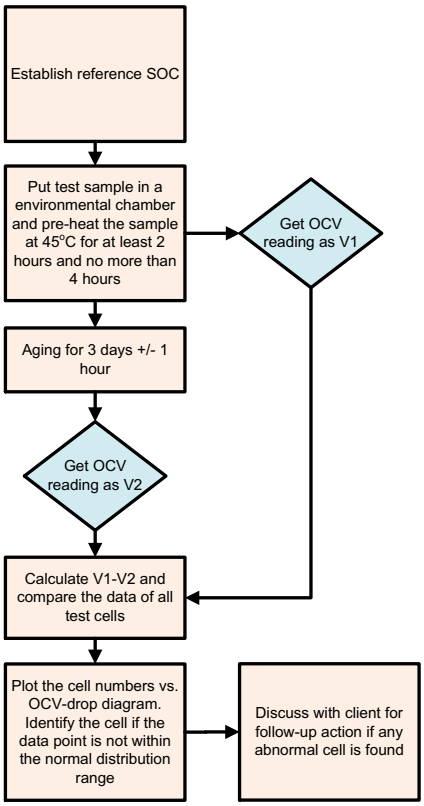

Figure 22 Test Procedure for Aging Sorting Test

Test Equipment

Figure 23 shows the samples setup for aging sorting and the environmental chamber. The customized chamber was made by KSON with temperature controls allowing conditions between -40 to 150 ˚C +/-1 ˚C. It was designed for destructive battery testing so it is equipped with fire suppression and anti-explosion functions.

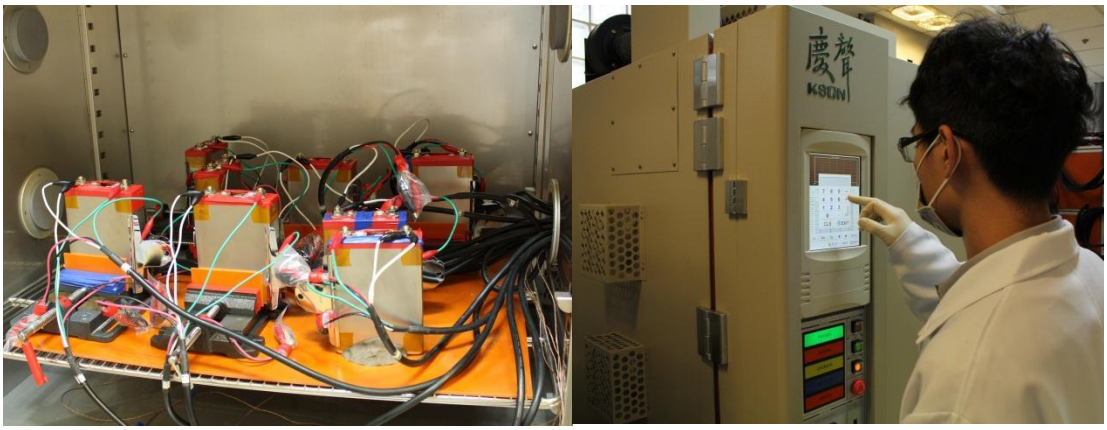

Figure 23 Test setup for Aging Sorting Test (Left) and Environmental Chamber Control Panel (Right)

Electrical Tests

Within this category, cells were connected to battery conditioning equipment to be charged or discharged. Rate capacity measurements, initial discharging profile, and cold pulse charge tests are categorized as pure electrical tests. Though the 1C discharge heat flux and IR thermal imaging under high rate discharging include electrical loading, they are considered thermal tests and are described in the subsequent section.

Rate Capacity Measurements

Even if the usage history of a battery is known, some basic electrical properties of the cells should be measured to act as a reference for other measurements in a forensic investigation. One of the key items is reversible rate capacity. Increased capacity fade can be suggestive of a long usage history or aging effects. The variation of capacity between cells within a single battery can also act as a key index to identify a cell or grouping of cells with potential internal anomalies.

Technical Note: The scale of capacity fade in a lithium ion cell can be attributed to different mechanisms[73], such as side reactions during overcharging or over-discharging, passive film formation,

[73] P. Arora et al., Capacity Fade Mechanisms and Side Reactions in Lithium-Ion Batteries, J. Electrochem. Soc., volume 145, issue 10, pp. 3647-3667, 1998.

active material dissolution and others. Capacity fading rate can also be an index to differentiate variation between cells after the battery has been used for some extended period of time.

Test Methodology

Figure 24 shows the test procedure for rate capacity measurements. The test samples were setup inside the environmental chamber with the temperature controlled at 25 °C. Before test, all cable connections to terminals were well secured to minimize joule heating effects at the connecting point. A single thermocouple was attached on positive terminal (rivet) and another one to negative terminal. An additional voltage measurement meter was connected to cell casing to negative or positive terminal to get the half-cell voltage reading while testing.

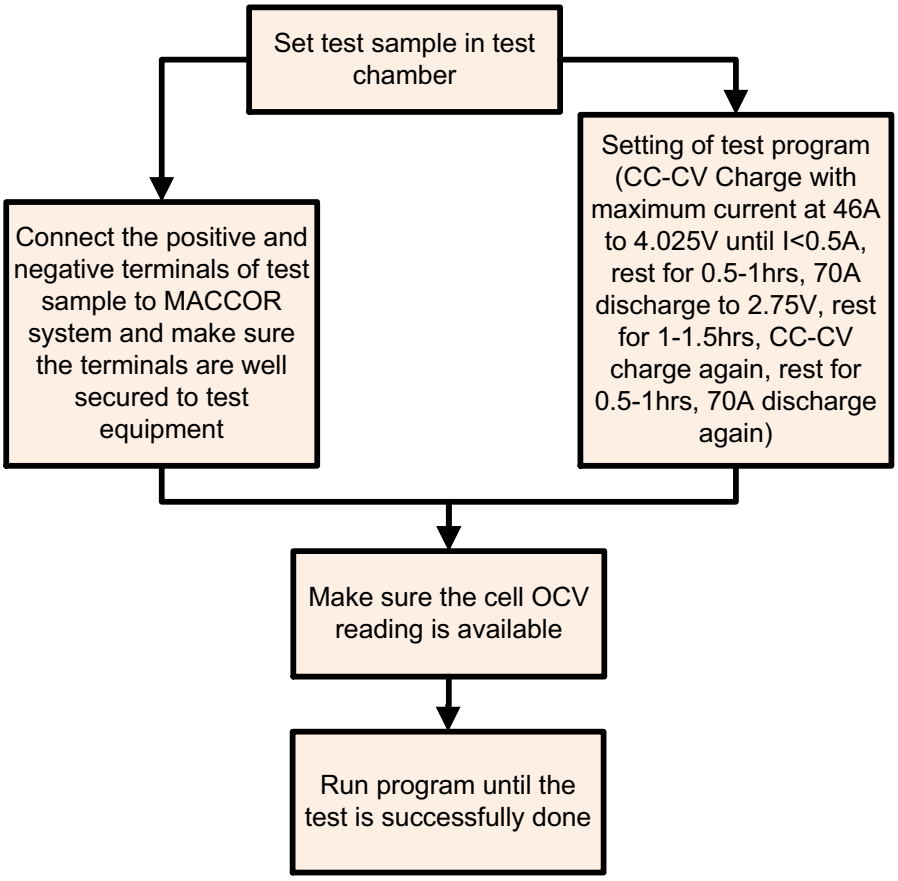

Figure 24 Test Procedure for Rate Capacity Measurement

The cell conditioning procedure consists of an initial step of establishing the reference SOC. For this step, the cell is subjected to actual charging/discharging conditions: charging at 46 A to 4.025 V in CC mode followed by CV mode until charge current is below 0.5 A. Allow the cell to rest for 30-60 minutes. Next the cell was subjected to a 70 A CC discharge to 2.75 V, allowed to rest for 60-90 minutes until the temperature stabilized at 25 +/- 2˚C. Then the cell was subjected to charging of 46 A to 4.025 V in CC mode followed by CV until 0.5 A. Once again the cell was allowed to rest for 30-60 minutes until a temperature of 25 +/- 2˚C was reached. Final step consisted of 70 CC discharge of a cell to 2.75 V. For safety purposes, if a reading above 70 ˚C was recorded from thermocouples, then the system automatically suspended the test and purged the chamber with cooling air. Figure 25 shows the sample setup for the capacity measurement on LVP65 cell.

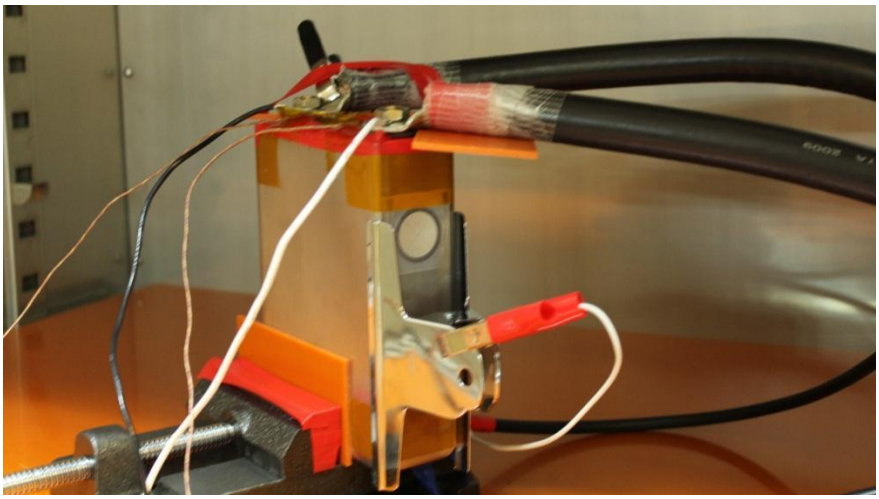

Figure 25 Setup for Capacity Measurements

Test Equipment

The cell conditioning was carried out using the MACCOR system 4000 serious (Figure 26) with a maximum output of 50 V/250 A. The accuracy on voltage and current controls was within 0.025% maximum. Test chambers are KSON chambers were described previously.

Figure 26 MACCOR 4000 Series

Initial Discharging Profile

The initial discharge profile at 25 ˚C was extracted from the rate capacity measurements. The discharge profile at any other temperature was found by testing the cells at a 70 A constant current mode until 2.75 V cut-off voltage at that particular temperature. However, test samples required several hours within a chamber to reach set point temperature.

Cold Pulse Charge Test

The objective of the test was to determine the internal characteristics of a cell when subjected to a pulse charge under cold conditions.

Test Methodology

1. The test was run on using 2 cells each at a different temperature. One at 25 °C and -18 °C.

2. Each cell was conditioned to 100% SOC (CC-CV to 4.025 V with the maximum charging current 46 A until current is below 0.5 A) at a temperature of 25 °C.
3. The cell was setup in an environmental chamber and soaked under the temperature setpoint for at least 2.5 hours.
4. EIS measurements were taken and then a connection to the MACCOR system was established.
5. Test is run first for pattern A for 2000 cycles with a rest period of only 0.1 second followed by another run pattern B for 1200 cycles.
    a. 19 Amp spikes with a period of 240 milliseconds, rise time of 41 ms and current rise of 500 Amps/sec. (Figure 27)
    b. 2.7 Amp spikes with a 560 ms period, the same 41 millisecond rise time and current rise of 65 Amps/sec. (Figure 28)
6. Repeat 5 times steps 4 and 5 and then take one more EIS measurement.
7. After the completion of the test, the cells were subjected to DPA.

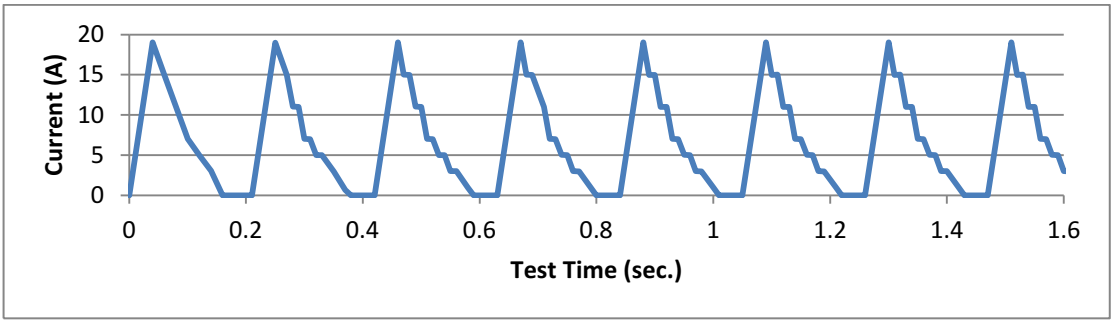

Figure 27 Pattern A in Cold Pulse Charge test

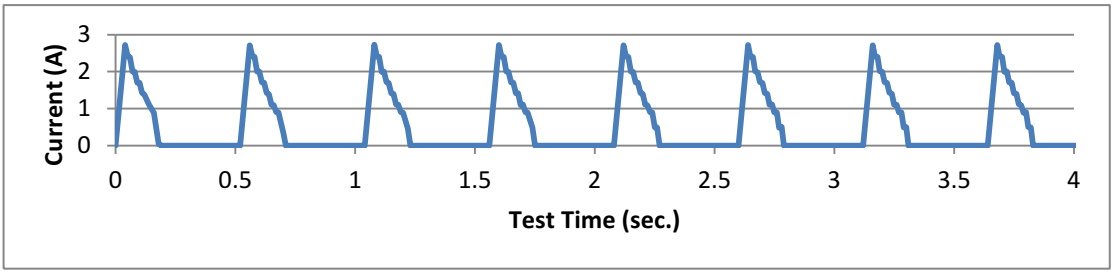

Figure 28 Pattern B in Cold Pulse Charge test

Test Equipment

The key equipment included the KSON chamber, the MACCOR system with the maximum rating at 80A/10V and the Verstat 4 system.

Thermal Analysis

The purpose of thermal analysis was to study the thermal behaviors or stability of LVP65 cell and its material or components. Within this category, heat capacity measurement, 1C discharge heat flux, IR thermal imaging under high rate discharge and ARC thermal abuse tests are covered.

Heat Capacity Measurement

Heat capacity is a thermal property that helps estimate enthalpy during battery charging or discharging. Heat capacity is generally not constant. Rather, it depends on the state variables of the thermodynamic system under study. In particular it is dependent on temperature itself, as well as on the pressure and the volume of the system.

Test Methodology

1. Preparation of test sample: 2 LVP65 cells are required for a single test. As shown in Figure 29, a heater sheet was inserted between 2 cells to create the test sample. This test sample was then placed in the center area of ARC chamber (Figure 30).
2. Next connected the cables of heater sheet to the power supply and attached the bomb thermocouple to the surface of test sample (Figure 31).
3. The ARC chamber was run using a program to measure heat capacity over a temperature range of 25 °C to 55 °C.
4. As the test sample was being heated, the ARC system traced the temperature readings from bomb thermocouple to maintain adiabatic conditions within the chamber.
5. Then heat capacity was calculated based on the following equation: $C_P = {}^{H}/_{m \times \Delta T}$

Note: First sample was tested twice with the cells at 100% SOC and 0% SOC. If the average heat capacity of the sample under the two SOC conditions was within 10%, subsequent measurements

were made on test samples at 50% SOC only. If the variation was greater than 10%, then measurements were taken at both SOC conditions for all subsequent cells.

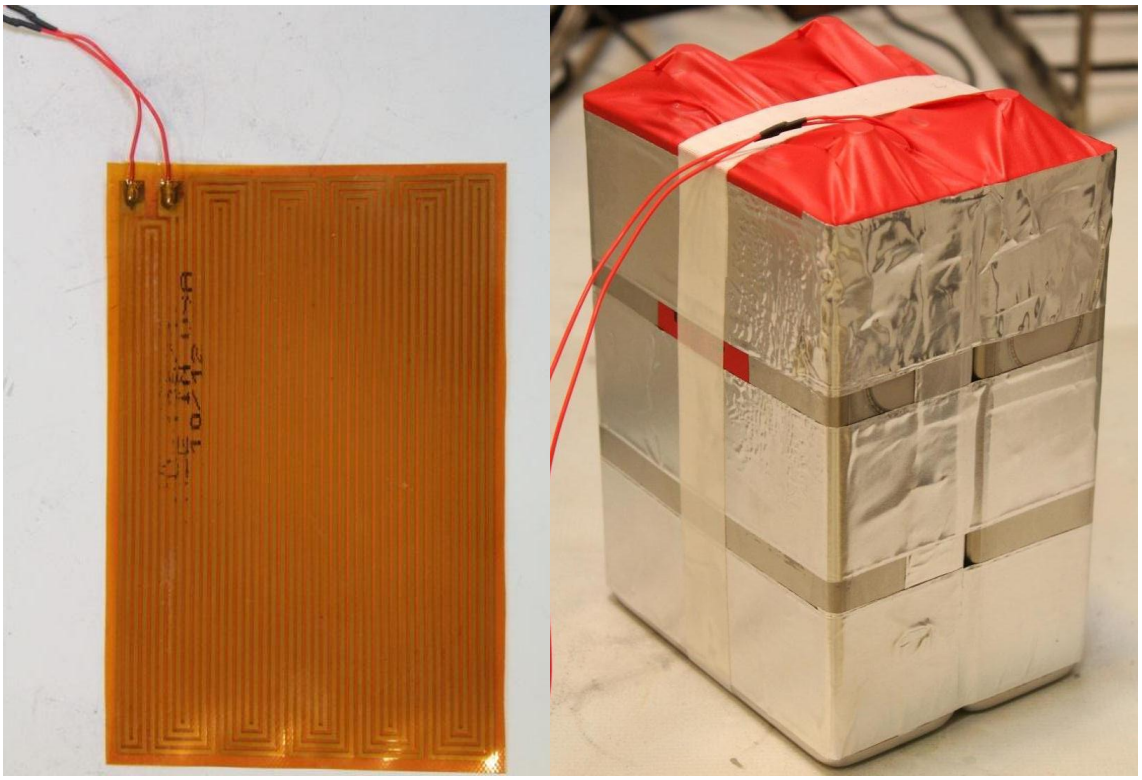

Figure 29 Preparation of Test Sample for Heat Capacity Measurements

Figure 30 Sample Setup in ARC Chamber

Figure 31 Power supply (Left) and Cell Connections to Power Supply (Right)

Test Equipment

The EV+ARC System (Figure 32) was used for heat capacity, heat flux and thermal abuse tests. The specification of the equipment is given below:

- Temperature range: room temperature to 300 °C
- Temperature measurement: Type N thermocouple
- Temperature sensitivity: 0.01 °C
- Temperature accuracy: 0.02 °C
- Exotherm detection sensitivity: 0.02 °C/min
- Exotherm tracking rate: to 20 °C/min
- Pressure measurement range: 0-50 bar
- Pressure measurement accuracy: 0.5%

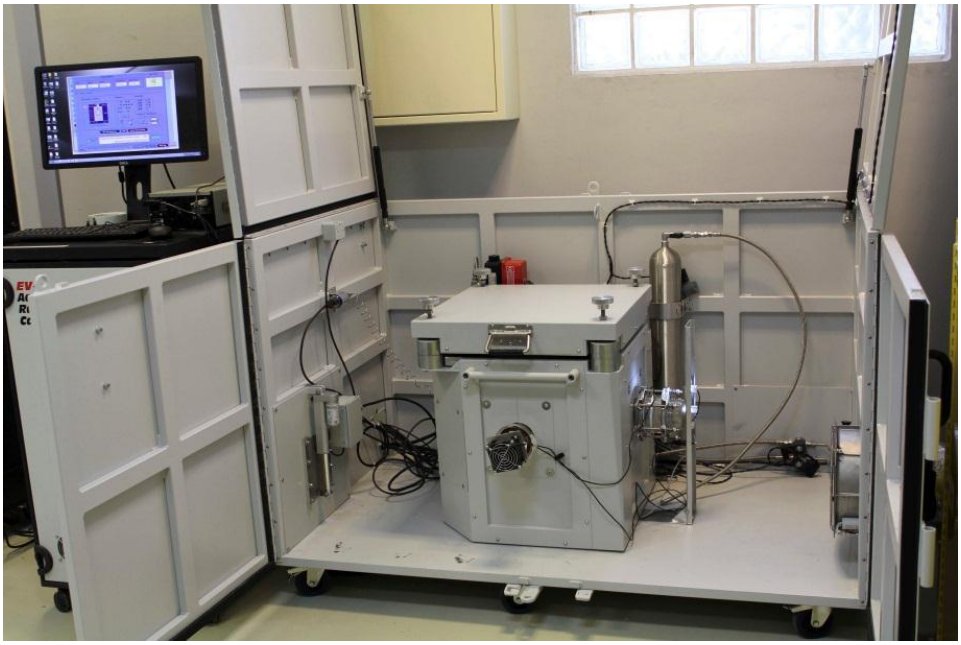

Figure 32 EV+ARC System

1C Discharge Heat Flux Test

The 1C Discharge heat flux test characterizes the 1C discharging efficiency of a single cell. The efficiency of a cell depends on the cell design and any aging effects. The data can also be used to characterize variations between cells.

Test Methodology

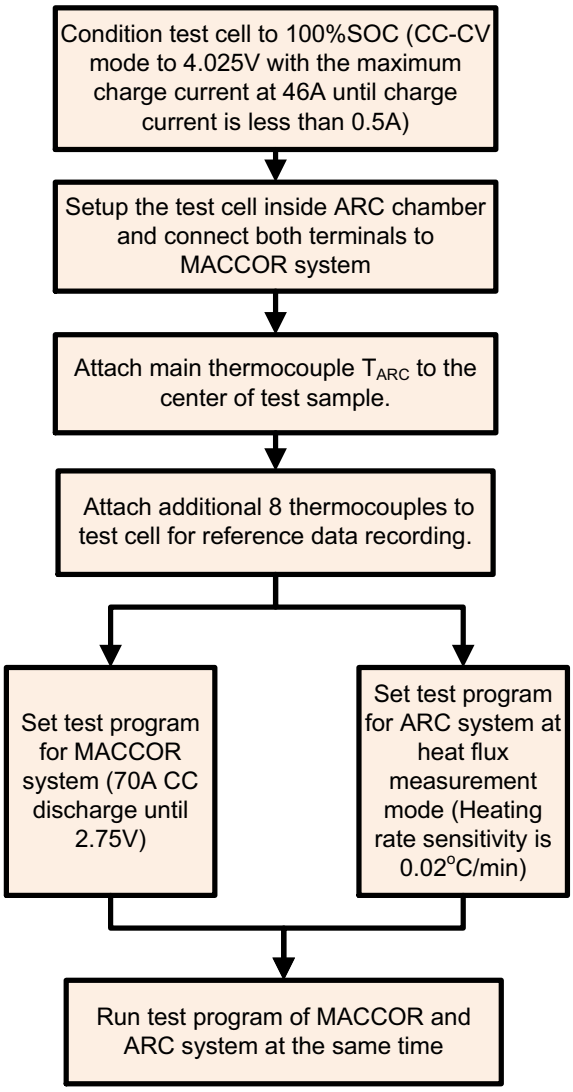

Figure 33 Procedure for 1C Discharge Heat Flux Test

1. The cell must be at 100% SOC. Cells were charged to 4.025 V under 25 °C using CC-CV mode with maximum charging current at 46 A until the current is less than 0.5 A. (see Figure 33)
2. The cell was setup inside of the ARC chamber and both terminals were connected to the MACCOR system.
3. The main thermocouple T_{ARC} was attached to the center of test sample. During testing, the system will trace the temperature from T_{ARC} to create the adiabatic conditions within the chamber. The maximum tracking rate is 20 °C/minute.
4. An additional 8 thermocouples were attached to the cell for reference. The locations of the 8 thermocouples are shown in Figure 34.

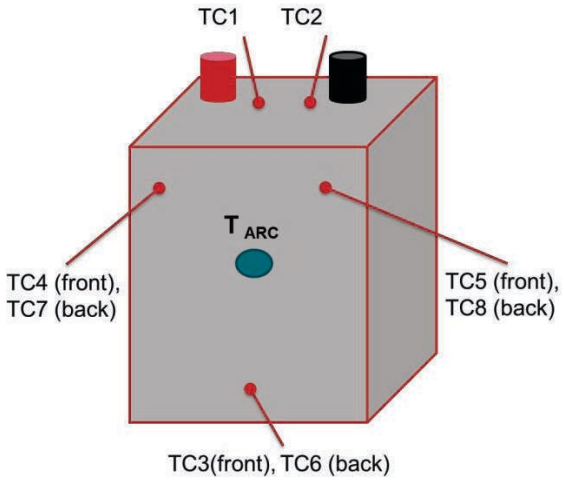

Figure 34 Positions of Thermocouples

5. Both the MACCOR system (70 A discharge to 2.75 V) and ARC system (Detecting heating rate sensitivity is 0.02 °C/min) were run concurrently.

Test Equipment

The MACCOR 4000 series with the maximum rating of 80 A/10 V and the EV+ARC system were used for the 1C Discharge Heat Flux test.

IR Thermal Imaging under High Rate Discharge

Purpose of IR thermal imaging test was to characterize any possible hot spots on the cell during APU start (high rate discharging). An IR thermal imaging camera helps develop surface temperature profiles of the cell to identify hotspots that might be missed with discreet thermocouple measurements. In addition, the contours can be used to select locations on the cell were thermocouples might best be installed.

Test Methodology

1. Selected 3 cells with highest capacity. Each Cell was charged to 100% SOC (Condition cell under 25 °C using CCCV mode to 4.025 V with the maximum current at 46 A until charging current is less than 0.5 A).
2. The cell was setup in the environmental chamber and connected to the terminals of the MACCOR system. In addition, the IR thermal imaging equipment was setup within the chamber (Figure 35).

Figure 35 Test Setup for IR Thermal Imaging test

3. The MACCOR system ran a simulation of the APU start: [redacted].
4. The frequency range of the IR thermal image capture was set to 1/60 Hz using a resolution mode of 320 x 240 pixels.
5. The cell was allowed to sit for at least 2.5 hours until thermal equilibrium was reached.
6. The APU start simulations were conducted at 3 different temperatures: -18 °C, 0 °C and 25 °C.

Test Equipment

The KSON environmental chamber, the MACCOR 4000 series with the maximum rating at 1000A/50V and the IR Imaging Camera InfRec R300 (Figure 36) were the key equipment used for this test.

Figure 36 IR Imaging Camera – InfRec R300

Thermal Abuse by Accelerating Rate Calorimetry (ARC)

The ARC equipment allows characterization of cells under thermal abuse. The ARC system will create adiabatic conditions so that all self-heating reactions generating more than a 0.02 °C/min temperature rise can be detected. For example, the initial on-set temperature (of self-heating) can be detected as the trigger for SEI decomposition. Also the temperature range for separator melting can be detected along with thermal runaway behavior can be observed. The adiabatic condition creates a worst case for cell heating as heat dissipation is minimized.

Technical Note: Exposure to high temperatures is a well-known contributor to unsafe operation of lithium-ion batteries. As a result, understanding how a battery will perform under thermal abuse is very helpful in quantifying the tolerance of a cell. All the reactions possibly activated by overheating the LVP65 type cells can be categorized as follows:[74, 75]

1. *Separator Melting*

   The separator is made of [redacted] with porous structure. Under normal condition, [redacted] will melt at around 130 °C and [redacted] at approximately 160 °C.

2. *Decomposition of Electrolyte*

   The solvent of electrolyte is organic. It will decompose when subjected to high temperatures. For example, $LiPF_6$ will interact with EC/EMC and lead to the material decomposition when the battery is heated to temperatures ranging from 125 °C to 180 °C. The decomposition of solvent will sometimes produce active products as well as gaseous substances to pressurize the cell. Generally, the decomposition will not result in excessive heat generation, but the side products will sometimes react further with electrodes at higher temperatures.

3. *The Reduction Reaction of Anode with Electrolyte*

   The SEI (Solid Electrolyte Interface) - a thin film has the same chemistry as liquid electrolyte but resides in a different phase - is easily formed on anode-separator interface. When the battery is slightly heated, the SEI formation will be enhanced. But the SEI film will melt if the battery is heated to 100 °C to 140 °C and will in turn, release small amount of heat.

4. *The Oxidation Reaction of Cathode with Electrolyte*

   When the temperature of battery exceeds 180 °C, decomposition reactions are likely to occur. If the heat cannot be dissipated effectively, it will eventually lead to cathode material decomposition and release more heat possibly leading to thermal runaway.

---

[74]E. P. Roth et al., "Thermal abuse performance of high-power 18650 Li-ion cells", Journal of Power Sources, vol. 128, pp. 308-318, 2004.

[75]Z. Z. Guo et al., "Introduction of the Safety of Li-ion Battery and the Thermal analysis Technology of Electrode Materials", Industrial Materials Magazine, No. 236, 2006.

5. Decomposition of Electrode Materials

The electrode materials usually decompose at high temperatures. Once the reaction is initiated, heat may be generated. Moreover, decomposition of the cathode will even produce oxygen gas, which may contribute to combustion however the amounts are quite small. For example, the $LiCoO_2$ battery will decompose and release gaseous oxygen under 200 °C to 240 °C as follows:

$$Li_{1/2}CoO_{2(S)} \rightarrow \frac{1}{2}LiCoO_{2(S)} + \frac{1}{6}Co_3O_{4(S)} + \frac{1}{6}O_{2(g)} \uparrow$$

Test Methodology

Two test cells at 0% SOC and 100% SOC were used for thermal abuse using the ARC. The ARC uses a heat-wait-seek mode to characterize the cell behaviors as the cell is heated. The test procedure is shown in Figure 37. The detection of temperature rate sensitivity is calibrated down to 0.01 °C/min but the temperature rate threshold for tracing is set at 0.02 °C/min. The temperature scan range is from 50 °C to 305 °C and the temperature rise step 5 °C with 40 minutes waiting time for each waiting stage.

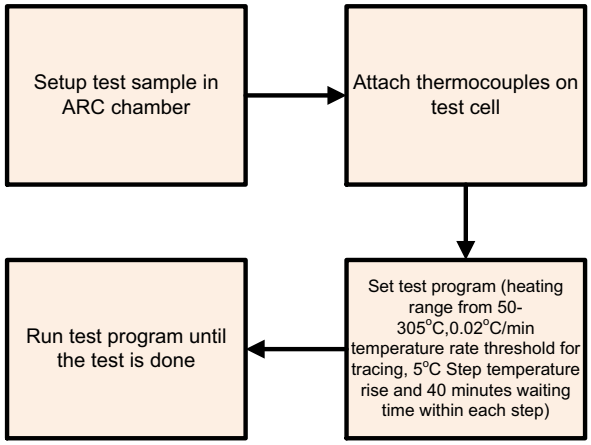

Figure 37 Test procedure for ARC Thermal Abuse (heat-wait-seek) test

Test Equipment

The EV+ARC system was the key equipment used for this test.

Cell DPA, Material Analysis and CT scan

DPA of cells was conducted at 100% SOC. There is an important safety concern associated with disassembling a fully charged, high energy cell. The detailed procedure is given in Appendix A. The cell weight and open circuit voltage (OCV) of each cell were also measured prior to disassembly process. As the materials inside a cell are very sensitive to oxygen exposure and the presence of moisture from air, cell disassembly and material preparation were performed inside an argon filled glove box to ensure safety and sample integrity. In this section, the analytical techniques used for material physical/chemical analysis of the disassembled cell components are described below.

Viscosity Measurements

The measurement was performed using a Brookfield model DV2TLV cone and plate viscometer with spindle CPA-40Z (Figure 38), where the temperature was controlled with a circulation bath. The required liquid volume for measurement can be only 0.5 mL for the electrolyte. This test method measures the torque (shear stress) required to rotate a disk in the fluid at a known speed (shear velocity) to yield the dynamic viscosity of the fluid.

Figure 38 Viscometer for electrolyte characterization

Electrical Conductivity Measurements

The ionic conductivity of the liquid was measured by means of a HANNA HI 8733 portable conductivity meter. The electrolyte sample and a meter probe are sealed in a glass tube to prevent the solvents from evaporation. The tube is immersed in an ethanol bath, which is able to maintain a stable environment from -50 to 50°C (Figure 39). Since the $LiPF_6$ salt is readily decomposed while exposed to ambient moisture, the test is performed in the Ar-filled glove box.

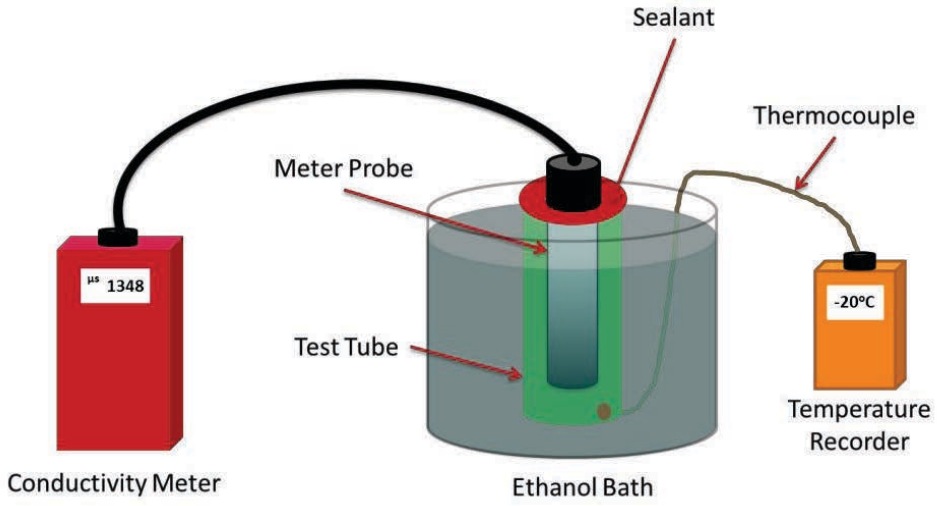

Figure 39 Illustration of the Setup for Electrical Conductivity

Induced Coupled Plasma (ICP)

The chemical evaluation of the electrolyte was performed by using inductively Coupled Plasma (ICP) technique for inorganic element analysis in this study. The model of Inductively Coupled Plasma Optical Emission Spectrophotometer (ICP-OES) was Perkin Elmer OPTIMA2100DV. The calibration curve was generated based on the concentrations of 0, 0.1, 0.5, and 1.0 ppm for each identified element.

Thermogravimetry (TGA)

The Thermogravimetry technique measures the weight loss of testing material at elevated temperature, which is used to evaluate the thermal stability of cathode and anode materials in

lithium ion cells. The decomposition temperature of the materials can then be determined. The TGA test for this project was performed with temperature ramping rate of 10 °C per minute in nitrogen purge environment by using the TA Instruments Q500 TGA.

Differential Scanning Calorimetry (DSC)

The DSC measures the heat flow changes of a sample as it is subjected to a prescribed temperature program in a controlled atmosphere. Thus, the DSC can provide the information on key temperature set points at which the material experiences physical or chemical changes. For this project, the DSC was employed to detect the chemical reactivity of the charged cathode or anode materials. The DSC test was performed with temperature ramping rate of 10 °C per minute in nitrogen purge environment by using TA Instruments Q2000 Differential Scanning Calorimeter. Each sample for DSC measurement was packed in a stainless steel pan and then crimp-sealed in Argon filled glove box.

Scanning Electron Microscopy (SEM)/Energy Dispersive X-Ray Spectroscopy (EDS)

JEOL Fields Emission Scanning Electron Microscope, JEOL FE-SEM JSM 6701 was used to observe the morphology of cell components including separator, anode and cathode materials (Figure 40). The SEM provides high image resolution up to 1 nm at 15 kV and 2 nm at 1 kV. The Oxford INCAx-act EDS was use for element identification. The EDS detector, known as a SDD (Silicon Drift Detector), guarantees a resolution in compliance with ISO 15632:2002.

Figure 40 SEM/EDS system for inspection

CT scan

CT scan is a nondestructive way to image the internal physical structure of a cell. The CT scan is often used by the battery manufacturers to ensure the proper alignment of electrode sheets and to

detect the presence of anomalies within a cell. In this investigation, the CT scan was used to observe and asses the internal construction of the cell design and any variations between samples.

Test Methodology

The CT scan was conducted using the test parameters 180-220 kV and 180-400 μA, under off-set mode, which is the mode that capture better resolution for sample dimension larger than 10 cm in width, with the presence of filter (0.5-2.5 mm thickness copper plate). The best resolution will allow identification of components no smaller than 0.3 mm. That is, any anomaly that is smaller than this dimension cannot be recognized by the CT scan images. That is also the reason it is difficult to distinguish the anode and cathode layers in a jelly-roll winding as the thickness of a layer is about 0.1 mm and the thickness of separator is 25 μm. Figure 41 shows the test setup of the CT scan. One challenge was to make sure that the X-ray signal can be received by the receiver (detector). A relatively large sample with heavy metal construction will usually require setting the accelerating voltage for X-ray source generation to more than 190 kV with a current flow of more than 150 mA. A filter is also required during testing because under the high power setting to protect the detector from damage under the high power settings.

Below is the summary of the key test parameters for the CT scan on LVP65 cells:

- Accelerating Voltage for X-ray generator: 180-220 kV
- Setting of current flow: 180 μA-400 μA
- Mode: offset
- Filter: 0.5 mm to 2.5 mm
- Temperature: Ambient laboratory conditions

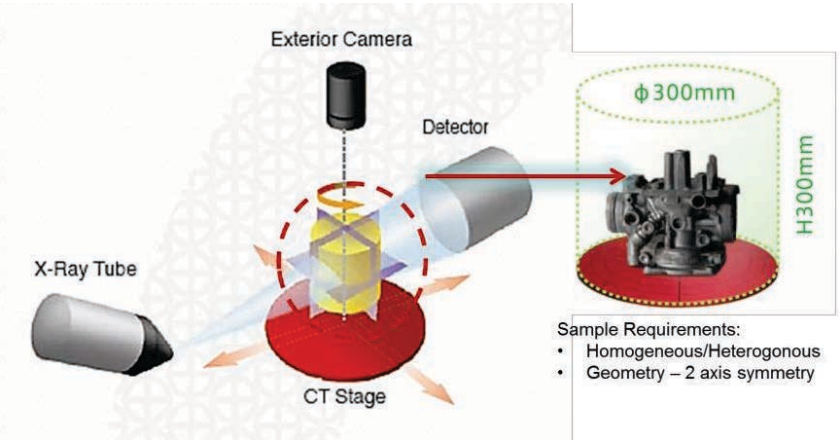

Figure 41 Setup of CT scan test

Test Equipment

The Shimadzu 225CT (Figure 42) was the CT scan model used for the analysis. The equipment has a maximum voltage rating at 225 kV.

Figure 42 Shimadzu 225CT

CELL LEVEL TEST RESULTS AND DISCUSSION

This section discusses the results from cell level testing. The data were analyzed and grouped into several categories: (1) cell design and observations; (2) basic cell performance and cell to cell variation; (3) thermal properties and temperature-dependent characteristics; and (4) miscellaneous.

Cell Design and Observations

LVP65 cells consist of a prismatic construction with 3 jelly-rolls (or windings) stacked in parallel as shown in Figure 43[76]. One observation is that there is ultrasonic welding of both sides of the current collector connected to positive and negative terminals. Such a construction may introduce more stress and create edges deformation of jelly-rolls. Any deformation within the electrode assembly can cause poor contact between electrode and separator, which is soaked with electrolyte, and may act as a site for dendrite formation or growth due to the uneven current distribution.[77] Figure 44 shows a CT scan image of the side view of the jelly rolls. The width of center jelly-roll, W2, is approximately 5-10% less than the width of the outer jelly rolls, W1 and W3. Compression of the center jelly roll will lead to higher and non-homogeneous stresses. Figure 45 also shows another example of deformations in the jelly rolls that may result in poor contact between electrode sheets and separator.

Figure 46 shows a photo of the internal components of a disassembled cell at 100% SOC. While the anode is saturated with lithium (such as LiC_6), the anode active material will turn a yellowish color with slightly metal-like gloss. Otherwise, the active material will be a brown color if anode is only partially saturated with lithium ions or black color if the cell is at a low SOC. Clearly the edge of the anode sheet exhibits a non-uniform darker color. Therefore the lithium ions are not traveling through the shortest path from cathode to anode during charging due to the poor contact between the electrode sheets to separator layer. It is in such areas that there is possibility of lithium plating and dendrite growth. Finally uneven permeability of the wrinkled separator could also result in uneven current density distribution, which can also lead to dendrite formation[78].

---

[76] NTSB document, "L-B-9461(A) Cell Element Assembly.pdf".

[77] F. Orsini et al., "In situ Scanning Electron Microscopy (SEM) observation of interfaces within plastic lithium batteries", Journal of Power Sources, vol. 76, pp. 19-29, 1998.

[78] S. S. Zhang, "A review on the separators of liquid electrolyte Li-ion batteries", Journal of Power Sources, vol. 164, pp. 351-364, 2007.

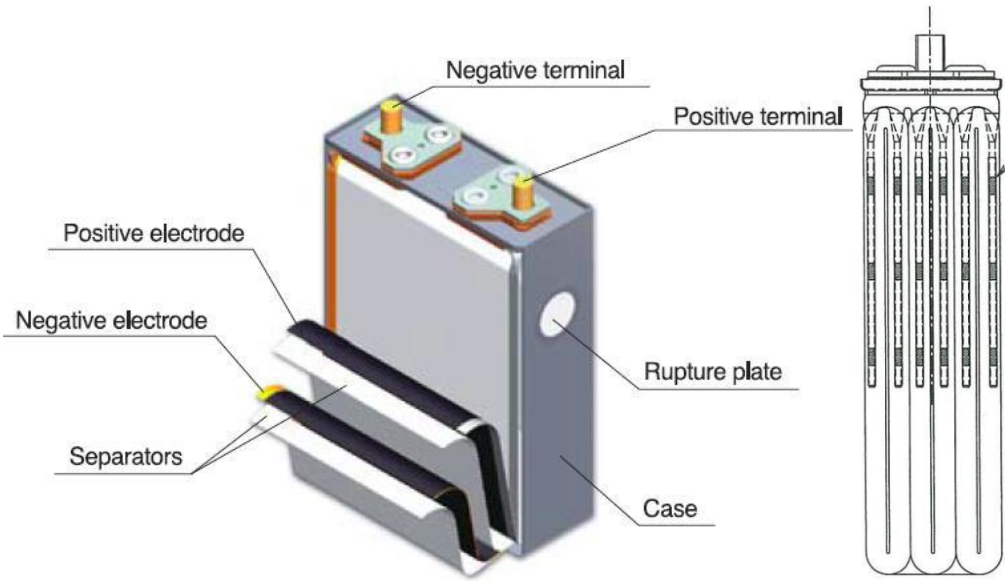

Figure 43 LVP65 Cell Construction

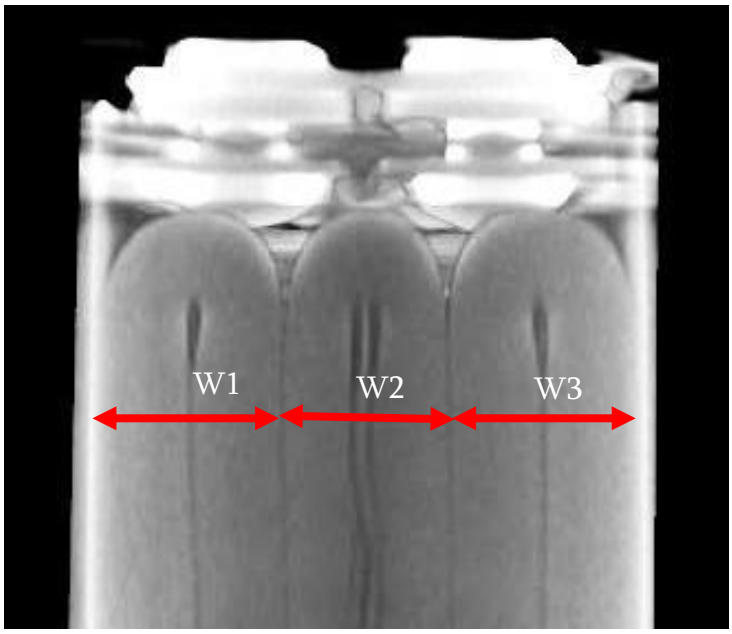

Figure 44 CT Scan image showing Cross-section view of top portion of Cell

Figure 45 Cell CT Scan image with outlines indicating regions with non-uniform Jelly Roll Stress

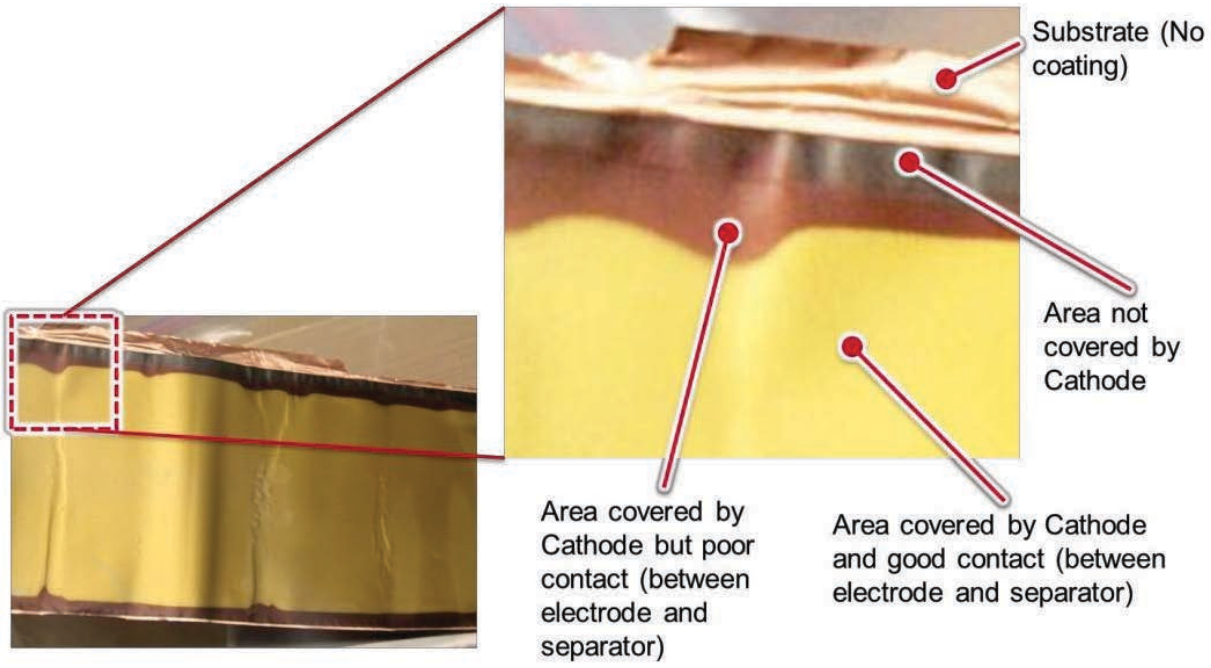

Figure 46 Photo of Anode Electrode Sheet of LVP65 Cell at 100% SOC

Figure 47 shows a photo of a disassembled cell. The non-uniform distribution of lithium-ions on anode surface is visible as dark regions showing low lithium ion saturation. These dark regions coincide with wrinkles as these folds create non-uniform contact between electrode sheet and separator. As can be seen in the same photo, there are regions near the wrinkles where no dark regions exist. So the presence of wrinkles is a necessary but not sufficient condition for ionic non-uniformity. Based on a review of cell CT scans, all the cells exhibited internal winding wrinkling or localized deformations. Such wrinkling may be created during cell assembly process when the three windings are inserted manually into the cell casing. It is also possible that localized deformation of the windings could result from exposure to vibrations.

The CT scan image in Figure 48 also reveals the differences in local density by the uneven gray coloration throughout the jelly roll. This imbalance in the distribution of lithium-ions on anode could, over the long term, cause polarization and result in localized material degradation and internal anomalies.

Figure 47 Wrinkles on Electrode Sheets and Separator

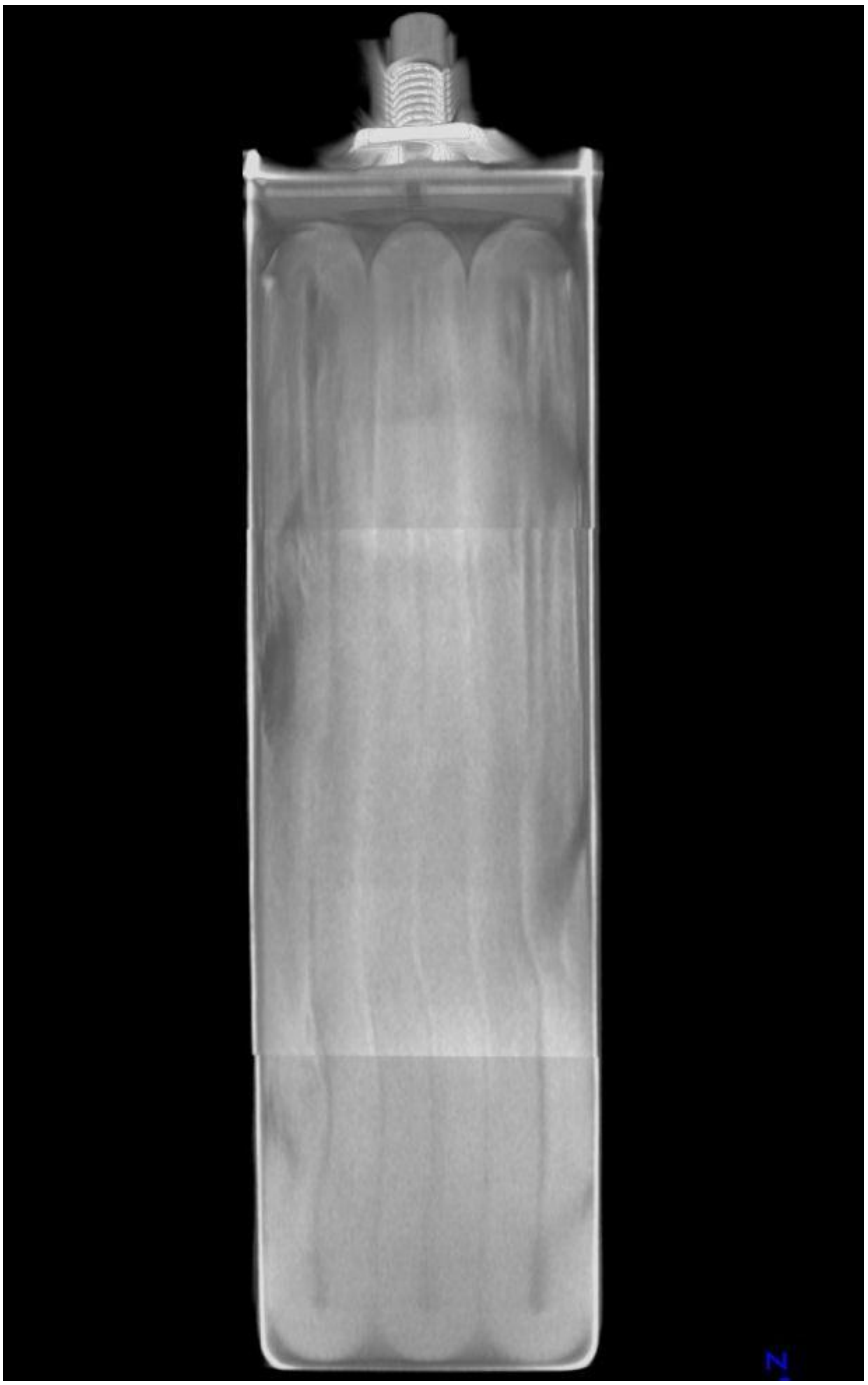

Figure 48 Cell CT scan image showing Uneven Compression of Jelly Rolls

Observations from Cell DPA

Next results from disassembled cells are examined more closely. As a baseline, when the anode coating is yellowish gold this indicates that the Li-intercalated carbon was in the structure of LiC_6 (Figure 49). For the anode in different stoichiometric states (LiC_x, $x>6$), the carbon anode will exhibit a dark color. The cathode is generally grayish black, and the chemical formula of the active material is Li_xCoO_2.

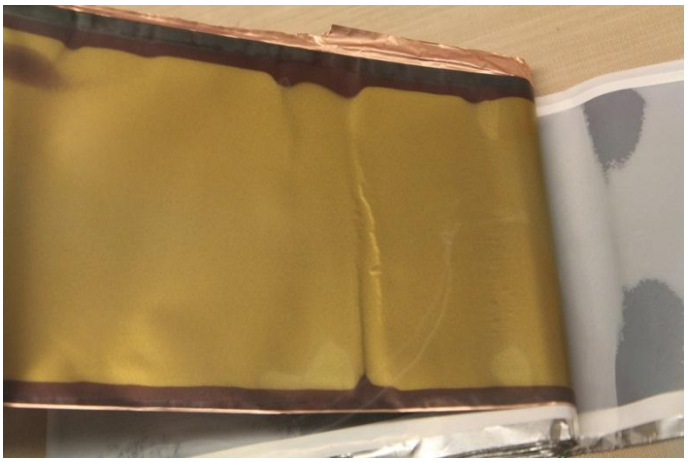

Figure 49 Photo of Electrodes of Disassembled Windings

Morphology Examinations

The results of morphology assessments for the cathode and anode materials using the SEM/EDS equipment are shown in Table 3. Since the cells were cycled and fully charged before disassembly, passivation layers (SEI) agglomerated on anode materials could be observed from the images. The SEI film on the surface of carbon particles are formed from the decomposition of electrolyte during cycling, and are generally composed of lithium fluoride (LiF), lithium oxide (Li_2O), lithium carbonate (Li_2CO_3), lithium alkyl carbonates ($ROCO_2Li$) and lithium alkoxides (ROLi), but the composition of SEI will change depending upon exact electrolyte composition. [79,80]

[79] V. Agubra and J. Fergus, "Lithium ion battery anode aging mechanisms", Materials, Vol. 6, 2013, pp. 1310-1325.

[80] O. Gullbrekken, Thermal characterization of anode materials for Li-ion batteries, Norwegian University of Science and Technology, 2012.

Table 3 Morphology for materials from Asset 412 cell 5

	Cathode	Anode
SEM Image	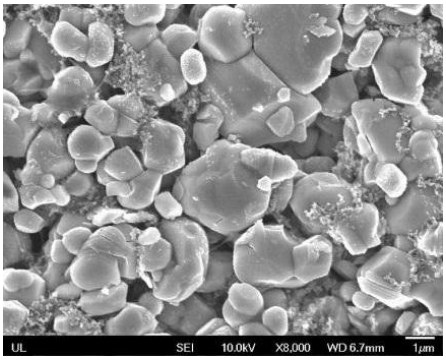	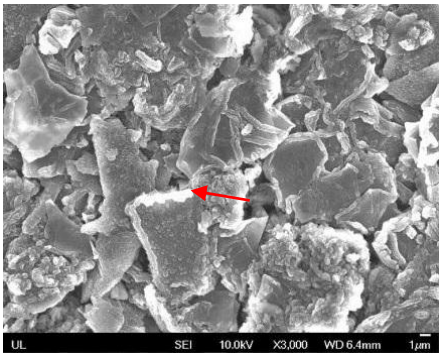
EDS analysis	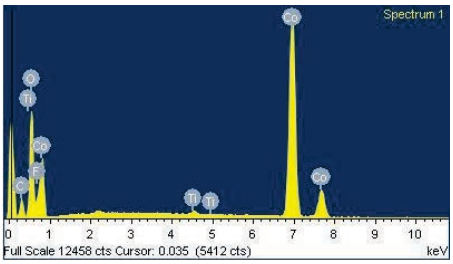	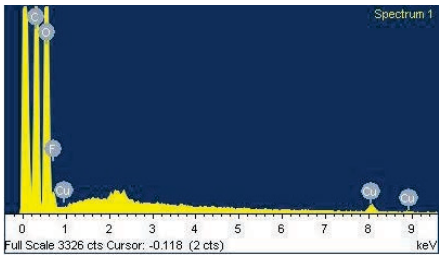
Active material	Lithium cobalt oxide	Carbon
Particle size	approximately 2 to 5 µm	approximately 10 to 15 µm
Morphology	Spherical	Flake

- Wrinkles

Wrinkles on separators could be observed in the disassembled windings, as shown in Figure 50. These non-uniformities could be a consequence of the winding and insertion processes discussed previously. Further examination of the morphology of the [redacted] separators by scanning electron microscope (SEM) shows that the pore sizes of the normal, unwrinkled sites and wrinkled sites were similar (Figure 51). However, portions of the wrinkled sites on the separator appear to have denser structure.

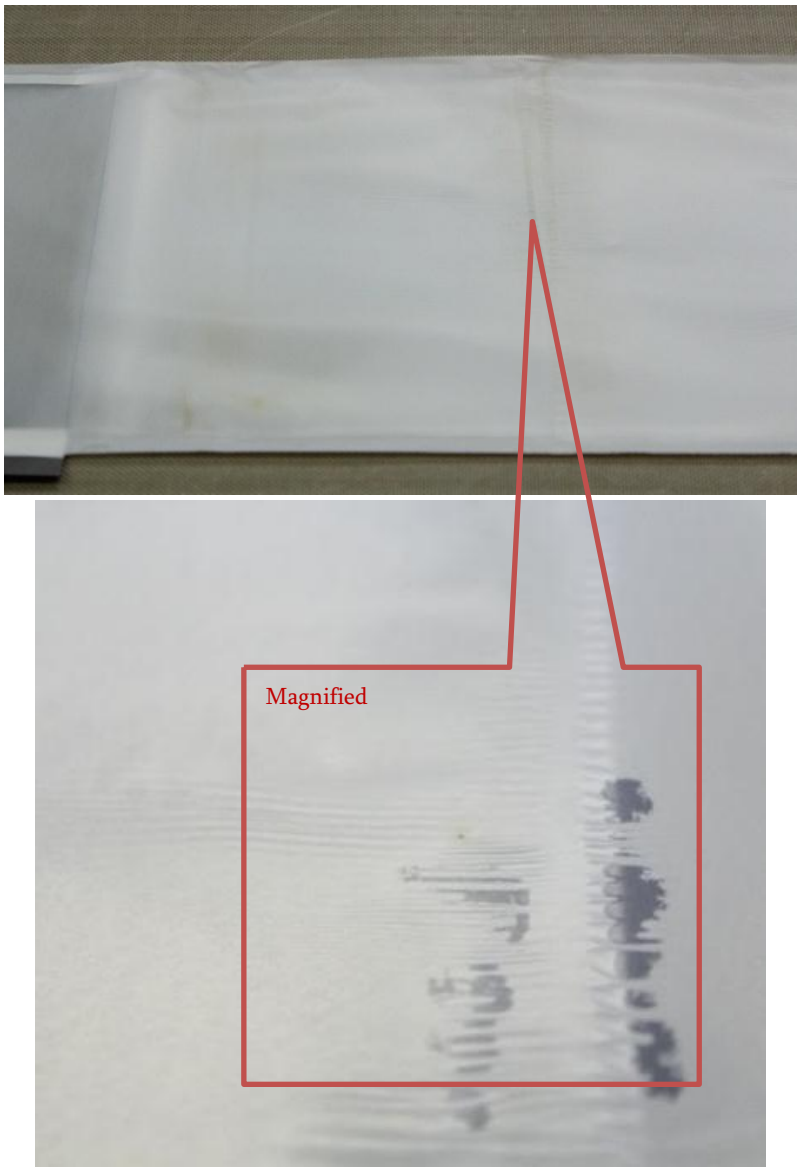

Figure 50 Photos of wrinkles on the separator

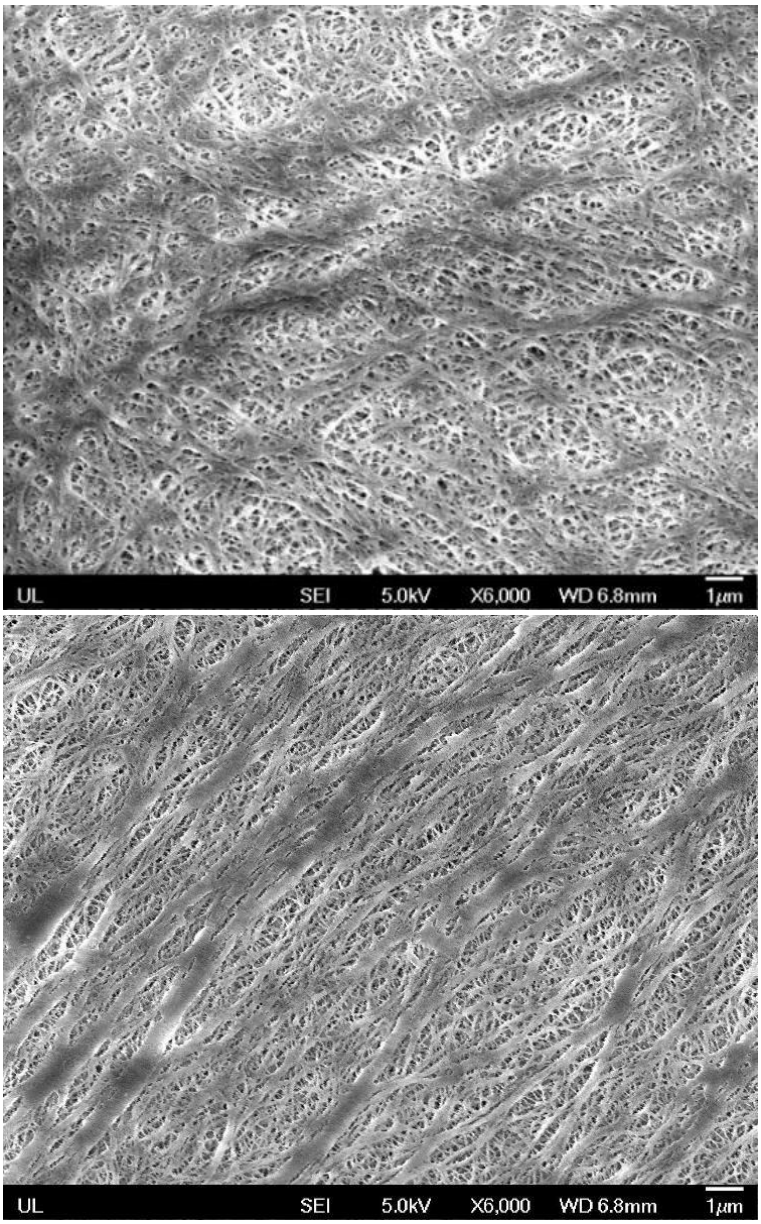

Figure 51 SEM images of Unwrinkled (top) and Wrinkled Separator sections (bottom)

Wrinkles on the separators can interfere with the ion transportation during cycling and resulted in non-uniform over potential on the electrodes during charge/discharge process. As shown in Figure 52, some dark areas appeared beneath the wrinkled separators indicating less lithium amounts intercalated in the carbon anode. Moreover, a serrated-like pattern was observed at some locations along the length of the winding. In these samples, the solvent has mostly evaporated. In some of

them, the growth of silvery white branching crystals was discovered at the tip of serrated pattern, as shown in Figure 53.

Figure 52 Wrinkled Separator and Non-uniform Coloration on Anode

Anodes with serrated patterns were observed in asset 412 cell 3, cell 5, and cell 6. Among the three cells, cell 6 was the worst case with the greatest number of needle-like crystals on the anode surface

while cell 3 only had the fewest observable crystal structures on the anode. In addition, outer windings had more serious serrated patterns than the center windings. It may be hypothesized that the center windings with higher compressive stresses should have better electrodes/separator contact for ion transportation during charging. Because cell 3 had very few serrated patterns on the anode, pulse charging at low temperature did not seem to be the dominant factor in the formation of such needle-like crystals in this study.

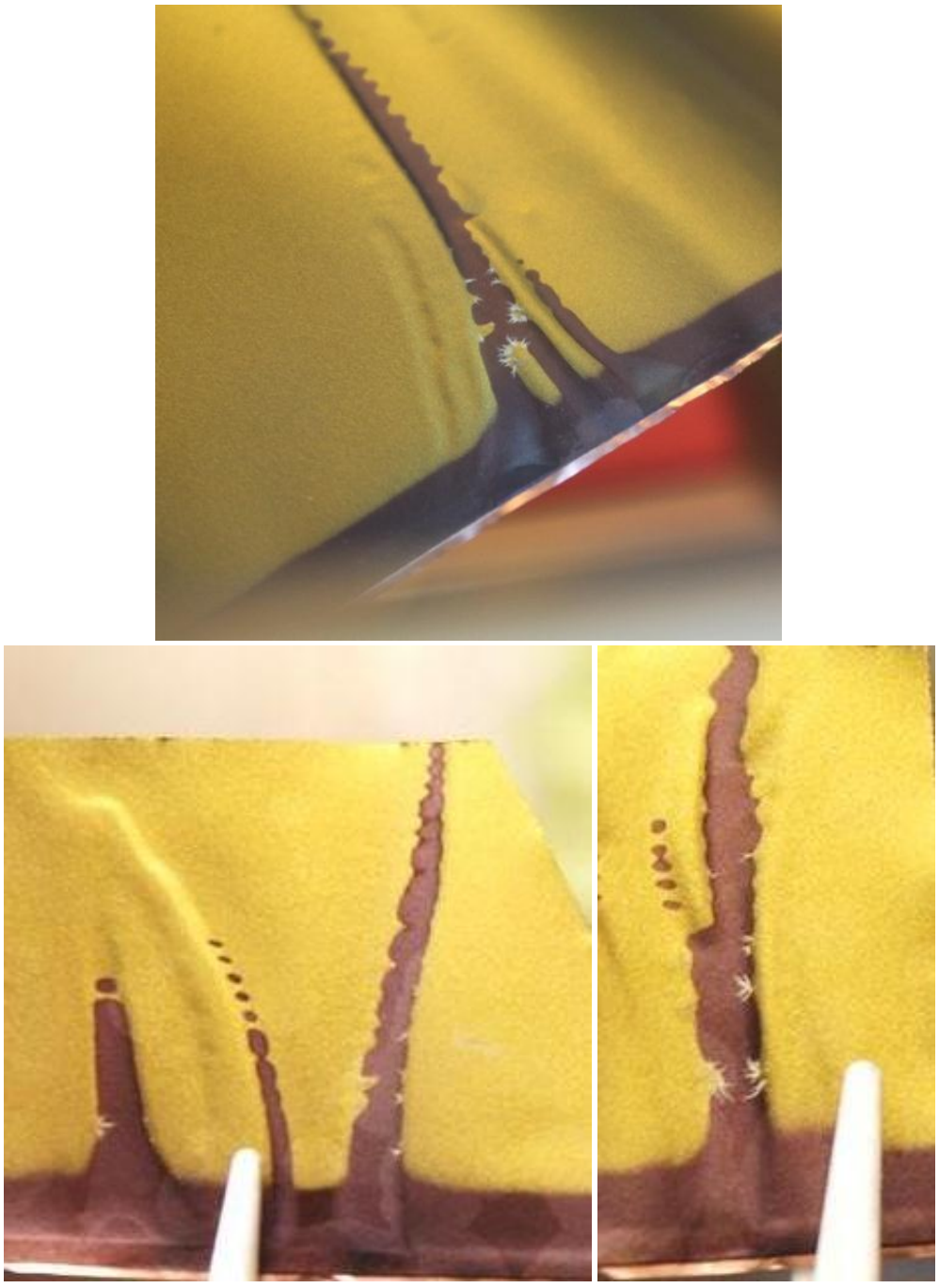

Figure 53 Branching Crystals on the Anode (white conical object is pointer)

- Dendrite

From our observations, the branching crystals and yellowish anode material (LiC_6) darkened upon removal of the anode sample from the argon filled glove box, and that the crystals would disappear within 15 minutes exposure in air. In the glove box, however, they could be stable for weeks in a well-controlled environment. Thus the crystal is very active and can react with the air (or moisture) immediately. Figure 54 shows how the crystals on the anode changes in air. In addition, the crystals appeared after the electrolyte evaporated during unwinding of the jelly roll, but they could not be rinsed away with dimethyl carbonate (DMC), one of the co-solvents in the electrolyte. These observations may indicate that these surface crystals contained lithium compounds.

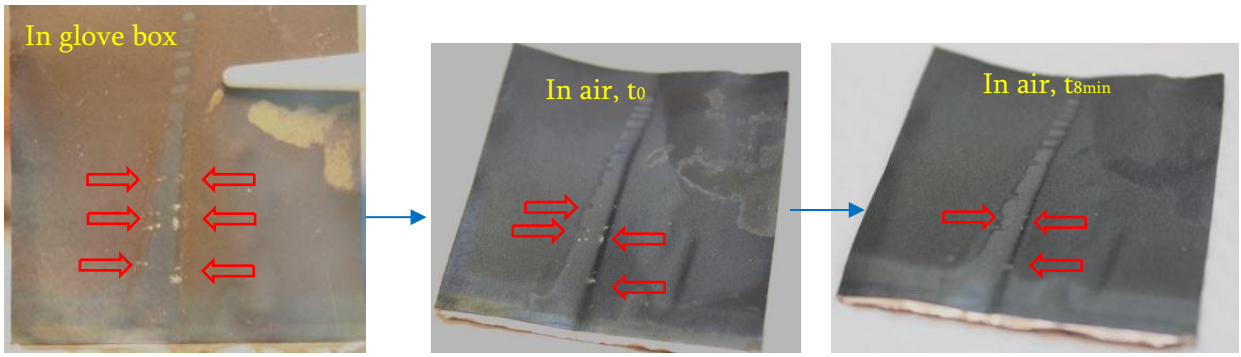

Figure 54 Evolution of Silvery Crystals when Exposed to Atmosphere (red arrow indicates the locations of needle-like crystals)

To further investigate the morphology of these crystals on the anode, an additional examination was performed by using electron microscope. A special protective process was taken to prevent the anode sample from reacting with the air during sample transportation from glove box to SEM for inspection. From the SEM, the branching crystals observed in visual inspection were actually tiny flakes or particles gathered with a specific pattern covering the surface of carbon anode. Among these mossy particles, some dendritic structures protruded from the anode could be discovered under a higher magnification (Figure 55). The dendrites might grow in a columnar structure or some kind of entanglement crystal structure. The size of dendrite was on order of microns. Our EDS analysis revealed that the dendrite had very similar compositions to the nearby anode materials, including C, O, F and trace Cu, as shown in Figure 56.

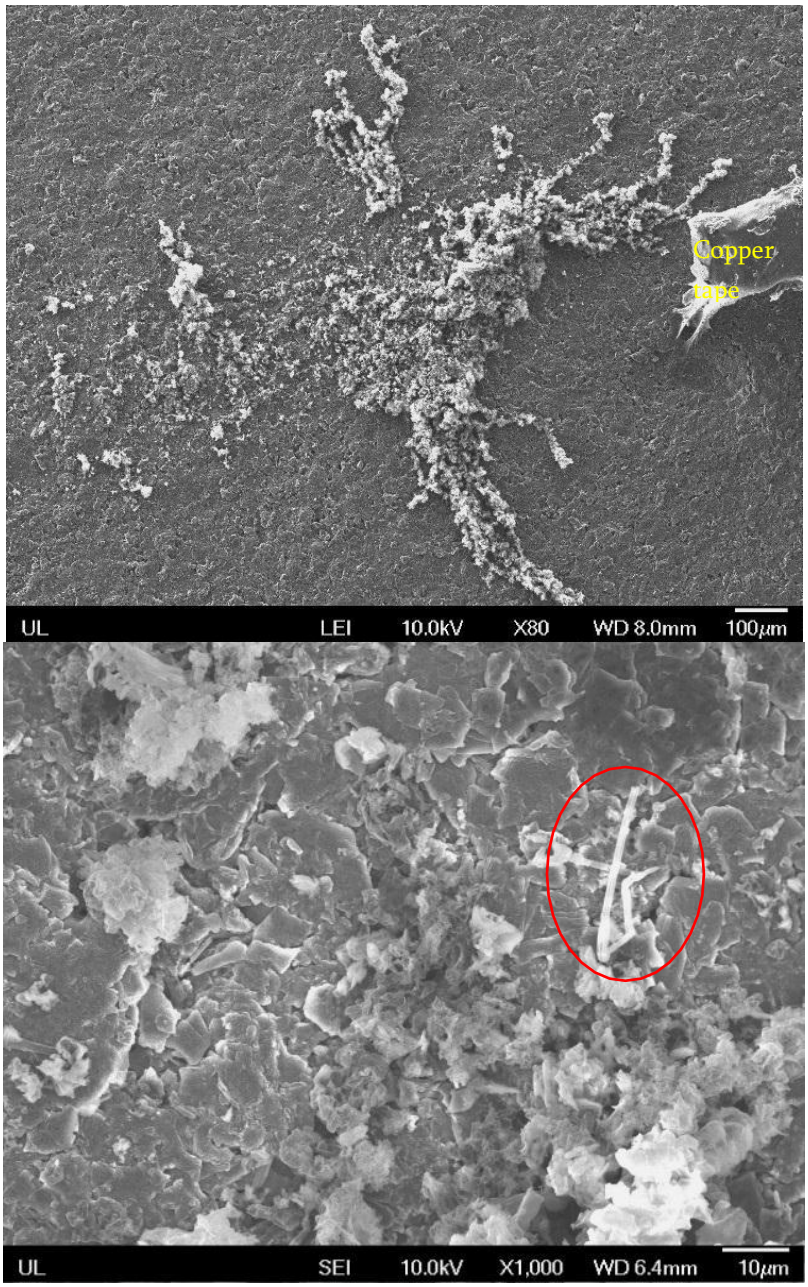

Figure 55 Morphology of Crystals on Anode (top) and Close-up of Dendrite (bottom)

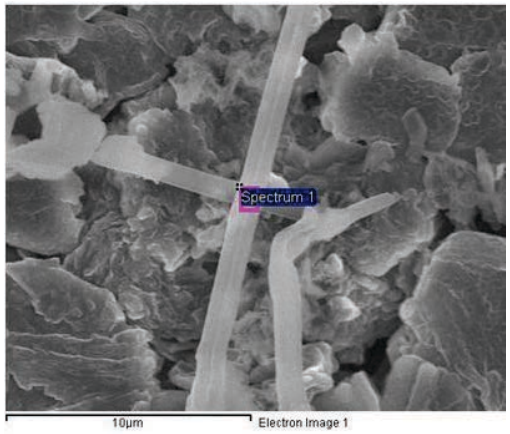

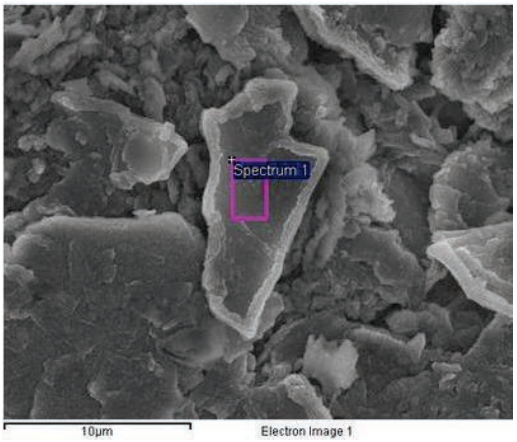

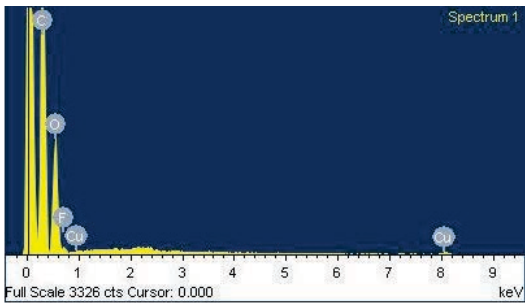

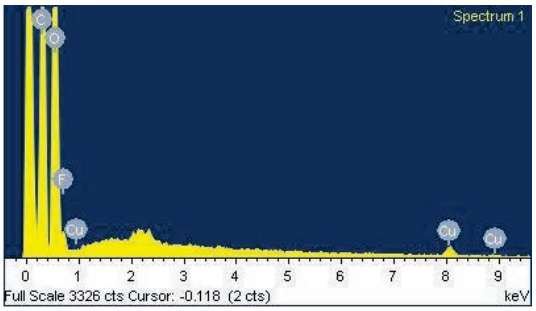

Element	Weight%	Atomic%
C	53.23	60/72
O	43.57	37.31
F	2.54	1.83
Cu	0.66	0.14
Totals	100.00	

Element	Weight%	Atomic %
C	39.49	47.10
O	55.66	49.83
F	3.74	2.82
Cu	1.11	0.25
Totals	100.00	

Figure 56 EDS analysis of dendrite (left) and anode material (right)

In our testing facility, the hookup EDS is generally applied for identifying composition of samples observed from SEM. However, since the EDS can only detect elements from atomic number 4 (Be) through 92 (U) and so in principle, lithium (atomic number 3) cannot be identified from this technique. Thus, the composition of the observed crystal like structure or dendrites cannot be definitively verified by EDS. Compared with the morphology of the lithium dendrites published in literatures[81,82], however, these observed protrusions are suspected to be metallic lithium dendrites

[81] F. Orsini et al., "In-situ SEM study of the interfaces in plastic lithium cells", J. of Power Sources, vol. 81, Iss. 81-82, 1999, pp. 918-921.

electro-deposited on the carbon anode (Figure 57) during cycling. The interesting thing here is that such branching crystals could also observed in Asset 412 cell 5, which only followed a standard charging protocol for LVP65 during its testing at UL.

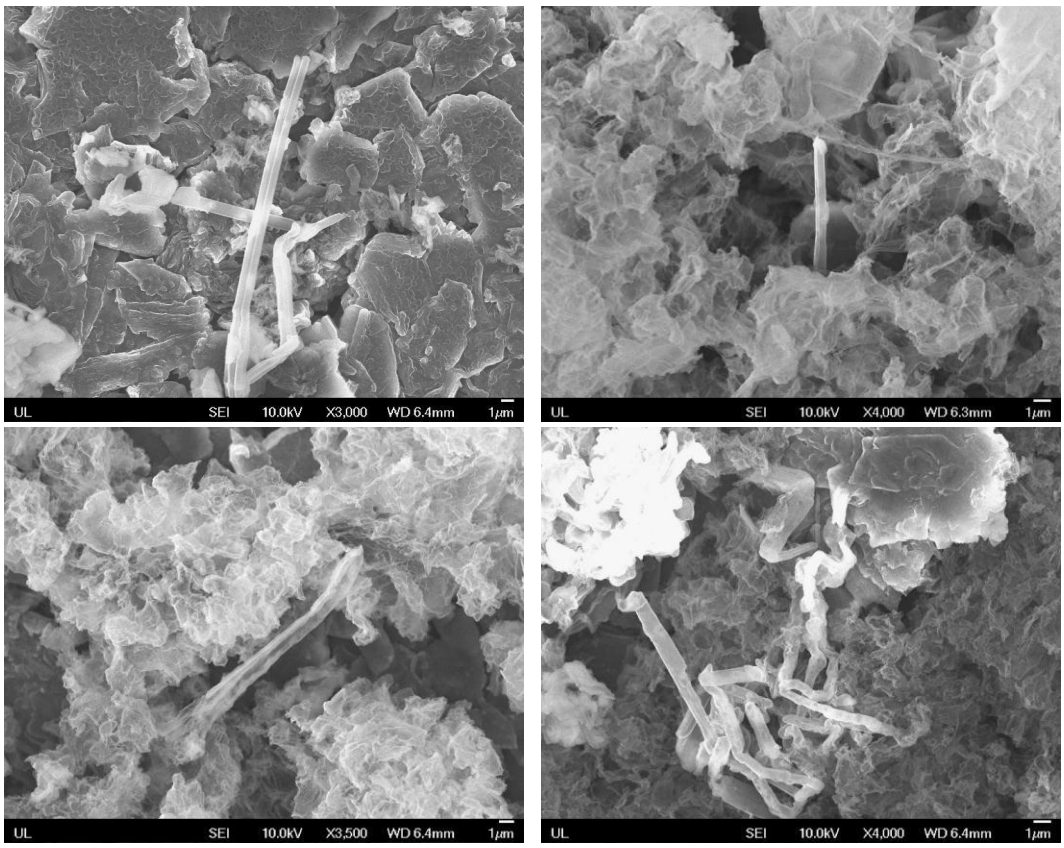

Figure 57 Dendrites observed on the Anode

Due to safety concerns that dendrites may lead to internal short circuits, there have been a number of studies on the formation mechanism of lithium dendrites in lithium ion cells. Some application circumstances such as high rate charging, low temperature cycling, or over-charge may induce lithium plating or dendrite formation on the graphite anode. The issue of lithium dendrite growth

[82] M. Dolle et al., "Live scanning electron microscope observations of dendritic growth in lithium/polymer cells", Electrochem. Solid-State Letters, vol. 5, Iss. 12, 2002, pp. A286-A289.

was thought to be governed mainly by current densities.[83] From what was observed in LVP65 cell, the formation of dendrites seemed to have very high correlation with the wrinkled separators/electrodes. A hypothesis may be formed: During the charging process, the wrinkled separator resulted in non-uniform current density distribution on the anode surface, so that the intercalation of lithium into the carbon structure followed the special patterns of the wrinkles on separator. That created some localized regions with high current densities on the anode and favored the formation of nucleation sites with reduced lithium. The reduced lithium then grew over time resulting in lithium dendrites. Such metallic dendrites may pierce through the separator leading to an internal short circuit of opposite electrodes or else break into small metal particles after several cycles where each new particle could become a possible internal failure site.

- Dark Spots on Cathode

As shown in Figure 58, some dark spots were observed on the cathode from Asset 412 cell 5. The comparison between the irregular spot with a normal region by using SEM/EDS examination is shown in

Figure 59. However, no significant difference in surface morphology or between the baseline region and spot was found according to the SEM/EDS analysis.

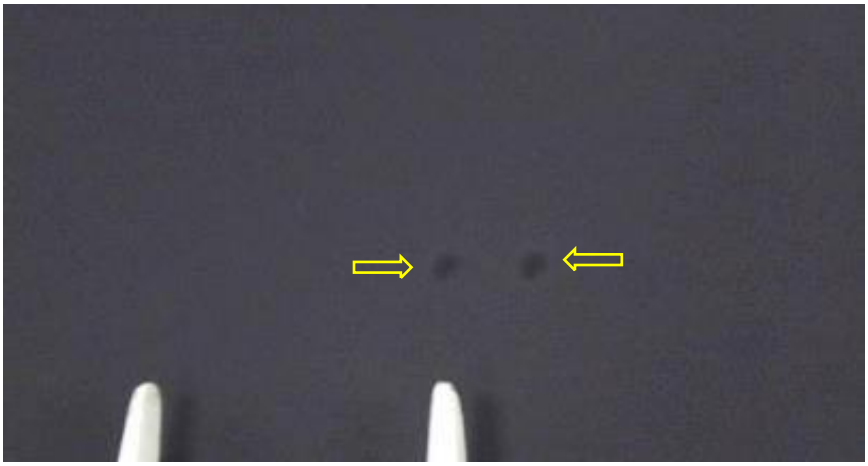

Figure 58 Dark spots on Cathode

[83] J.M. Tarascon and M. Armand, "Issues and challenges facing rechargeable lithium batteries", Nature, Vol. 414, Iss. 6861, 2001, pp. 359-367.

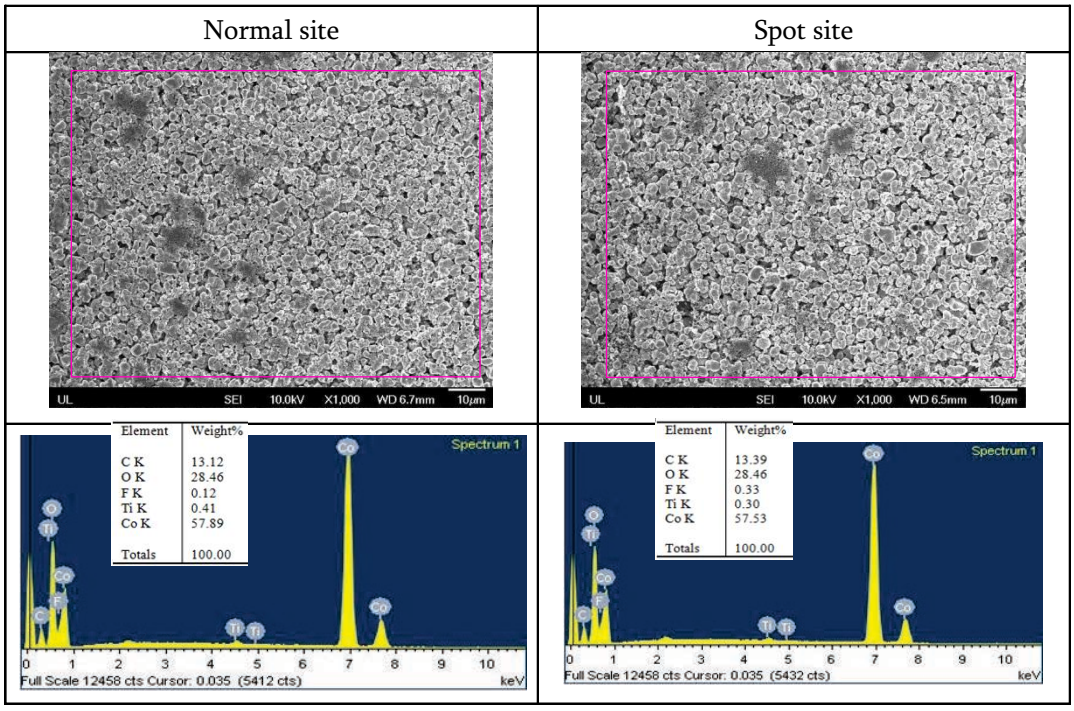

Figure 59 SEM image and EDS analysis for Dark Spots on Anode from Figure 58

Basic Cell Performance and Cell-to-Cell Variation

LVP65 cell is required to deliver high power and so it was designed with extremely low impedance and excellent high rate performance. As such it stands apart from the basic lithium ion cell that powers consumer electronics. In this section, data from different cells will be compared to assess variation. This last aspect is critical to the battery as it consists of eight cells.

Asset 436

Battery 436 was assigned for task A.1.c battery testing. However, before conducting any battery level testing, all cells were characterized to collect the baseline performance, filter potential faulty cells and ensure that cell to cell variation within a battery was minimized.

Rate Capacity and Electrochemical Properties

Table 4 shows the summary of capacity measurements on all cells of battery 436. According to the reversible capacity data recorded from the 2nd cycle, the capacity of all cells is between 73.490 Ah and 74.844 Ah, which amounts to variation less than 1.8%.

Table 4 Rate Capacity Measurement on Cells of Battery 436

	Rate Capacity (Ah)		
Sample	1st cycle (Ca_1)	2nd cycle (Ca_2)	Ca_2-Ca_1
436-1	73.757	73.943	0.186
436-2	74.686	74.844	0.158
436-3	73.322	73.490	0.168
436-4	74.375	74.643	0.268
436-5	74.092	74.148	0.056
436-6	74.478	74.605	0.127
436-7	74.154	74.225	0.071
436-8	73.801	73.901	0.1

It is normal that the capacity at 2nd cycle is a slightly higher than 1st cycle as the battery has been set at rest (open-circuit) for a certain period of time. During the rest period, the cell component materials become more stabilized. Therefore, more energy will be required to overcome the more stabilized passivation component[84] during 1st cycle after the cell being set open-circuit for long time.

Table 5 provides a comparison of the reversible capacity (under 70 A discharging) of all cells at 25 °C and -18 °C. It shows a 1% - 2% decay only in reversible capacity and 1-2 °C temperature rise under -18 °C due to the increase of cell impedance at low temperatures. However, during the test, cells are soaked in a forced air-circulated chamber, heat generated from cell will be taken away immediately.

[84] E. Peled et al., "Composition, depth profiles and lateral distribution of materials in the SEI built on HOPG-TOF SIMS and XPS studies", Journal of Power Sources, vol. 97-98, pp. 52-57, 2001.

That is, the actual temperature rise while discharging under -18 ˚C can be expected to be higher without the presence of active cooling.

Table 5 Comparison of Reversible Capacity at 25 ˚C and -18 ˚C (Battery 436)

	25 ˚C Data		-18 ˚C Data		
Sample	Reversible Capacity (Ca_2); Ah	Max. Temperature Rise; ºC	Reversible Capacity (Ca_3); Ah	Max. Temperature Rise; ºC	Retention (Ca_3/Ca_2*100%)
436-1	73.943	3.65	72.604	6.22	98.19
436-2	74.844	4.09	73.835	6.09	98.65
436-3	73.49	4.46	72.9	6.14	99.2
436-4	74.643	4.39	72.704	5.51	97.4
436-5	74.148	4.16	72.667	6.25	98
436-6	74.605	5.14	73.194	5.57	98.11
436-7	73.427	3.92	72.742	5.9	99.07
436-8	73.901	4.88	72.518	6.98	98.13

The OCV, 1 kHz AC resistance and EIS data for the eight cells from battery 436 are given in Table 6. All of the listed properties are within acceptable variations between the cells suggesting good consistency for this batch of cells.

Table 6 OCV, 1k Hz AC Resistance, and EIS data*1 (R_b and R_{ct}) of cells in battery 436

	25 ˚C Data		EIS(25 ˚C)		-18 ˚C Data		EIS(-18 ˚C)	
Sample	OCV; V	1kHz AC-R; m-Ohm	R_b; Ohm	R_{ct}; Ohm	OCV; V	1kHz AC-R: m-Ohm	R_b; Ohm	R_{ct}; Ohm
436-1	2.8847	0.29	0.00372	0.00017	2.9228	0.39	0.00546	0.01894
436-2	2.8744	0.325	0.00434	0.00053	2.9159	0.42	0.00202	0.02088
436-3	2.833	0.29	0.00393	0.00029	2.8818	0.42	0.00576	0.01544
436-4	2.8529	0.285	0.00396	0.00041	2.8996	0.375	0.00534	0.01656
436-5	2.8671	0.29	0.00394	0.0003	2.9166	0.415	0.00204	0.01606
436-6	2.8788	0.31	0.00421	0.0002	2.9276	0.42	0.00575	0.01745
436-7	2.8732	0.29	0.00396	0.00044	2.9167	0.4	0.00566	0.01664
436-8	2.8743	0.295	0.00385	0.0002	2.9217	0.42	0.00203	0.02007

Note *1: All measurements were made on cells under 0% SOC.

A Nyquist plot of the EIS measurements for all the cells from one battery is shown in Figure 60. As the internal impedance of the LVP65 cell is intrinsically low this makes the noise more prominent in the EIS measurements. So at 25 °C, almost no charge transfer resistance can be detected from the plot. Typically, a semi-circle of the EIS profile in medium to low range of AC frequency is easily observed. However, for this cell design, the semi-circle is not readily apparent indicating that the reaction rate of charge transfer (ion-exchange) is spontaneous[85]. However, at lower temperatures such as -18 °C, the charge transfer resistance (the semi-circle) can be readily observed. So at low temperatures, the ion-exchange rate becomes more dominant in the medium to low AC frequency range. Such a large increase in charge transfer resistance can be attributed to two principal effects: resistance of ion transport in solid-state and kinetics of the cell electrochemical reaction[86]. That is, the performance of the LVP65 cells may degrade when subjected to high rate charging or discharging at colder temperatures.

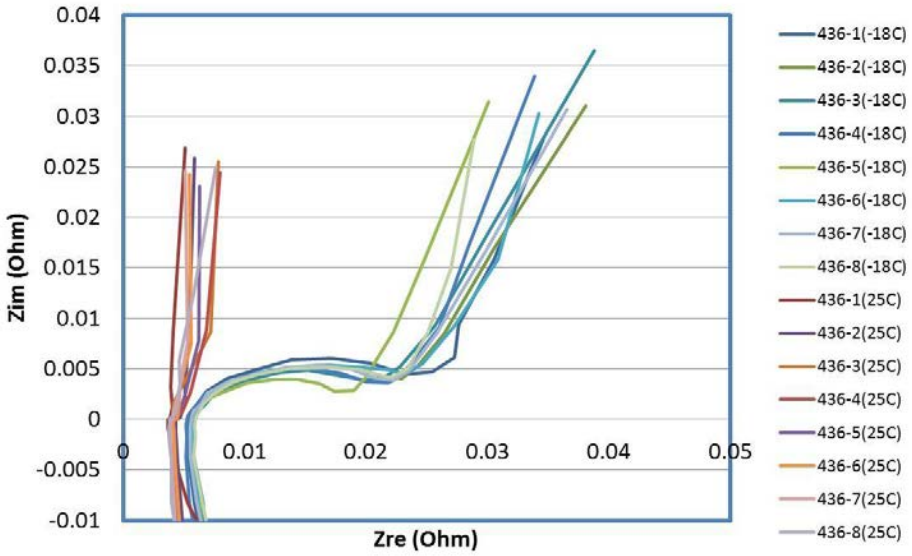

Figure 60 EIS measurements of Cells from Battery 436 under -18 °C and 25 °C

[85] B. Guo et al., "Nanostructured Co_3O_4 Materials: Synthesis, Characterization, and Electrochemical Behaviors as Anode Reactants in Rechargeable Lithium Ion Batteries", J. Phys. Chem. C, 114 (29), pp. 12805–12817, 2010.

[86] S. S. Zhang et al., "Electrochemical impedance study on the low temperature of Li-ion batteries", Electrochimica Acta 47, 7, pp1057-1061, 2004

Aging Sorting Test

The results from the aging sorting test of eight cells from a single battery are shown in Figure 61. Before the test, all cells were set to open-circuit for more than 10 days. However, no noticeable trend of voltage stabilization was observed during the 3 days of the aging sorting testing at 45 °C. Theoretically, 10 days for aging sorting testing of cells under room temperature is sufficient for a brand new production cell to stabilize. However, as these cells have been subjected to usage, it is possible that the internal state had changed such that stabilization was not readily achieved. Among this grouping of cells, cell 1 had the slowest increase in voltage. Cell 3 had the lowest voltage reading and also a small voltage-drop at the beginning of 2nd day. However, no abnormal characteristics in electrochemical properties of cell 3 were detected and the small voltage-drop (highlighted in Figure 61) was very short lived and the voltage rise resumed. However, it is possible that this cell contained a minor internal anomaly.

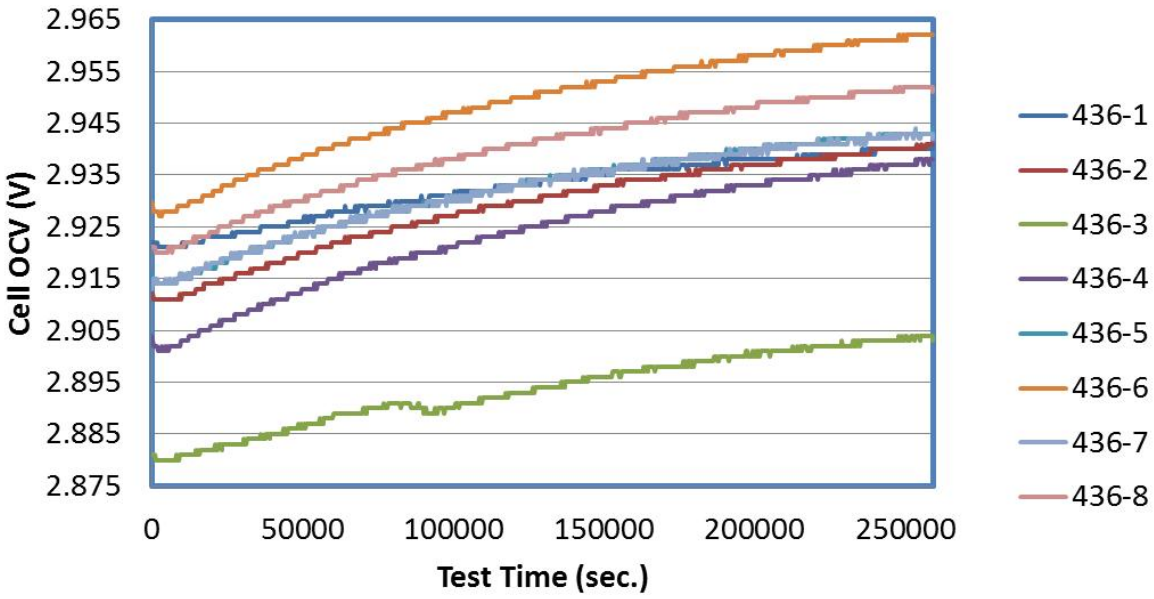

Figure 61 OCV Data during Aging Sorting Testing

Table 7 gives the summary of the absolute voltage difference before and after the aging sorting testing under 45 °C conditions, which is defined as "Delta-V". Cell 1 and cell 3 were the two cells with higher discharging rate than the other cells as the voltage increase is smaller than the others. One potential root cause could be internal material defects.

Table 7 Difference in Voltage Reading before and after Aging Sorting (Cells of Battery 436)

	Aging Sorting
Sample	Delta-V (V)
436-1	0.02
436-2	0.03
436-3	0.024
436-4	0.037
436-5	0.03
436-6	0.035
436-7	0.031
436-8	0.032

Discharging Profiles

Discharging profiles of all cells at 25 °C are given in Figure 62. HCV is the half-cell voltage, which is the voltage reading between the cell casing and the negative terminal. The voltage profiles show very little variation between cells. More variation in the HCV readings from cell to cell can be observed; this is expected as the cell casing is not a standard reference electrode.

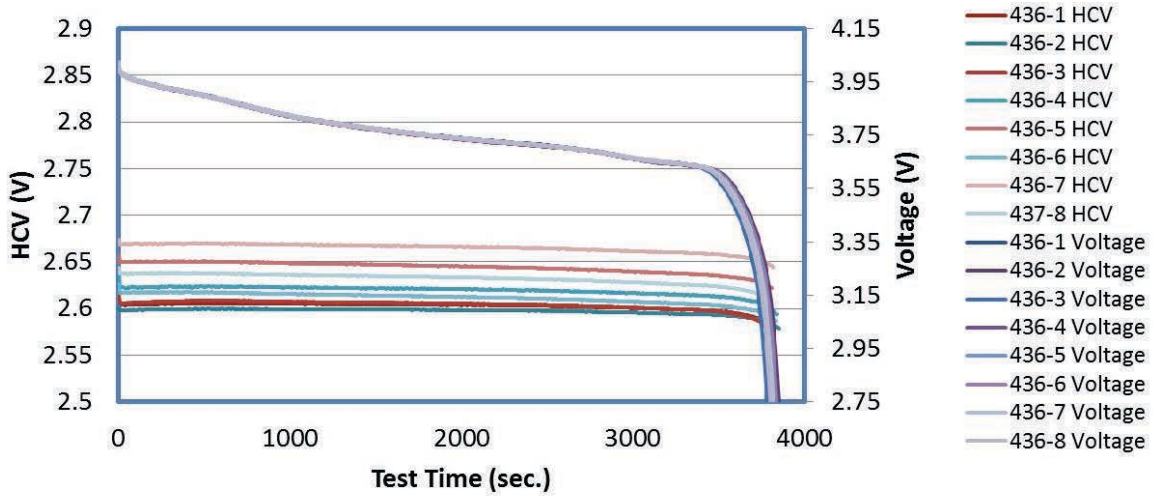

Figure 62 Discharging Profiles of Cells in Battery 436 under 25 °C

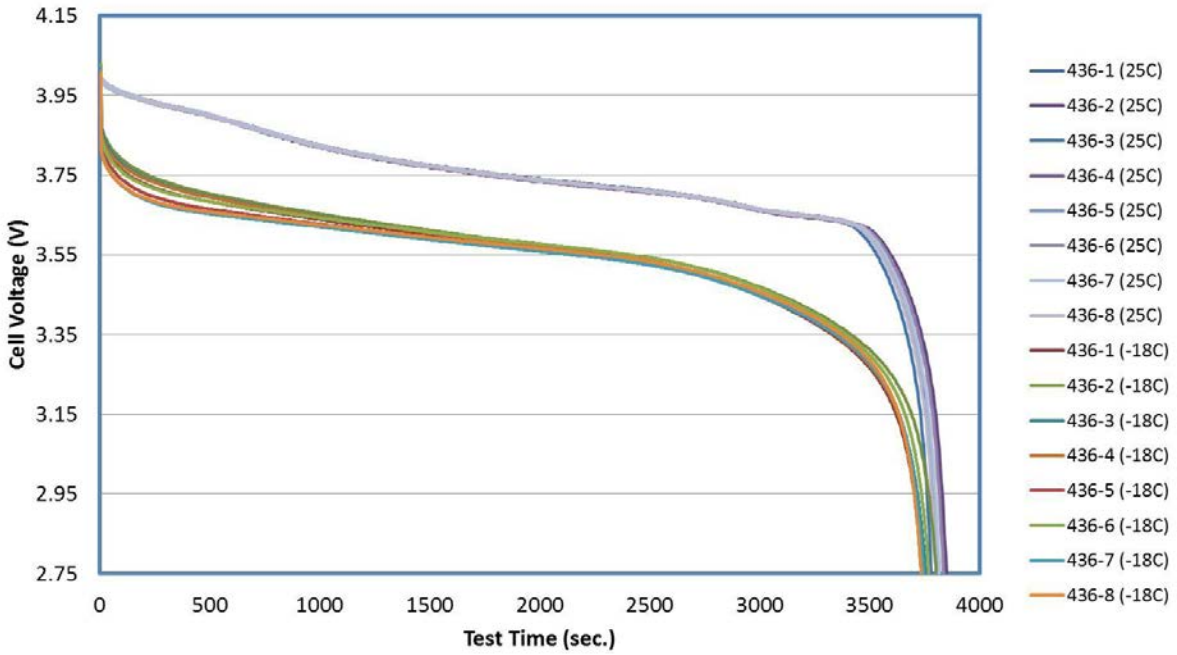

Figure 63 Discharging Profiles of Cells from Battery 436 at 25 ˚C and -18 ˚C

The discharging profiles of cells at 25 °C and -18 °C are compared in Figure 63. The cells show much lower voltage plateau under lower temperature conditions due to the higher internal resistance. For these cells, the working voltage under 70 A discharging and 25 °C is about 3.7 V, but it is 3.55-3.6 V only under -18 °C. The discharging profile of individual cell, tested at cell characterization stage, will be compared to the discharging profile after battery level tests to observe if any signal can be found that could be related to lithium plating issue[87].

Variation(s) between Cells of Battery 436

In summary, all the key electrochemical properties of the cells in battery 436 are compared in Figure 64. In general, the variations between cells are within an acceptable range and no internal anomalies were detected.

[87] S. S. Zhang et al., "Study of the charging process of a $LiCoO_2$-based Li-ion battery", Journal of Power Sources 160, pp1349–1354, 2006

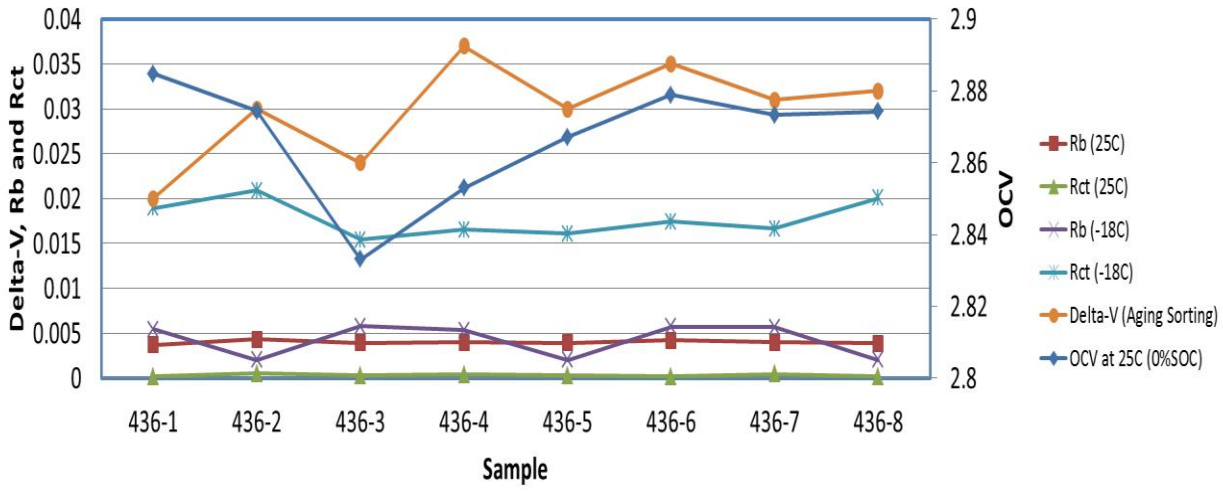

Figure 64 Summary of Key Electrochemical Properties of Cells from Battery 436

Asset 459

Battery 459 was selected for task A.1.a and A.1.b testing, both cell and battery level. However, again as a matter of good practice before conducting any battery level testing, all cells were characterized to collect the baseline performance of individual cell and cell to cell variations.

Rate Capacity and Electrochemistry Properties

Table 8 shows the summary of capacity measurement on all cells of battery 459. According to the reversible capacity data recorded from the 2nd cycle, the capacity of all cells was between 68.796 Ah and 71.824 Ah, which is about 4.2% variation. Therefore, there was more cell to cell variations battery 459 (4.2%) than that in battery 436 (1.8%). However, battery 459 may have had a longer or more severe usage history than battery 436 as the average reversible capacity in the cells of battery 459 (70.4 Ah) was lower than that in battery 436 (74.2 Ah). More charge-discharge cycles will always lead to more capacity fading. Therefore, battery 459 may be aged more.

Table 8 Rate Capacity Measurement on Cells of Battery 459

Rate Capacity (Ah)			
Sample	1st cycle (Ca_1)	2nd cycle (Ca_2)	Ca_2-Ca_1
459-1	70.256	70.661	0.405
459-2	69.513	69.724	0.211
459-3	71.323	71.563	0.24
459-4	68.52	68.966	0.446
459-5	71.253	71.658	0.405
459-6	69.511	69.878	0.367
459-7	71.504	71.824	0.32
459-8	68.449	68.796	0.347

Table 9 shows a comparison of reversible capacity (under 70 A discharging) of all cells at 25 °C and -18 °C. It shows a 1%-2% decay in reversible capacity and 3-4 °C temperature rise under -18 °C due to the increase of cell impedance at low temperature.

Table 9 Comparison of Reversible Capacity at 25 °C and -18 °C (Battery 459)

	25 °C Data		-18 °C Data		
Sample	Reversible Capacity (Ca_2); Ah	Max. Temperature Rise; °C	Reversible Capacity (Ca_3); Ah	Max. Temperature Rise; °C	Retention (Ca_3/Ca_2*100%)
459-1	70.661	3.19	69.334	6.63	98.12
459-2	69.724	3.51	68.381	7.24	98.07
459-3	71.563	2.77	70.297	6.17	98.23
459-4	68.966	4.15	67.679	5.81	98.13
459-5	71.658	2.74	70.702	5.34	98.67
459-6	69.878	2.54	68.747	7.1	98.38
459-7	71.824	2.33	70.778	5.53	98.54
459-8	68.796	3.57	67.853	6.1	98.63

The OCV, 1 kHz AC resistance and EIS data of the eight cells from battery 459 are given in

Table 10. All of the electrochemical properties were within acceptable variations between cells showing good consistency. The Nyquist plot of the EIS measurements is shown in Figure 65. The EIS profiles show very similar behaviors as the cells in battery 436.

Table 10 OCV, 1k Hz AC Resistance, and EIS data*1 (Rb and Rct) of cells in battery 459

	25°C Data		EIS(25°C)		-18°C Data		EIS(-18°C)	
Sample	OCV; V	1kHz AC-R; m-Ohm	R_b; Ohm	R_{ct}; Ohm	OCV; V	1kHz AC-R: m-Ohm	R_b; Ohm	R_{ct}; Ohm
459-1	2.9154	0.31	0.00434	0.00023	2.9151	0.44	0.00609	0.01361
459-2	2.9119	0.275	0.00364	0.00033	2.9105	0.415	0.00574	0.01086
459-3	2.9346	0.29	0.00389	0.00022	2.9318	0.43	0.00605	0.01275
459-4	2.9343	0.28	0.00373	0.00041	2.9337	0.42	0.00601	0.01251
459-5	2.9226	0.3	0.00405	0.0005	2.9109	0.37	0.00516	0.00964
459-6	2.9157	0.29	0.00398	0.00042	2.9136	0.42	0.00571	0.01184
459-7	2.9327	0.28	0.00395	0.00041	2.9284	0.41	0.00568	0.01275
459-8	2.9185	0.275	0.00369	0.00053	2.9157	0.42	0.00573	0.00874

Note *1: All measurements were made on cells under 0% SOC.

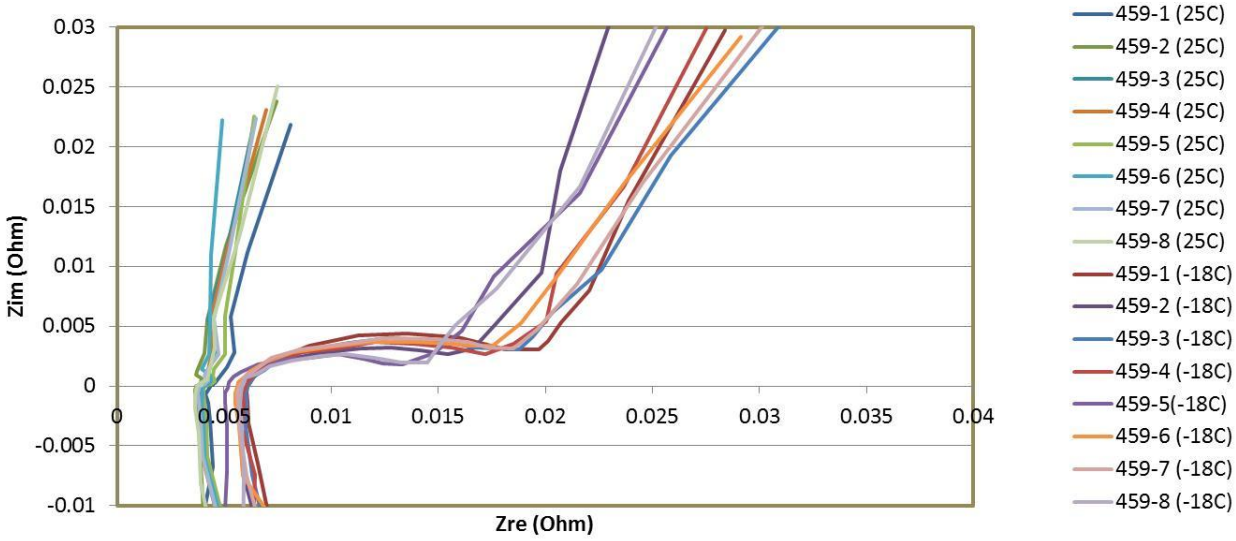

Figure 65 EIS measurements on Cells from Battery 459 under -18 °C and 25 °C

Aging Sorting Test

The test results from the aging sorting of battery 459 are shown in Figure 66. All the cells were set to open-circuit for more than 10 days before test. In addition, the aging time was extended to 8.5 days in total to investigate the timing for cell voltage to reach a stable reading. According to these extended test results, all cells reached a maximum cell potential by end of 8.5 day period when aging sorting under 45 °C conditions. Among all cells, cell 4 was the first cell that reached the maximum cell OCV and showed only slight decrease in the voltage reading after 7th to 8th day.

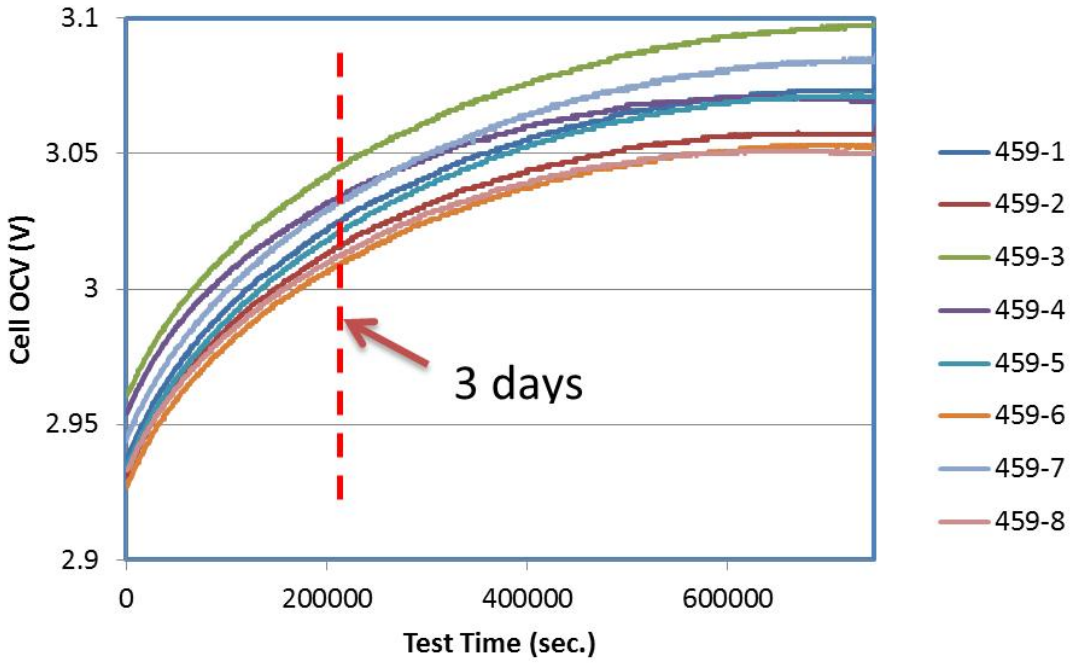

Figure 66 OCV reading during Aging Sorting on Cells of Battery 459

Table 11 gives the summary of voltage difference before and after the aging sorting testing under 45 °C conditions, which is defined as "Delta-V". Regardless of whether the duration of the test lasted 3 days or 8.5 days, all cells showed a similar trend in voltage change.

Table 11 Differences in Voltage Reading before and after Aging Sorting (Cells of Battery 459)

Aging Sorting		
Sample	Delta-V after 3 days; V	Delta-V after 8.5 days; V
459-1	0.096	0.155
459-2	0.092	0.144
459-3	0.092	0.155
459-4	0.086	0.131
459-5	0.095	0.155
459-6	0.089	0.141
459-7	0.097	0.16
459-8	0.087	0.133

Discharging Profiles

Discharging profiles of all cells under 25°C are given in Figure 67. HCV is half-cell voltage, which is the voltage reading between cell case to negative terminal. The voltage profiles show small variation between cells.

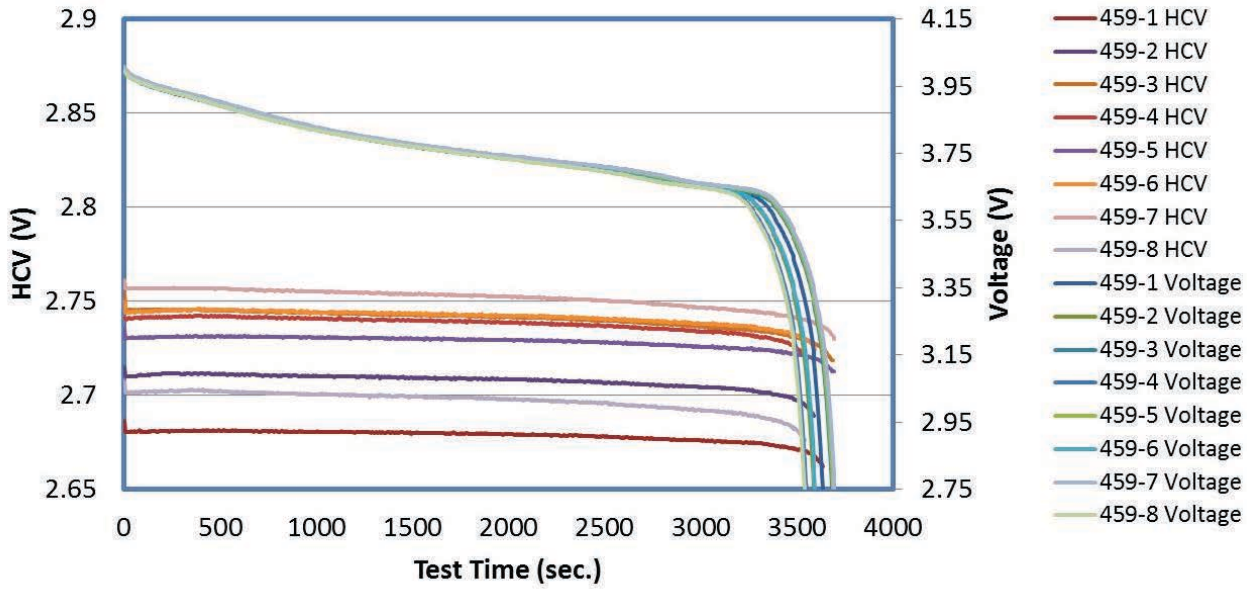

Figure 67 Discharging Profile of Cells from Battery 459 under 25 °C

The discharging profiles of cells under 25 ˚C and -18 ˚C conditions are shown in Figure 68. In general, the initial discharging profiles under -18 ˚C showed greater variations between cells than for the same cells under 25 ˚C conditions.

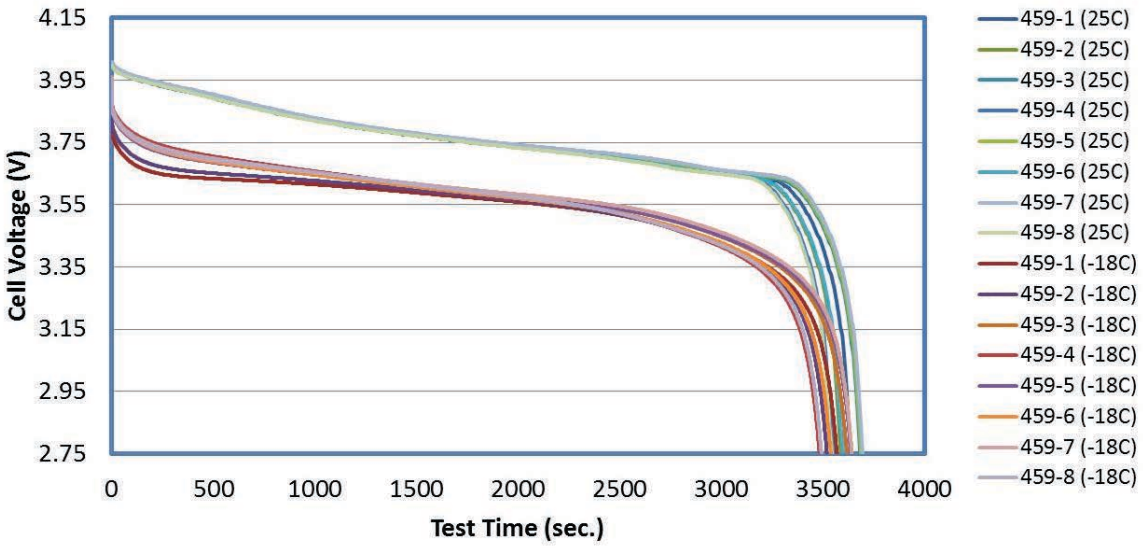

Figure 68 Discharging Profiles of Cells from Battery 459 under 25 °C and -18 °C

Variation(s) between Cells of Battery 459

The key electrochemical properties of the cells from battery 459 are compared in Figure 69. In general, the variations between cells were within acceptable range although the cell variations in battery 459 are larger than those from battery 436. No cell was identified as having a major internal flaw.

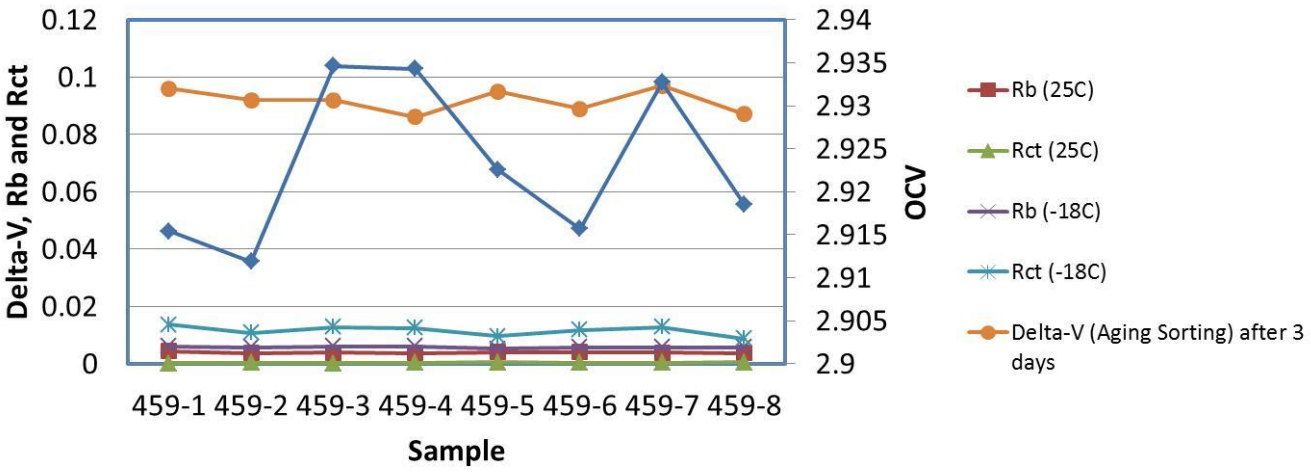

Figure 69 Key Electrochemical Properties for cells from Battery 459

Assets 412 and 376Table 12 shows the rate capacity of additional cells, cell 2 through cell 8 from battery 412 and cell 7 from battery 376. According to the test data, cells 3, 5, 6, and 7 of battery 412 have similar capacity ranging from 68 - 70 Ah. Cells 2 and 4 of battery 412 have similar capacity around 72 - 73 Ah. Cell 8 of battery 412 and cell 7 of battery 376 have more reversible capacity than other cells. The actual capacity of cell 7 of battery 376 was the highest (76.15 Ah) among all cells, which was almost the initial capacity of LVP65 cells. That is, the condition of cell 7 of battery 376 was very close to a new production cell. That is also possible that cell 7 of battery 376 has higher initial capacity than others as cells are grouped by capacity for assembly into a battery, and cells from battery 412 and 376 should be from different production lots. There was large variation in rate capacity between the cells of battery 412, the surviving battery from the 787 JAL incident in Boston. Hence all of the cells have been subjected possibly to different conditions causing different amounts of capacity fading.

Table 12 Rate Capacity of Cells from batteries 412 and 376

	Rate Capacity
Sample	2nd cycle*1
376-7	76.15
412-2	72.48
412-3	69.607
412-4	72.358
412-5	68.848
412-6	69.567
412-7	69.736
412-8	73.551

Note*1: Most of the cells are more than or close to 100%SOC as received. As a result, cell would be discharged first and then take the data at 2nd cycle as the baseline information.

The results from the aging sorting tests are shown in Figure 70. For this battery, the cells showed very different rates of change in the voltage. For example, Cell 8 of battery 412 even seemed to have a trend of decreasing voltage whereas for the others cells in battery 412, the voltages were increasing. The single cell from battery 376 exhibited a very stable voltage reading.

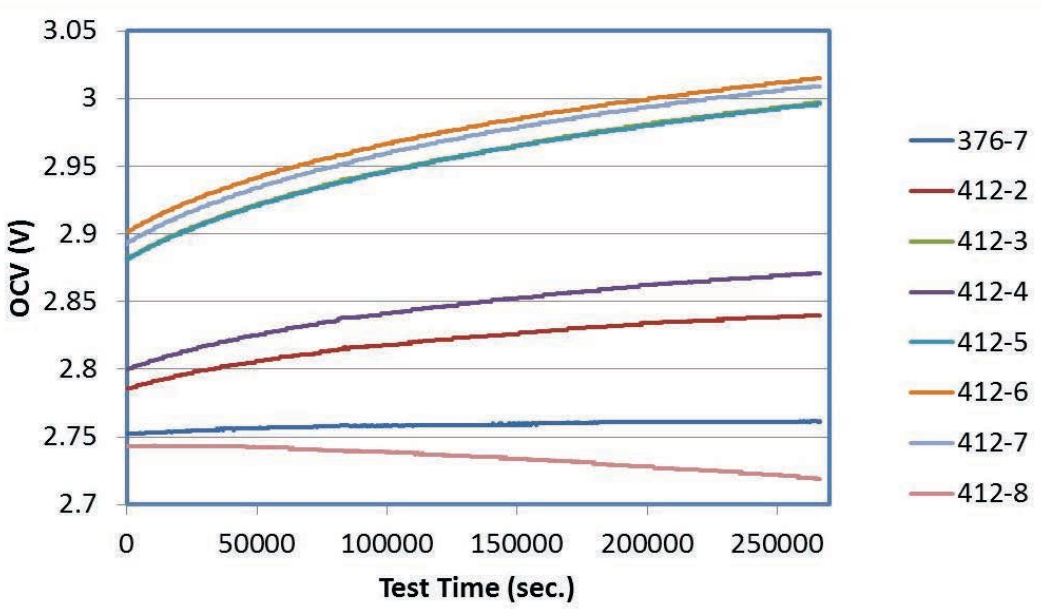

Figure 70 OCV reading during Aging Sorting testing on Cells of Batteries 412 and 376

Rate capacity and slope of OCV profile from the aging sorting test on those cells are summarized in

Table 13. Generally cells with higher reversible capacity will have smaller slope in OCV profile from aging sorting test. Next, using the data from the cells in battery 412 to correlate the reversible capacity to the slope of OCV (from the aging sorting test) leads to the results shown in Figure 71. A 2nd order polynomial fit was used to generate a regression relationship. The slope of the OCV profile from the aging sorting test appeared to be highly correlated to the condition of capacity fading in LVP65 cells. The OCV profile from the aging sorting test can act as a key index to aging within the LVP65 cell. Going further, this OCV profile from the aging sorting test can potentially be useful in developing state of health (SOH) parameter during operation.

Table 13 Rate Capacity and Slope of OCV profile from Aging Sorting test

	Rate Capacity	Aging Sorting
Sample	2nd cycle*1	Slope of OCV profile
376-7	76.15	0.3×10^{-7}
412-2	72.48	2×10^{-7}
412-3	69.607	4×10^{-7}
412-4	72.358	2×10^{-7}
412-5	68.848	4×10^{-7}
412-6	69.567	4×10^{-7}
412-7	69.736	4×10^{-7}
412-8	73.551	-0.9×10^{-7}

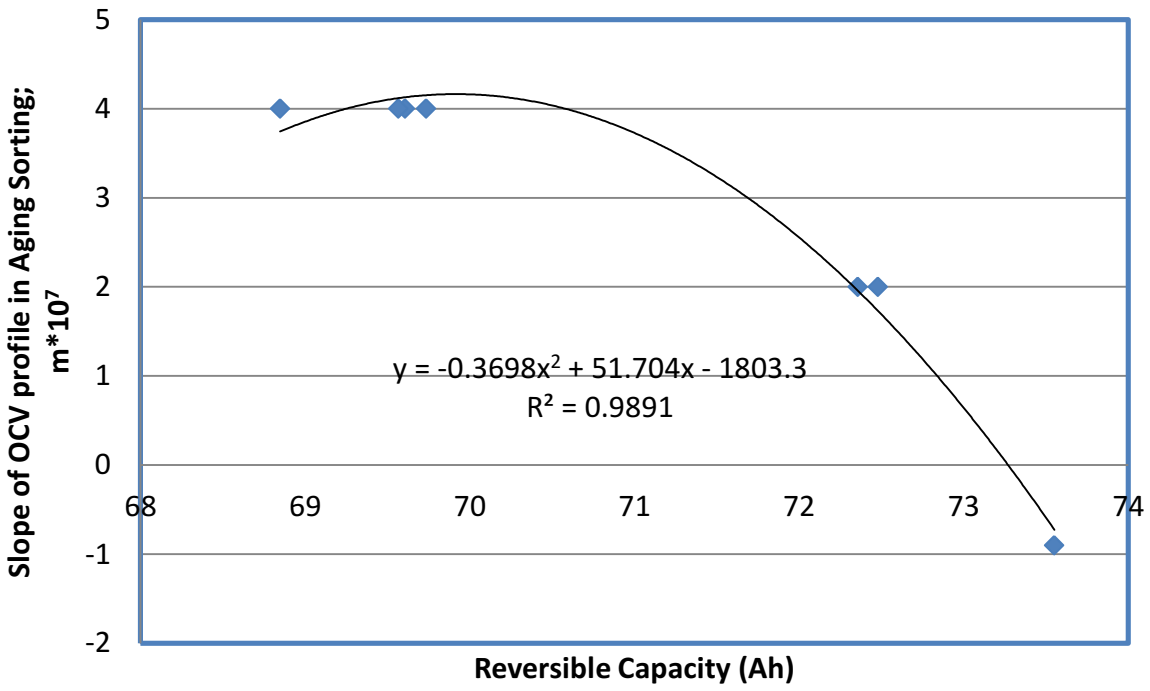

Figure 71 Regression Relationship between Capacity to Slope of OCV Profile (cells of battery 412)

Thermal Properties and Temperature-Dependent Characteristics

This section covers results for thermal characterization of the LVP65 cells by heat capacity measurement and 1C discharge heat flux test. Thermal performance was further analyzed by examining the EIS profile and even characterizing some select temperature dependent properties of the electrolyte. Finally, the tolerance of LVP65 cell to thermal abuse condition using an ARC will be presented.

Thermal Property

All cells of battery 459 were used for the heat capacity measurement and 1C discharge heat flux test. Heat capacity was needed to estimate the total enthalpy while cell charging or discharging. However, the heat capacity can change depending upon the SOC. Therefore, heat capacity (C_p) measurements were taken at 0% SOC and 100% SOC. If the variation in heat capacity was less than 10%, then subsequent heat capacity measurements were simply taken at 50% SOC for all remaining cell samples. Figure 72 shows the comparison of heat capacity data between the sample at 0% SOC, 50%

SOC and 100% SOC. The measurements were made starting from room temperature up to 55 °C. However, more test variations can be induced in the initial heat stage as there will be more temperature gradient within large LVP65 cell under heater power up stage. Figure 73 shows the ramp up in power and temperature during the test. We excluded the data point before 34 °C and only analyzed the data point from 34 °C to 55 °C for more accurate analysis.

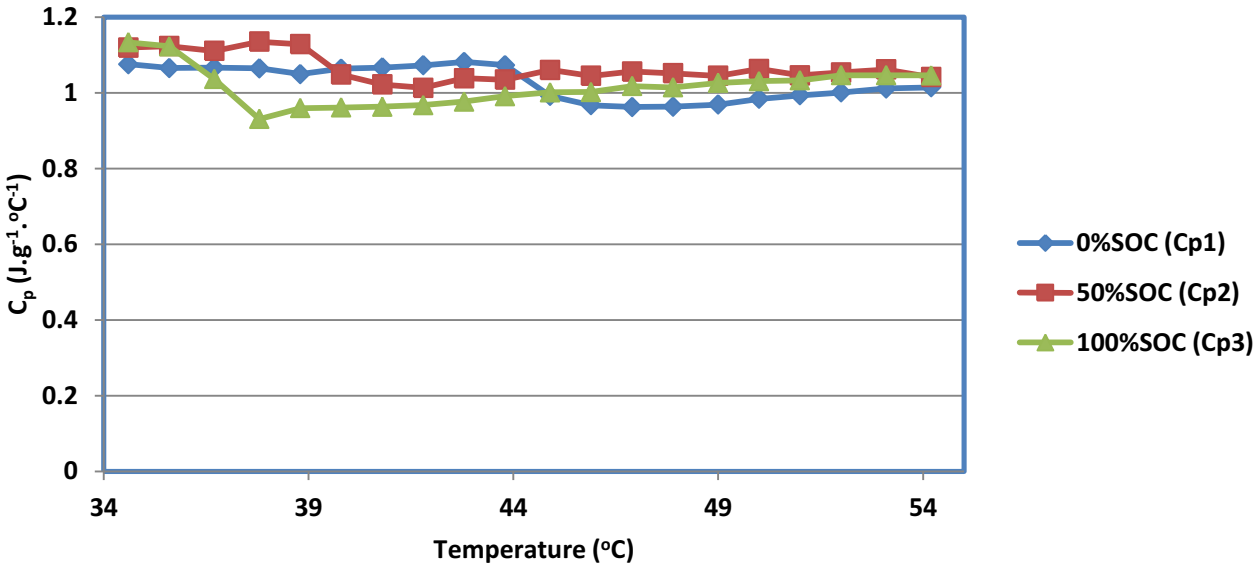

Figure 72 Cell Heat Capacity under 0%, 50% and 100% SOC Conditions

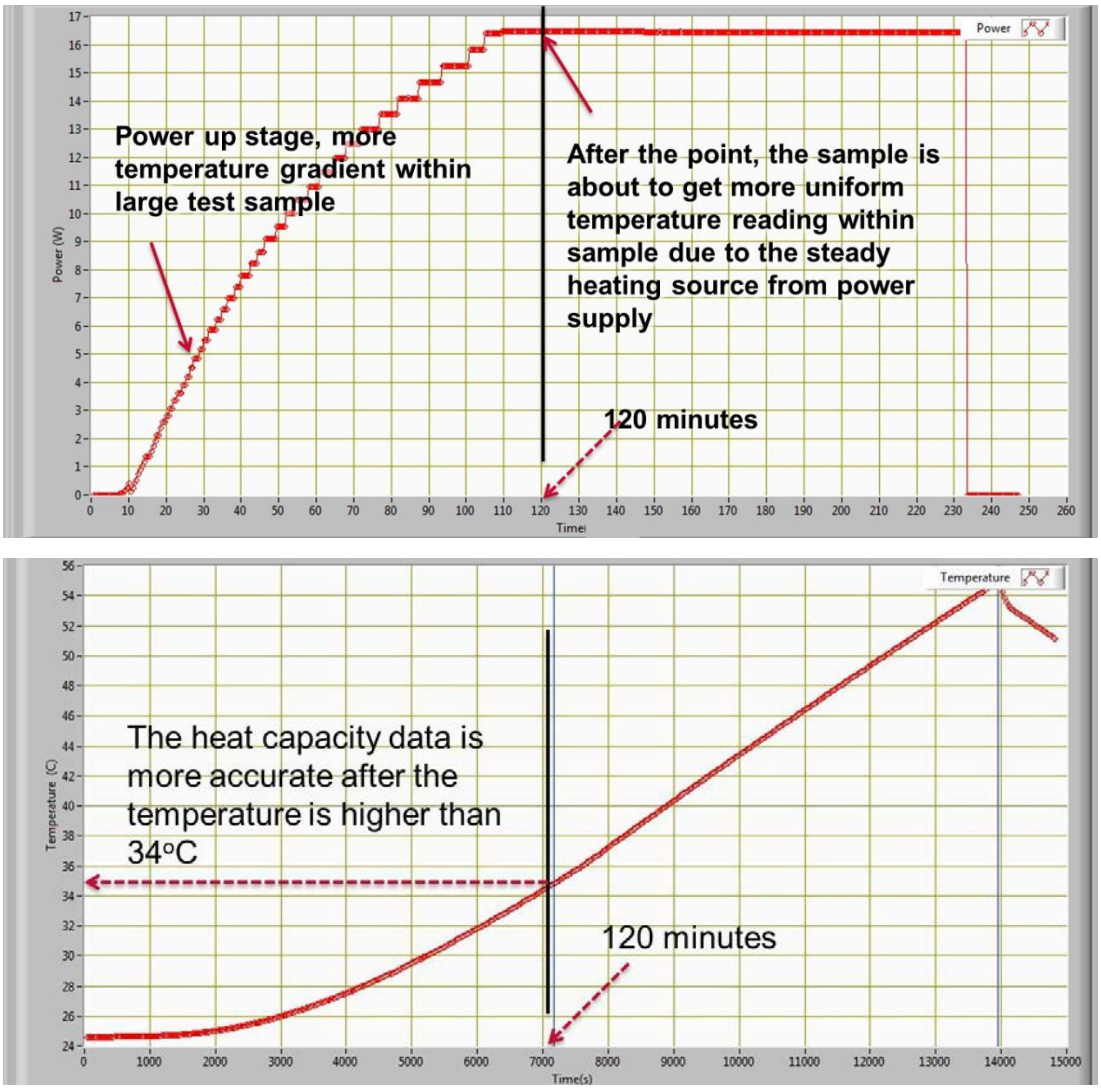

Figure 73 Power up Profile (top) and Temperature Reading (bot) during Heat Capacity Measurement

The data of C_p measurements on test samples (cell 1 and 2 of battery 459) at 0% SOC and 100% SOC are given in Table 14. There was only one point with a greater than 10% variation but the average variation is 1.11%. Therefore, using a 50% SOC as the basis for heat capacity measurements of these cells was acceptable.

Table 14 Heat Capacity Data

Heat Capacity			
Temperature	0%SOC (Cp1)	100%SOC (Cp2)	Variation(%); (Cp2-Cp1)/Cp1*100%
34.6	1.075787	1.133438	5.358960463
35.6	1.065442	1.123111	5.412683187
36.7	1.066568	1.036508	-2.818385701
37.8	1.064888	0.931042	-12.56902134
38.8	1.049552	0.959674	-8.563463268
39.8	1.063915	0.961198	-9.654624665
40.8	1.066872	0.963508	-9.688509962
41.8	1.072841	0.967787	-9.79213136
42.8	1.081504	0.976858	-9.675969761
43.8	1.07307	0.991359	-7.614694288
44.9	0.991912	1.001359	0.952403036
45.9	0.967124	1.002452	3.652892494
46.9	0.962507	1.017749	5.73938683
47.9	0.963438	1.014777	5.328728989
49	0.969035	1.026389	5.918671668
50	0.984319	1.030856	4.727837215
51	0.993573	1.03294	3.962164833
52	1.001005	1.046658	4.56071648
53.1	1.011615	1.046483	3.446765815
54.2	1.014496	1.046234	3.128449989
Average	1.02697315	1.015519	-1.115331009

Figure 74 shows the test results for heat capacity on the cells of battery 459 at 50% SOC. Most of the variation between cells appeared to occur below 40 °C. As the temperature increased above 40 °C, the readings stabilized over this short temperature range. The detailed data is summarized in

Table 15. The average heat capacity of all cells is about 1.00 to 1.07 **J/g**·℃, which amounts to approximately 7% variation between the cells.

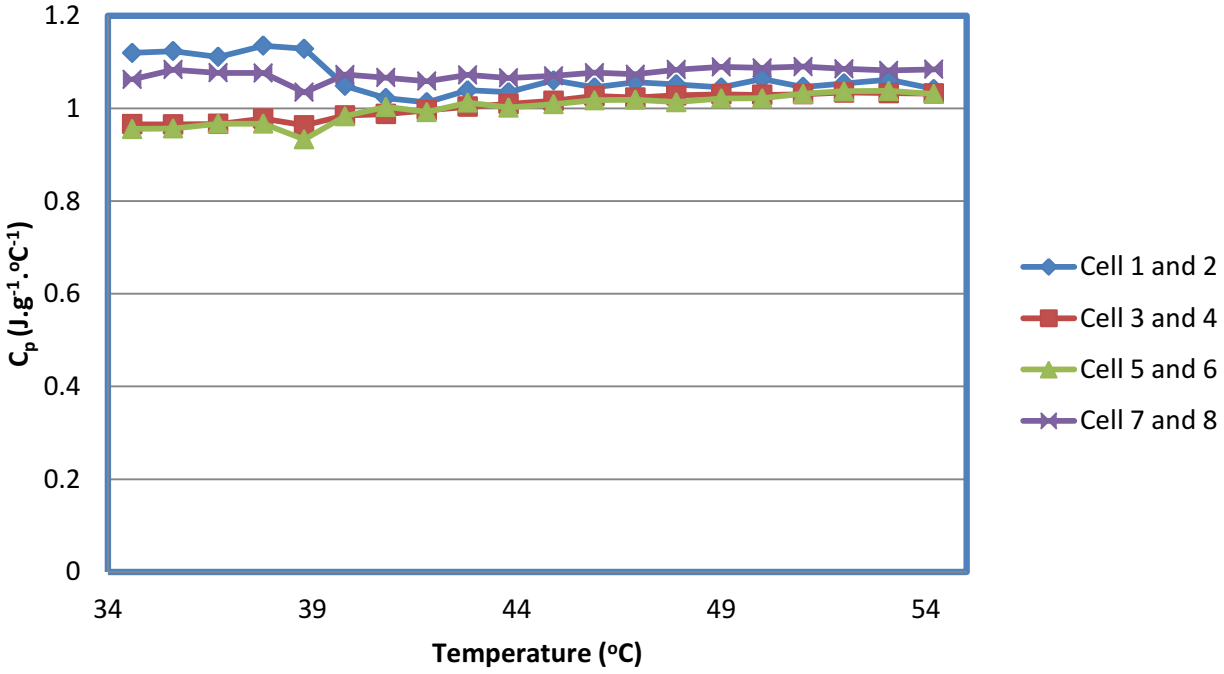

Figure 74 Heat Capacity Measurements on Cells from Battery 459 (at 50% SOC)

Table 15 Heat Capacity of Cells in Battery 459

	Heat Capacity; $J/g \cdot °C$			
Temperature; °C	Cell 1 and 2	Cell 3 and 4	Cell 5 and 6	Cell 7 and 8
34.6	1.119778	0.965533	0.955634	1.062281
35.6	1.123379	0.965366	0.956763	1.083504
36.7	1.110943	0.966273	0.966901	1.076678
37.8	1.135254	0.977611	0.96696	1.076194
38.8	1.128558	0.963343	0.933222	1.03454
39.8	1.048223	0.984606	0.983026	1.072619
40.8	1.022144	0.98773	1.003255	1.066356
41.8	1.013135	0.995859	0.992221	1.05847
42.8	1.03883	1.003628	1.012527	1.071946
43.8	1.034856	1.00928	1.001669	1.065583
44.9	1.060444	1.016325	1.009128	1.070015
45.9	1.045059	1.026516	1.017528	1.076768
46.9	1.056362	1.023069	1.018719	1.073567
47.9	1.051697	1.028117	1.013358	1.083519
49	1.045042	1.030541	1.021292	1.08931
50	1.063149	1.028865	1.021754	1.087307
51	1.046235	1.030527	1.031339	1.0899
52	1.053746	1.034076	1.036894	1.085288
53.1	1.062022	1.032805	1.037559	1.081559
54.2	1.041656	1.0316	1.031212	1.084185
Average	1.0650256	1.0050835	1.00054805	1.07447945

Knowing the heat capacity of the cells allows an estimate of the heat generated during the cell discharging process. The heat flux test was conducted using ARC chamber while the cell is subjected to 70 A CC discharging. When the temperature on cell casing is changing, the ARC system will always track the cell surface temperature to maintain adiabatic conditions, no heat exchange between sample and test chamber. Figure 75 shows the temperature profile for cell 1 from Battery 459 under the heat flux test. The maximum temperature rise for the overall discharging process under the simulated adiabatic condition was 16.4 °C. So the total heat (H_{1C}) generated was:

1.065 g (mass of cell) × 1.065 $J/g \cdot ℃$ (*heat capacity of the cell*) × 16.4 ℃(*temperature rise*) = 47911.9 Joules

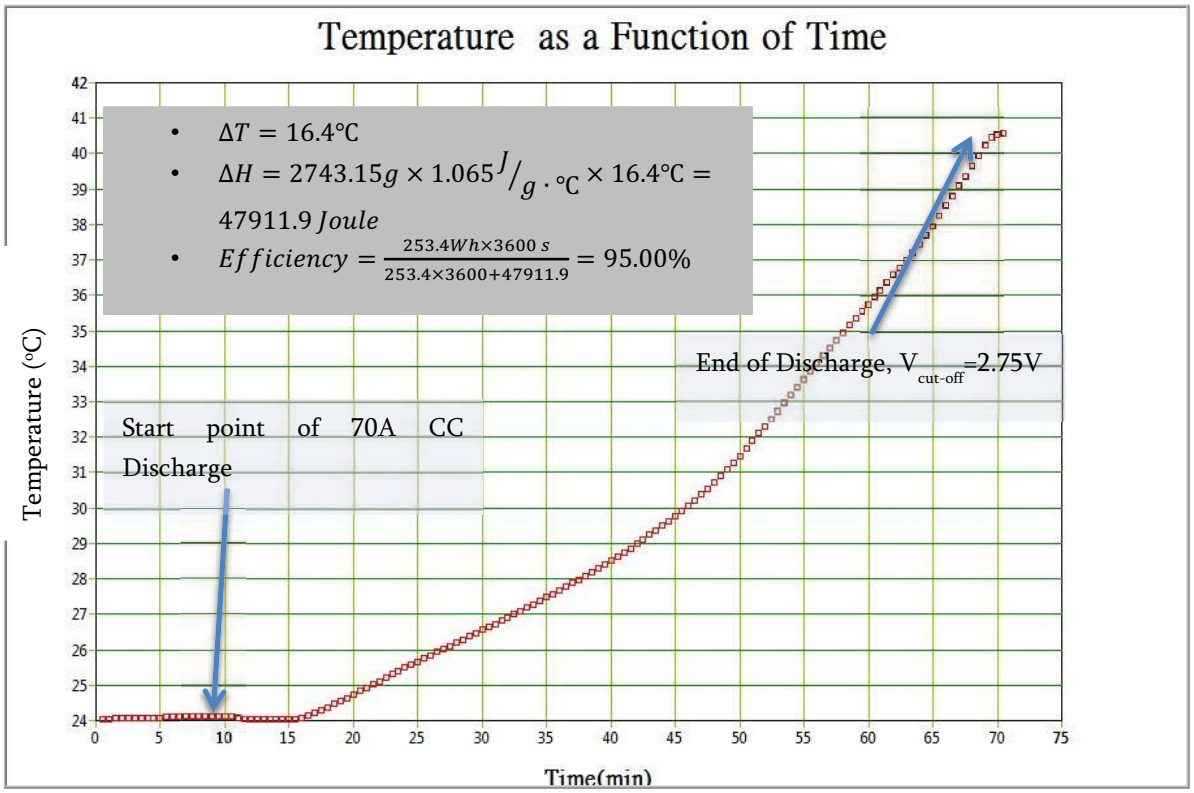

Figure 75 Temperature Profile of 459-Cell 1 during the 1C Heat Flux test (ARC)

Once the 70 A discharging was complete, there was 253.4 Wh of electrochemical energy (E_{ech}) obtained from the cell which is sufficient to run many consumer electronics. Next is a formula to calculate efficiency of the cell.

$$Electrochemistry\ energy/Total\ energy \times 100\%$$

The total energy term is based on contributions from two sources, the electrochemical energy and the heat generated during the discharging process. Hence the efficiency of the cell under 1C discharging is:

$$253.4\ Wh \times 3600\ s \cdot hour^{-1} / (253.4 \times 3600 + 47911.9)\ Joule \times 100\% = 95.00\%$$

So approximately 5% of the total cell energy is dissipated when subjected to a single 70 A discharging cycle.

Table 16 summarizes the results of similar calculations for other cells in Battery 459. That maximum temperature rise during 1C discharging was approximately 15 to 17 °C with the discharging efficiency of ranging from 95% to 95.4%. The data from these cells showed very good consistency.

Table 16 Thermal Properties and Efficiency of 70 A Discharging for the Cells in Battery 459

	459-1	459-2	459-3	459-4	459-5	459-6	459-7	459-8
Mass (g)	2743.2	2759.1	2737.8	2760.5	2749.2	2759.6	2751.5	2760.6
C_p $(J/g \cdot °C)$	1.065	1.065	1.005	1.005	1.001	1.001	1.074	1.074
ΔT (°C)	16.4	15.0	17.0	15.5	16.1	15.7	16.1	15.6
E_{ech} **(Wh)**	253.4	250.1	256.8	248.4	257.0	245.4	256.8	253.2
$H_{1C}(Joule)$	47912.7	44076.6	46775.3	43001.7	44306.4	43369.1	47577.3	46252.2
Efficiency (%)	95.00	95.33	95.18	95.41	95.43	95.32	95.11	95.17

During the heat flux test, temperature readings at different locations on the cell casing were measured to determine temperature uniformity. An example of the measurement on cell 1 (from battery 459) is shown in Figure 76. The profile of TC1 (red dotted line) shows the temperature on the rivet for the cathode and TC2 (blue dotted line) shows the temperature on the rivet for the anode. The maximum temperature reading occurred on the cathode rivet followed by the anode rivet. Except for TC1 and TC2, all other temperature profiles (TC2-TC8) exhibited less than 1 °C between the different locations. TC1 readings were about 4-5 °C higher than any other locations on the cell case and TC2 readings were about 1-3 °C higher than other locations. Higher temperature readings on the cathode as compared to the anode can be explained as follows: (1) the substrate of anode is copper, which is more conductive than aluminum, the substrate of cathode; (2) the active material of

anode is graphite or carbon, which is more conductive than $LiCoO_2$ cathode material[88]. It is important to note that with a cell casing surface temperature variation less than 1 °C under 70 A discharging, the temperature variation within the cell could possibly be at least 4-5 °C.

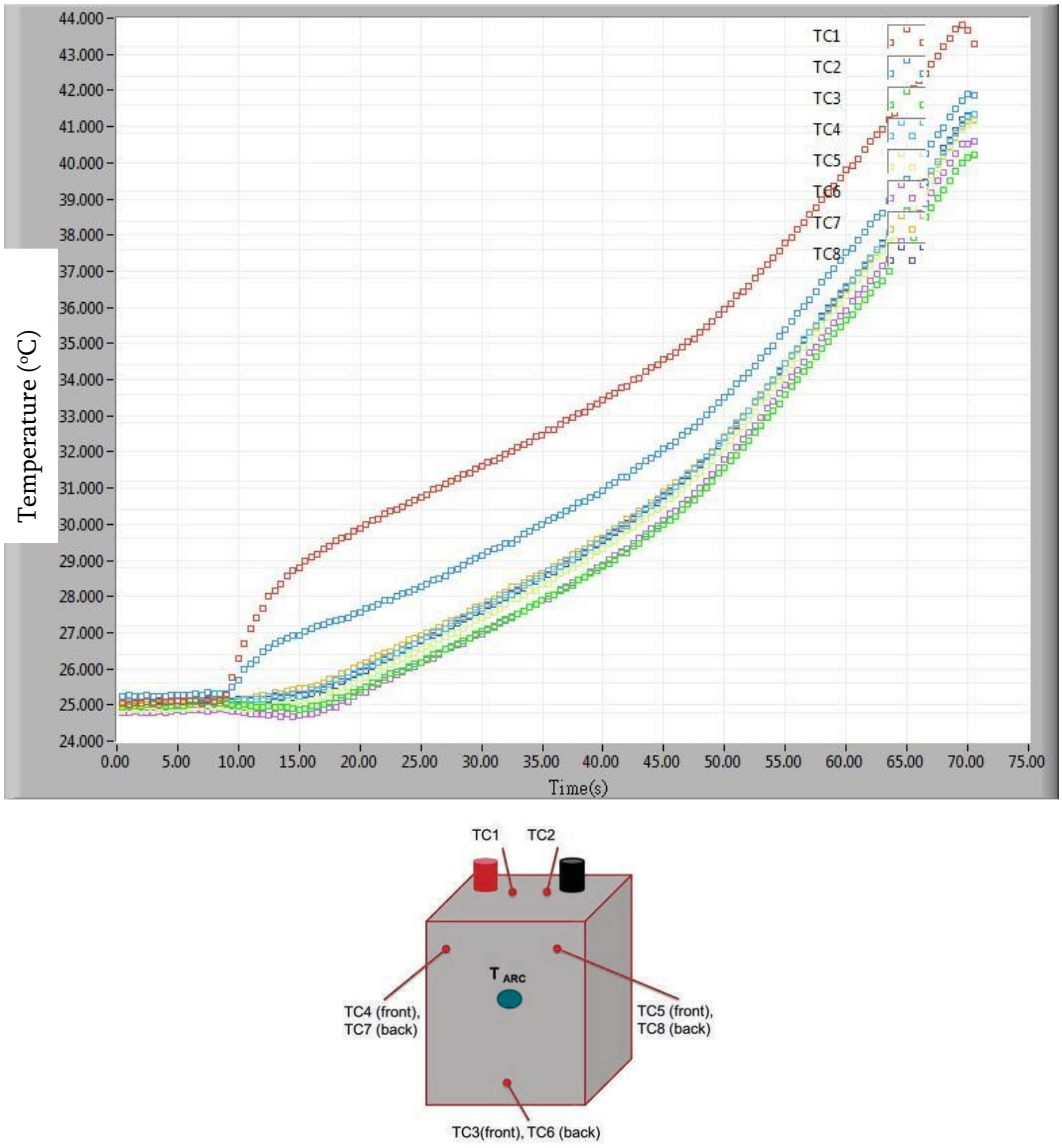

Figure 76 Temperature Profiles at different location on cell casing while Heat Flux test (Cell 1 from battery 459)

[88] To enhance the conductivity of cathode material, the conductive agent, graphite, is usually mixed with the active materials in cathode.

Study of Temperature-Dependent Characteristics

This section covers the temperature dependent characteristics of LVP65 cells by analyzing the electrochemical properties such as EIS and 1 kHz AC resistance. As these electrochemical properties are highly dependent upon the electrolyte properties, electrolyte characterization was also carried out.

Electrochemical Properties

The electrochemical properties (OCV, 1 kHz Resistance, EIS:R_b and EIS:R_{ct}) of a cell are the most fundamental parameters defining its performance. For these cells, it was necessary to characterize the key electrochemical properties over a temperature range from 40 ˚C to -40 ˚C. By monitoring changes in these parameters, a nondestructive approach can be devised to possibly correlate the presence of dendrites as a consequence of cold temperature charging tests conducted on the LVP65 cells.

The sample for the investigation was cell 2 of battery 412, the surviving battery from the JAL incident in Boston. The cell was first conditioned to a 0% SOC. Then EIS measurements were taken over the temperature range from 40 ˚C to -40 ˚C and are shown in Figure 77. Both the charge transfer resistance and capacitance increased with decreasing temperature where the data scale from -40 ˚C simply dwarfs the data from higher temperature. To observe the behavior at other temperatures, another plot without the data from -40 ˚C is shown Figure 78. The data shows how the bulk material resistance, charge transfer resistance and capacitance effect at electric double layers became dramatically larger when the temperature was lowered from 0 ˚C to 20 ˚C.

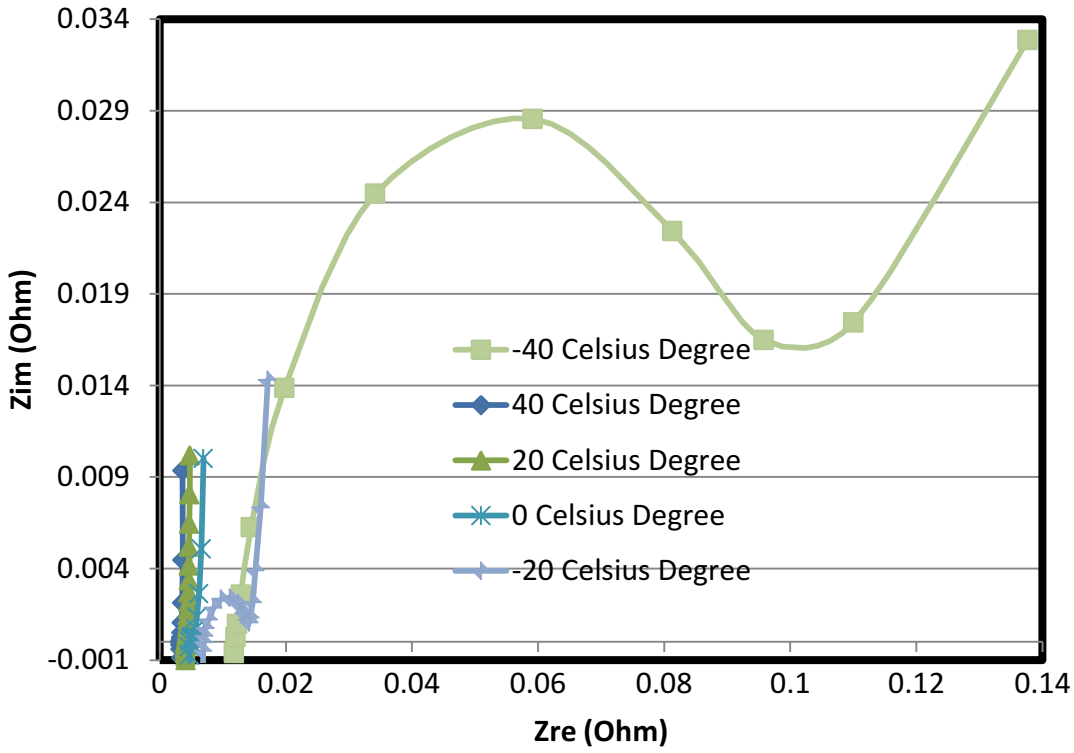

Figure 77 EIS measurements on Cell 2 from Battery 412 under 40, 20, 0, -20 and -40 °C

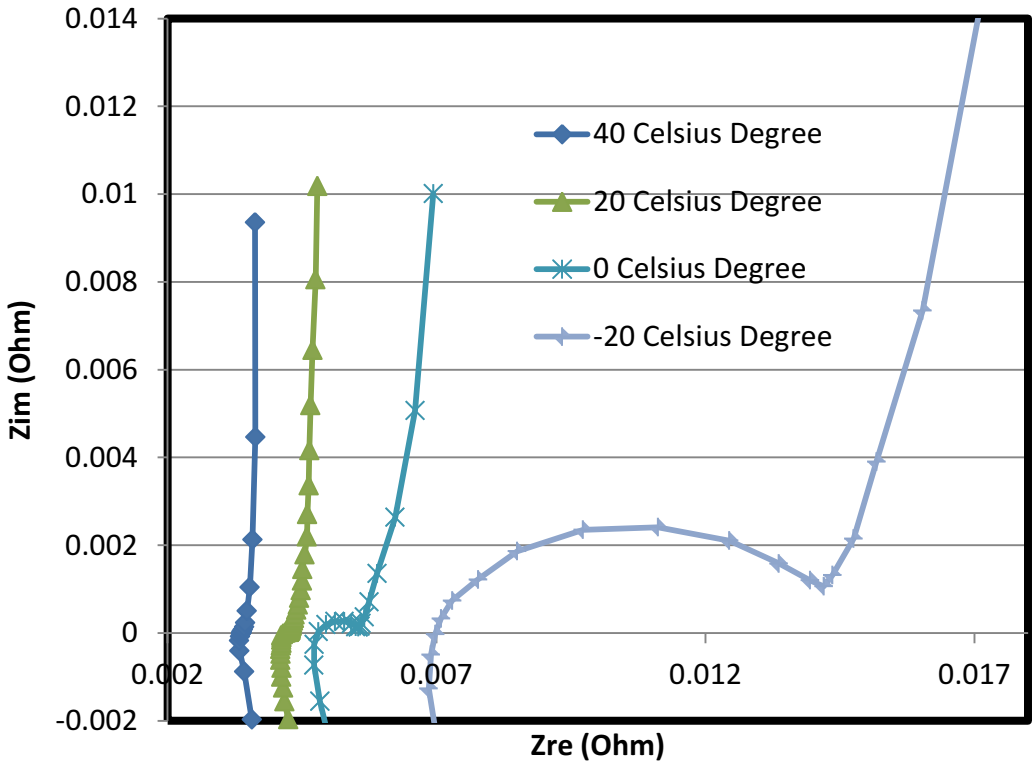

Figure 78 EIS measurements of Cell 2 from Battery 412 under 40, 20, 0, and -20 °C

All of the measured key electrochemical properties from the EIS are plotted in Figure 79 with a listing of the same values in Table 17. The charge transfer resistance (R_{ct}) showed the most significant changes as the temperature was lowered. As the R_{ct} increased with decreasing temperature, electrochemical reactions such as ion exchange at the electrical double layers could not be completed so that some lithium-ion likely accumulated at the electrolyte/electrode interface. Therefore, lithium metal is likely to be formed due to the polarization effect at anode under charging. Hence R_{ct} can theoretically act as a parameter to assess changes in the internal state of the cell due to lithium plating/dendrite formation and growth under cold temperature charging conditions.

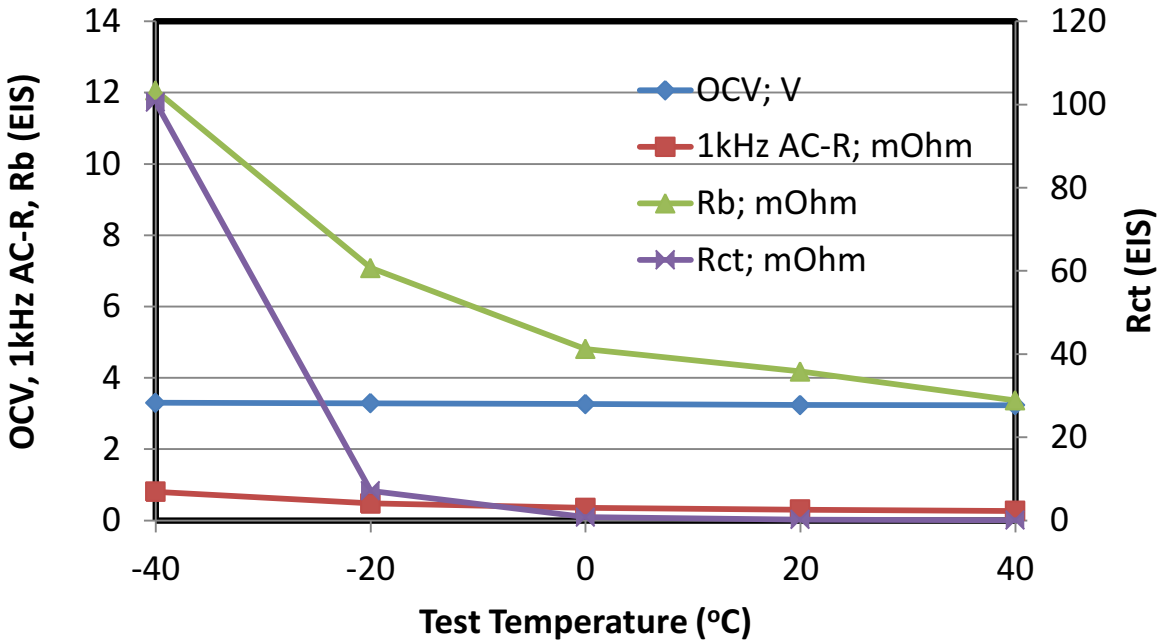

Figure 79 Key Electrochemical Properties of Cell 2 from Battery 412 as a function of Temperature

Table 17 Key Electrochemical Properties of Cell 2 from Battery 412 as a function of Temperature

Temperature; °C	OCV; V	1kHz AC-R; m-Ohm	Rb; m-Ohm	Rct; m-Ohm
40	3.2327	0.27	3.37	0.074
20	3.2394	0.305	4.18	0.22
0	3.2668	0.355	4.81	0.79
-20	3.2857	0.48	7.08	7.12
-40	3.2988	0.805	12.06	100.53

R_b represents the resistance of bulk material as the AC frequency range is high and so in an electrochemical system there is no induced polarization effects. Basically, R_b captures the overall resistance consisting of separator, electrodes, substrates and electrolyte. Among all of the components, electrolyte is the only material that is in a liquid state for this cell design. Therefore, the electrolyte is likely sensitive to changes in temperature and so there may be a strong correlation between R_b and some key electrolyte properties such as viscosity and conductivity. Such electrolyte properties can affect the resistance of ion transport between the electrodes.

Electrolyte Characterization

The electrolyte for lithium ion cells is typically a lithium salt dissolved in a mixture of organic solvents. An ideal electrolyte solvent should be able to dissolve salts to sufficient concentrations, so as to be a good ionic conductor and electronic insulator, remain inert to all cell components, have wide operating range, and fail safely.[89] For general commercial lithium ion cells, mixing different organic solvents is common. Selection of suitable solvents is very critical and based on application needs. According to the information from GS-Yuasa, the formulation of the electrolyte is lithium hexafluorophosphate ($LiPF_6$) in a mixture of ethylene carbonate (EC), dimethyl carbonate (DMC) and ethylmethyl carbonate (EMC) with some stabilizer additives. [redacted] The use of ternary solvents in LVP65 cell is intended to meet demanding requirements of the electrolyte for the specific aircraft application. Every solvent has its own function in the electrolyte. EC can provide the protection layer on the surface of the graphite to prevent continuous electrolyte reduction and self-discharging, increase the degree of dissociation of the Li salt, and provide high permittivity. DMC and EMC decrease the viscosity of the solution and have low dielectric constant, which can facilitate the ion transport through the electrolyte. EMC can also decrease the freezing point of the solution (Table 18). The EC/DMC/EMC ternary solvent system has been reported for several low temperature applications.[90, 91]

Table 18 Select Properties of Electrolyte Solvents for LVP65

Solvent	Structure	Molecular weight	Freezing point (°C)	Boiling point (°C)	Viscosity (cP)	Dielectric constant
EC	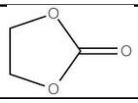	88	35-38	248	1.90 (at 40°C)	89.78
DMC	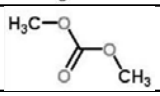	90	2~4	91	0.59 (at 20°C)	3.107
EMC	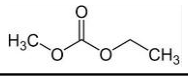	104	-55 ~-53	110	0.65 (at 25°C)	2.958

[89] K. Xu, "Nonaqueous liquid electrolytes for lithium-based rechargeable batteries", Chem. Rev., vol. 104, Iss. 10, 2004, pp. 4303-4418.

[90] E.J. Plichta, M. Hendrickson, R. Thompson, G. Au, W.K. Behl, M.C. Smart, B.V. Ratnakumar, and S. Surampudi, "Development of low temperature Li-ion electrolytes for NASA and DoD applications", J. Power Sources, vol. 94, Iss. 2, 2001, pp. 160-162.

[91] D. Yaakov, Y. Gofer, D. Aurbach, and I. C. Halalay, "On the study of electrolyte solutions for Li-ion batteries that can work over a wide temperature range", J. Electrochem. Soc., vol. 157, Iss. 12, 2010, pp. 1383-1391.

Since the operational and storage temperature window of LVP65 cell are highly dependent upon the performance of the electrolyte, it was necessary to measure some key properties of the electrolyte over a temperature range of -40 to 40 °C. To access the electrolyte, destructive teardown of the cell was necessary with extreme care in extraction of the electrolyte to prevent contamination (Figure 80). Two main properties of the electrolyte were measured, the electrical conductivity and viscosity of the electrolyte which are shown in Figure 81. The viscosity data measured at -40 °C exhibited some anomalies due to some issues with the measurement. Viscosity and electrical conductivity have an inverse correlation as a function of temperature. The data shows that once temperatures reached below 0 °C there was a dramatic change in each property.

Figure 80 Drained Electrolyte (left) and Electrical Conductivity Measurements (right)

These results demonstrate how select electrolyte and electrochemical properties are highly correlated and can provide insight into the changing internal state of the cell. Together with the previous analysis where the electrolyte characteristics were correlated to the AC impedance of the LVP65 cell, a set of parameters is available to assess the performance of the cell under a range of conditions.

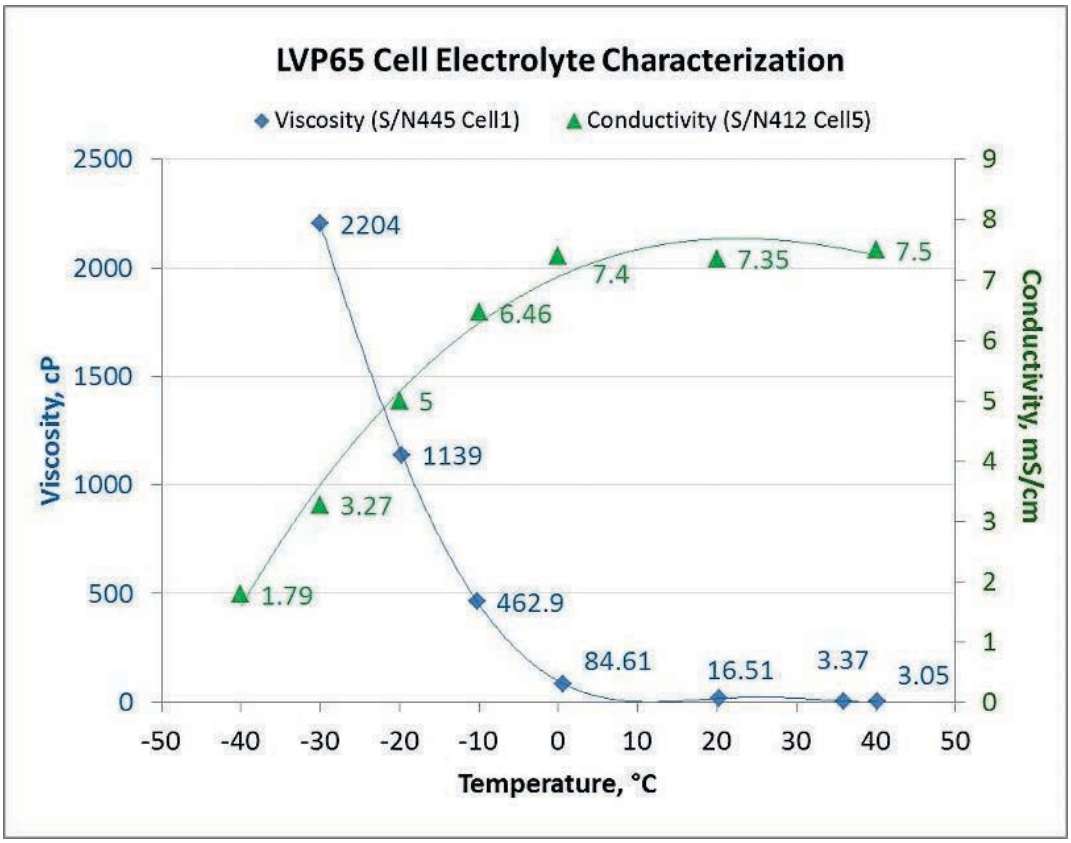

Figure 81 Electrolyte Viscosity and Electrical Conductivity as a function of Temperature

Next, to investigate the elemental composition of the electrolyte, three electrolyte samples were drained from cell 3, cell 5, and cell 6 from battery 412 and analyzed by using ICP. The dilution solution was made of 2% nitric acid (HNO_3) in de-ionized water, which was also used in blank test (Table 19).

Table 19 Sample Description for ICP test

Sample Identification	Description	Comments
Blank dilution solution	2% of HNO_3 solution	As the Blank test and dilution solution
#412 Cell3	Brown Liquid	100 times diluted with dilution solution
#412 Cell5	Brown Liquid	100 times diluted with dilution solution
#412 Cell6	Brown Liquid	100 times diluted with dilution solution

Table 20 ICP Test Results on Electrolyte: 1st measurements

	Elements in mg/L										
	Li	P	Al	Cu	Ca	Mg	K	Na	Ba	B	Cd
Blank	0.7	ND	0.4	1.5	1.4	0.1	1.6	6.2	ND	0.8	ND
#412-3	8539	39300	4.6	3.8	27.5	4.9	21.9	30.4	0.1	1.7	ND
#412-5	9089	43830	1.2	9.7	7.0	1.0	24.3	42.6	0.1	2.0	ND
#412-6	8567	38660	65.6	50.3	40.2	9.3	26.4	54.6	0.6	2.0	ND

	Elements in mg/L										
	Cr	Co	Fe	Mn	Si	Sr	Sn	Ti	Zn		
Blank	0.2	0.1	ND	0.1	0.8	ND	ND	ND	ND		
#412-3	0.2	1.1	5.5	2.4	5.8	0.1	0.1	ND	2.0		
#412-5	0.3	1.2	2.2	0.5	4.7	ND	0.7	ND	1.4		
#412-6	0.4	1.4	2.8	0.9	4.7	0.2	0.1	ND	2.6		

Table 20 shows the results from the ICP tests. For Cell 6, some elements (Al, Cu, Ca, and Mg) were found in relatively higher concentration. There was some suspicion of contamination during the cell DPA. Therefore the tests were repeated but the electrolyte was filtered before running and ICP tests conducted for the three cells. The 2nd round of results is shown in the table below.

Table 21 ICP Test Results on Electrolyte: 2nd measurements

	Elements in mg/L										
	Li	P	Al	Cu	Ca	Mg	K	Na	Ba	B	Cd
Blank	0.7	ND	0.1	0.7	0.8	ND	1.1	2.7	ND	1.1	ND
#412-3	8871	33820	2.0	1.2	6.3	ND	26.6	37.7	ND	4.6	ND
#412-5	9780	40250	2.4	4.0	17.4	1.2	34.1	44.1	0.2	0.2	ND
#412-6	8874	37710	1.1	1.5	4.8	ND	28.9	30.9	0.4	1.7	ND

	Elements in mg/L										
	Cr	Co	Fe	Mn	Si	Sr	Sn	Ti	Zn		
Blank	ND	ND	ND	ND	0.9	ND	ND	ND	ND		
#412-3	0.5	1.3	3.4	ND	4.7	ND	0.2	0.2	0.7		
#412-5	0.3	1.4	6.4	ND	11.9	0.2	0.9	0.3	3.2		
#412-6	0.6	1.0	5.8	ND	7.0	ND	0.5	0.2	1.0		

For this 2nd round of measurements, there was no significant variation in the elements traced in the three different electrolyte samples. Therefore, the unusually high concentration of Al, Ca, and Mg that appeared in the analysis of the 1st extracted samples were probably particulate contaminants in electrolyte (Figure 82). These particles very likely had a source in the broken pieces of cutting wheels used during cell disassembly. Figure 83 shows the composition analysis of the cut-off wheels. The Ca and Al are part of the abrasives in cut-off wheels.

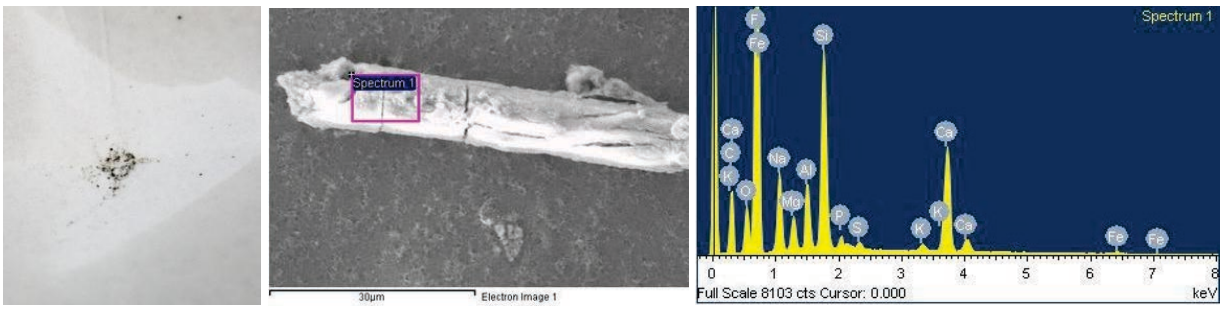

Figure 82 Particles Filtered from Electrolyte

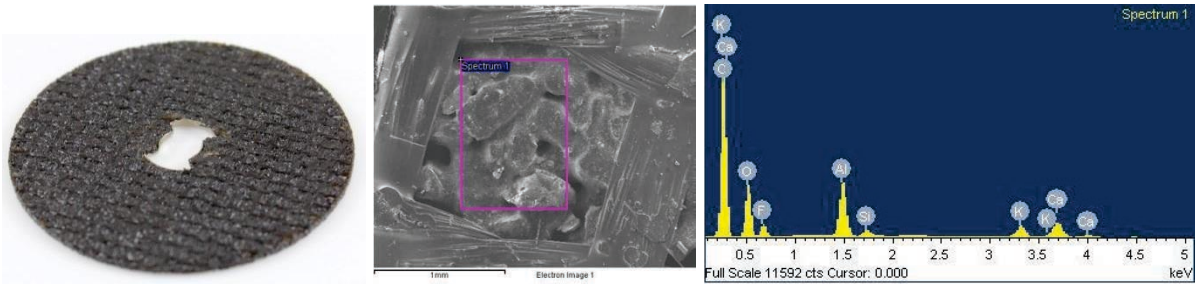

Figure 83 Elemental Analysis of Cut-off Wheel

Thermal Abuse and Application Scope of Temperature

To investigate the tolerance of LVP65 cell design to thermal abuse, cell 2 and cell 4 from battery 412, were subjected to adiabatic heating via an ARC. As internal faults responsible for safety issues generally lead to internal heating, this test can be insightful about the thermal stability of the cell. The thermal stability of the cell is dependent not only the cell design but also SOC so one cell was set to 0% SOC and a second cell was set to 100% SOC.

Thermal Abuse via ARC

Figure 84 shows the ARC test results of cell 2 from battery 412. The SOC of the test sample was set to 0%. The ARC is programmed to run a heat-wait-seek procedure to maintain adiabatic conditions by matching the heating rate of the cell as measured by a temperature reading on the surface of the cell. According to the test data, the self-heating rate did not exceed 0.02 °C/min up to 180 °C. Above 155 °C, no cell self-heating was detected. The self-heating rate at each temperature step is plotted in Figure 85. The initial self-heating was triggered when temperatures exceeded 60 °C. The heating rate continues to increase where at 125 °C, it reaches 0.05 °C/min. At that point, the separator starts melting and absorbs some heat, temporarily decreasing the heating rate. As the separator is melting, an internal short-circuit (ISC) can occur. However, as the cell was set to 0% SOC and most of the reactive materials within the cell likely slowly decomposed or reacted with anode, cathode or electrolyte, no large self-heating was observed post separator melt-down.

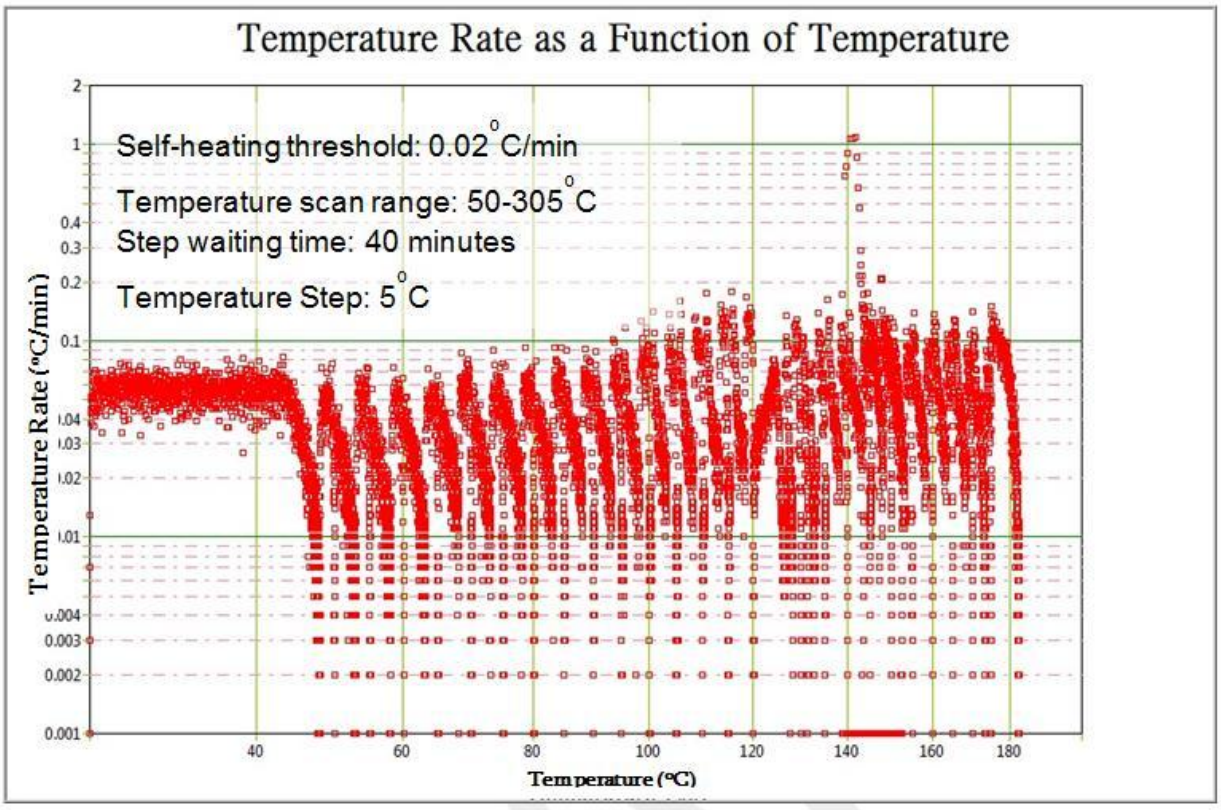

Figure 84 ARC heat-wait-seek test on Cell 2 from battery 412 set to 0% SOC

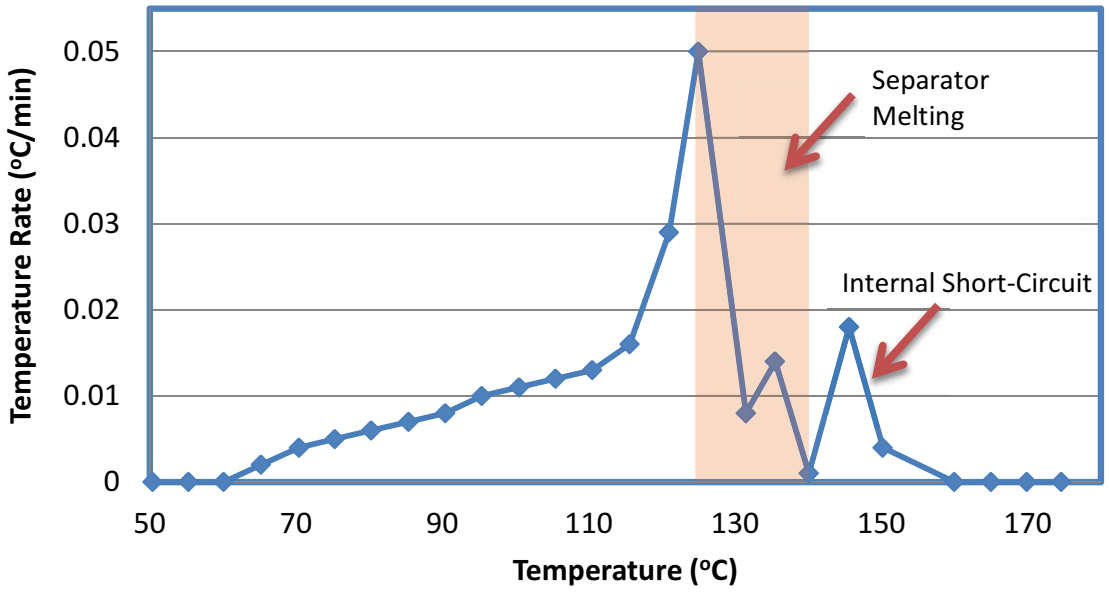

Figure 85 Self-heating Rate in ARC (Cell 2 from Battery 412 at 0% SOC)

Cell 4 from battery 412 was also tested by at a 100% SOC. The test result is shown in Figure 86 and the specific self-heating rate at each temperature step is given in Figure 86. For the LVP65 cell at 100% SOC, the self-heating rate exceeded 0.02 °C/min starting at temperatures around 80-85 °C. The separator melted around 130 °C followed by triggering of an ISC. In this case, the cell experienced thermal runaway. Looking at the self-heating rate data, self-heating appears to be detected for temperatures starting around 60 °C, similar to the results for cell 2 which was set to 0% SOC. This suggests that from a safety point of view, 60 °C may be an appropriate application limit for cell usage. These results do not imply that there will be immediate safety issue if the cells are exposed to conditions within the 60 to 70 °C. However, there may be safety concerns for the cell to be used during normal usage after the thermal aging. Safety issues could arise for these cells in the temperature range of 60 to 70 °C as there may be some damage to the SEI layer between electrode and electrolyte reducing this important protection layer[92].

[92] P. Verma et al., "A review of the features and analyses of the solid electrolyte interphase in Li-ion batteries", Electrochimica Acta, vol. 55, pp. 6332-6341, 2010.

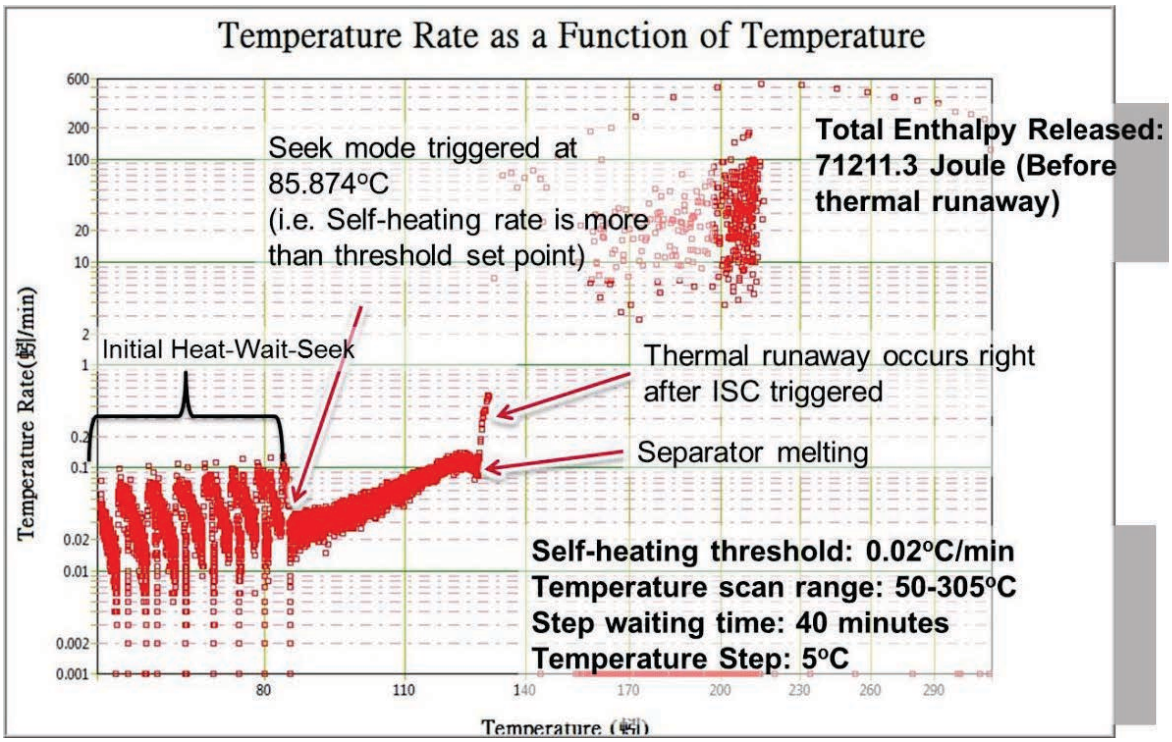

Figure 86 ARC heat-wait-seek test on Cell 4 from Battery 412 set to 100% SOC

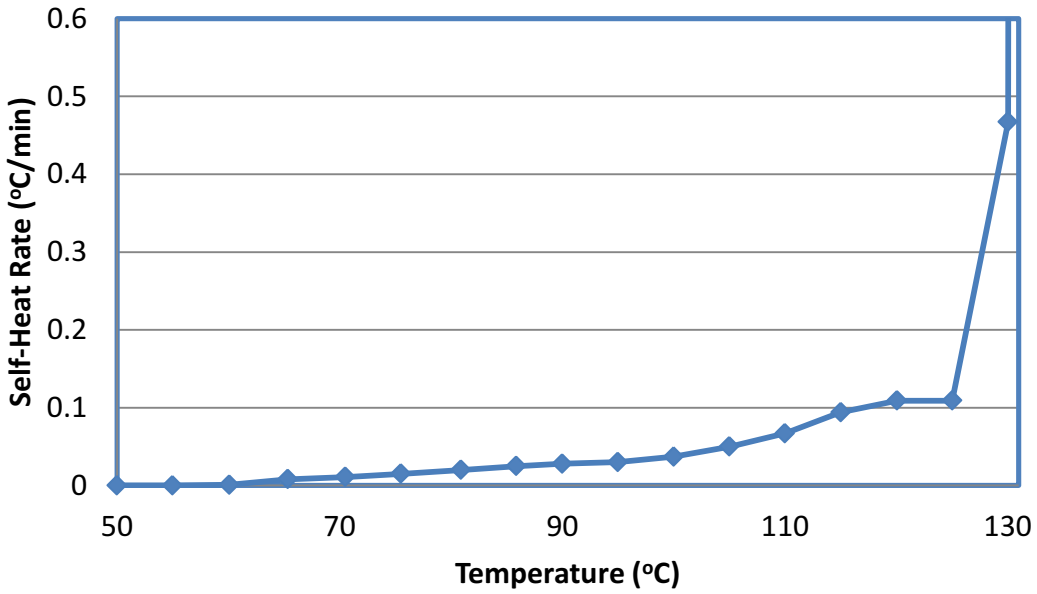

Figure 87 Self-heating Rate under ARC (Cell 4 of Battery 412, 100% SOC)

The CT scan images of cell 2 and cell 4 from battery 412 after the ARC thermal abuse testing are shown in Figure 88 and Figure 89. In both case, swelling of the cell casing was observed without any rupture of the metal casing. There were signs of venting and the electrode layer structure still appeared intact in cell 2 from battery 412 where no thermal runaway was observed. For cell 4 thermal runaway burned most of the active materials. In these tests, the vent activated as it should without loss of cell case mechanical integrity.

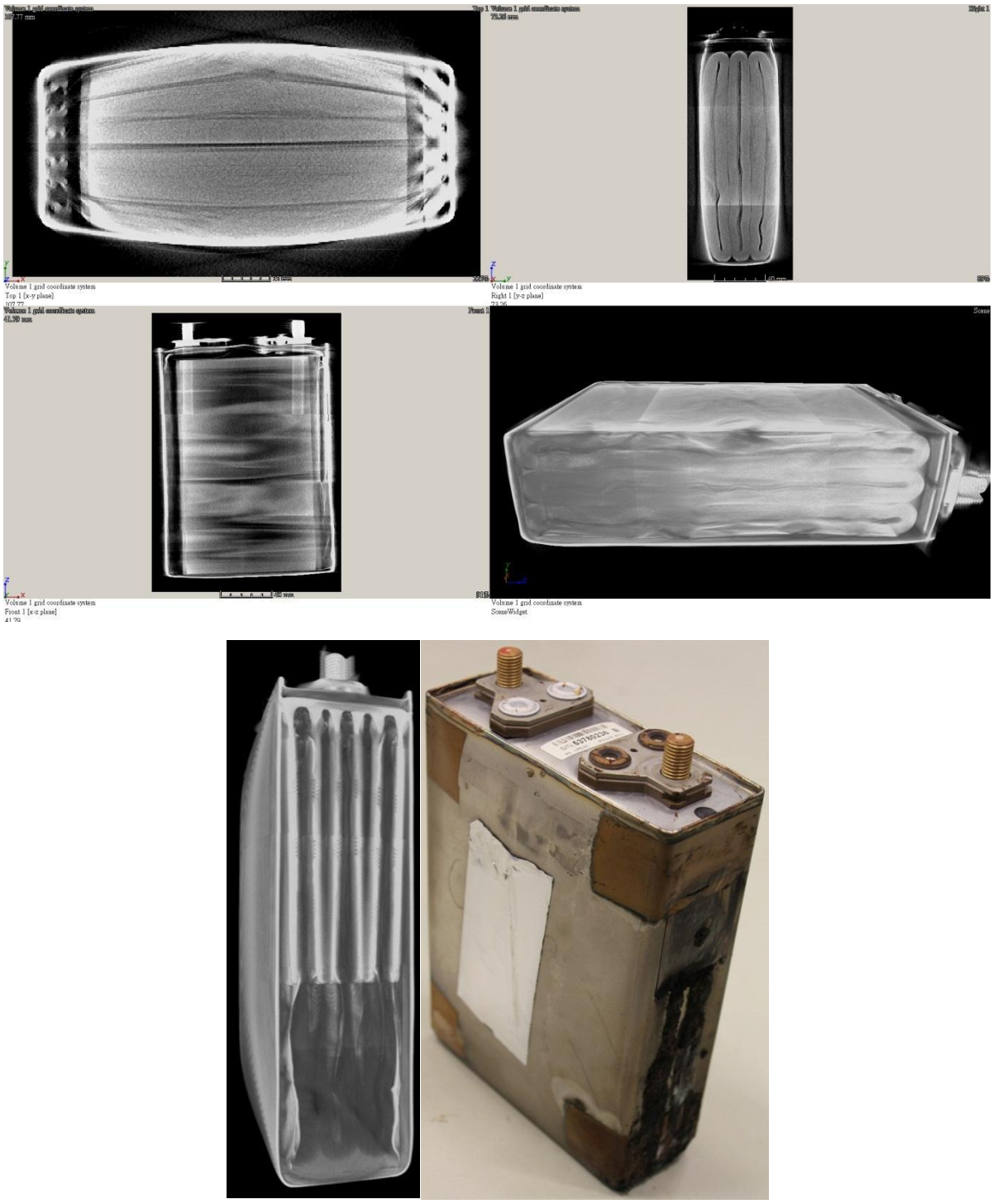

Figure 88 CT Scan images of Cell 2 from Battery 412 after ARC test

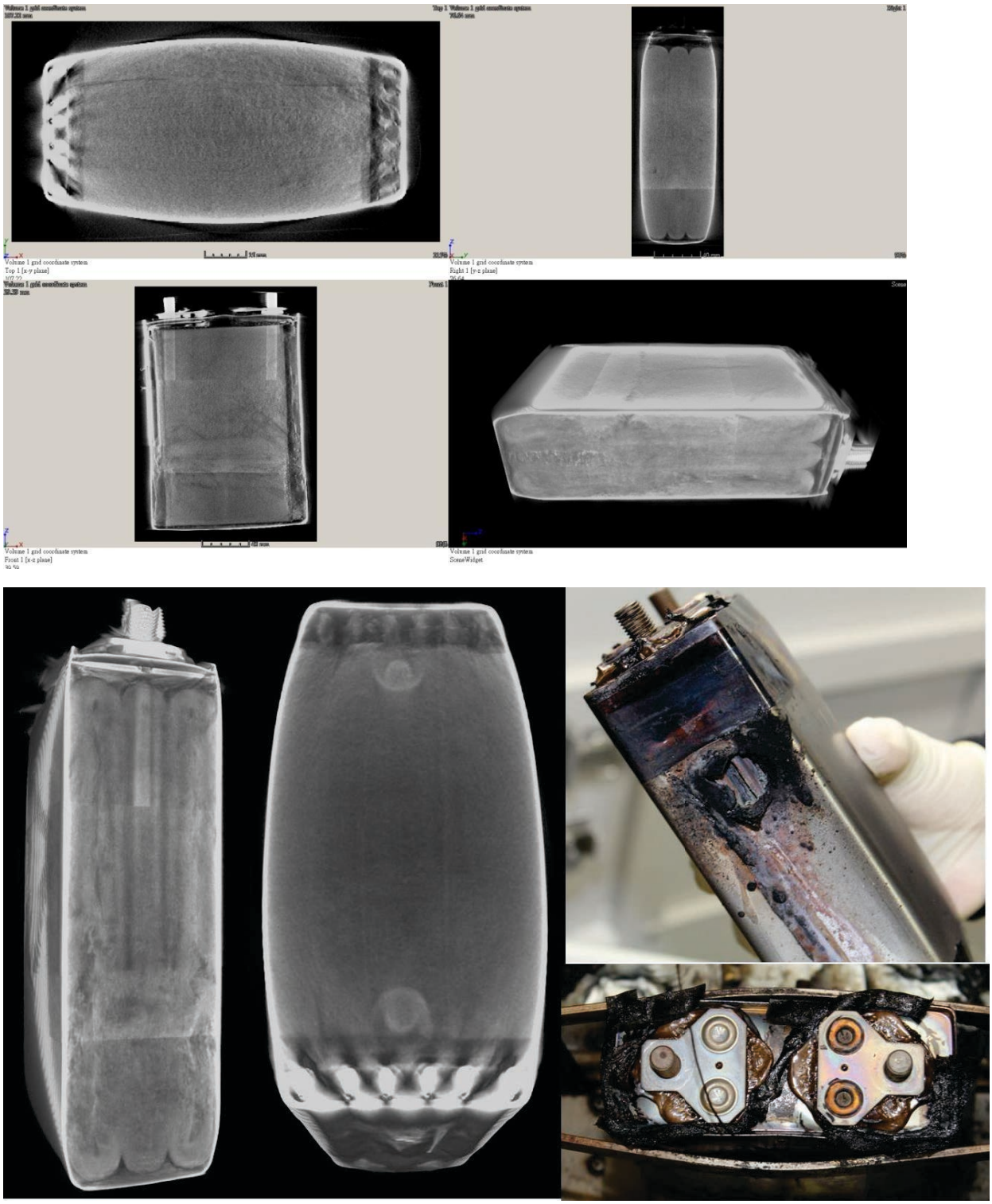

Figure 89 CT Scan images of Cell 4 from Battery 412 after ARC test

Thermal Stability of Cathode/Anode Materials

Charged lithium cobalt oxide (Li_xCoO_2, x<1) is thermally unstable, and it can decompose to release oxygen at temperatures above 200 °C.[93] However, it has been reported that the $Li_{0.5}CoO_2$ with solvents EC+DEC could initiate decomposition at temperatures as low as 130 °C.[94] Therefore, it is important to quantify the decomposition temperature for the cathode active material in the LVP65 construction. Thermogravimetric analysis (TGA) was used to analyze the cathode materials from three disassembled cells and the results are shown in Figure 90. Since the cathode materials were not rinsed out prior to TGA testing, the first weight loss stage (from 65 to 115 °C) on the TGA curve resulted from the evaporation of remaining solvents in the material.

The onset temperature for cathode material decomposition, based on the TGA, is approximately 240 °C. The results from the three cells, cell 3, cell 5 and cell 6 from battery 412 are consistent, which revealed that the additional pulse charging process in this investigation had very little effect on the thermal stability of cathode materials. This may be due to the fact that the cell was nearly fully charged prior to the pulse charging step, so that the chemical states of the lithium cobalt oxide materials from the three different cells were similar. The TGA analysis maybe cannot distinguish differences accurately for the cells in such a state.

The decomposition of Li_xCoO_2 can be generally represented by the following equation:

$$Li_xCoO_2 \rightarrow xLiCoO_2 + \left(\frac{1}{3}\right)Co_3O_4 + \left(\frac{1-x}{3}\right)O_2$$

The activation energy of the decomposition reaction varies with the level of delithiation of lithium cobalt oxide (amount of Li in the structure). The degradation of cathode materials can be triggered even earlier if lithium is continuously drawn out from the layered structure of lithium cobalt oxide in overcharged cells.

---

[93] Y. Baba and S. Okada, "Thermal stability of Li_xCoO_2 cathode for lithium ion battery", Solid State Ionics, vol. 148, Iss. 3-4, 2002, pp. 311-316.

[94] D. D. MacNeil and J. R. Dahn, "The reaction of charged cathodes with nonaqueous solvents and electrolytes: I. $Li_{0.5}CoO_2$ batteries and energy conversion", J. Electrochem. Society, vol. 148, Iss. 11, 2001, pp. A1205-A1210.

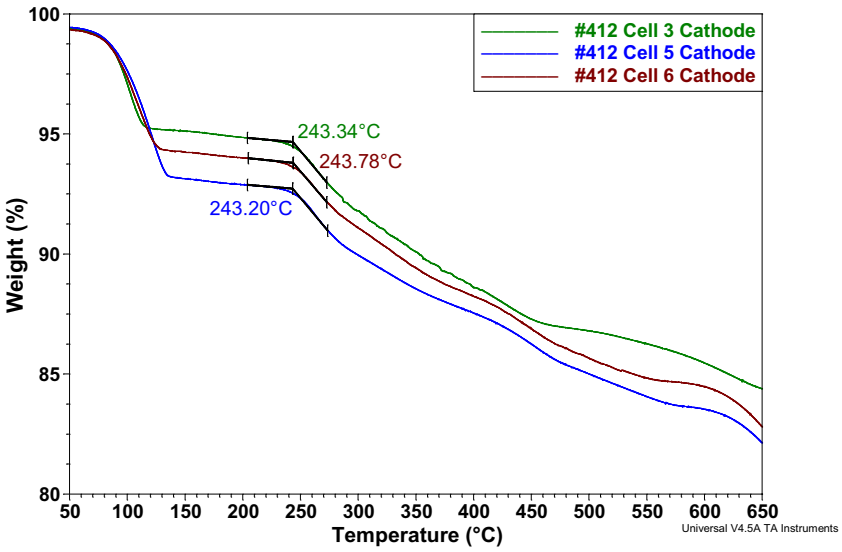

Figure 90 TGA curves of Cathode Materials

To further analyze the thermal behaviors of the materials in LVP65 cell, the differential scanning calorimetry (DSC) technique was employed on components extracted from cell 3, cell 5 and cell 6 from battery 412. The DSC measurements for cathode and anode materials are shown in Figure 91, which are quite consistent with results reported in other published studies. For the charged cathode materials, the exotherm begins at around 190 °C is possibly caused by a phase transition of delithiated Li_xCoO_2 and decomposition of the solvent with the active cathode surface (SEI layers). The peak at around 220 – 230 °C was caused by oxygen release from the decomposition of Li_xCoO_2. The small peaks above 250 °C could be from the reactions of the electrolyte.[95,96] As for the anode materials, a small exothermic peak at 100 °C is associated with conversion of the metastable SEI layer to a stable SEI.[97] Then, a mild heat generation starting at 125 °C continues until another peak at 250 °C where there was a sharp heat release peak at 270 °C. From 125 to 200 °C, the slight exothermic response was caused by the heterogeneous reaction between electrolyte solvent diffused into carbon particles and

[95] Y. Baba and S. Okada, "Thermal stability of Li_xCoO_2 cathode for lithium ion battery", Solid State Ionics, vol. 148, Iss. 3-4, 2002, pp. 311-316.

[96] J. Yamaki et al., "Thermal stability of electrolytes with Li_xCoO_2 cathode for lithiated carbon anode", J. Power Sources, vol. 119, 2003, pp. 789-793.

[97] J. Yamaki et al., "Thermal stability of graphite anode with electrolyte in lithium0ion cells", Solid State Ionics, vol. 148, Iss. 3-4, 2002, pp. 241-245.

react with lithium ion, which thus formed new SEI on graphite anode. While heating above 200°C, the first significant exothermic reaction can be ascribed to the decomposition of the electrolyte, and the second peak is generally believed to be a consequence of the breakdown of SEI.[98]

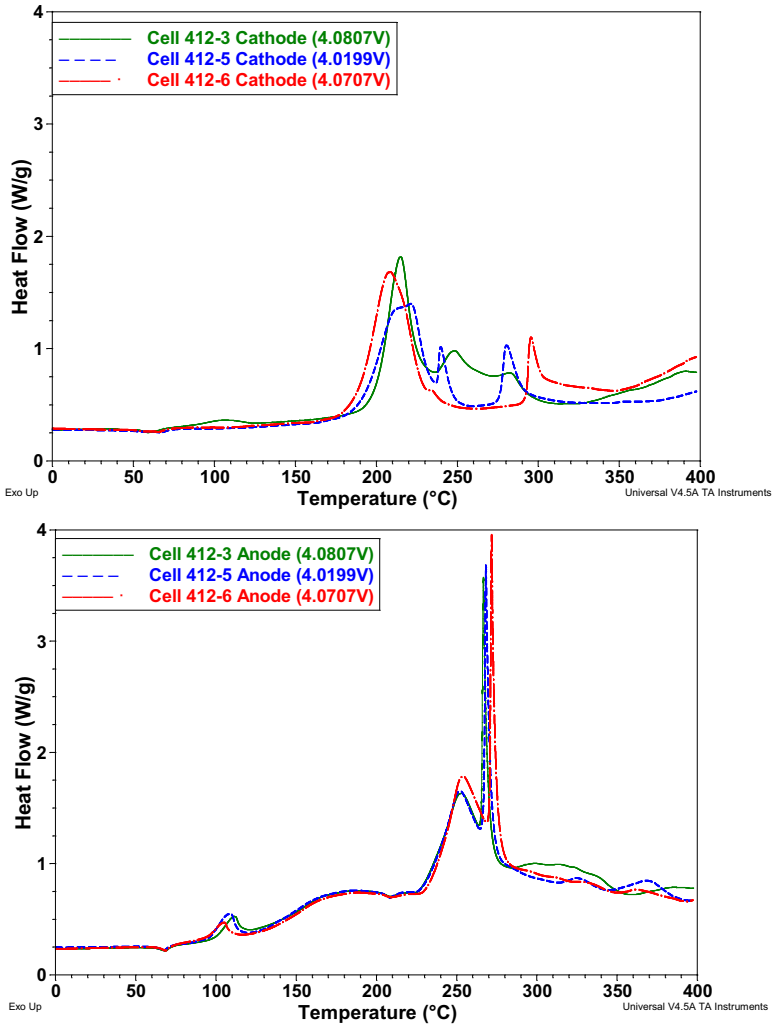

Figure 91 DSC Results for Cathode (top) and Anode (bot)

The thermal behaviors of the cathode and anode for a single cell are superimposed for comparison purposes in Figure 92. At elevated temperatures, the heat release from the anode material was more significant than that from cathode. In general, measurements taken from the DSC and TGA were not under adiabatic conditions. Hence, it is reasonable the trigger temperature for exothermic reactions

[98] O. Haik et al.,"On the thermal behavior of lithium intercalated graphites batteries and energy storage" J. Electrochem. Society, vol. 158, Iss. 8, 2011, pp. A913-A923.

measured in the DSC and TGA lead to a higher self-heating signal than that from thermal abuse via ARC. Besides, there were no electrochemical reactions involved in DSC and TGA analyses but electrochemical heat can be generated after melting down of separator in an ARC test. However, the exothermic reaction data from the DSC can be compared with the data from the ARC. The initial self-heating in LVP65 cell (i.e. starting from 60-65 ˚C) can be correlated to initial thermal degradation of the SEI layer with some side reactions between the anode and electrolyte. The middle stage of self-heating can be correlated to the reactions involving the anode with the electrolyte, and the final stage of exothermic reactions can be related to the decomposition of electrode materials.

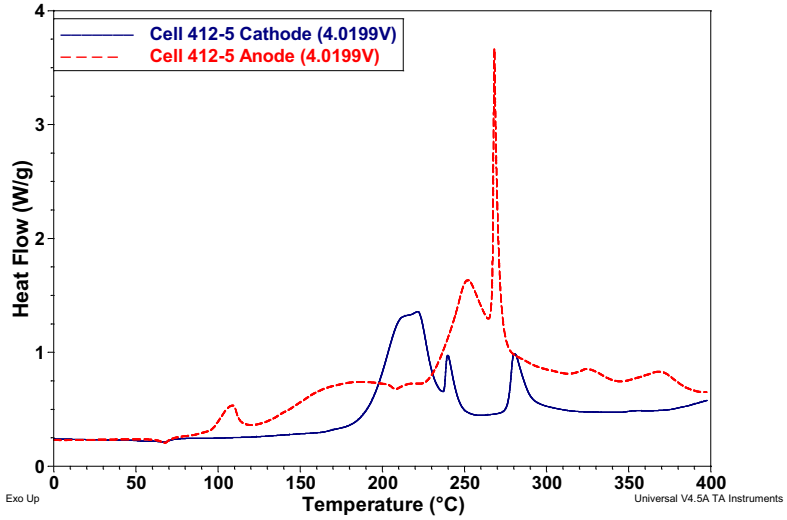

Figure 92 Cathode and Anode Exotherms for Cell 5 from Battery 412

Pulse Charge and IR Imaging

This section covers two additional tests whose intent was to understand the cell response under different charging/discharging conditions. One condition involved subjecting a cell to a pulse charge test. The purpose of this test was to understand if pulse noise at the end of the normal charge cycle adversely affected cell behavior. The 2nd test involved subjecting a cell to simulated APU start during controlled ambient conditions to determine whether localized hot spots were occurring on the cell.

Pulse Charge Test under -18 ˚C and 25 ˚C

Cell 3 and cell 6 from battery 412 were used for cold pulse charging test under -18 ˚C and 25 ˚C conditions, respectively. EIS measurements were recorded on the cells before and after each cold

pulse charging cycle for comparison. Due to time constraints, five cycles were conducted for each cell. However, only the data at -18 °C could be analyzed as the current output of the LVP65 cell under 100% SOC introduces a current level that causes a high noise to signal ratio in the EIS measurements for temperatures at 25 °C.

The EIS profiles of the cell 3 (test under -18 °C) are given in Figure 93. The scale of semi-circle can be seen shrinking after each cycle. After five cycles, the charge transfer resistance (R_{ct}) of the cell (2.7 m-Ohm) was reduced by 28.9% from the original R_{ct} (3.8m-Ohm) measured before the start of the pulse testing. The reduced R_{ct} indicates a decreasing polarization effect so that the lithium plating/dendrite is theoretically less likely to happen.

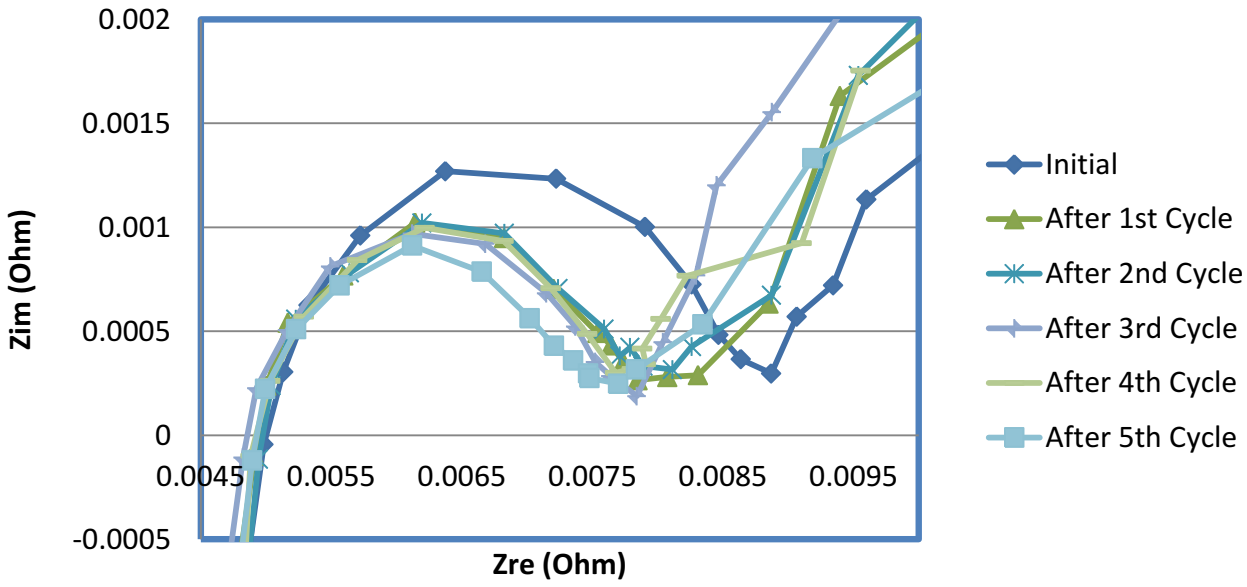

Figure 93 EIS Profiles before and after Pulse Charge test under -18 °C (Cell 3 of Battery 412)

Table 22 gives the summary of the pulse charge test results for -18 °C and 25 °C conditions. The cells were also disassembled and the electrolyte drained out for further characterization. Dendrite formation was observed on cell 6, which was pulse charged under 25 °C. Dendrites were also observed in cell 5, which was not subjected to the pulse test, but simply subjected to CC-CV charging to 4.025 V only. Comparing the inspection results for cell 5 and cell 6, more dendrites were visible in cell 6 than in cell 5.

Evidence of dendritic anomaly could not be found in cell 3, which was subjected to cold pulse charging at -18°C. In this case, the cell history is required to help identify the potential cause. For cell 3, the EIS profile showed less polarization after pulse charge cycles which means the possibility for dendrite formation can be potentially reduced[99]. However, these cells suggest that the presence of wrinkles could encourage dendrite formation within the cell during application usage.

Table 22 Test Summary of Pulse Charge Test and DPA under 25 °C and -18 °C

Sample	Cell 5 from battery 412 (For reference only – not subjected to pulse charging)	Cell 3 from battery 412	Cell 6 from battery 412
Test	Electrolyte characterization	Cold Pulse Charge under -18 °C	Cold Pulse Charge under 25 °C
Finding from DPA	• More wrinkles in jelly-rolls • Evidence of dendritic anomalies 	• Wrinkles in jelly-rolls but less saw-tooth patterns • No evidence of dendritic anomalies 	• More wrinkles in jelly-rolls • Evidence of dendritic anomalies 
EIS	No comments	EIS data shows the polarization effect is getting smaller after pulse charge -	No comments

IR Thermal Imaging during Simulated APU start

Cell 3 from battery 459 was selected for IR Thermal Imaging test under simulated APU start at -18, 0 and 25 °C conditions. In addition, cells 5 and 7 were also selected for APU start simulation but

[99] C. Brissot et al., "Dendritic growth mechanisms in lithium/polymer cells", Journal of Power Sources, Vol. 81-82, pp. 925-929, 1999.

instrumented with additional thermocouples with the IR thermal imaging camera. The positions of thermocouples (TC1, TC2, TC3, TC4, TC5 and TC6) are shown in Figure 94. All of the temperature data was recorded at a sampling rate of 1 Hz.

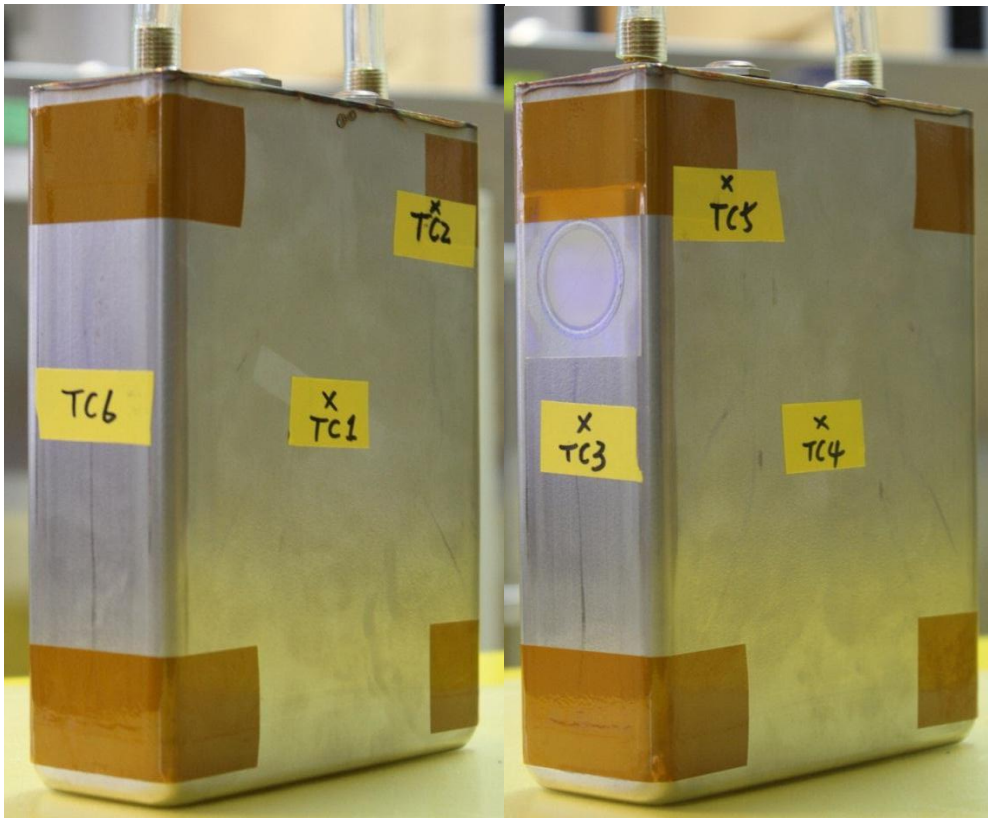

Figure 94 Positions of Thermocouples for APU Start Simulation

Figure 95 and Figure 96 show the IR imaging and thermocouples readings, respectively, under -18 °C conditions. From the thermal image, three points, P1, P2 and P3, were selected. Some areas such as the corners and top area of the cell casing can lead to a false high reading. The reason is that there was a tape in those areas and the emissivity for the taping materials is different from that of the metal casing. As calibration of the IR camera requires input on the emissivity of the material, for now an estimate for emissivity of stainless steel was inputted and so there will be some error. The main purpose of the IR camera was to capture potential hot spots that might be missed from a discrete number of thermocouples. According to the data from IR camera, the maximum temperature rise before and after APU start was more than 18 °C for the APU start simulation even under such cold conditions as -18 °C. However, the temperature reading from thermocouples showed approximately

24 ˚C temperature rise as maximum. It is expected that the maximum temperature rise shall occur around cathode terminal. Convection currents within the test chamber may also have an effect on the temperature readings.

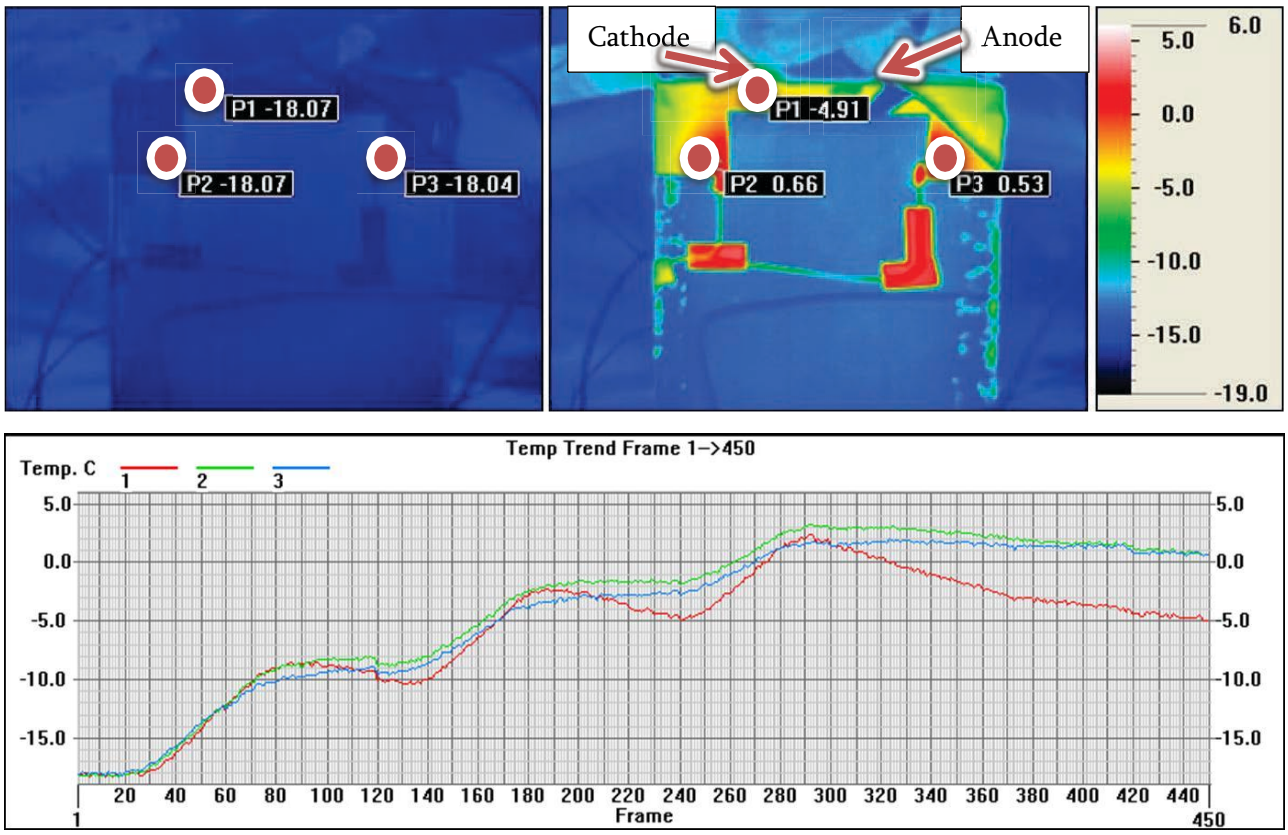

Figure 95 IR Thermal Imaging Data of Cell 3 from Battery 459 during APU start at -18 ˚C

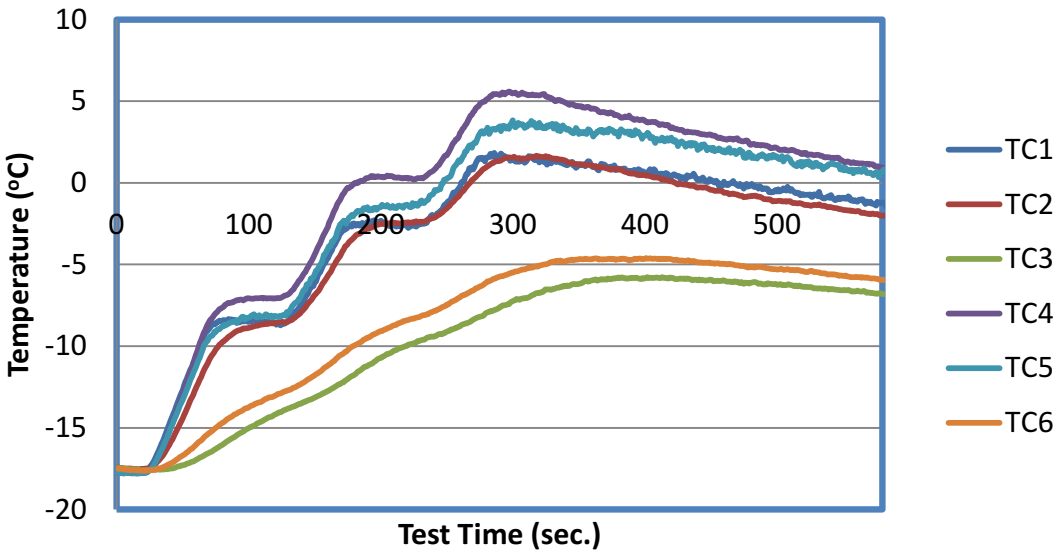

Figure 96 Thermocouple Data on cell 3 from Battery 459 during APU start at -18 °C

Similarly, Figure 97 shows the IR imaging of cell 3 from battery 459 during APU start simulation under 0 °C. According to the IR imaging, P1, which was closer to cathode terminal, showed the largest temperature rise (18 °C) among all. According to Figure 98, the maximum temperature rise based on thermocouple readings was about 15 °C. For the APU start under 0 °C, the location for the maximum rise in temperature will generally be in proximity of the cathode terminal.

The data for 25 °C test temperature is given in Figure 99 and Figure 100. Similar to 0 °C test conditions, the maximum temperature rise occurs around cathode terminal and was approximately 14 °C according to IR imaging and 8 °C according to the thermocouples. Likewise, the temperature profiles of cell 5 and cell 7 of battery 459 for APU start simulation under -18 °C, 0 °C and 25 °C are given in Figure 101, Figure 102 and Figure 103, respectively. The temperature profiles for all that cells at identical temperature condition were similar. Among all different test temperatures, the lowest temperature can always introduce more impedance (and polarization effect) within cell so that the observed temperature rise can be larger.

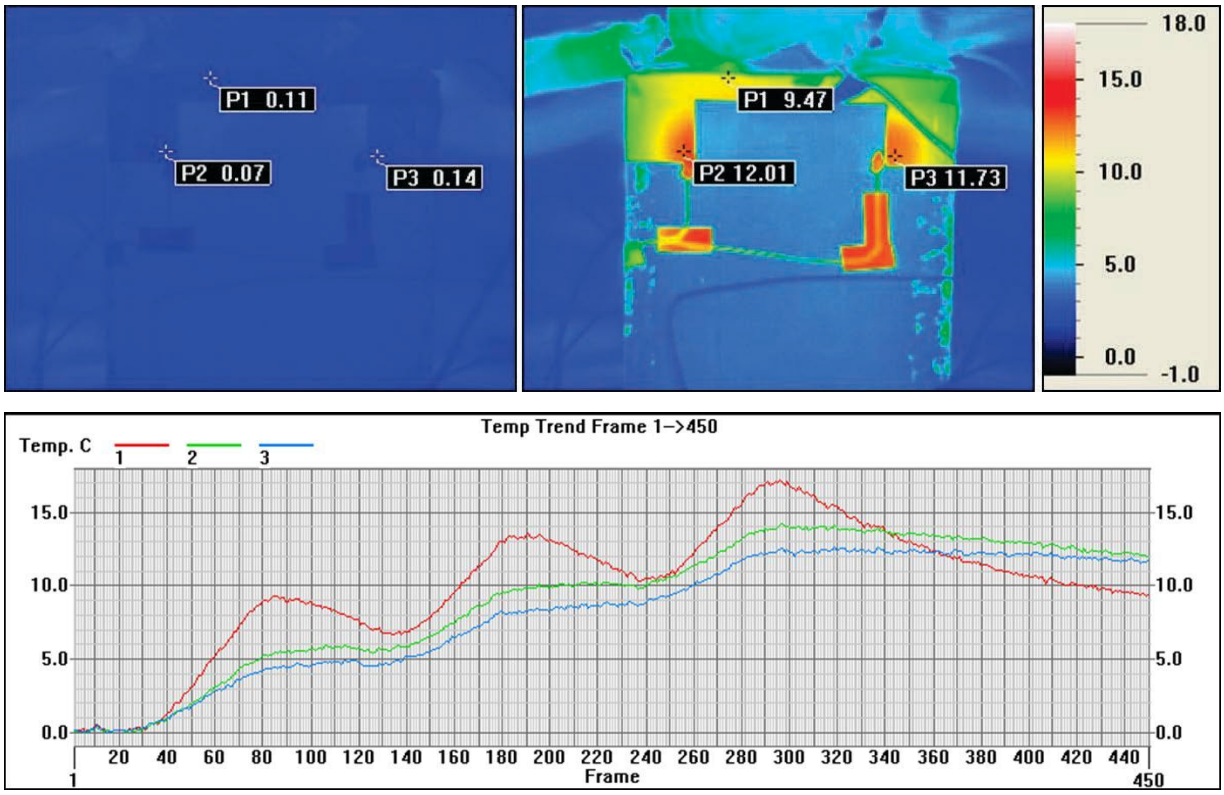

Figure 97 IR Thermal Imaging of Cell 3 from Battery 459 during APU start at 0 °C

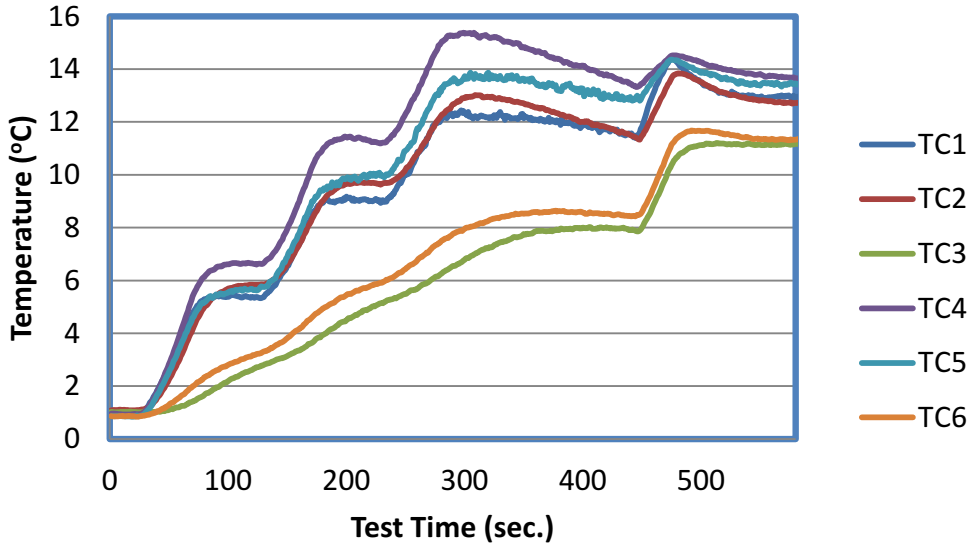

Figure 98 Thermocouple Data from cell 3 of Battery 459 during APU start at 0 °C

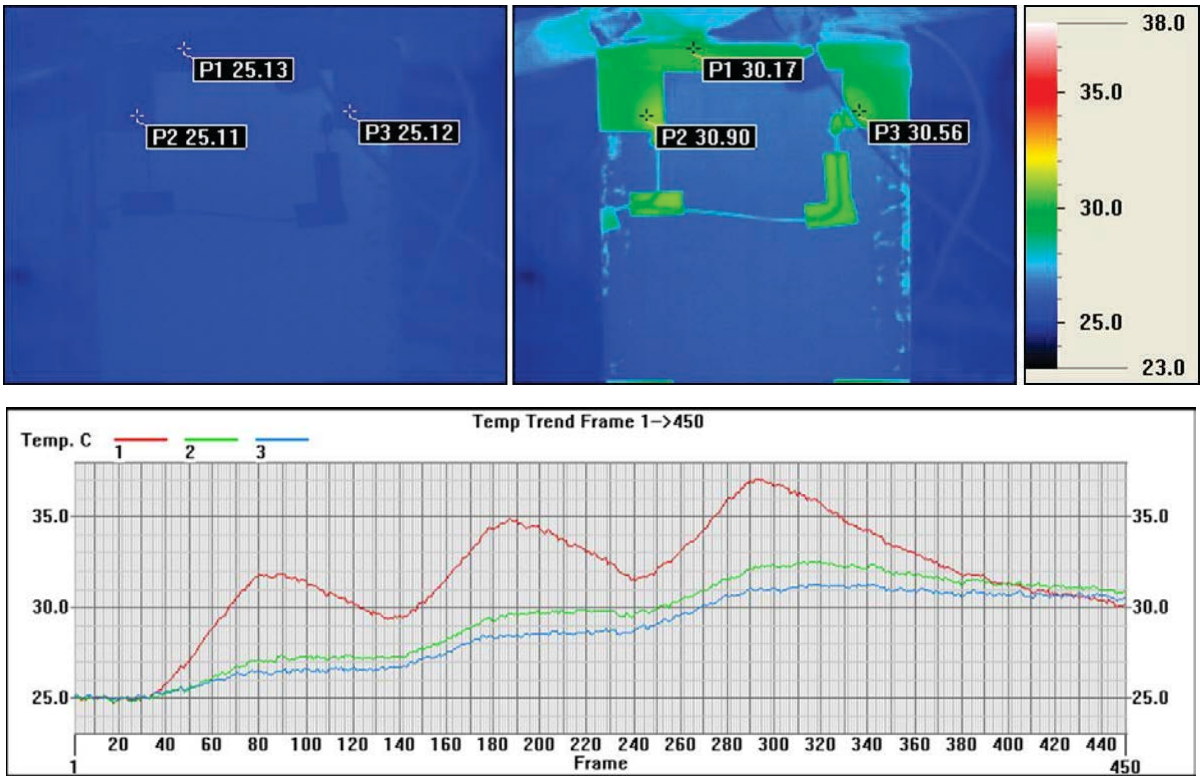

Figure 99 IR Thermal Imaging of Cell 3 from Battery 459 during APU start at 25 °C

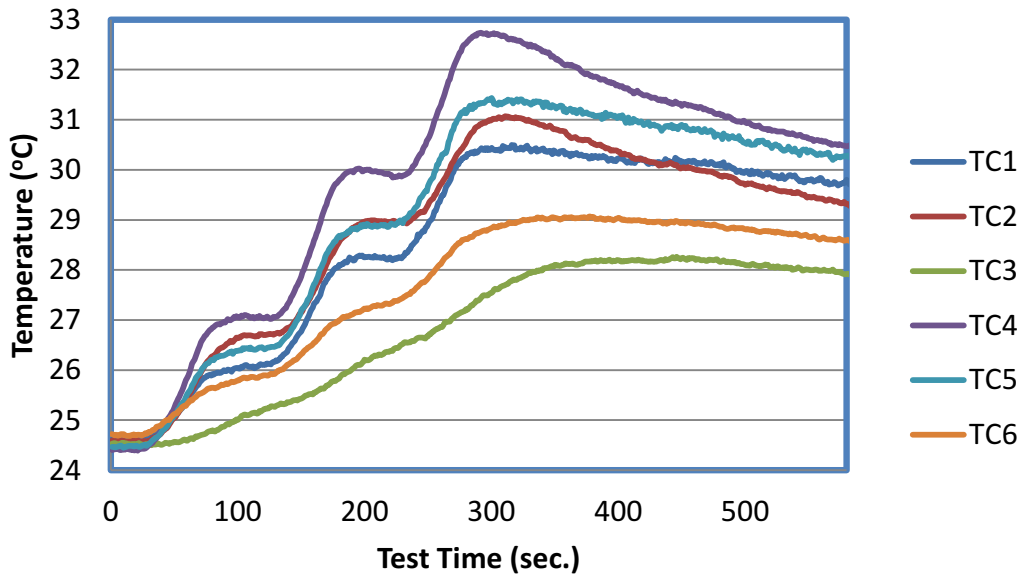

Figure 100 Thermocouple Data from cell 3 of Battery 459 during APU start at 25 °C

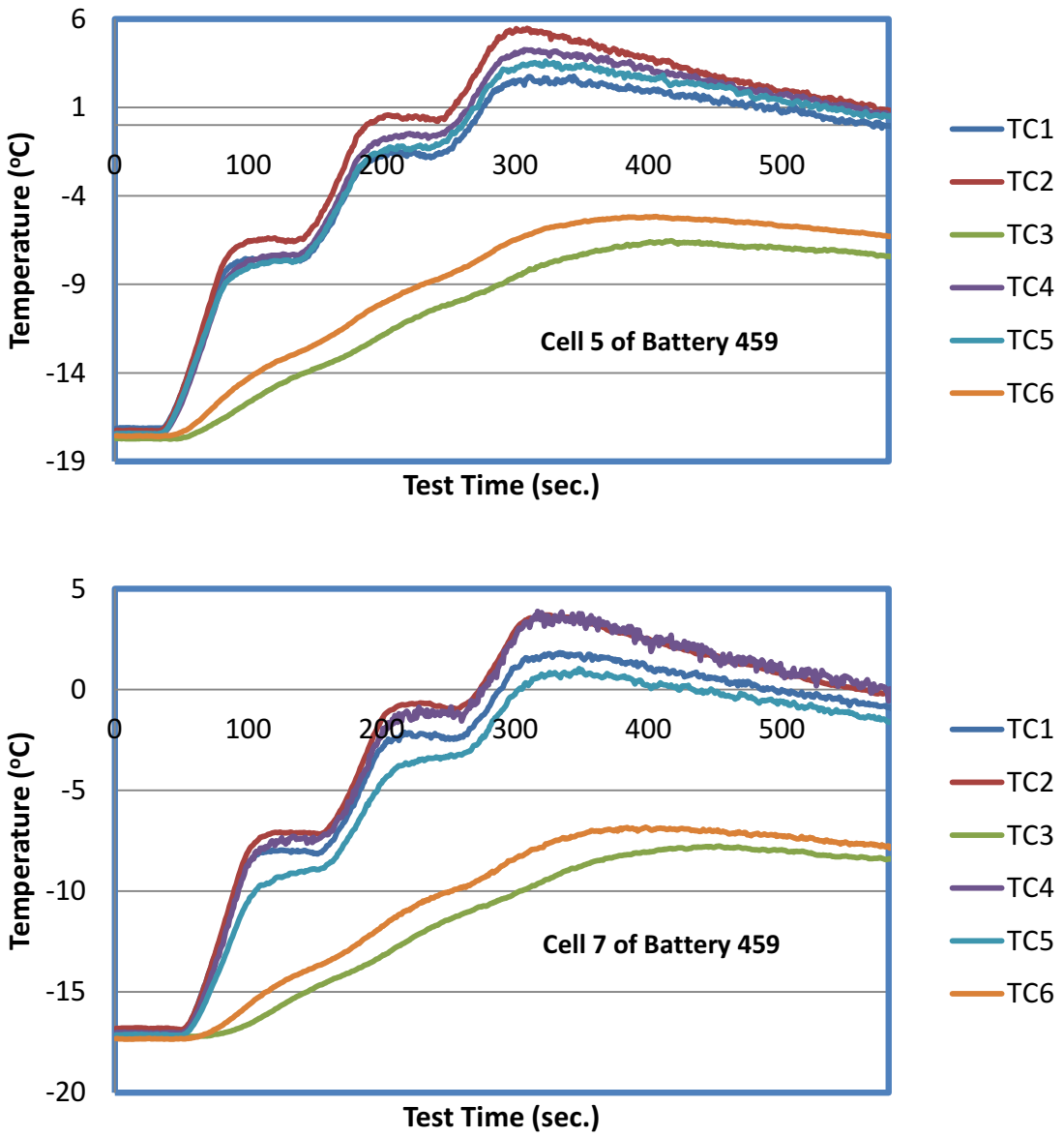

Figure 101 Thermocouple Data from cell 5 and cell 7 of Battery 459 during APU start simulation at -18 °C

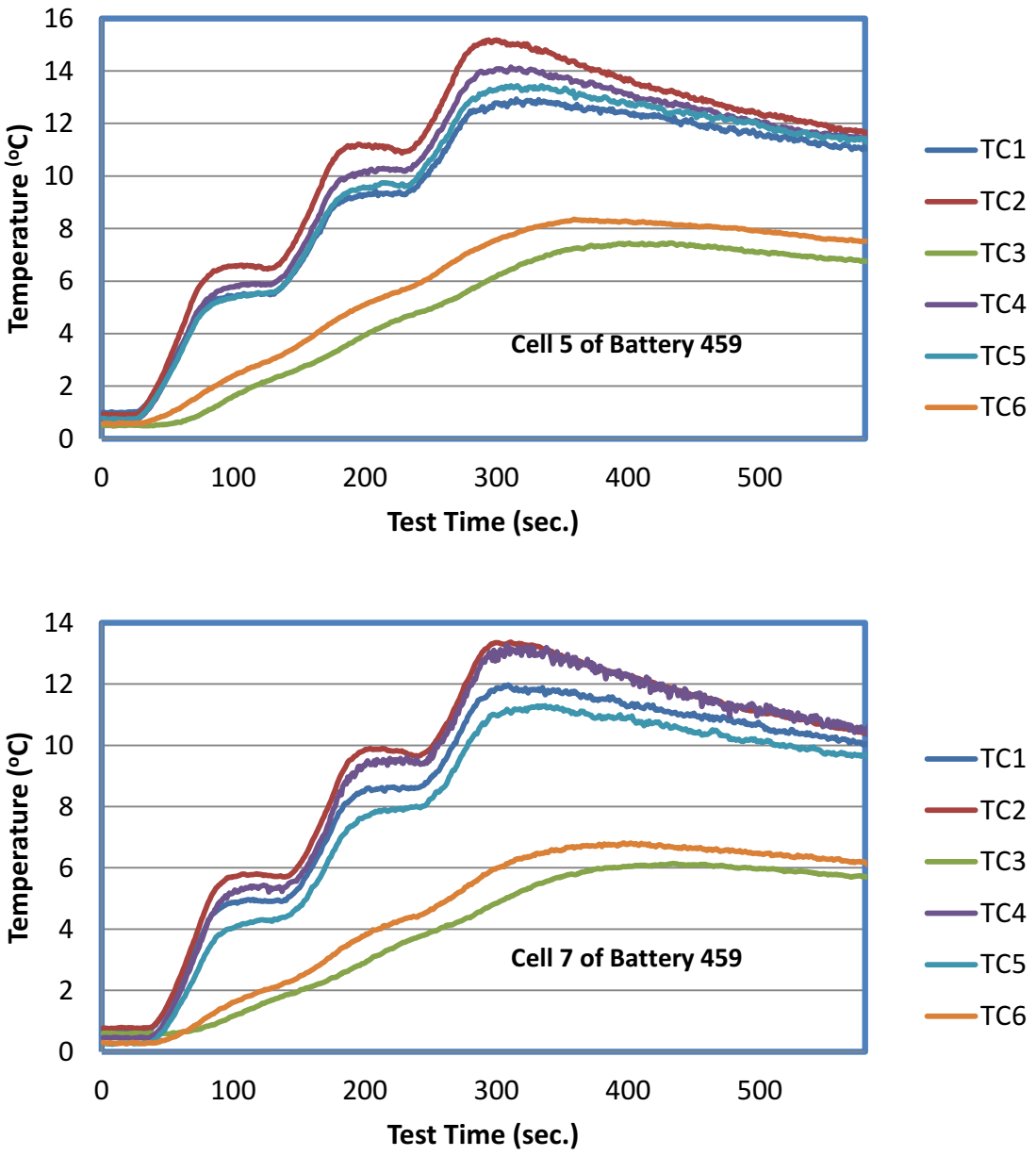

Figure 102 Temperature readings from Thermocouples on cell 5 and cell 7 of Battery 459 while APU start at 0 °C

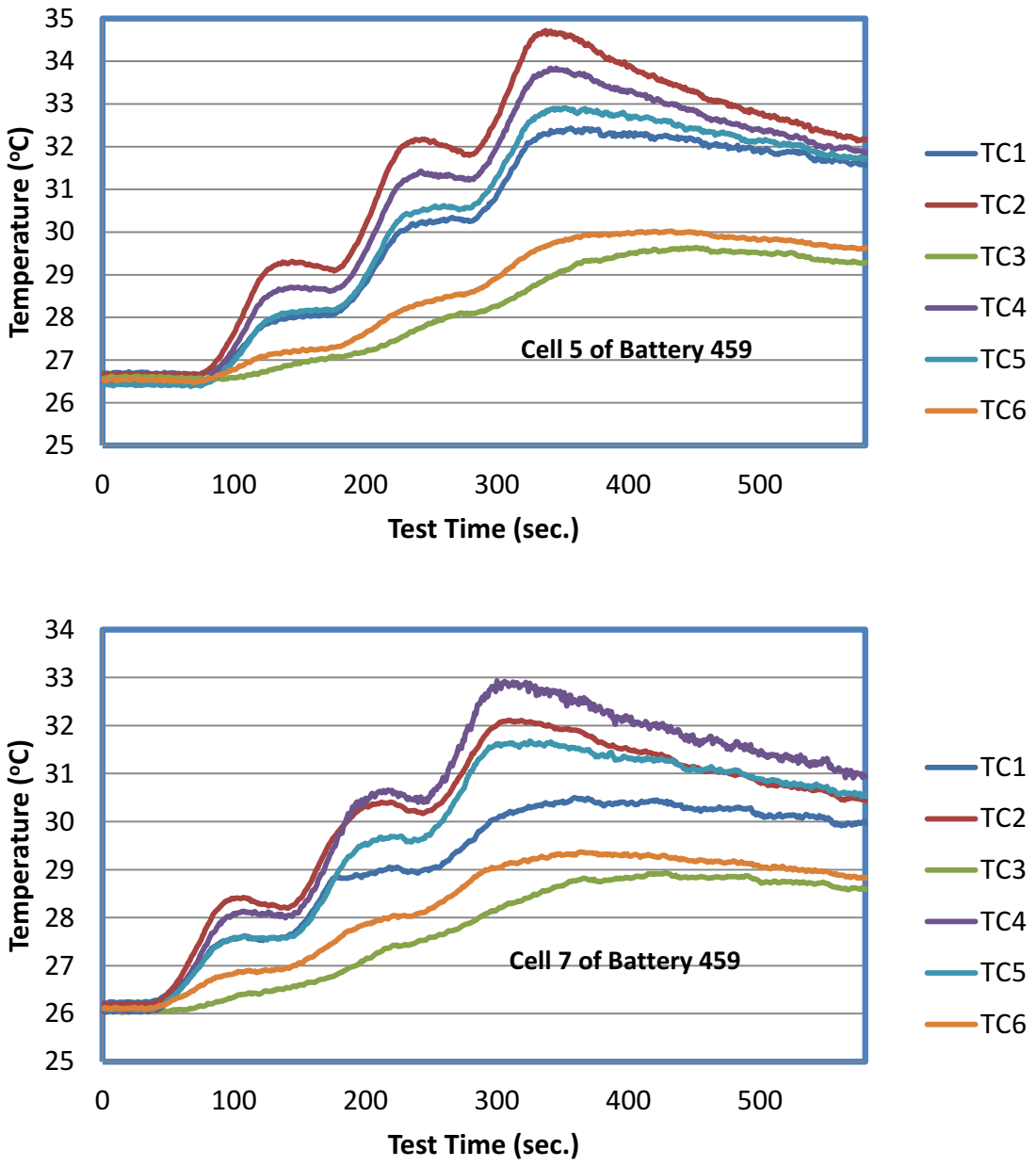

Figure 103 Thermocouple Data on cell 5 and cell 7 from Battery 459 during APU start at 25 °C

With the temperature rise data from APU start simulations under different test temperature and the heat capacity of LVP65 cell, discharging efficiency of the cell as the function of temperature can be estimated. Using cell 7 of battery 459 as the example, the mass, heat capacity and the maximum

temperature rise at the first high rate discharging step [redacted] in APU start are all summarized in

Table 23. In addition, the relation between discharging efficiency and test temperature is further sketched in Figure 104. The lower test temperature will always induce greater impedance within cell, thereby generating more heat and lowering discharging efficiency.

Table 23 Calculation of Discharging Efficiency in 1st run of APU start [redacted] under 25, 0 and -18°C

Test Sample	Cell 7 of Battery 459 (M=2751.5g, C_p = 1.074 $J/g \cdot$ °C)		
Test Temperature	25 °C	0 °C	-18 °C
Max. Temperature Rise; ΔT	2 °C	5 °C	11 °C
Electrical Energy; E	99 kJ	90 kJ	77 kJ
Heat Generation; $H=M*C_p*\Delta T$	6 kJ	15 kJ	32 kJ
Discharging Efficiency; E/(E+H)*100%	94.3%	85.7%	70.6%

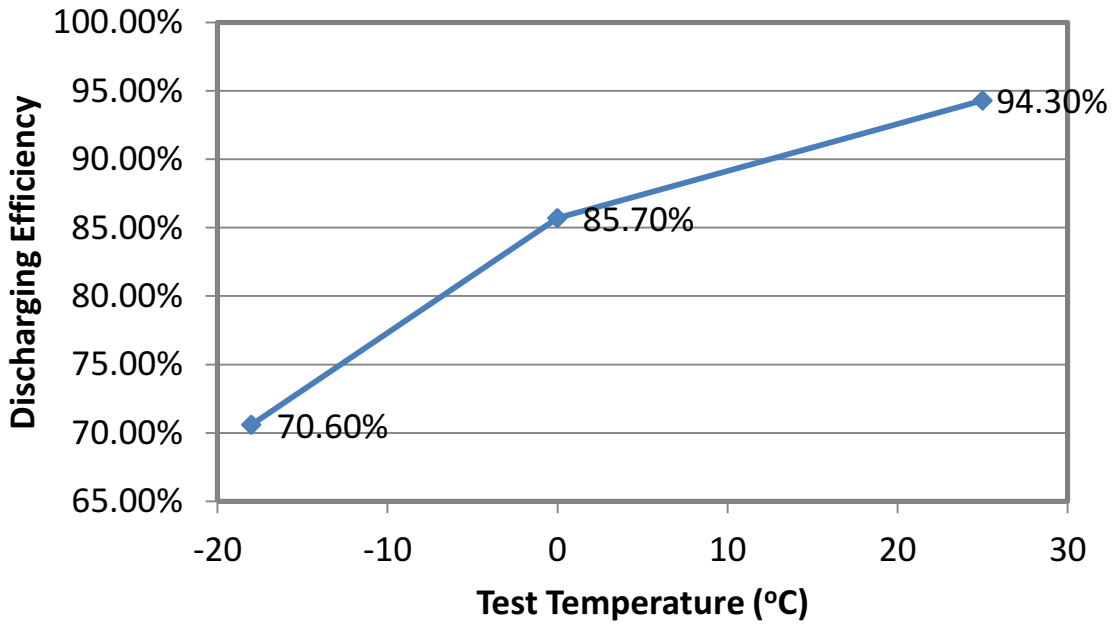

Figure 104 Relation between Test Temperature and Discharging Efficiency in 1st run of APU start [redacted] on Cell 7 of Battery 459

In addition, the current and voltage profiles from cell 3, 5 and 7 of battery 459 during APU start at -18, 0 and 25 ˚C are shown in Figure 105, Figure 106, and Figure 107. The voltage drop was increasing as the cell was discharged under lower temperatures. The voltage readings for cell 3 and cell 5 reached the minimum voltage specifications of 2.75 V during the first cycle of discharging under -18 ˚C. Only cell 7 could be operated normally with the voltage reading staying above 2.75 V. That also means the polarization effect under low temperature was getting better.

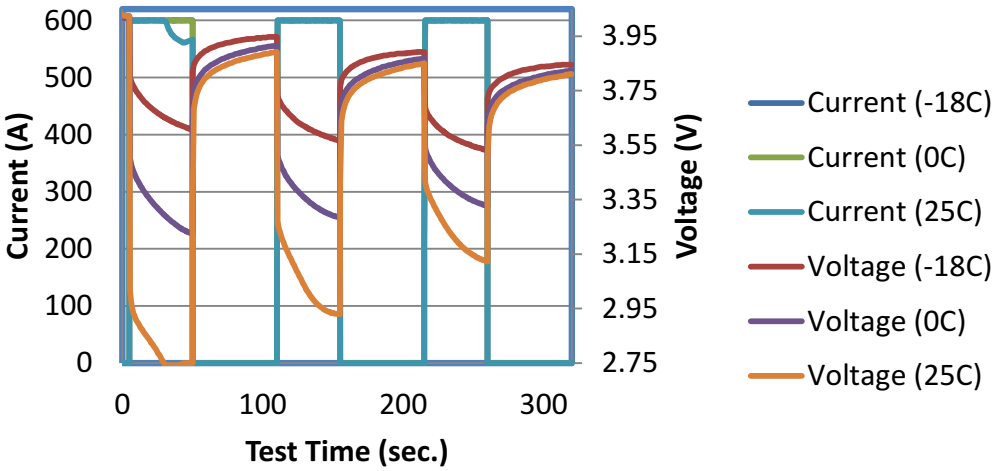

Figure 105 Voltage and Current Profiles of Cell 3 from Battery 459 during APU start at -18 ˚C, 0 ˚C and 25 ˚C

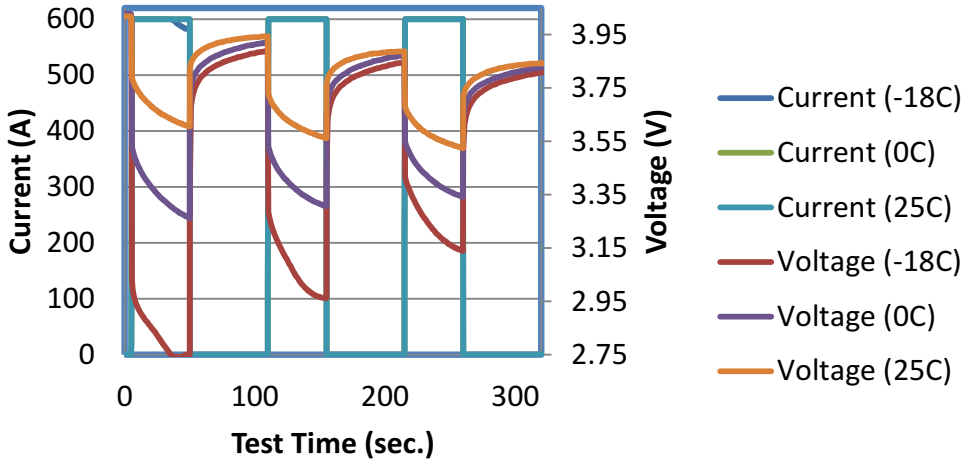

Figure 106 Voltage and Current Profiles of cell 5 from Battery 459 during APU start at -18 ˚C, 0 ˚C and 25 ˚C

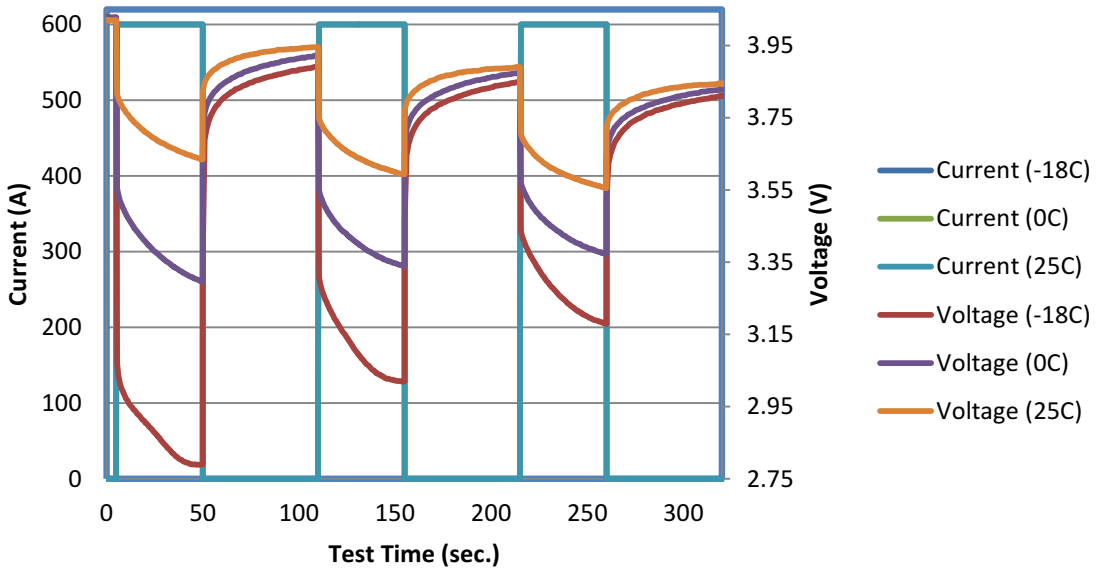

Figure 107 Voltage and Current Profiles of Cell 7 from Battery 459 during APU start at -18 ˚C, 0 ˚C and 25 ˚C

BATTERY LEVEL TEST DESCRIPTIONS

Simulated APU Starts

Testing described under task A.1.B of the contract was designed to study the effect of auxiliary power unit (APU) starts on the battery with the battery charging system. The APU start was performed at different ambient conditions. Upon the receipt of the battery #459, a 'Battery Inspection Datasheet' documented the condition of the device prior to the formal testing. This datasheet measured and recorded several key criteria such as battery voltage, cell voltage, AC / DC resistances, ambient conditions, and serial numbers (see Appendix B).

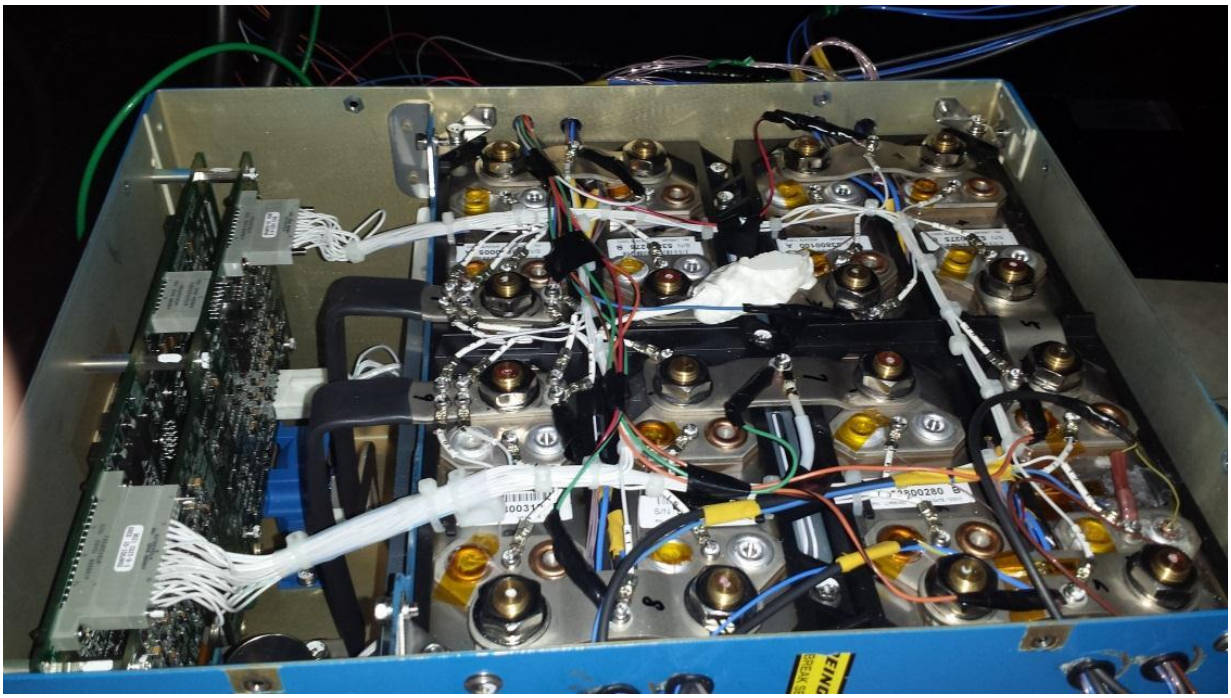

Figure 108 Instrumented Battery Assembly

Instrumentation

- 8 thermocouples were installed on each cell, except for cell #6 which was instrumented with 16 thermocouples.

- The voltage at each cell and the overall assembly was monitored throughout all tests.
- A strain gauge was added to the large face of each cell in the assembly.
- Communication Signals from the Battery Management Unit (BMU) were monitored.
- Current from test system and on the ground conductor was monitored utilizing Hall Effect Current Sensors.
- Infrared images were taken of the battery with the cover removed during the last cycle of each test to provide full field temperature contours.
- Some additional instrumentation:
    - Strain Gauge to the top of Cell 5.
    - Strain Gauge to the Cell 5 / Cell 6 Tie Bus Bar.
    - Voltage Measurement from the rivet on the positive terminal of cell 5 to the rivet plate on the positive terminal of cell 5.

APU Start Testing Procedure

The intent was to charge the battery utilizing the typical aircraft battery charger and simulate three APU starts. The battery / battery charger system was connected directly to a programmable DC Load which was programmed to discharge the battery (Figure 109). The DC Load consisted of a high power programmable DC load manufactured by NH Research, Model 4760.

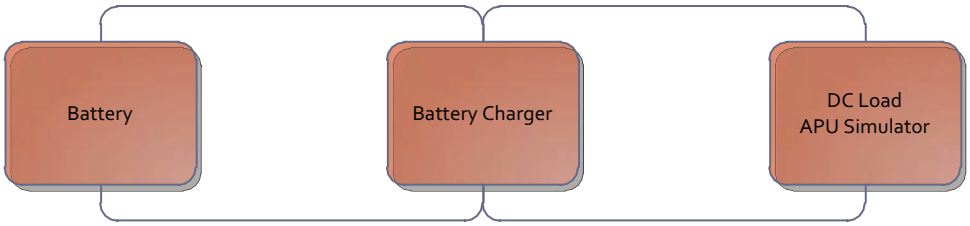

Figure 109 Basic Topology of Test Circuit

- Charging Procedure – The battery was charged utilizing the airplane battery charger which applies a constant current mode of 46 amperes until a voltage of 32.2 volts is reached. Once

32.2 volts is reached the charging device is switched to constant voltage mode which will maintain the 32.2 volt condition.

- Discharging Procedure – The battery was discharged utilizing a constant power draw of 18 kW for 45 seconds. The load was then switched off for 60 seconds. The load was again switched into the circuit for 45 seconds. This was repeated for a total of 3 times simulating APU starts with two rest periods.

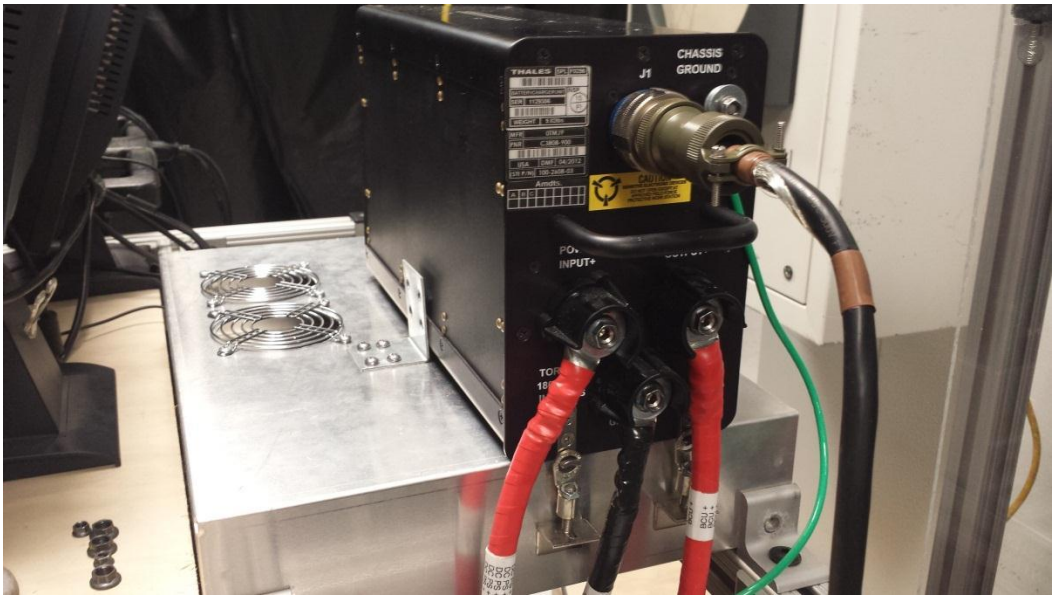

Figure 110 Battery Charger Installed onto 19.8 CFM Forced Ventilation Box

The battery charger was allowed to charge the battery throughout the entire discharge cycle (3 APU starts). At the end of the discharge cycle the battery charger was allowed to fully charge the battery. This entire test was repeated for a total of 5 times per ambient temperature (15 APU starts per ambient temperature). The test was first completed as 25 °C, 0 °C and then -18 °C. During the last 3 APU starts the test was performed with the cover of the battery removed. This allowed infrared thermal imaging of the top of the cells.

Figure 111 Battery Connections in the Test Chamber

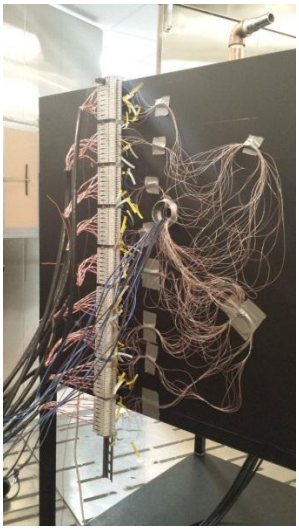

Figure 112 Thermocouple Connections Outside of the Chamber

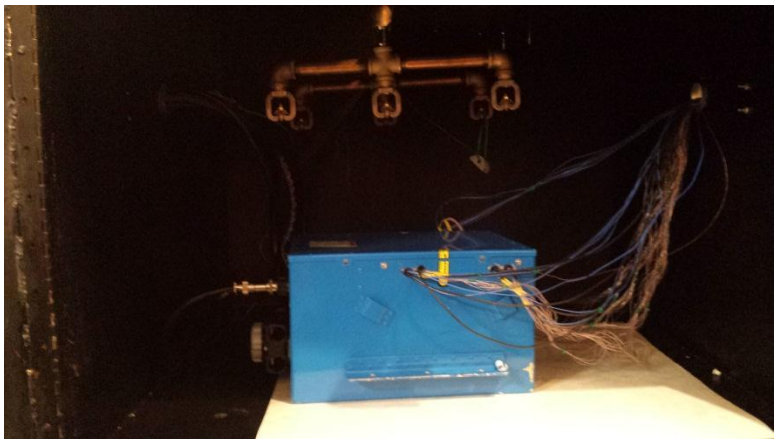

Figure 113 Battery in Test Chamber

Current Oscillations and Interruptions

Testing described under task A.1.C was designed to study the effect of current oscillations and interruptions on the internal state of the cells. The current interruptions were introduced during the constant current (CC Mode) portion of the battery charge procedure. The current oscillations were introduced in the constant voltage (CV Mode) portion of the battery charge procedure. The test plan was designed to first generate a control (clean) signal response. The data from this clean section could then provide a comparative benchmark for the abnormal current loading tests. Upon the receipt of the battery #436, a 'Battery Inspection Datasheet' documented the condition of the device prior to formal testing. This datasheet measured and recorded several key criteria such as battery voltage, cell voltage, AC/DC resistances, ambient conditions, and serial numbers (see Appendix B).

Instrumentation

- 8 thermocouples were installed on each cell, except for cell #6 which was equipped with 16 thermocouples.
- The voltage at each cell and the overall assembly was monitored throughout all tests.
- A strain Gauge was installed on the large face of each cell in the assembly.
- Communication Signals from the Battery Management Unit (BMU) were monitored.
- Current from test system and on the ground conductor were monitored utilizing Hall Effect Current Sensors.

Clean Test Procedure

This testing was designed to establish a baseline performance for the cells in the battery. The basic idea was to charge the battery utilizing a clean constant current source and a clean constant voltage source. The battery was connected directly to programmable regenerative DC power Source/Load which was programmed to charge and discharge the battery. The clean testing was conducted without the battery charger in the circuit.

Figure 114 Clean Battery Cycling Circuit Topology

The DC Regenerative Load / Source consisted of a high power battery charge / discharge test system manufactured by NH Research, Model 9200-4960. During the testing the battery will be charged and discharged with is to be defined as follows:

- Charging Procedure – The battery was charged utilizing a constant current mode of 46 amperes until a voltage of 32.2 volts was reached. Once 32.2 volts was reached the charging device was switched to constant voltage mode which maintained the 32.2 volt for the duration of the soak.
- Discharge Procedure – The battery was discharged utilizing a constant current draw of 50 amperes until the battery voltage reached 31.0 volts. The load was then switched to a constant current draw of 10 amperes until the battery voltage reached 30.9 volts. The load was then switched to a constant draw of 5 amperes until the battery voltage reached 30.8 volts. Once a voltage of 30.8 volts was reached the discharge process was halted.

This process was run three times. In each test the battery was discharged and charged. The battery was initially in a discharged state. During the first test the battery was charged and exposed to 8 hours in the constant voltage mode. During the 2nd and 3rd tests the battery was discharged and then charged and exposed to 2 hours in the constant voltage mode.

Noisy Test Procedure

The intent of this test was to assess the effects that current oscillations and interruptions might have on the battery/cell. The basic test methodology was similar to the Clean Test Procedure. The variable in the Noisy testing was that current interruptions were artificially created and the current oscillations from the normal aircraft battery charger were allowed to progress.

- Current Interruptions – The current interruptions were artificially created only during the constant current portion of the charging cycle. The interruption was created by introducing a repeatable 15 millisecond interruption in the current. The aircraft battery charger responded to this current interruption with its own 175 millisecond interruption in current. To maximize any effect that the current interruption may have on the battery/battery charger system the current interruptions were performed three times during each constant current charge. The three current interruptions were introduced 10 minutes after the start of the constant current charge and 30 seconds apart.

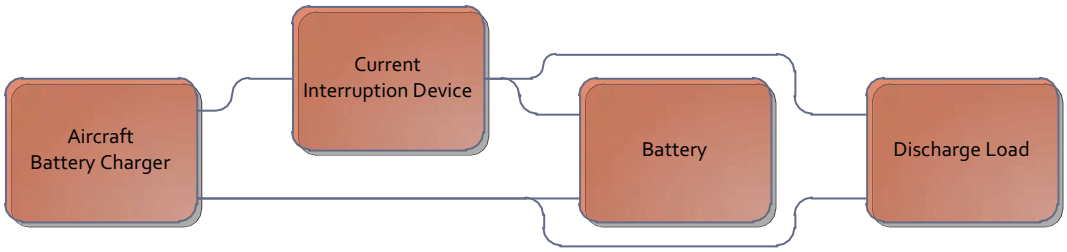

Figure 115 Noisy Testing Circuit Topology

- Current Oscillations – The current oscillations were introduced by the aircraft battery charger during constant voltage mode under normal operating conditions. The current oscillations start when the aircraft battery charger is in constant voltage mode and delivering less than 2.0 amps. The oscillations lasted for about 5 minutes and then degraded to 0 amps. During the current oscillations the current swings approximately 2 amperes.

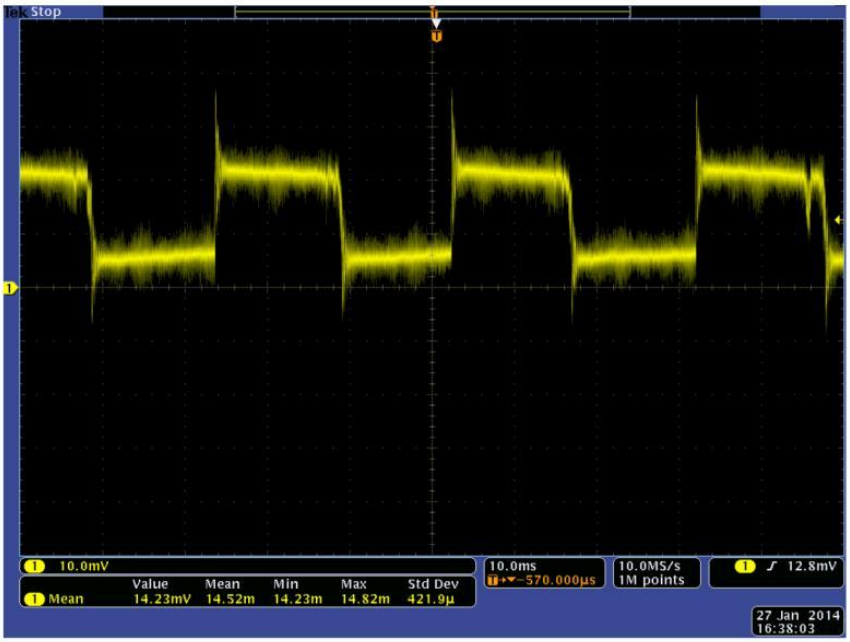

Figure 116 Current Oscillation Present on the Battery Charger (Scope Screen Image)

Similar to the clean test procedure, this process was repeated three times. In each test the battery was discharged and charged. The battery was initially in a discharged state. During the first test the battery was charged and exposed to 8 hours in the constant voltage mode. During the 2nd and 3rd tests the battery was discharged and then charged and exposed to 2 hours in the constant voltage mode.

BATTERY LEVEL TEST RESULTS AND DISCUSSION

Simulated APU Starts

Because the APU starts were performed on a constant power load on battery 459, the current draw trended higher and higher for each APU start since the battery voltage was dragged down. The currents averaged approximately 620 Amperes at 25 °C, 670 Amps at 0 °C, and 940 Amps at -18 °C. The battery management unit (BMU) Hall-effect current sensor (HECS) readings were beyond the measurable scale during the APU starts (Figure 117). The three negative spikes indicated that the APU load being applied reached a maximum at about 370 Amperes. The current signal then turned positive indicating the aircraft battery charger working in the constant current mode. This was then followed by a downward slope as the charger was working in constant voltage mode.

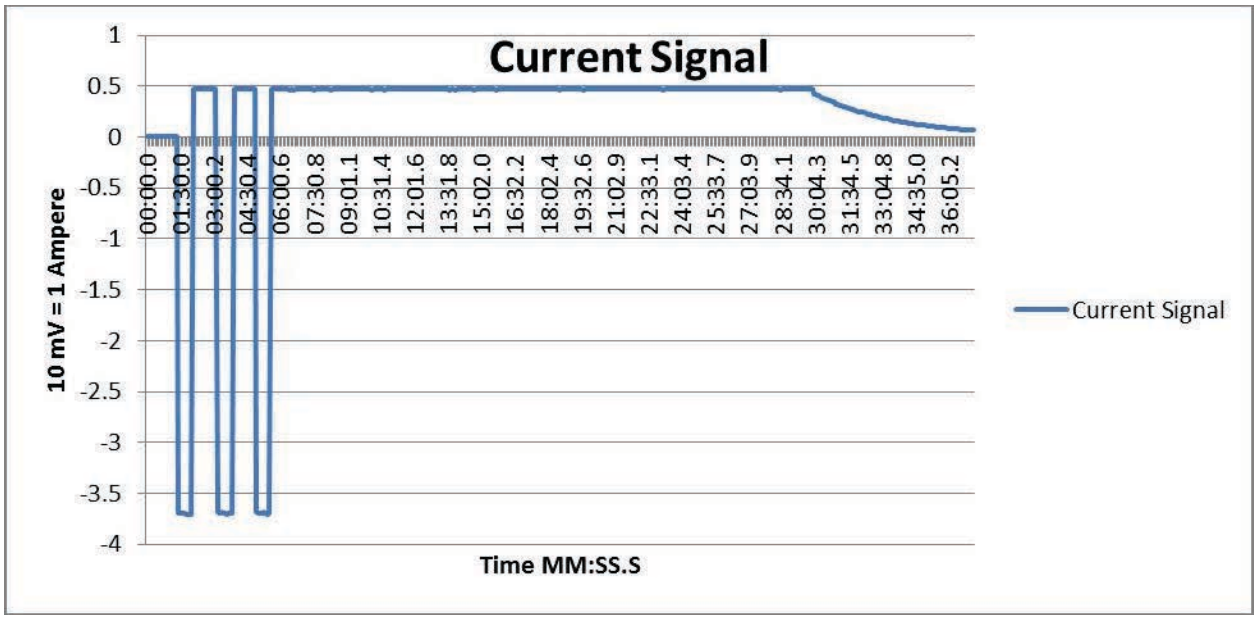

Figure 117 Current Signal Data from BMU HECS

The temperature data from the thermocouples installed on cell 7 from battery 459 under ambient conditions of 25 °C is shown in Figure 118. The three spikes in the data were generated by the three APU starts. As these are cell surface temperatures, they will likely be lower and lag temperature rise within the cell. The data from all the thermocouples were generally in sync except for two outliers. The two thermal outliers were always for thermocouples located on the rivets of the cell. Figure 119

shows a typical thermal recording of the battery without the cover. The higher temperature outlier was always located on the positive (aluminum) terminal of a cell.

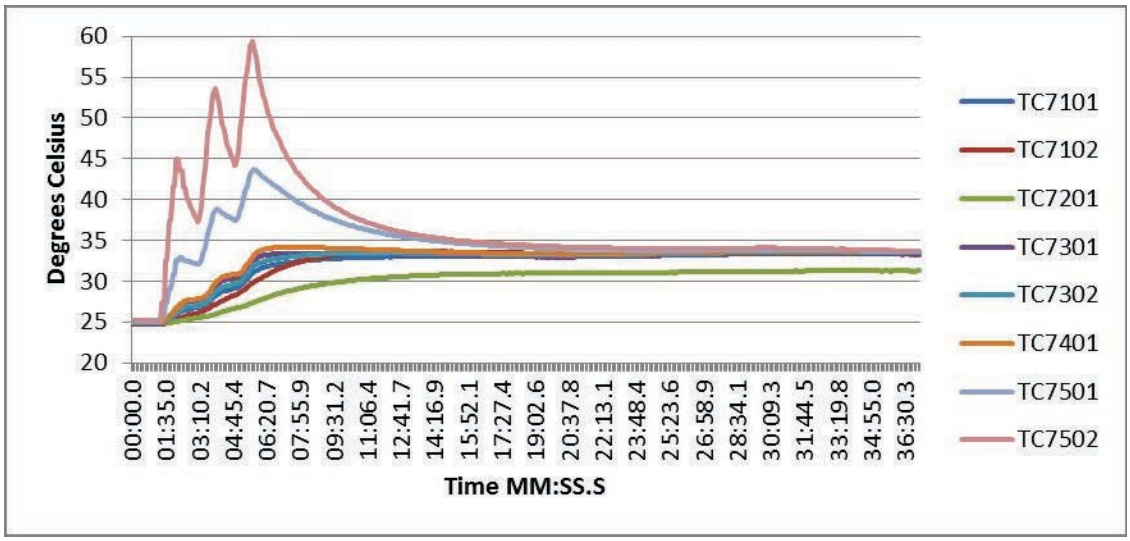

Figure 118 Thermocouple Data from Cell 7

The high temperatures on the positive terminal of cell 5 were of particular concern. They reached about 125 °C (Figure 119 and Figure 120). There was also a trend for some of the rivet thermocouple readings to record higher peak temperatures as additional APU starts were simulated.

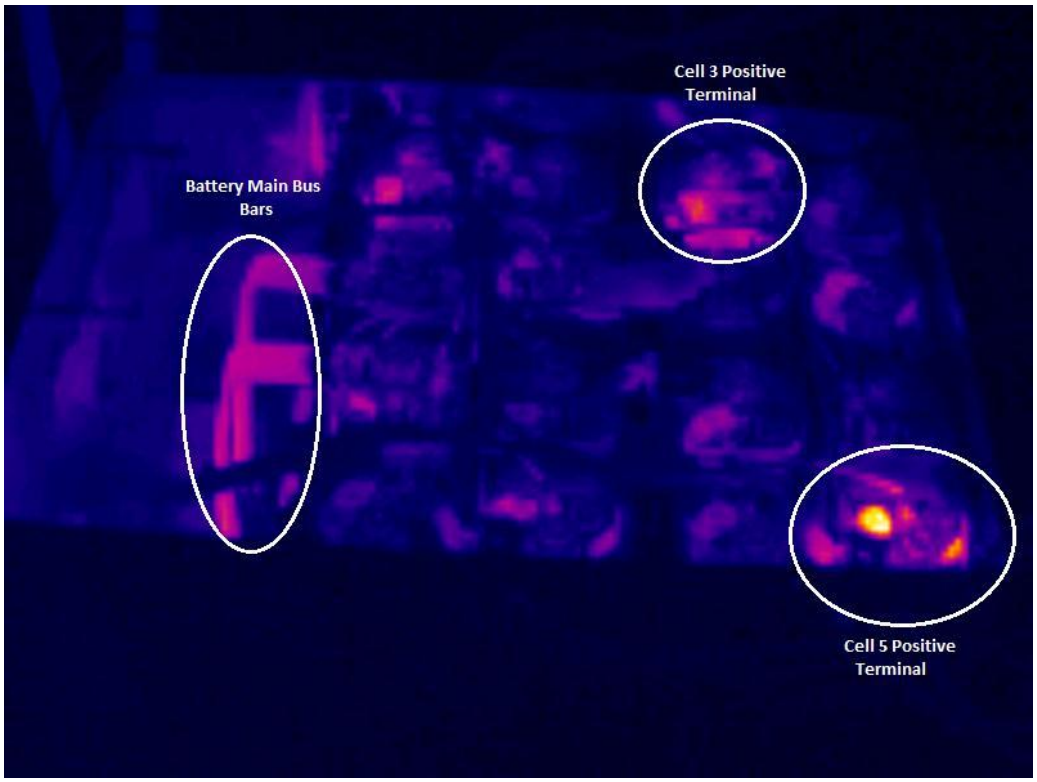

Figure 119 Infrared Thermal Image of the Battery During APU Loading

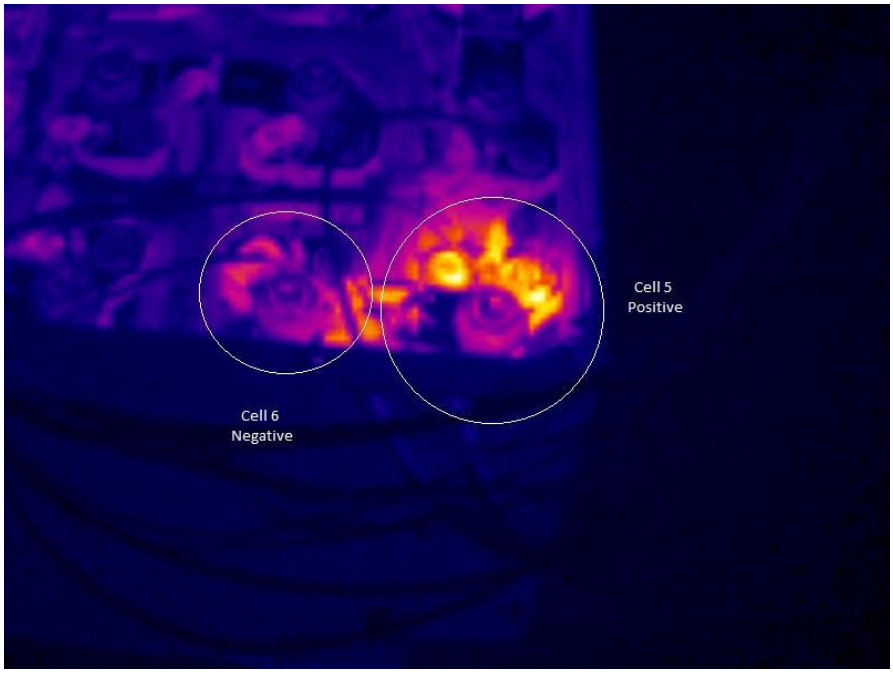

Figure 120 Close-up of the Hot Spot on Cell #5

Next examining the strain gauge data, the cells were clearly swelling. Even this data showed an initial triple local maximum coincident with the three APU start simulations. Figure 121 shows an example of strain gauge readings typical of the cells in the battery.

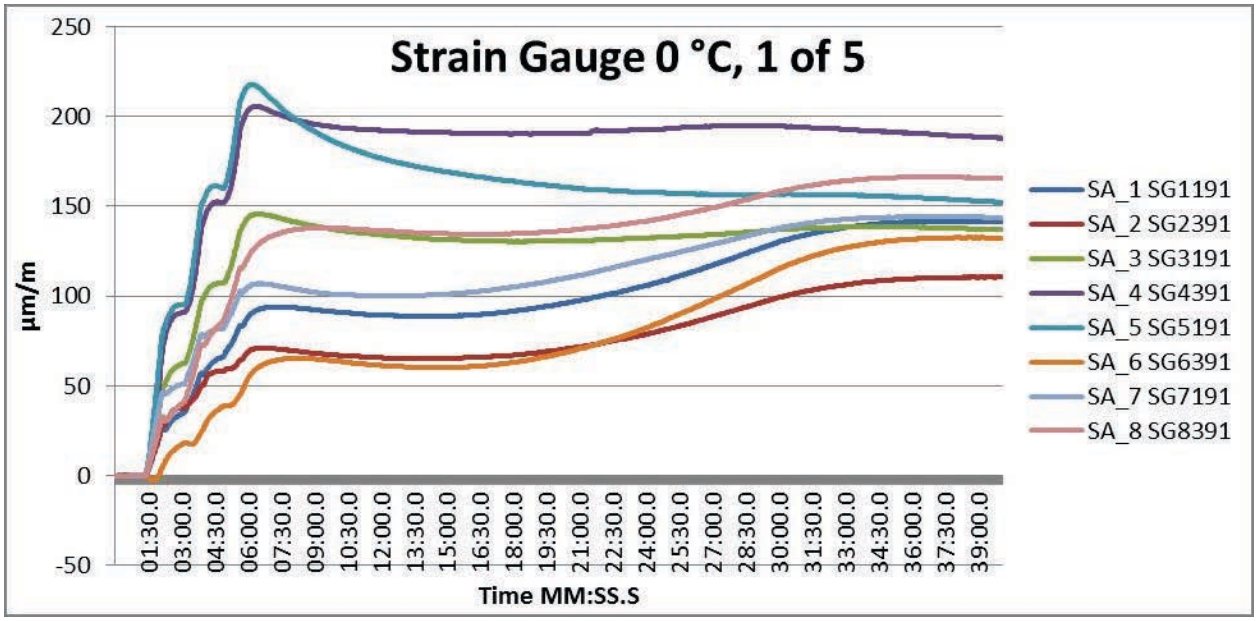

Figure 121 Typical Strain Gauge Data from A.1.B testing under 0 °C conditions

There were a few unusual strain gauge readings only during the 25 °C testing (Figure 122). During most of the APU starts, cell 1, cell 2 and cell 6 were under compression at this temperature. The data recorded on cell 2 displayed very unusual behavior. However, there were no thermal or electrical anomalies to indicate issues with the cell. Thereafter, strain gauge readings from cell 2 only showed tension for all tests at lower ambient temperatures.

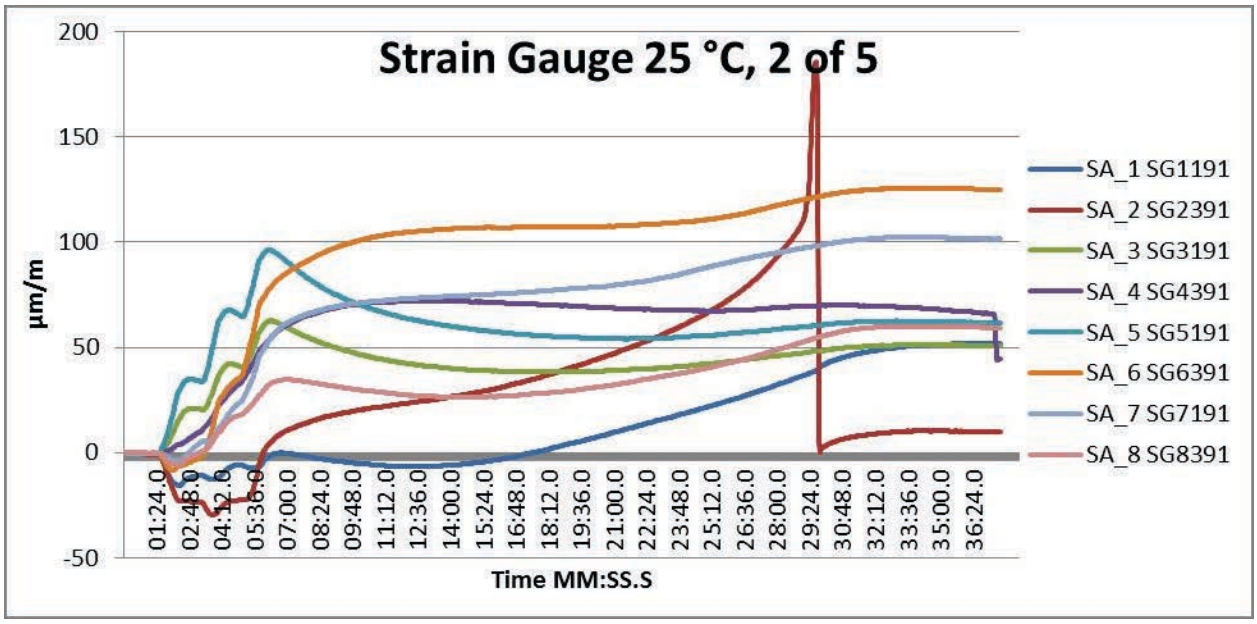

Figure 122 Strain Gauge for Cell 2 during APU, 25 °C, 2 of 5

There were issues with the running the testing at -18 °C. The test setup stopped operating after approximately 22 seconds into the first 45 second APU start. The issue was unresolved due to timing constraints.

The voltages across the cells were fairly consistent during charging across all testing. Cell balancing appeared to begin once the cells were above 4.00 Volts. The cells were fairly unbalanced during discharge. At some points there was a 0.05 Volt difference between the cells. Refer to Appendix B for more details on the data.

APU Start Test EIS measurements

The EIS data before and after the test are shown in Figure 123. Only cell 5 showed an abnormal shift in R_b (bulk material resistance) among all the EIS comparison data. As battery 459 was tested 5 times subjected to APU simulation only, the aging effect was not expected to be a dominant factor to cause a noticeable change in bulk material resistance[100]. However, given the fact that abnormal heating at

[100] H. Kim et al., "Electrochemical Performances of Lithium-Ion Polymer Battery with Polyoxyalkylene glycol acrylate-Based Gel Polymer Electrolyte", Journal of Materials for Electrochemical Systems 9, 15-20, 2006.

the rivet for the positive terminal of cell 5 was observed during testing, it is reasonable to suspect that some internal material decomposition had taken place due to the abnormal heating. Such changes within the cell can alter the ohmic resistance of bulk material and hence register as a change R_b value of the EIS. This strongly shows the value of EIS in non-destructively gaining information on the internal state of a cell. Regarding the comparison of R_{ct} (charge transfer resistance) data, cell 1 and cell 5 showed almost no change before and after APU cycles. Cell 3 and cell 7 showed a slight decrease in the charge transfer resistance (about 10% decreasing) after A.1.b test. However, the remaining cells, 2, 4, 6 and 8, showed more apparent increase in charge transfer resistance (about 20%-100%). Now small magnitude variations in the R_{ct} value can be easily caused by test setup variations or high sensitivity to cell sample settings such as SOC. But the larger magnitude changes in R_{ct} are consequential and suggest excess local heating at the electrical double layer that can accelerate the degradation of interfacial layers. This shows up as an increase in charge transfer resistance[101, 102]. In other words, the high rate discharging protocol defined in APU start may have an unfavorable short-term effect on cell performance and safety under low temperature conditions. The stability of SEI layer has been demonstrated to be an important contributor to safe operation of lithium-ion batteries[103].

[101] J. W. Braithwaite et al., "Corrosion of lithium-ion battery current collectors", Journal of Electrochemical Society, vol. 146, pp. 448-456, 1999.

[102] J. S. Kim et al., "Characteristics of surface films formed at a mesocarbon microbead electrode in a Li-ion battery", Journal of Power Sources, vol. 91, pp. 172-176, 2000.

[103] P. G. Balakrishnan et al., "Safety mechanisms in lithium-ion batteries", Journal of Power Sources, vol. 155, pp. 401-414, 2006.

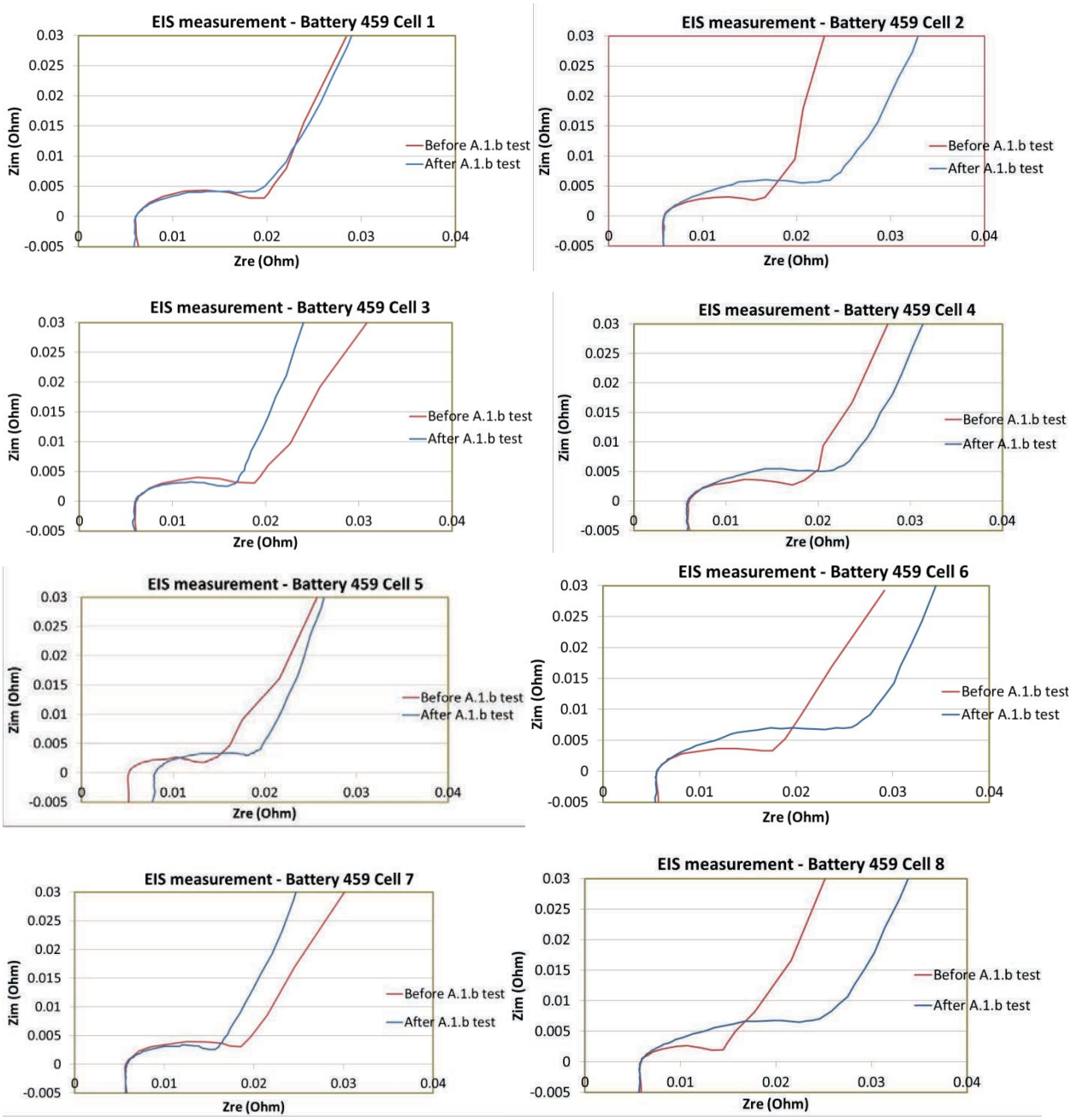

Figure 123 Comparison of EIS data before and after A.1.b test for Cells from Battery 459

Noisy Testing

For noisy testing of battery 436, the signal consisted of a 15 millisecond interruption in the current as shown in Figure 124.

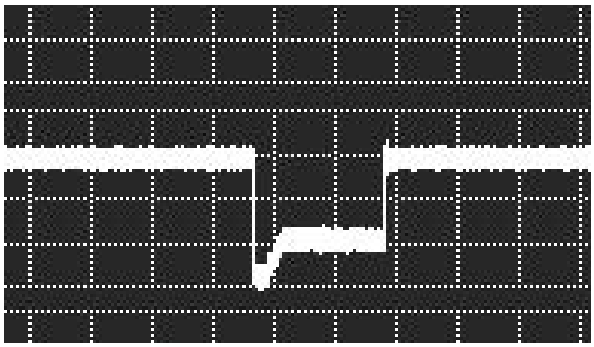

Figure 124 Scope Capture of the Current Interruption (BITE)

Current oscillations were also introduced during the noisy battery testing and the signal is shown in Figure 125.

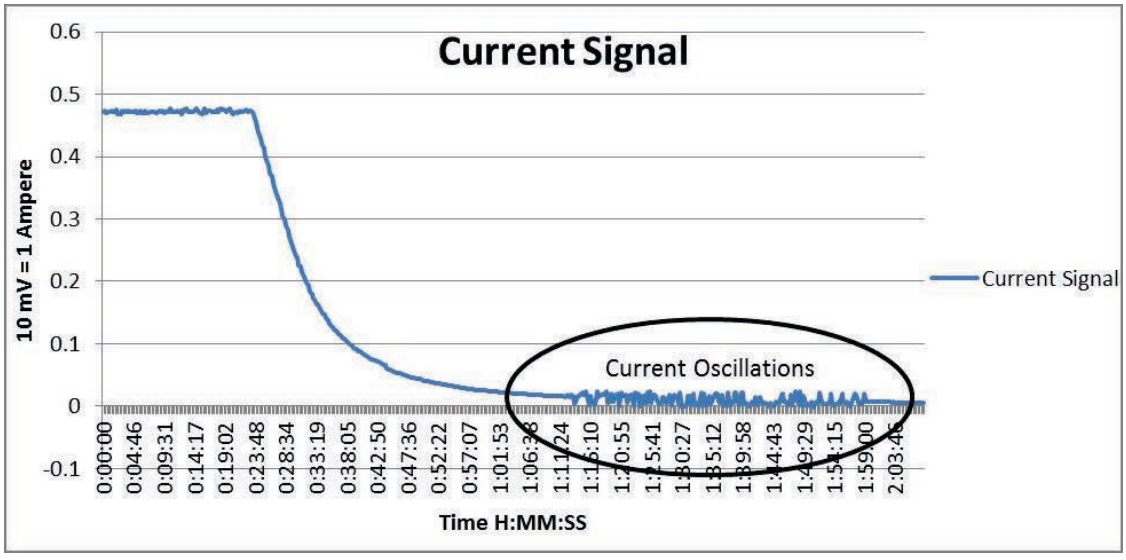

Figure 125 Partial Graph of Current Signal Data from BCU HECS of Noisy Test

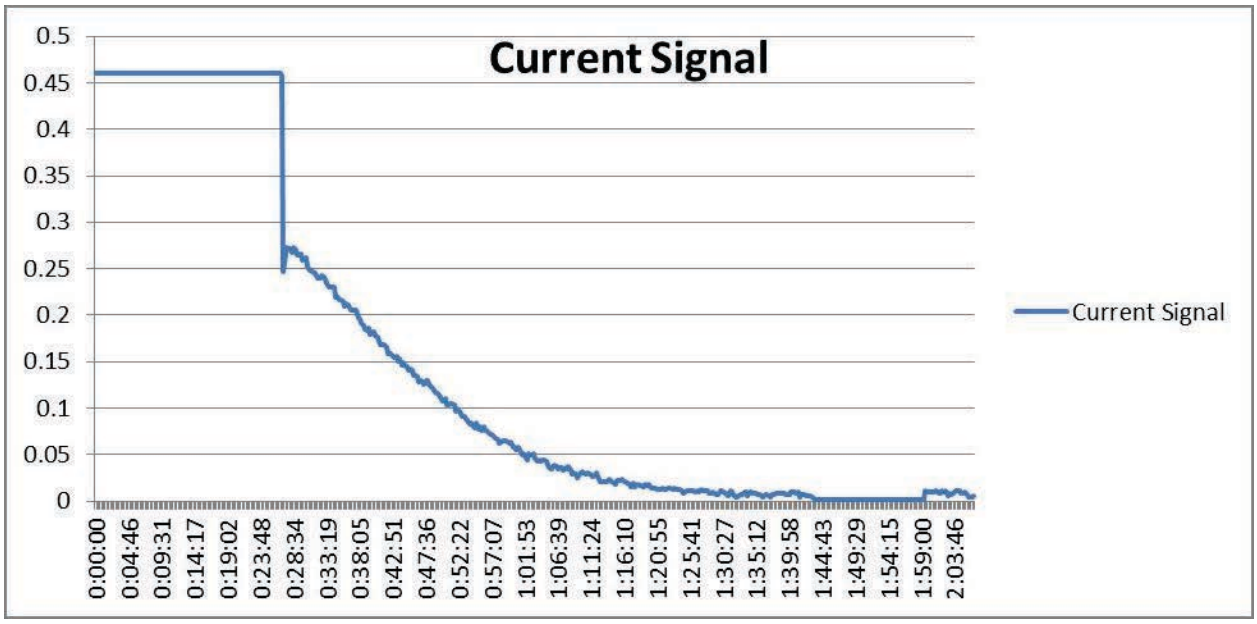

Figure 126 Partial graph of Current Signal Data from BCU HECS of Clean Test

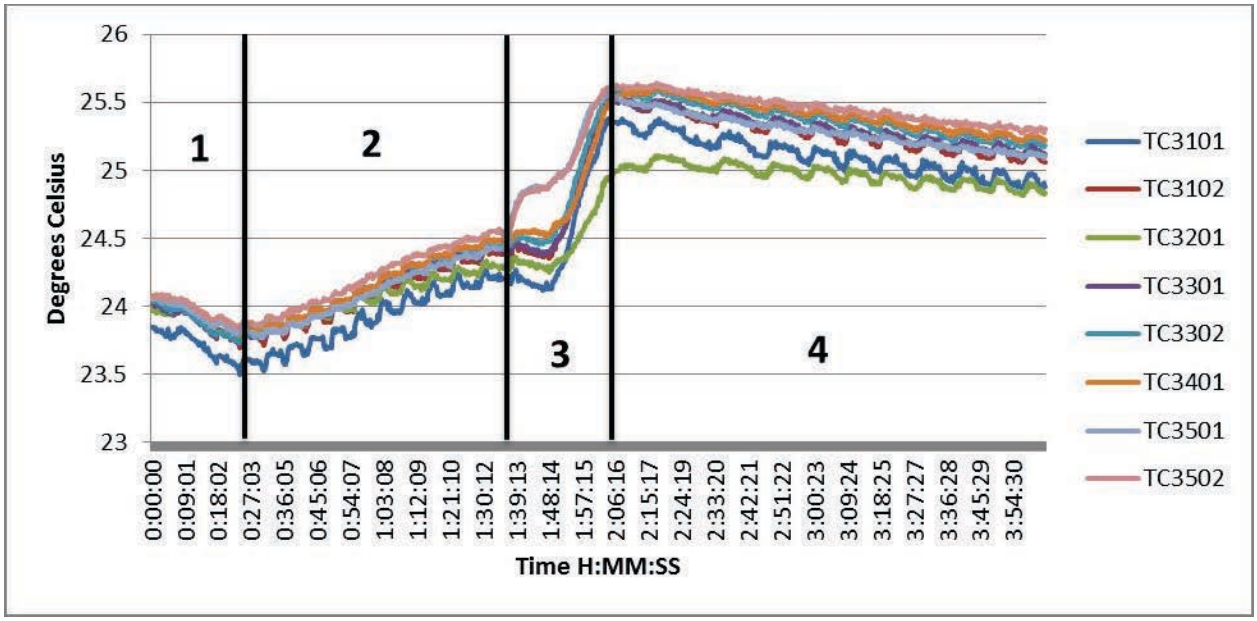

Figure 127 Typical Cell Surface Temperatures Recorded During A.1.c testing

For the Noisy Testing on the battery 436, the cell temperatures were barely higher than those measured during the clean testing. In general, the thermocouple readings ranged from 23 °C to 26 °C and all followed the same basic pattern shown in Figure 127. The temperature data can be divided into zones as follows:

- Zone 1 – slight cooling of the cells during discharge.
- Zone 2 –slight and steady increase in temperatures. This is likely due to the thermal lag between the cell surface temperature and the internal thermal state of the cell.
- Zone 3 – slight cooling as an initial endothermic thermal reaction to the constant current mode of the charge. The two raised outliers are typical of the thermal response seen for these cells and are associated with high temperatures on the rivets of the cell. The endothermic reaction is then overtaken by other heat sources and temperature of the cell spikes to a maximum.
- Zone 4 –slight cooling as a latent thermal reaction to constant voltage mode of the charge cycle.

The strain gauge data recorded compression during the discharging and tension during the charge cycles. The compression and tension of the cells was not uniform across the cells and there was always a consistent outlier (Cell 1 in Battery 439, Cell 5 in battery 459) throughout all the testing. The strain gauge data also followed the same basic model as for the temperature (Figure 128):

- Zone 1 – compression during the discharge.
- Zone 2 – Rapid rise in tension during the constant current portion of the charge.
- Zone 3 – Slow settling during the constant voltage mode portion of the charge.

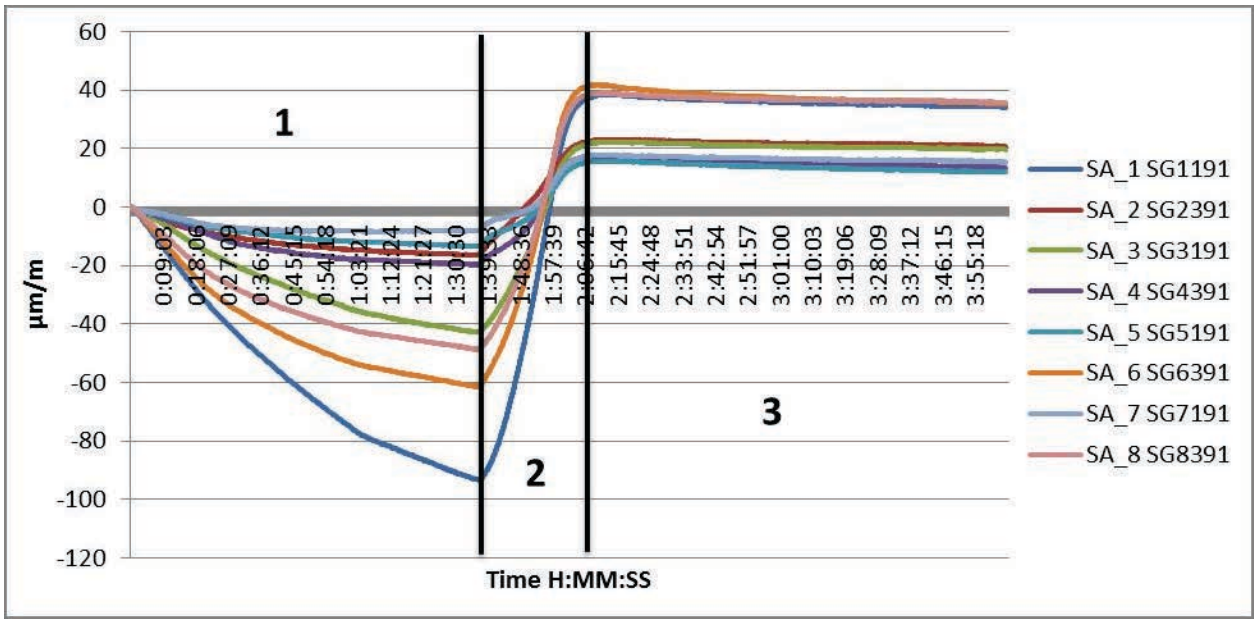

Figure 128 Strain Gauge Data recorded during A.1.c Testing

There was no discernible difference in the strain gauge data between the Clean Testing and Noisy Testing. The voltages across the cells were fairly consistent throughout all the testing. Cell balancing did appear to begin once the cells were above 4.00 Volts. Typically the cells voltages differed by as much as 0.01 volt.

Noisy Test EIS measurements

The comparison of EIS data before and after A.1.c testing is shown in Figure 129[104]. There is almost no change in the bulk resistance, R_b. Except for cell 5, all other cells showed a decrease in R_{ct} (charge transfer resistance) after A.1.c test. The EIS has indicated that the pulse noise has no discernible (or possibly favorable) effect on the battery performance. Cell 5 showed a small increase in R_{ct} after A.1.c test. However, as the magnitude was small, this could simply be measurement error, and so there was no concern specific to cell 5 as no abnormal heating of the cell was observed during A.1.c testing.

[104] EIS data from cell 1 is not shown due to data loss.

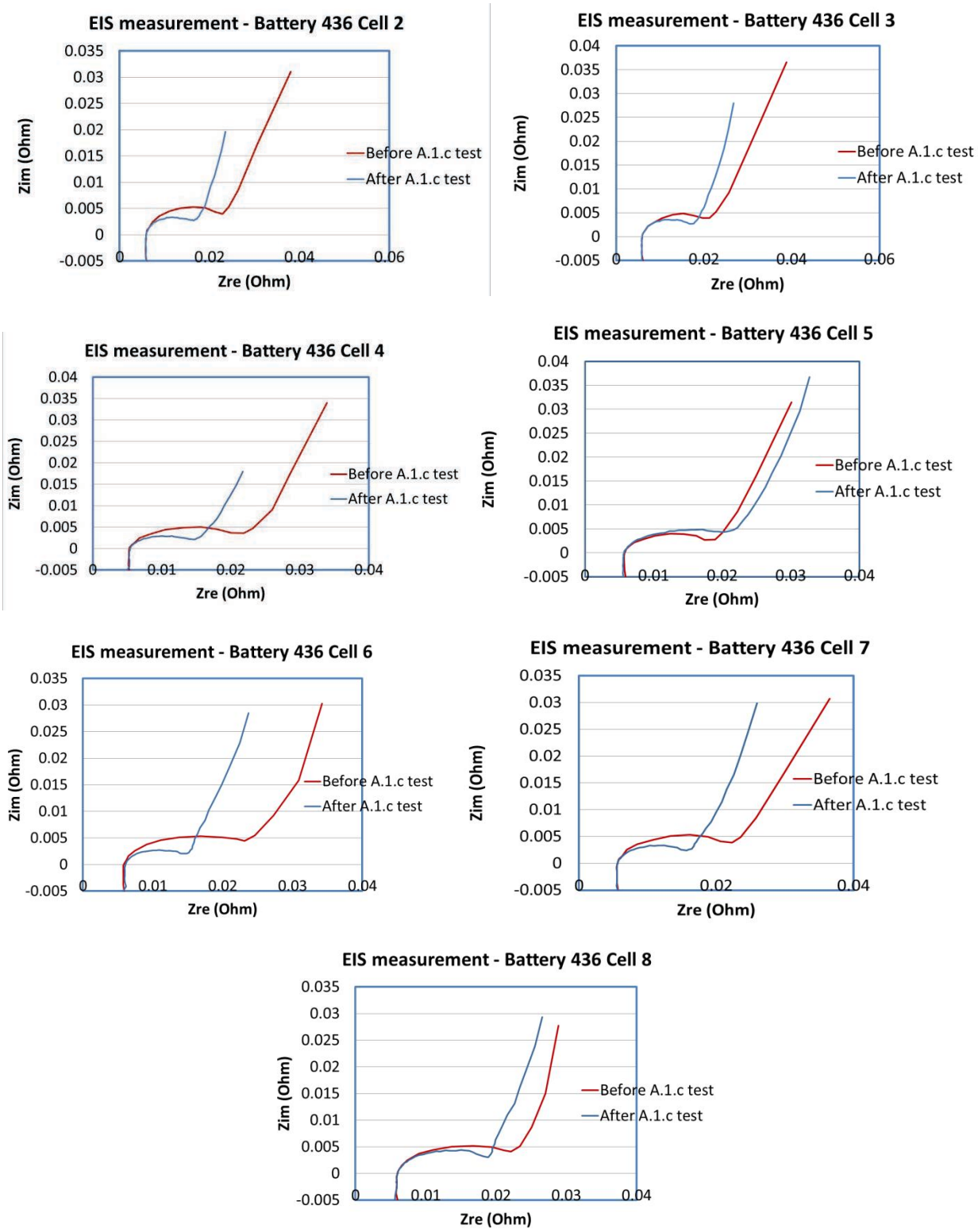

Figure 129 EIS measurements before and after A.1.c test for Cells on Battery 436

APPENDIX A

The cyclic field use of a lithium ion cell drives internal physical and chemical changes that create new considerations for safe disassembly that are not present during the assembly process[105]. For cells with metallic cases, disassembly requires cutting actions which generate heat and possibly sparks. For this particular Asset, the amount of stored energy when fully charged can pose a serious safety concern and so additional precautions must be taken. Regardless, the disassembly of the battery and cell requires a careful methodology that can capture evidence of environmental conditions or manufacturing issues on very thin substrates. In this section, the battery and cell disassembly process is described in detail on steps that deviate from the procedures provided by Boeing in the following documents: (1) Ebron, V.H., et al., Lithium Ion Battery Tear Down Procedure, creation date: 2/28/13, and (2) EQA Battery Examination Sheet – Phase 1, Revision Level R4, date: 2/22/13. Additional risks during storage, handling and disposal of such energetic devices were covered by internal UL safety standard operating procedures requiring some revisions and are not described in this report.

Battery Disassembly

To disassemble a battery to allow for re-assembly requires careful documentation of each component and construction details. Also the cells within the battery had to be removed to cell level testing. The disassembly process had to be reversible so that all components can be for follow-up battery testing. The overall procedure for battery disassembly is shown in Figure A.1 below. Some measurements such as cell OCV and AC/DC resistance will be taken on a cell while still in the battery box and also on a cell outside of the battery box.

[105] N. Willard et al., Disassembly methodology for conducting failure analysis on lithium-ion batteries, Journal of Material Science: Materials in Electronics, Vol. 22, 2011.

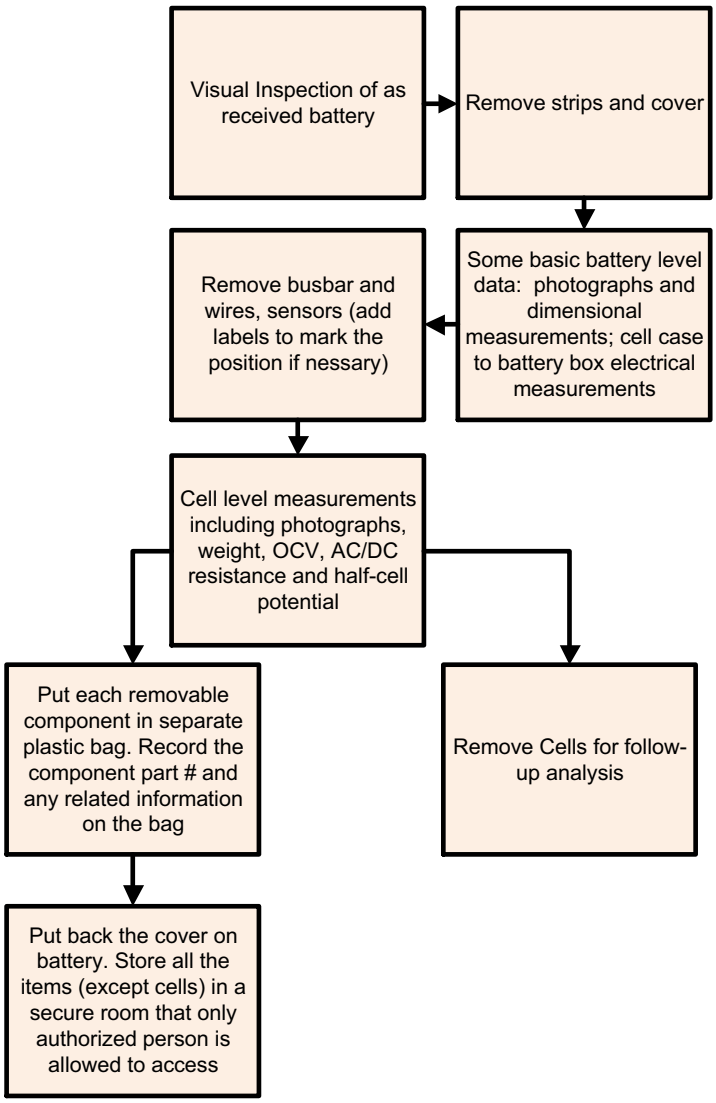

Figure A.1 Flow Chart of Battery Disassembly Process

During battery disassembly, 1k AC impedance was using HIOKI 3561 equipment at mini-Ohm scale. DC resistance and cell OCV were measured by Fluke 289 equipment. All steps in battery disassembly were carried out in laboratory conditions of 20-25 ˚C.

Cell Disassembly

Disassembly of fully charged cells requires tremendous care and caution. UL has experience and processes in place to safely handle small and large format batteries and will always review of any

documentation provided by manufacturer. Nevertheless, no system is full-proof and new lessons are learned with each case.

- One aspect of the cell process requires a thermocouple that was attached to the cell casing while the cell was set to open circuit for at least 6 hours under room temperature. Under these conditions, the cell should not overheat or swell. If it does, this suggests internal faults and extra caution if a decision to conduct DPA is still made.
- A cell casing cutting method developed by UL can minimize the deformation of metal casing and generation of contaminants internally. The cutting process involved scoring 2 parallel lines around the top of the casing side, near the top cover, similar to the tabs on a shipping package (Figure A.2). Then a lateral through cut at one corner of the case establishes a starting point for the unrolling of the thin sliver of casing between the 2 scored regions. A simple wrench can be used to grasp the initial part of the casing and roll the casing without deforming the casing into the windings or near the terminal cover.
- The electrolyte can be drained out from the open case and then sealed in a polypropylene bottle for further analysis.

Figure A.2 Photograph of cell access technique and drained electrolyte

- After drawing out the windings from the metal case and removing the wrap materials, the head current collectors are cut first for separating the three windings. Then, the welded current collectors of each winding are cut as well for winding unroll. In order to prevent the materials from reacting with ambient moisture and oxygen, the whole unroll processes are carried out in the Ar-filled glove box.

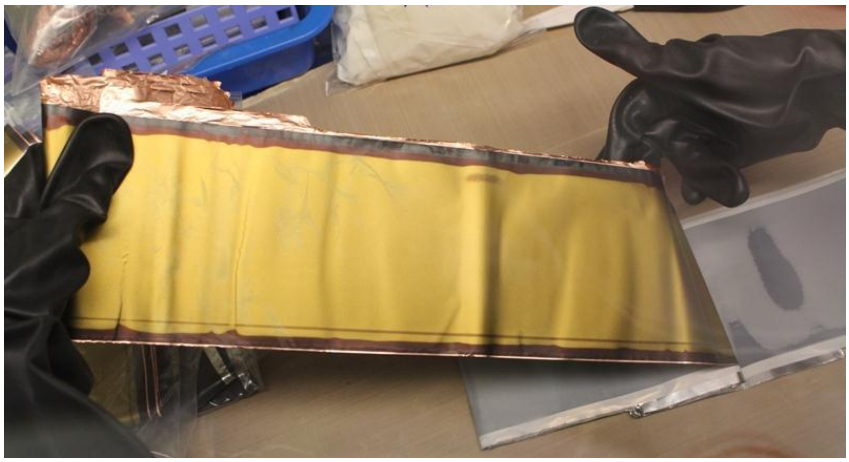

Figure A.3 Photograph of unroll winding and visual inspection

- The preliminary visual inspection is applied for the unrolled electrodes. If any anomaly-like spot is discovered, additional examination will proceed by SEM/EDS analysis.
- The samples prepared for material thermal analysis (TGA and DSC) are scraped from the cathode and anode electrodes without additional solvent rinse.

Battery Assembly with Sensors

To monitor the temperature and cell size changes of LVP65 cells for battery subjected to specific experimental condition afterward, 8 thermocouples (TCs) and 1 stain gauge (SG) were installed on each cell except cell 6 before battery assembly. For Cell 6, 16 TCs and 1 SG were attached for more data recording.

A thin layer of glue was pasted on the surface of cell prior to attaching any TCs to avoid measurement interference. The resistance between the wire and cell case was checked again after installing TC on cell. For SG, the resistance should be 350Ω ± 0.3% before and after installing on cell. Figure A.4 shows cells with installed TCs (pink and blue wires) and SGs (black wire).

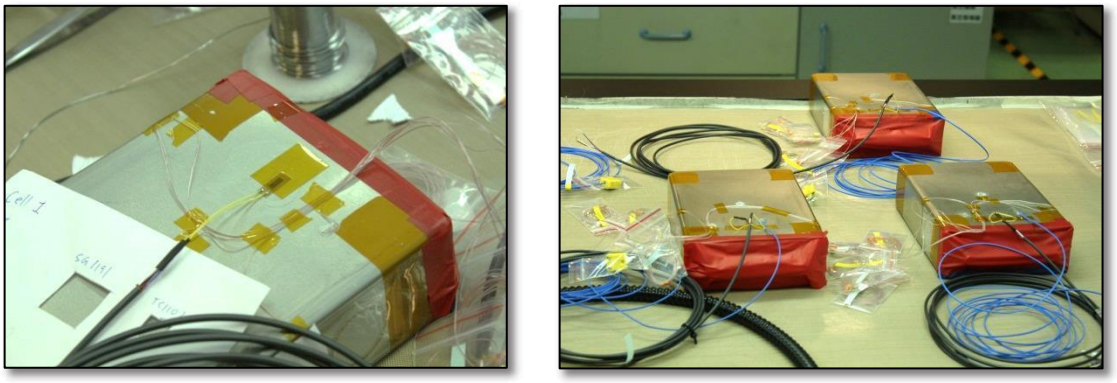

Figure A.4 Cell with thermocouples and strain gauge

Below is the detailed procedure for cell preparation:

1. Locate the position of TCs. Prior to attaching any TC, paste a thin layer of SICOMET glue on the surface of cell for insulation (Figure A. 5).

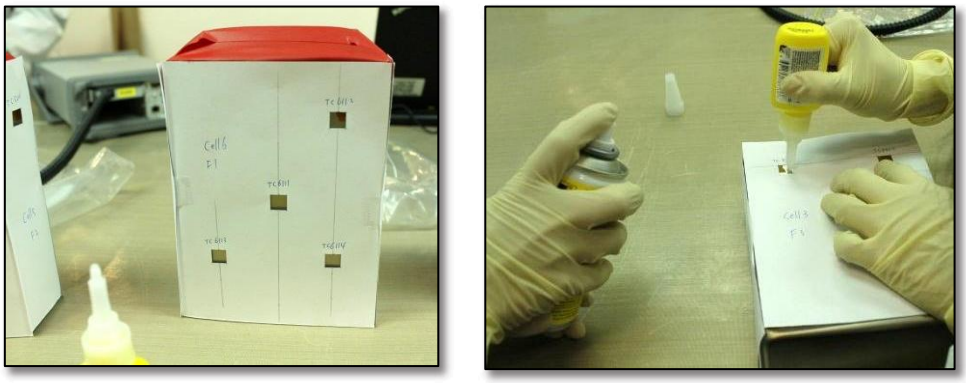

Figure A. 5 **Preparation for installation of thermocouples**

2. Check the resistance of TC (not open) and SG (350Ω ± 0.3%), and then install TC and SG on Cell (Figure A. 6).

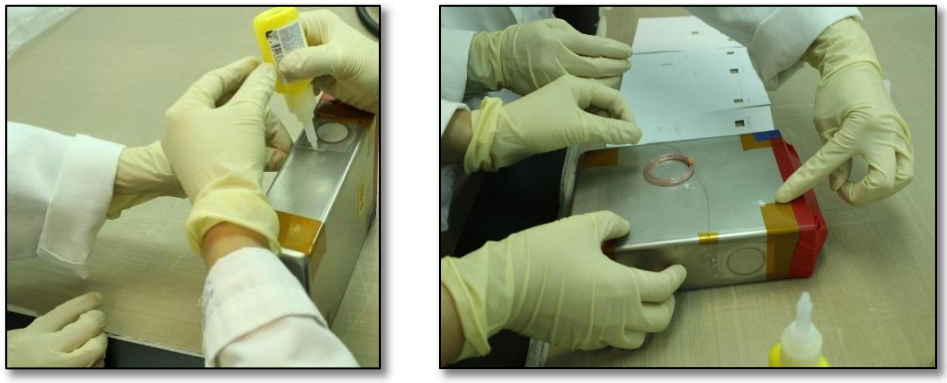

Figure A. 6 **Installation of thermocouples**

3. Check the resistance between the wire and cell case to make ensure electrical insulation (Figure A. 7). Check the resistance of SG (350Ω ± 0.3%) again, and then place the wires and label into separate bag.

Figure A. 7 **Resistance check after installation of thermocouple on cell**

4. Redirect the TC wires to the cell phase with SG, and bind the wires to one bunch with tapes (Figure A.4).

TC and SG Installation Layout

Thermocouple

OMEGA 5TC-TT-J-40_72, PFA-insulated Thermocouples, type J calibration 72" long, 40 gauge, stripped lead termination.

Strain gauge

HBM 1-LY41-6/350, one measuring grid, linear strain gage calibrated, carrier and cover: polyimide / measuring grid foil: constantan, measuring grid length in 6 mm, α for ferritic steel, measuring grid resistance in 350 ohms.

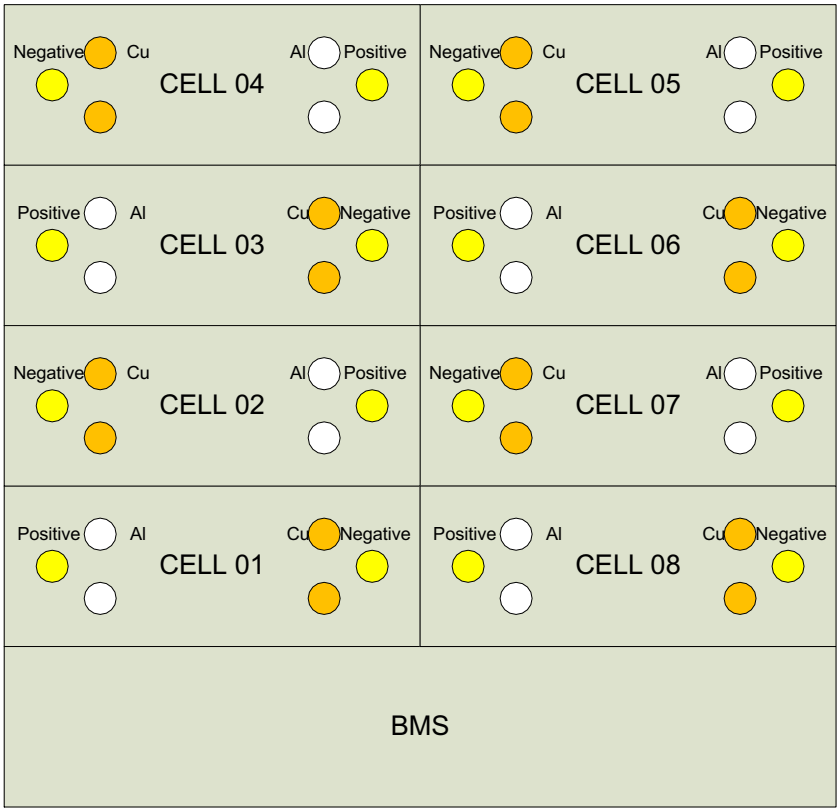

Layout of thermocouples and strain gages on cells 1 (Standard)

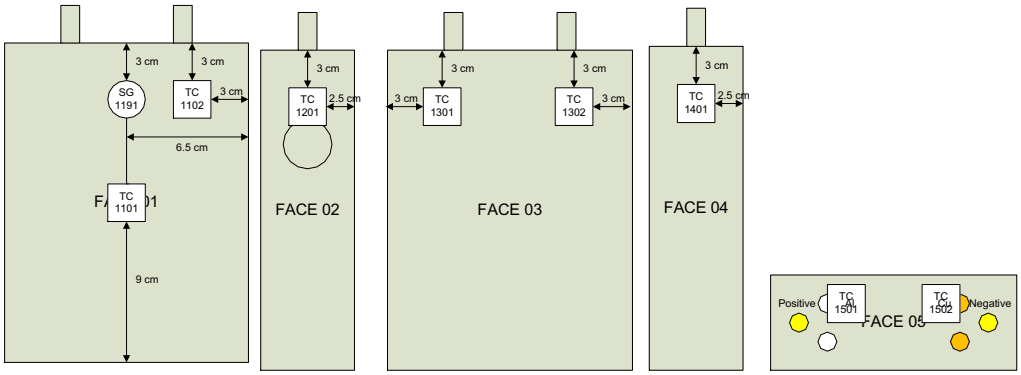

Layout of thermocouples and strain gages on cells 2 (Standard)

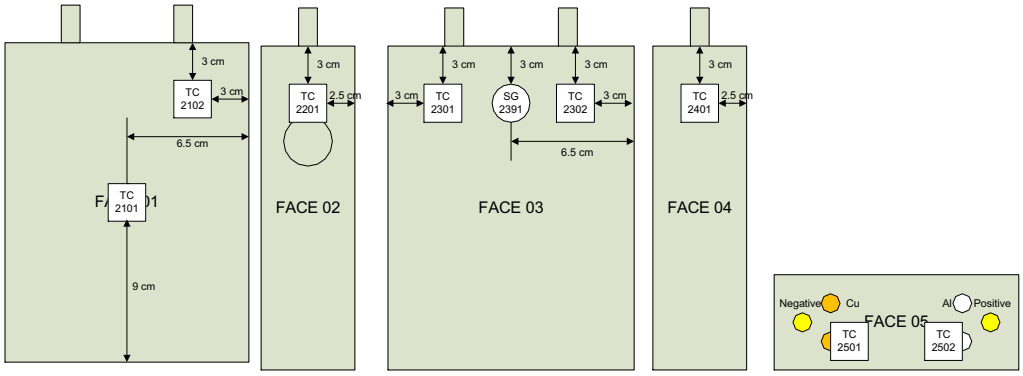

Layout of thermocouples and strain gages on cells 3 (Standard)

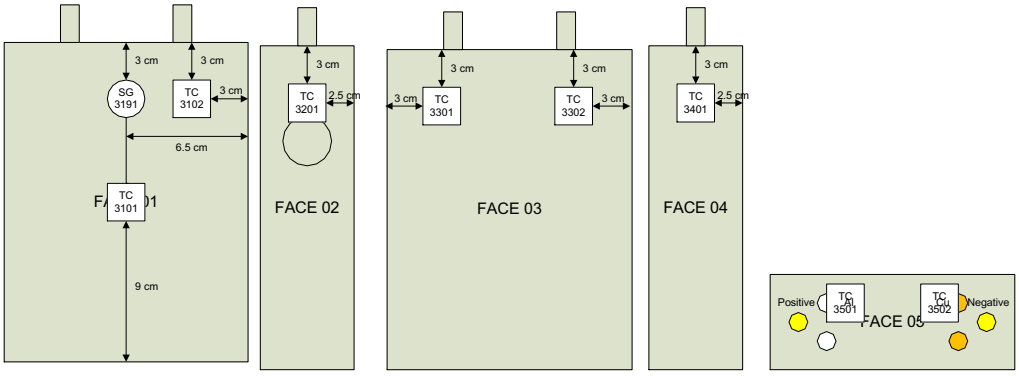

Layout of thermocouples and strain gages on cells 4 (Standard)

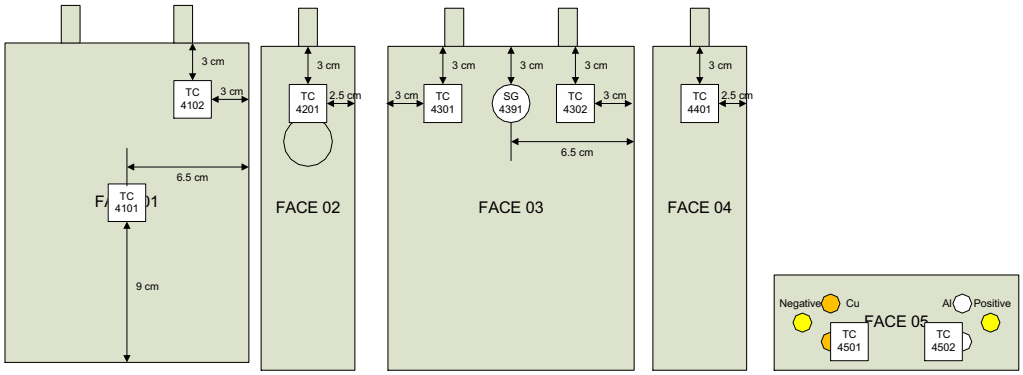

Layout of thermocouples and strain gages on cells 5 (Standard)

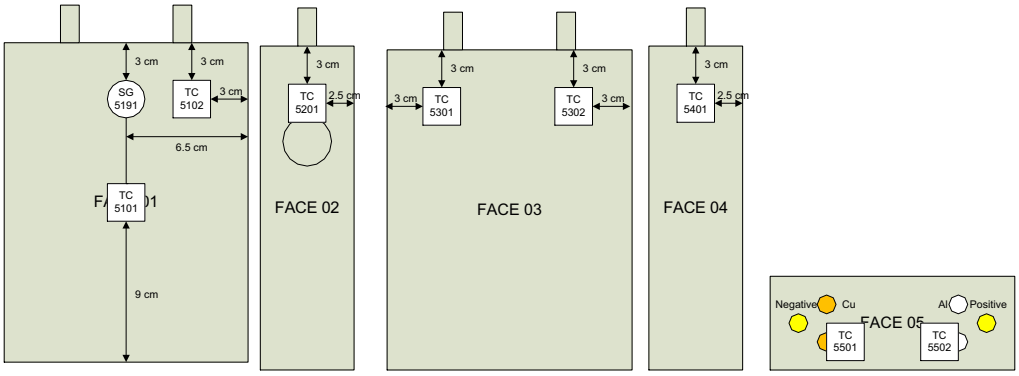

Layout of thermocouples and strain gages on cells 6 (Special)

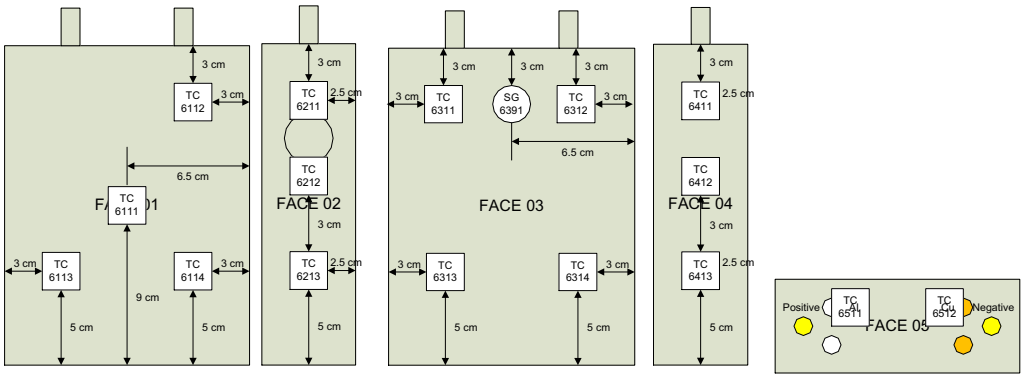

Layout of thermocouples and strain gages on cells 7 (Standard)

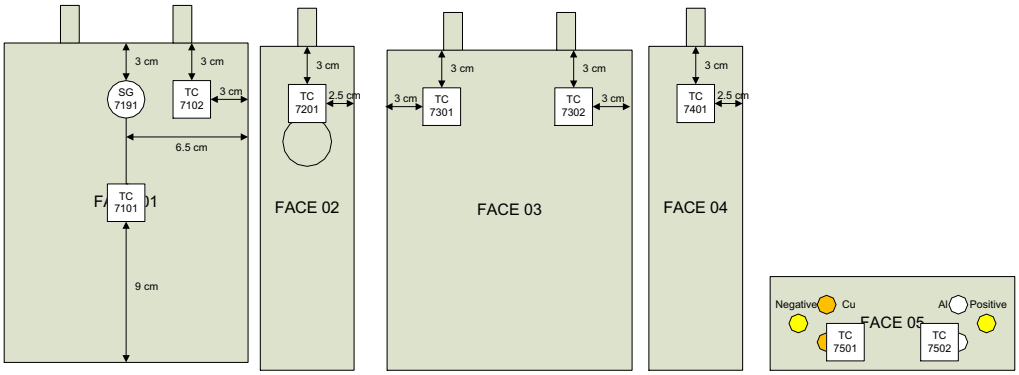

Layout of thermocouples and strain gages on cells 8 (Standard)

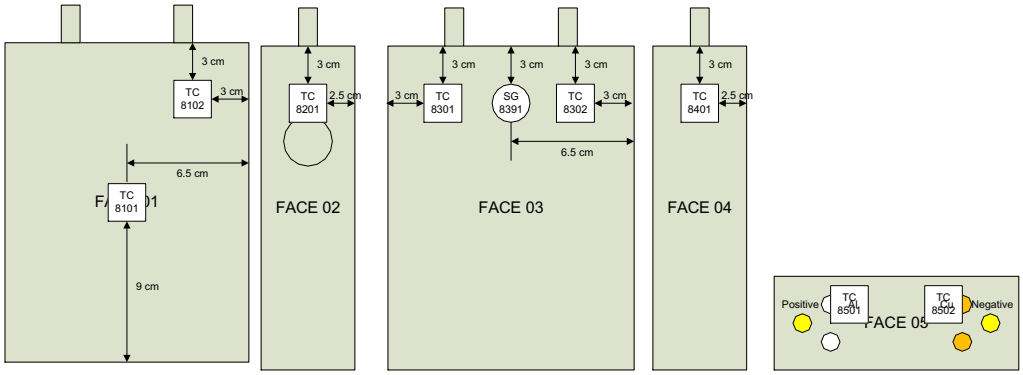

Layout of holes for signal lines

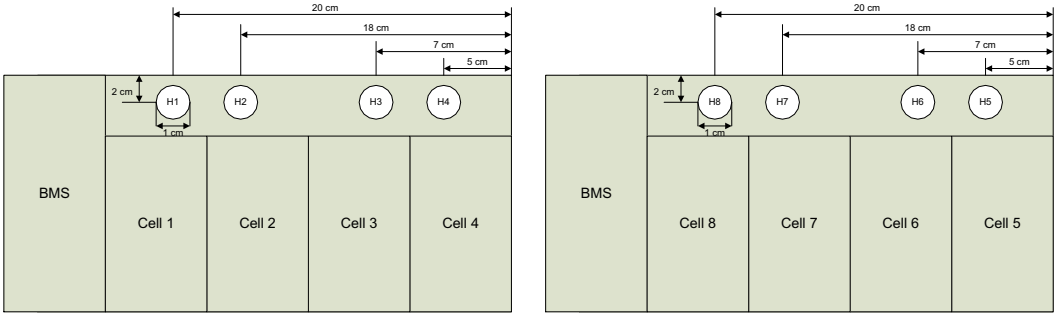

Layout of signal lines

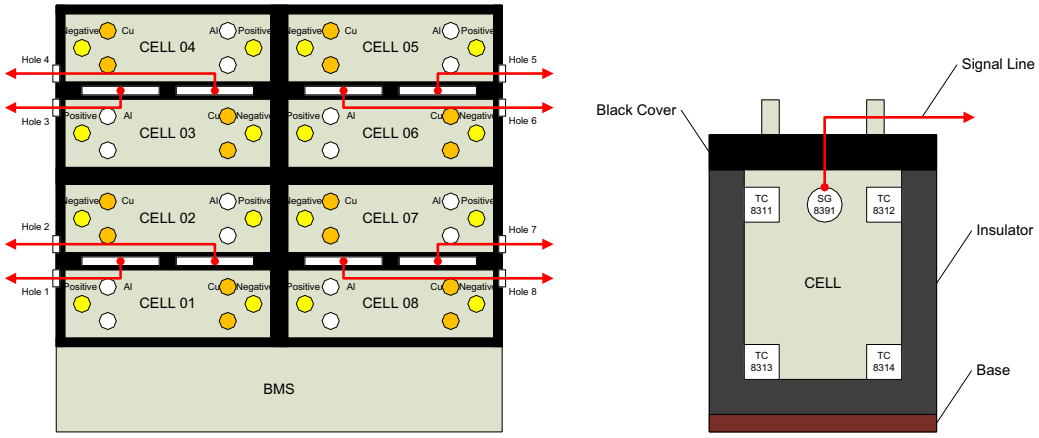

It must be very careful to prevent any accidental external short while installing cells with TCs and SGs into battery case. To save extra spaces for TC and SG wires, the direction of plastic U-shape spacer between cells has been changed to upside-down. The wires should be passed through upper fixation frame of the module and the pre-drilled holes on the sides of battery box. Visual inspection and resistance check for wires are performed to make sure that the TCs and SGs are not broken during cell installation.

Below is the detailed procedure for battery assembly:

1. Install Cell 1 with TCs and SG, put in plastic spacer 3 (Component # 150) and 4 (Component # 160), then install Cell 2 with another plastic spacer 3 (Component # 150).
2. Install Cell 8 and 7 in the same way, and then pass the wires of TCs and SGs through upper fixation frame of the module (Component # 180) as Figure A. 8.

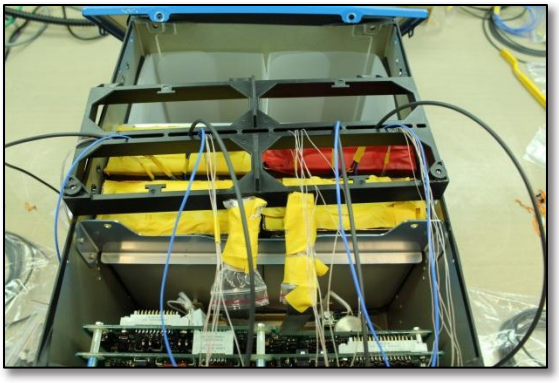

Figure A. 8 The distribution of TC and SG wires while installing cells

3. Remove the tape on Cell terminals from each Cell unit and assemble upper fixation frame of the module (Component # 180). Visual inspect the wires and check their resistances (Figure A. 9).

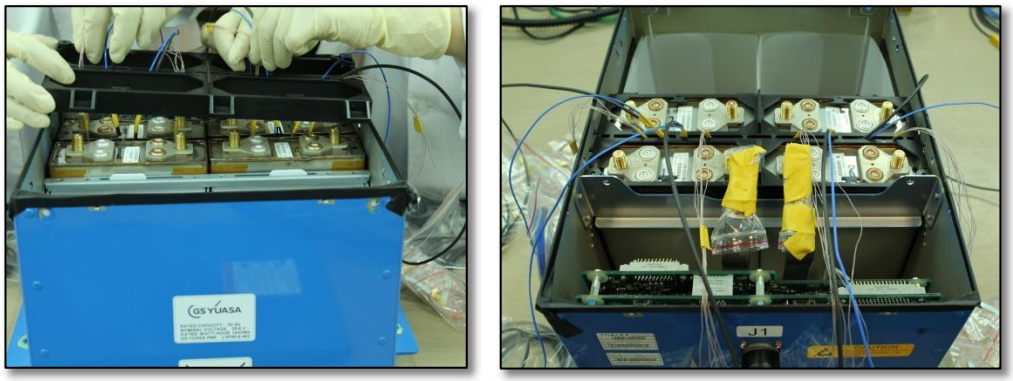

Figure A. 9 Installation of upper fixation frame of the module

4. Stick two TCs on the positive and negative rivet of each Cell respectively.
5. Pass wires of TCs and SGs through the pre-drilled holes on the sides of battery box as Figure A. 10.

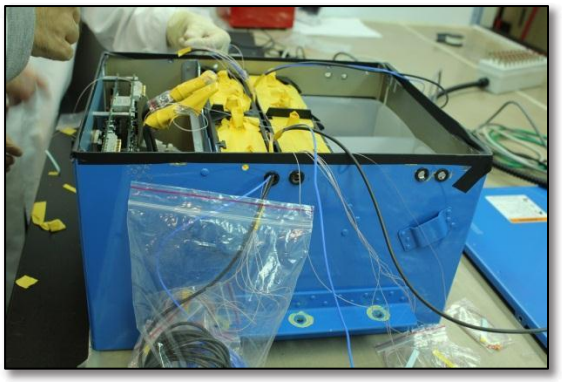

Figure A. 10 Passing wires through holes on battery box

6. Repeat the same procedure for Cell 3, 4, 5 and 6.
7. Measure the voltage of each Cell, it should be about 3.70V ~ 3.75V according to charging condition.
8. Fix the upper fixation frame of the module (Component # 180).
9. Set the hexagon nuts (Component # 210) to hexagonal holes of the upper fixation frame of the module (Component # 180), and then temporarily fix the corner metal fitting (Component # 200) to the upper fixation frame of the module (Figure A.11).

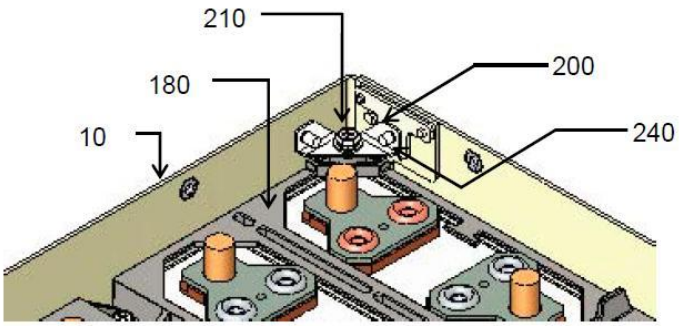

Figure A.11 Cell fixture frame and corner nut

10. Fix the upper fixation frame of the module (Component # 180) to the central metal fitting of battery box.
11. Fix the corner metal fittings (Component # 200) to the battery box. Torque value shall be 160 cN.m
12. Fix the contactor ASSAY (Component # 550) to the supporter and cell terminal. Torque value shall be 153 kgf-cm (Figure A. 12).
13. Fix the HECS cooper bar ASSY (Component # 520A) to the connector and cell terminal with attachment nut and spring washer. Torque value shall be 153 kgf-cm (Figure A. 12).

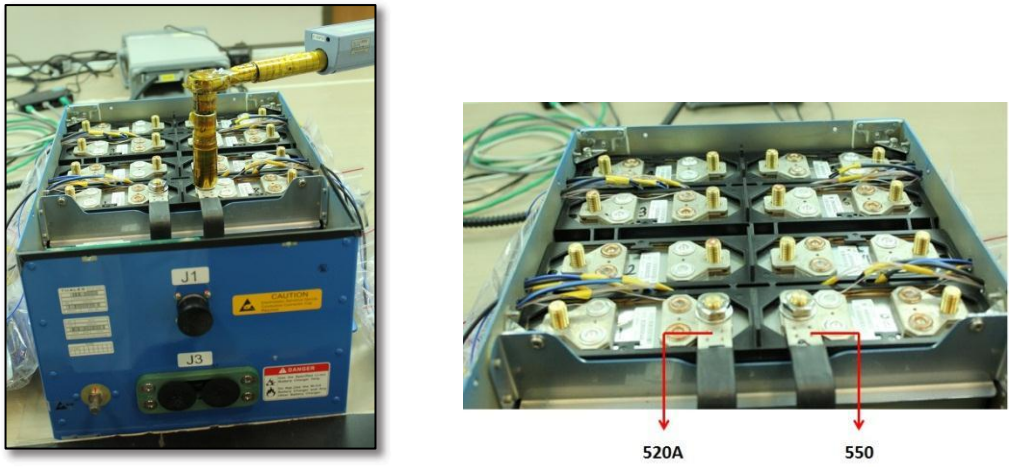

Figure A. 12 Connection of contactor ASSAY and HECS copper bar ASSAY

14. Fix the connection copper bar 2, 4, 6 and 8. Torque value shall be 153 kgf-cm (Figure A. 13). Please notice the wires of TCs and SGs are putting under the connection copper bar.

Figure A. 13 Installation of connection copper bar 2, 4, 6 and 8

15. Fix the connection copper bar 3 and 7. Torque value shall be 153 kgf-cm (Figure A. 14).

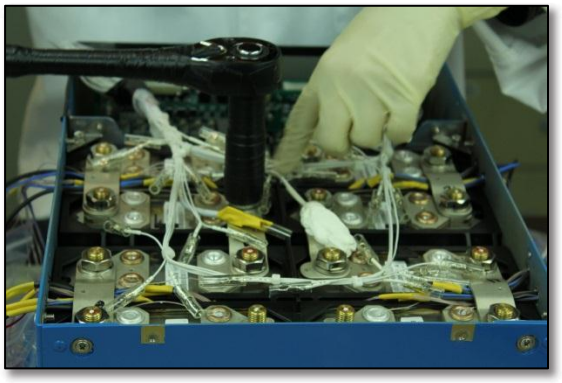

Figure A. 14 Installation of connection copper bar 3 and 7

16. Before fix the main and sub harness, label wire 33-A, 43-I, 38-E and Th2-G. Be careful temporary not fix these four screws. Then fix the main harness and then the sub harness (Figure A. 15). Torque value of the screws shall be 60 cN.m.

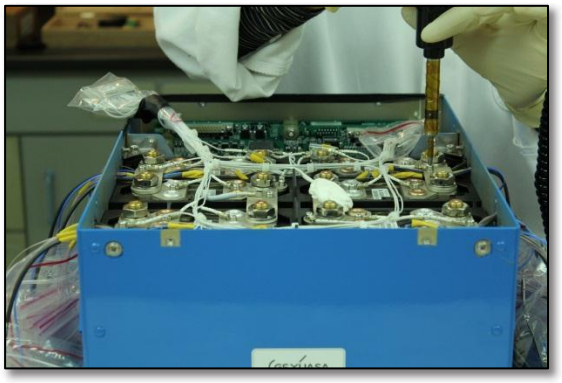

Figure A. 15 Installation of main and sub harness

17. Fix the connection copper bar 5. Torque value shall be 153 kgf-cm. And then fix the screw of 38-E and Th2-G. Torque value of the screws shall be 60 cN.m.
18. Connect the HECS contactor harness (Component # 360).
19. Plug in the main harness and the sub harness to the main BMU and the sub BMU respectively, and then fix them with attached screws of the square type connector.
20. Fix the screws of wire 33-A and 43-I. Torque value of the screws shall be 60 cN.m.
21. Tie the harness (Figure A. 16).

Figure A. 16 Completion of inside installation

22. Measure the open circuit voltage of the battery at terminal J3, the open circuit voltage of the re-assembled battery is about 30V.
23. Set the upper insulation cover (Component # 40).
24. Fix the battery box cover to the battery box. Torque value of the screws shall be 160 cN.m.
25. Set the belt. The attached TCs and SGs are packed in separate bags and carefully fixed on the top of battery cover before shipment, as shown in Figure A. 17.

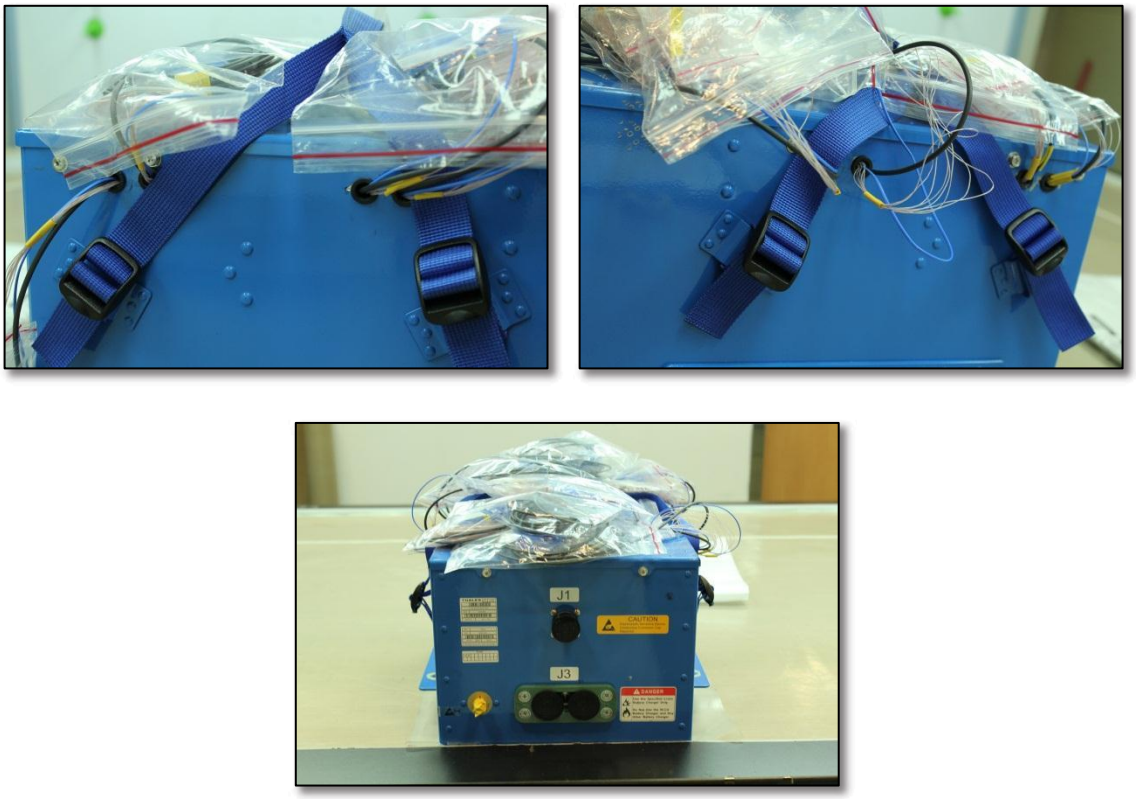

Figure A. 17 Assembled battery

26. Put the battery into the transport box and ready for shipment (Figure A. 18).

Figure A. 18 Battery in shipping box

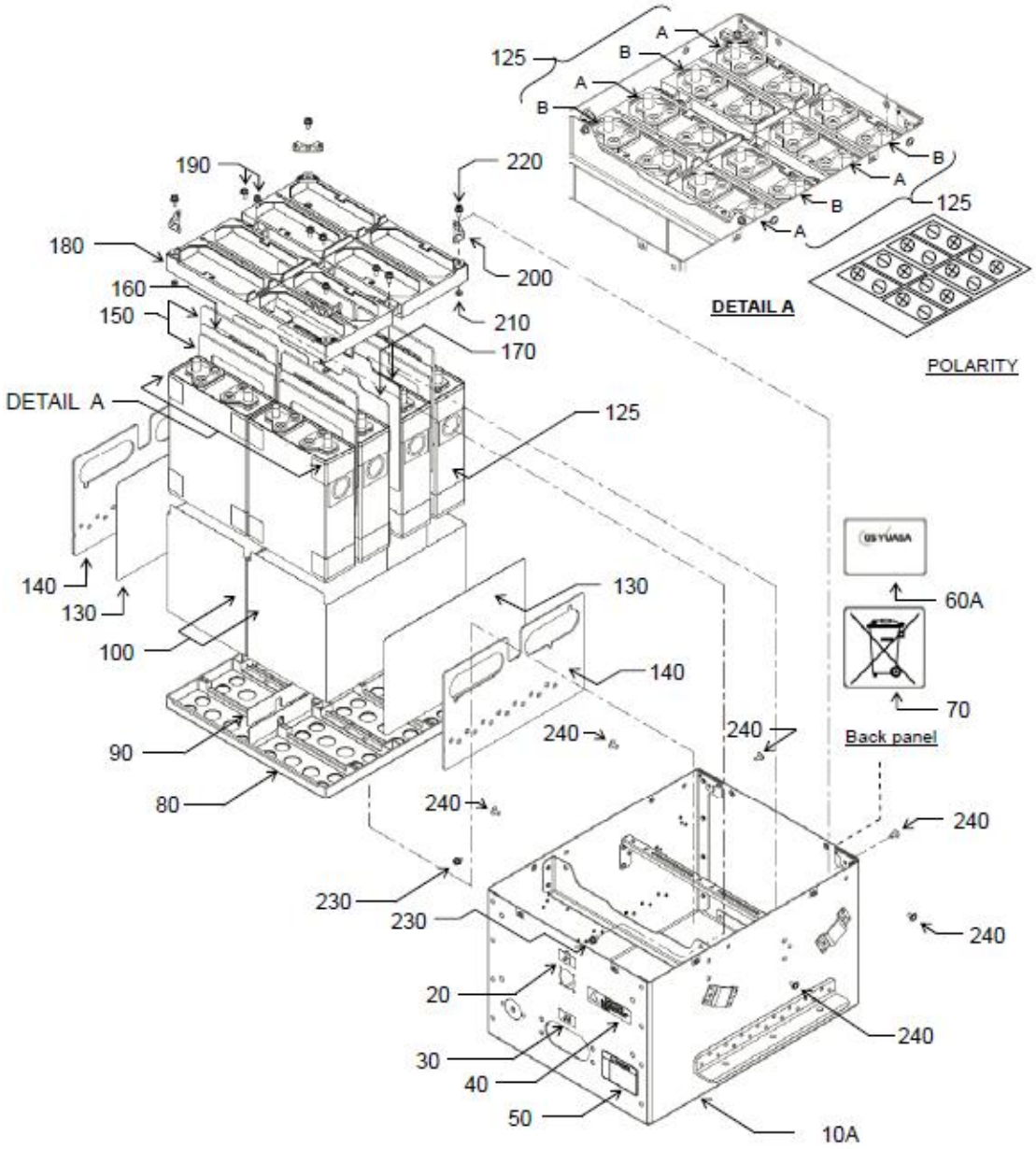

Figure A.19 Components and reference item numbers of battery

APPENDIX B

Inspection Datasheets

Battery Inspection # 436 Datasheet

Battery Part Number: B3856-901

Battery Serial Number: 436
Battery Voltage at Receipt: 29.851V
Ambient Temperature (In Degrees F) at Examination: 22.7 °C
Humidity at Examination: 41.8%

SHIPPING CONTAINER EXAMINATION

	Condition of Shipping Container
Container top	Unremarkable
Container sides	Unremarkable
Container bottom	N/A

BATTERY VOLTAGE TEST

Caution: Electro Static Discharge Sensitive protection is required.
WARNING! Full battery voltage potential is present!
Personal protective equipment is required.

Remove cap from J3 terminal.
Using a Fluke model 287 multimeter measure the battery voltage through J3. Positive terminal is on the right hand side. Meter set on AUTO.

Equipment Documentation

Equipment	Model	Property Number	Calibration Date
TRUE RMA MULTIMETER	Fluke 287	80544	2013-02-28

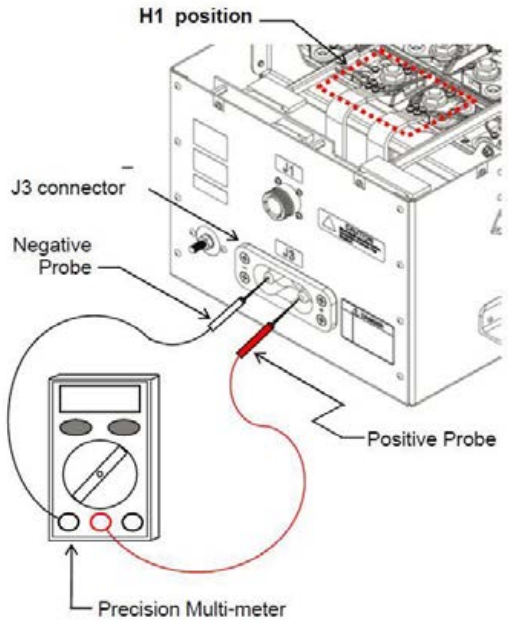

Battery Voltage Test

Record Voltage: 29.851V
Replace cap.

SHIPPING CONTAINER EXAMINATION

Caution: Electro Static Discharge Sensitive protection is required.
WARNING! Full battery voltage potential is present!
Personal protective equipment is required.

IPL #	IPL Nomenclature	Inspection Results
50A	Cover	Unremarkable
90	Carrying Strap	Unremarkable
60	Screws	Unremarkable
70	Warning Label	Unremarkable
	Additional Labels	Unremarkable
30	Box Assy. (right side)	Unremarkable
240 F2	Screws	Unremarkable
	Rivets	Unremarkable
	Tamper Tape	Unremarkable
	Additional Labels	N/A
100	Strap Adjuster	Unremarkable
30	Box Assy. (back side)	Unremarkable

240 F2	Cover Screws	Unremarkable
	Box screws	Unremarkable
	Rivets	Unremarkable
	Labels	Unremarkable
30	Box Assy. (left side)	Unremarkable
240 F2	Cover Screws	Unremarkable
	Rivets	Unremarkable
	Tamper Tape	Unremarkable
100	Strap Adjuster	Unremarkable
	Box screws	Unremarkable
30	Box Assy. (front)	Unremarkable
	Part ID Labels	Unremarkable
	Other Labels	Unremarkable
	J1 Connector w/cover	Unremarkable
	J1 Connector remove cover	N/A
420A	Cover Screws	Unremarkable
270	J3 Connector w/cover	Unremarkable
	J3 Connector cover removed	N/A
280	Box Screws	Unremarkable
310	Gasket	Unremarkable
	Case Ground Terminal	Unremarkable
230	Rivets	Unremarkable
240	Nut	Unremarkable
250	Washer	N/A
	Box Assy. (bottom)	N/A

VISUAL EXAMINATION OF CONTROL AREA

Caution: Electro Static Discharge Sensitive protection is required.
WARNING! Full battery voltage potential is present!
Personal protective equipment is required.

Visually examine the printed circuit boards (PCB), wiring and connectors.
Any material to be collected by BR&T shall be collected by BR&T prior to continuing any phase of the examination.

IPL #	IPL Nomenclature	Inspection Results
	Fwd PCB	Unremarkable
	Aft PCB	Unremarkable
210	Sub Harness (LH)	Unremarkable
160	Main Harness (RH)	Unremarkable
30	Box Floor	Unremarkable

30	Box sidewalls	Unremarkable
	Fwd PCB Connector	Unremarkable
	Aft PCB Connector	Unremarkable
560	Contactor	Unremarkable
563	Contactor Bolt	N/A
565	Contactor Washer	N/A

REMOVE INSULATION COVER AND EXAMINATION OF CELL COMPARTMENT

Caution: Electro Static Discharge Sensitive protection is required.
WARNING! Full battery voltage potential is present!
Personal protective equipment is required.

Perform a visual examination of the battery cells for damage, discoloration debris DO NOT TOUCH! If collection of material is required, do it at this point (BR&T).

IPL #	IPL Nomenclature	Inspection Results
40	Insulation Cover Underside	Unremarkable
520A	Negative Bar	Unremarkable
550	Positive Bar	Unremarkable
660	Bolts	N/A
620	Insulation positive	Unremarkable
540	Insulation negative	Unremarkable
180F2	Fixation Frame	Unremarkable
190F2	Bolts	Unremarkable
200F2	Corner Fittings	Unremarkable
220F2	Bolts	Unremarkable
189	Right Thermister screw	Unremarkable
	Left Thermister Potting	Unremarkable

Record Battery Cell Serial Numbers

CAUTION

Caution: Electro Static Discharge Sensitive protection is required.
WARNING! Full battery voltage potential is present!
Personal protective equipment is required.

Perform a visual examination of the battery cells for damage, discoloration debris DO NOT TOUCH! If collection of material is required, do it at this point.
Document serial numbers, manufacturing date, part number and any additional data printed on each cell.

Cell 4 S/N: 53800036 B P/N: LVP65-002 Mfg. date: 11/2012	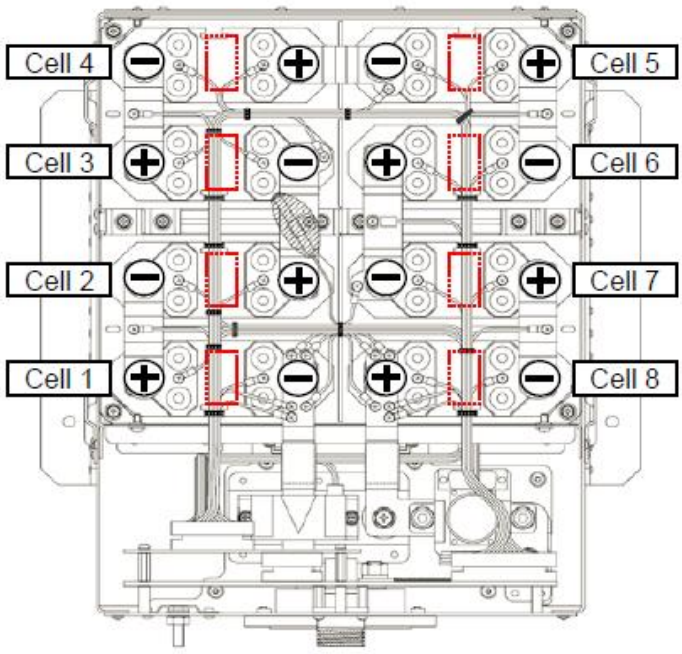	Cell 5 S/N: 53800056 A P/N: LVP65-002 Mfg. date: 11/2012
Cell 3 S/N: 53800045 A P/N: LVP65-002 Mfg. date: 11/2012		Cell 6 S/N: 53800040 B P/N: LVP65-002 Mfg. date: 11/2012
Cell 2 S/N: 53800029 B P/N: LVP65-002 Mfg. date: 11/2012		Cell 7 S/N: 53800057 A P/N: LVP65-002 Mfg. date: 11/2012
Cell 1 S/N: 53800044 A P/N: LVP65-002 Mfg. date: 11/2012		Cell 8 S/N: 53800066 B P/N: LVP65-002 Mfg. date: 11/2012

Cell numbering, Cell polarity

and Description of Cell

Note: Red marking on terminals indicates the positive terminal studs.

Battery Cell Compartment Examination (visible portion only)

Caution: Electro Static Discharge Sensitive protection is required.
WARNING! Full battery voltage potential is present!
Personal protective equipment is required.

IPL #	IPL Nomenclature	Inspection Results
	Examine Dielectric Separators	Unremarkable
160	Main Harness (RH)	Unremarkable
210	Sub Harness (LH)	Unremarkable
125F2	Cell 1	Unremarkable
	Wires	Unremarkable
	Connections	Unremarkable
180	Mounting Screws	Unremarkable
490	Nuts	Unremarkable
500	Washers	Unremarkable
680	Connection Bar Cell 1 to Cell 2	Unremarkable
690	Nuts	Unremarkable
700	Washers	Unremarkable
520A	Primary Bus Bar (Negative)	Unremarkable
125F2	Cell 2	Unremarkable
	Wires	Unremarkable
	Connections	Unremarkable
180	Mounting Screws	Unremarkable
740	Connection Bar Cell 2 to Cell 3	Unremarkable
690	Nuts	Unremarkable
700	Washers	Unremarkable
125F2	Cell 3	Unremarkable
	Wires	Unremarkable
	Connections	Unremarkable
180	Mounting Screws	Unremarkable
680	Connection Bar Cell 3 to Cell 4	Unremarkable
690	Nuts	Unremarkable
700	Washers	Unremarkable
125F2	Cell 4	Unremarkable
	Wires	Unremarkable
	Connections	Unremarkable
180	Mounting Screws	Unremarkable
710	Connection Bar Cell 4 to Cell 5	Unremarkable
690	Nuts	Unremarkable

700	Washers	Unremarkable
125F2	Cell 5	Unremarkable
	Wires	Unremarkable
	Connections	Unremarkable
180	Mounting Screws	Unremarkable
680	Connection Bar Cell 5 to Cell 6	Unremarkable
690	Nuts	Unremarkable
700	Washers	Unremarkable
125F2	Cell 6	Unremarkable
	Wires	Unremarkable
	Connections	Unremarkable
180	Mounting Screws	Unremarkable
770	Connection Bar Cell 6 to Cell 7	Unremarkable
690	Nuts	Unremarkable
700	Washers	Unremarkable
125F2	Cell 7	Unremarkable
	Wires	Unremarkable
	Connections	Unremarkable
180	Mounting Screws	Unremarkable
680	Connection Bar Cell 7 to Cell 8	Unremarkable
690	Nuts	Unremarkable
700	Washers	Unremarkable
125F2	Cell 8	Unremarkable
	Wires	Unremarkable
	Connections	Unremarkable
180	Mounting Screws	Unremarkable
690	Nuts	Unremarkable
700	Washers	Unremarkable
490	Nuts	Unremarkable
500	Washers	Unremarkable
530	Primary Bus Bar (Positive)	Unremarkable

Battery Cell Swelling

125	Battery Cell Pack	Unremarkable	

Battery Cell Moisture

125	Battery Cell Pack	Unremarkable	

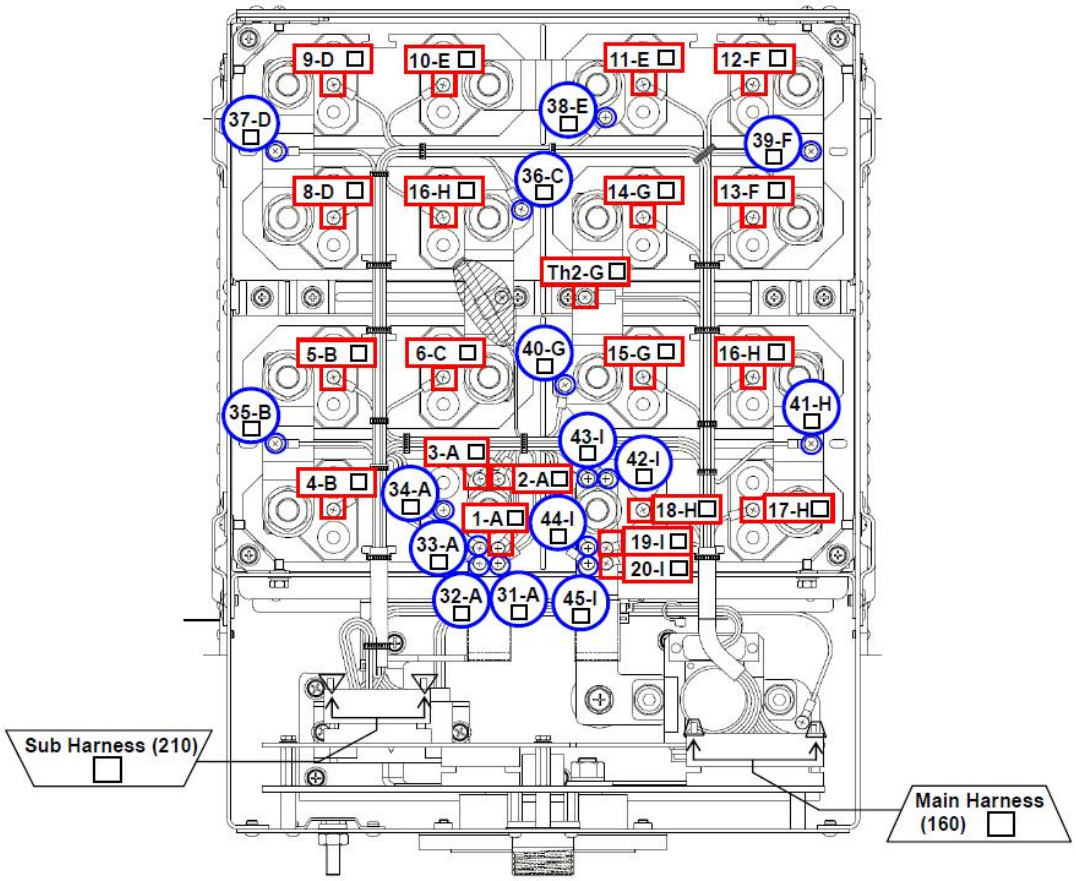

Location designations for monitoring harness attachments.

Left	Cable Ties	Unremarkable	436_0848
Right	Cable Ties	Unremarkable	436_0848

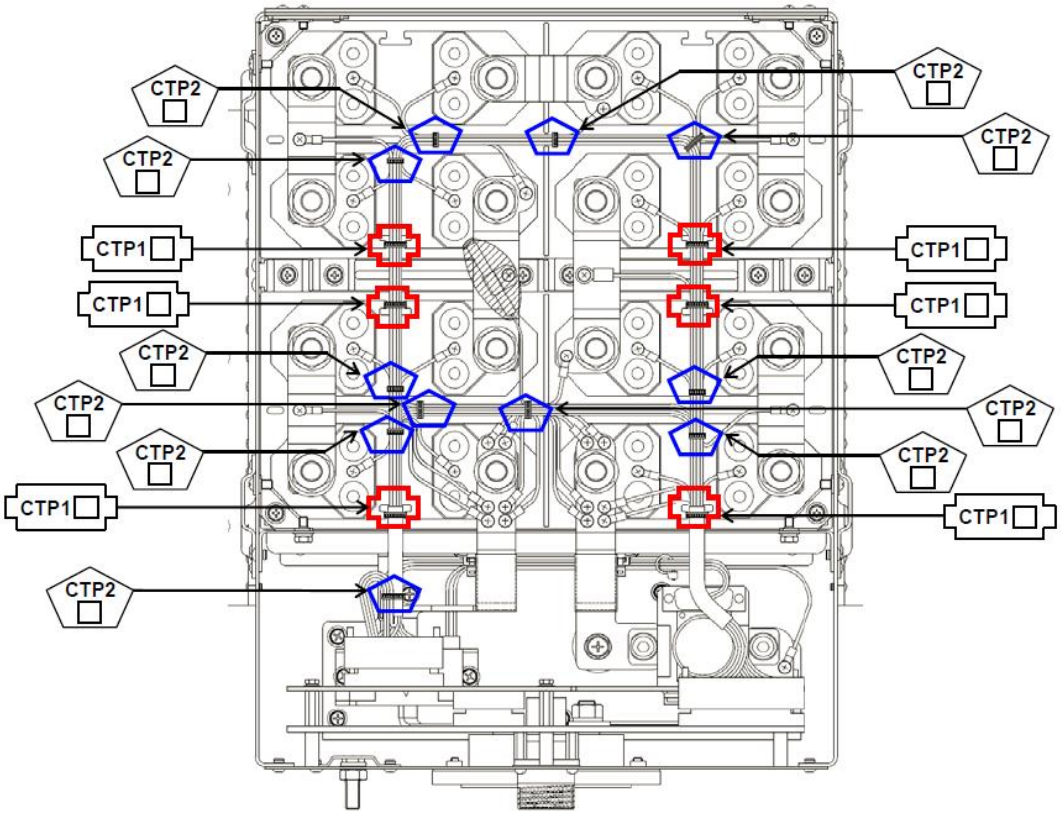

Wire Tie Locations

Battery Cell Voltage Test

Caution: Electro Static Discharge Sensitive protection is required.
WARNING! Full battery voltage potential is present!
Personal protective equipment is required.

Note: Red marking on terminals indicates the positive terminal.
Remove cap from J3 terminal (IPL 270).
Using an Agilent model 3440A multimeter measure the battery voltage through J3 (this is a repeat test). Positive terminal is on the right hand side. Meter set on AUTO range.
Using an Agilent model 3440A multimeter to measure the battery voltage through H1. Positive terminal is on the right hand side. Meter set on AUTO range.

Warning: (Pay attention to polarity)

(2) Battery Voltage Test

Measurement item	Results	Criteria	Pass	Reject
Battery voltage through J3 connector	V	22 V or higher	☐	☐
Battery voltage at H1 position	V			

Remarks:
Measure the voltage at H1 position when the above result is out of the criteria.
The voltage of H1 position is the voltage between the negative terminal of Cell 1 and the positive terminal of Cell 8.
Refer to the right figure.

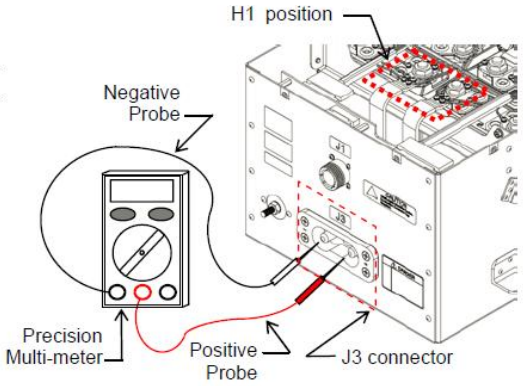

Battery Voltage Test

Record Voltage J3: 29.851V
Record Voltage H1: 29.851V
Replace J3 cap.

Equipment Documentation:

Equipment	Model	Property Number	Calibration Date
TRUE RMA MULTIMETER	Agilent 3440A	50635	2013-02-05

Using a Agilent, measure the voltage of each cell, positive to negative terminals; record results.

Cell #	Voltage (Criteria 2.1V to 4.2V)
	Results
1	3.7307 V
2	3.7271 V
3	3.7351 V
4	3.7386 V
5	3.7298 V
6	3.7322 V
7	3.7303 V
8	3.7311 V

Battery Cell Individual Voltage Test per Service Bulletin

Caution: Electro Static Discharge Sensitive protection is required.
WARNING! Full battery voltage potential is present!
Personal protective equipment is required.

Note: Red marking on terminals indicates the positive terminal.
The following additional cell resistance tests (with battery cover removed) also need to be performed. Note: this test was intended for a fully charged battery.
Using an Agilent 3440A multimeter to measure the voltage of each cell and record results.

Cell #	Positive to Case	Negative to Case	Cell Voltage (sum)
	Results (VDC)	Results (VDC)	Results (VDC)
1	1.0575V	2.6720V	3.7295V
2	1.0535V	2.6725V	3.7260V
3	1.0562V	2.6744V	3.7306V
4	1.0625V	2.6747V	3.7372V
5	1.0324V	2.6964V	3.7288V
6	1.0783V	2.6527V	3.7310V
7	1.0060V	2.7233V	3.7293V
8	1.0315V	2.6991V	3.7306V

Additional Battery Test

Measure resistance between negative terminal of J3 to the case ground stud using a Fluke model 287 multimeter.

J3 Negative Terminal to Case Ground:	OL
J3 Positive Terminal to Case Ground:	OL

Measure the resistance of the positive and negative terminal of each cell to case ground stud using a Fluke model 289 multimeter.

Cell 1 Positive Terminal to Case Ground	OL
Cell 2 Positive Terminal to Case Ground	OL
Cell 3 Positive Terminal to Case Ground	OL
Cell 4 Positive Terminal to Case Ground	OL
Cell 5 Positive Terminal to Case Ground	OL
Cell 6 Positive Terminal to Case Ground	OL
Cell 7 Positive Terminal to Case Ground	OL
Cell 8 Positive Terminal to Case Ground	OL

Cell 1 Negative Terminal to Case Ground	OL
Cell 2 Negative Terminal to Case Ground	OL
Cell 3 Negative Terminal to Case Ground	OL
Cell 4 Negative Terminal to Case Ground	OL
Cell 5 Negative Terminal to Case Ground	OL
Cell 6 Negative Terminal to Case Ground	OL
Cell 7 Negative Terminal to Case Ground	OL
Cell 8 Negative Terminal to Case Ground	OL

Measure the resistance between each individual cell case and the battery case ground stud using a Fluke model 287 multimeter.

Cell #	Cell Case to Battery Case Ground
	Results
1	OL
2	OL
3	OL
4	OL
5	OL
6	OL
7	OL
8	OL

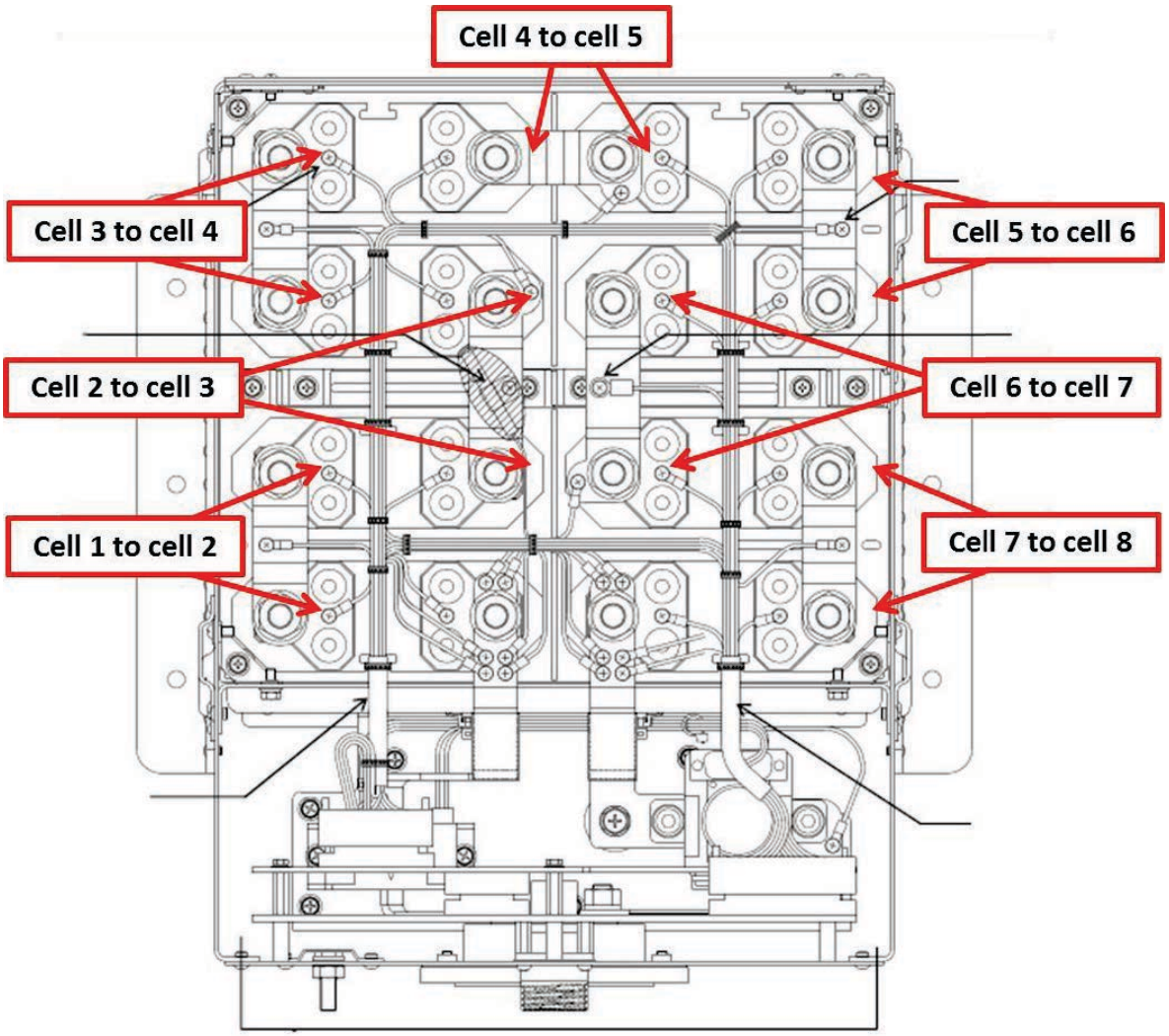

Cell to cell test locations

Battery Inspection # 459 Datasheet

Battery Part Number: B3856-901
Battery Serial Number: 459
Battery Voltage at Receipt: 29.851V
Ambient Temperature (In Degrees F) at Examination: 22.0 degree C
Humidity at Examination: 54%
Battery Voltage Test

Caution: Electro Static Discharge Sensitive protection is required.
WARNING! Full battery voltage potential is present!
Personal protective equipment is required.

Remove cap from J3 terminal.
Using a Fluke model 289 multimeter measure the battery voltage through J3. Positive terminal is on the right hand side. Meter set on AUTO.

Equipment Documentation

Equipment	Model	Property Number	Calibration Date
TRUE RMA MULTIMETER	Fluke 287		

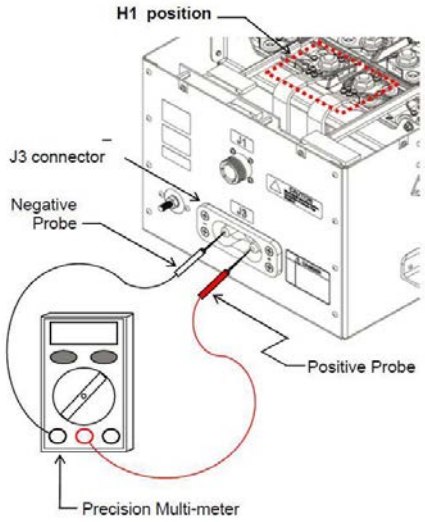

Battery Voltage Test

Record Voltage: 29.851V
Replace cap.

Shipping Container Examination

Caution: Electro Static Discharge Sensitive protection is required.
WARNING! Full battery voltage potential is present!
Personal protective equipment is required.

IPL #	IPL Nomenclature	Inspection Results
50A	Cover	Unremarkable
90	Carrying Strap	Unremarkable
60	Screws	Unremarkable
70	Warning Label	Unremarkable
	Additional Labels	NA
		Dent can be observed on the four corners of cover

30	Box Assy. (right side)	Unremarkable
240 F2	Screws	Unremarkable
	Rivets	Unremarkable
	Tamper Tape	Unremarkable
	Additional Labels	NA
100	Strap Adjuster	Unremarkable

30	Box Assy. (back side)	Unremarkable
240 F2	Cover Screws	Unremarkable
	Box screws	Unremarkable
	Rivets	Unremarkable
	Labels	Unremarkable

IPL #	IPL Nomenclature	Inspection Results
30	Box Assy. (left side)	Unremarkable
240 F2	Cover Screws	Unremarkable
	Rivets	Unremarkable
	Tamper Tape	Unremarkable
100	Strap Adjuster	Unremarkable
	Box screws	Unremarkable

30	Box Assy. (front)	Unremarkable
	Part ID Labels	Unremarkable
	Other Labels	Unremarkable
	J1 Connector w/cover	Unremarkable
	J1 Connector remove cover	Unremarkable
420A	Cover Screws	Unremarkable

270	J3 Connector w/cover	Unremarkable
	J3 Connector cover removed	Unremarkable
280	Box Screws	Unremarkable
310	Gasket	NA
	Case Ground Terminal	Unremarkable
230	Rivets	Unremarkable
240	Nut	Unremarkable
250	Washer	NA

IPL #	IPL Nomenclature	Inspection Results
	Box Assy. (bottom)	NA

Internal Battery Examination – Remove Battery Box Cover

Caution: Electro Static Discharge Sensitive protection is required.
WARNING! Full battery voltage potential is present!
Personal protective equipment is required.

Remove the carrying strap prior to removing the top cover. Verify the strap adjuster conditions. Document the bond and ground locations.

IPL #	IPL Nomenclature	Inspection Results
90	Carrying Strap	Unremarkable
100	Strap Adjusters	Unremarkable

Remove the cover (Item No. 50A)

IPL #	IPL Nomenclature	Inspection Results
50A	Cover (interior)	Unremarkable
80	Packing	Unremarkable
40	Insulation Cover	White resin contamination

Visual Examination of Control Area

Caution: Electro Static Discharge Sensitive protection is required.
WARNING! Full battery voltage potential is present!
Personal protective equipment is required.

Visually examine the printed circuit boards (PCB), wiring and connectors.

Any material to be collected by BR&T shall be collected by BR&T prior to continuing any phase of the examination.

IPL #	IPL Nomenclature	Inspection Results
	Fwd PCB	Unremarkable
	Aft PCB	Unremarkable
210	Sub Harness (LH)	Unremarkable
160	Main Harness (RH)	Unremarkable
30	Box Floor	NA
30	Box sidewalls	NA
	Fwd PCB Connector	Unremarkable
	Aft PCB Connector	Unremarkable
560	Contactor	Unremarkable
563	Contactor Bolt	Unremarkable
565	Contactor Washer	NA

Remove Insulation Cover and Examination of Cell Compartment

Caution: Electro Static Discharge Sensitive protection is required.
WARNING! Full battery voltage potential is present!
Personal protective equipment is required.

Perform a visual examination of the battery cells for damage, discoloration debris DO NOT TOUCH! If collection of material is required, do it at this point (BR&T).

IPL #	IPL Nomenclature	Inspection Results
40	Insulation Cover Underside	White resin contamination
520A	Negative Bar	Unremarkable
550	Positive Bar	Unremarkable
660	Bolts	Unremarkable
620	Insulation positive	Unremarkable
540	Insulation negative	Unremarkable
180F2	Fixation Frame	Unremarkable
190F2	Bolts	Unremarkable
200F2	Corner Fittings	Unremarkable
220F2	Bolts	Unremarkable
189	Right Thermister screw	Unremarkable
	Left Thermister Potting	Unremarkable

Record Battery Cell Serial Numbers

CAUTION

Caution: Electro Static Discharge Sensitive protection is required.
WARNING! Full battery voltage potential is present!
Personal protective equipment is required.

Perform a visual examination of the battery cells for damage, discoloration debris DO NOT TOUCH! If collection of material is required, do it at this point.
Document serial numbers, manufacturing date, part number and any additional data printed on each cell.

Cell 4 S/N: 53800275 B P/N: LVP65-002 Mfg. date: 12/2012	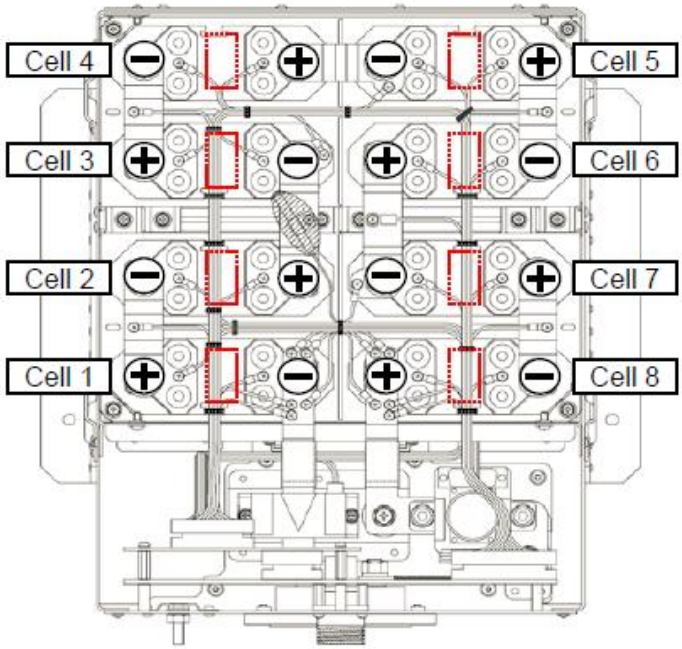	Cell 5 S/N: 53800163 A P/N: LVP65-002 Mfg. date: 12/2012
Cell 3 S/N: 53800100 A P/N: LVP65-002 Mfg. date: 11/2012		Cell 6 S/N: 53800280 B P/N: LVP65-002 Mfg. date: 12/2012
Cell 2 S/N: 53800276 B P/N: LVP65-002 Mfg. date: 12/2012		Cell 7 S/N: 53800208 A P/N: LVP65-002 Mfg. date: 12/2012
Cell 1 S/N: 53800005 A P/N: LVP65-002 Mfg. date: 11/2012		Cell 8 S/N: 53800319 B P/N: LVP65-002 Mfg. date: 12/2012

Cell numbering, Cell polarity andDescription of Cell S/N

Note: Red marking on terminals indicates the positive terminal studs.

Battery Cell Compartment Examination (visible portion only)

Caution: Electro Static Discharge Sensitive protection is required.
WARNING! Full battery voltage potential is present!
Personal protective equipment is required.

IPL #	IPL Nomenclature	Inspection Results
	Examine Dielectric Separators	NA
160	Main Harness (RH)	Unremarkable
210	Sub Harness (LH)	Unremarkable

125F2	Cell 1	Unremarkable
	Wires	Unremarkable
	Connections	Unremarkable
180	Mounting Screws	Unremarkable
490	Nuts	Unremarkable
500	Washers	Unremarkable
680	Connection Bar Cell 1 to Cell 2	Unremarkable
690	Nuts	Unremarkable
700	Washers	Unremarkable
520A	Primary Bus Bar (Negative)	Unremarkable

125F2	Cell 2	Unremarkable
	Wires	Unremarkable
	Connections	Unremarkable
180	Mounting Screws	Unremarkable
740	Connection Bar Cell 2 to Cell 3	Unremarkable
690	Nuts	Unremarkable
700	Washers	Unremarkable

125F2	Cell 3	Unremarkable
	Wires	Unremarkable
	Connections	Unremarkable
180	Mounting Screws	Unremarkable
680	Connection Bar Cell 3 to Cell 4	Unremarkable
690	Nuts	Unremarkable
700	Washers	Unremarkable

IPL #	IPL Nomenclature	Inspection Results

125F2	Cell 4	Unremarkable
	Wires	Unremarkable
	Connections	Unremarkable
180	Mounting Screws	Unremarkable
710	Connection Bar Cell 4 to Cell 5	Unremarkable
690	Nuts	Unremarkable
700	Washers	Unremarkable

125F2	Cell 5	Unremarkable
	Wires	Unremarkable
	Connections	Unremarkable
180	Mounting Screws	Unremarkable
680	Connection Bar Cell 5 to Cell 6	Unremarkable
690	Nuts	Unremarkable
700	Washers	Unremarkable

125F2	Cell 6	Unremarkable
	Wires	Unremarkable
	Connections	Unremarkable
180	Mounting Screws	Unremarkable
770	Connection Bar Cell 6 to Cell 7	Unremarkable
690	Nuts	Unremarkable
700	Washers	Unremarkable

125F2	Cell 7	Unremarkable
	Wires	Unremarkable
	Connections	Unremarkable
180	Mounting Screws	Unremarkable
680	Connection Bar Cell 7 to Cell 8	Unremarkable
690	Nuts	Unremarkable
700	Washers	Unremarkable

IPL #	IPL Nomenclature	Inspection Results
125F2	Cell 8	Unremarkable
	Wires	Unremarkable
	Connections	Unremarkable
180	Mounting Screws	Unremarkable
690	Nuts	Unremarkable
700	Washers	Unremarkable
490	Nuts	Unremarkable
500	Washers	Unremarkable
530	Primary Bus Bar (Positive)	Unremarkable

Battery Cell Swelling

125	Battery Cell Pack	Unremarkable

Battery Cell Moisture

125	Battery Cell Pack	Unremarkable

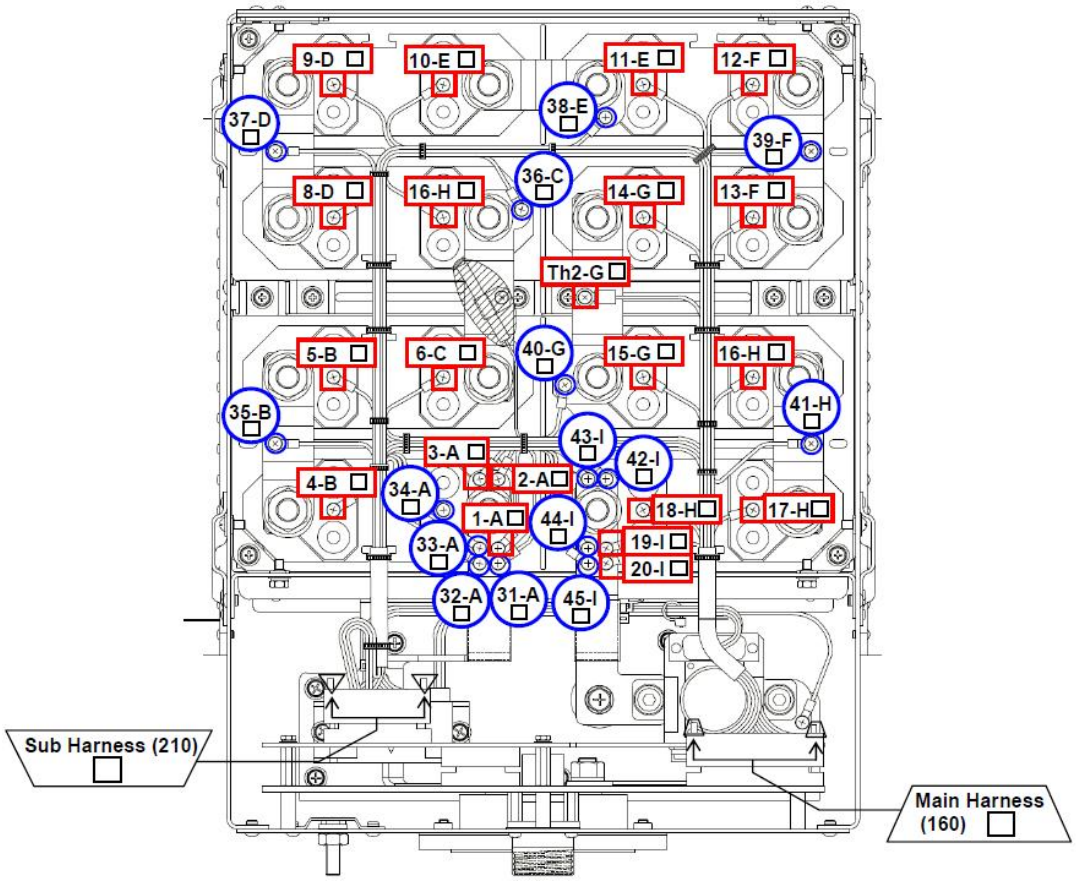

Location designator for monitoring harness attachements

Left	Cable Ties	Unremarkable
Right	Cable Ties	Unremarkable

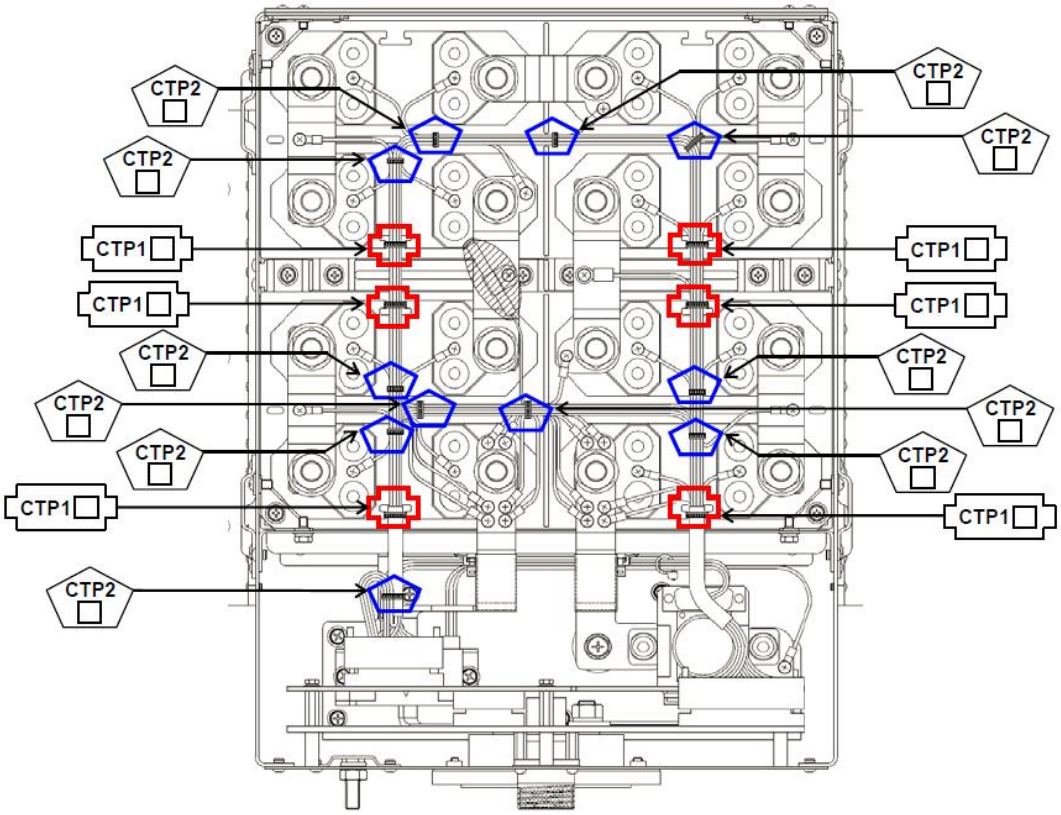

Wire Tie Locations

Battery Cell Voltage and 1kHz Resistance Tests

Caution: Electro Static Discharge Sensitive protection is required.
WARNING! Full battery voltage potential is present!
Personal protective equipment is required.

Note: Red marking on terminals indicates the positive terminal.

Remove cap from J3 terminal (IPL 270).

Using a Fluke model 289 multimeter measure the battery voltage through J3 (this is a repeat test). Positive terminal is on the right hand side. Meter set on AUTO range.

Using a Fluke model 289 multimeter measure the battery voltage through H1. Positive terminal is on the right hand side. Meter set on AUTO range.

Warning: (Pay attention to polarity)

(2) Battery Voltage Test

Measurement item	Results	Criteria	Pass	Reject
Battery voltage through J3 connector	V	22 V or higher	☐	☐
Battery voltage at H1 position	V			

Remarks:
Measure the voltage at H1 position when the above result is out of the criteria.
The voltage of H1 position is the voltage between the negative terminal of Cell 1 and the positive terminal of Cell 8.
Refer to the right figure.

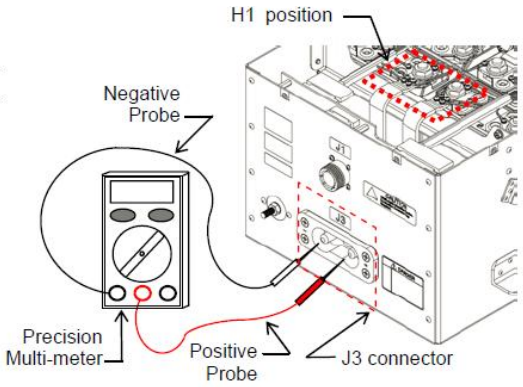

Battery Voltage Test

Record Voltage J3: 29.851V
Record Voltage H1: 29.851V
Replace J3 cap.

Equipment Documentation:

Equipment	Model	Property Number	Calibration Date
TRUE RMA MULTIMETER	Fluke 289		
BATTERY HiTESTER	HIOKI 3561		

Using a Hioki battery tester, measure the voltage of each cell, positive to negative terminals; record results.

Cell #	Voltage (Criteria 2.1V to 4.2V)
	Results
1	3.7259
2	3.7244
3	3.7416
4	3.7246
5	3.7424
6	3.7256
7	3.7424
8	3.7226

Using a Hioki battery tester, measure AC1 kHz resistance; record results.
Positive terminal on the cell to negative terminal on each cell.

Cell #	AC1kHz (<0.1 ohms)
	Results
1	0.31 mΩ
2	0.28 mΩ
3	0.33 mΩ
4	0.29 mΩ
5	0.35 mΩ
6	0.28 mΩ
7	0.29 mΩ
8	0.28 mΩ

Battery Cell Individual Voltage Test per Service Bulletin

Caution: Electro Static Discharge Sensitive protection is required.
WARNING! Full battery voltage potential is present!
Personal protective equipment is required.

Note: Red marking on terminals indicates the positive terminal.
The following additional cell resistance tests (with battery cover removed) also need to be performed. Note: this test was intended for a fully charged battery.
Using a Fluke 289 multimeter, measure the voltage of each cell and record results.

Cell #	Positive to Case	Negative to Case	Cell Voltage (sum)
	Results (VDC)	Results (VDC)	Results (VDC)
1	1.3065V	2.4184V	3.7249V
2	2.3755V	1.3480V	3.7235V
3	1.3276V	2.4127V	3.7403V
4	1.3330V	2.3900V	3.7230V
5	1.6681V	2.0734V	3.7415V
6	1.6709V	2.0536V	3.7245V
7	1.4112V	2.3300V	3.7412V
8	1.5141V	2.2075V	3.7216V

Additional Battery Test

Measure resistance between negative terminal of J3 to the case ground stud using a Fluke model 289 multimeter.

J3 Negative Terminal to Case Ground:	OL
J3 Positive Terminal to Case Ground:	OL

Measure the resistance of the positive and negative terminal of each cell to case ground stud using a Fluke model 289 multimeter.

Cell 1 Positive Terminal to Case Ground	OL
Cell 2 Positive Terminal to Case Ground	OL
Cell 3 Positive Terminal to Case Ground	OL
Cell 4 Positive Terminal to Case Ground	OL
Cell 5 Positive Terminal to Case Ground	OL
Cell 6 Positive Terminal to Case Ground	OL
Cell 7 Positive Terminal to Case Ground	OL
Cell 8 Positive Terminal to Case Ground	OL

Cell 1 Negative Terminal to Case Ground	OL
Cell 2 Negative Terminal to Case Ground	OL
Cell 3 Negative Terminal to Case Ground	OL
Cell 4 Negative Terminal to Case Ground	OL
Cell 5 Negative Terminal to Case Ground	OL
Cell 6 Negative Terminal to Case Ground	OL
Cell 7 Negative Terminal to Case Ground	OL
Cell 8 Negative Terminal to Case Ground	OL

Measure the resistance between each individual cell case and the battery case ground stud using a Fluke model 289 multimeter.

Cell #	Cell Case to Battery Case Ground
	Results
1	OL
2	OL
3	OL
4	OL
5	OL
6	OL
7	OL
8	OL

Measure the resistance from the positive terminal of the connecting link to the negative terminal of the adjoining cell in series (Fig. 6). Using Hioki battery tester.

Cell #	AC1kHz (<0.1 ohms)
	Results

1 to 2	0.04 mΩ
2 to 3	0.04 mΩ
3 to 4	0.04 mΩ
4 to 5	0.04 mΩ
5 to 6	0.05 mΩ
6 to 7	0.04 mΩ
7 to 8	0.05 mΩ

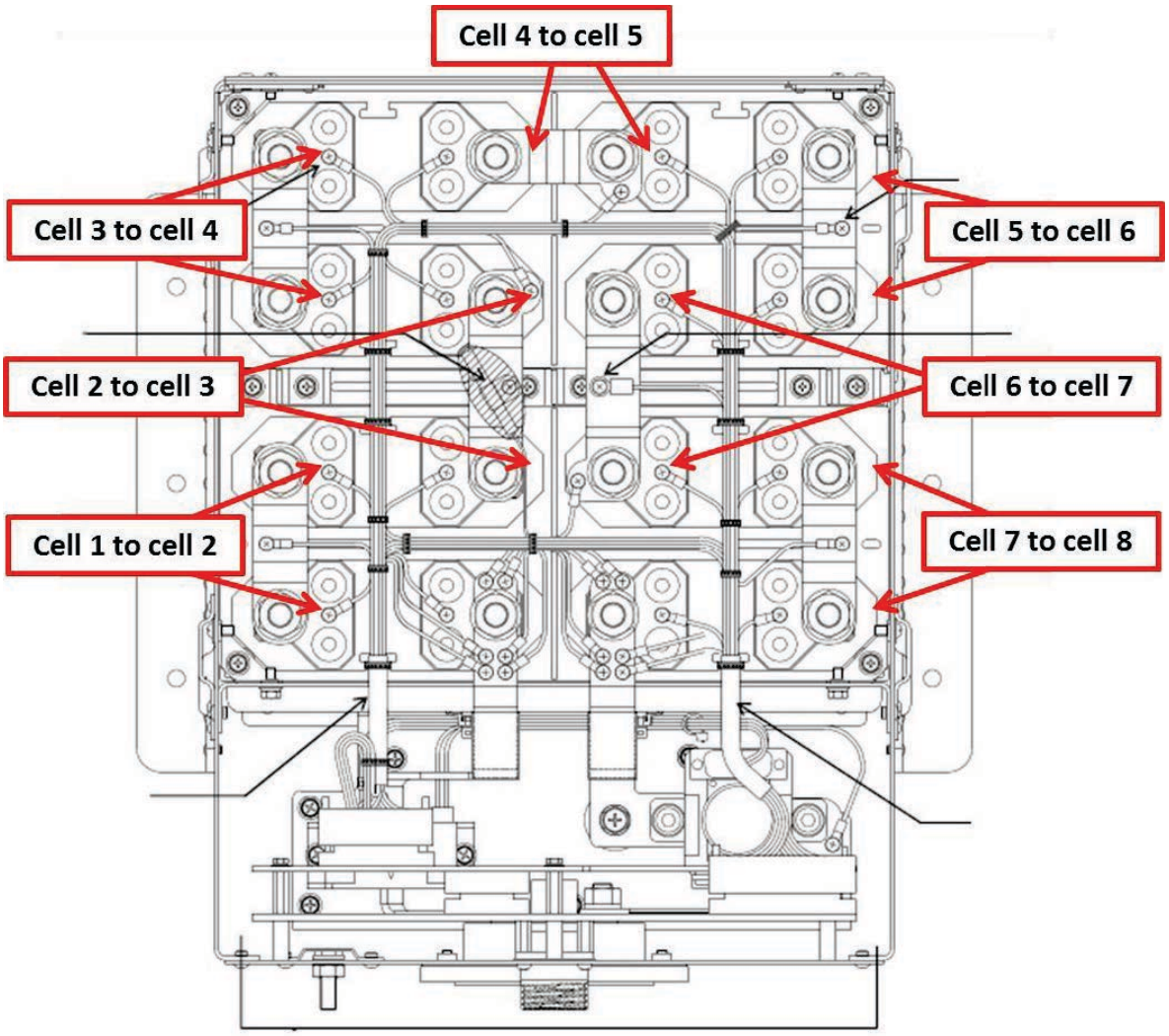

Cell to Cell Test Locations

Bonding Resistance Test

Caution: Electro Static Discharge Sensitive protection is required.
WARNING! Full battery voltage potential is present!
Personal protective equipment is required.

Bonding Resistance

If all of the parameters of the battery testing are within specifications, conduct the following tests.

Using a Hioki battery tester measure the resistance between the ground stud nut (IPL 240) to the non-coated area adjacent to the ground stud.

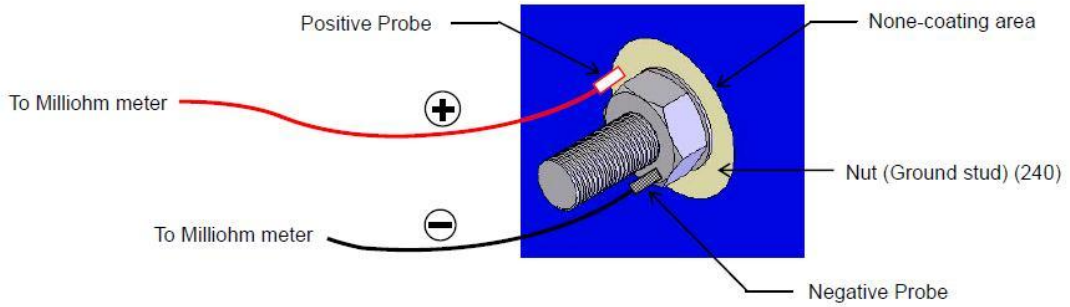

Bonding Resistance Test Setup

Bonding Resistance	0.18 Ω	(Criteria <0.001 Ohm)

DC Resistance Measurements

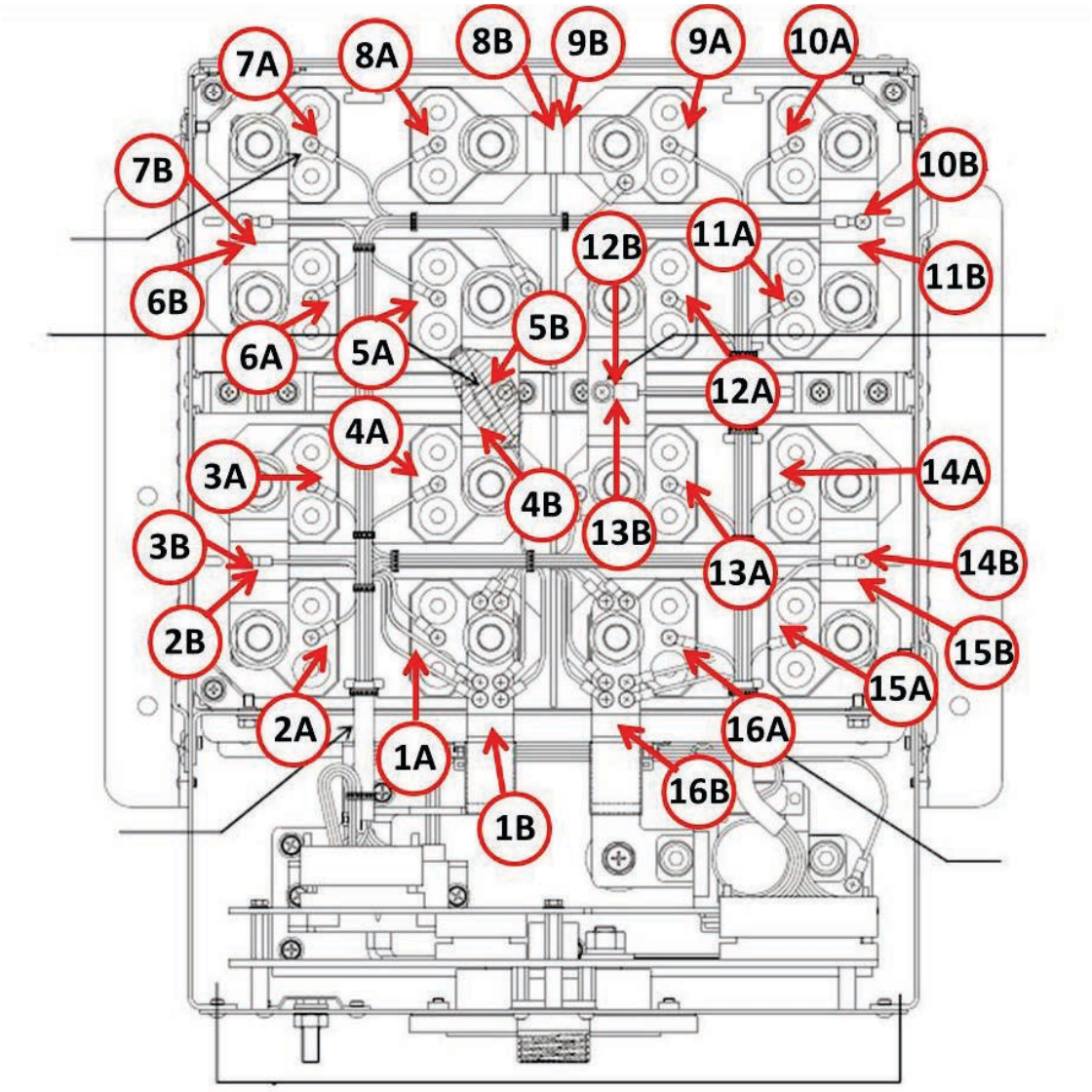

DC Resistance Measurement Locations

Equipment Documentation:

Equipment	Model	Property Number	Calibration Date
TRUE RMA MULTIMETER	Fluke 289		

Procedure:

Measurements to be made at positions shown on previous page, from center of bus bar (link) to point on terminal plate between rivets (not on wiring screw).
Note: Center of bus bar for measurements 4B and 5B may be inaccessible due to white resin. Closest points to resin are acceptable measurement points.
Apply equal, firm pressure on both contacts of each probe at measurement positions until meter indicates measurement has been made (green lights flash).
Record DC resistance.
Results:

Measurement	Value *(mOhms)*
1A – 1B	0.08 Ω
2A – 2B	0.08 Ω
3A – 3B	0.08 Ω
4A – 4B	0.08 Ω
5A – 5B	0.08 Ω
6A – 6B	0.08 Ω
7A – 7B	0.08 Ω
8A – 8B	0.08 Ω
9A – 9B	0.08 Ω
10A – 10B	0.08 Ω
11A – 11B	0.08 Ω
12A – 12B	0.08 Ω
13A – 13B	0.09 Ω
14A – 14B	0.08 Ω
15A – 15B	0.09 Ω
16A – 16B	0.09 Ω

More Battery Level Test Data

This section contains the graphed summary of the data recorded during testing.

Task A.1.B – 25C, 1 of 5

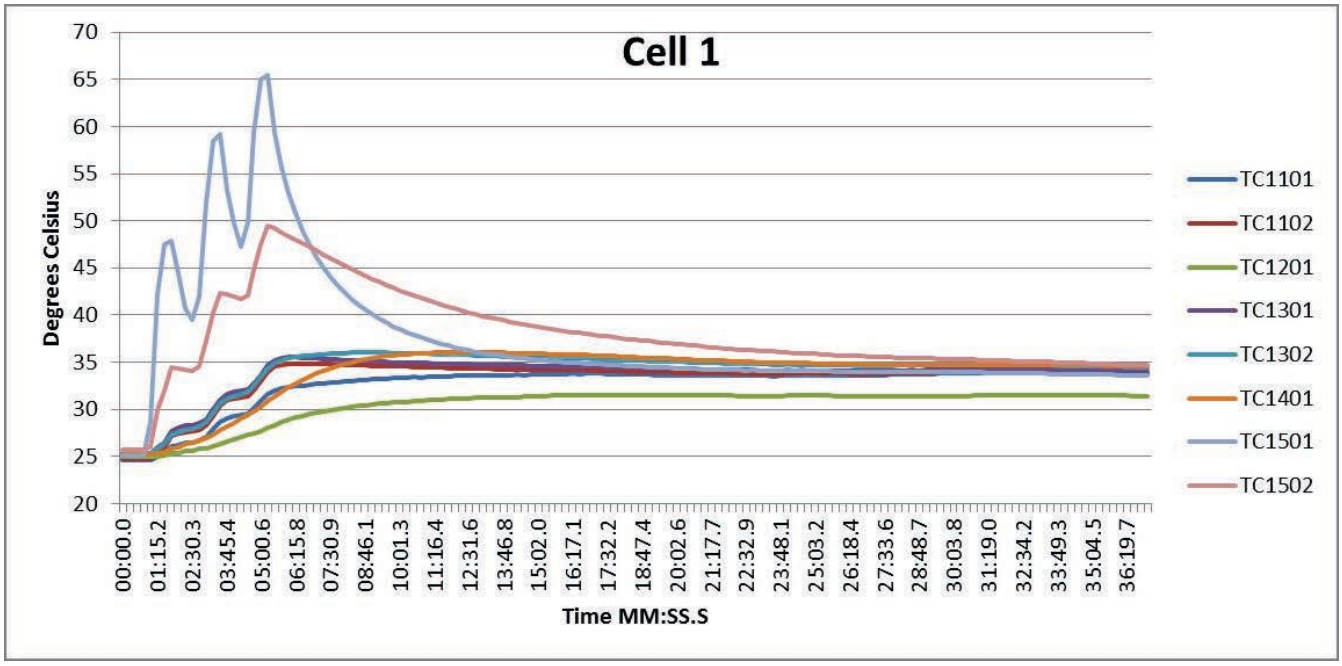

Figure B.1: Task A.1.B, 25 °C, 1 of 5, Cell 1 Temperatures

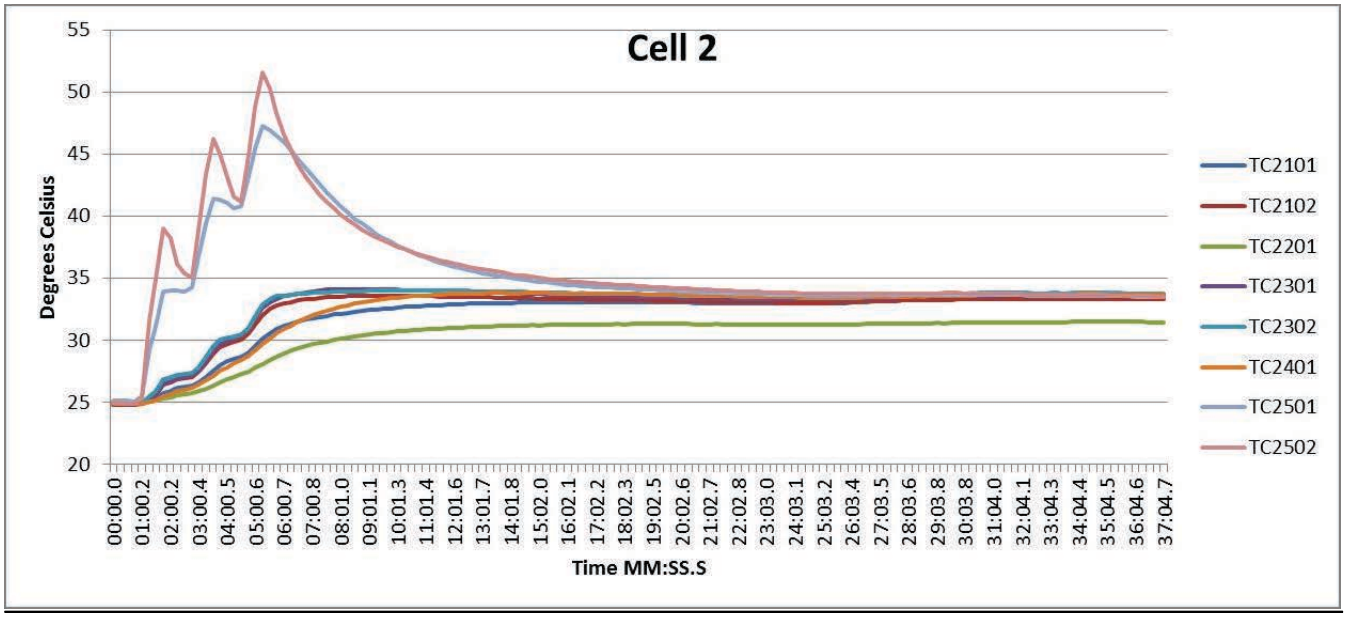

Figure B.2: Task A.1.B, 25 °C, 1 of 5, Cell 2 Temperatures

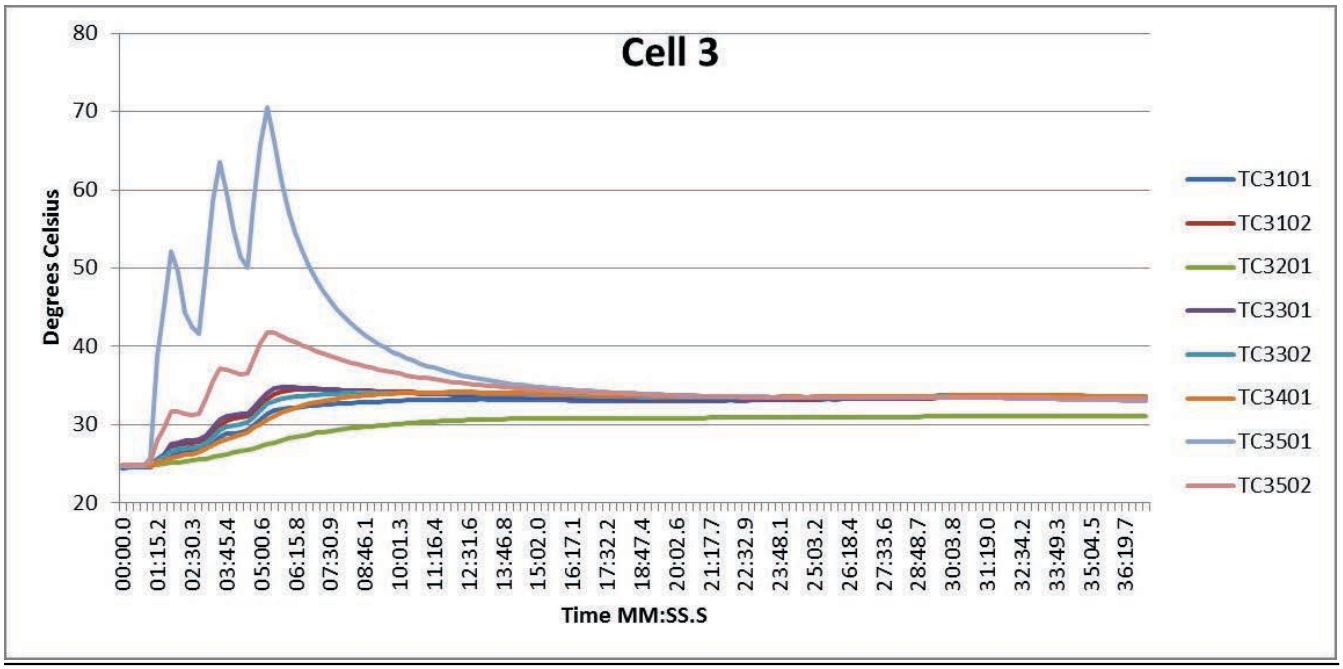

Figure B.3: Task A.1.B, 25 °C, 1 of 5, Cell 3 Temperatures

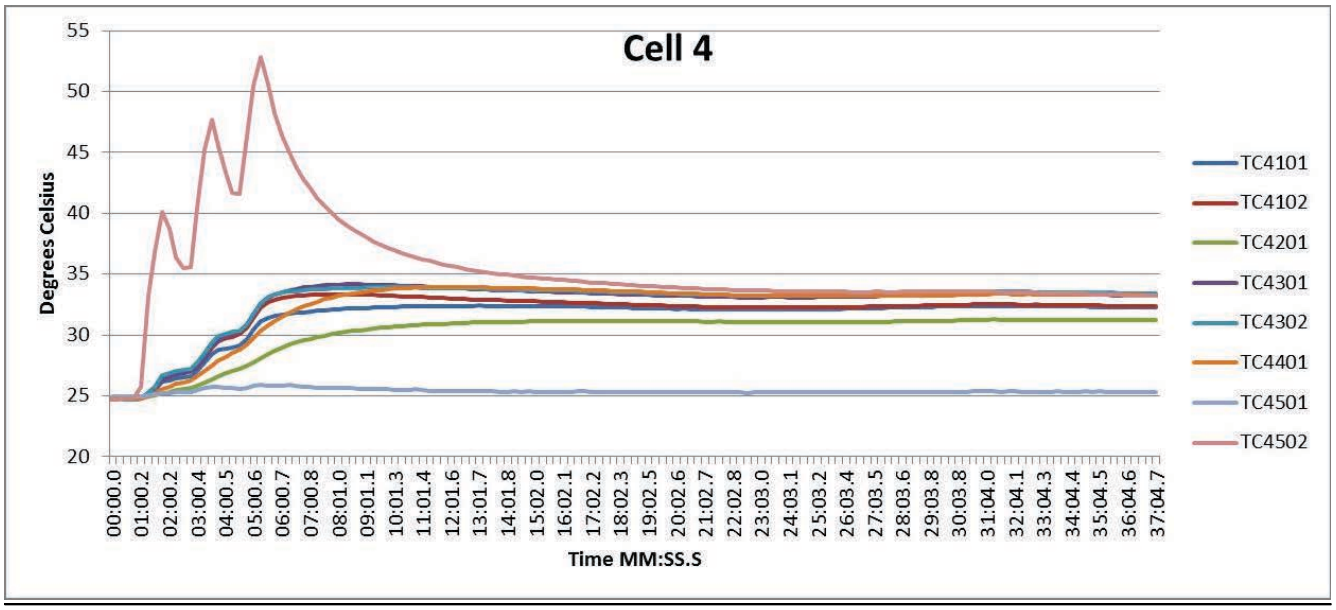

Figure B.4: Task A.1.B, 25 °C, 1 of 5, Cell 4 Temperatures

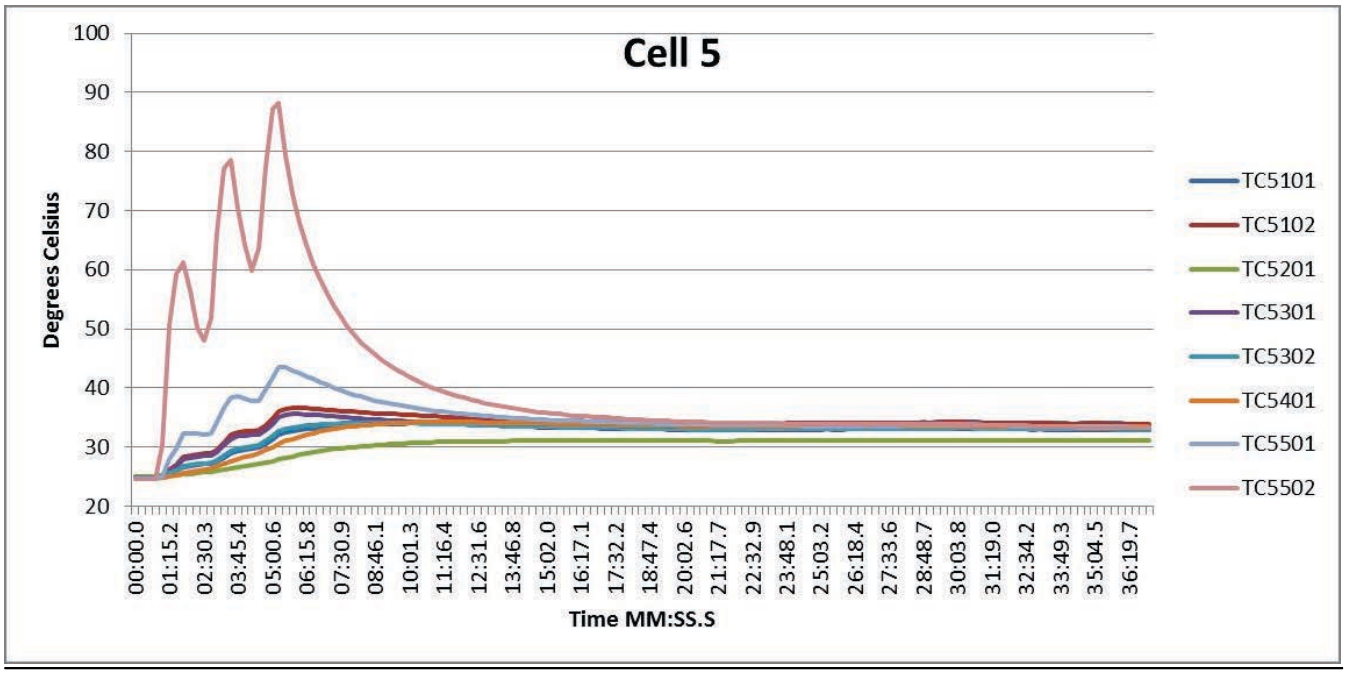

Figure B.5: Task A.1.B, 25 °C, 1 of 5, Cell 5 Temperatures

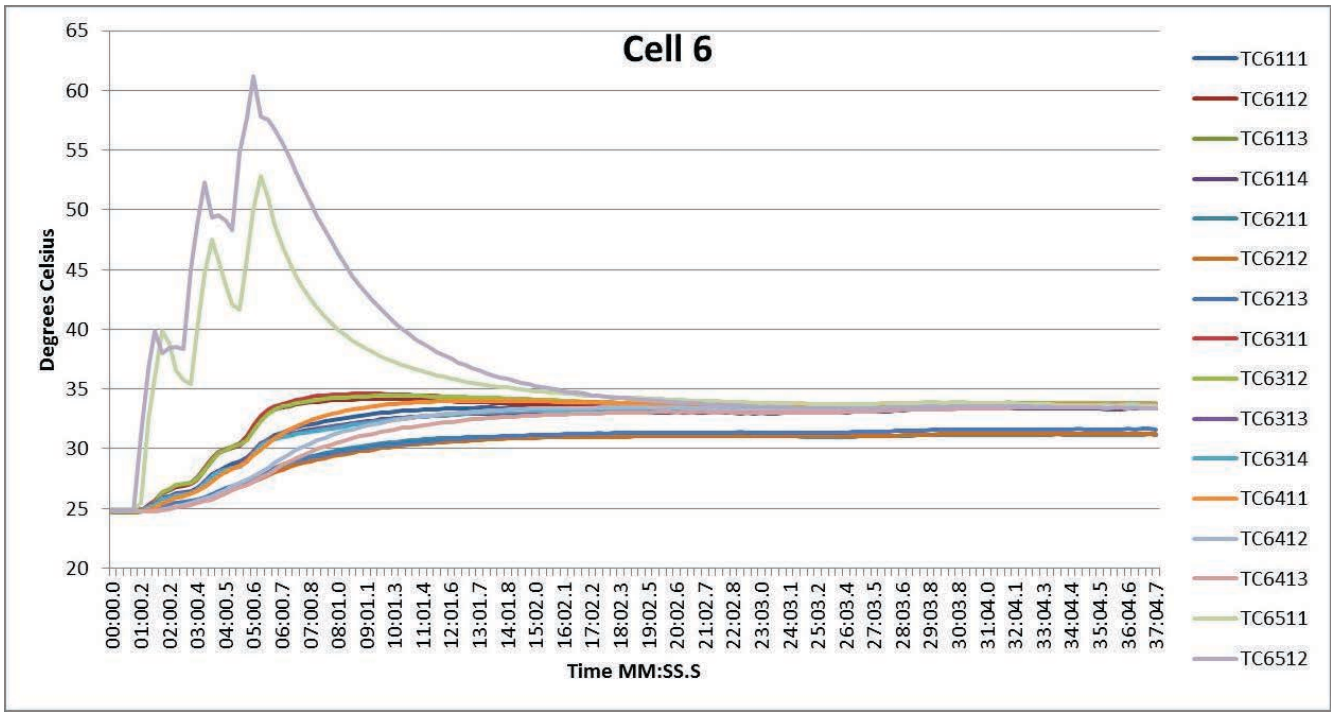

Figure B.6: Task A.1.B, 25 °C, 1 of 5, Cell 6 Temperatures

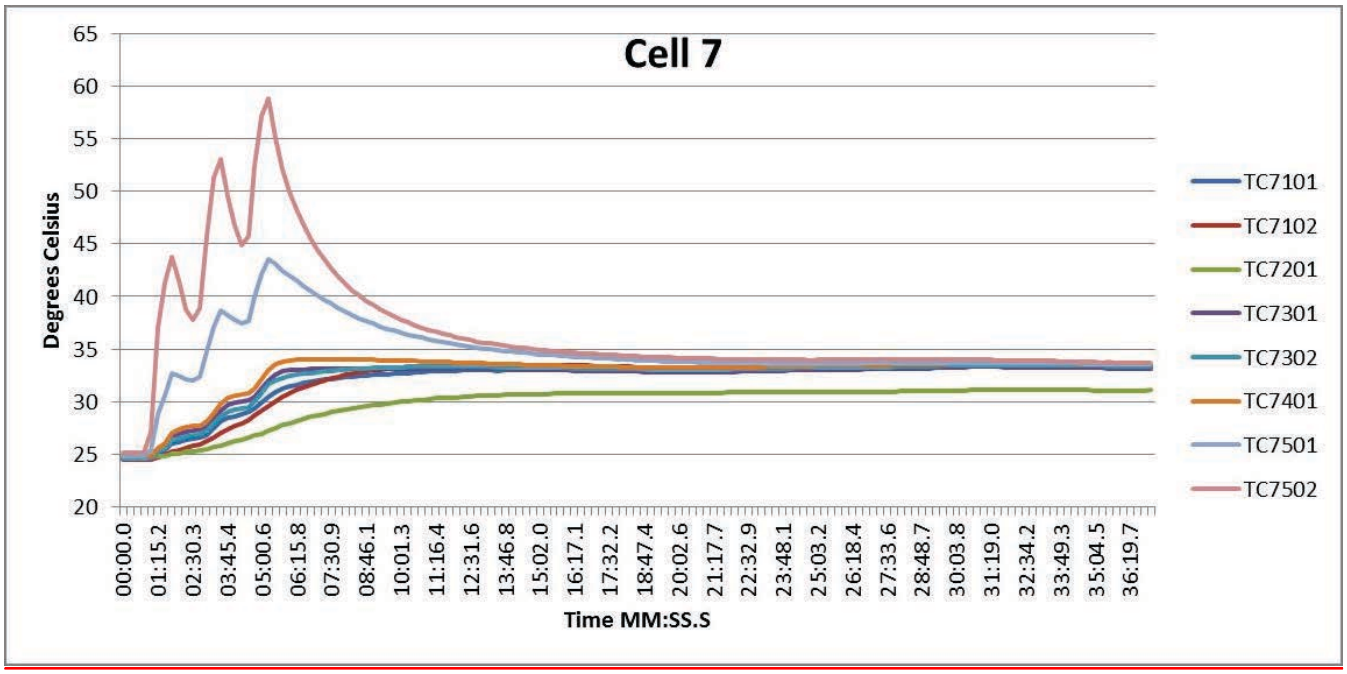

Figure B.7: Task A.1.B, 25 °C, 1 of 5, Cell 7 Temperatures

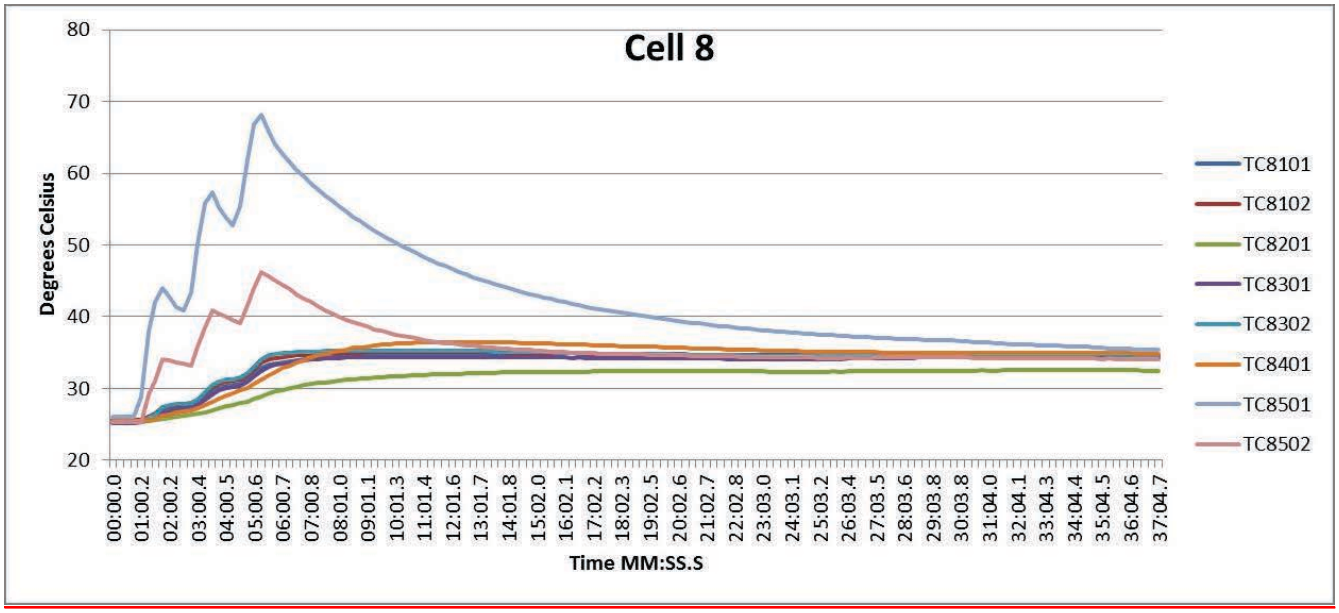

Figure B.8: Task A.1.B, 25 °C, 1 of 5, Cell 8 Temperatures

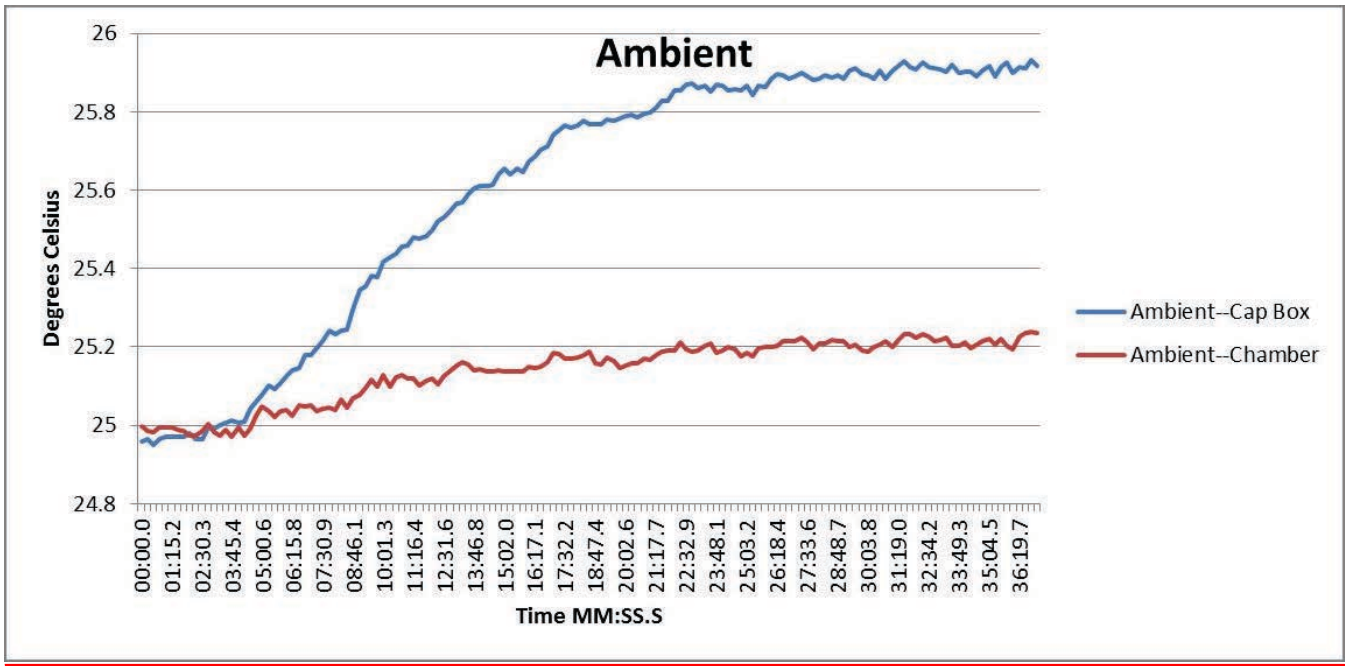

Figure B.9: Task A.1.B, 25 °C, 1 of 5, Ambient Temperatures

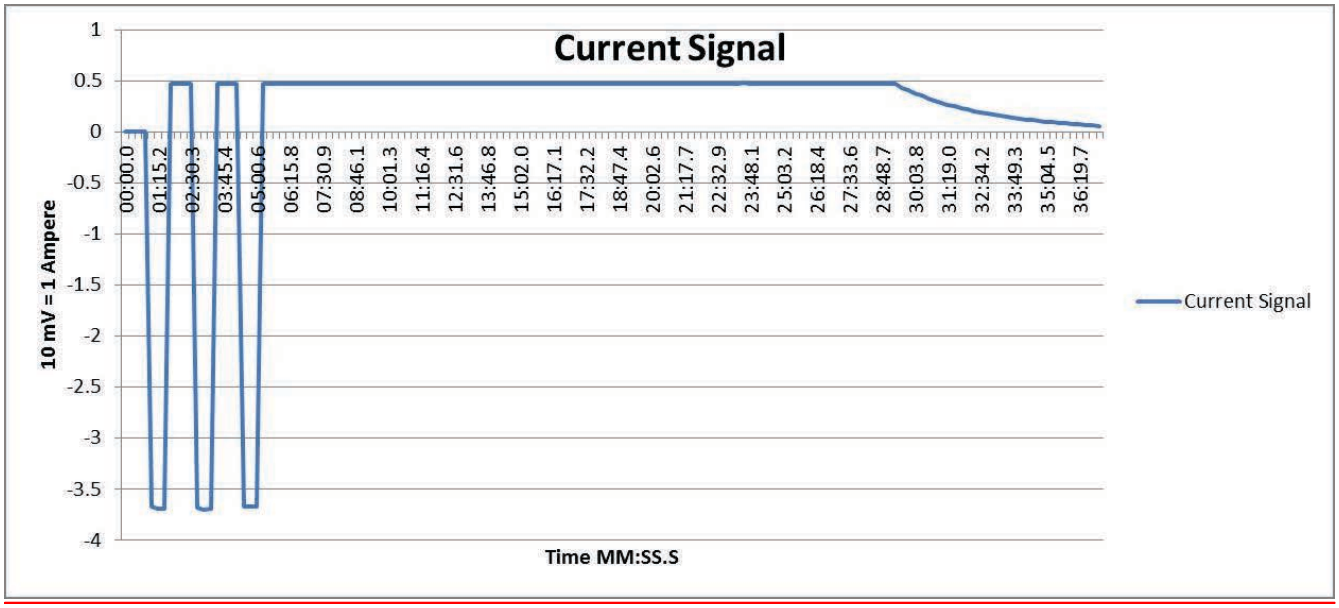

Figure B.10: Task A.1.B, 25 °C, 1 of 5, Current Signal from BMU HECS

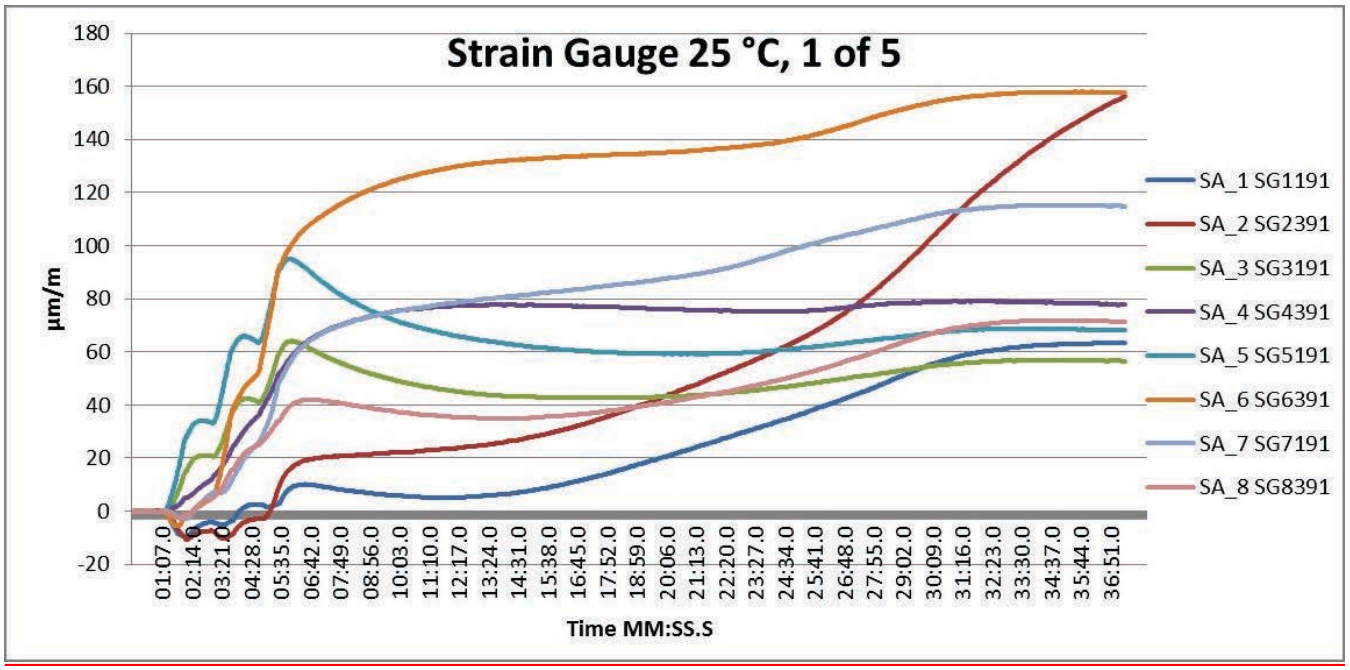

Figure B.11: Task A.1.B, 25 °C, 1 of 5, Strain Gauge

Task A.1.B – 25 °C, 2 of 5

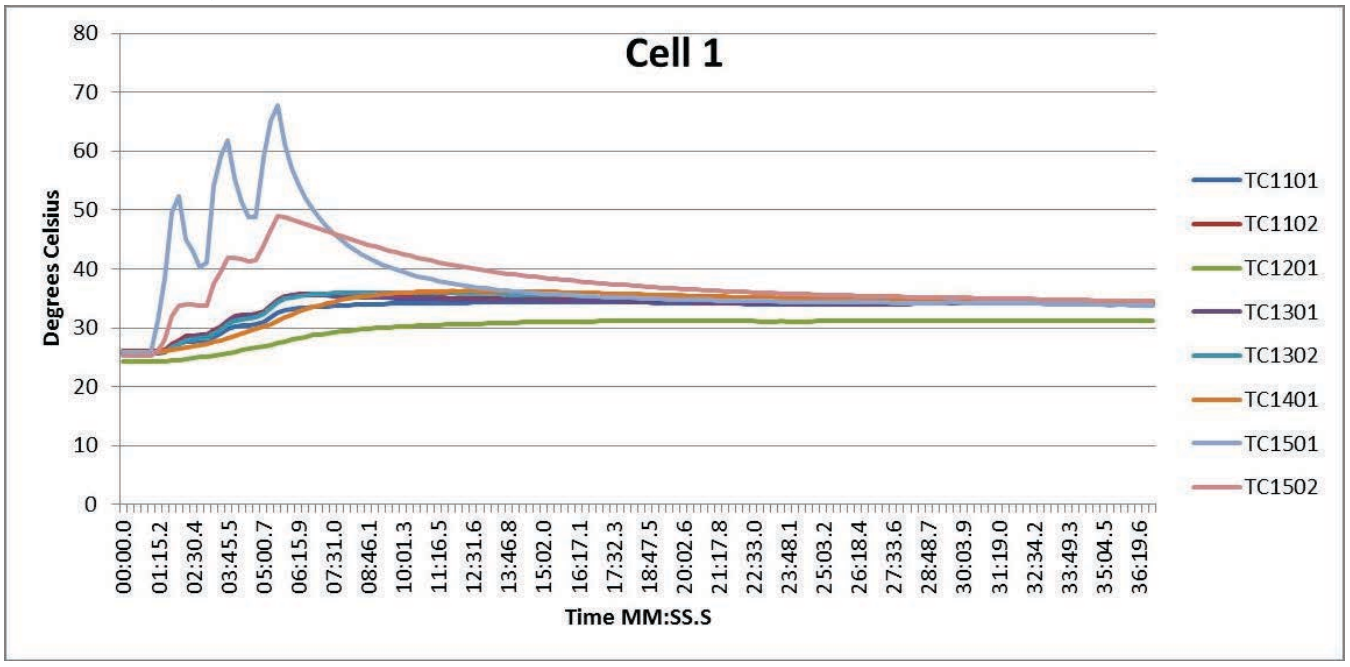

Figure B.12: Task A.1.B, 25 °C, 2 of 5, Cell 1 Temperatures

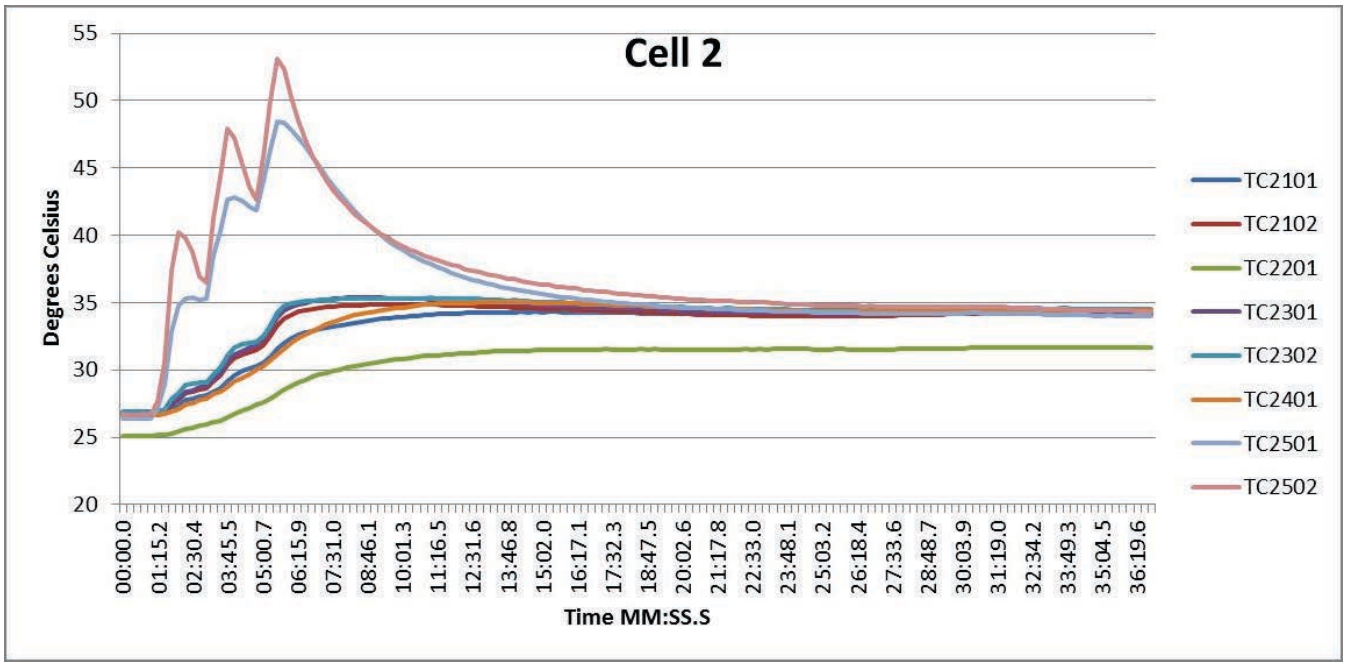

Figure B.13: Task A.1.B, 25 °C, 2 of 5, Cell 2 Temperatures

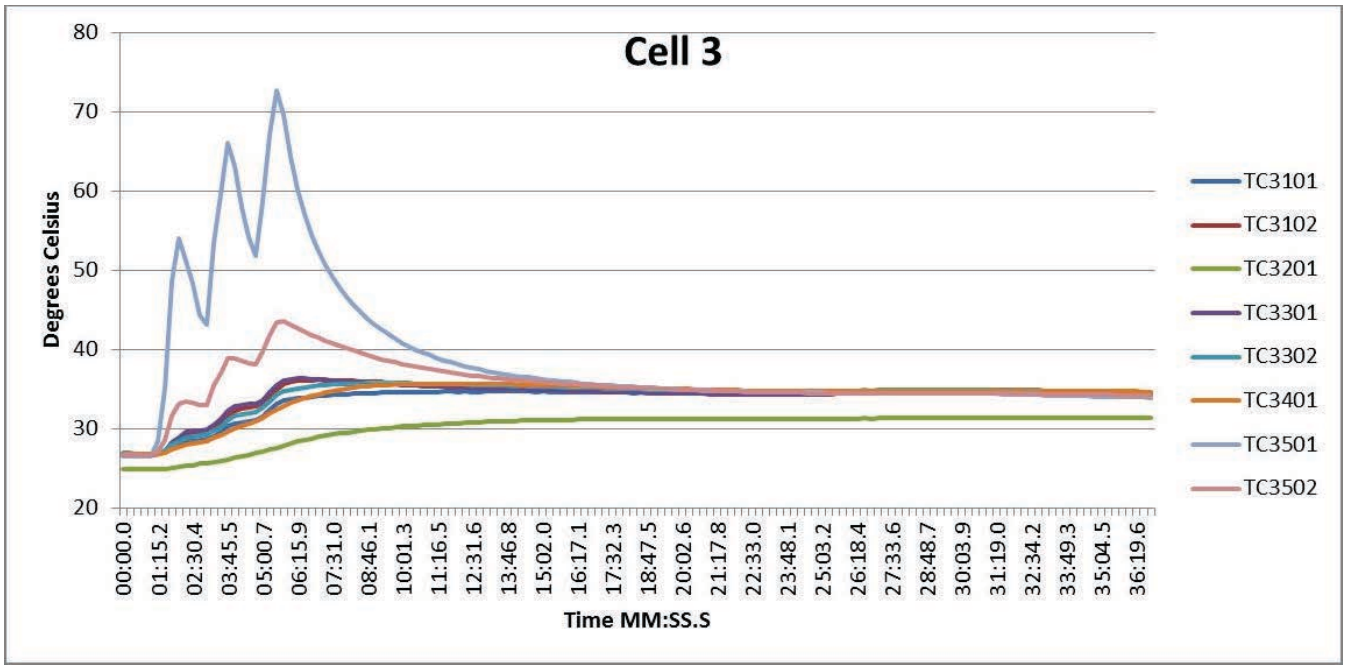

Figure B.14: Task A.1.B, 25 °C, 2 of 5, Cell 3 Temperatures

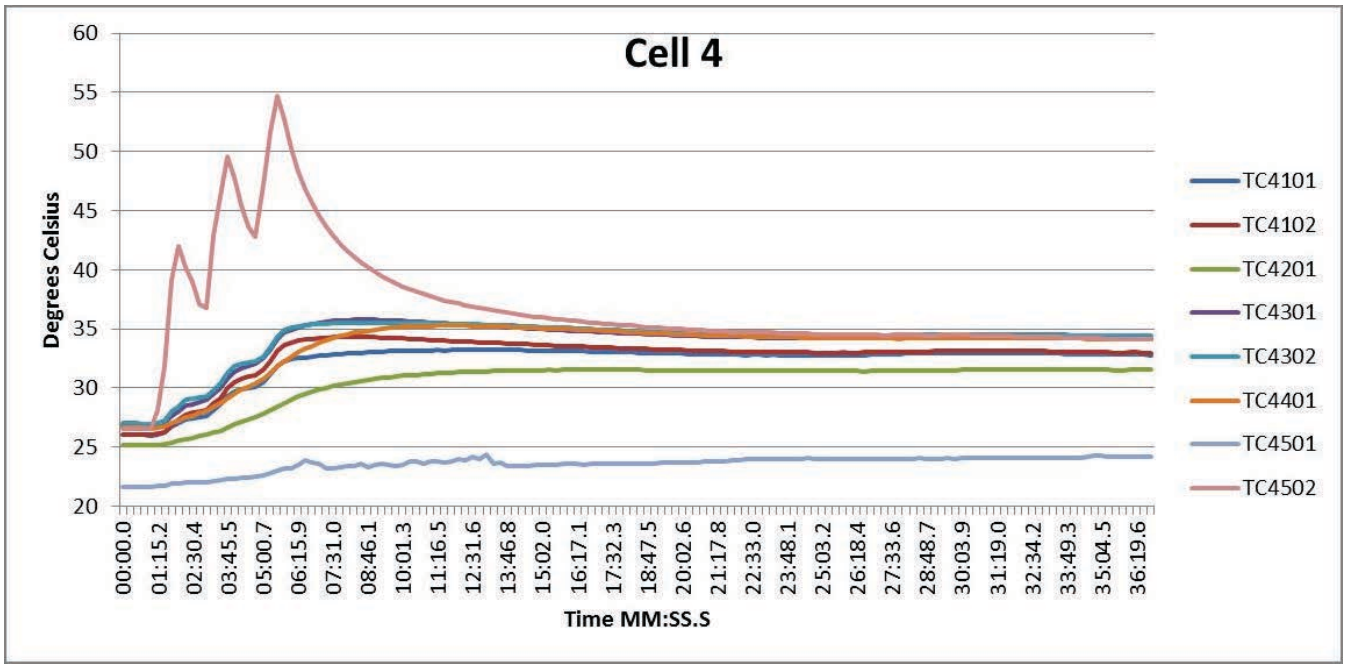

Figure B.15: Task A.1.B, 25 °C, 2 of 5, Cell 4 Temperatures

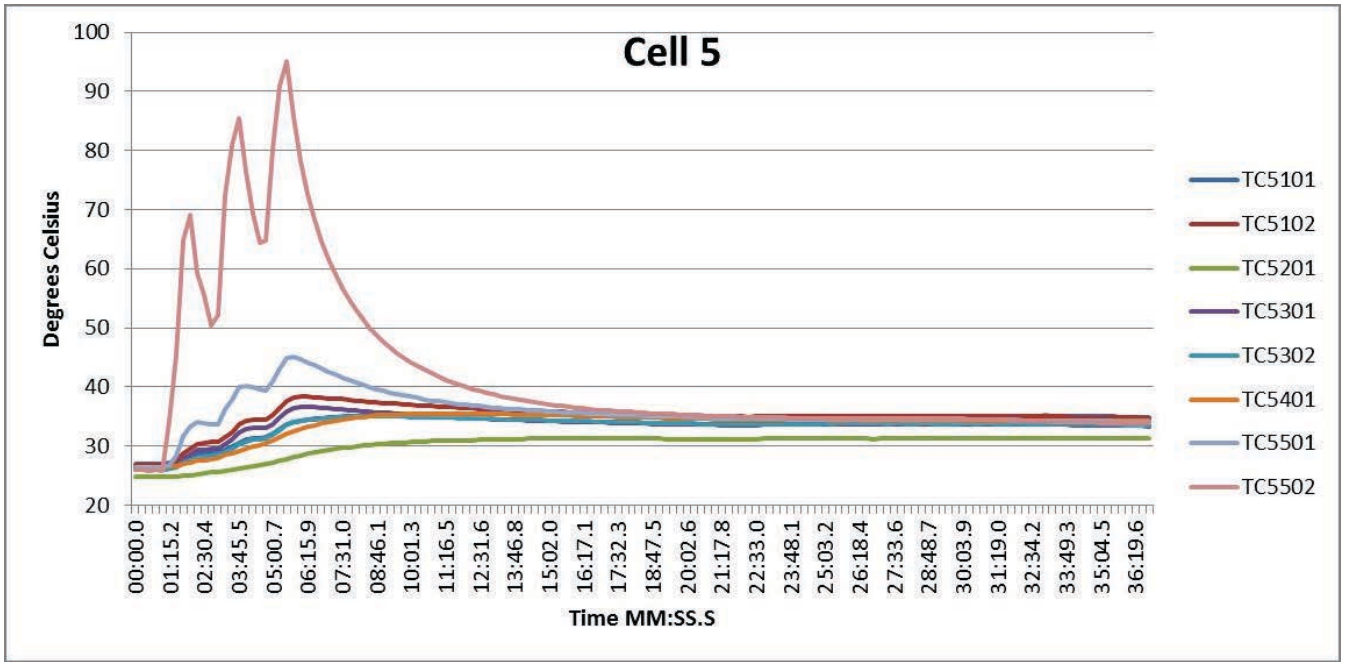

Figure B.16: Task A.1.B, 25 °C, 2 of 5, Cell 5 Temperatures

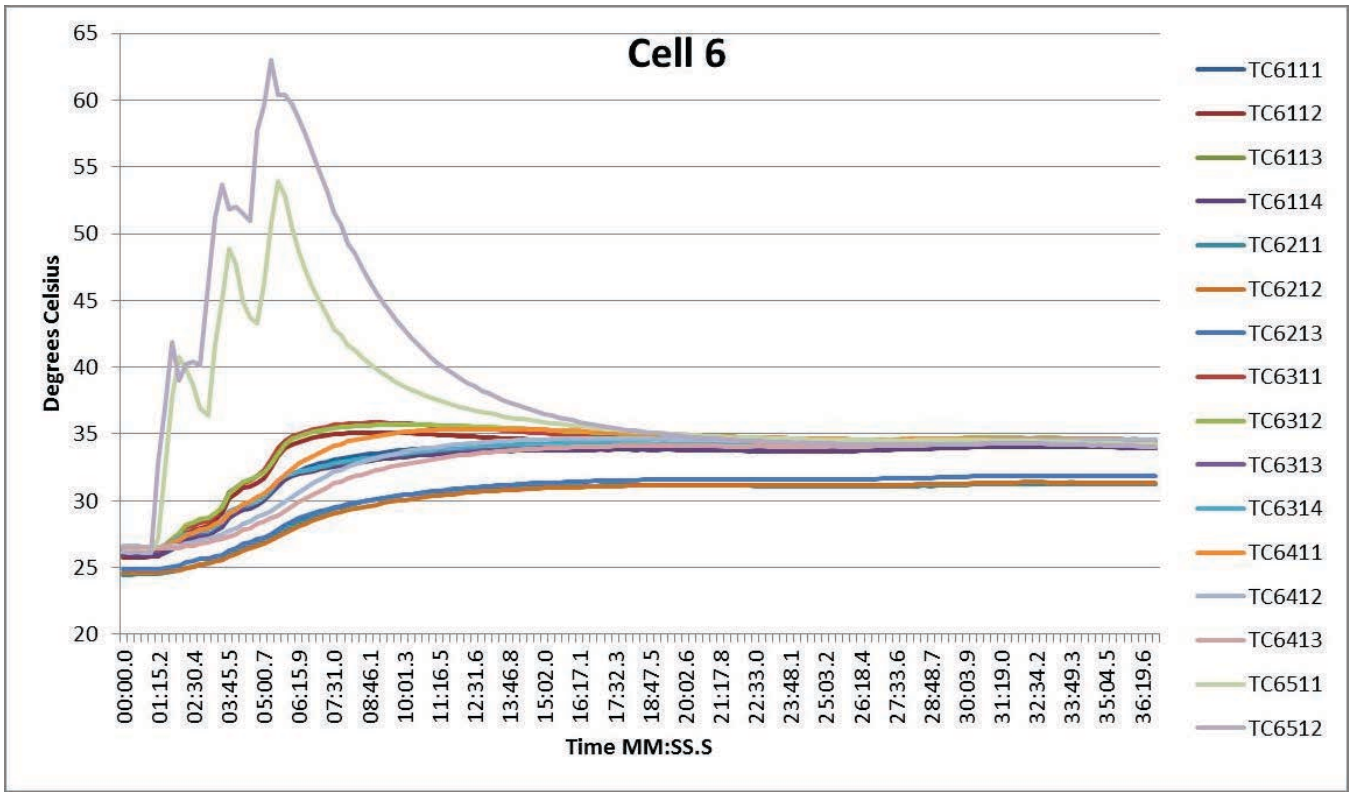

Figure B.17: Task A.1.B, 25 °C, 2 of 5, Cell 6 Temperatures

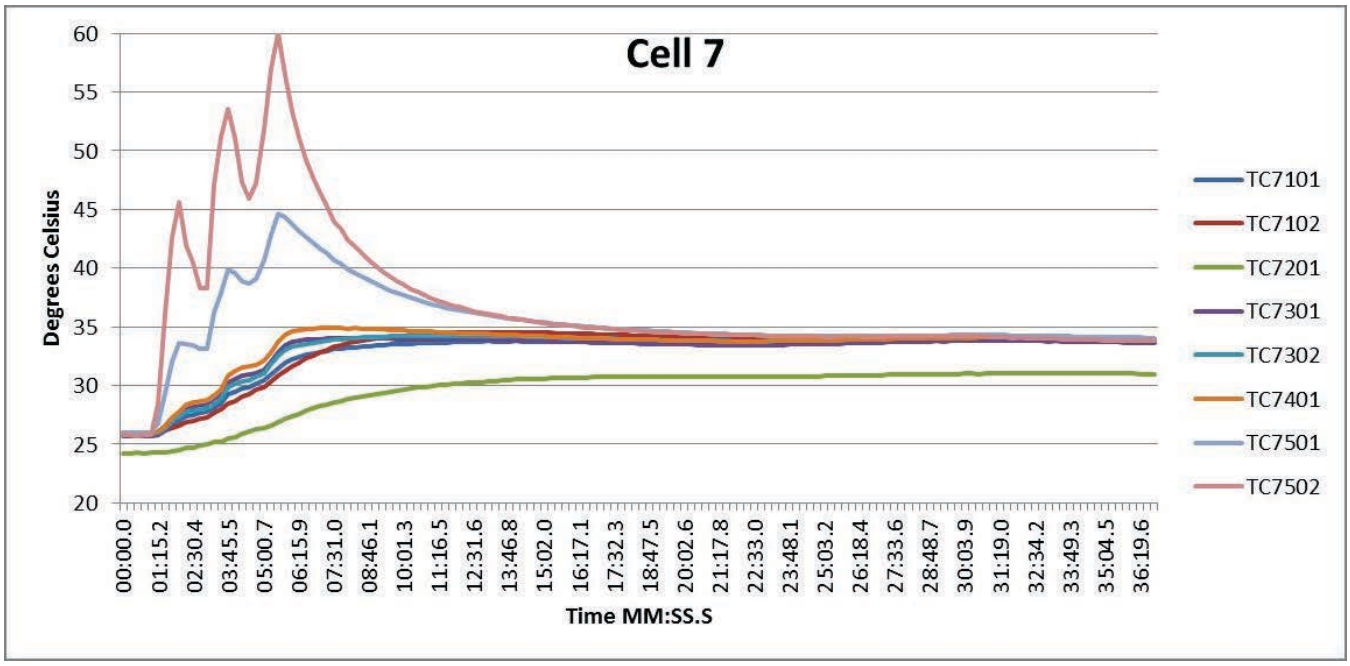

Figure B.18: Task A.1.B, 25 °C, 2 of 5, Cell 7 Temperatures

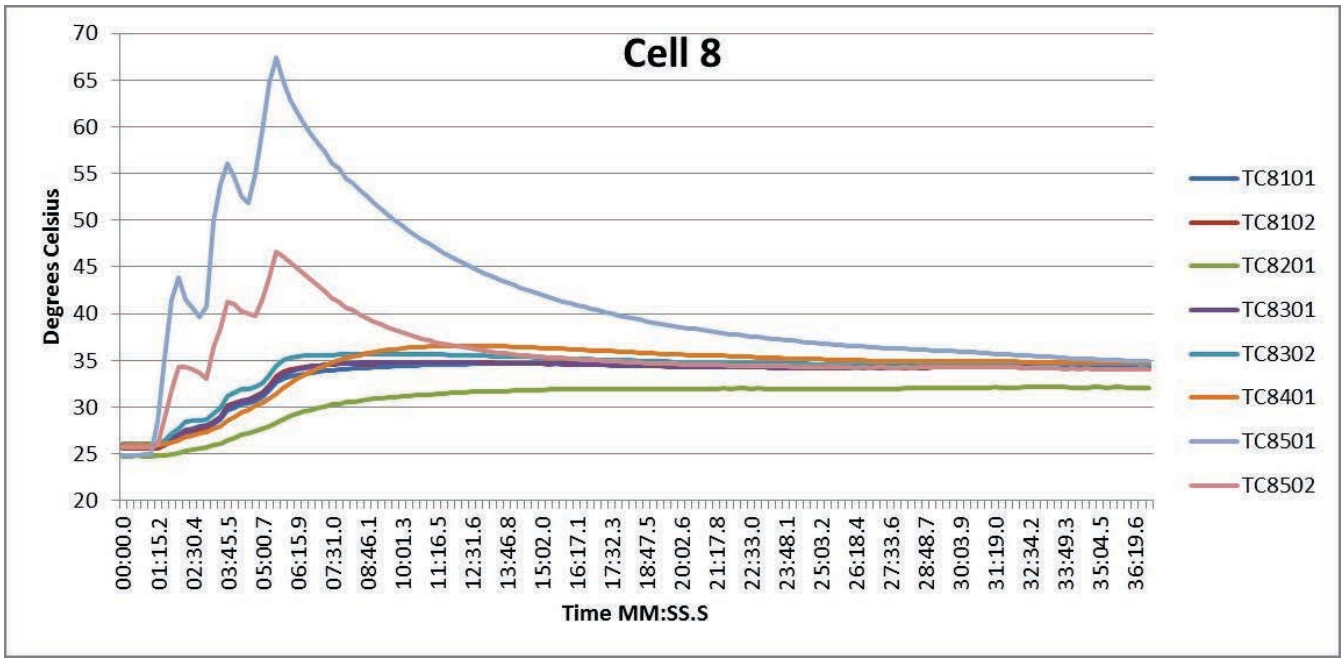

Figure B.19: Task A.1.B, 25 °C, 2 of 5, Cell 8 Temperatures

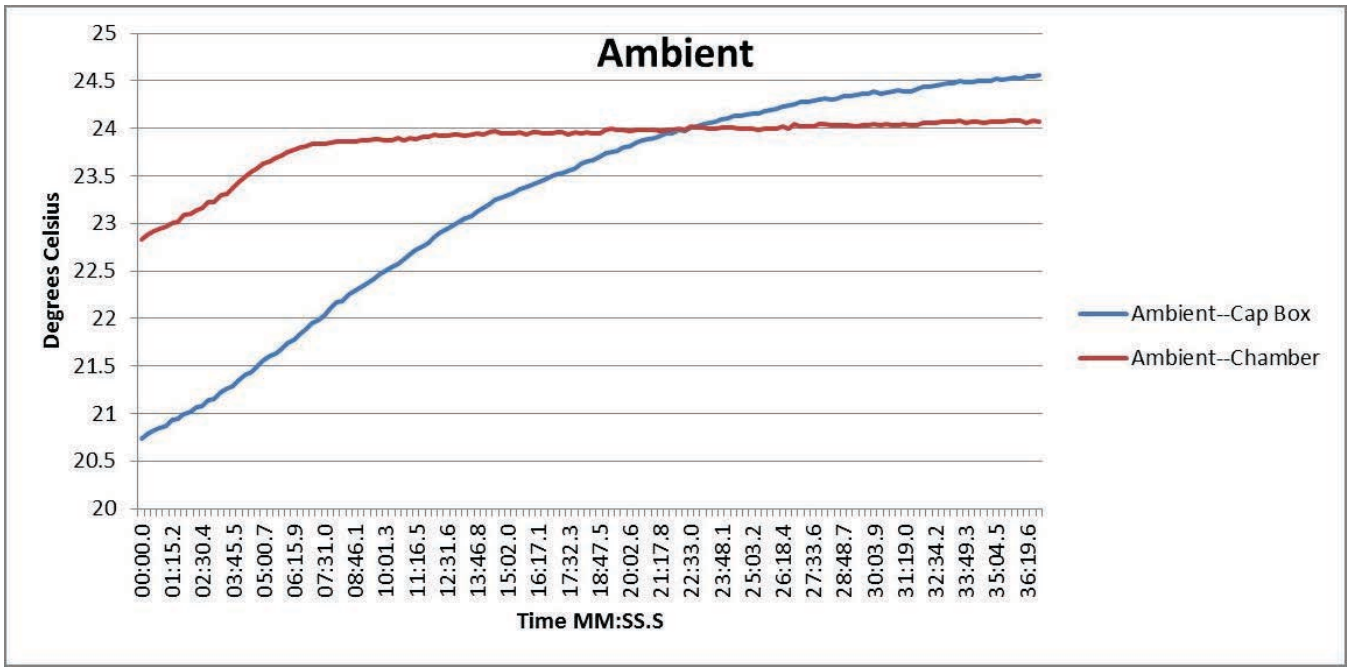

Figure B.20: Task A.1.B, 25 °C, 2 of 5, Ambient Temperatures

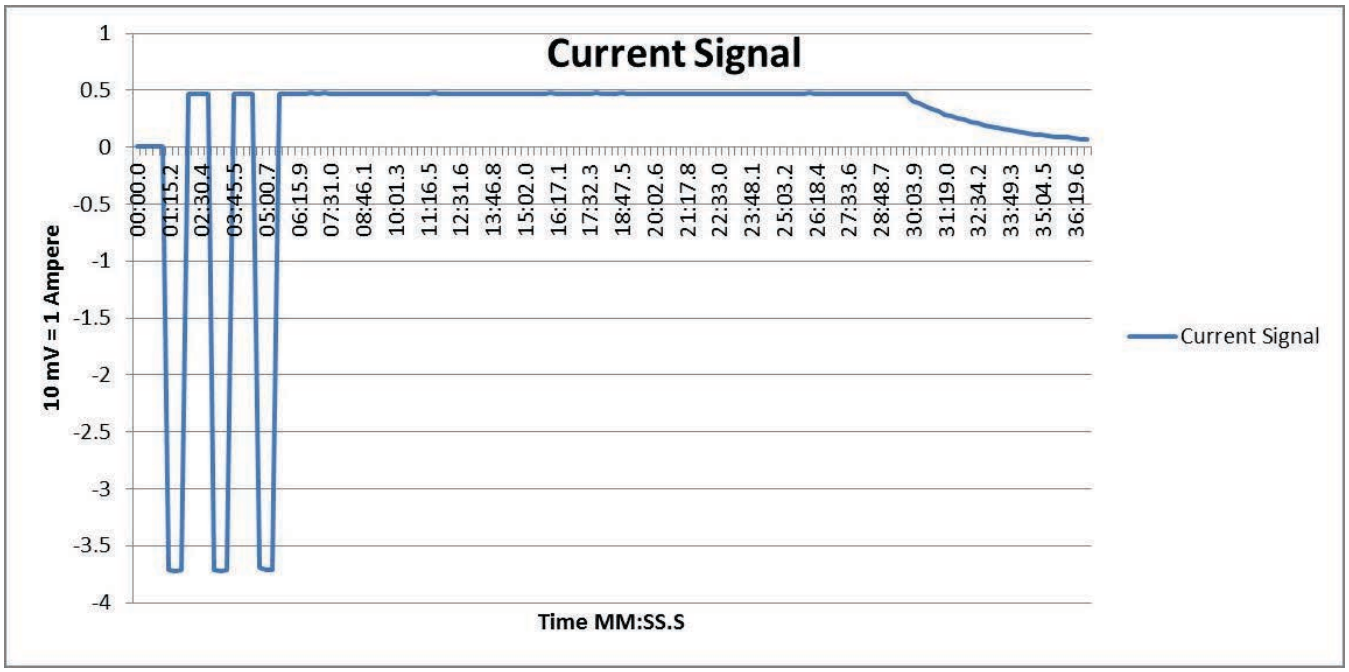

Figure B.21: Task A.1.B, 25 °C, 2 of 5, Current Signal from BMU HECS

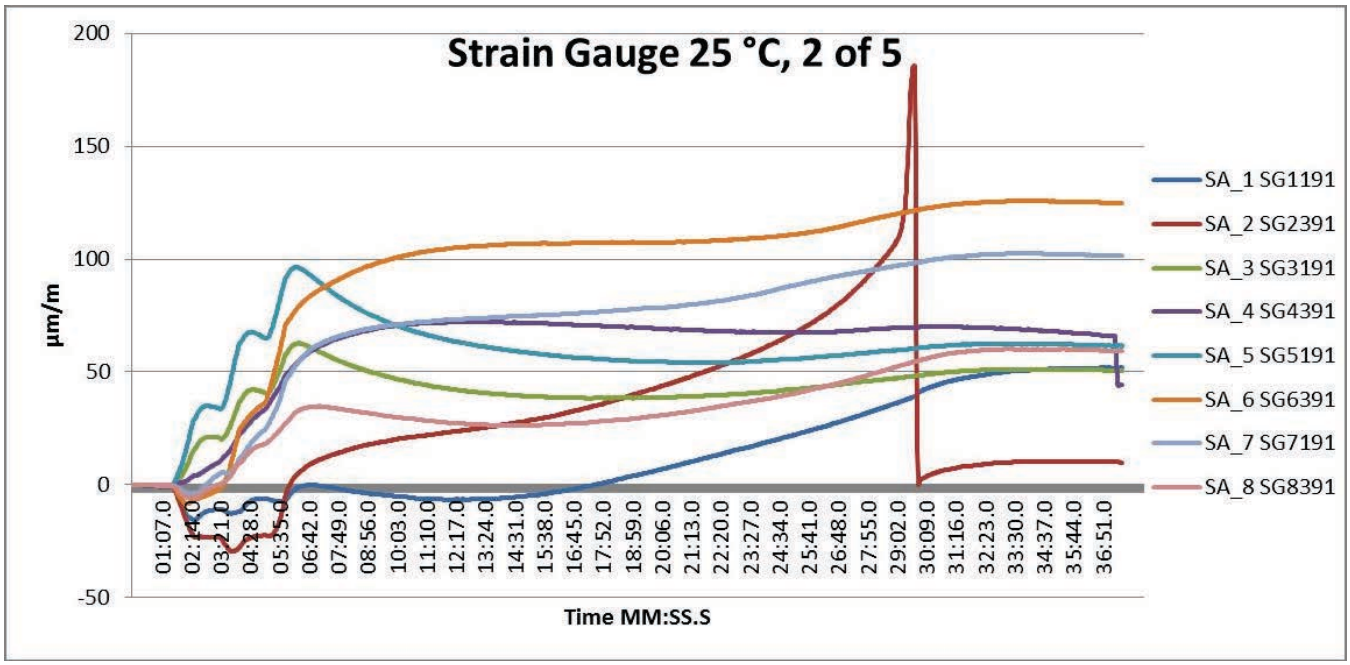

Figure B.22: Task A.1.B, 25 °C, 2 of 5, Strain Gauges

Task A.1.B – 25 °C, 3 of 5

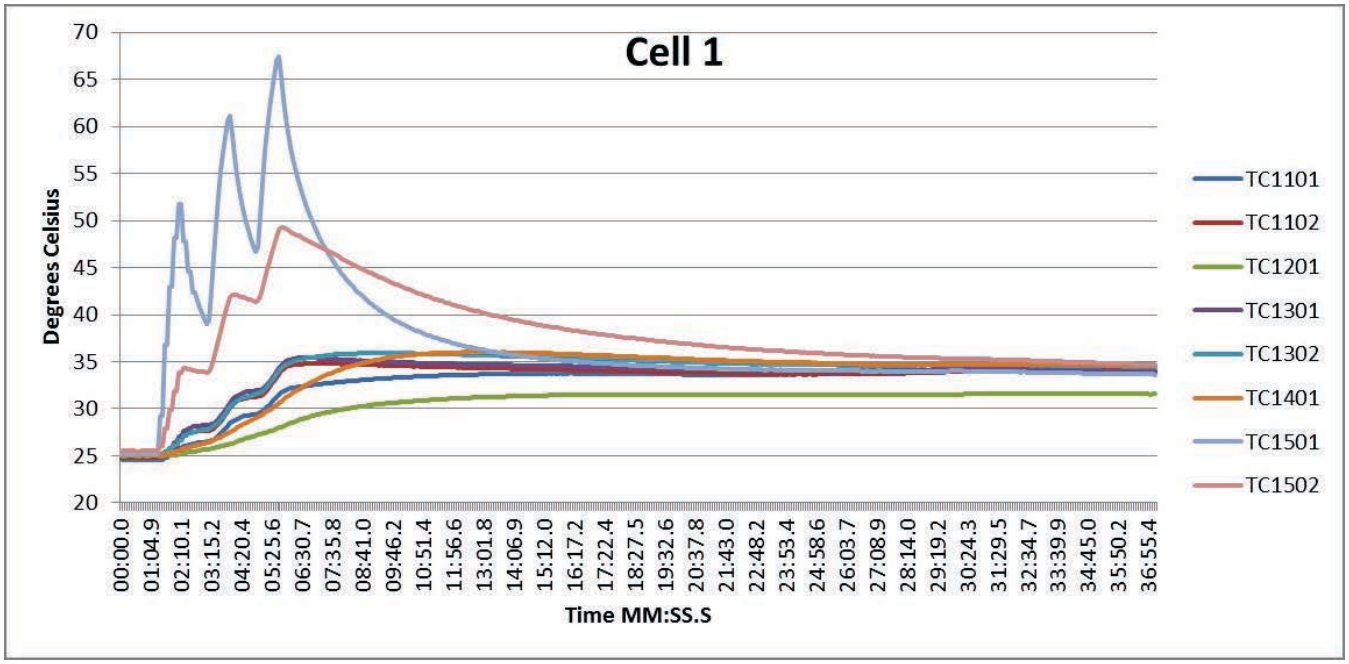

Figure B.23: Task A.1.B, 25 °C, 3 of 5, Cell 1 Temperatures

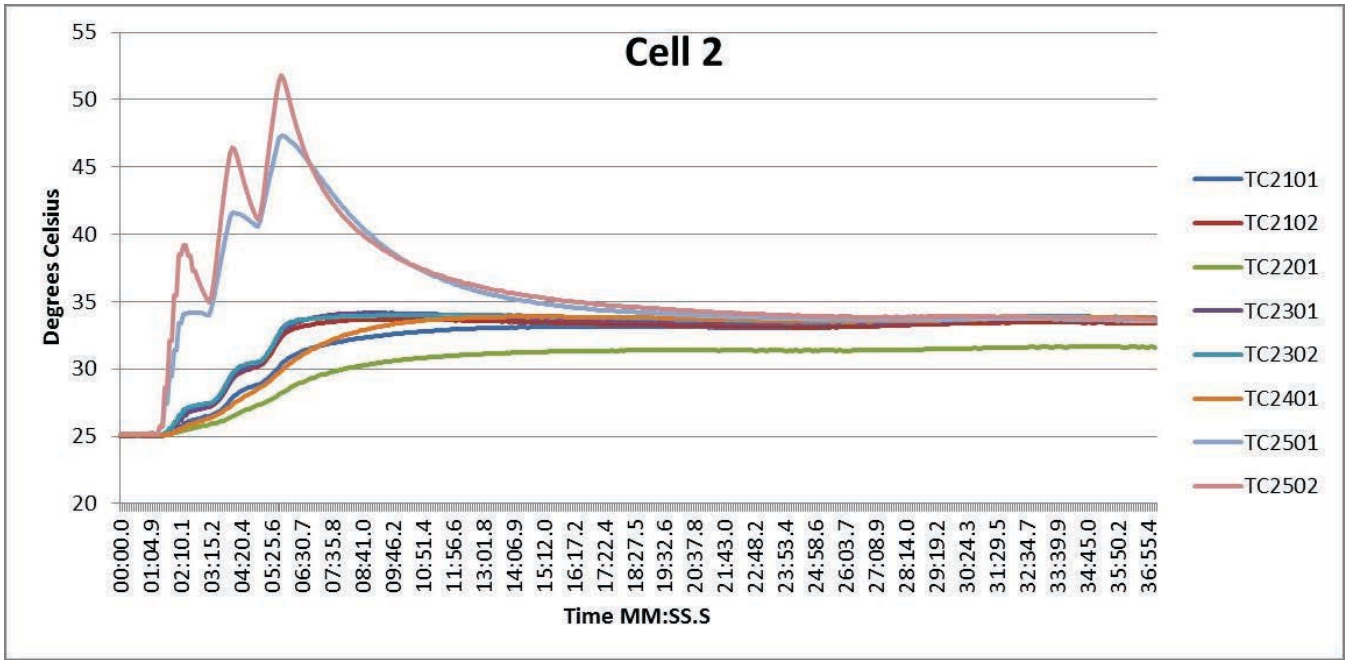

Figure B.24: Task A.1.B, 25 °C, 3 of 5, Cell 2 Temperatures

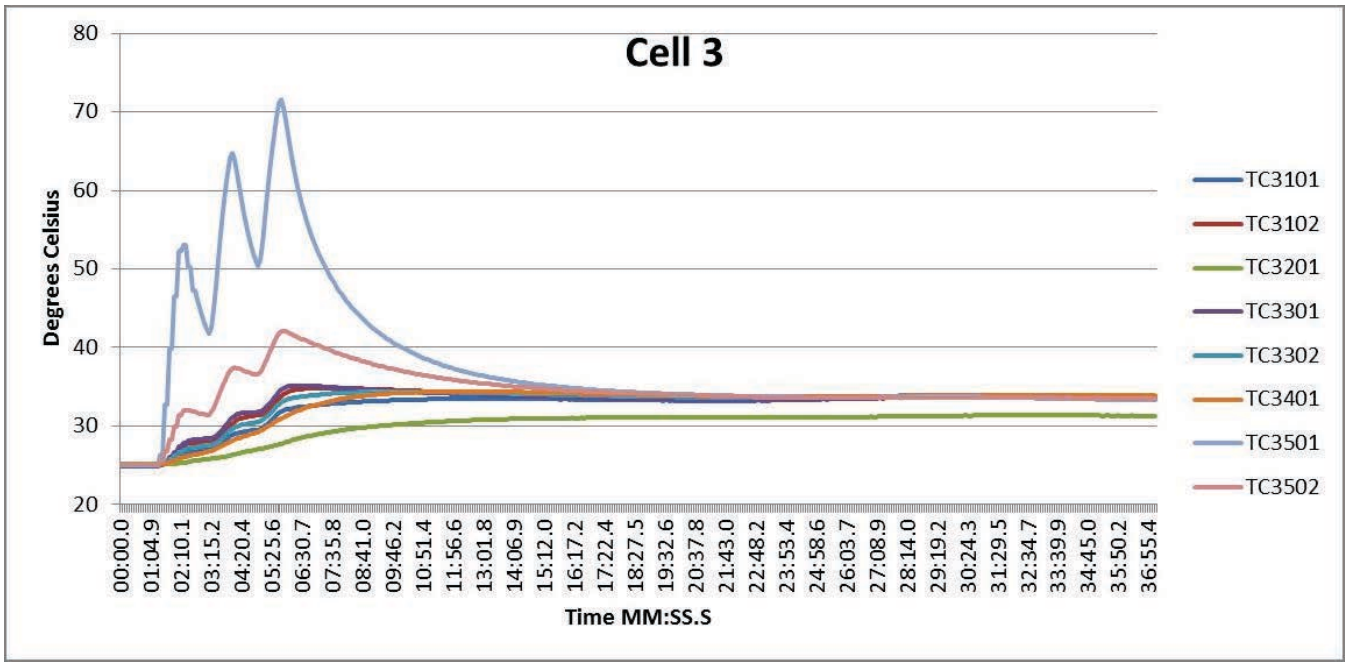

Figure B.25: Task A.1.B, 25 °C, 3 of 5, Cell 3 Temperatures

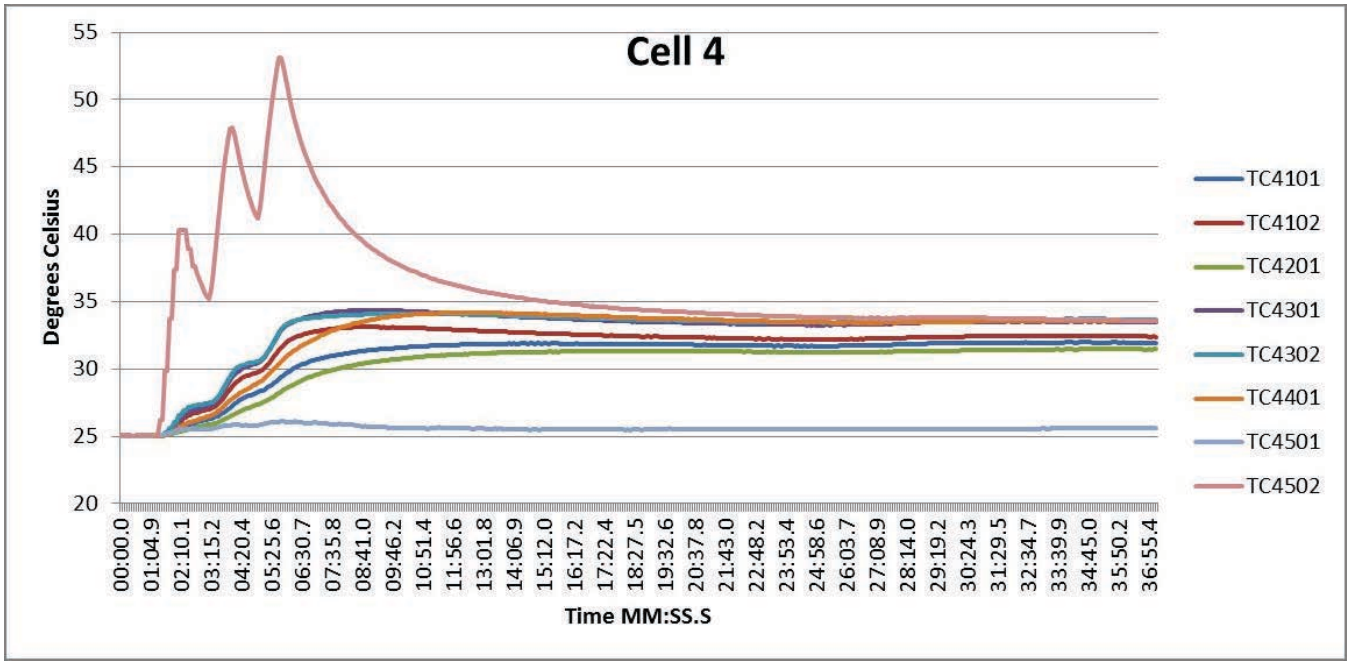

Figure B.26: Task A.1.B, 25 °C, 3 of 5, Cell 4 Temperatures

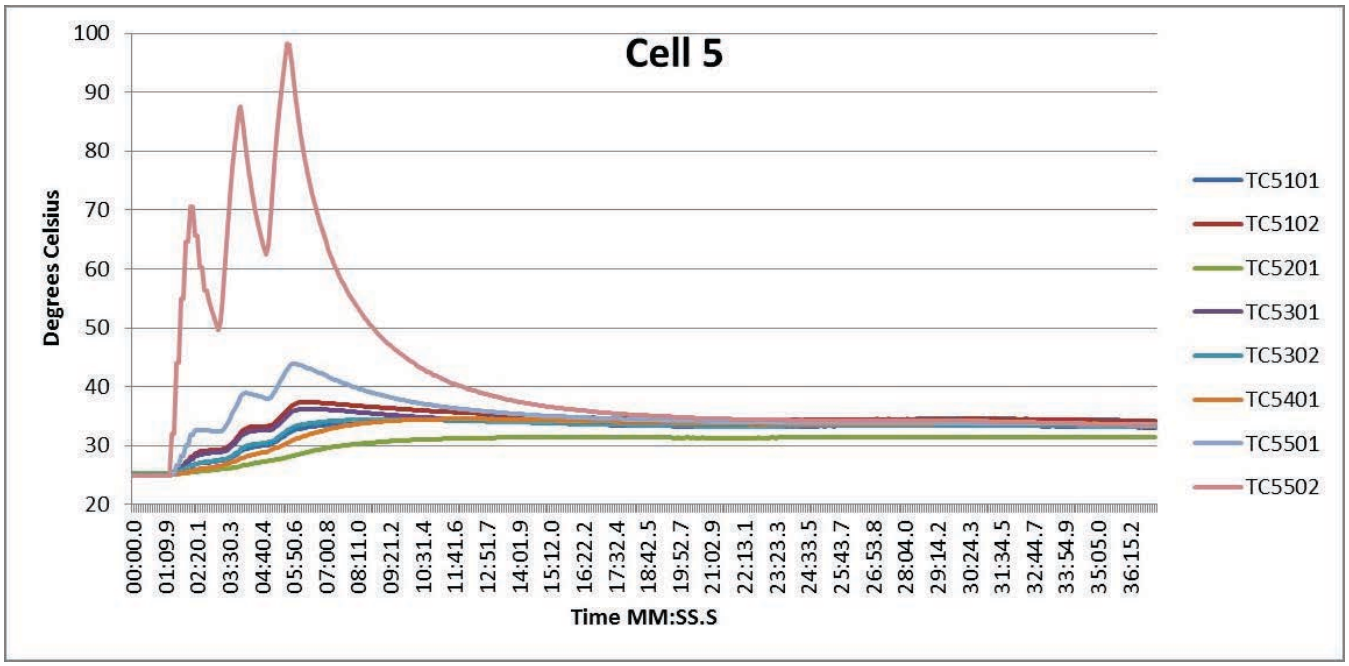

Figure B.27: Task A.1.B, 25 °C, 3 of 5, Cell 5 Temperatures

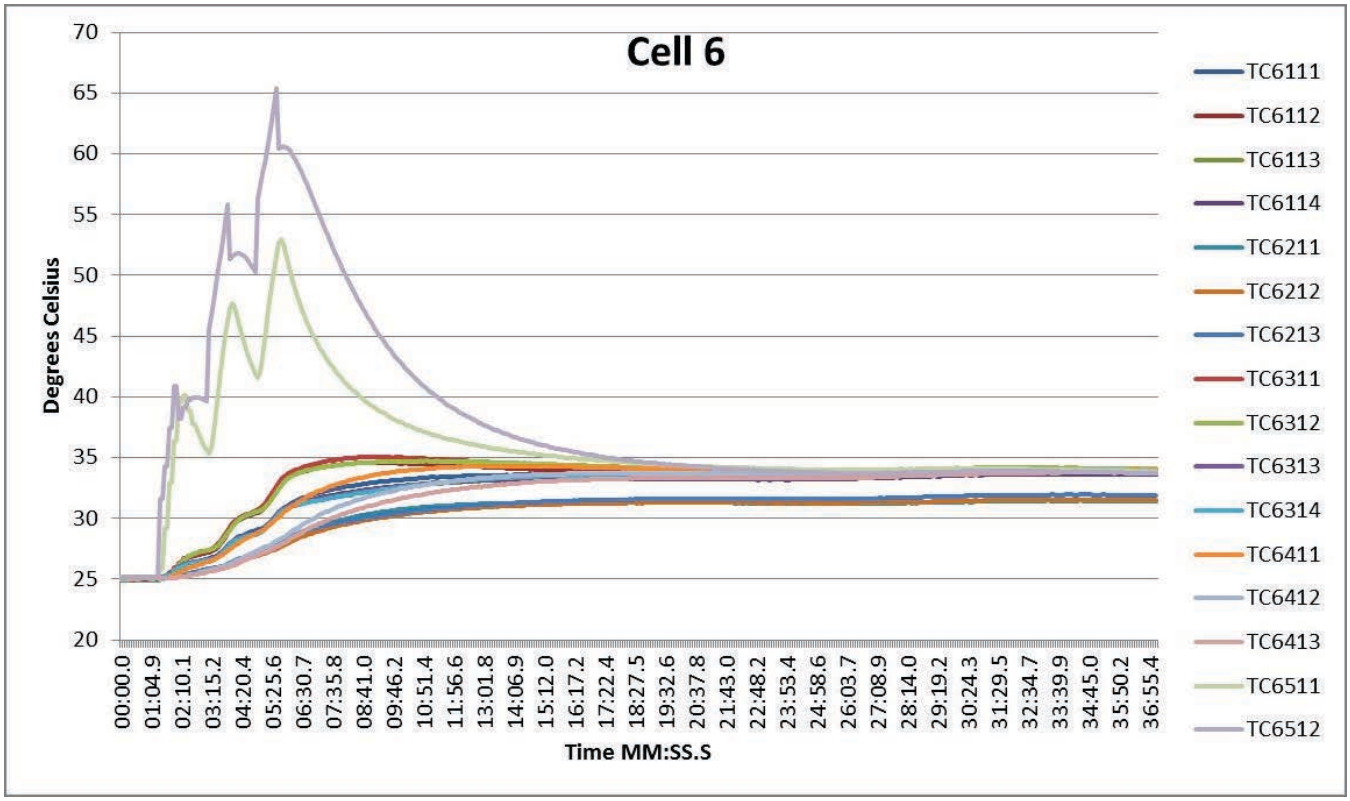

Figure B.28: Task A.1.B, 25 °C, 3 of 5, Cell 6 Temperatures

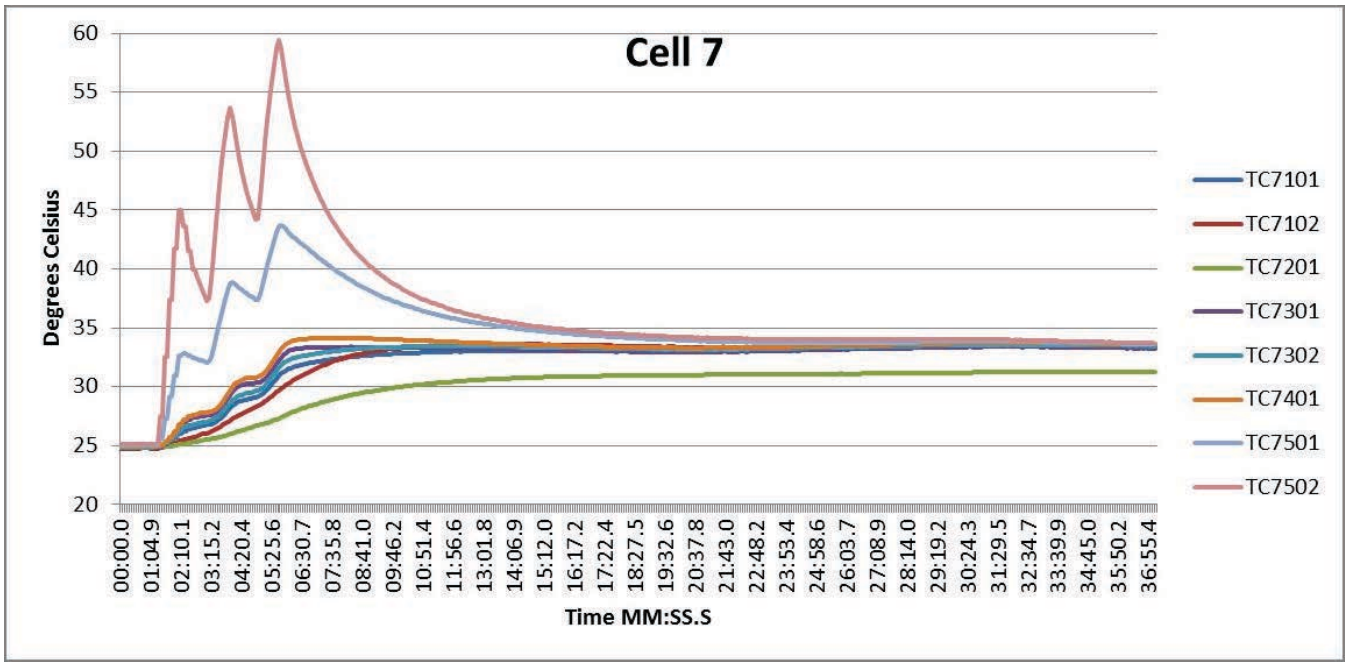

Figure B.29: Task A.1.B, 25 °C, 3 of 5, Cell 7 Temperatures

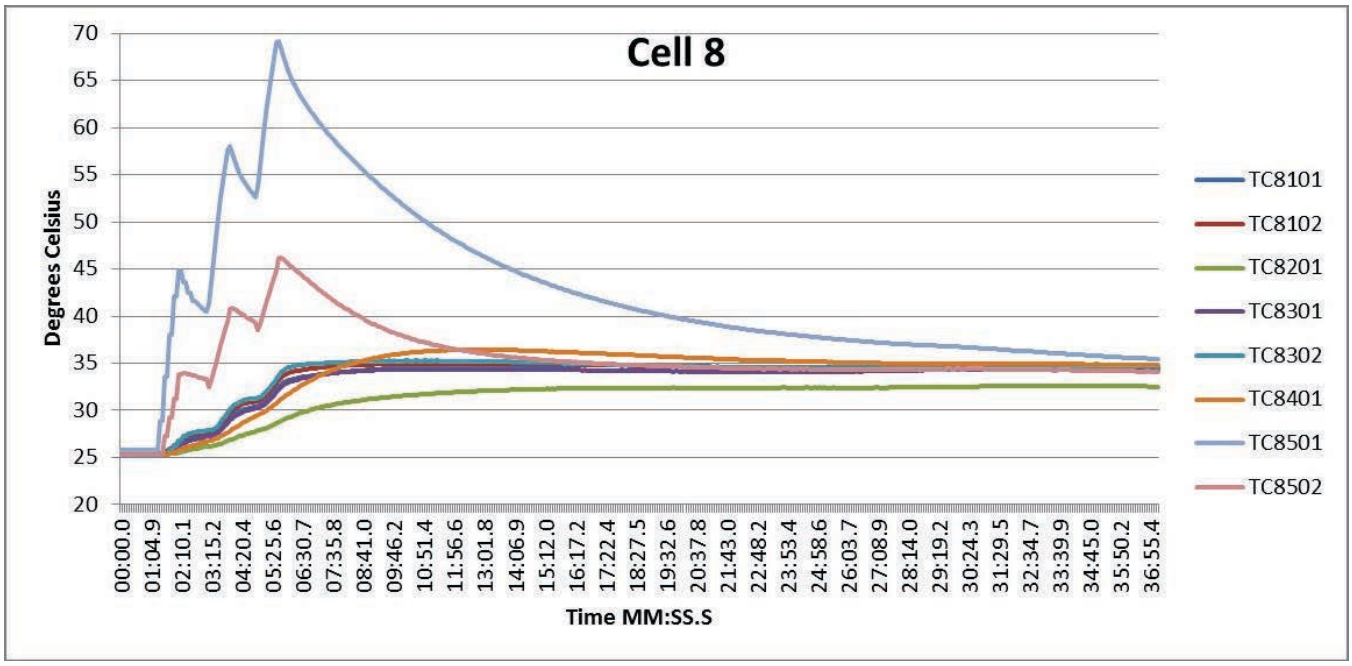

Figure B.30: Task A.1.B, 25 °C, 3 of 5, Cell 8 Temperatures

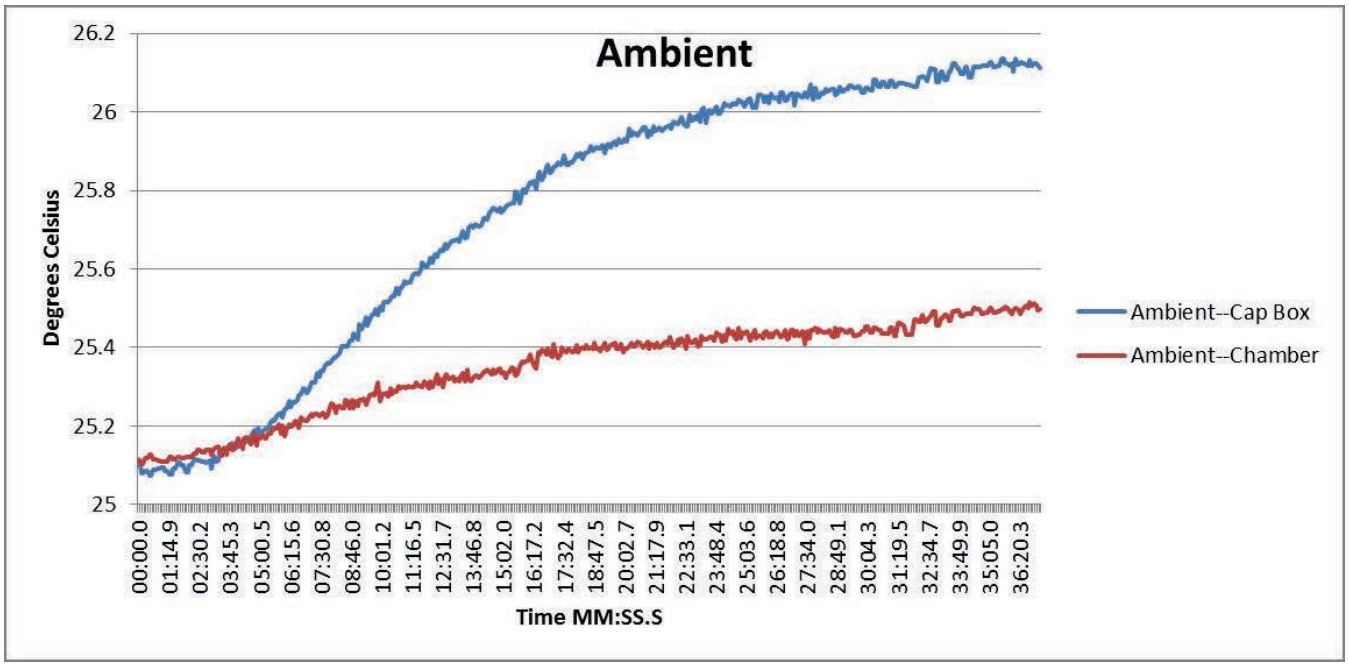

Figure B.31: Task A.1.B, 25 °C, 3 of 5, Ambient Temperatures

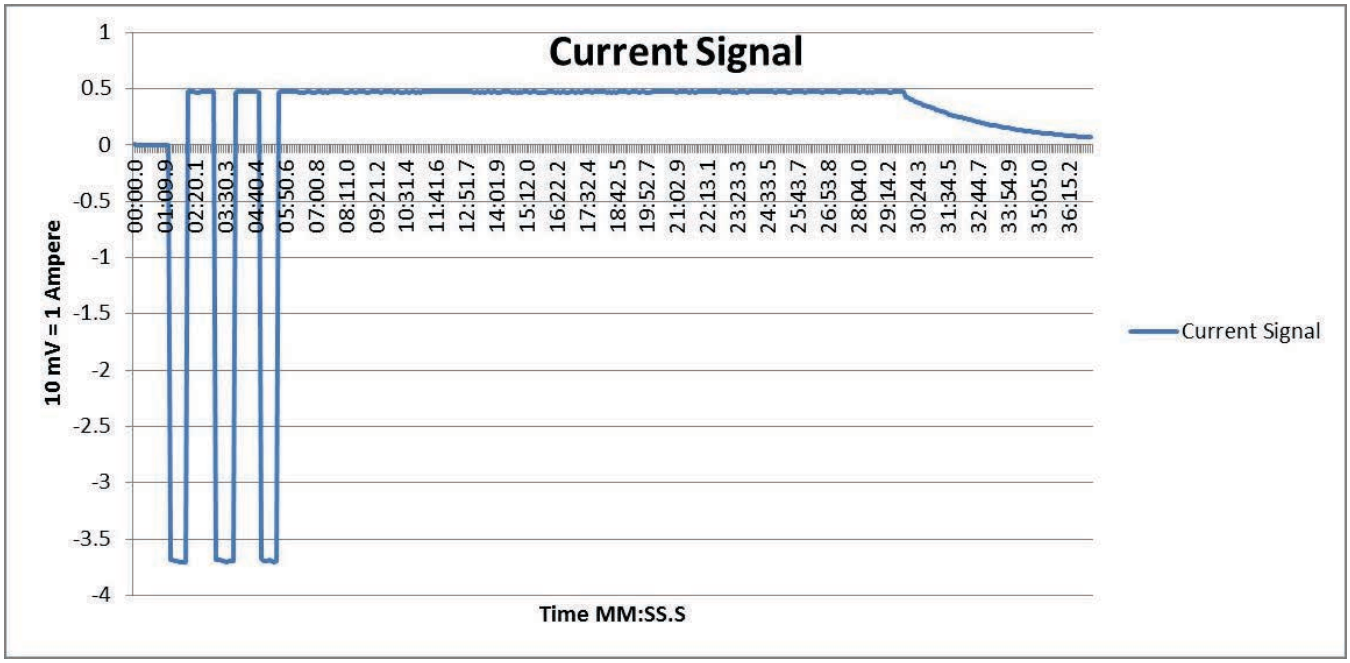

Figure B.32: Task A.1.B, 25 °C, 3 of 5, Current Signal

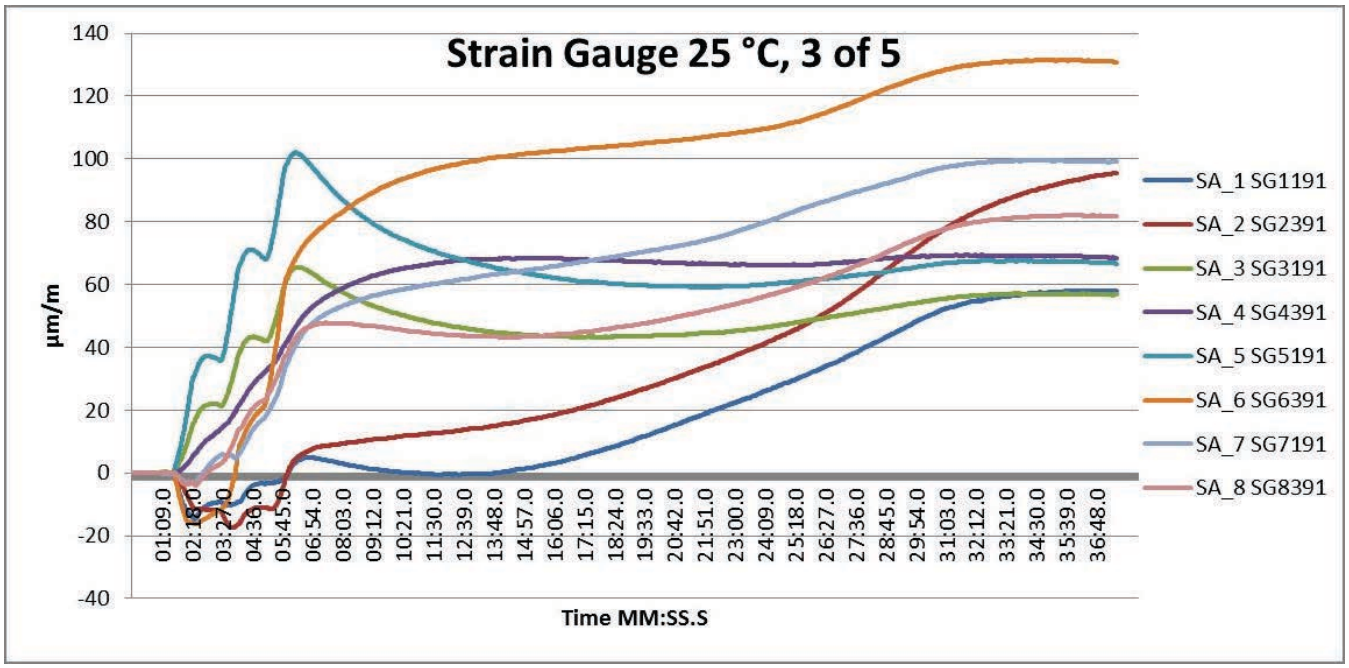

Figure B.33: Task A.1.B, 25 °C, 3 of 5, Strain Gauges

Task A.1.B – 25 °C, 4 of 5

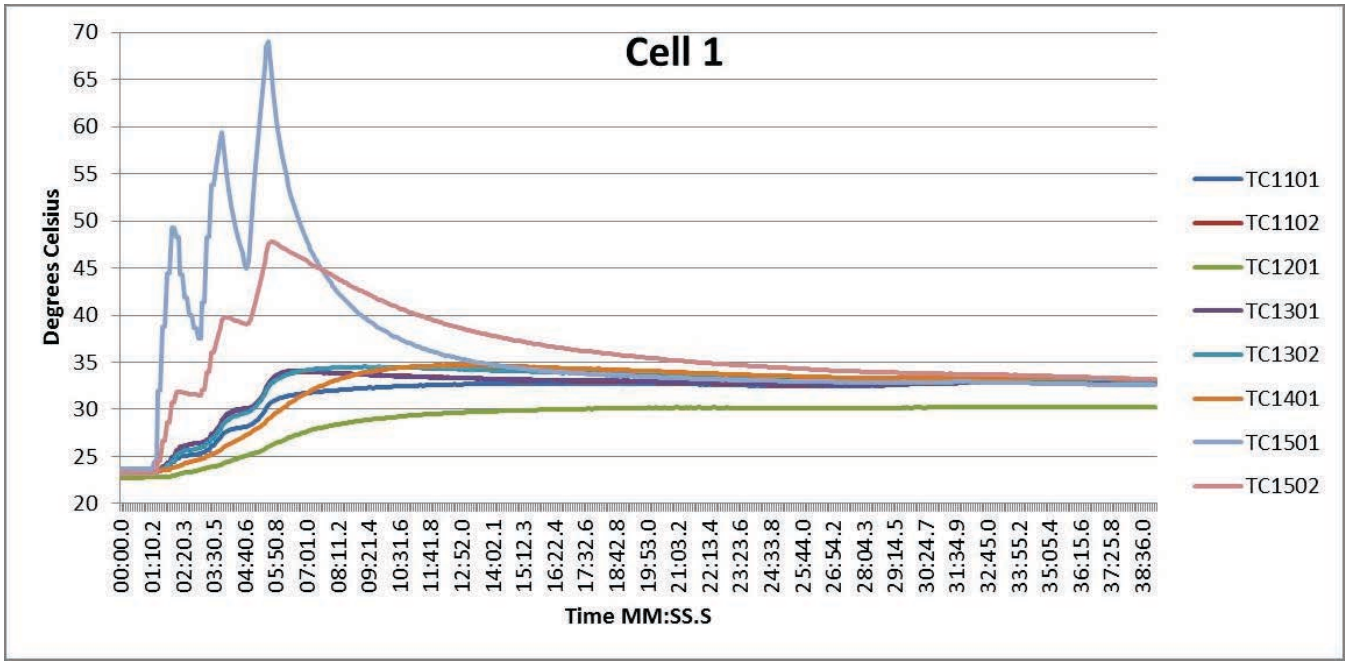

Figure B.34: Task A.1.B, 25 °C, 4 of 5, Cell 1 Temperatures

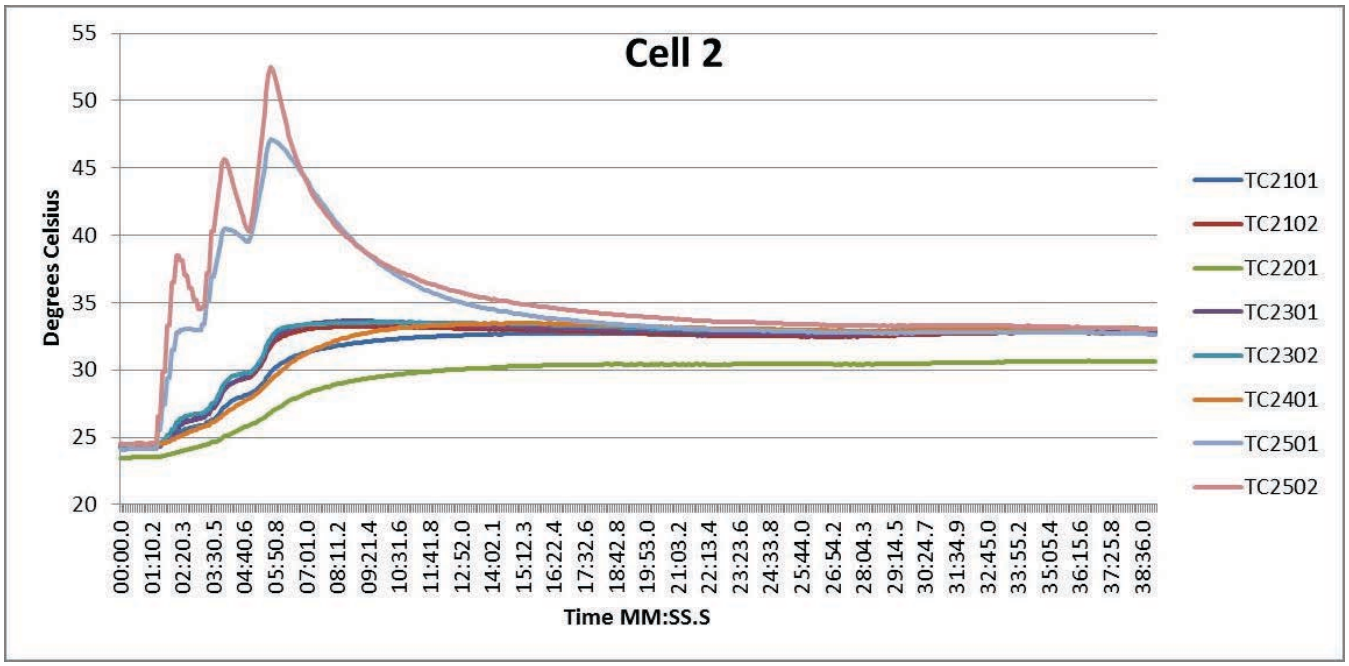

Figure B.35: Task A.1.B, 25 °C, 4 of 5, Cell 2 Temperatures

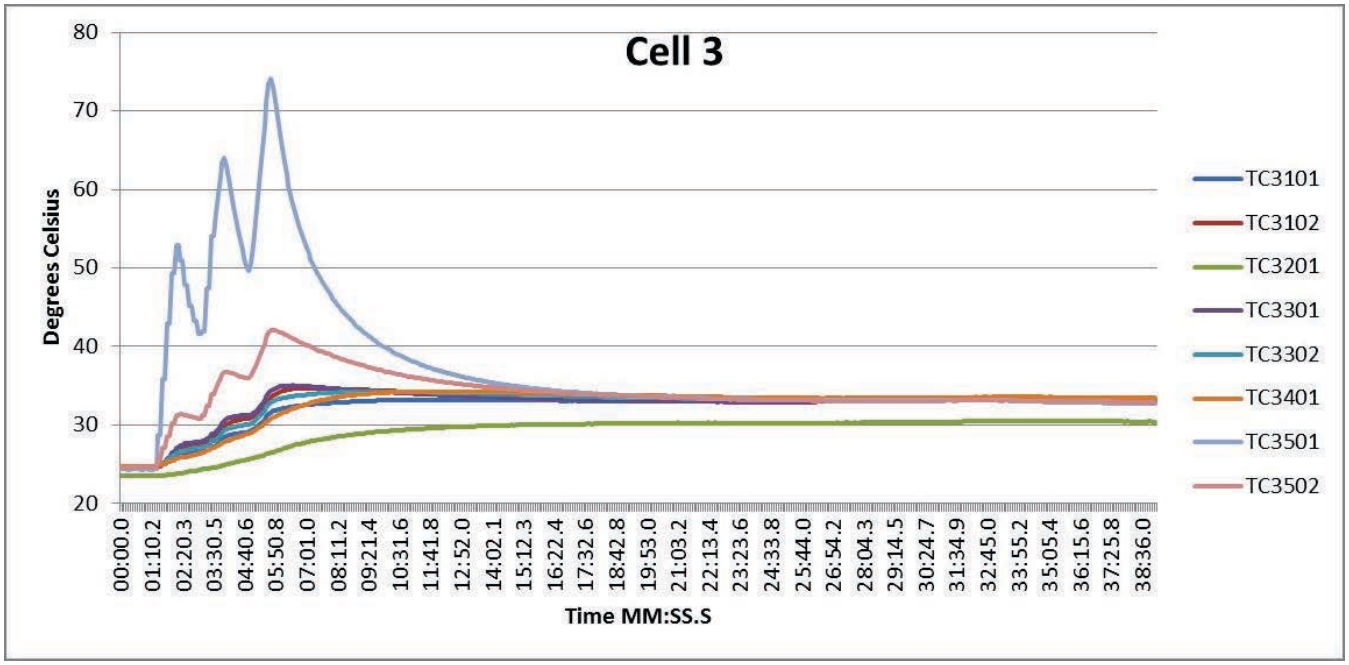

Figure B.36: Task A.1.B, 25 °C, 4 of 5, Cell 3 Temperatures

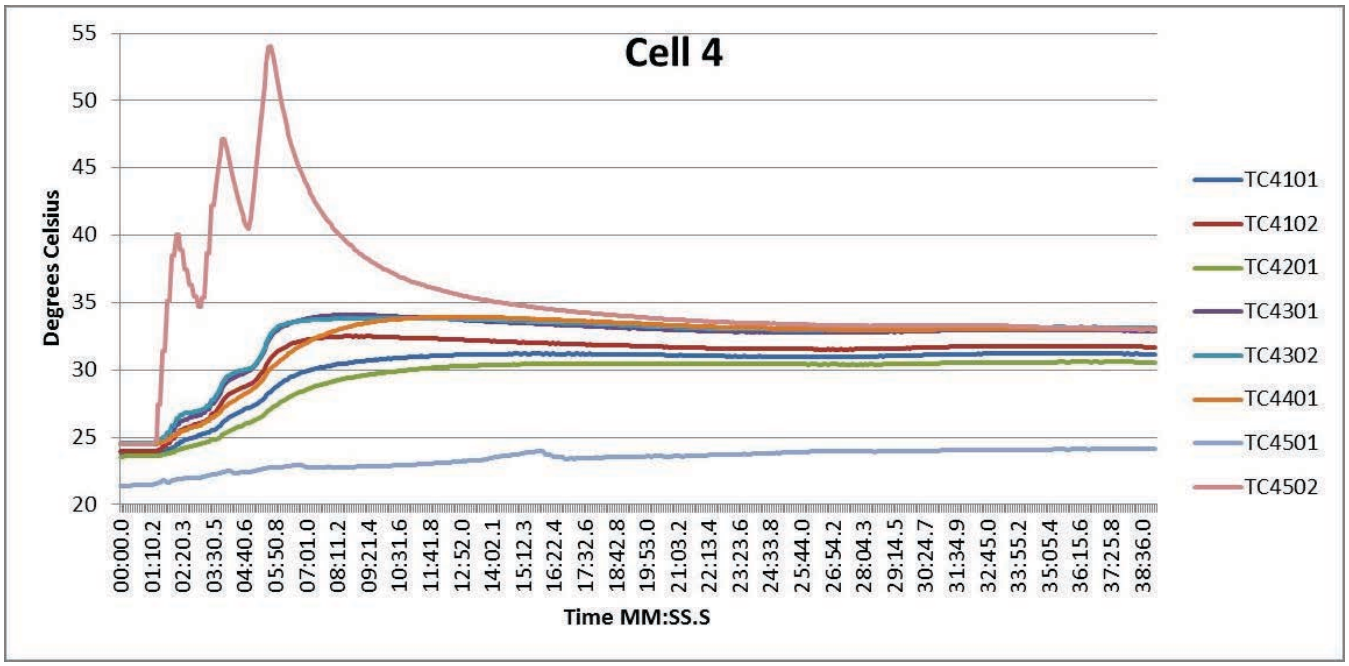

Figure B.37: Task A.1.B, 25 °C, 4 of 5, Cell 4 Temperatures

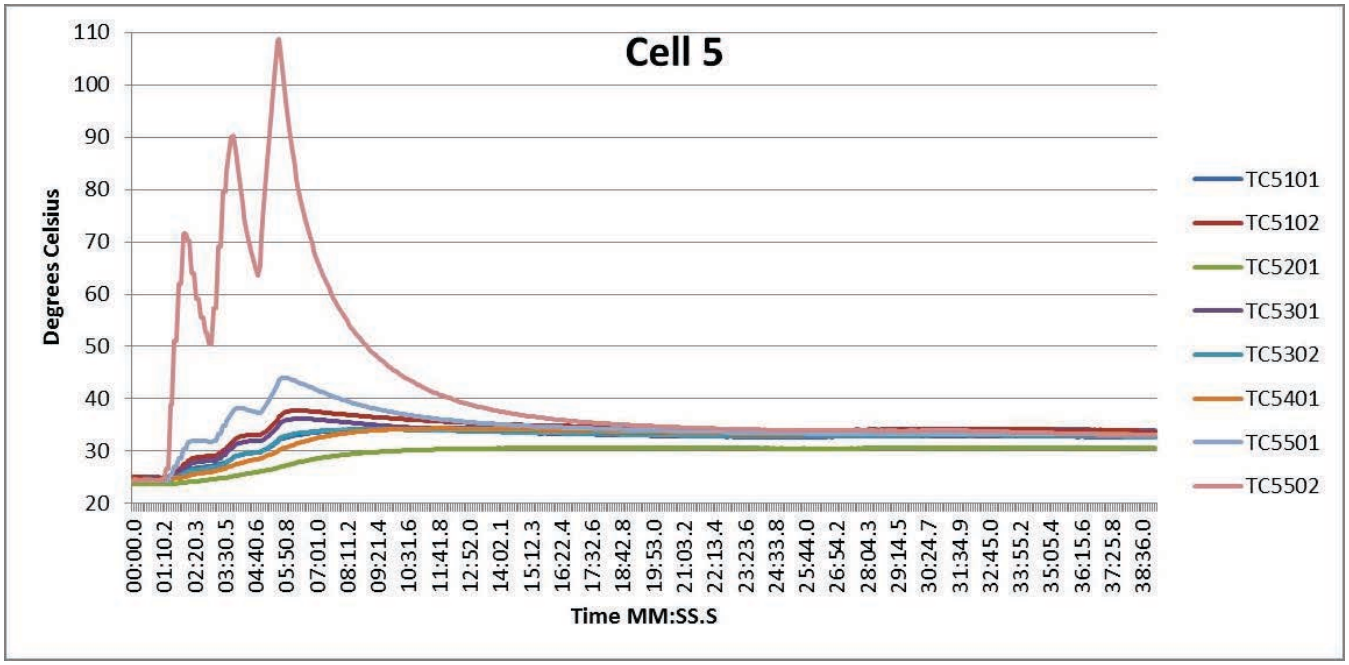

Figure B.38: Task A.1.B, 25 °C, 4 of 5, Cell 5 Temperatures

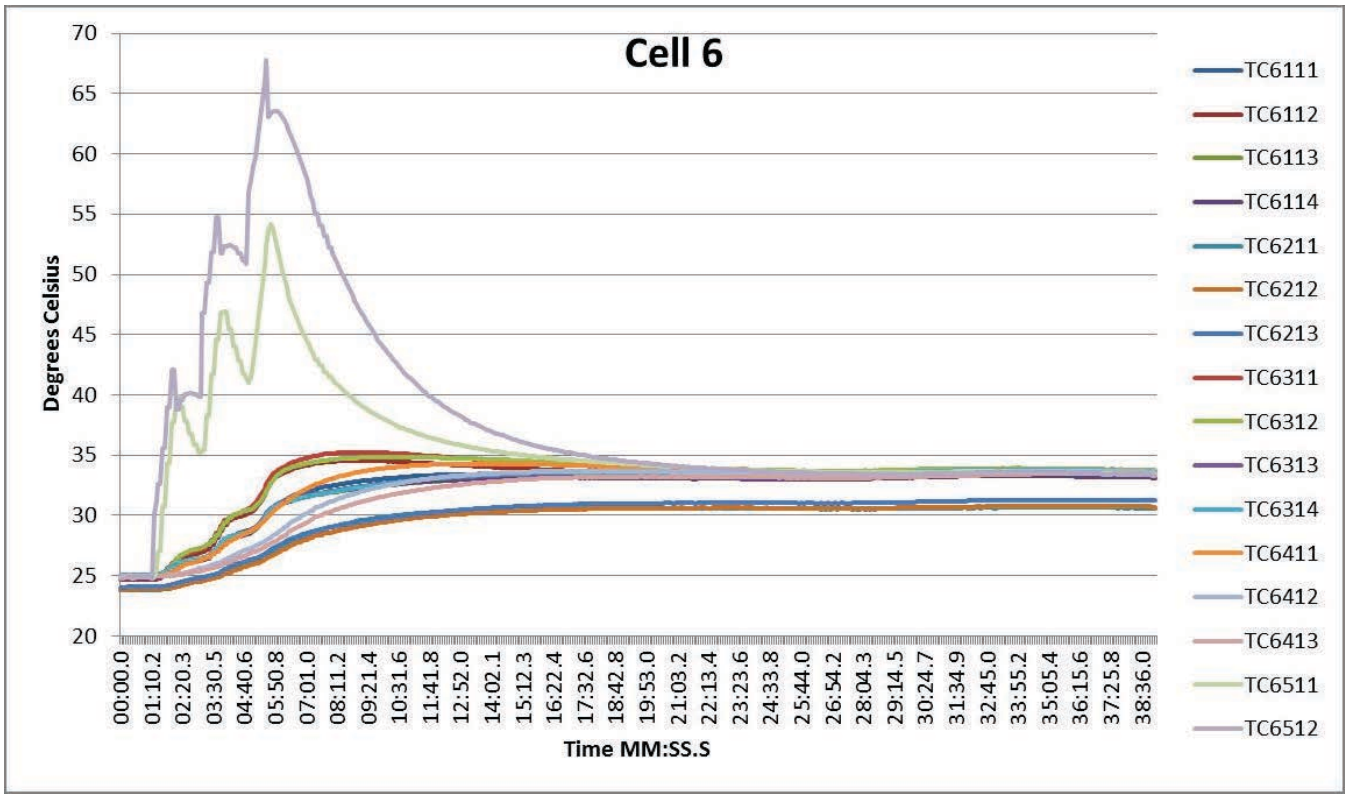

Figure B.39: Task A.1.B, 25 °C, 4 of 5, Cell 6 Temperatures

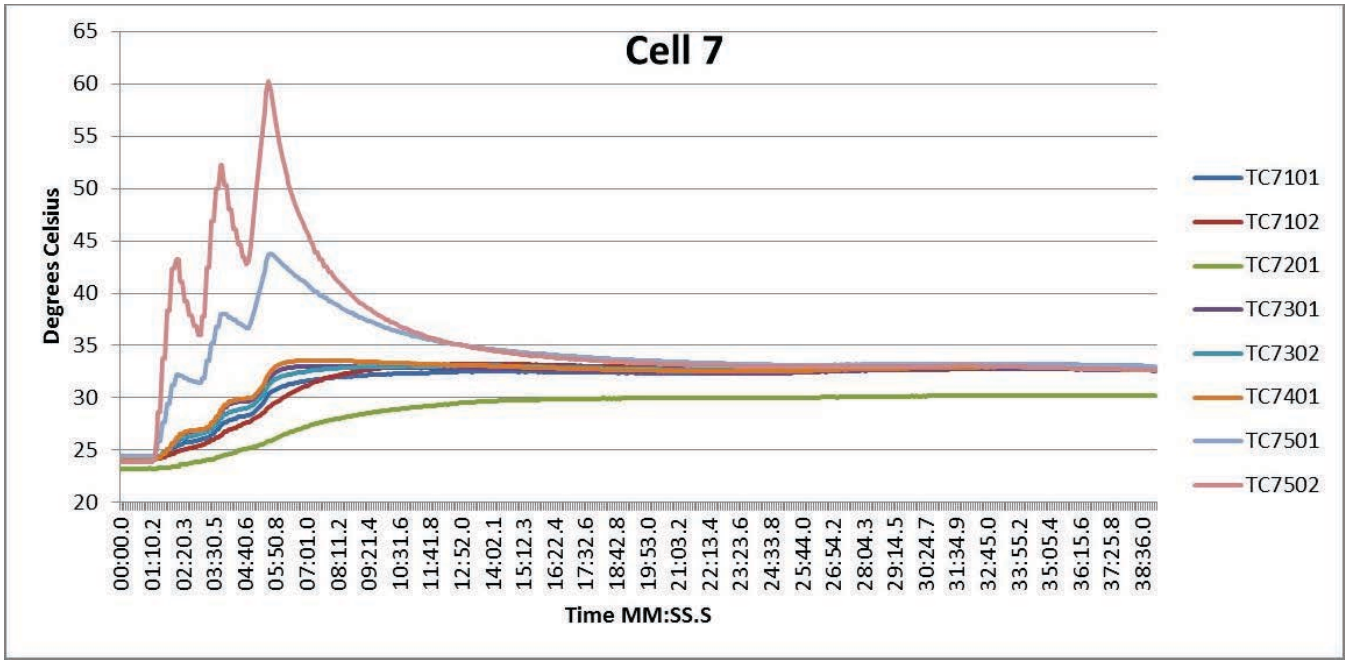

Figure B.40: Task A.1.B, 25 °C, 4 of 5, Cell 7 Temperatures

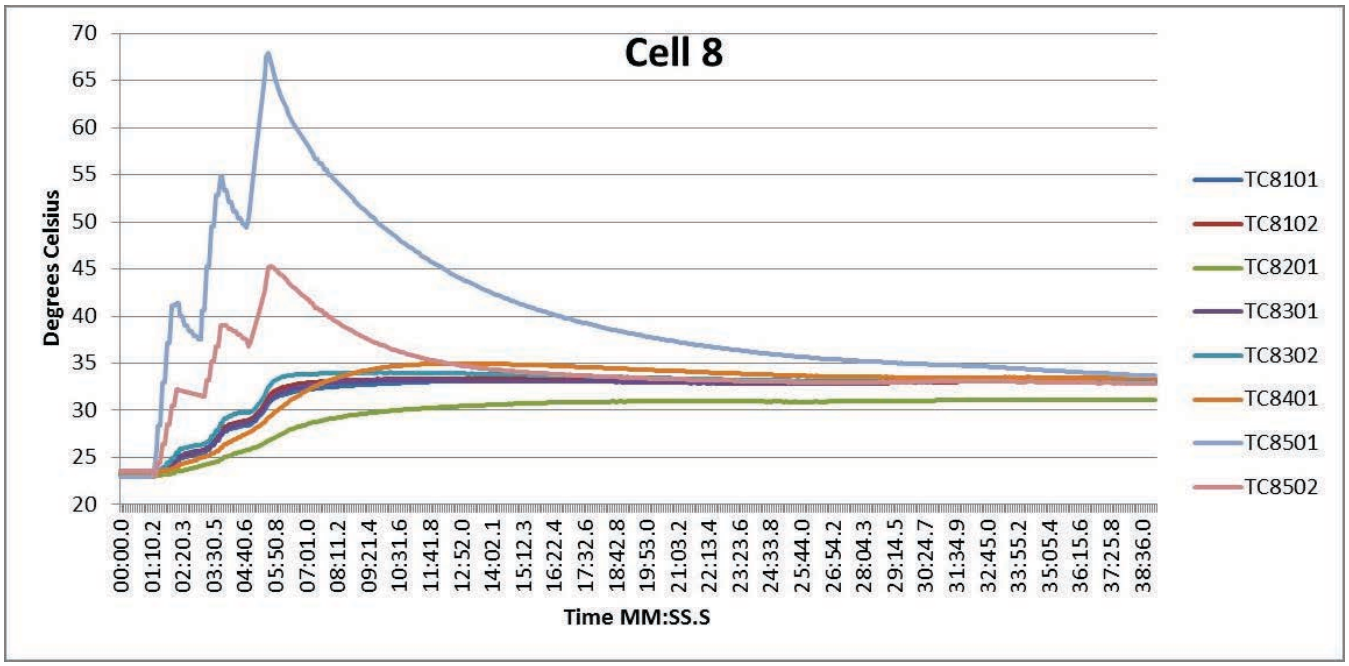

Figure B.41: Task A.1.B, 25 °C, 4 of 5, Cell 8 Temperatures

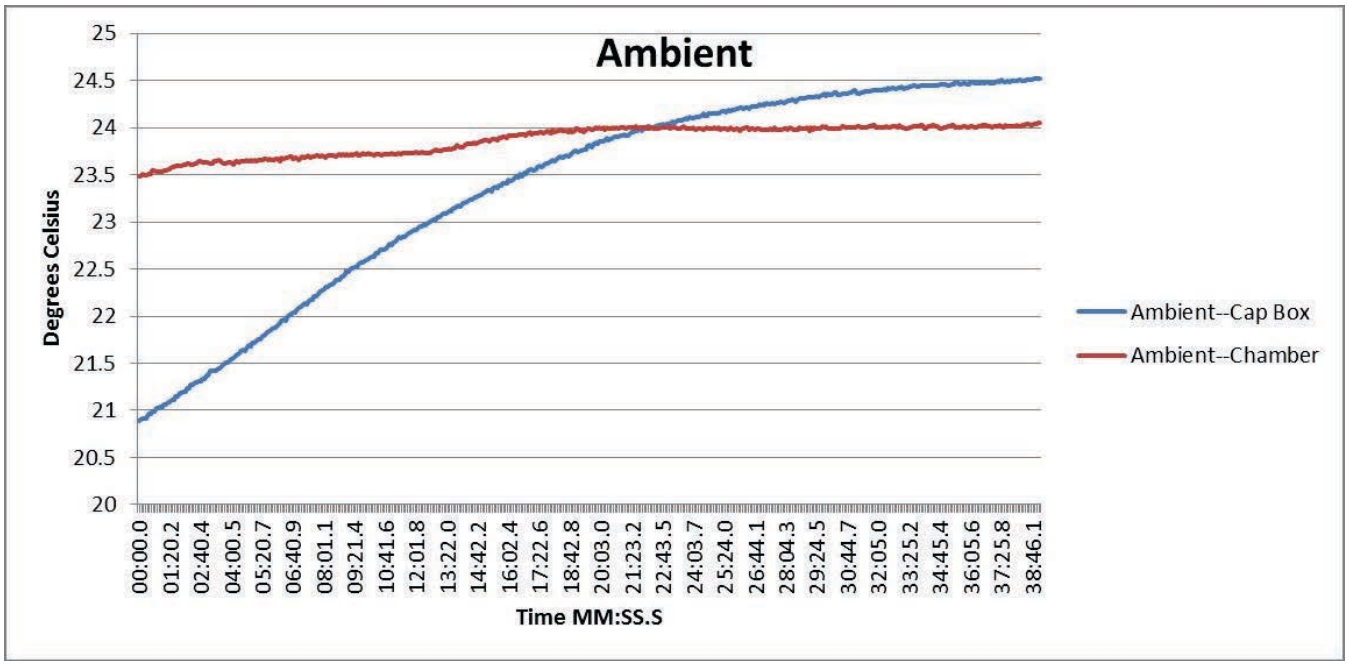

Figure B.42: Task A.1.B, 25 °C, 4 of 5, Ambient Temperatues

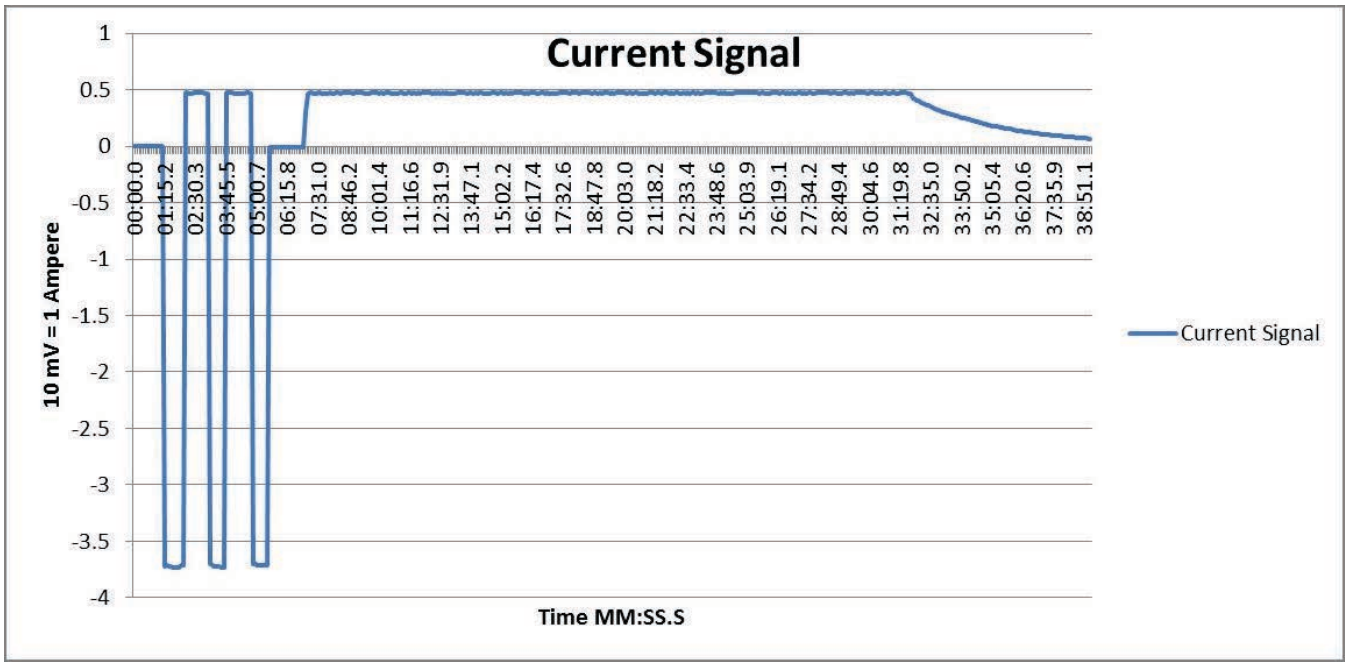

Figure B.43: Task A.1.B, 25 °C, 4 of 5, Current Signal from BMU HECS

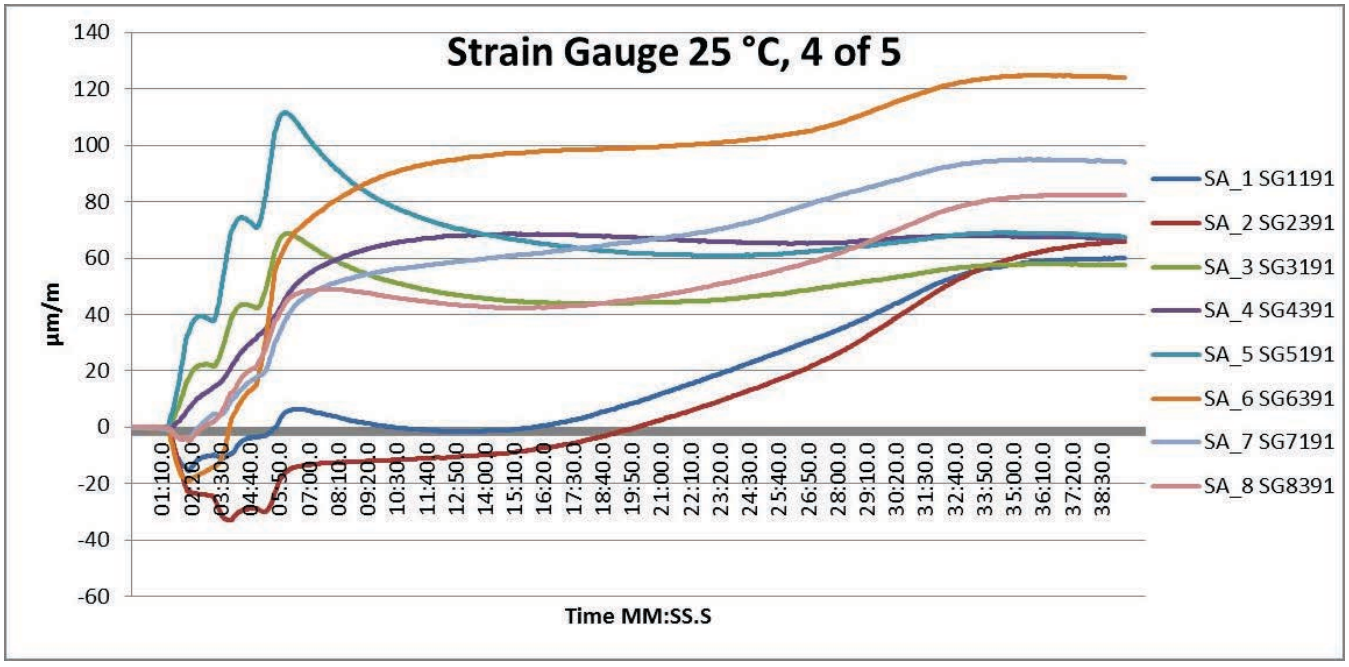

Figure B.44: Task A.1.B, 25 °C, 4 of 5, Strain Gauges

Task A.1.B – 25 °C, 5 of 5

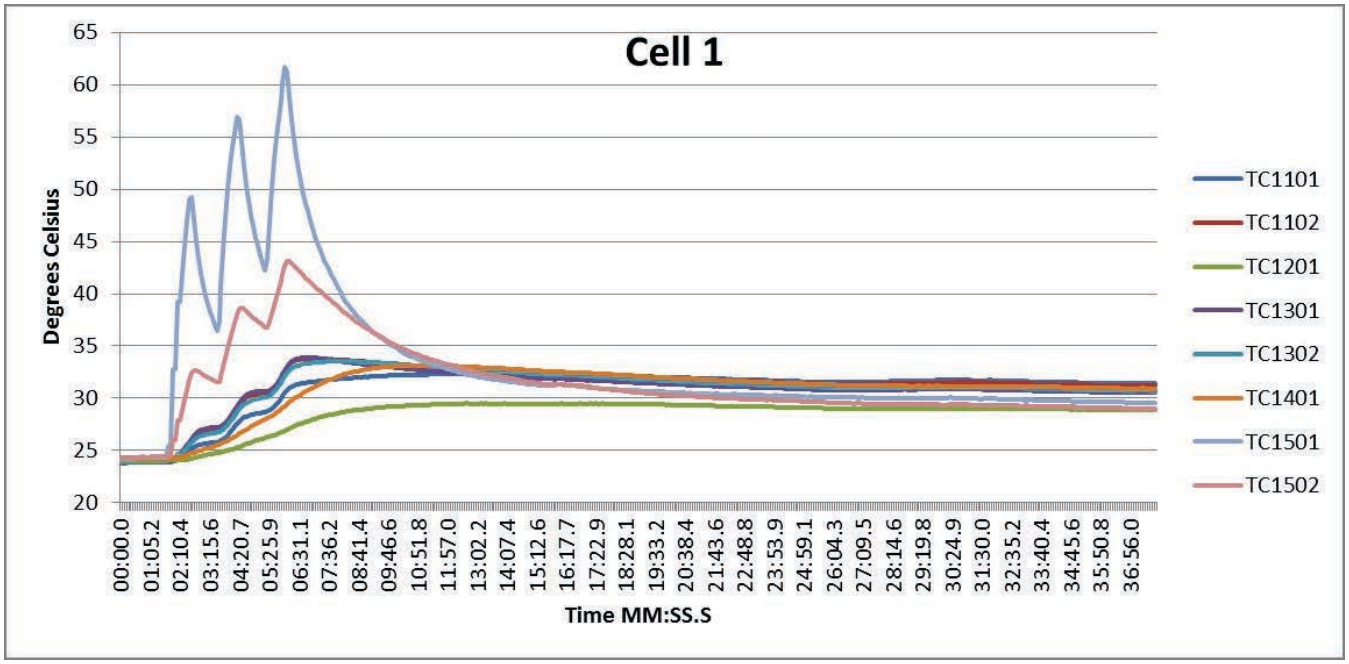

Figure B.45: Task A.1.B, 25 °C, 5 of 5, Cell 1 Temperatures

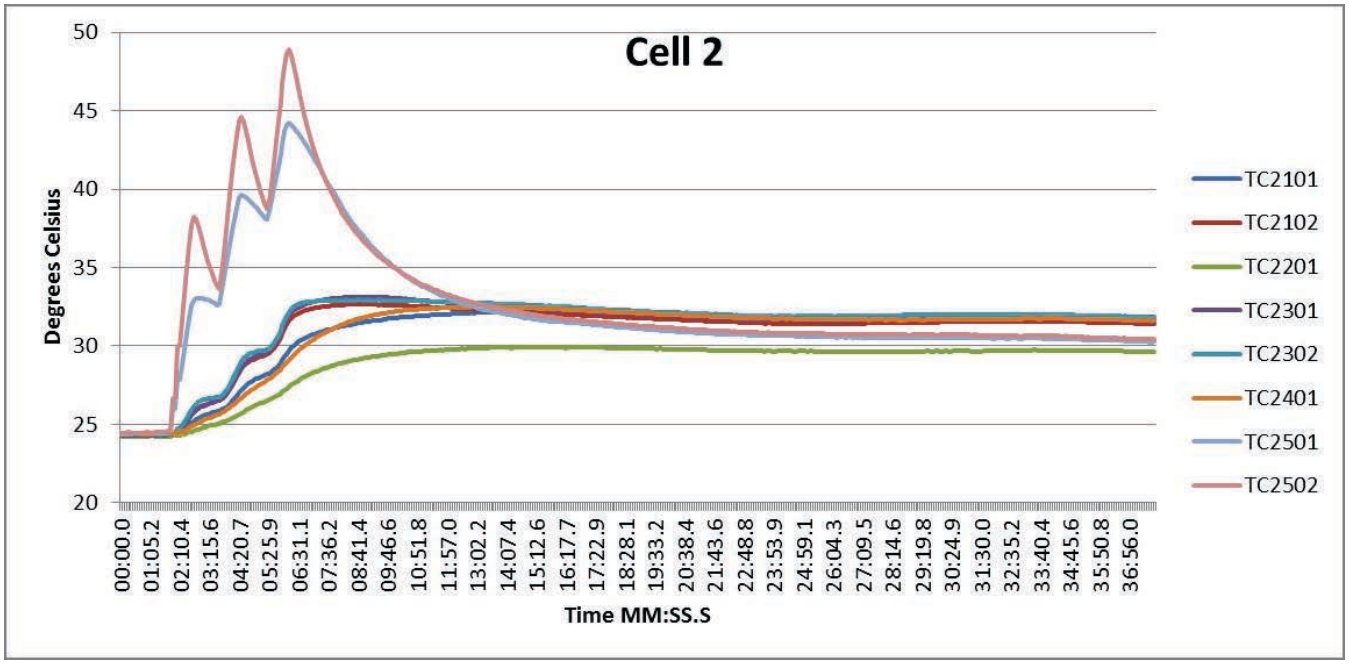

Figure B.46: Task A.1.B, 25 °C, 5 of 5, Cell 2 Temperatures

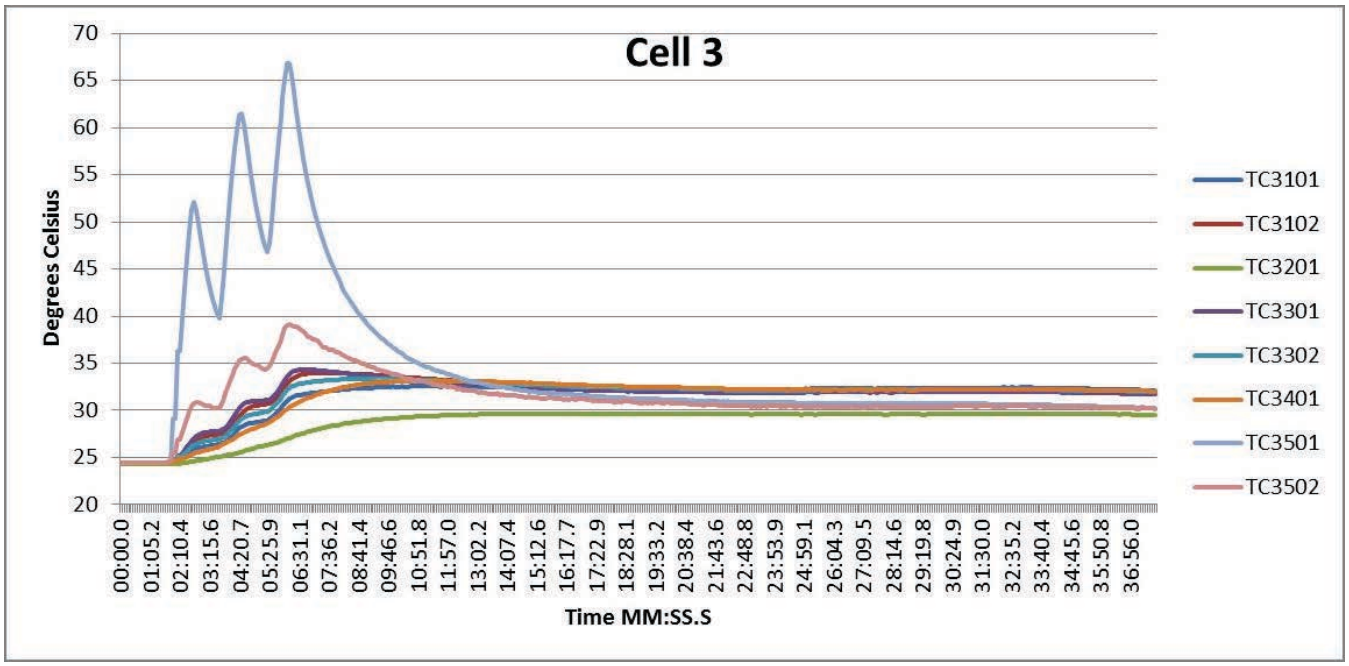

Figure B.47: Task A.1.B, 25 °C, 5 of 5, Cell 3 Temperatures

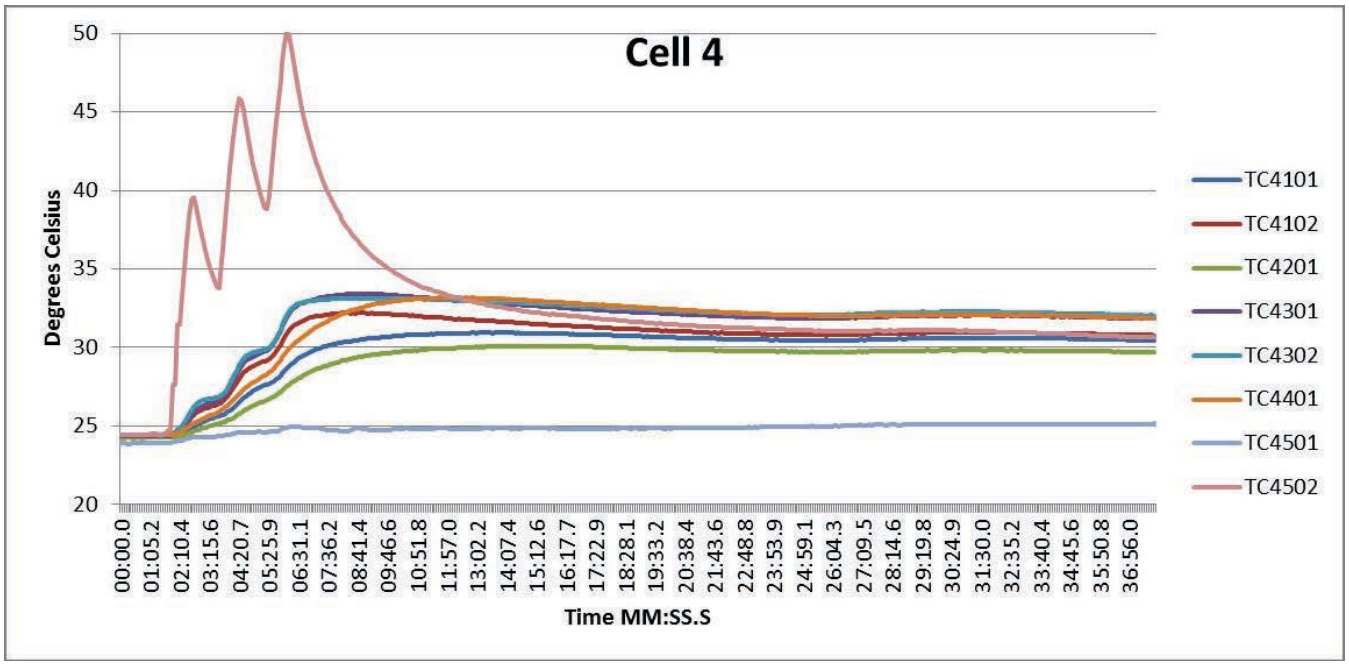

Figure B.48: Task A.1.B, 25 °C, 5 of 5, Cell 4 Temperatures

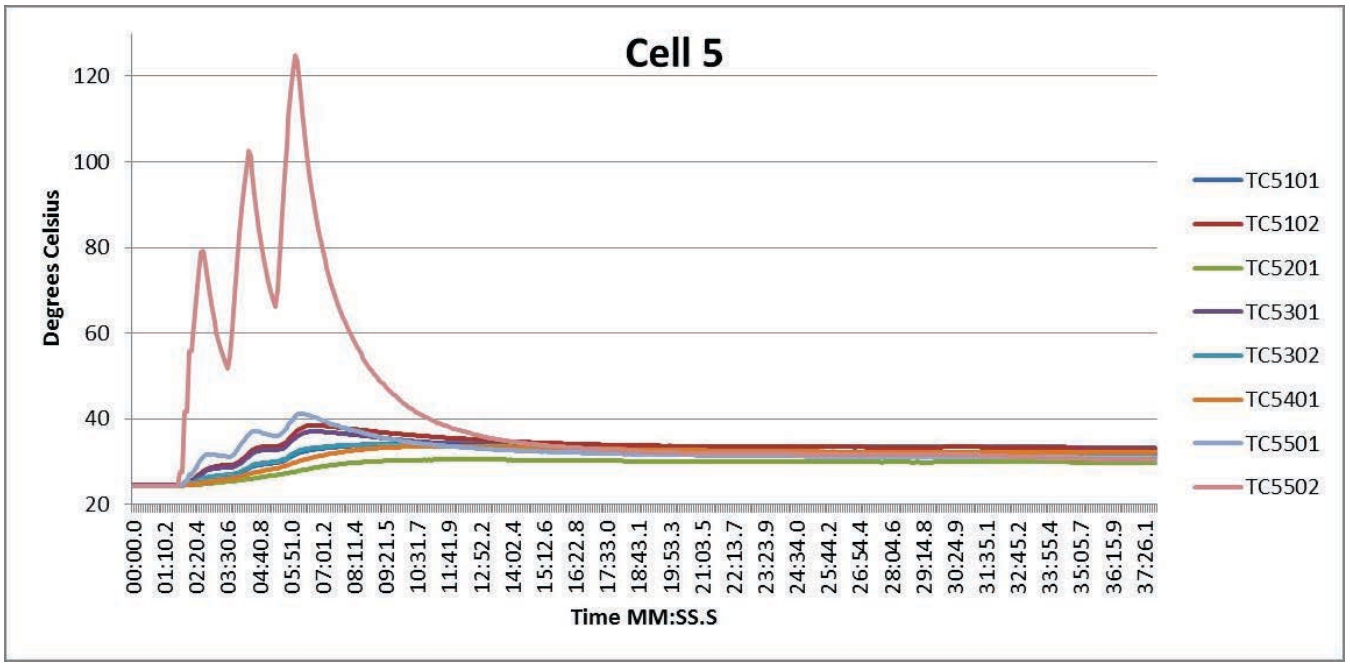

Figure B.49: Task A.1.B, 25 °C, 5 of 5, Cell 5 Temperatures

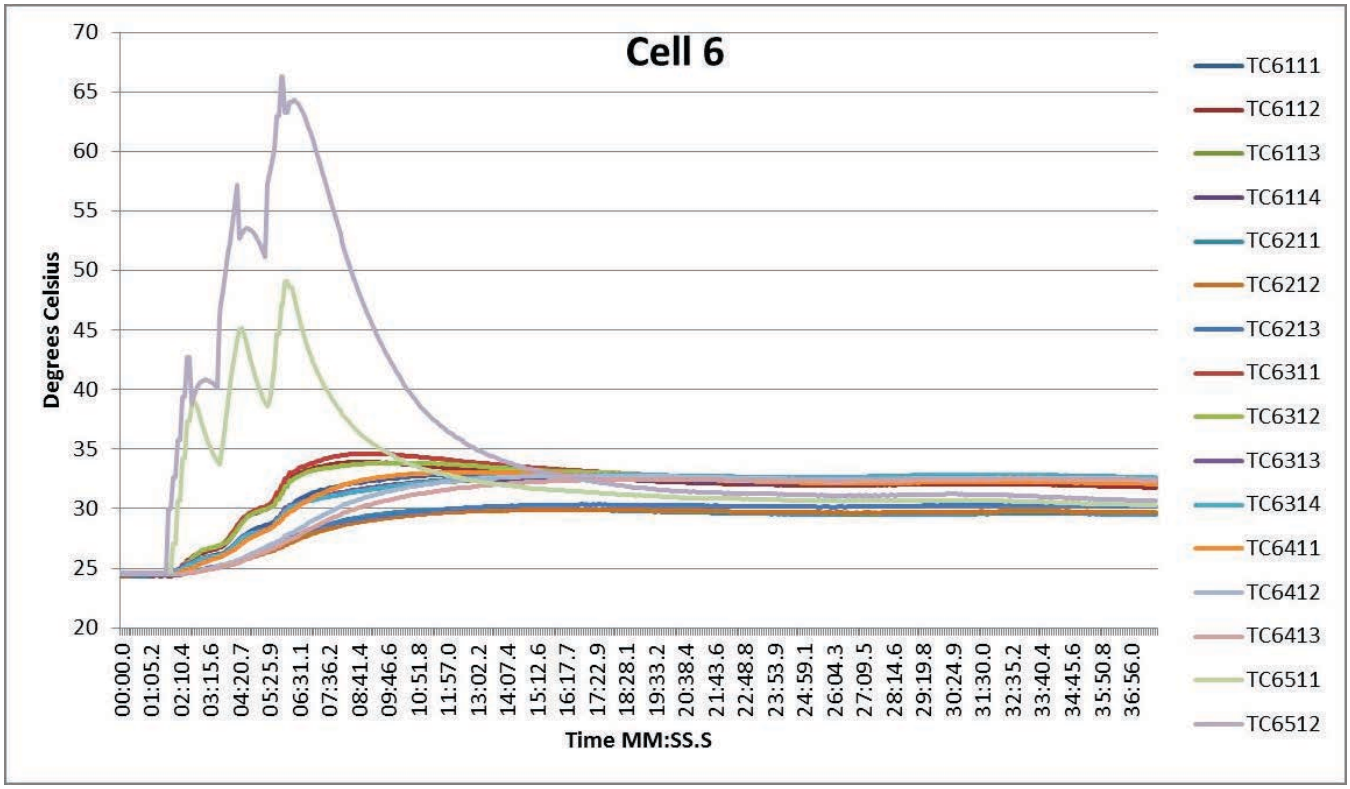

Figure B.50: Task A.1.B, 25 °C, 5 of 5, Cell 6 Temperatures

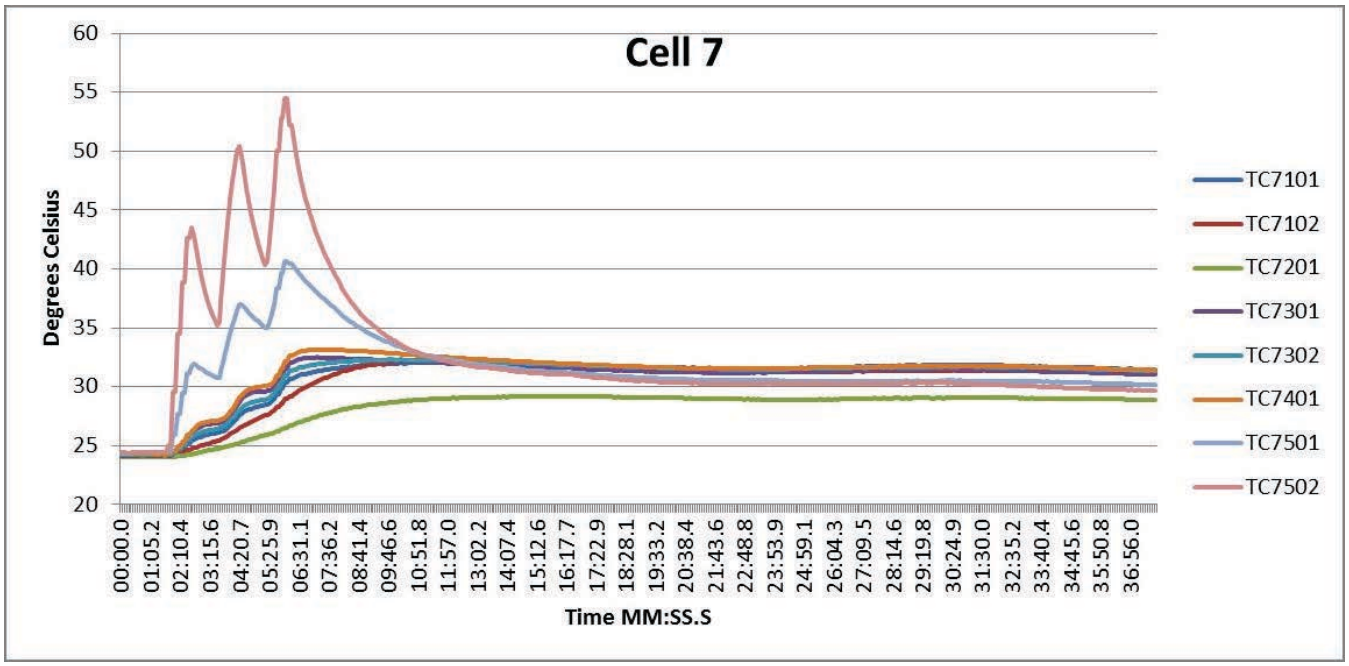

Figure B.51: Task A.1.B, 25 °C, 5 of 5, Cell 7 Temperatures

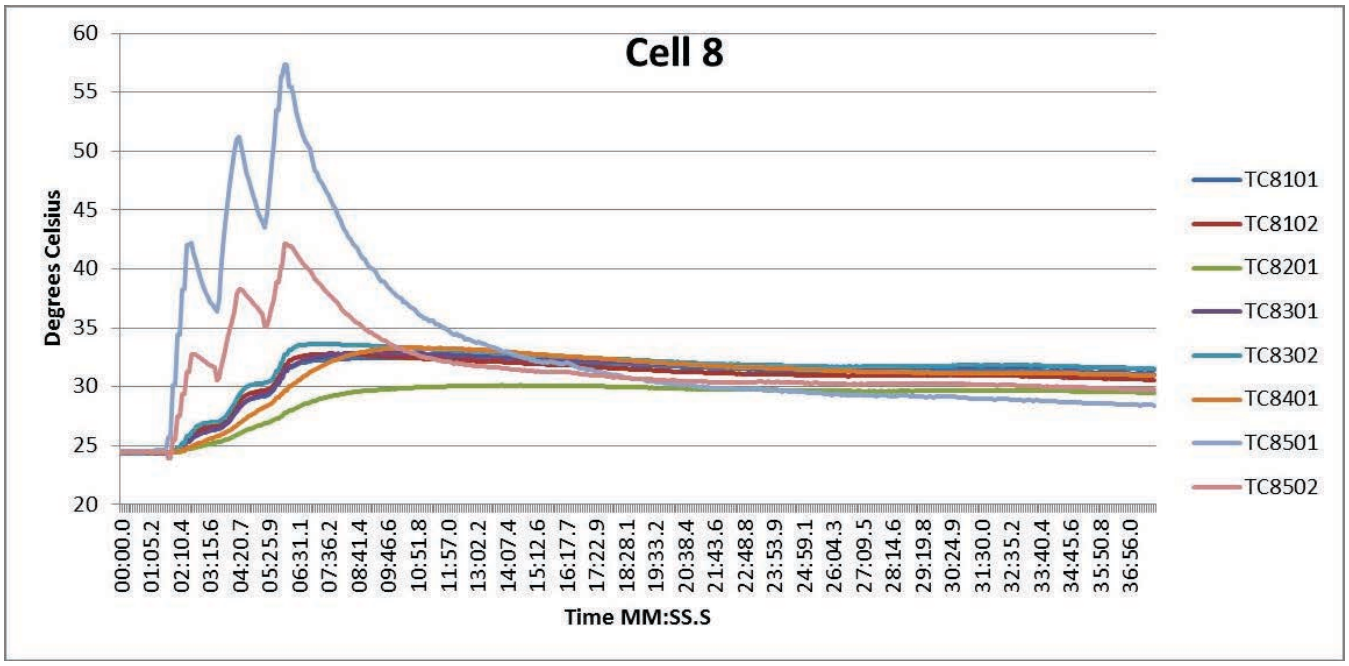

Figure B.52: Task A.1.B, 25 °C, 5 of 5, Cell 8 Temperatures

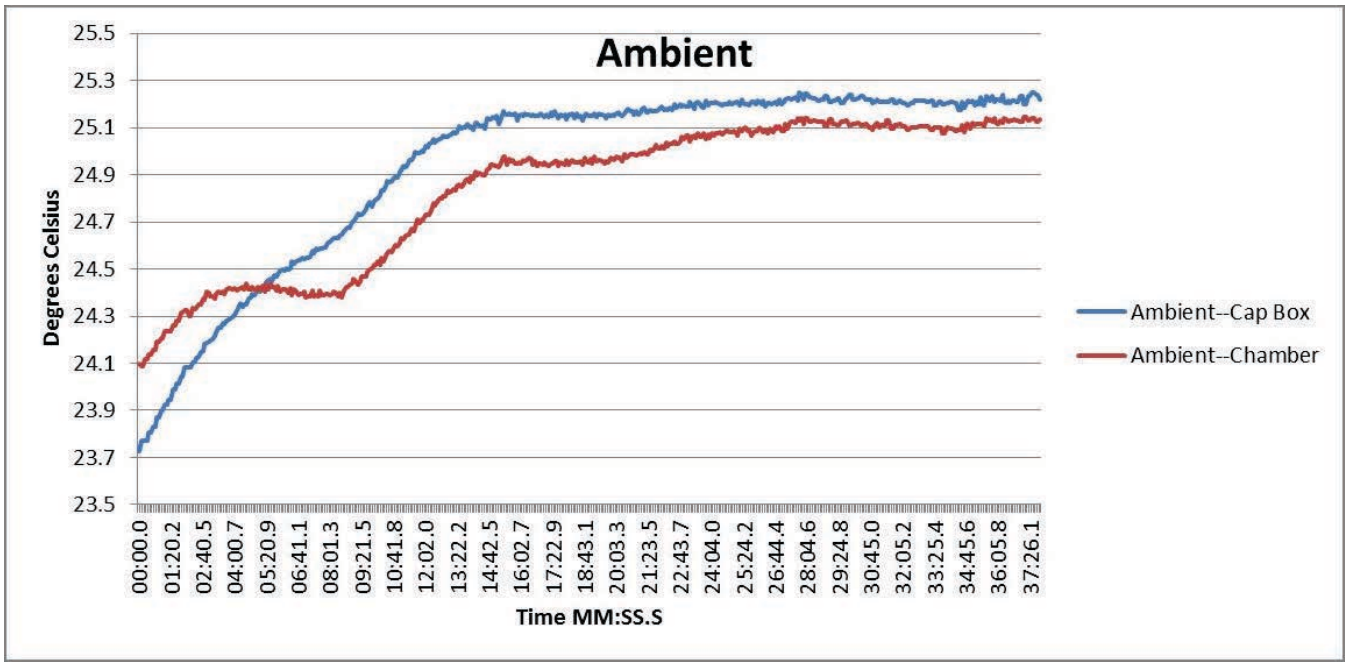

Figure B.53: Task A.1.B, 25 °C, 5 of 5, Ambient Temperatures

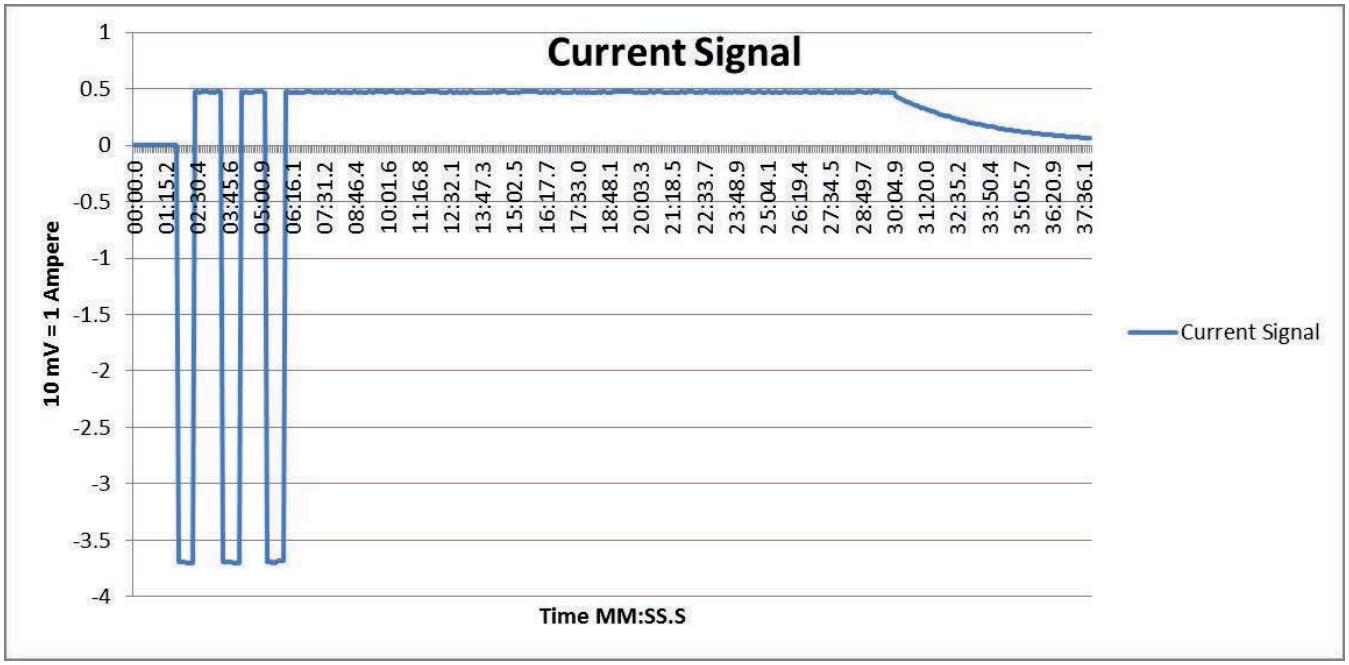

Figure B.54: Task A.1.B, 25 °C, 5 of 5, Current Signal from BMU HECS

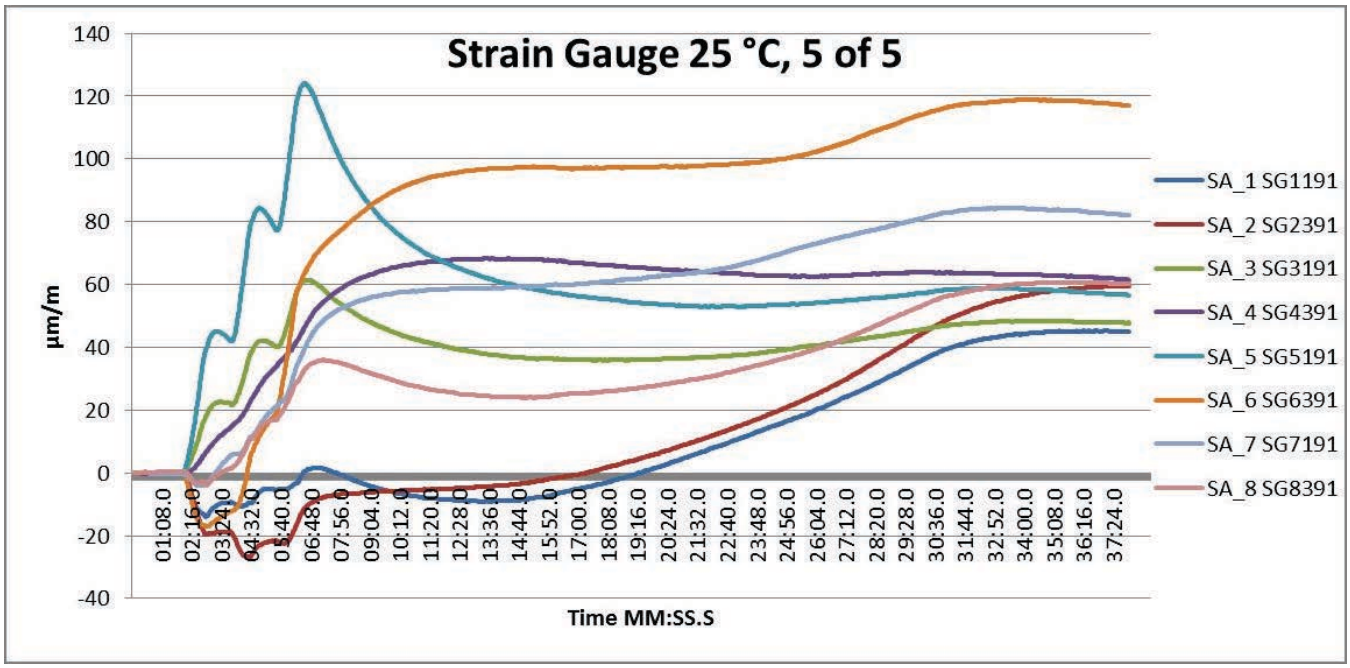

Figure B.55: Task A.1.B, 25 °C, 5 of 5, Strain Gauges

Task A.1.B – 0 °C, 1 of 5

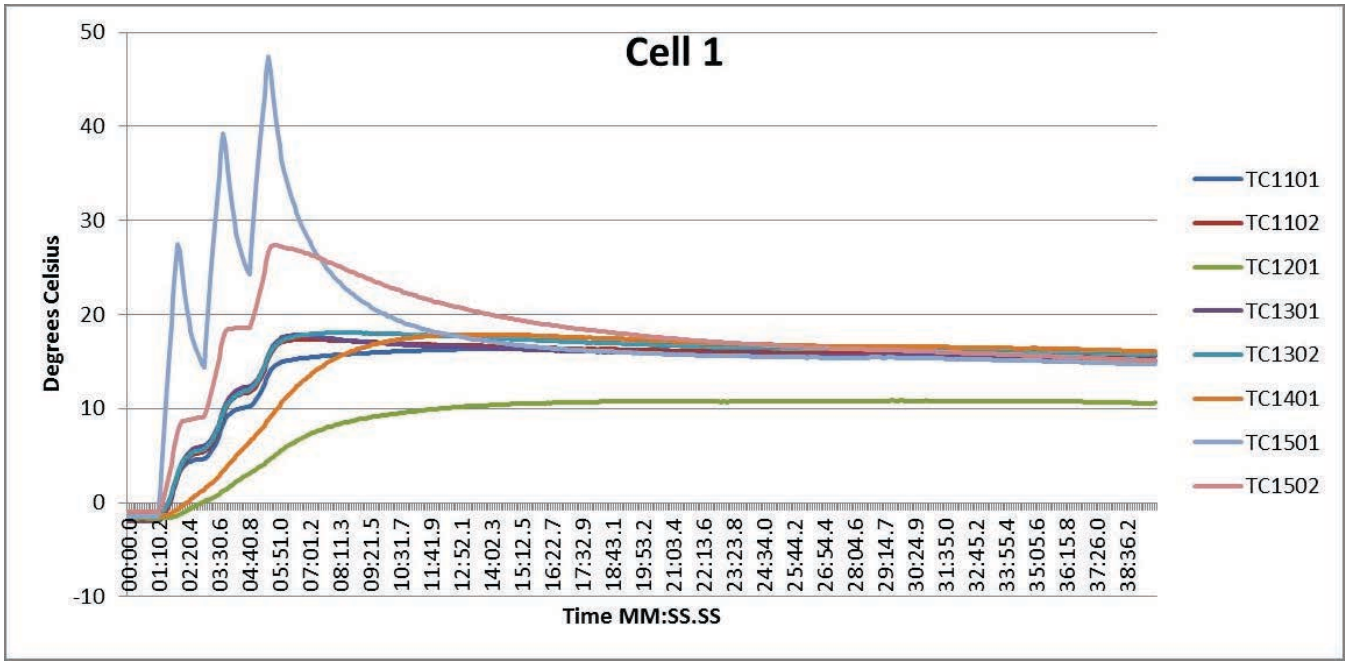

Figure B.56: Task A.1.B, 0 °C, 1 of 5, Cell 1 Temperatures

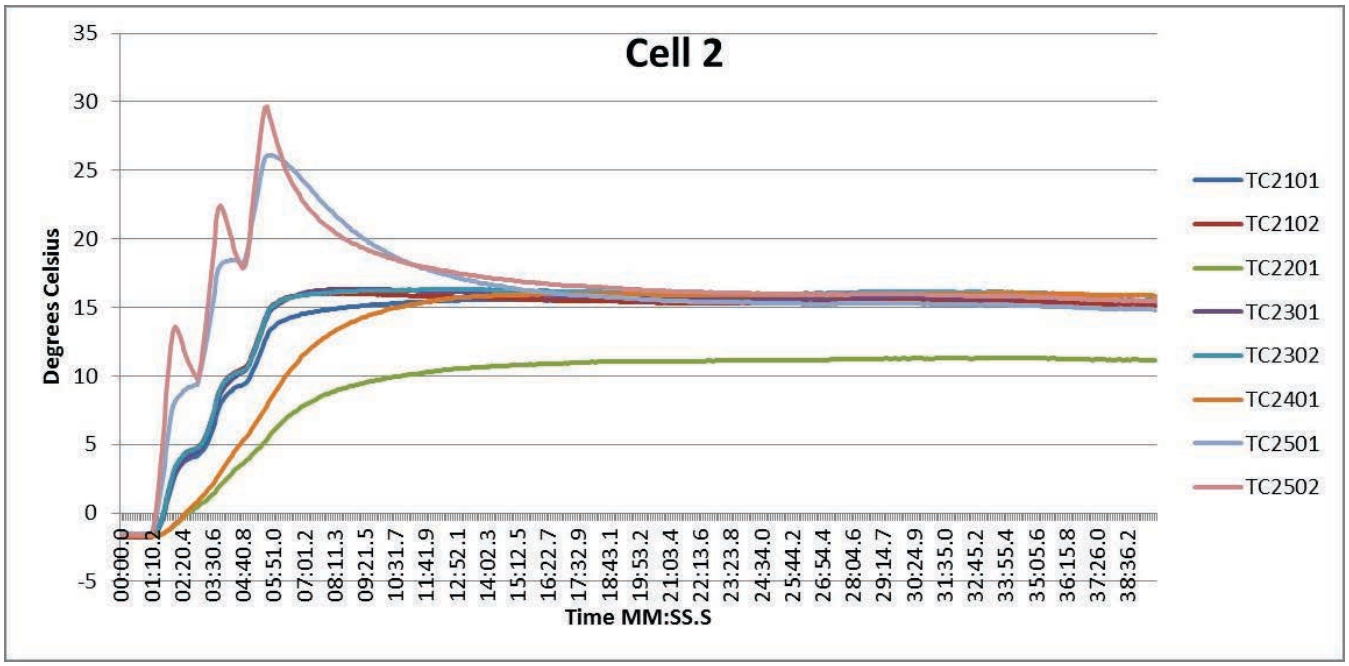

Figure B.57: Task A.1.B, 0 °C, 1 of 5, Cell 2 Temperatures

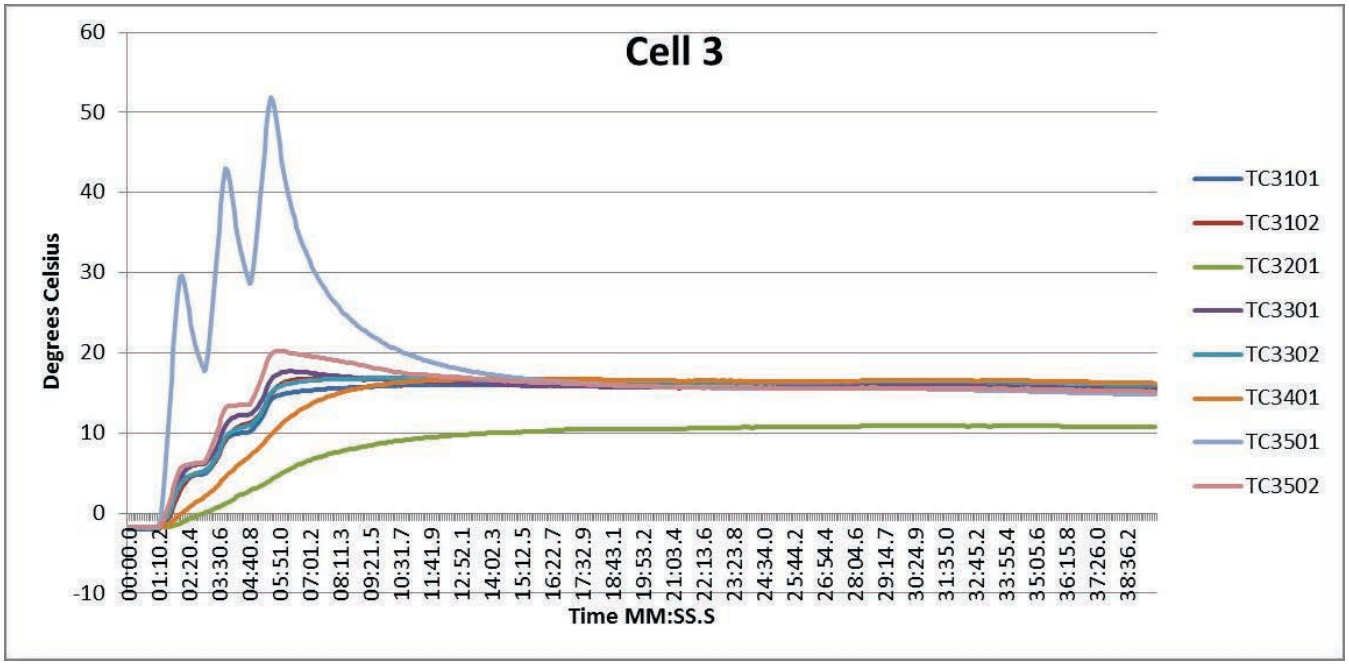

Figure B.58: Task A.1.B, 0 °C, 1 of 5, Cell 3 Temperatures

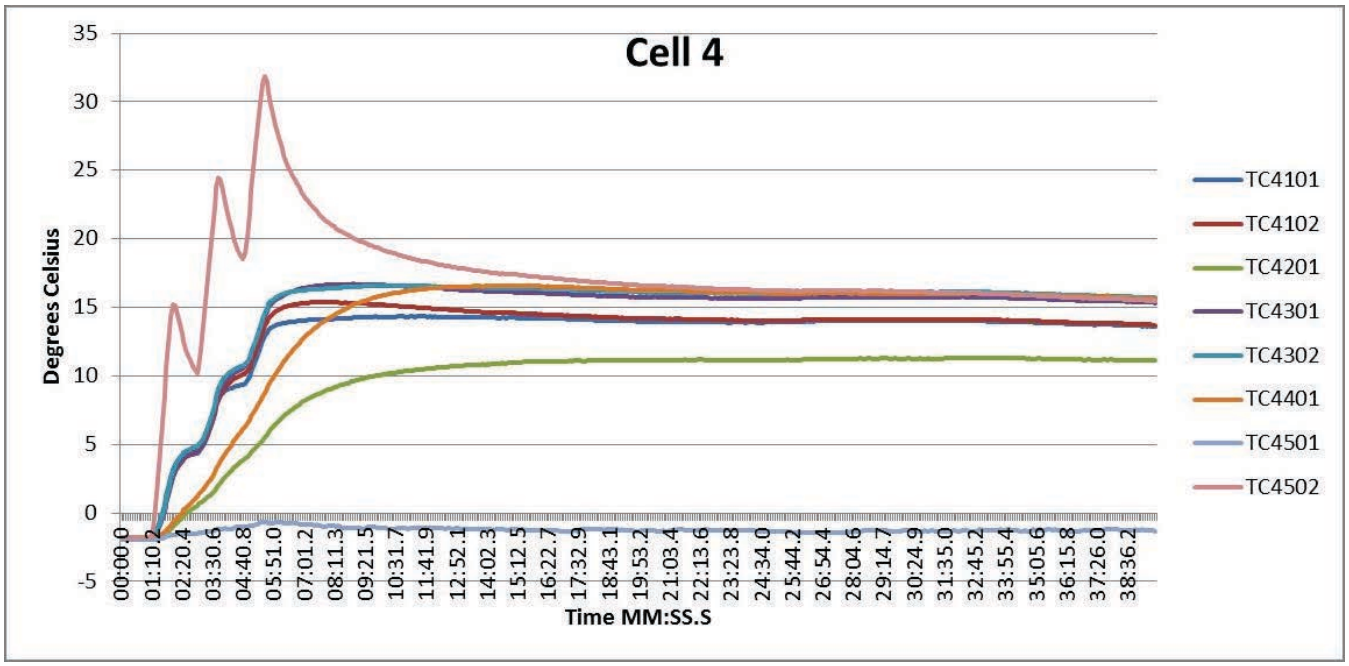

Figure B.59: Task A.1.B, 0 °C, 1 of 5, Cell 4 Temperatures

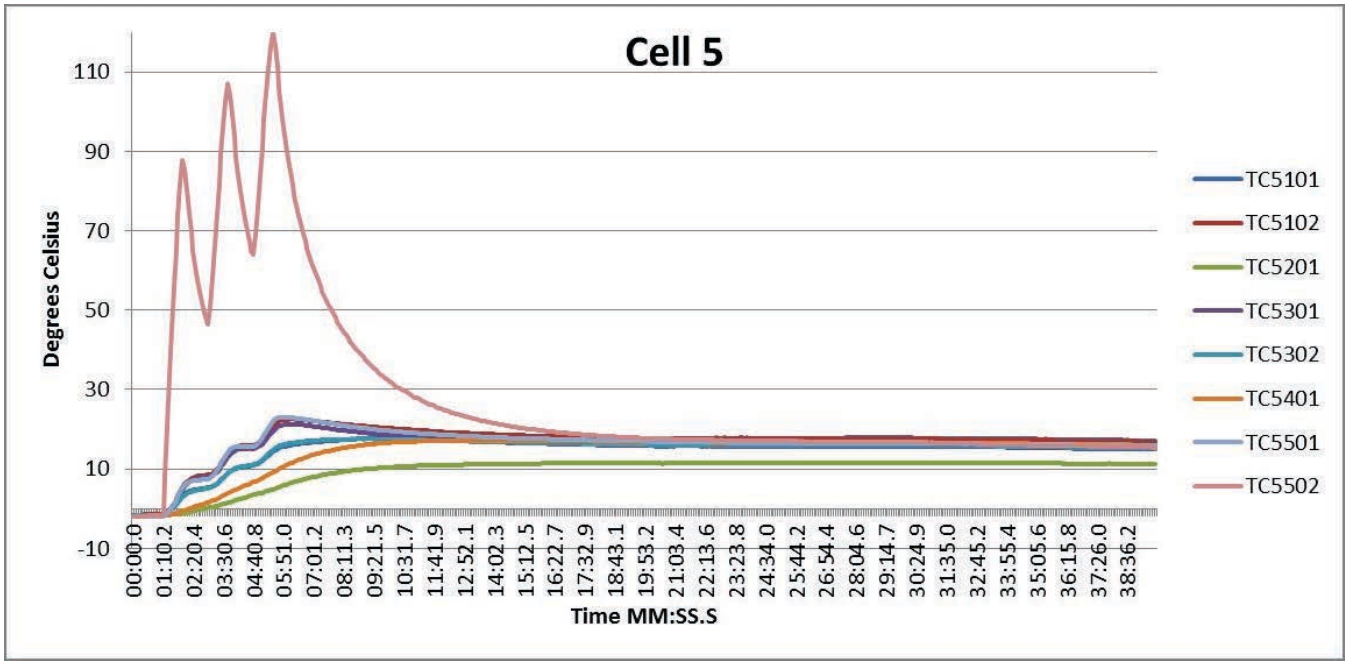

Figure B.60: Task A.1.B, 0 °C, 1 of 5, Cell 5 Temperatures

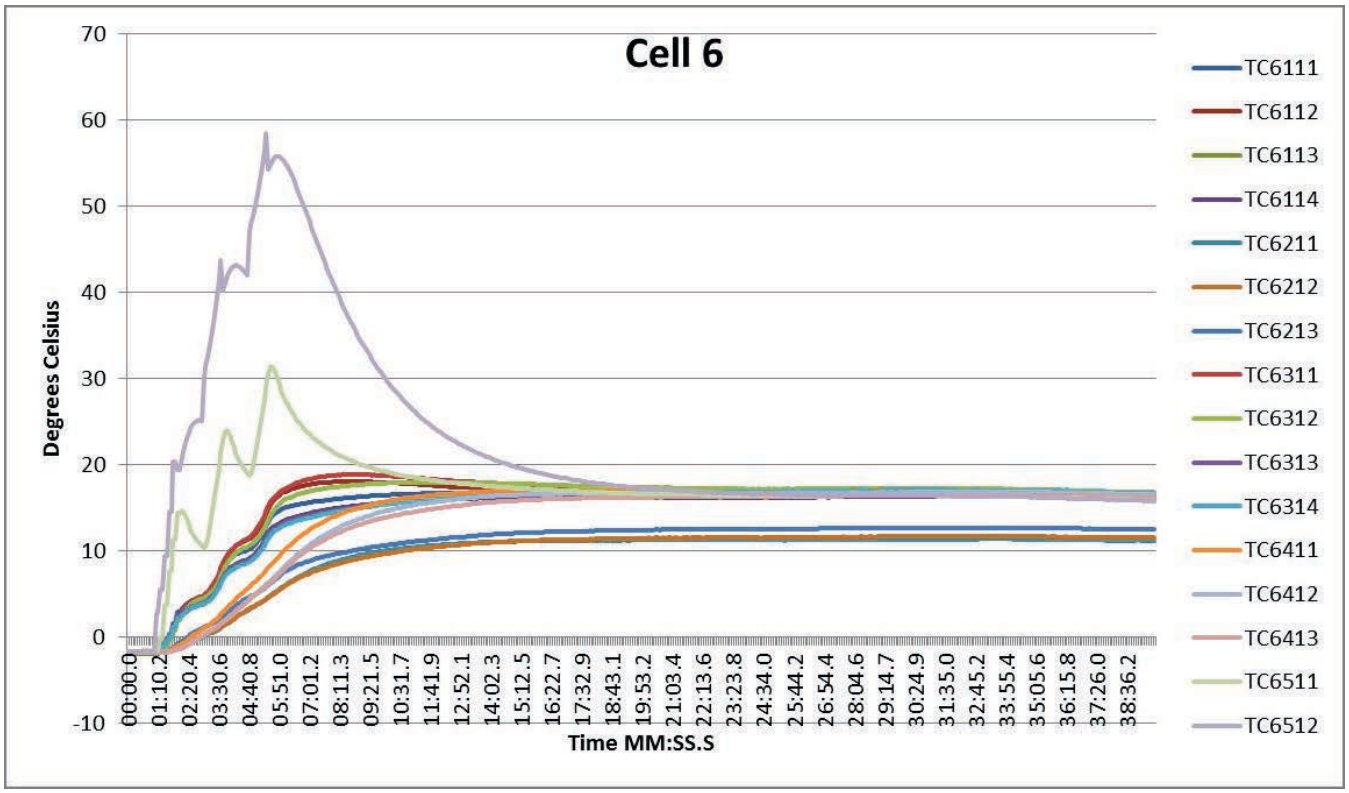

Figure B.61: Task A.1.B, 0 °C, 1 of 5, Cell 6 Temperatures

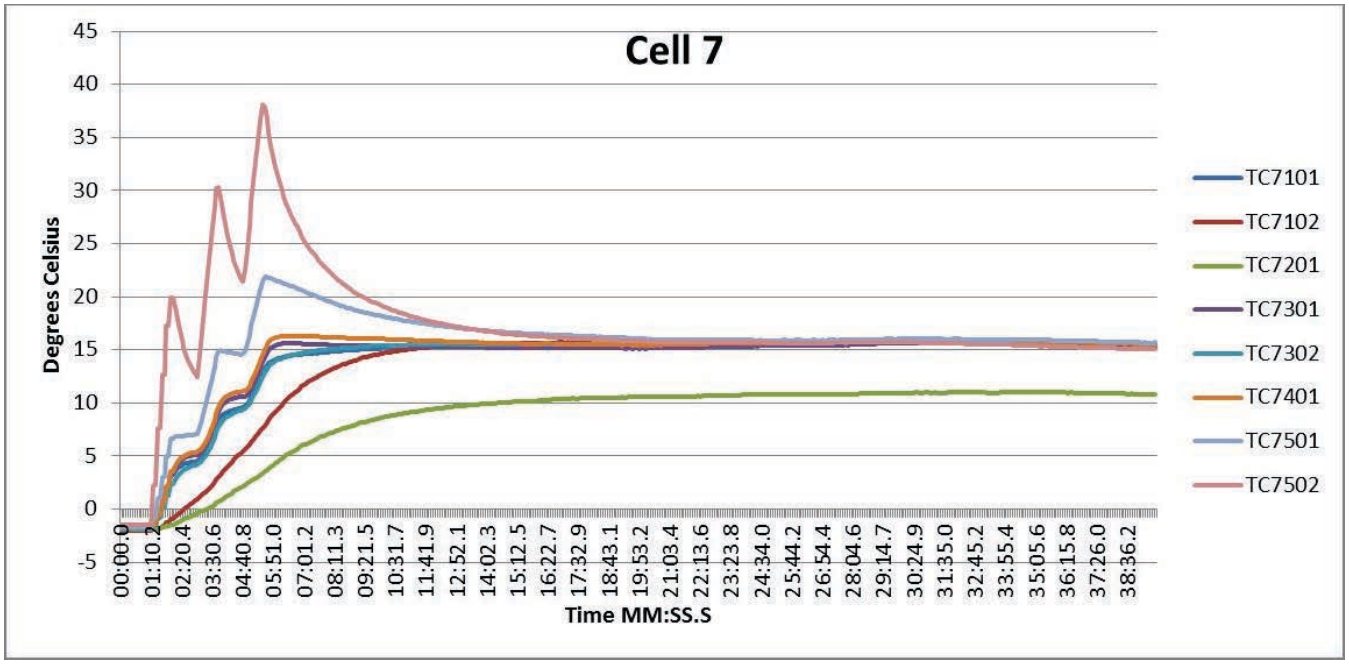

Figure B.62: Task A.1.B, 0 °C, 1 of 5, Cell 7 Temperatures

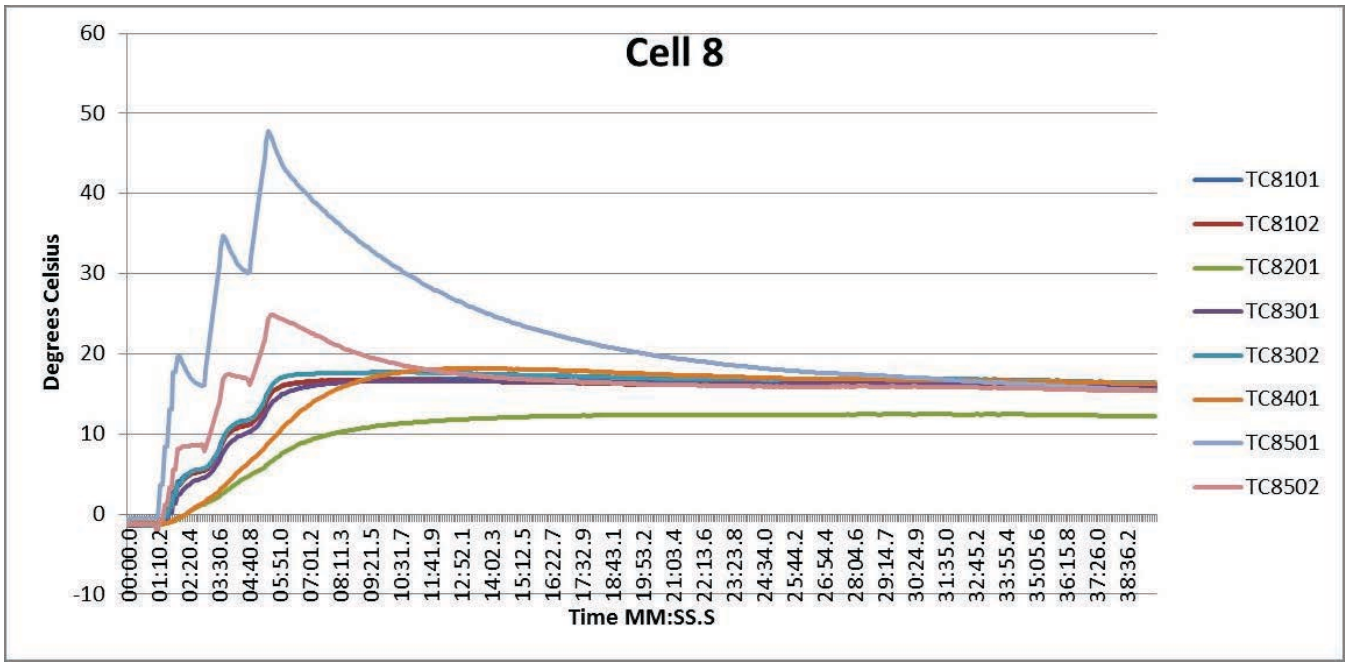

Figure B.63: Task A.1.B, 0 °C, 1 of 5, Cell 8 Temperatures

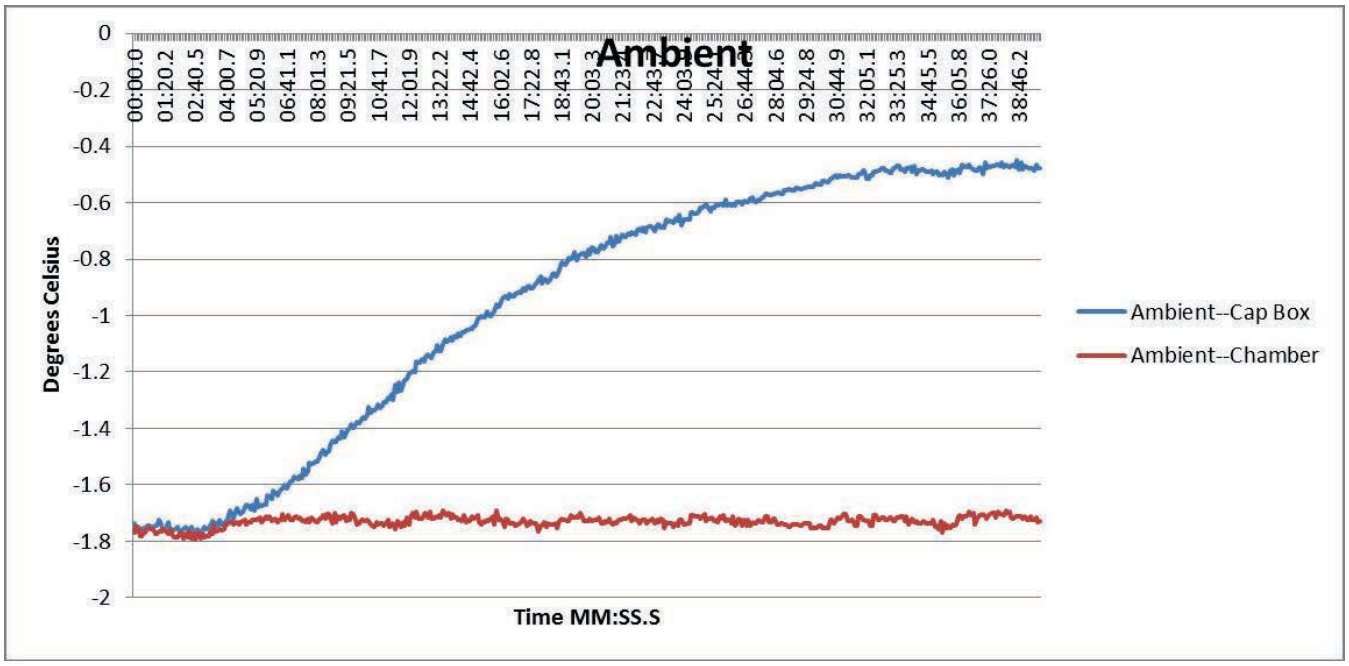

Figure B.64: Task A.1.B, 0 °C, 1 of 5, Ambient Temperatures

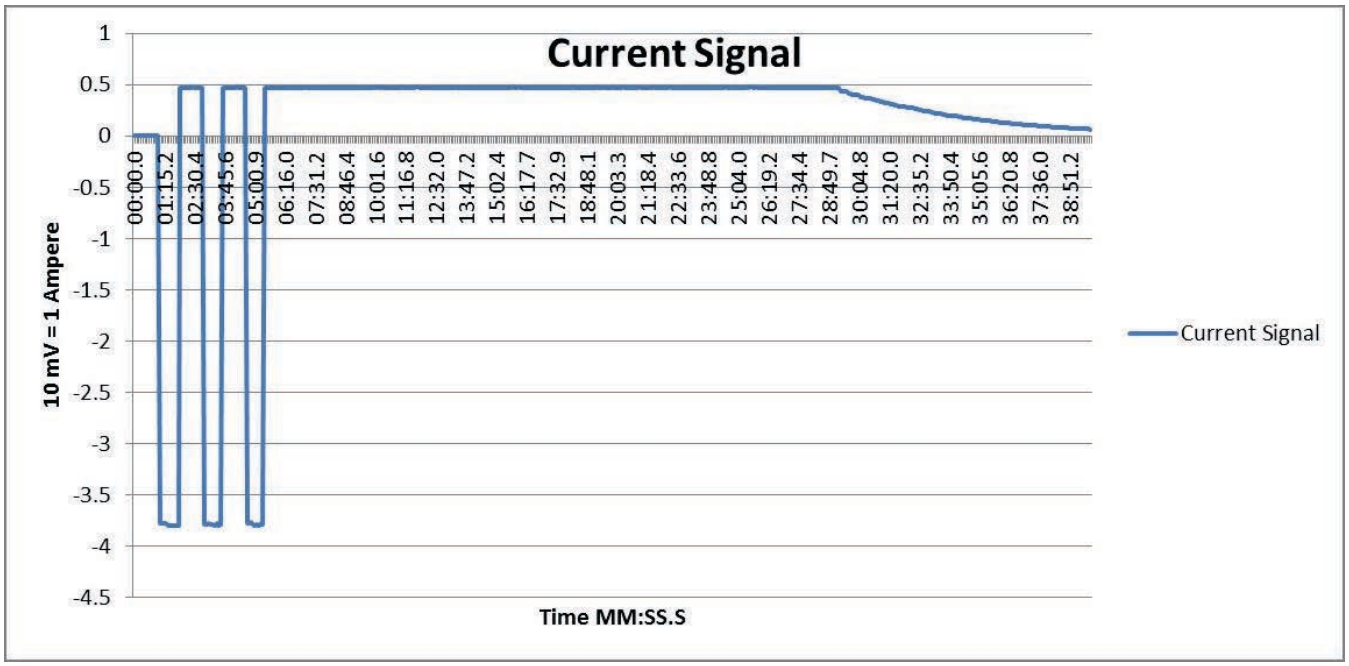

Figure B.65: Task A.1.B, 0 °C, 1 of 5, Current Signal from BMU HECS

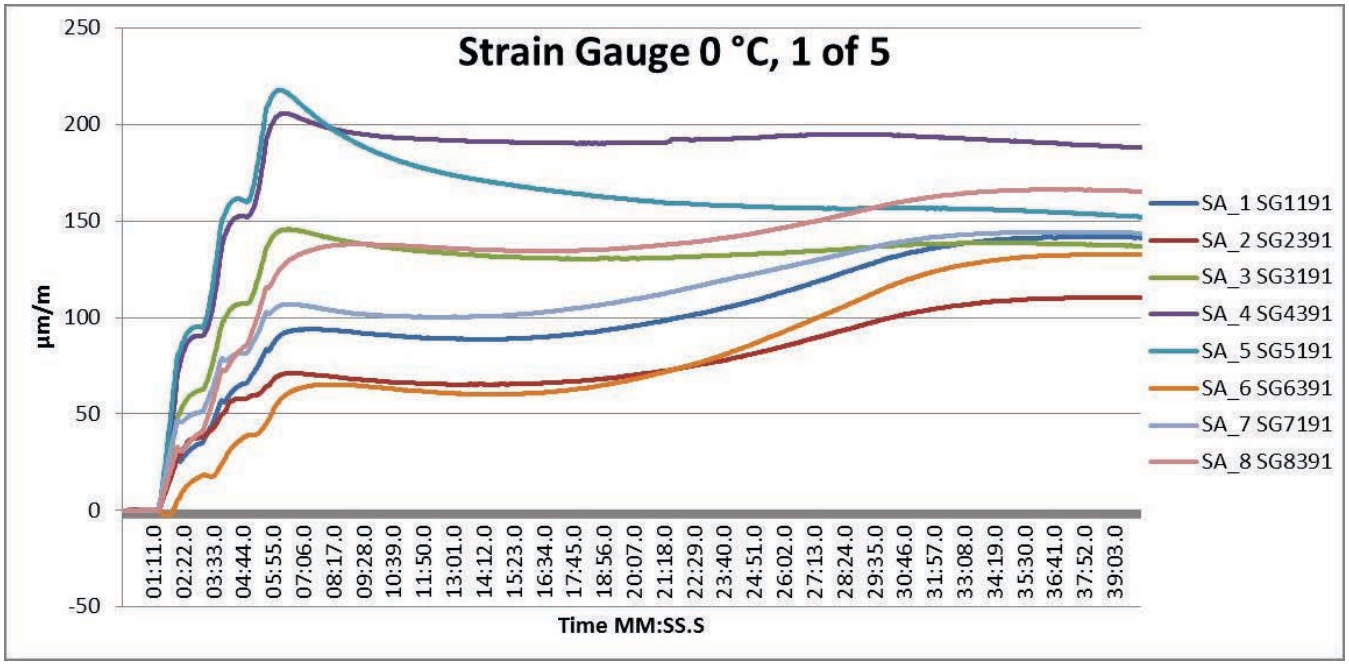

Figure B.66: Task A.1.B, 0 °C, 1 of 5, Strain Gauges

Task A.1.B – 0 °C, 2 of 5

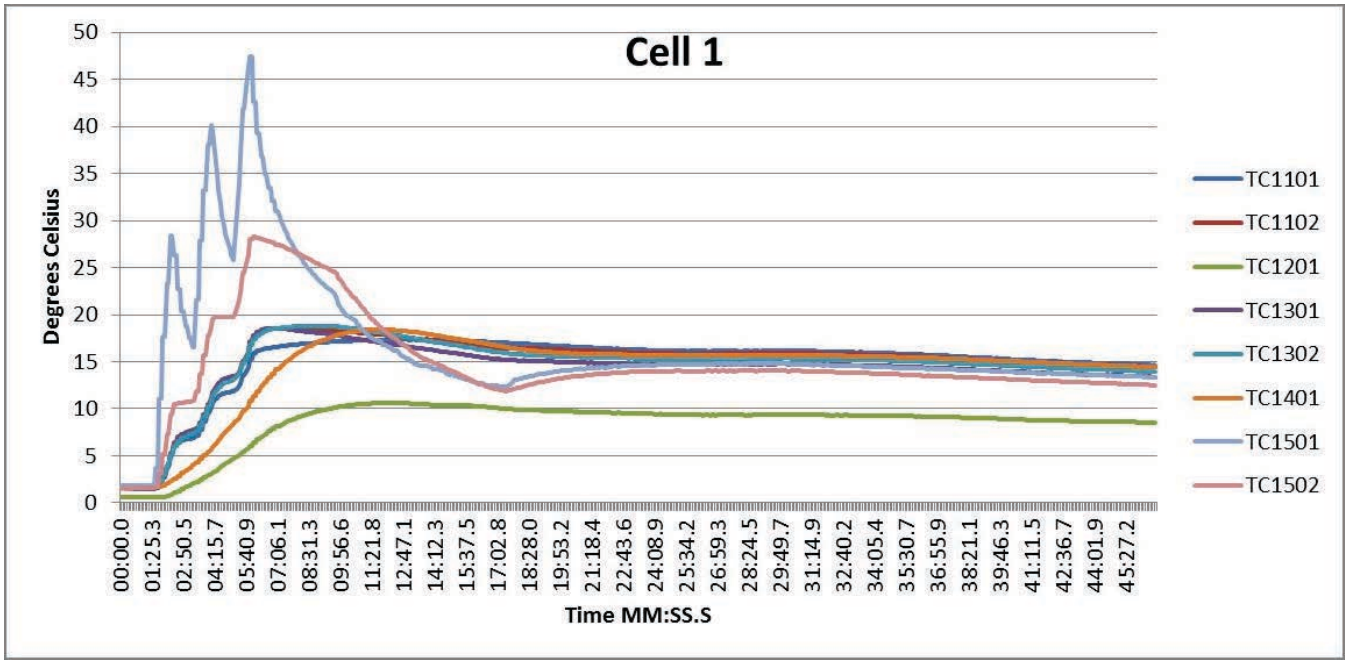

Figure B.67: Task A.1.B, 0 °C, 2 of 5, Cell 1 Temperatures

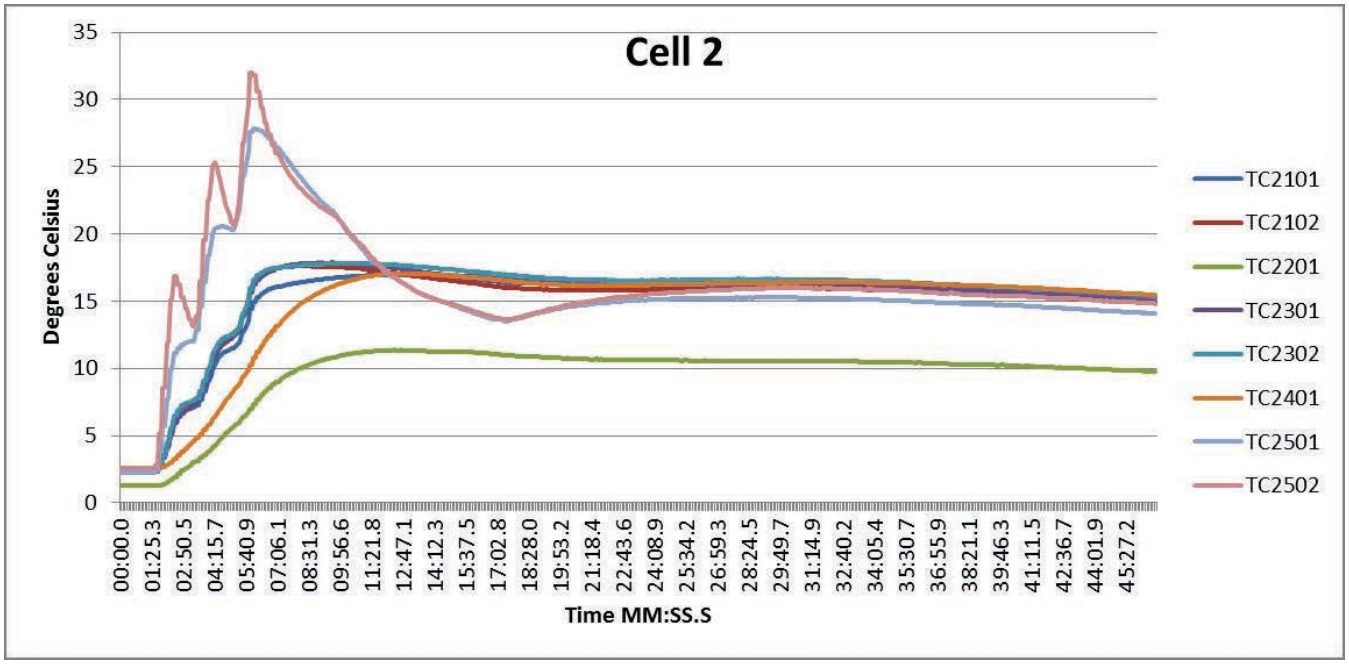

Figure B.68: Task A.1.B, 0 °C, 2 of 5, Cell 2 Temperatures

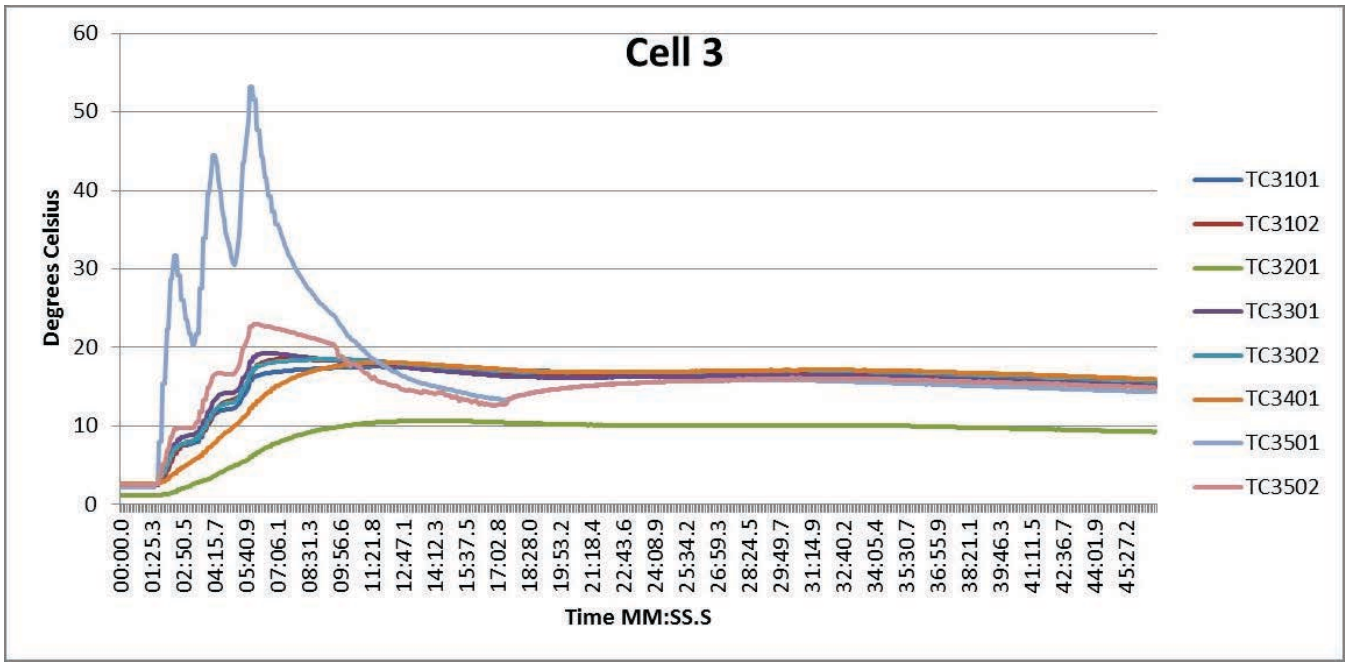

Figure B.69: Task A.1.B, 0 °C, 2 of 5, Cell 3 Temperatures

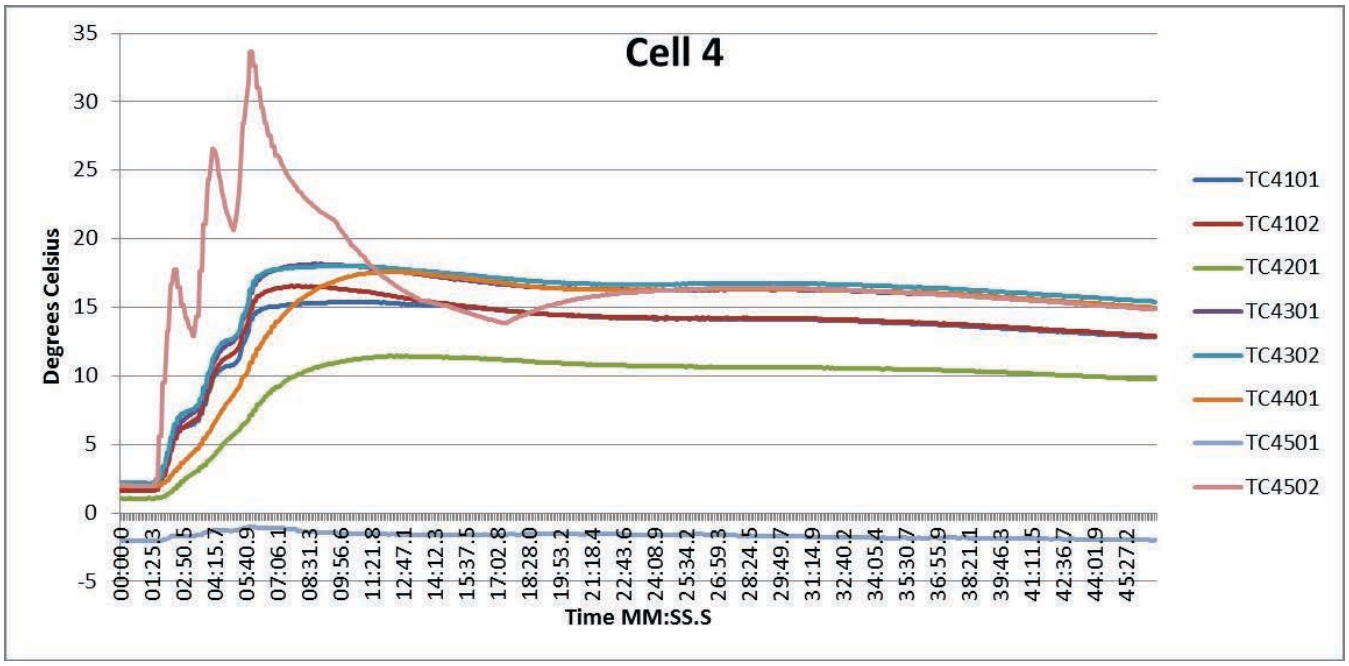

Figure B.70: Task A.1.B, 0 °C, 2 of 5, Cell 4 Temperatures

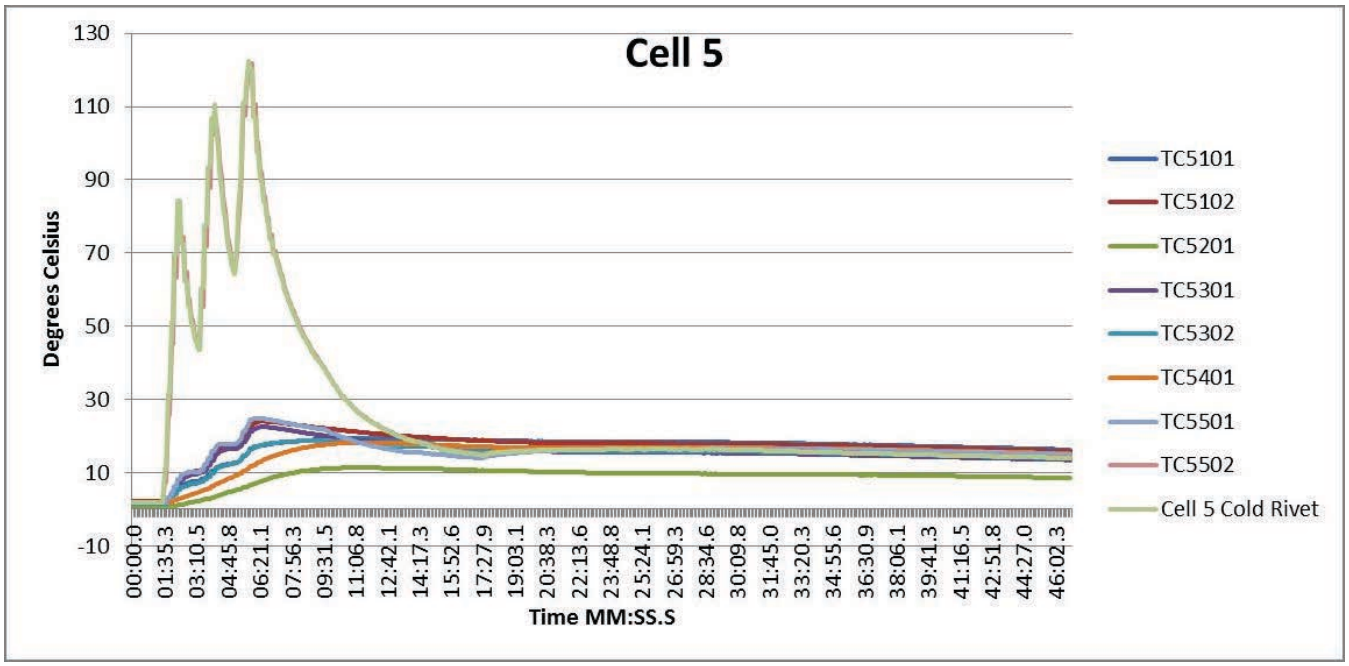

Figure B.71: Task A.1.B, 0 °C, 2 of 5, Cell 5 Temperatures

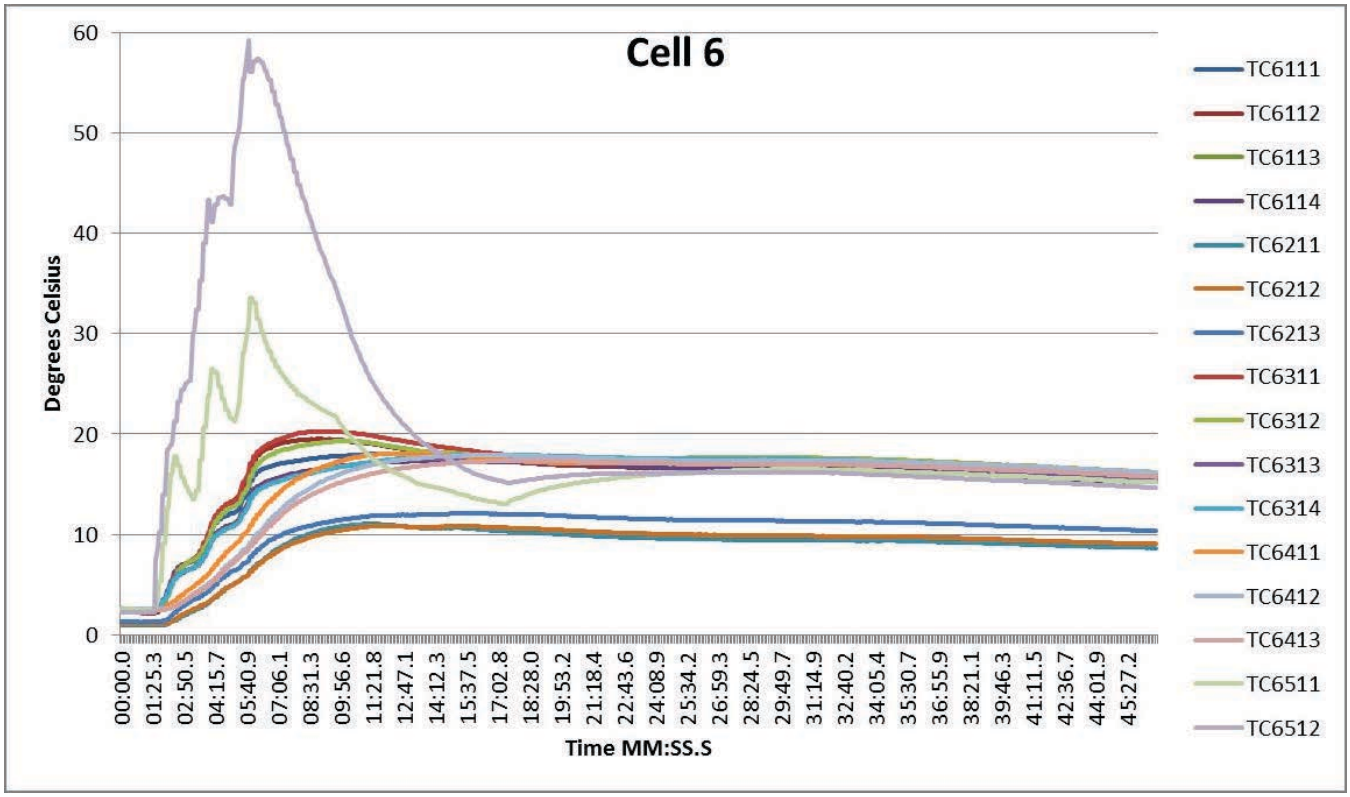

Figure B.72: Task A.1.B, 0 °C, 2 of 5, Cell 6 Temperatures

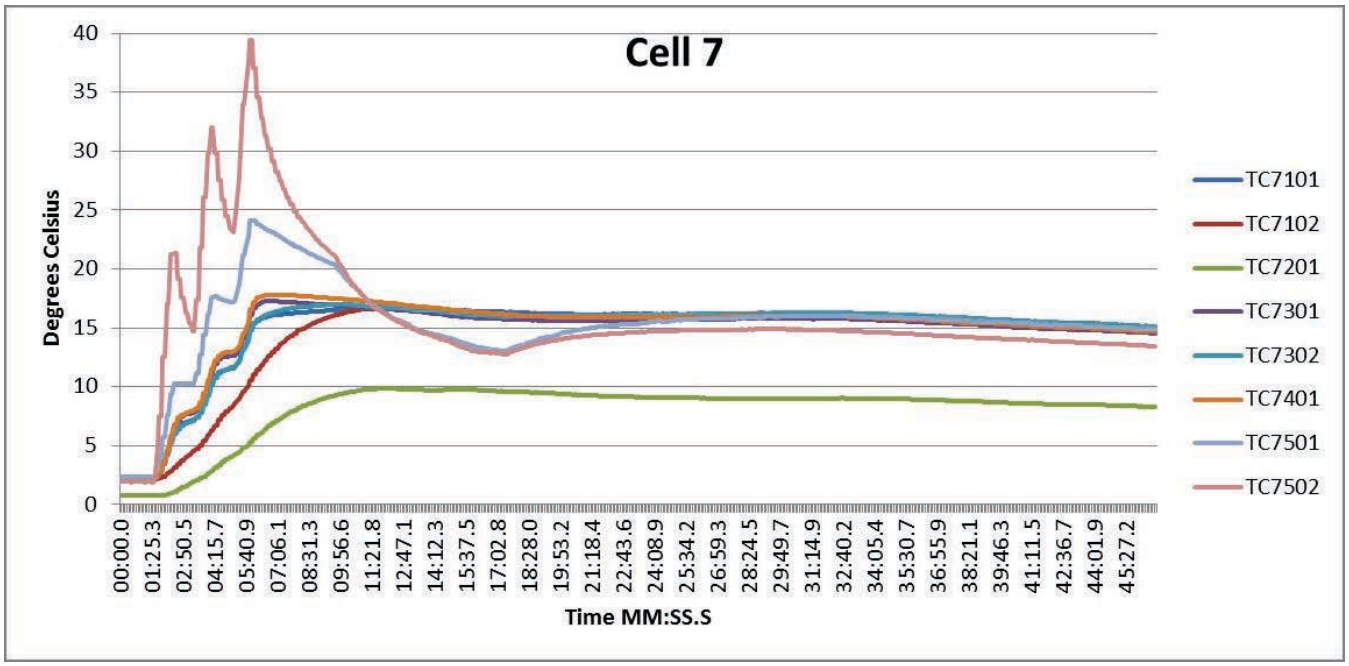

Figure B.73: Task A.1.B, 0 °C, 2 of 5, Cell 7 Temperatures

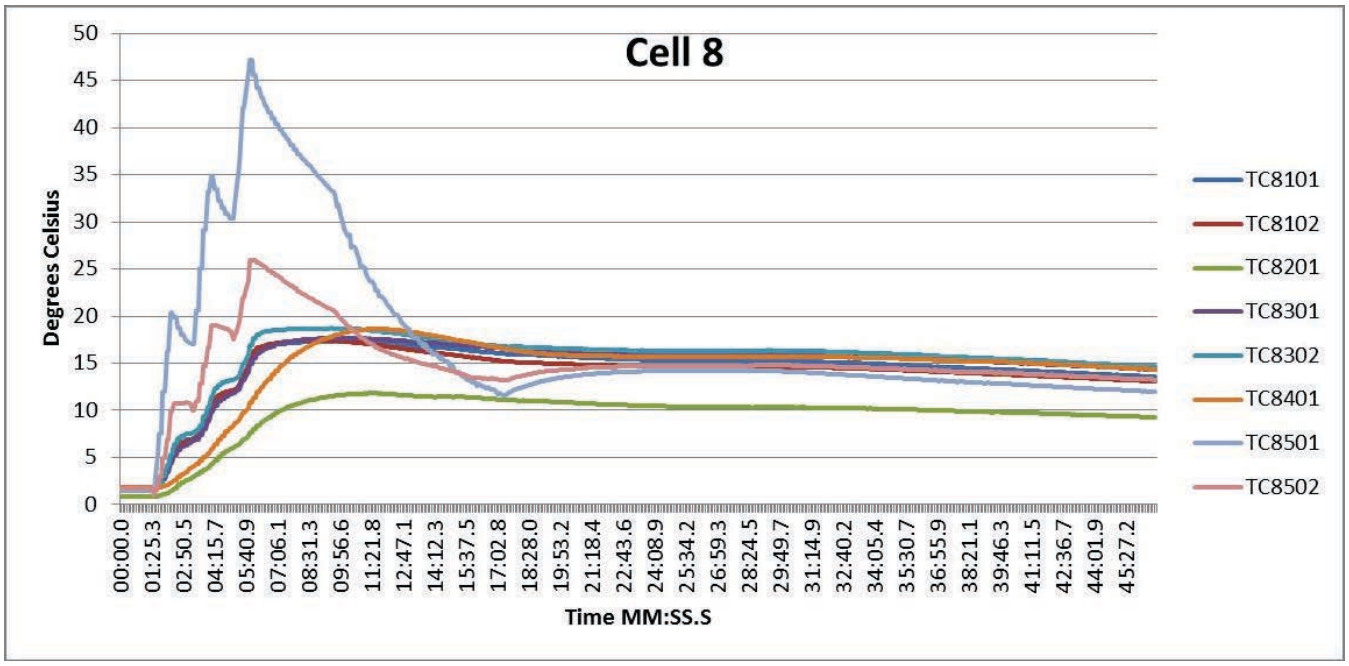

Figure B.74: Task A.1.B, 0 °C, 2 of 5, Cell 8 Temperatures

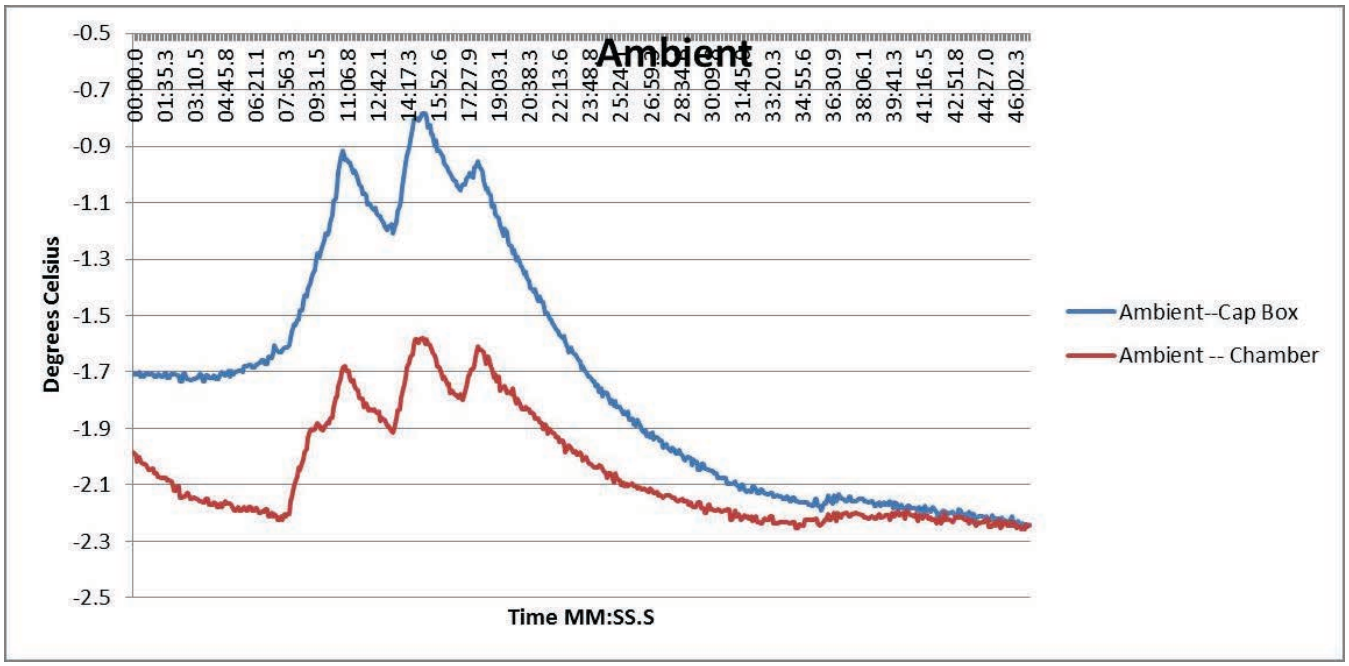

Figure B.75: Task A.1.B, 0 °C, 2 of 5, Ambient Temperatures

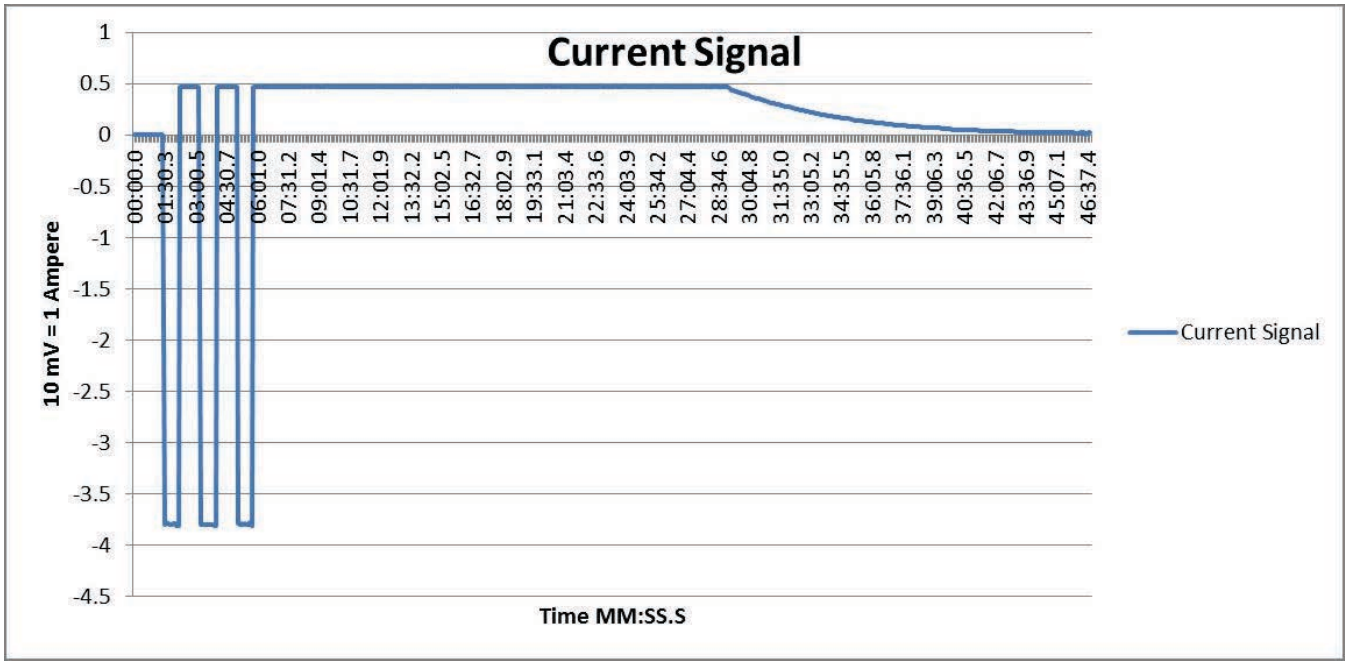

Figure B.76: Task A.1.B, 0 °C, 2 of 5, Current Signal from BMU HECS

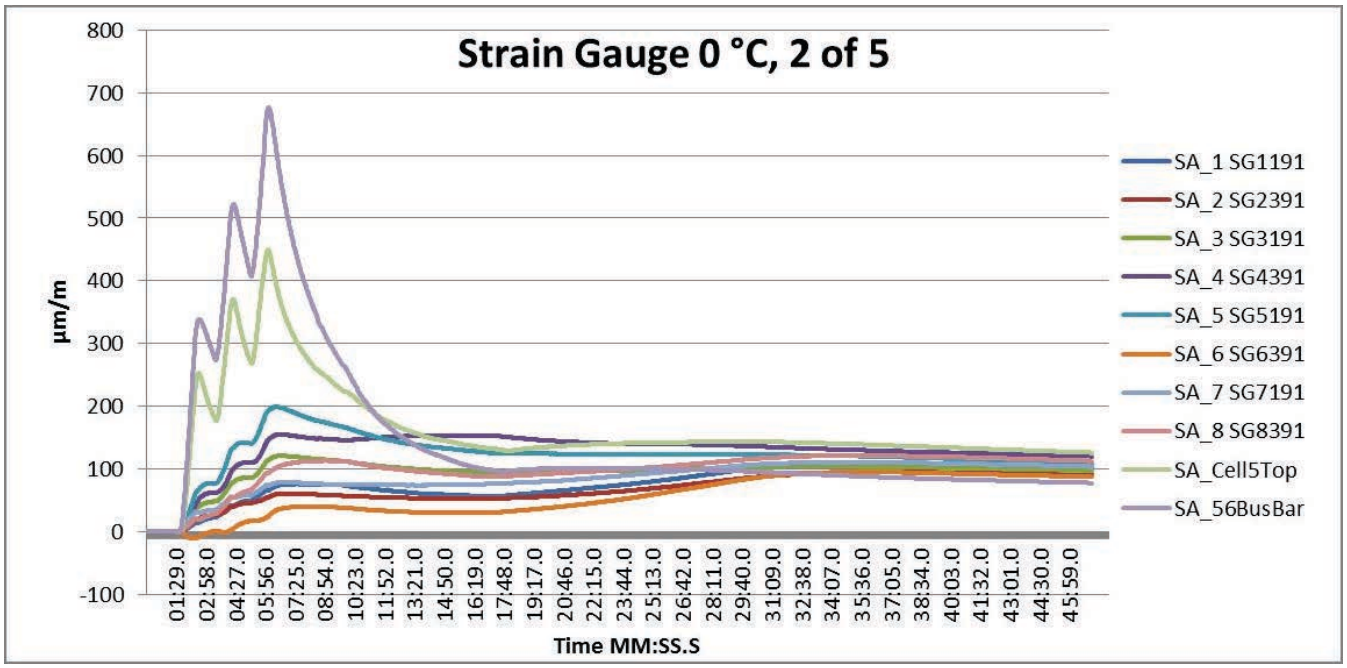

Figure B.77: Task A.1.B, 0 °C, 2 of 5, Strain Gauges

Task A.1.B – 0 °C, 3 of 5

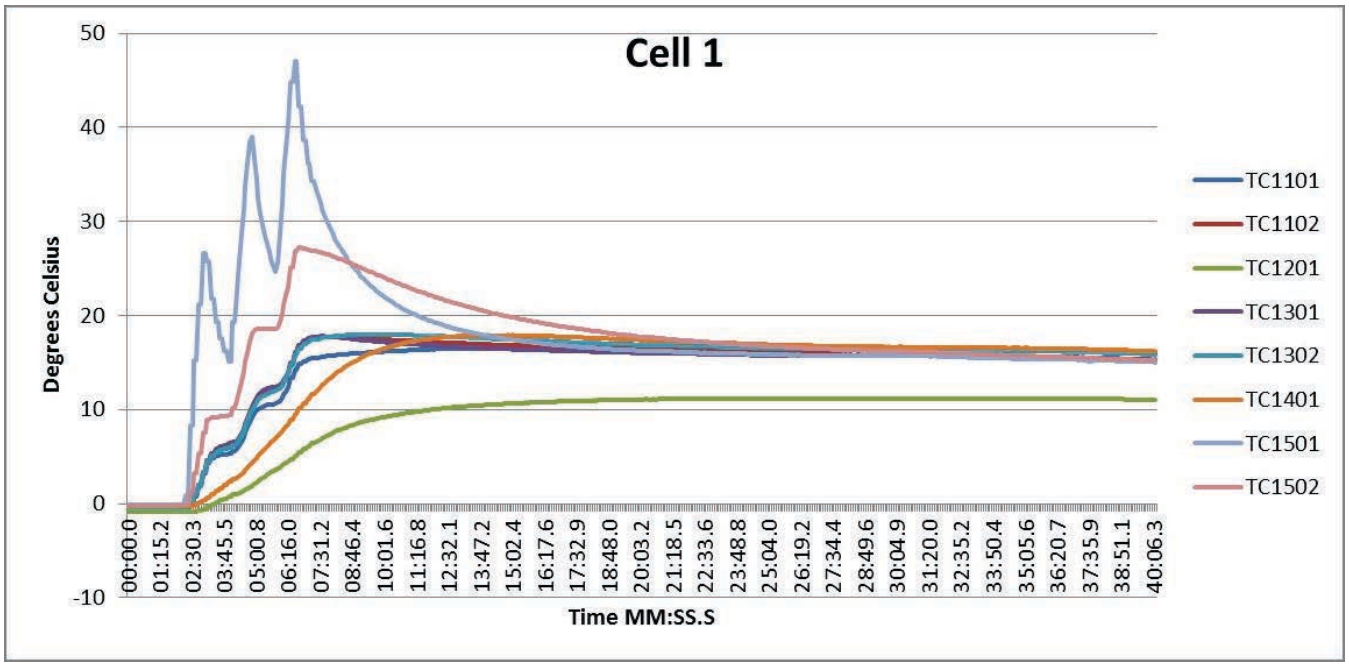

Figure B.78: Task A.1.B, 0 °C, 3 of 5, Cell 1 Temperatures

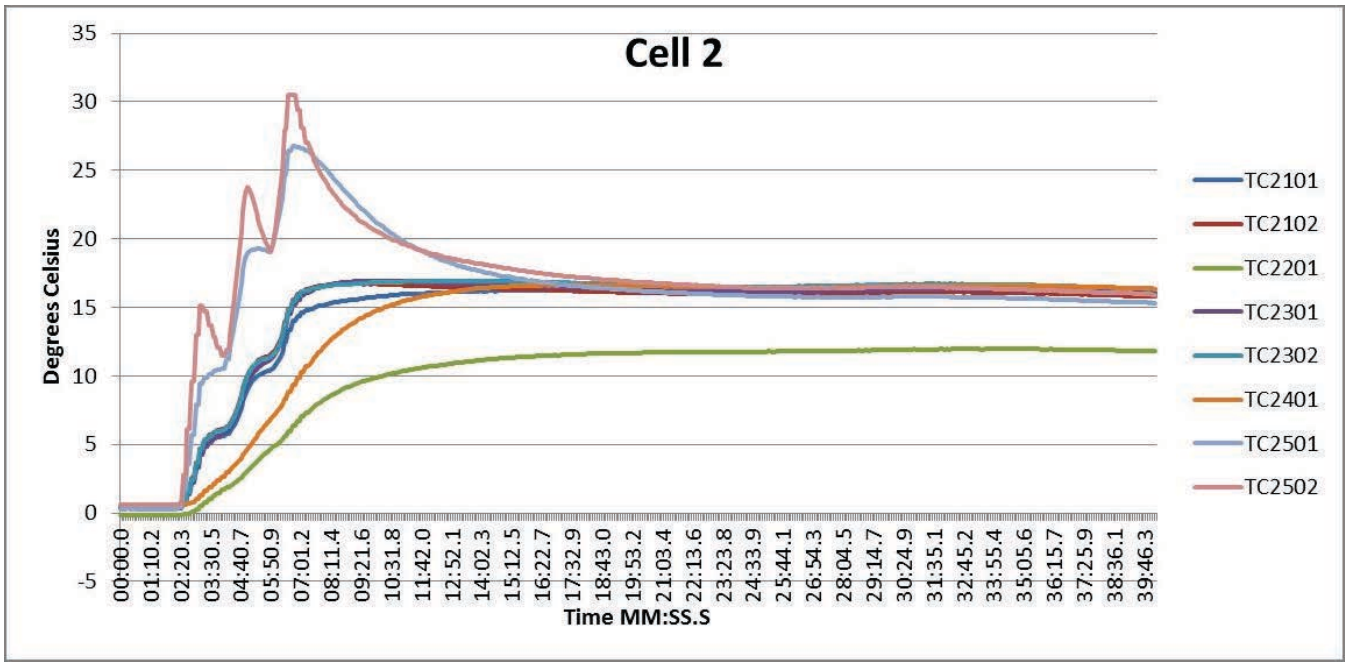

Figure B.79: Task A.1.B, 0 °C, 3 of 5, Cell 2 Temperatures

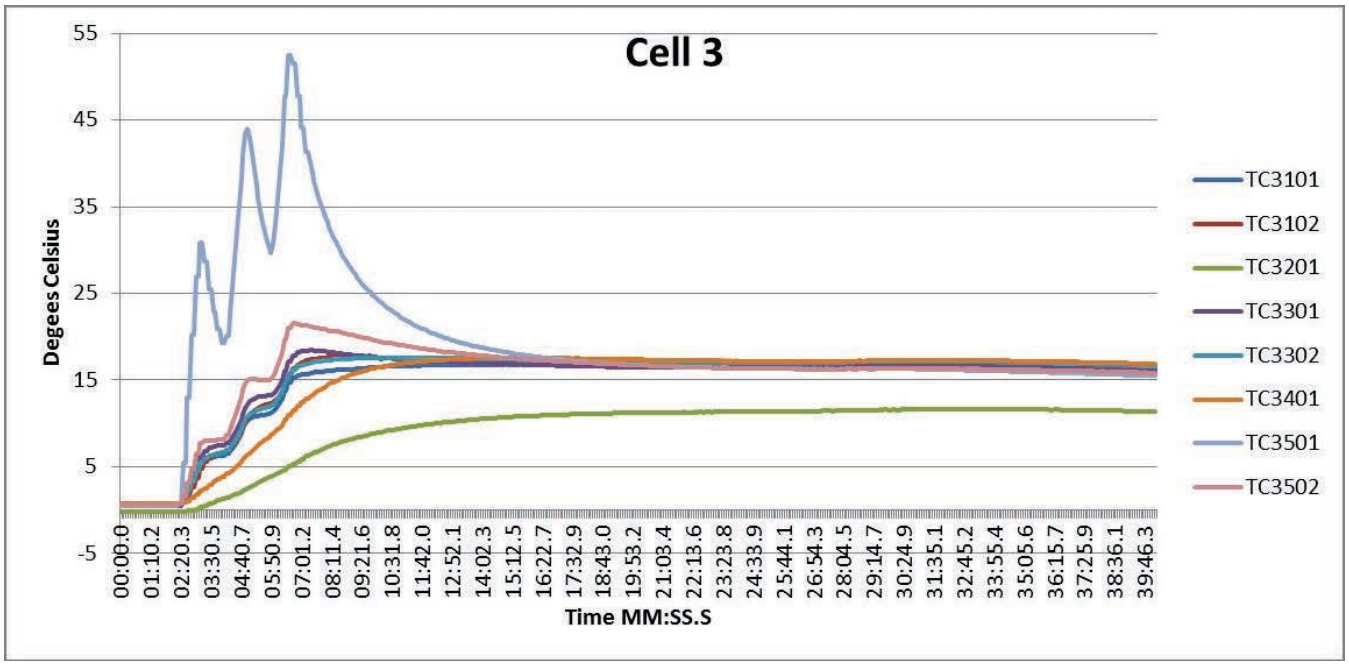

Figure B.80: Task A.1.B, 0 °C, 3 of 5, Cell 3 Temperatures

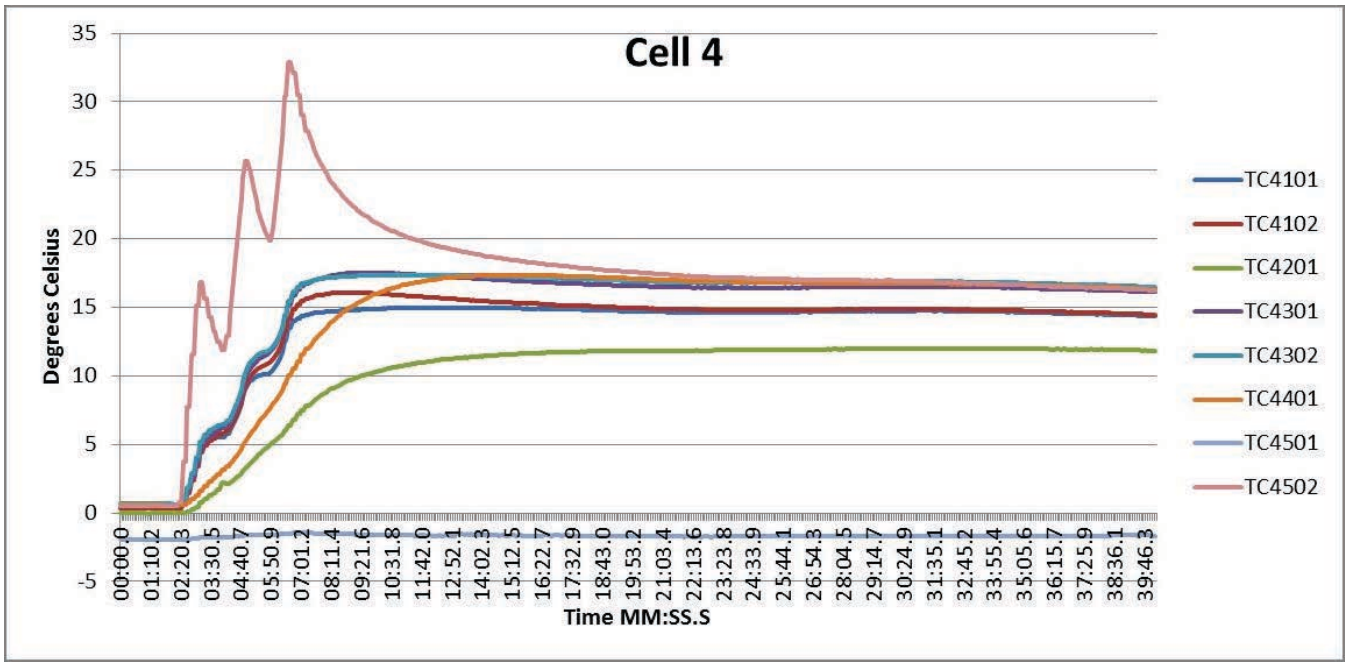

Figure B.81: Task A.1.B, 0 °C, 3 of 5, Cell 4 Temperatures

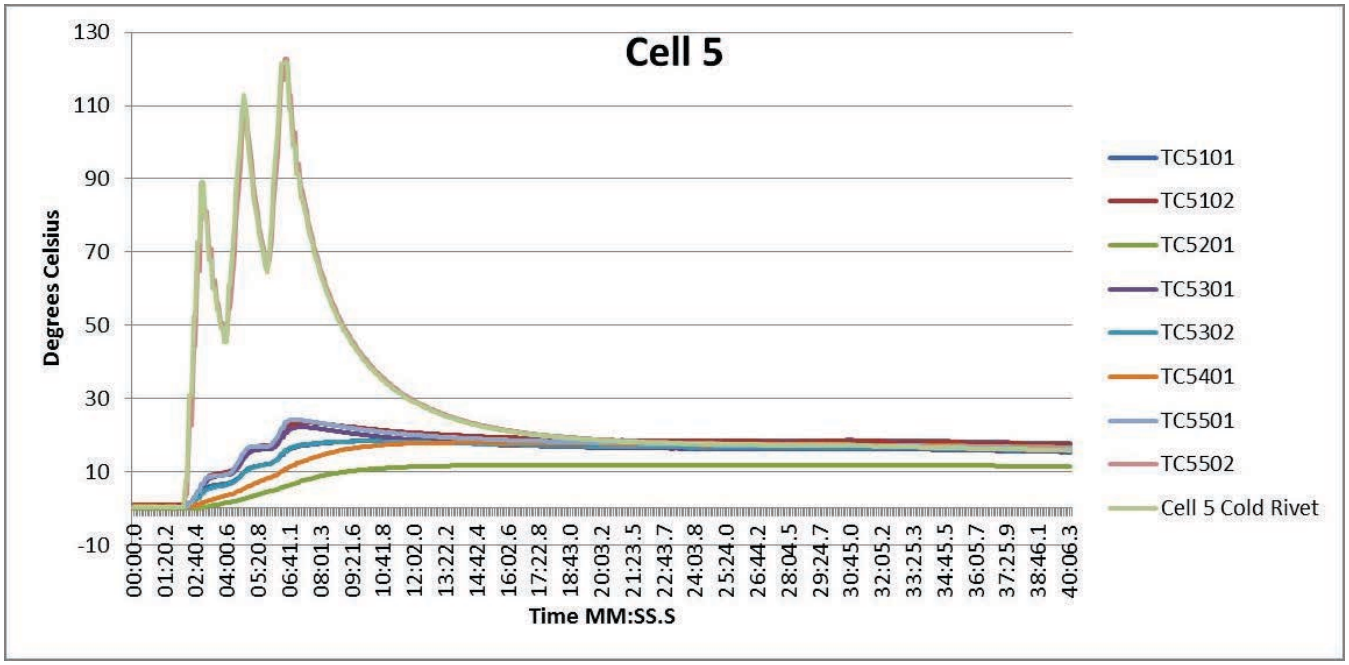

Figure B.82: Task A.1.B, 0 °C, 3 of 5, Cell 5 Temperatures

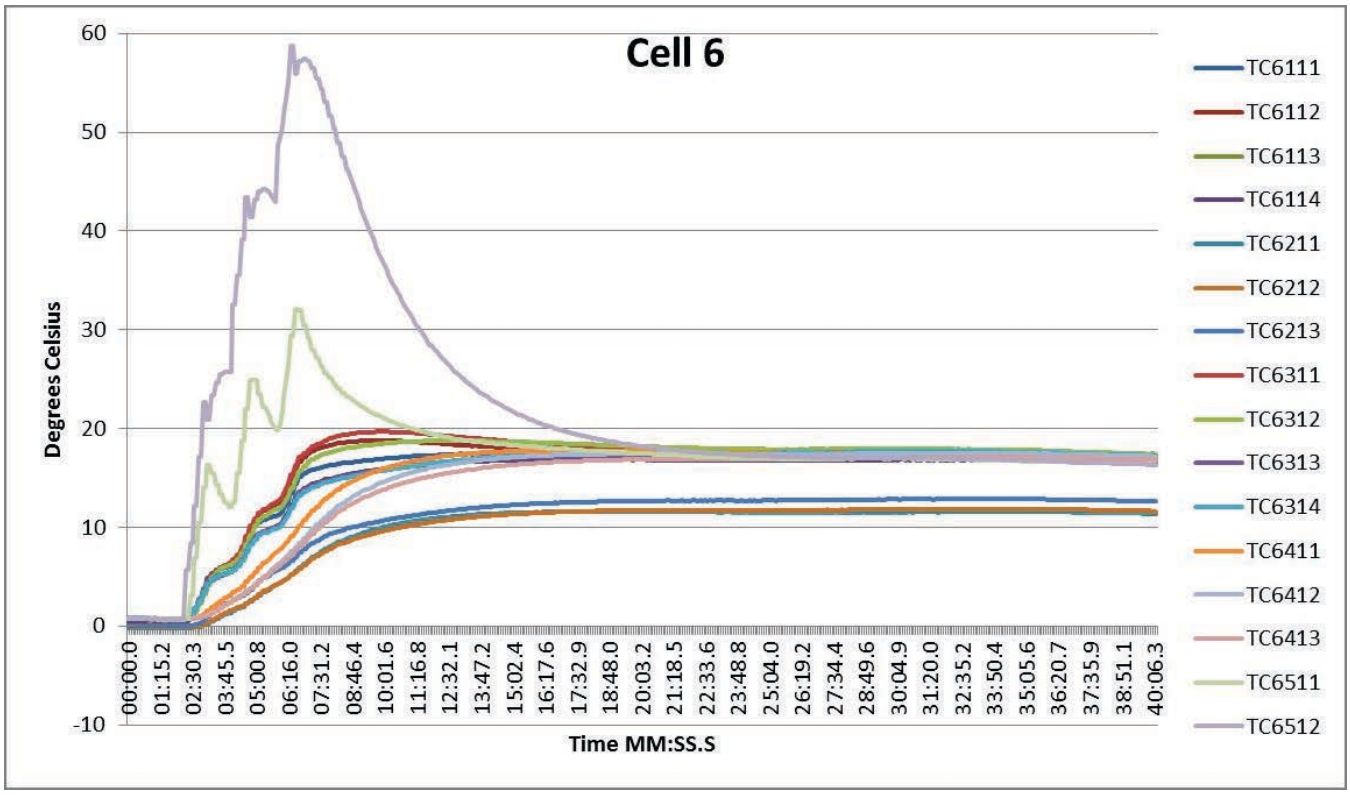

Figure B.83: Task A.1.B, 0 °C, 3 of 5, Cell 6 Temperatures

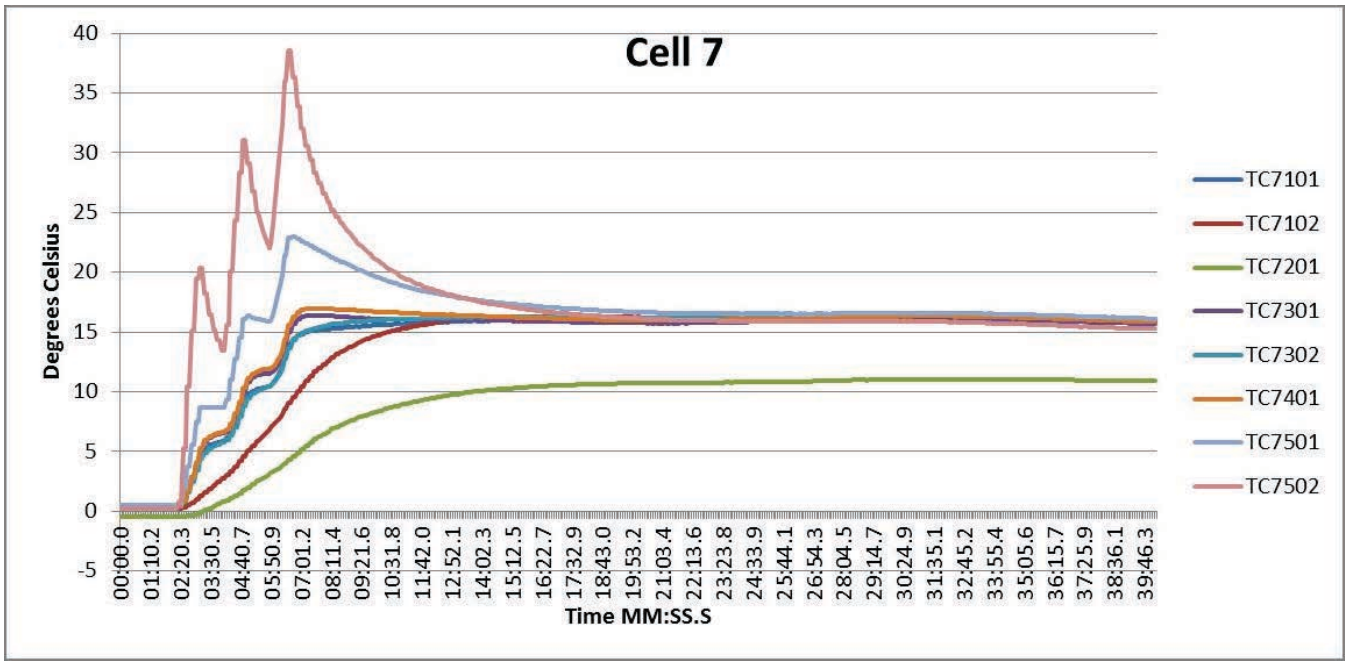

Figure B.84: Task A.1.B, 0 °C, 3 of 5, Cell 7 Temperatures

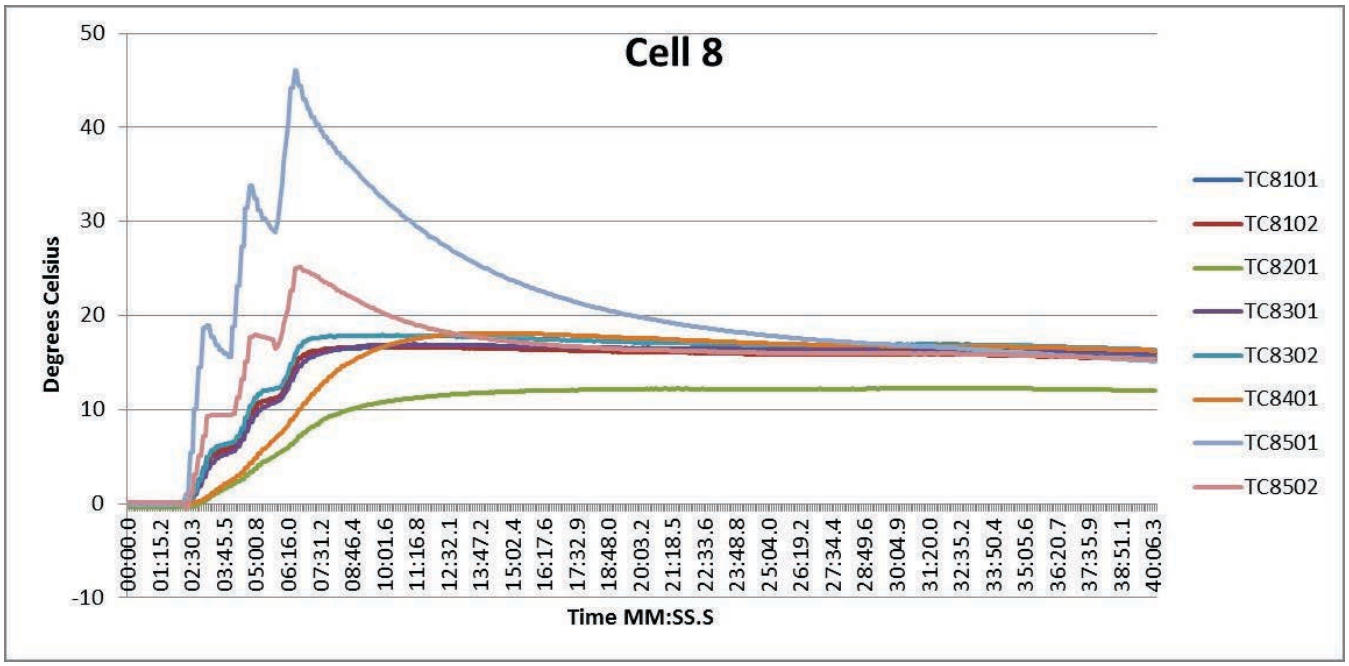

Figure B.85: Task A.1.B, 0 °C, 3 of 5, Cell 8 Temperatures

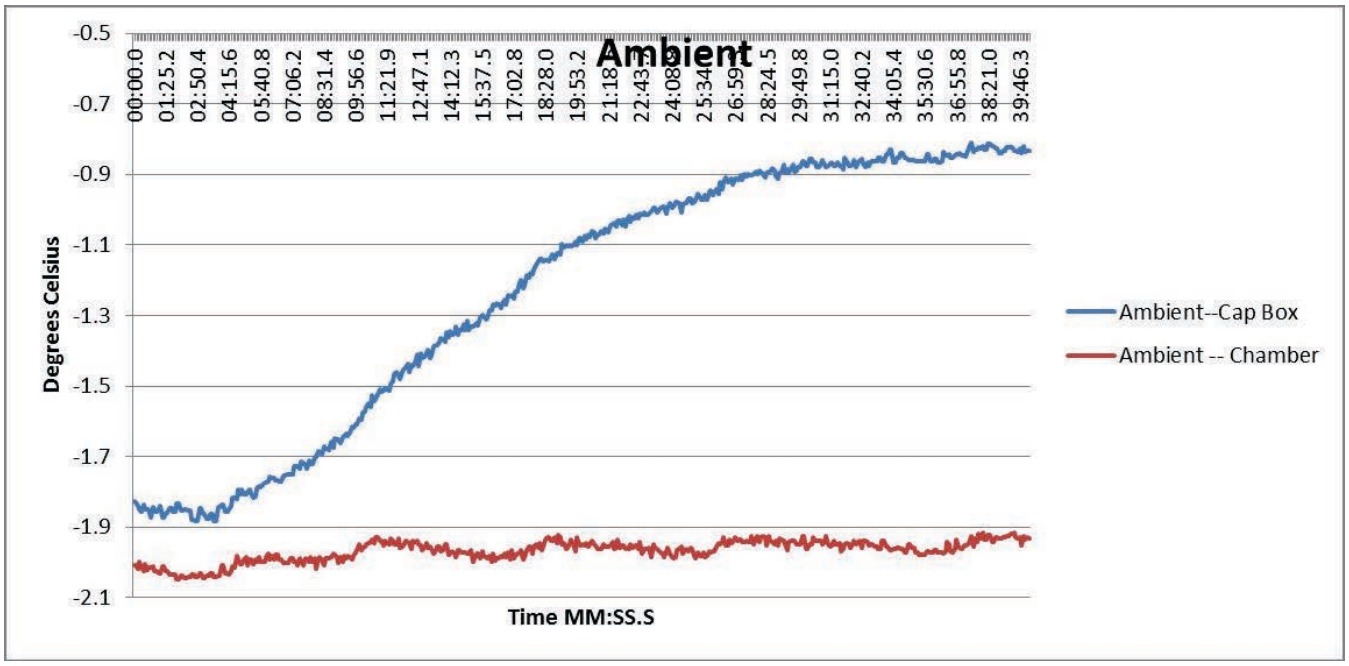

Figure B.86: Task A.1.B, 0 °C, 3 of 5, Ambient Temperatures

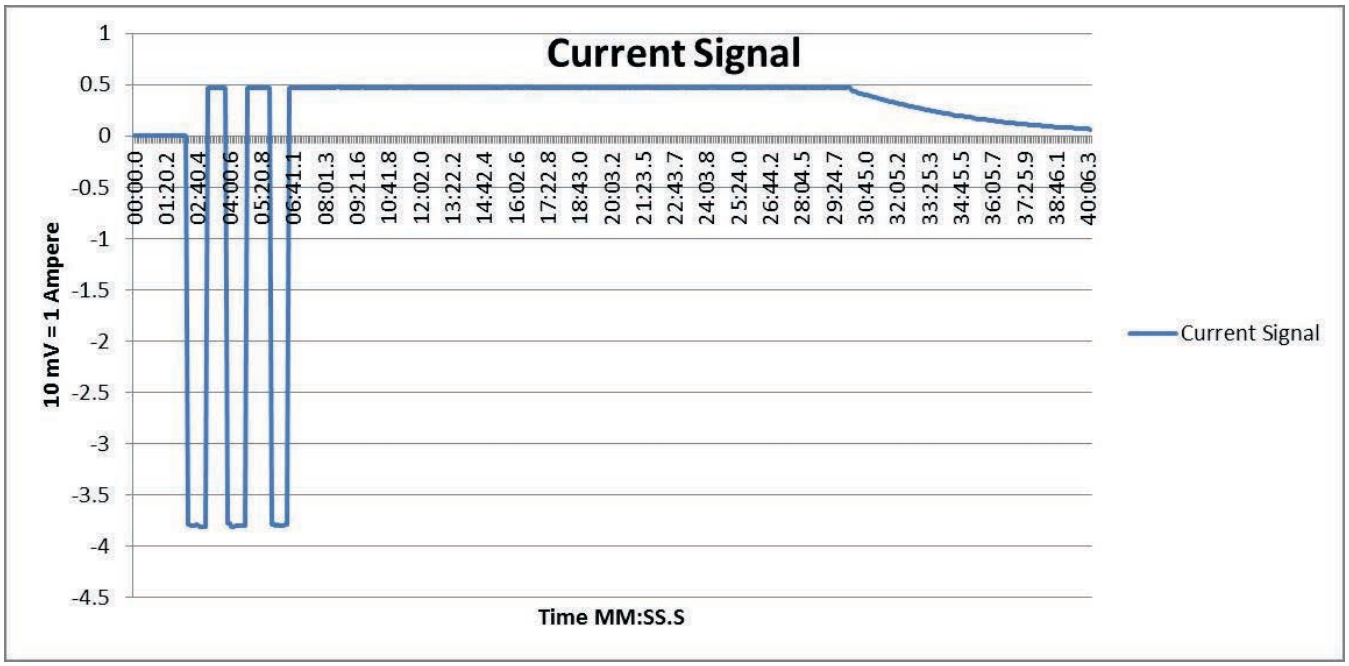

Figure B.87: Task A.1.B, 0 °C, 3 of 5, Current Signal from BMU HECS

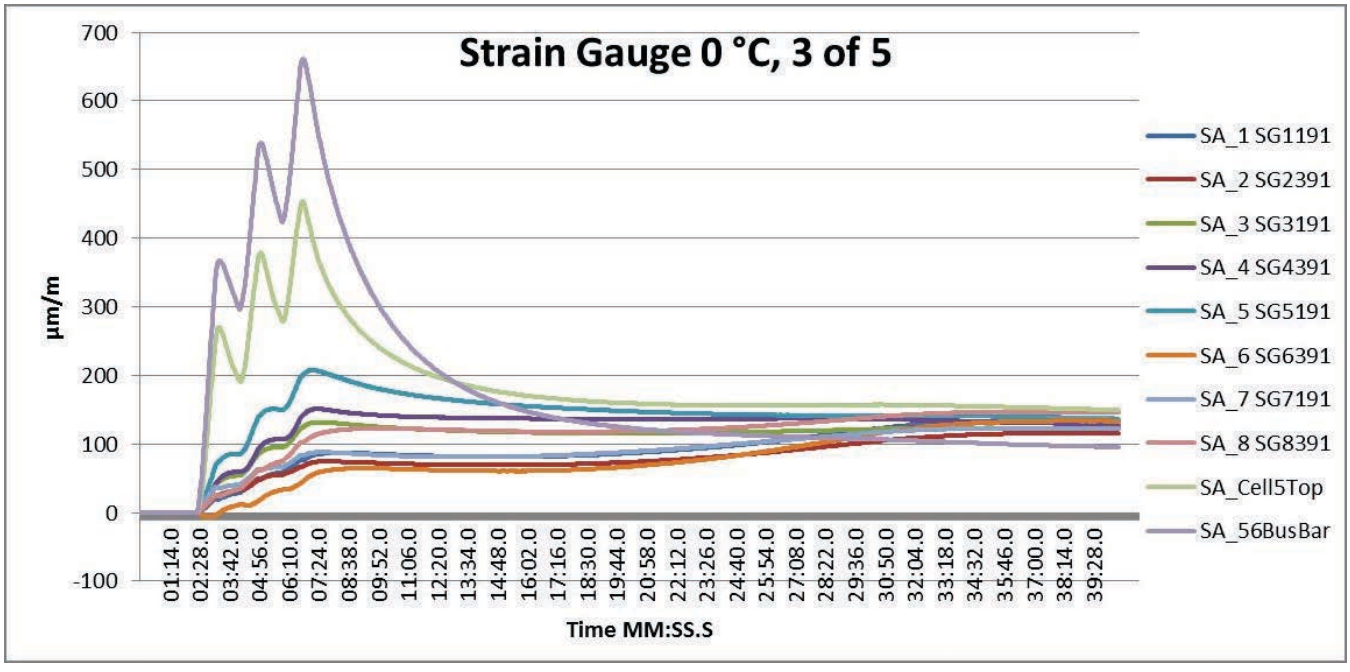

Figure B.88: Task A.1.B, 0 °C, 3 of 5, Strain Gauges

Task A.1.B – 0 °C, 4 of 5

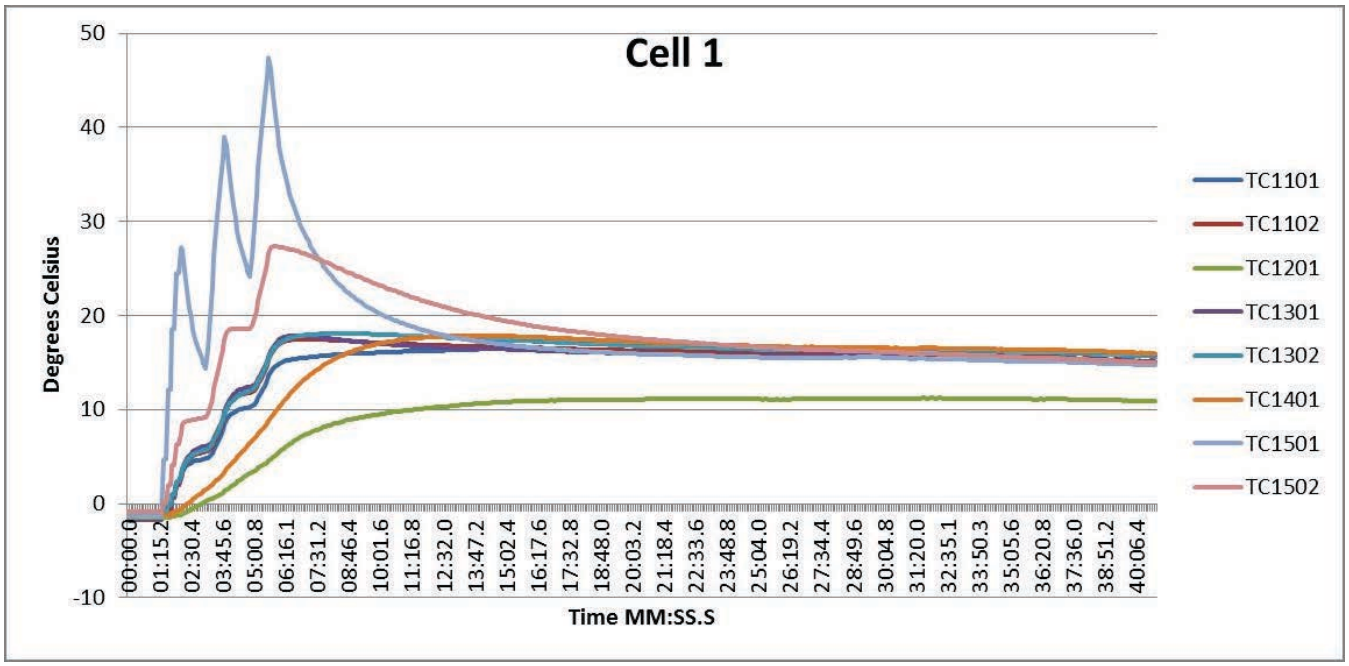

Figure B.89: Task A.1.B, 0 °C, 4 of 5, Cell 1 Temperatures

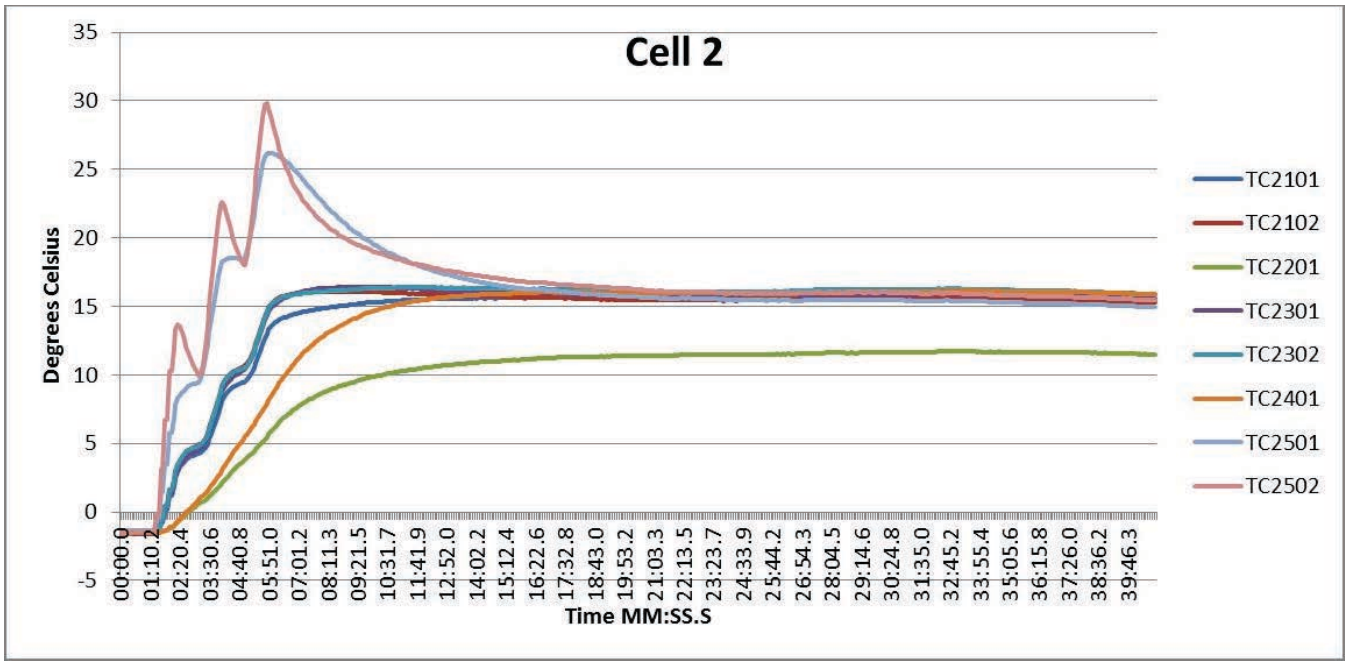

Figure B.90: Task A.1.B, 0 °C, 4 of 5, Cell 2 Temperatures

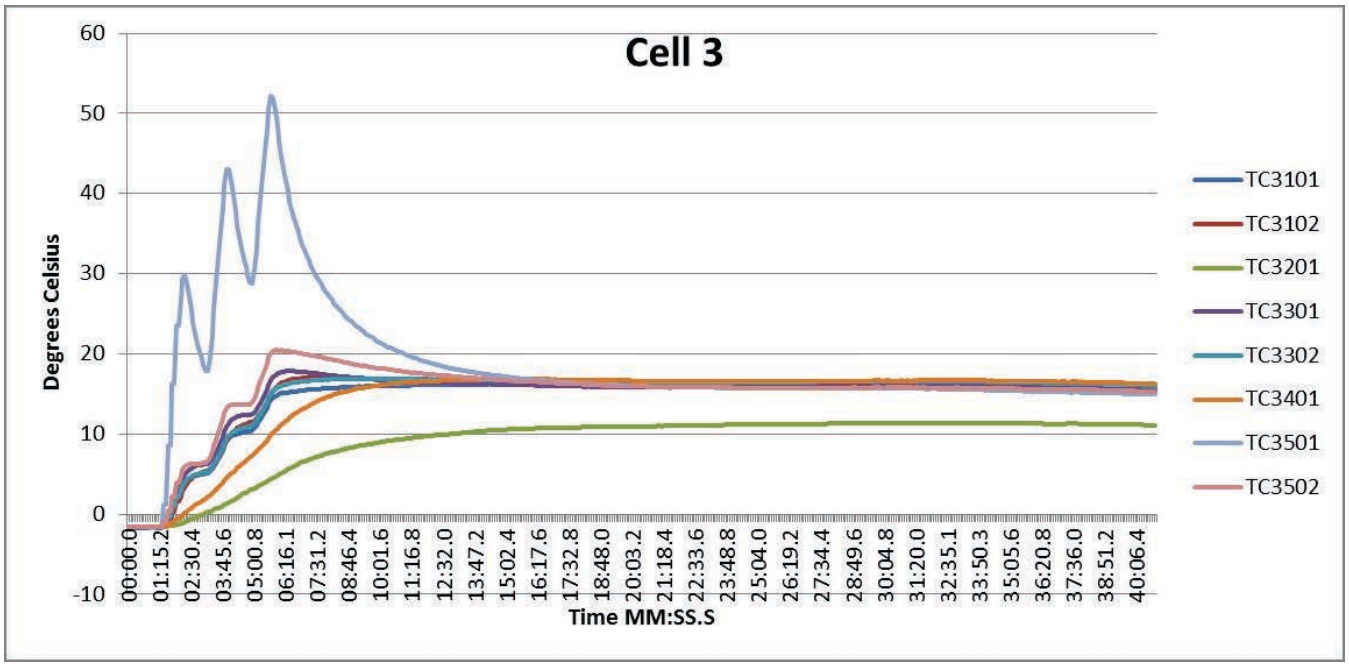

Figure B.91: Task A.1.B, 0 °C, 4 of 5, Cell 3 Temperatures

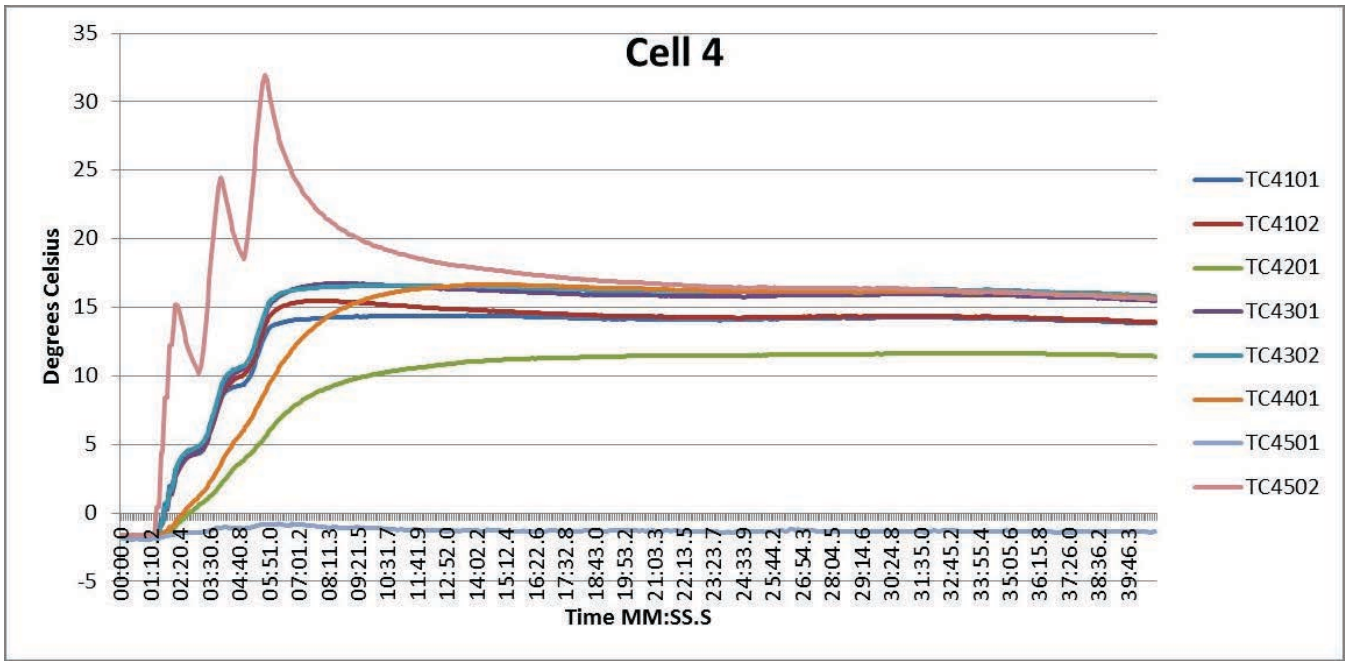

Figure B.92: Task A.1.B, 0 °C, 4 of 5, Cell 4 Temperatures

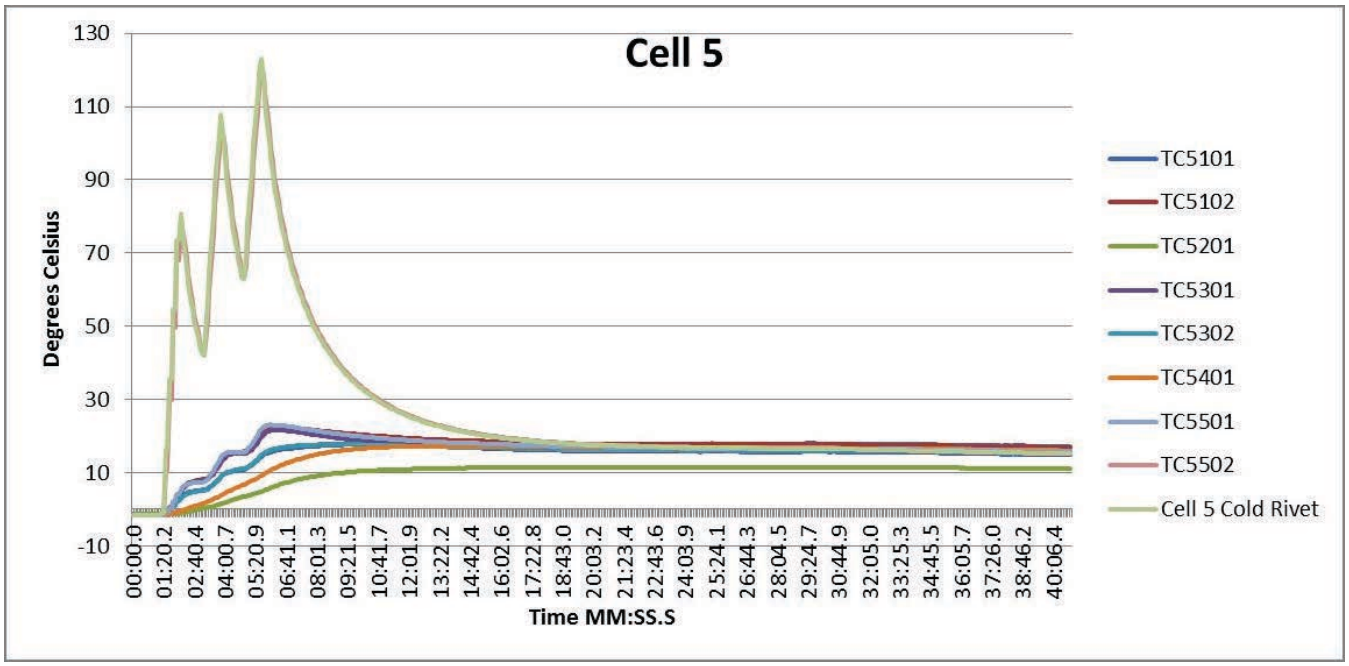

Figure B.93: Task A.1.B, 0 °C, 4 of 5, Cell 5 Temperatures

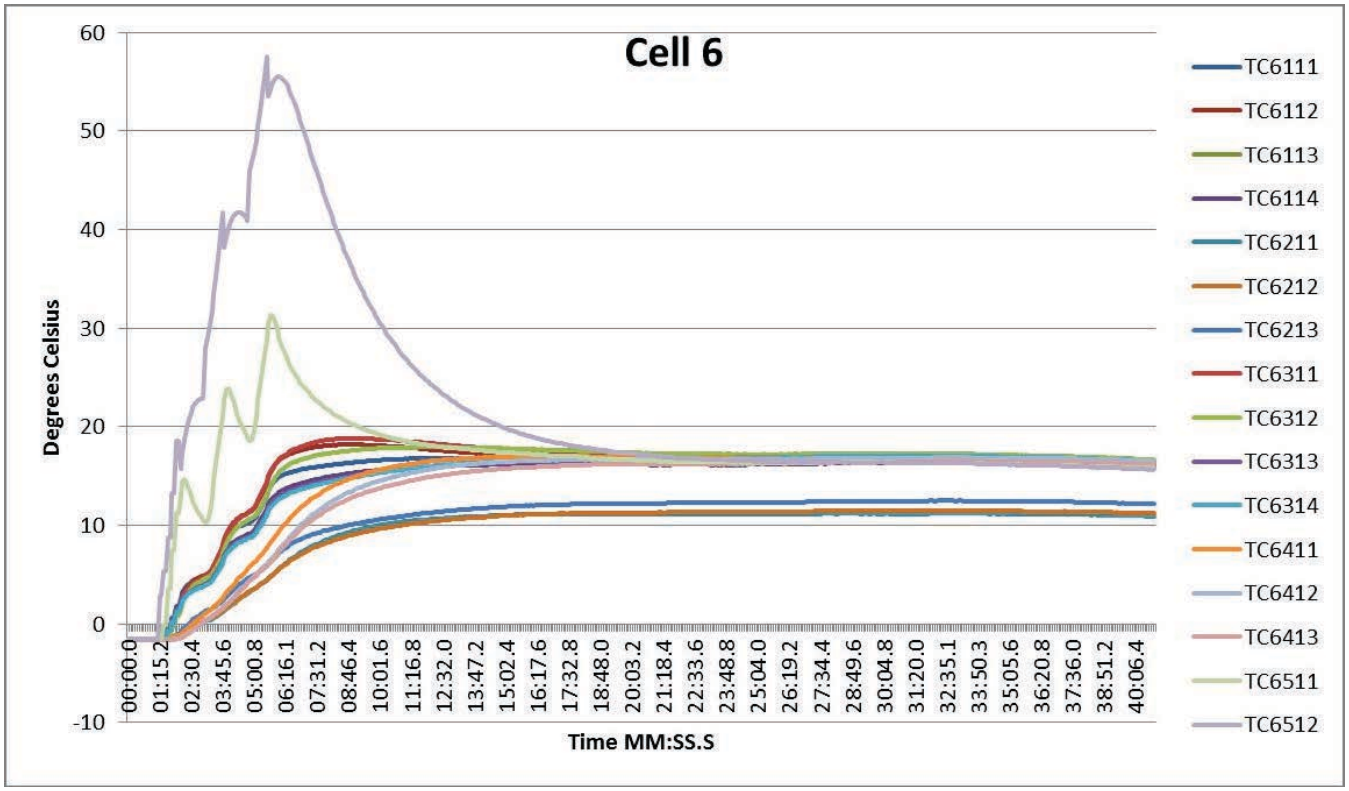

Figure B.94: Task A.1.B, 0 °C, 4 of 5, Cell 6 Temperatures

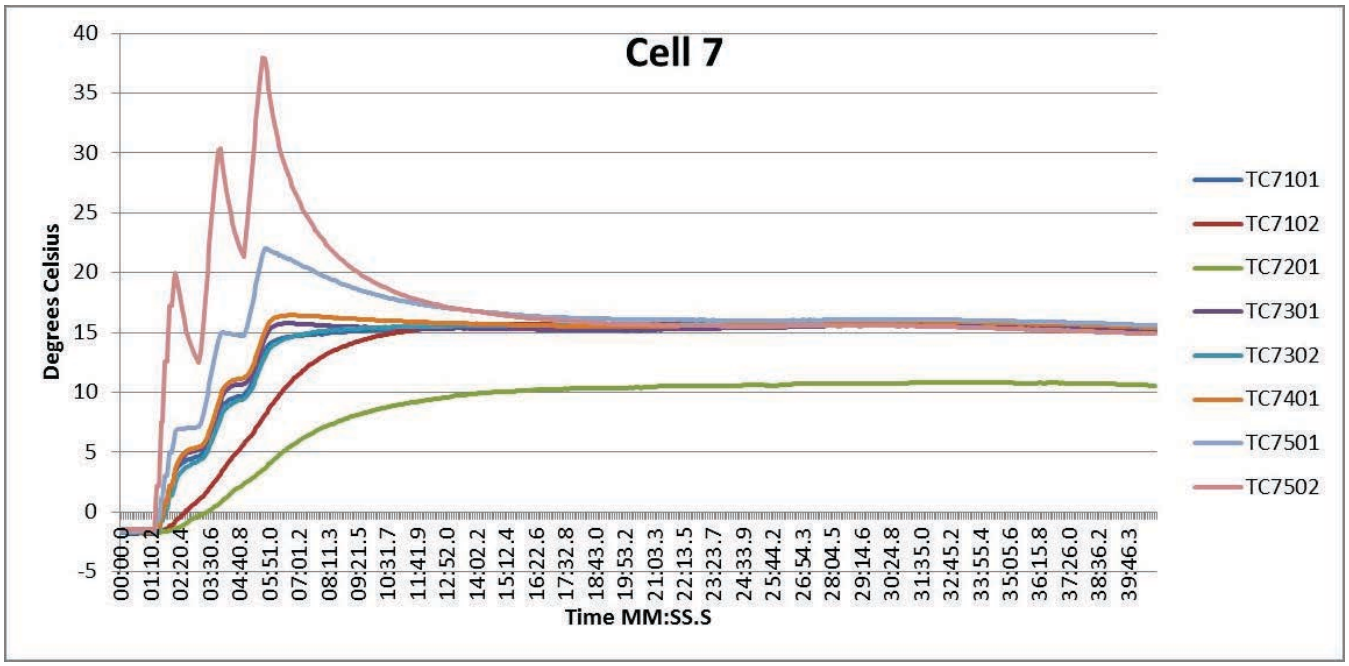

Figure B.95: Task A.1.B, 0 °C, 4 of 5, Cell 7 Temperatures

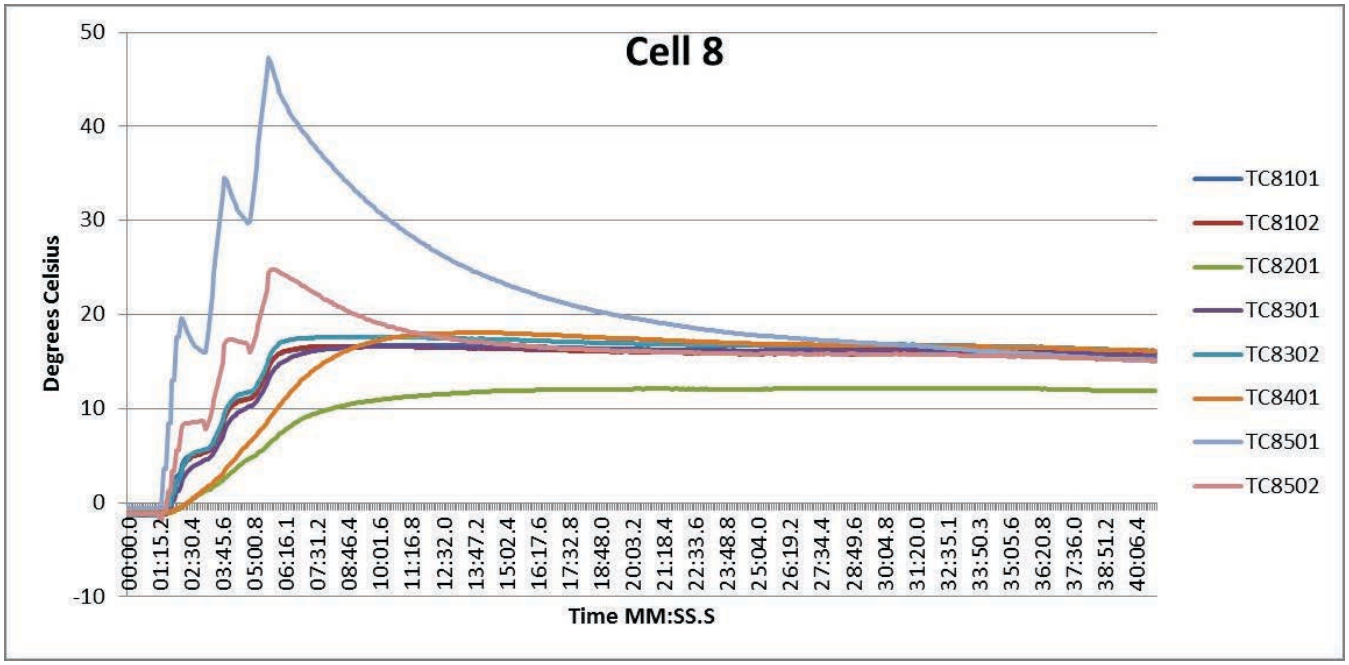

Figure B.96: Task A.1.B, 0 °C, 4 of 5, Cell 8 Temperatures

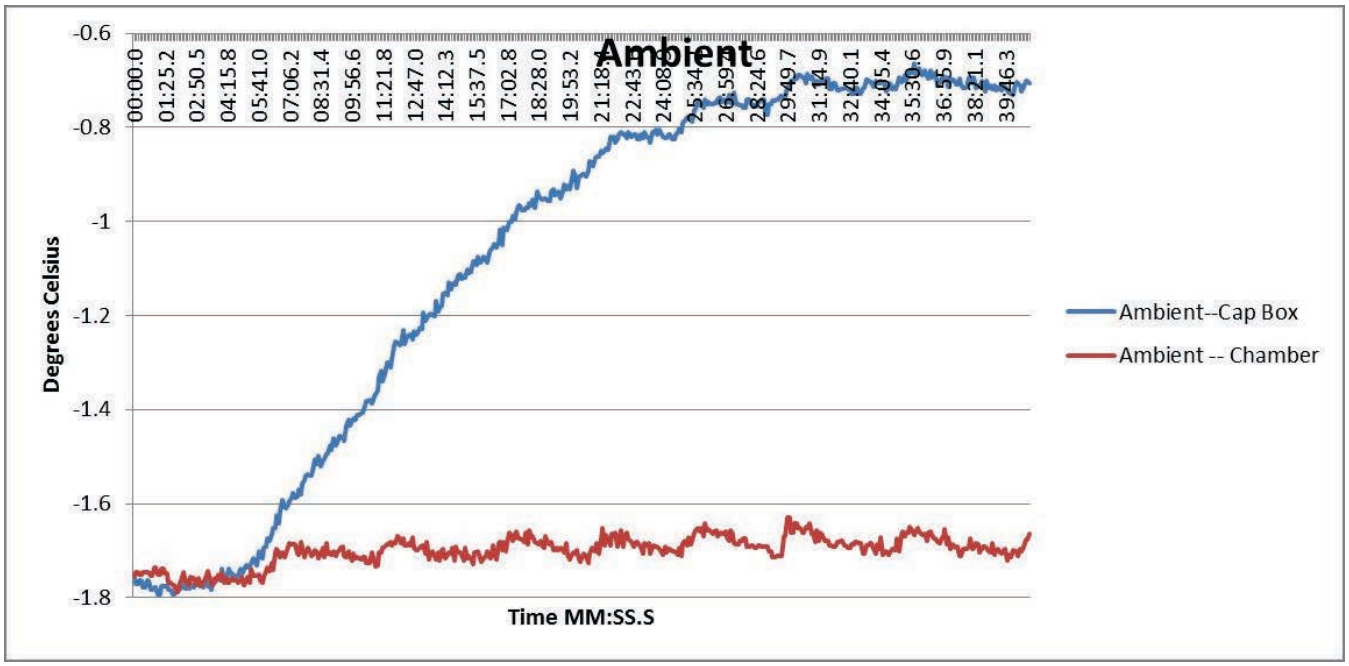

Figure B.97: Task A.1.B, 0 °C, 4 of 5, Ambient Temperatures

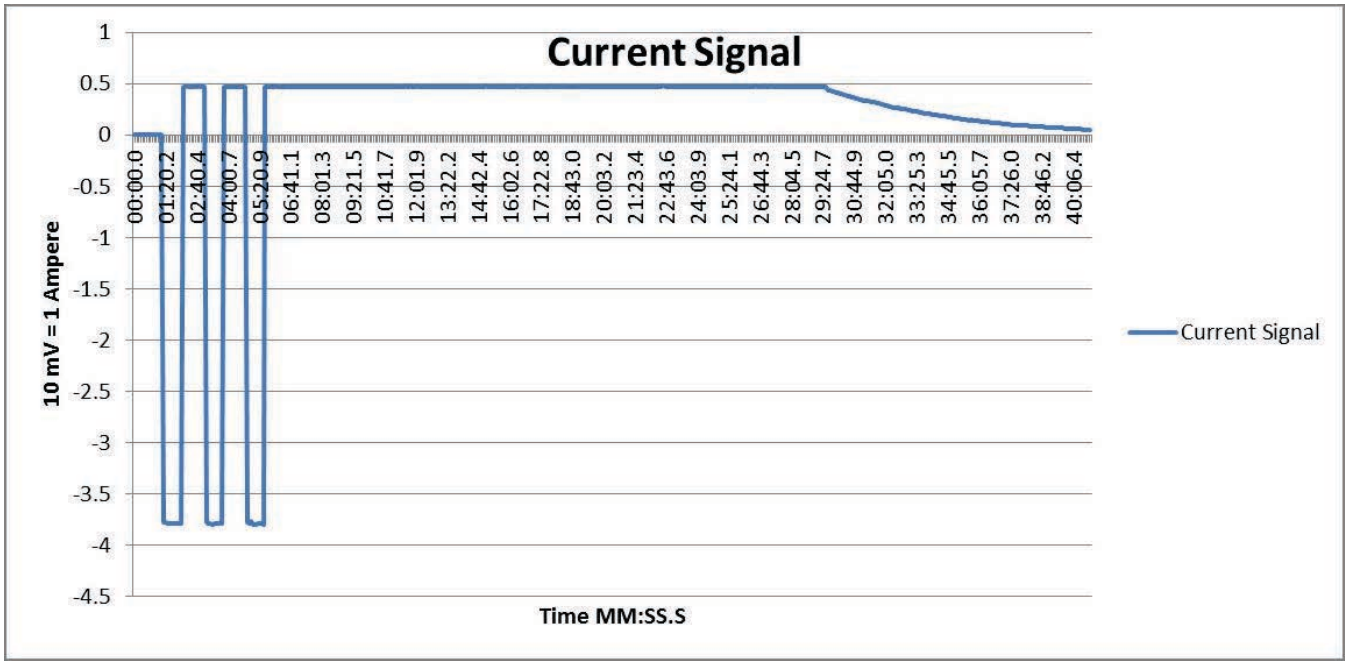

Figure B.98: Task A.1.B, 0 °C, 4 of 5, Current Signal from BMU HECS

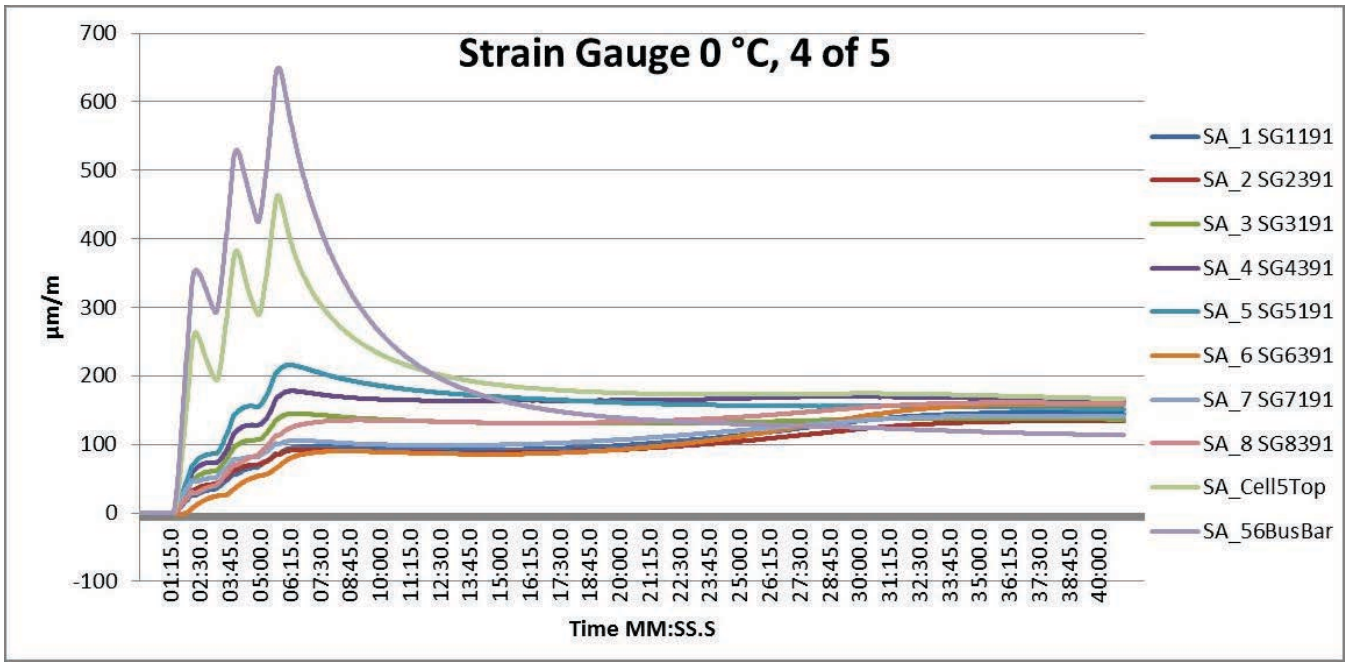

Figure B.99: Task A.1.B, 0 °C, 4 of 5, Strain Gauges

Task A.1.B – 0 °C, 5 of 5

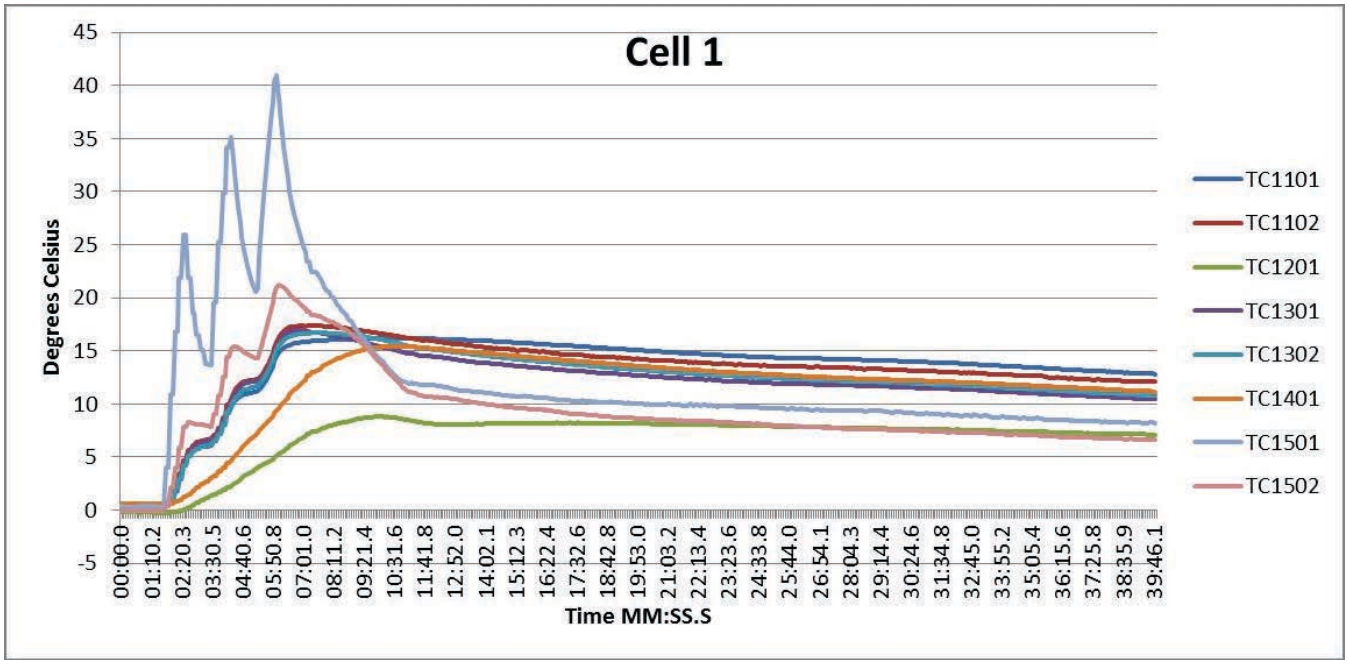

Figure B.100: Task A.1.B, 0 °C, 5 of 5, Cell 1 Temperatures

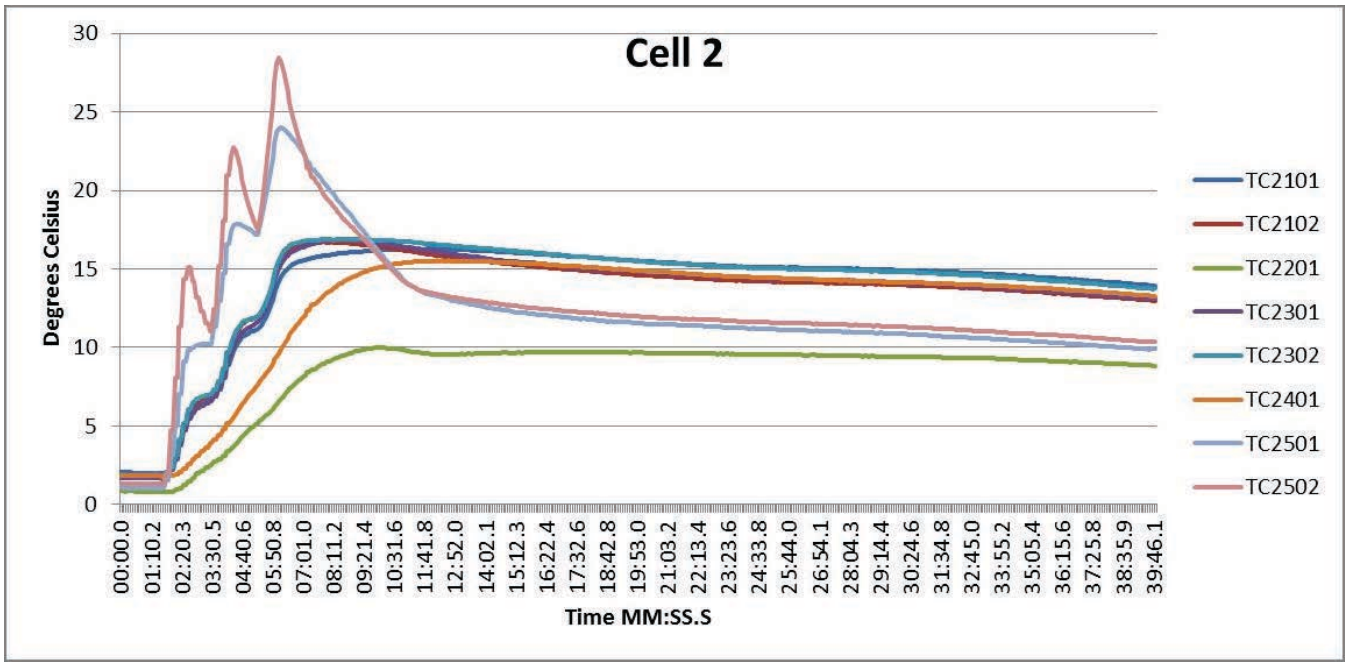

Figure B.101: Task A.1.B, 0 °C, 5 of 5, Cell 2 Temperatures

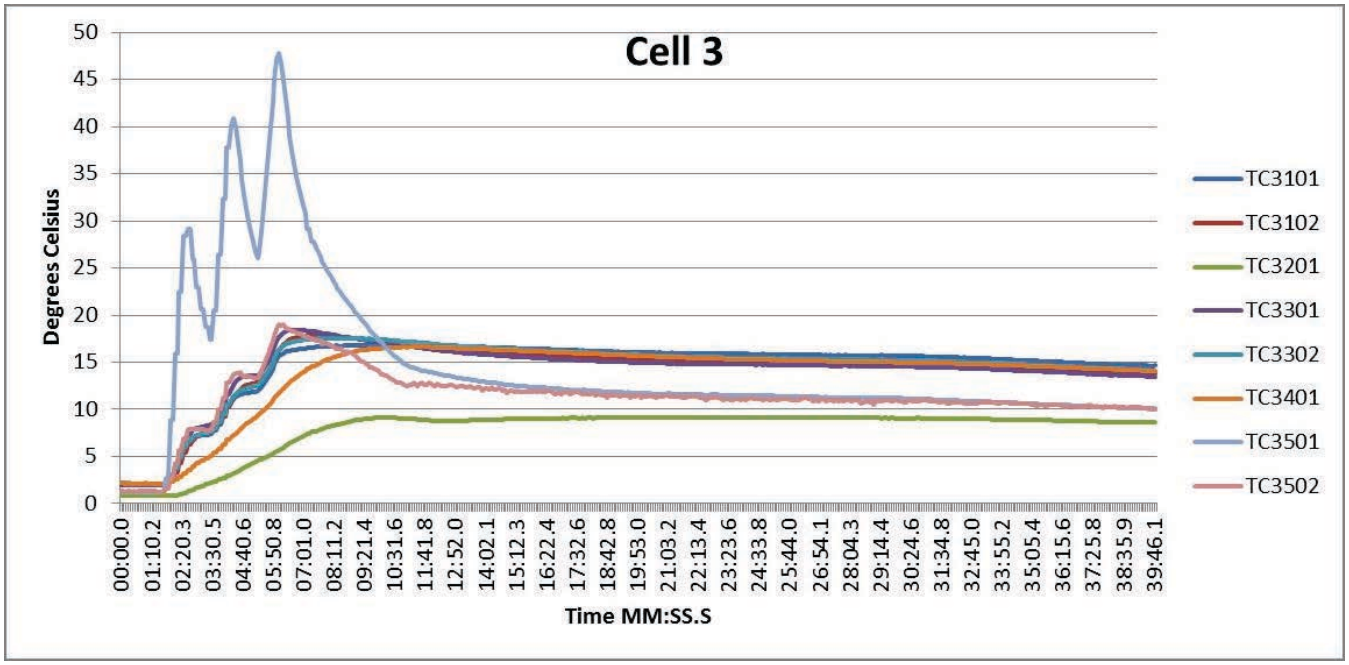

Figure B.102: Task A.1.B, 0 °C, 5 of 5, Cell 3 Temperatures

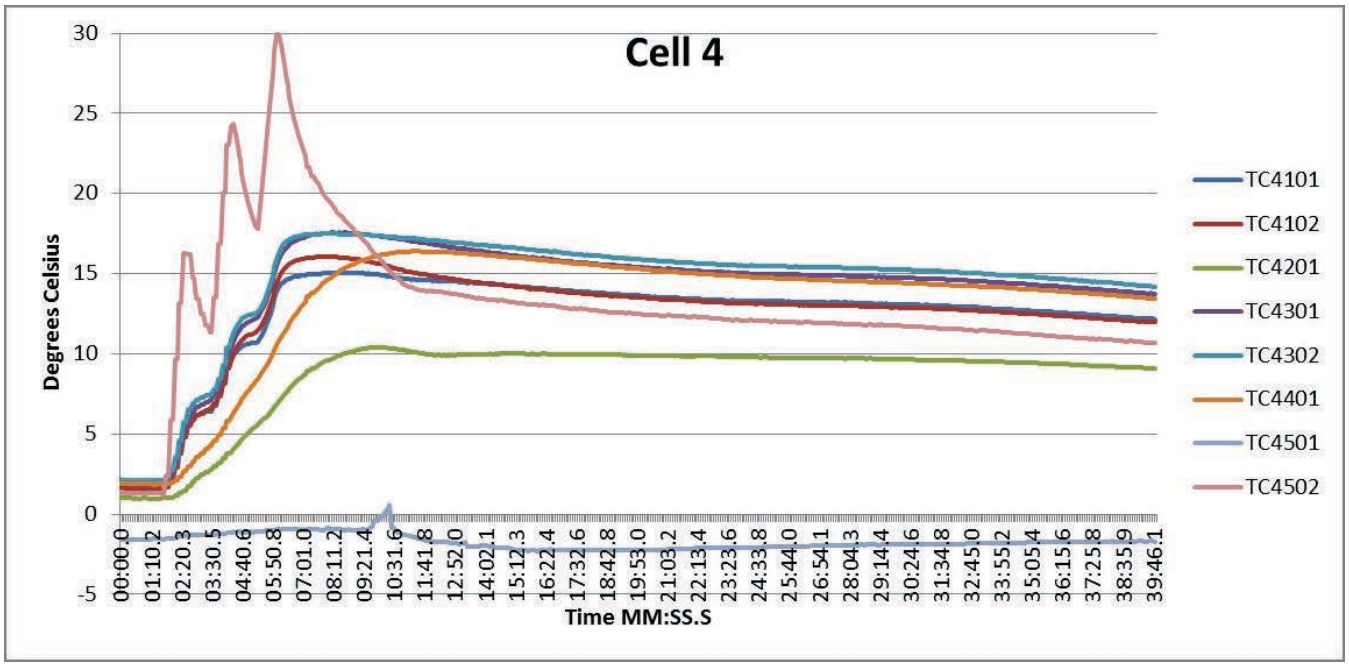

Figure B.103: Task A.1.B, 0 °C, 5 of 5, Cell 4 Temperatures

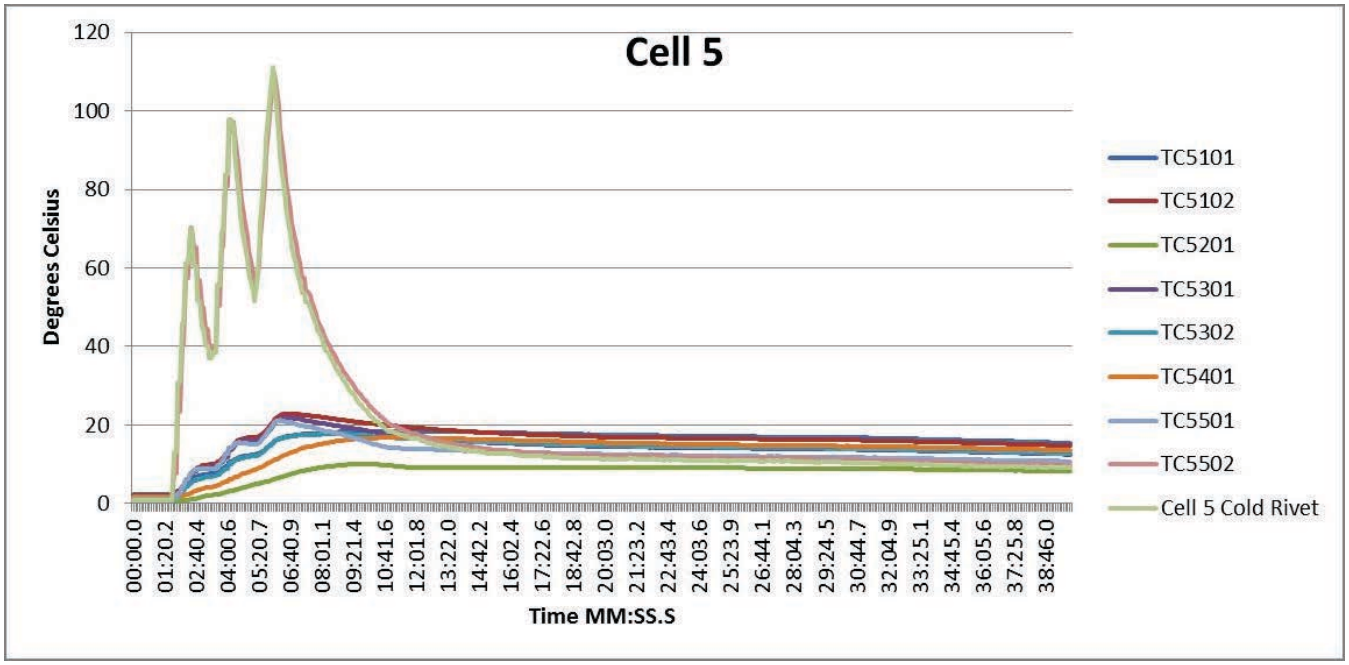

Figure B.104: Task A.1.B, 0 °C, 5 of 5, Cell 5 Temperatures

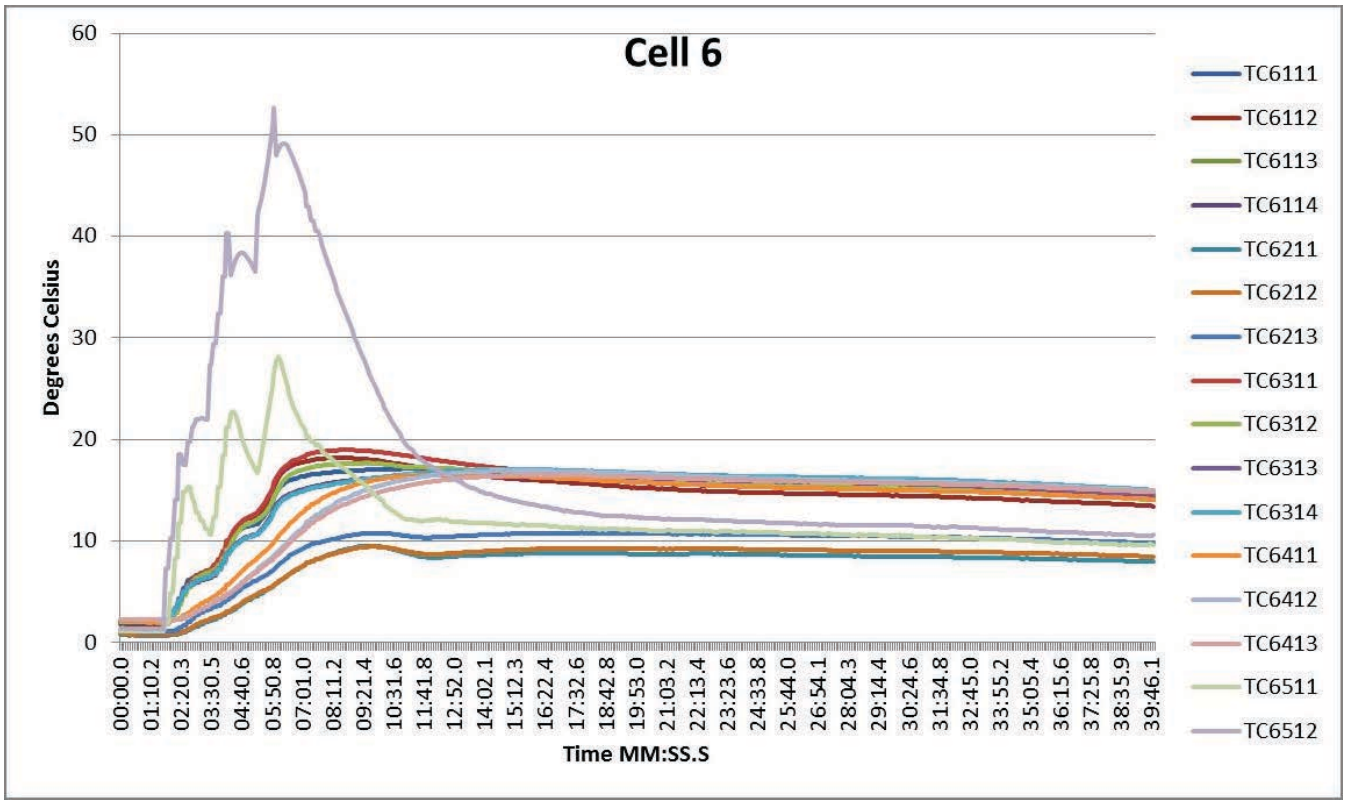

Figure B.105: Task A.1.B, 0 °C, 5 of 5, Cell 6 Temperatures

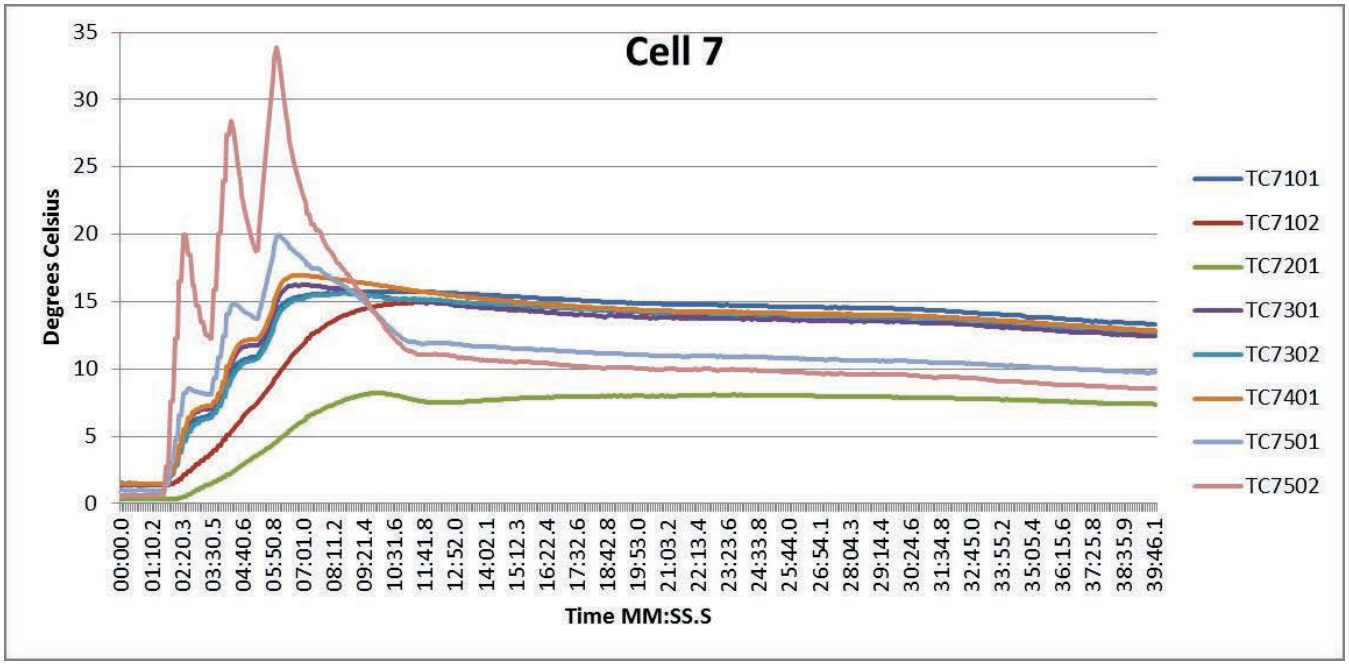

Figure B.106: Task A.1.B, 0 °C, 5 of 5, Cell 7 Temperatures

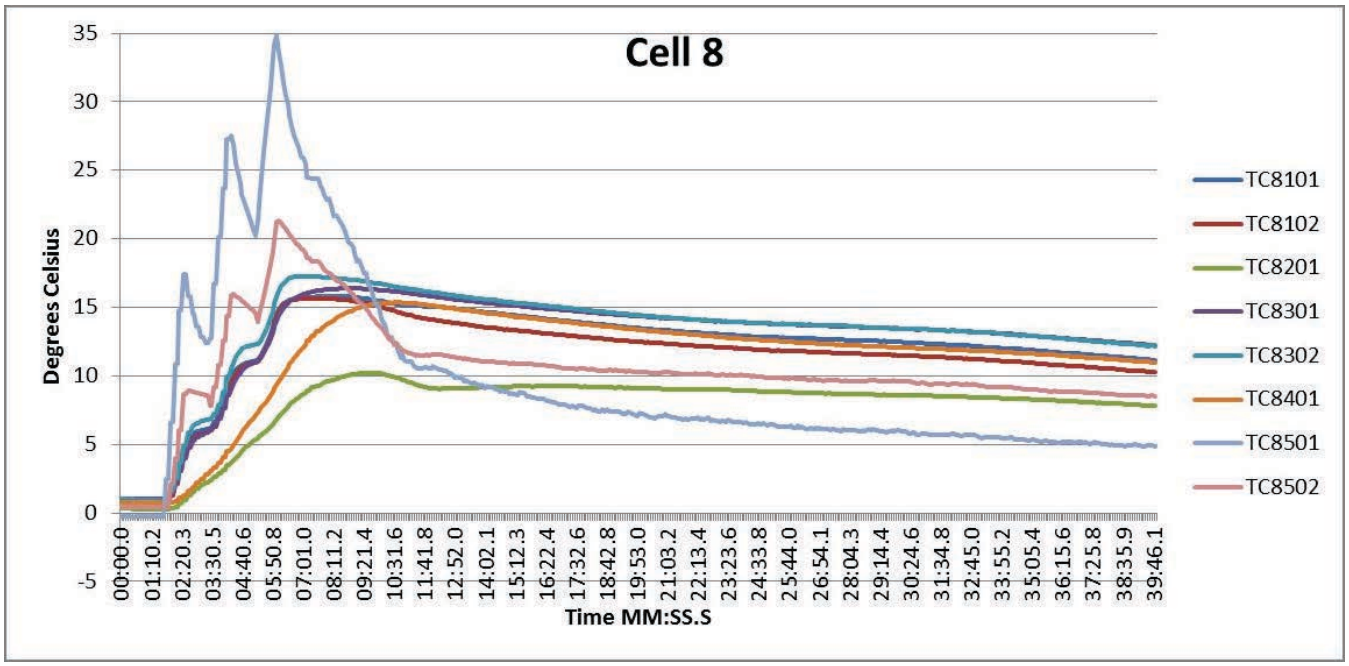

Figure B.107: Task A.1.B, 0 °C, 5 of 5, Cell 8 Temperatures

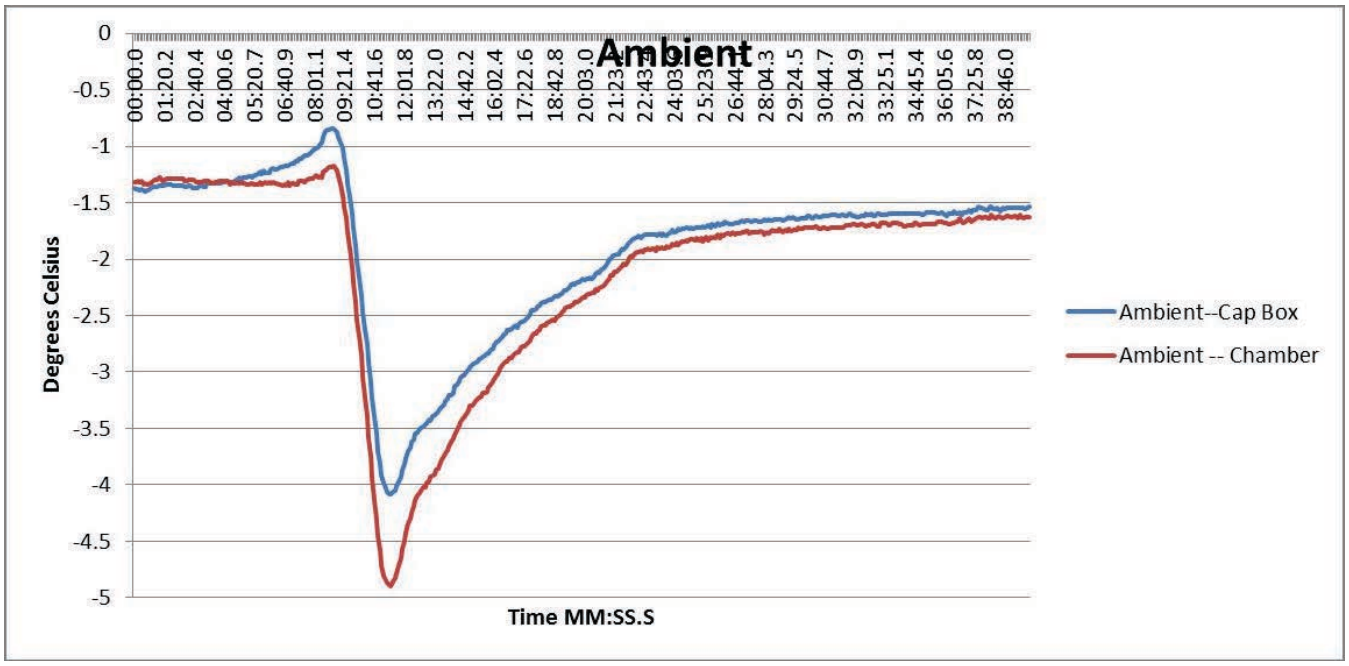

Figure B.108: Task A.1.B, 0 °C, 5 of 5, Ambient Temperatures

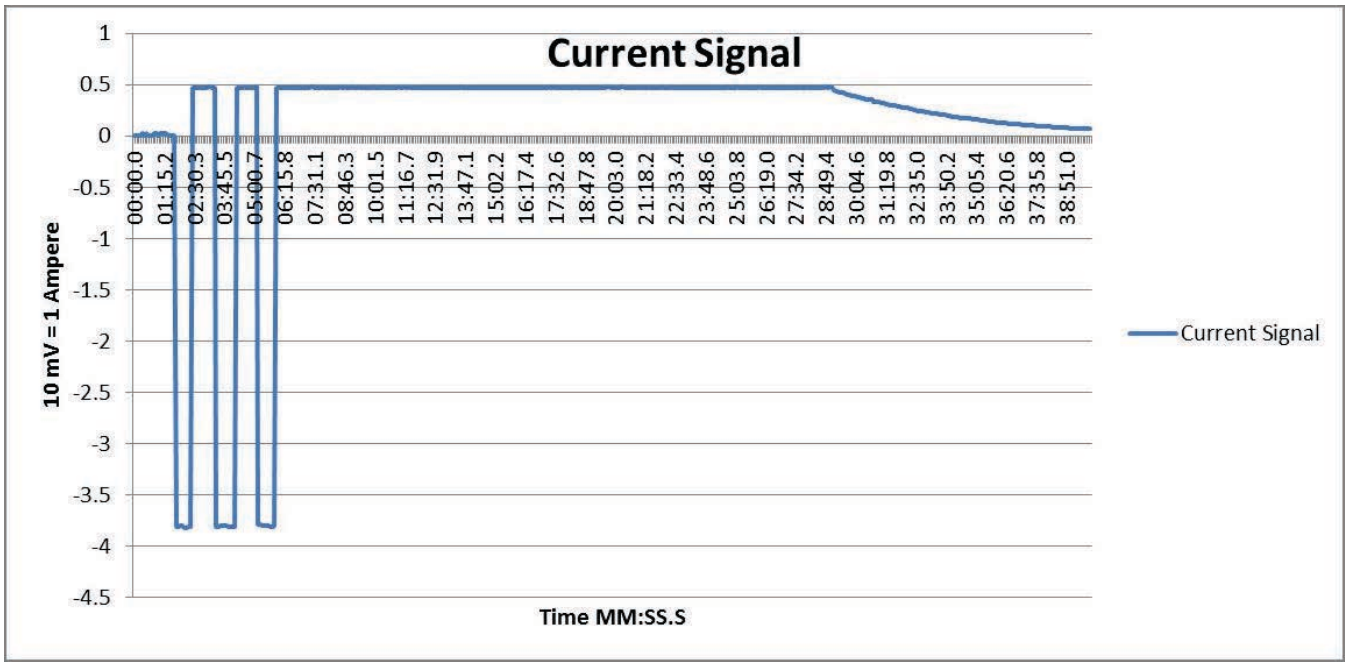

Figure B.109: Task A.1.B, 0 °C, 5 of 5, Current Signal from BMU HECS

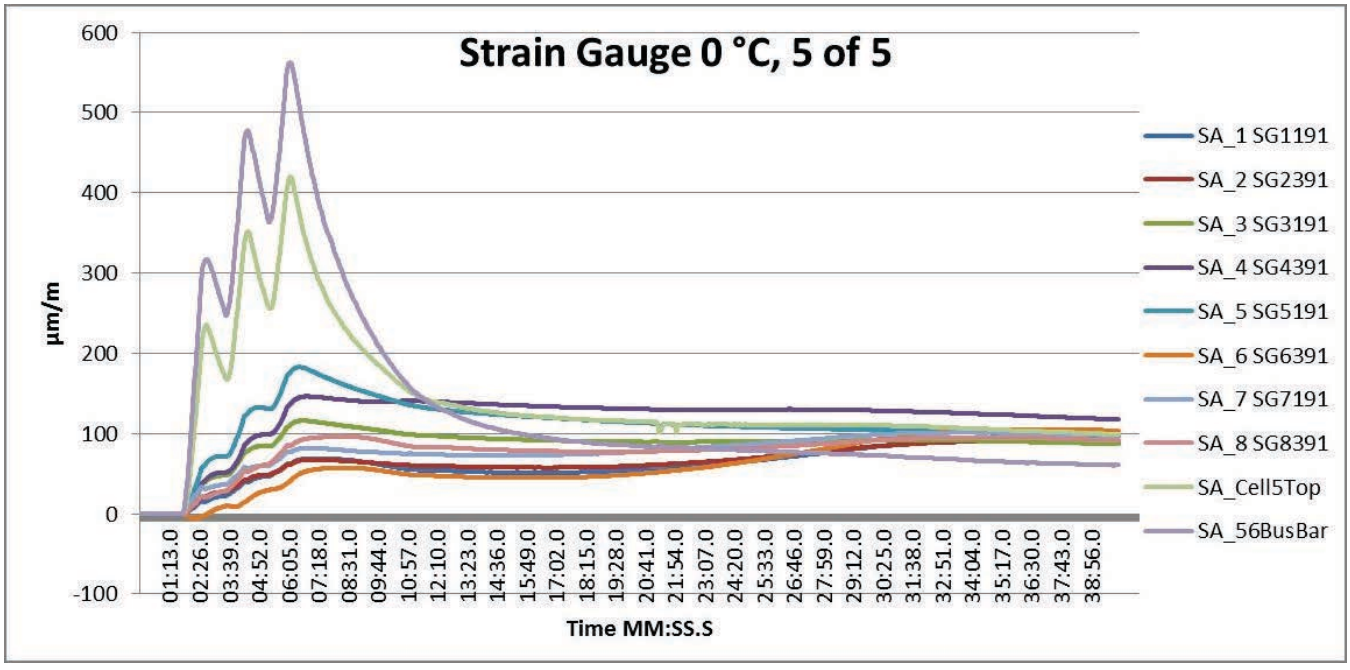

Figure B.110: Task A.1.B, 0 °C, 5 of 5, Strain Gauges

Task A.1.B – -18 °C, 1 of 5

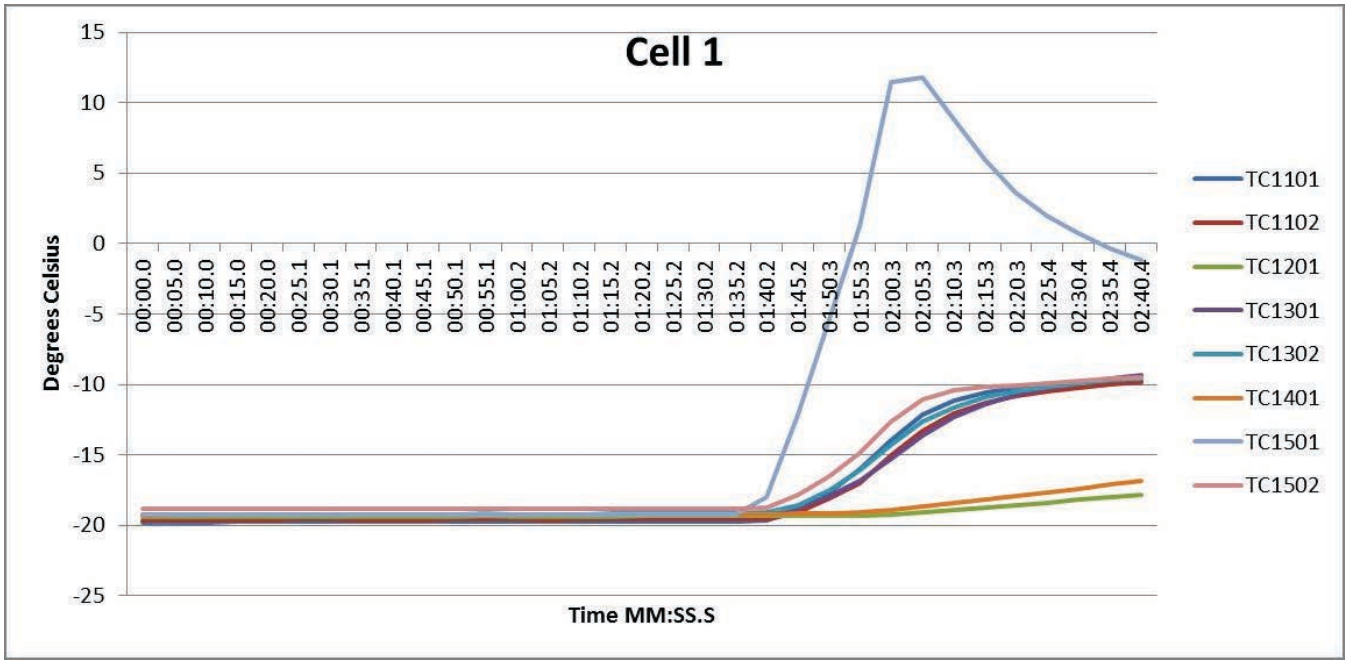

Figure B.111: Task A.1.B, -18 °C, 1 of 5, Cell 1 Temperatures

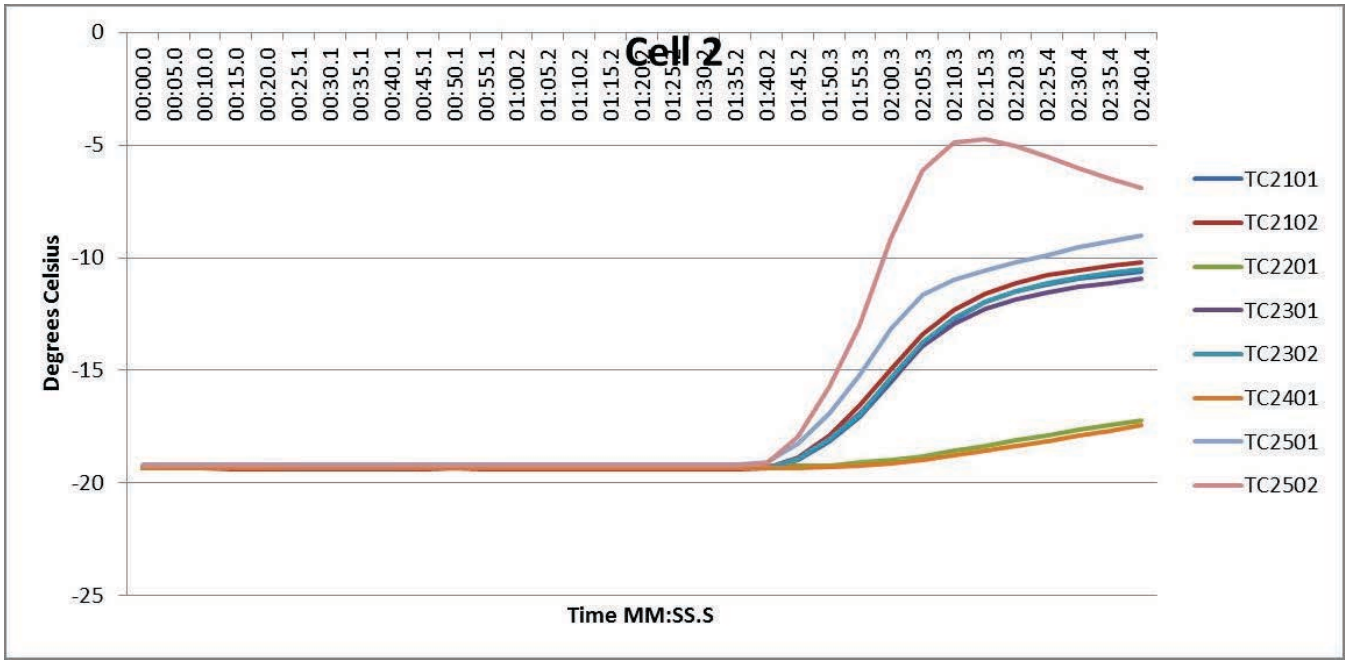

Figure B.112: Task A.1.B, -18 °C, 1 of 5, Cell 2 Temperatures

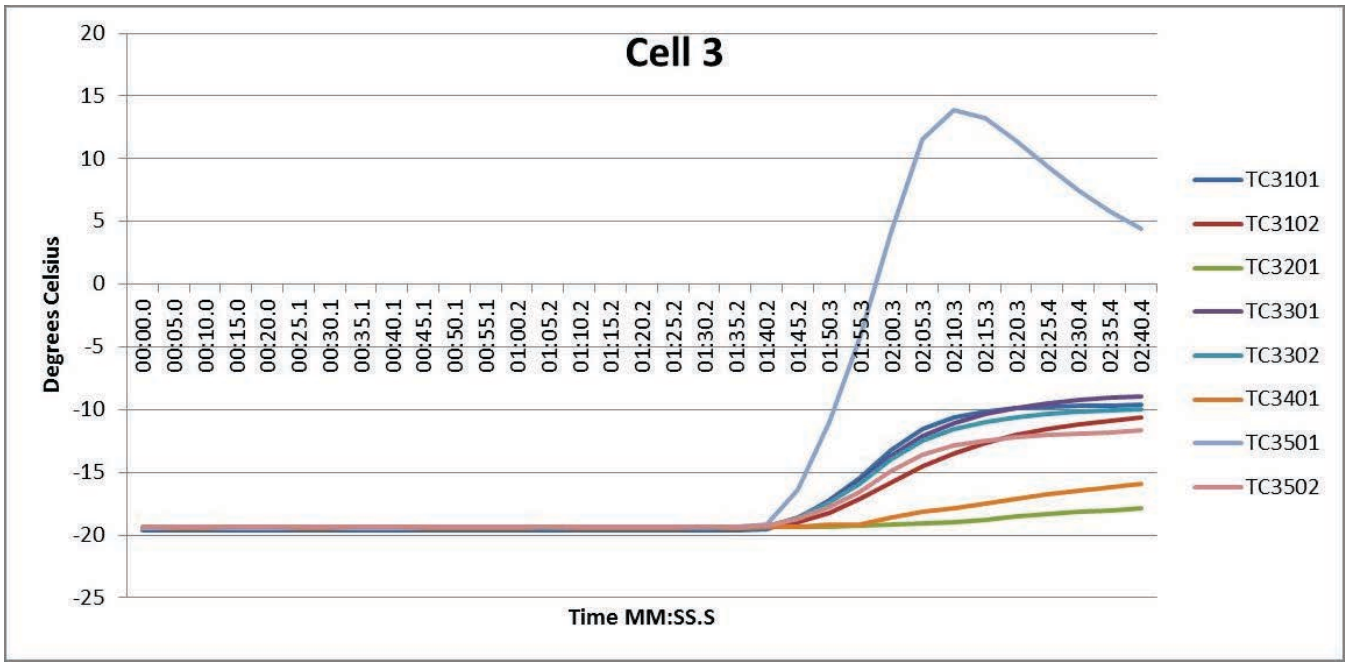

Figure B.113: Task A.1.B, -18 °C, 1 of 5, Cell 3 Temperatures

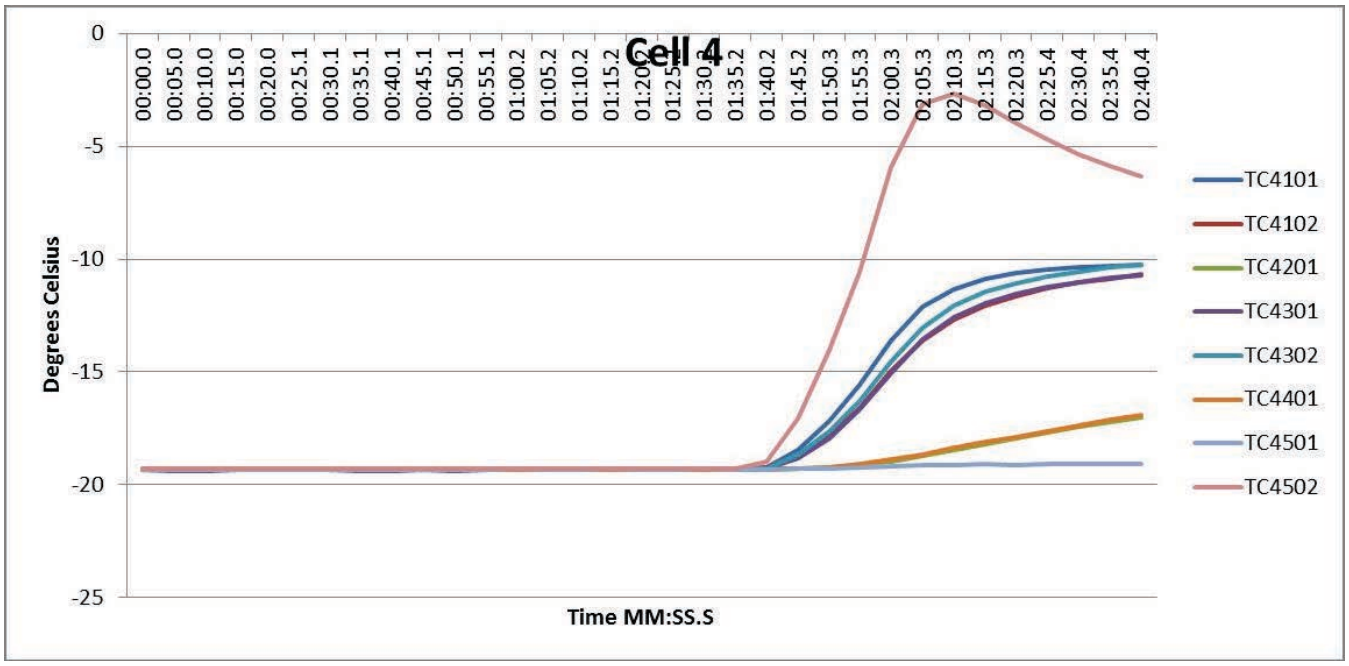

Figure B.114: Task A.1.B, -18 °C, 1 of 5, Cell 4 Temperatures

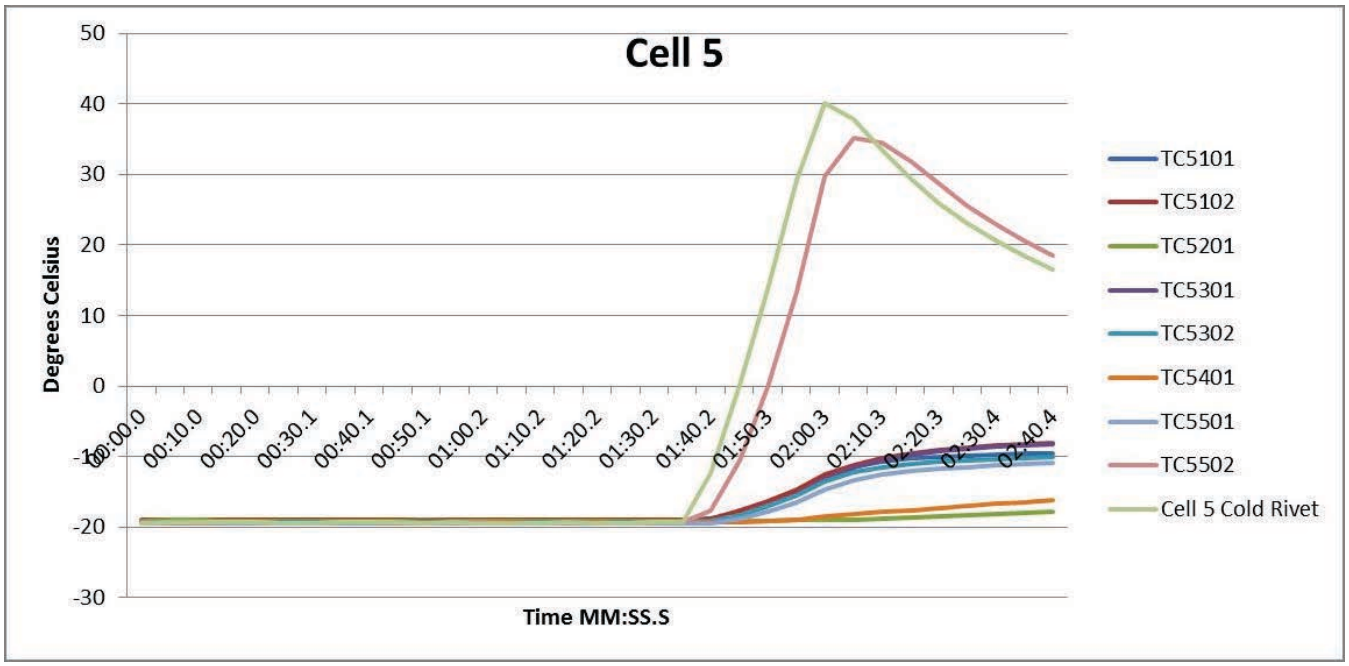

Figure B.115: Task A.1.B, -18 °C, 1 of 5, Cell 5 Temperatures

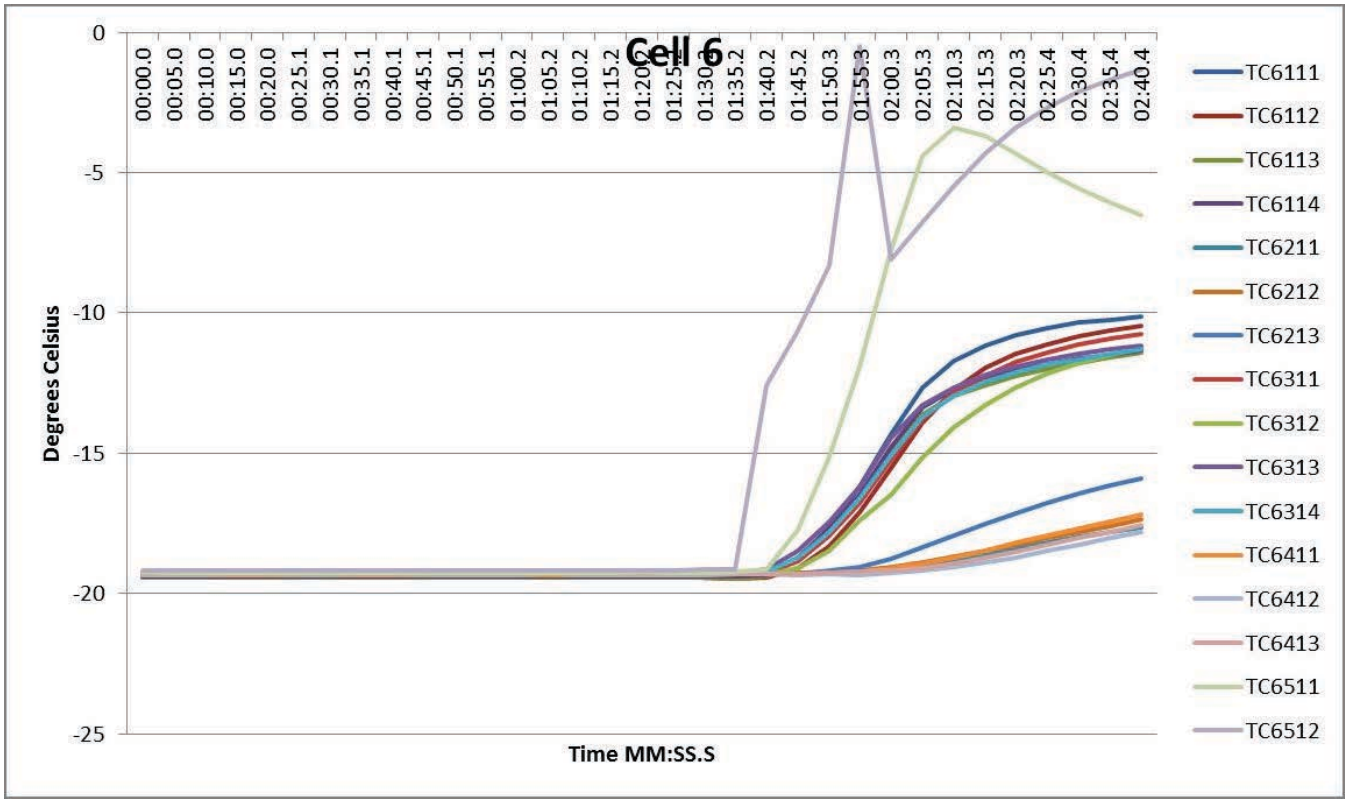

Figure B.116: Task A.1.B, -18 °C, 1 of 5, Cell 6 Temperatures

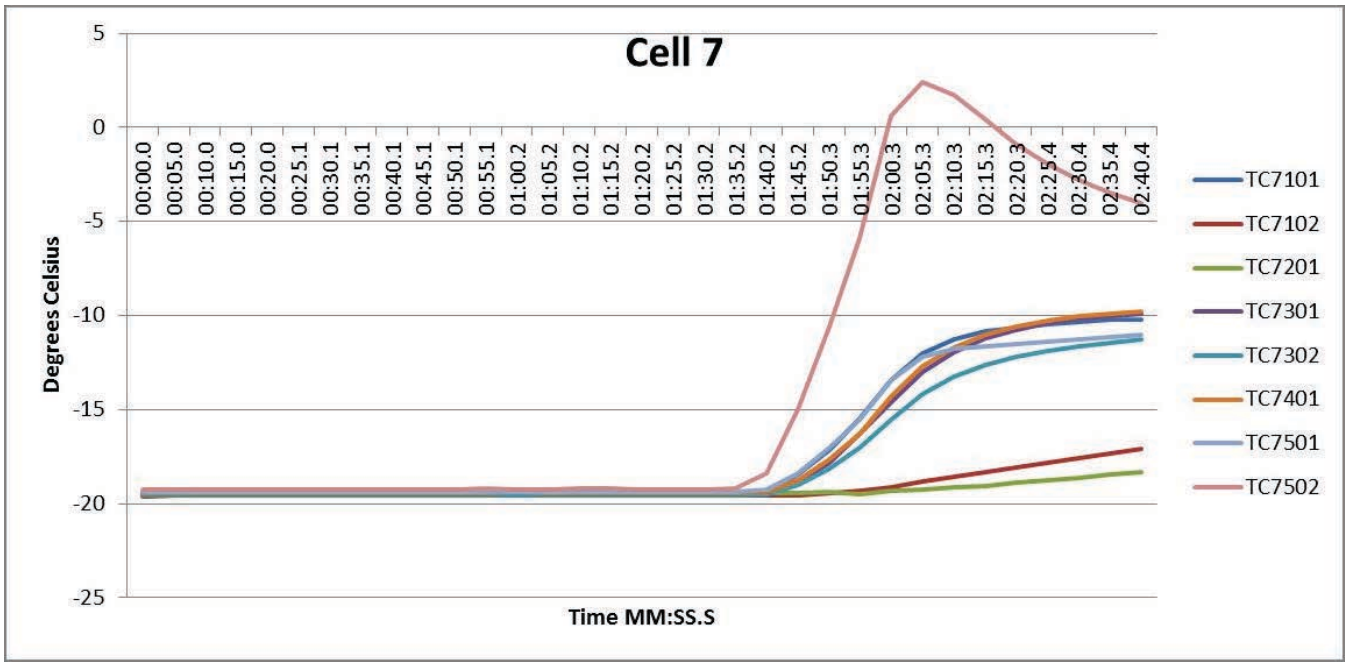

Figure B.117: Task A.1.B, -18 °C, 1 of 5, Cell 7 Temperatures

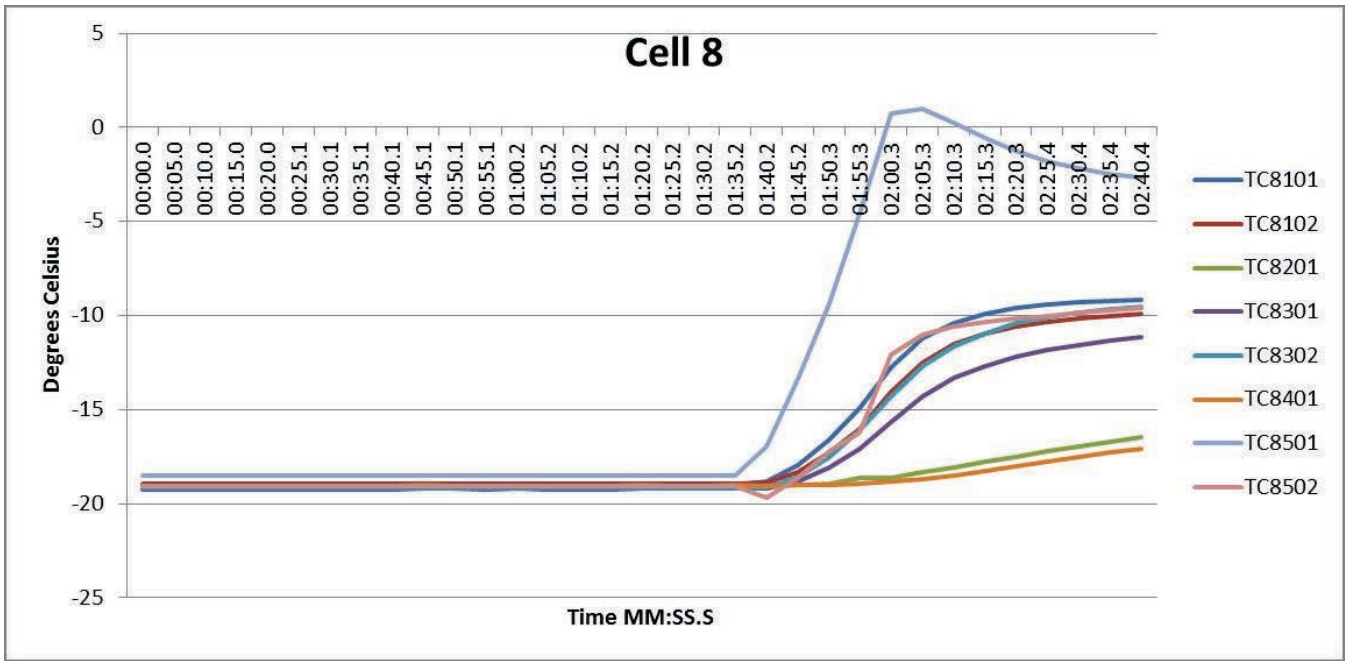

Figure B.118: Task A.1.B, -18 °C, 1 of 5, Cell 8 Temperatures

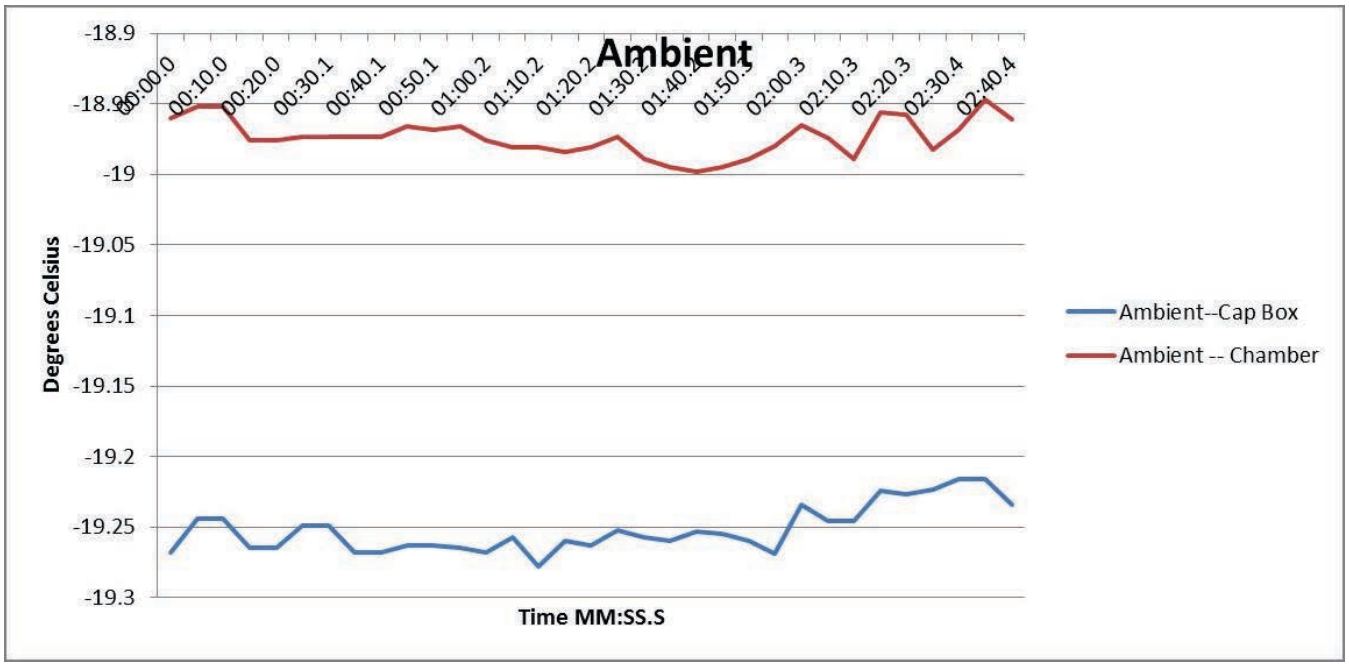

Figure B.119: Task A.1.B, -18 °C, 1 of 5, Ambient Temperatures

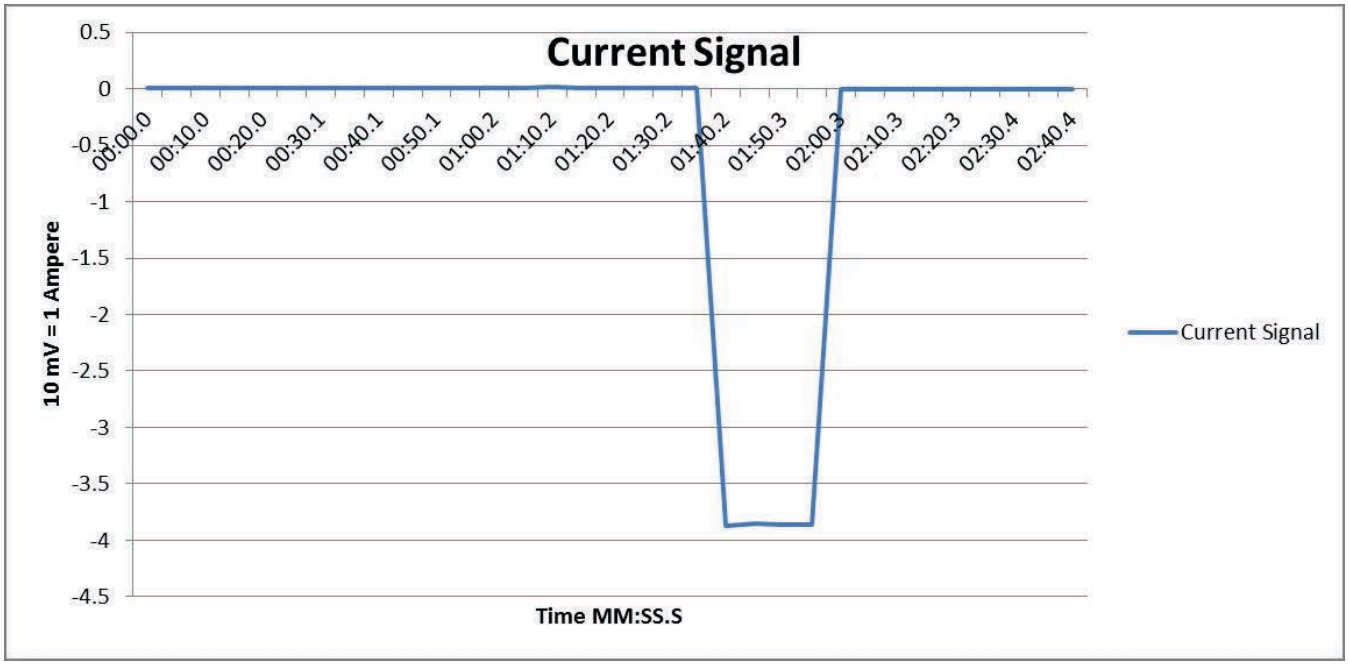

Figure B.120: Task A.1.B, -18 °C, 1 of 5, Current Signal from BMU HECS

Task A.1.C – Clean, 8-Hour

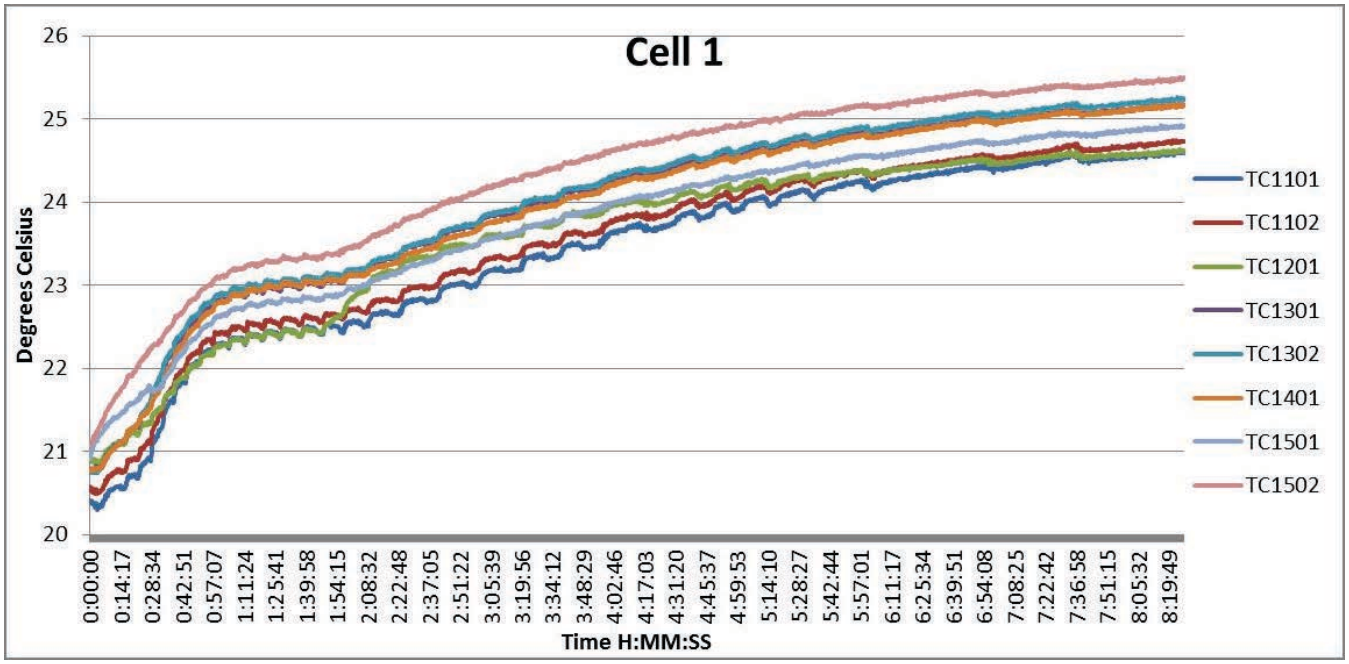

Figure B.121: Task A.1.C, Clean, 8-Hour, Cell 1 Temperatures

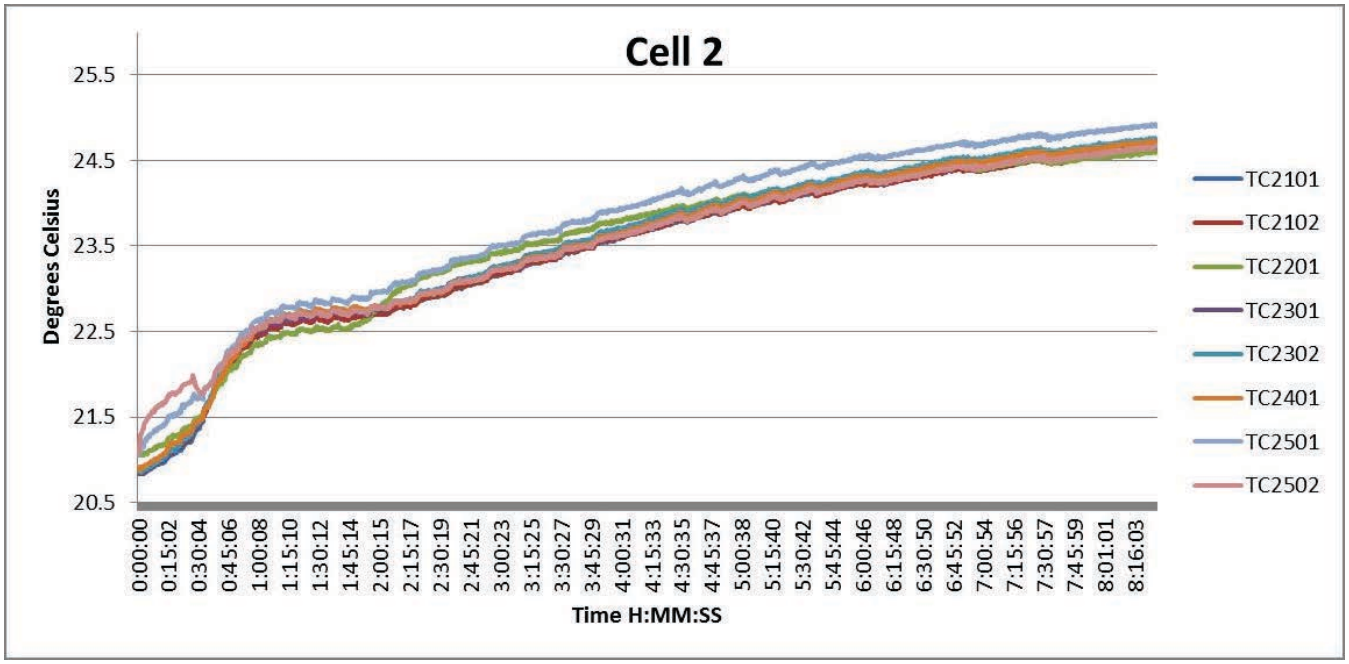

Figure B.122: Task A.1.C, Clean, 8-Hour, Cell 2 Temperatures

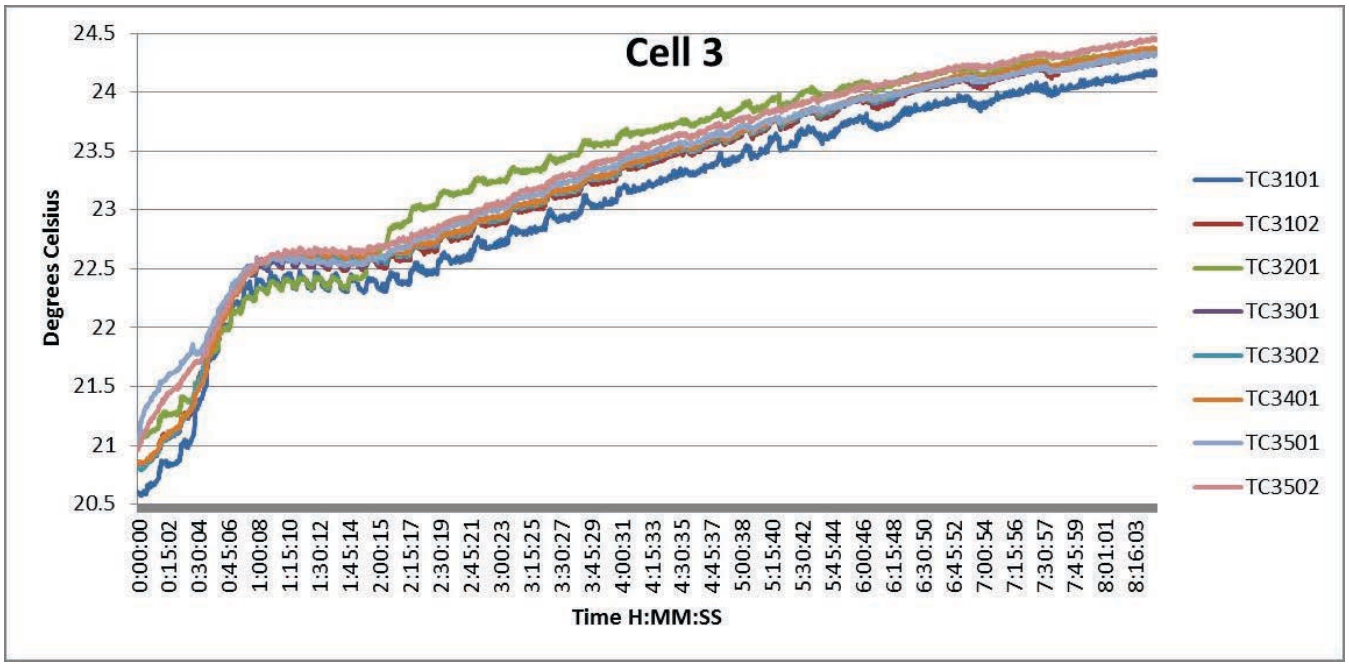

Figure B.123: Task A.1.C, Clean, 8-Hour, Cell 3 Temperatures

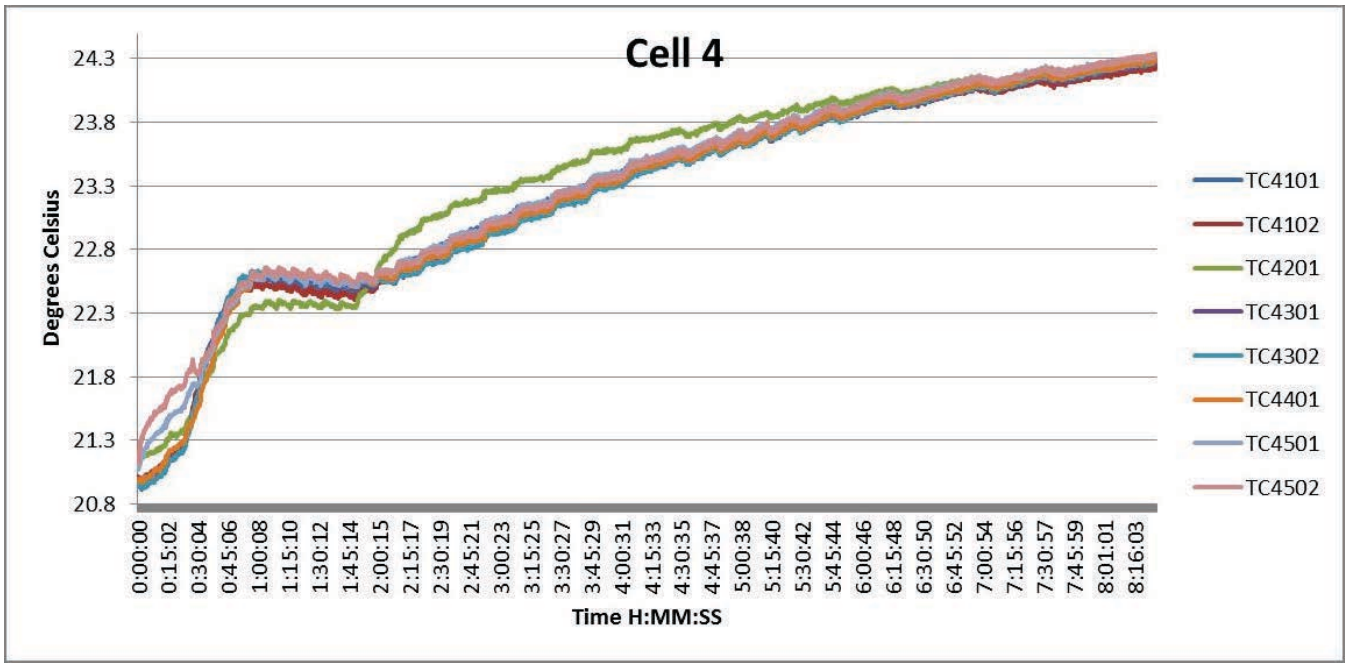

Figure B.124: Task A.1.C, Clean, 8-Hour, Cell 4 Temperatures

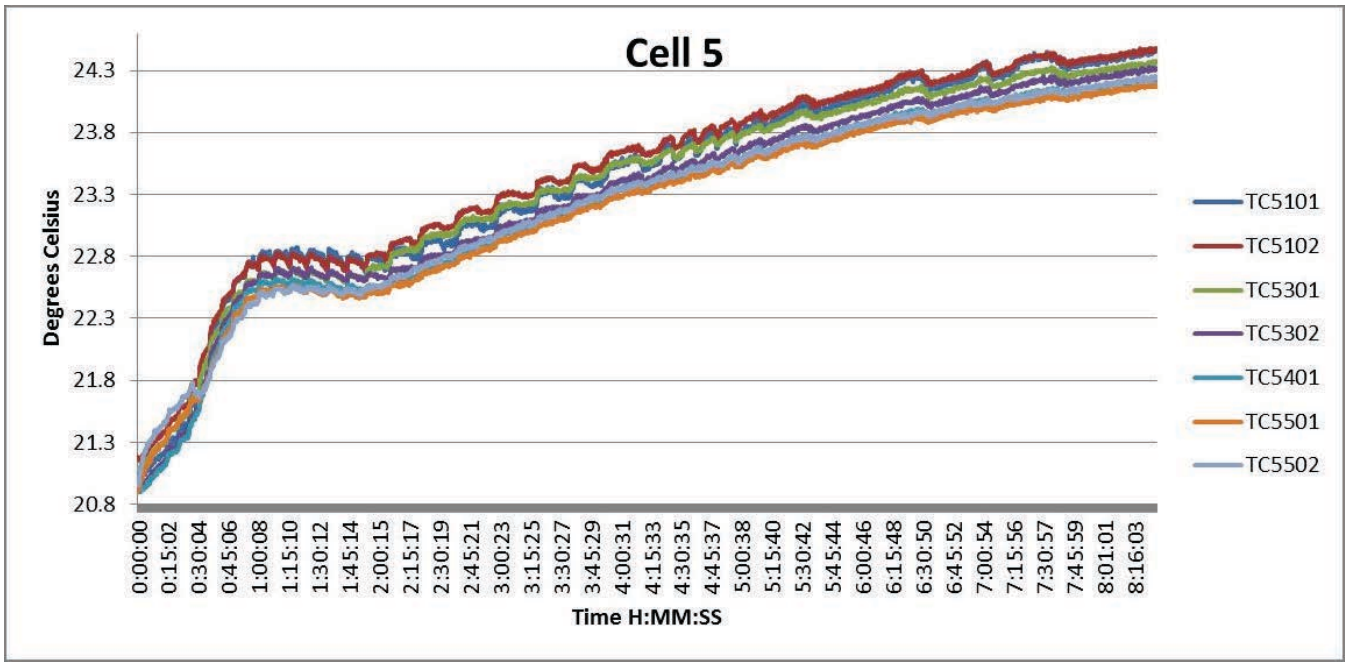

Figure B.125: Task A.1.C, Clean, 8-Hour, Cell 5 Temperatures

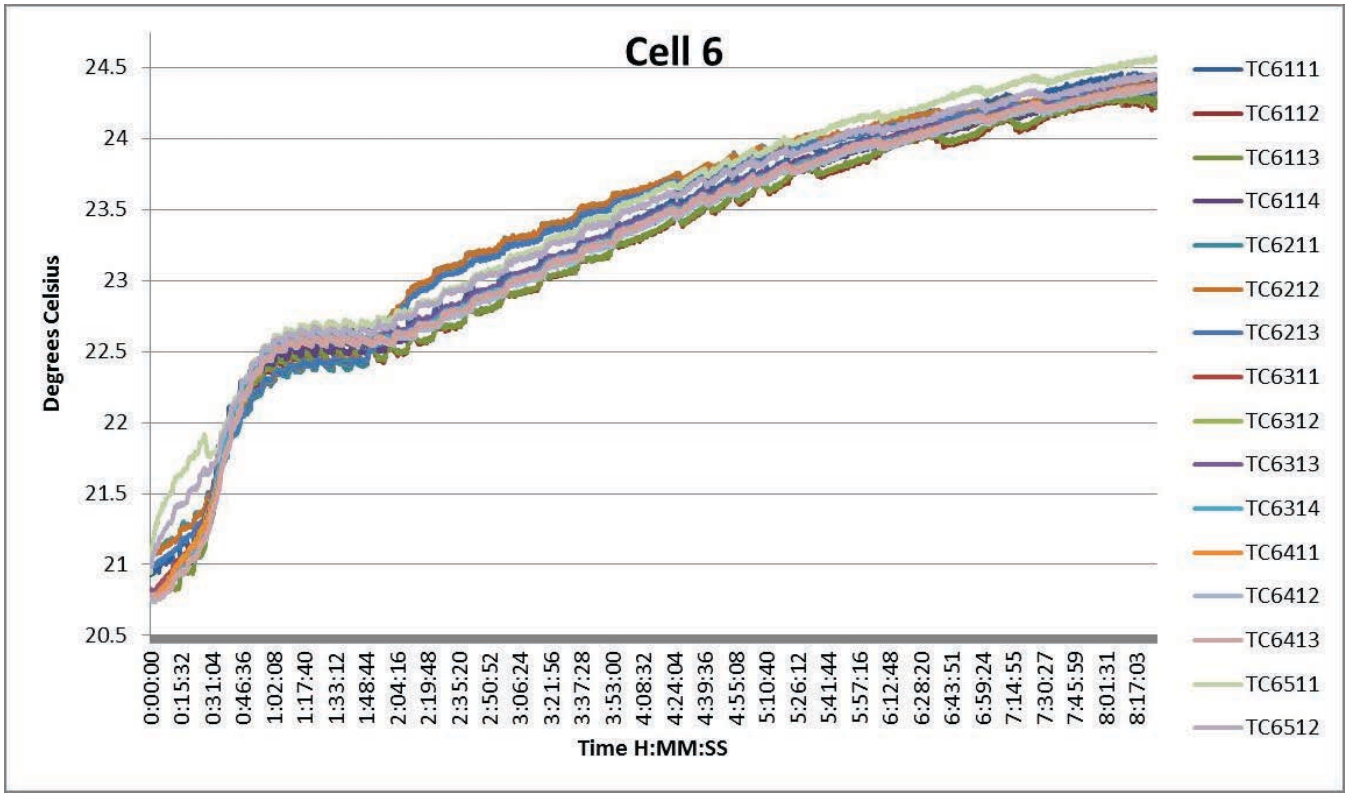

Figure B.126: Task A.1.C, Clean, 8-Hour, Cell 6 Temperatures

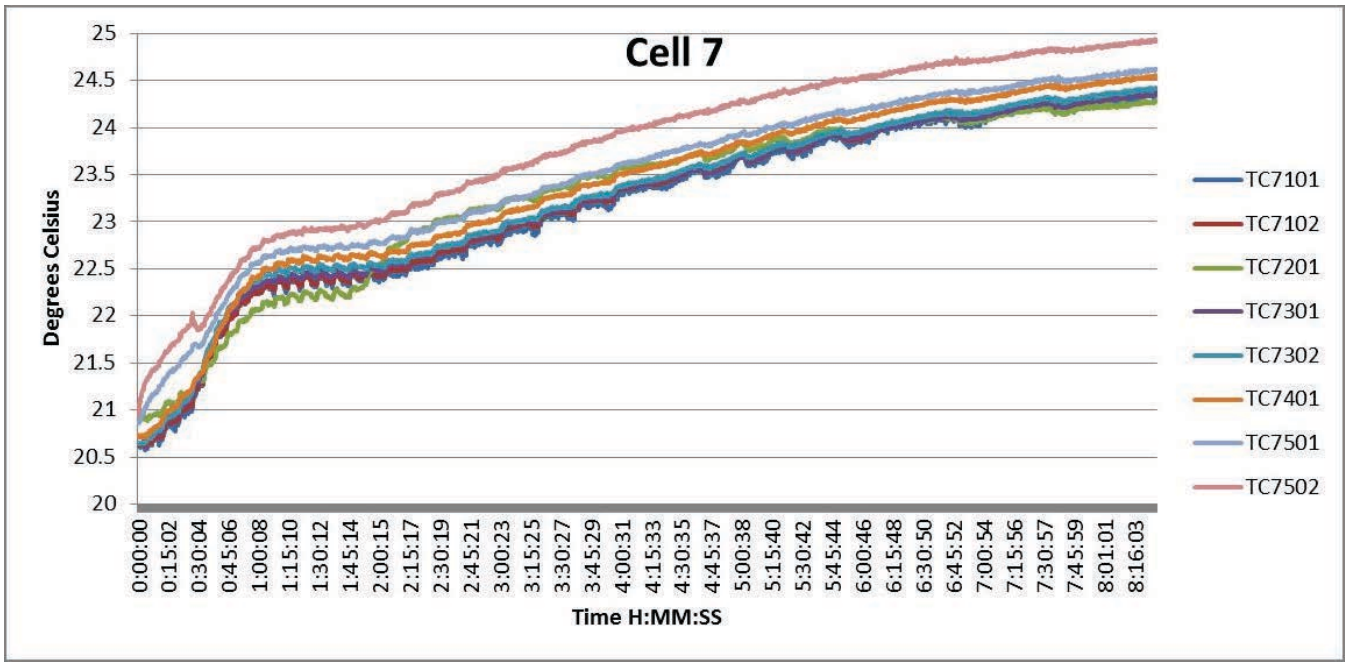

Figure B.127: Task A.1.C, Clean, 8-Hour, Cell 7 Temperatures

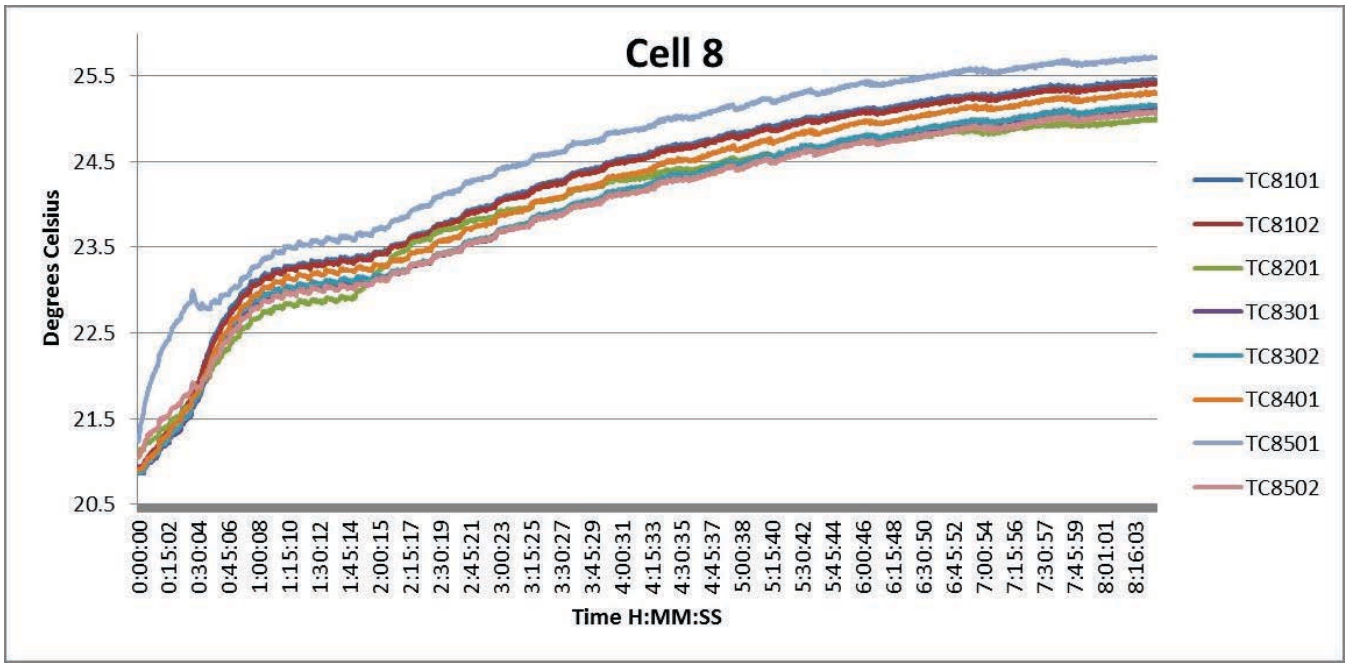

Figure B.128: Task A.1.C, Clean, 8-Hour, Cell 8 Temperatures

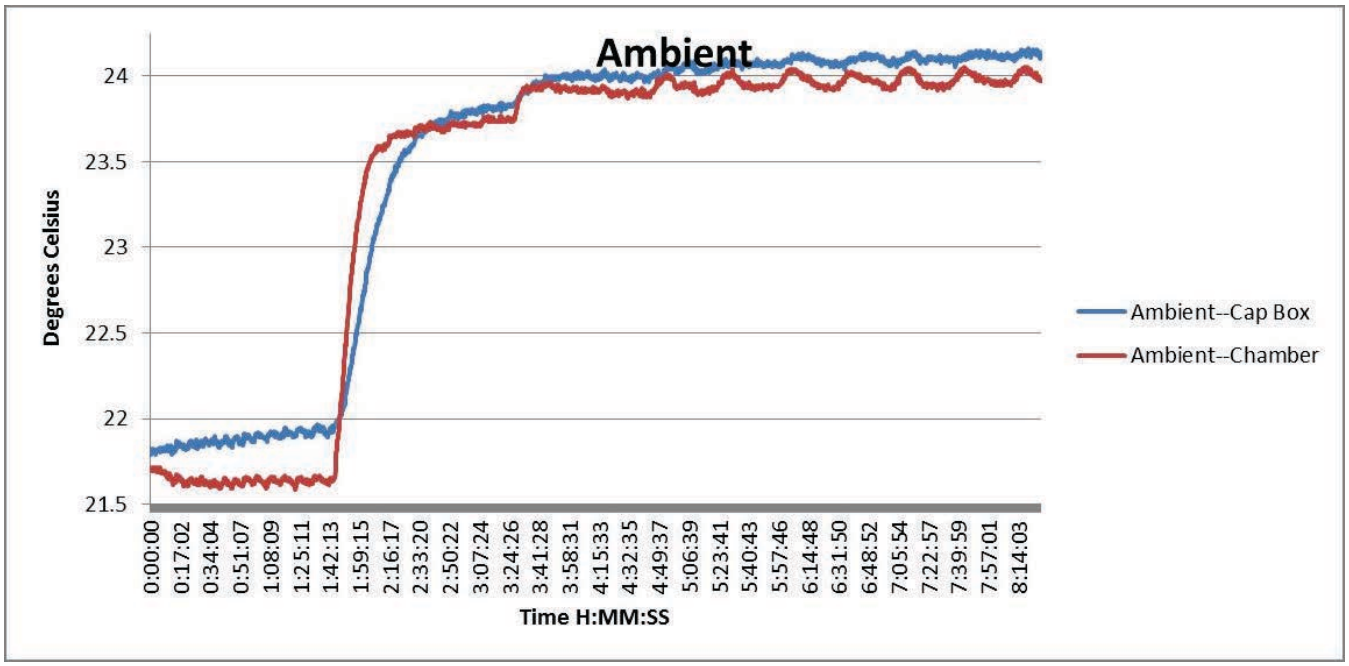

Figure B.129: Task A.1.C, Clean, 8-Hour, Ambient Temperatures

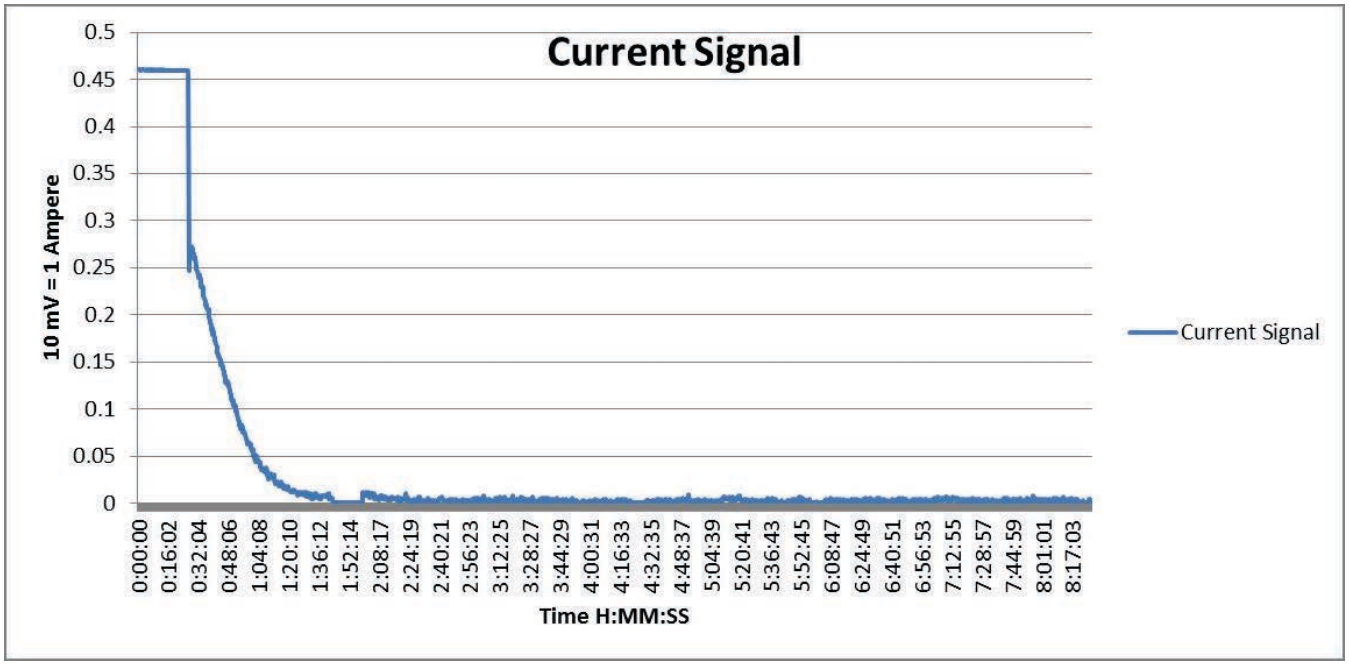

Figure B.130: Task A.1.C, Clean, 8-Hour, Current Signal from BMU HECS

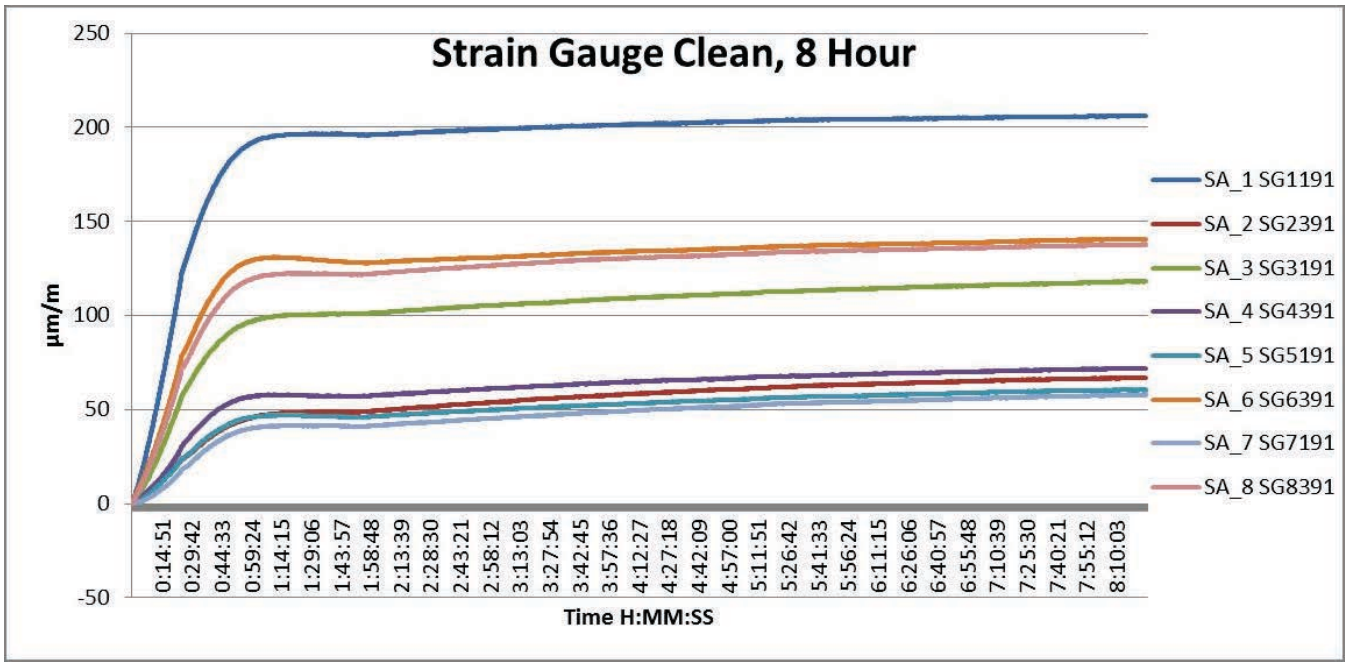

Figure B.131: Task A.1.C, Clean, 8-Hour, Strain Gauges

Task A.1.C – Clean, First 2-Hour

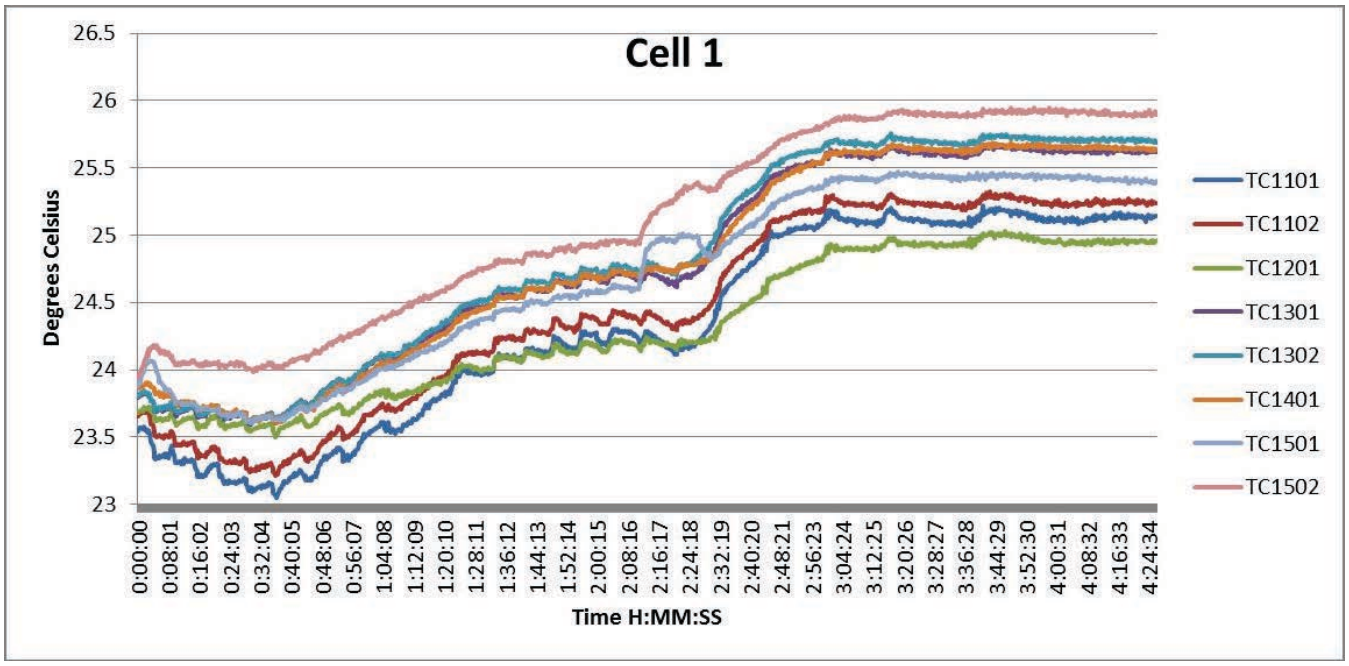

Figure B.132: Task A.1.C, Clean, First 2-Hour, Cell 1 Temperatures

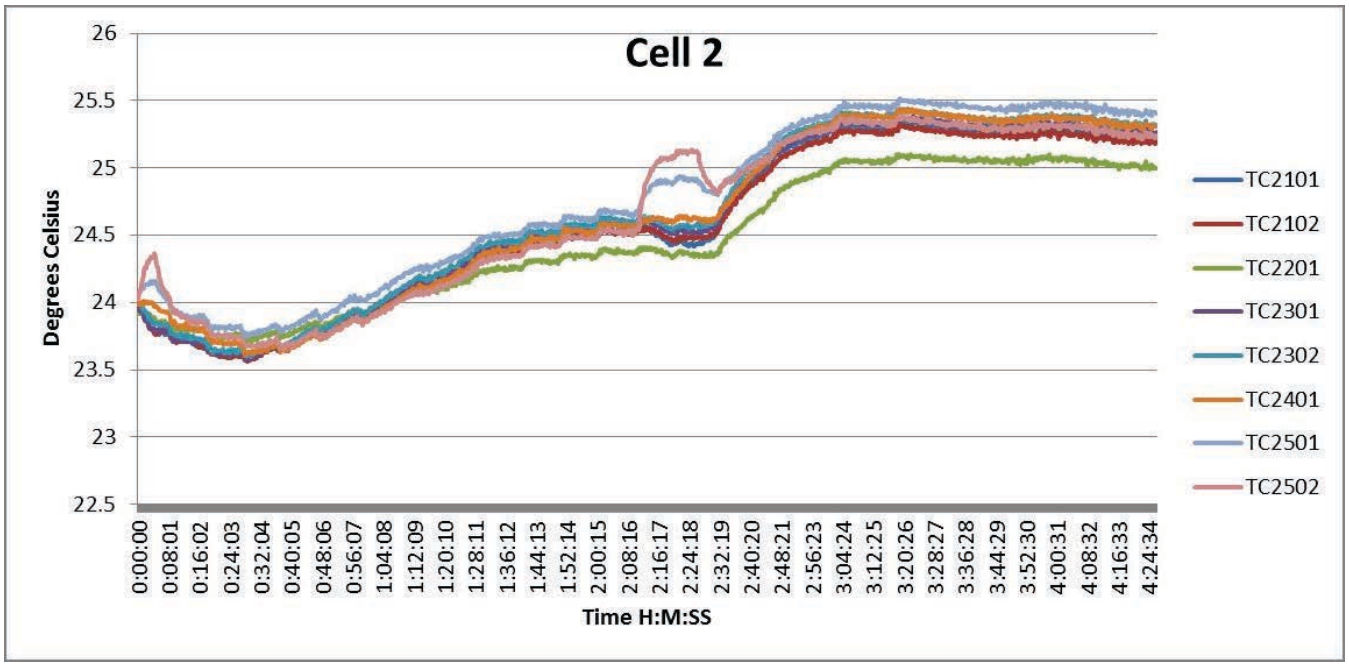

Figure B.133: Task A.1.C, Clean, First 2-Hour, Cell 2 Temperatures

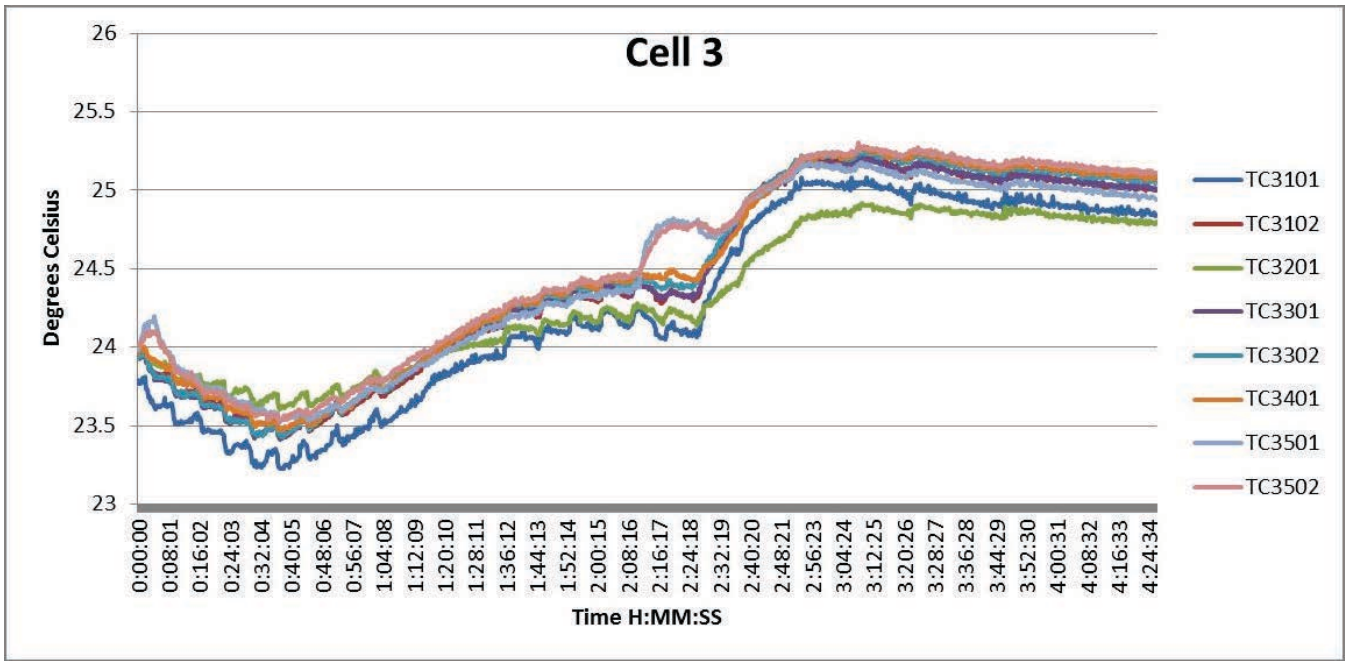

Figure B.134: Task A.1.C, Clean, First 2-Hour, Cell 3 Temperatures

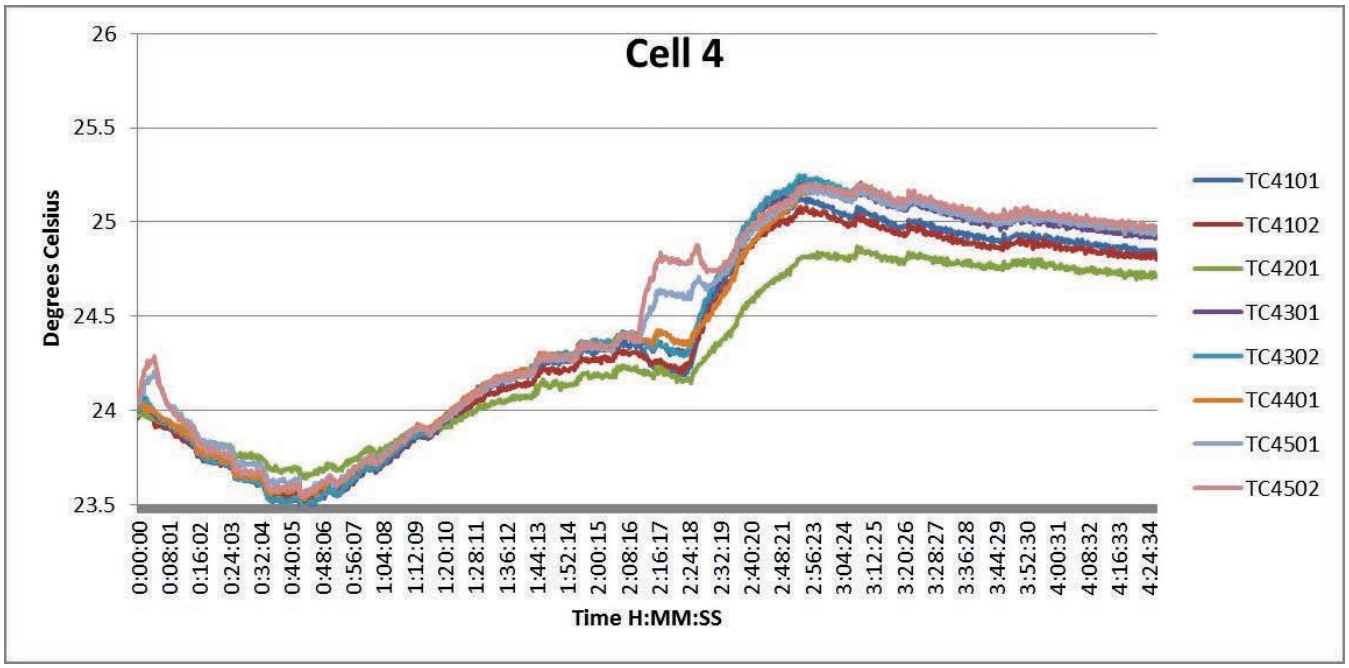

Figure B.135: Task A.1.C, Clean, First 2-Hour, Cell 4 Temperatures

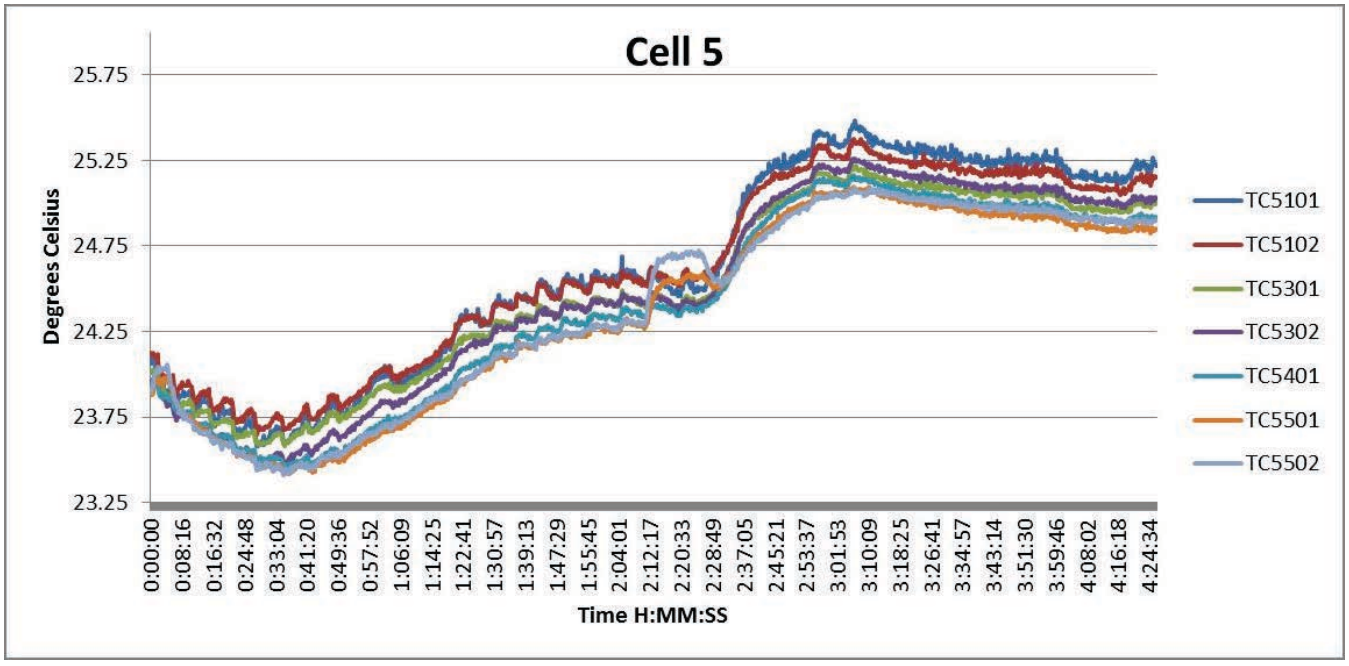

Figure B.136: Task A.1.C, Clean, First 2-Hour, Cell 5 Temperatures

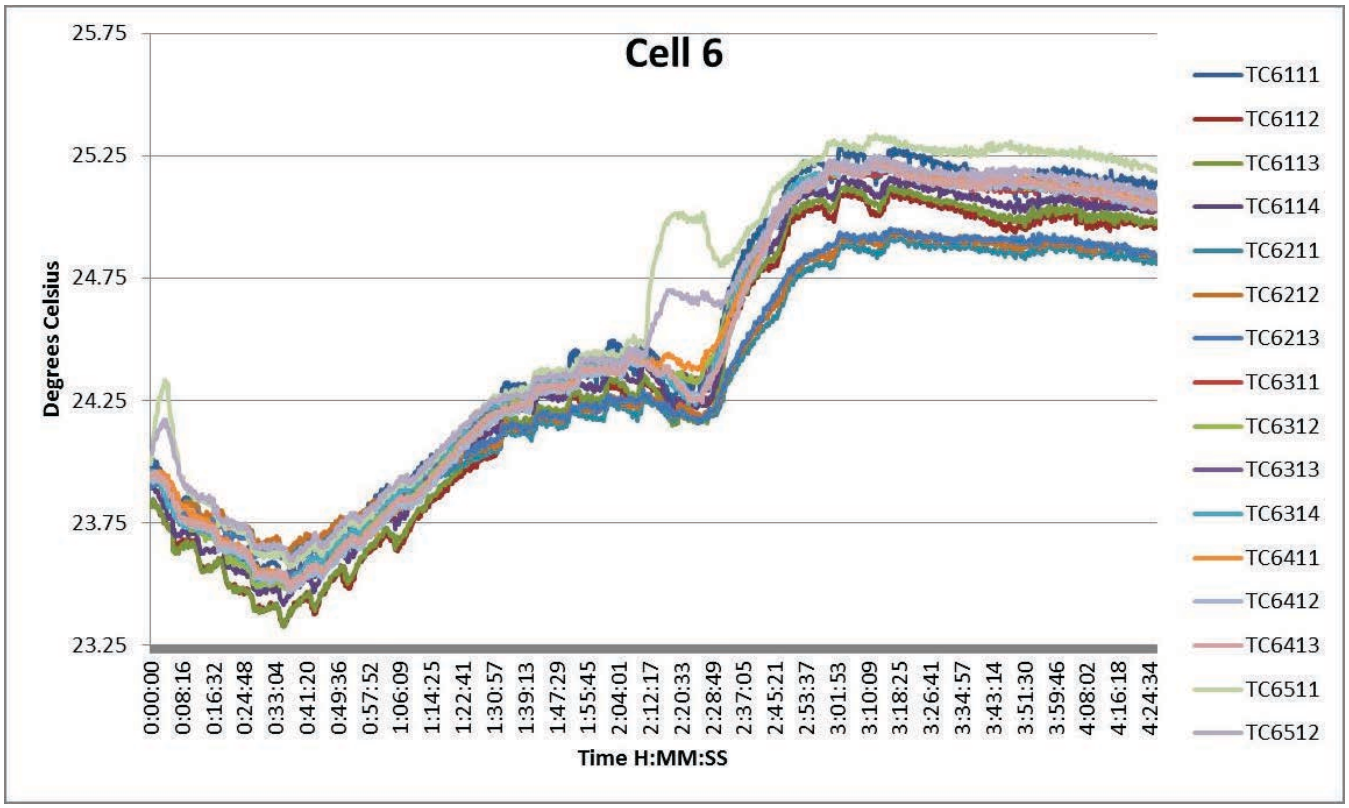

Figure B.137: Task A.1.C, Clean, First 2-Hour, Cell 6 Temperatures

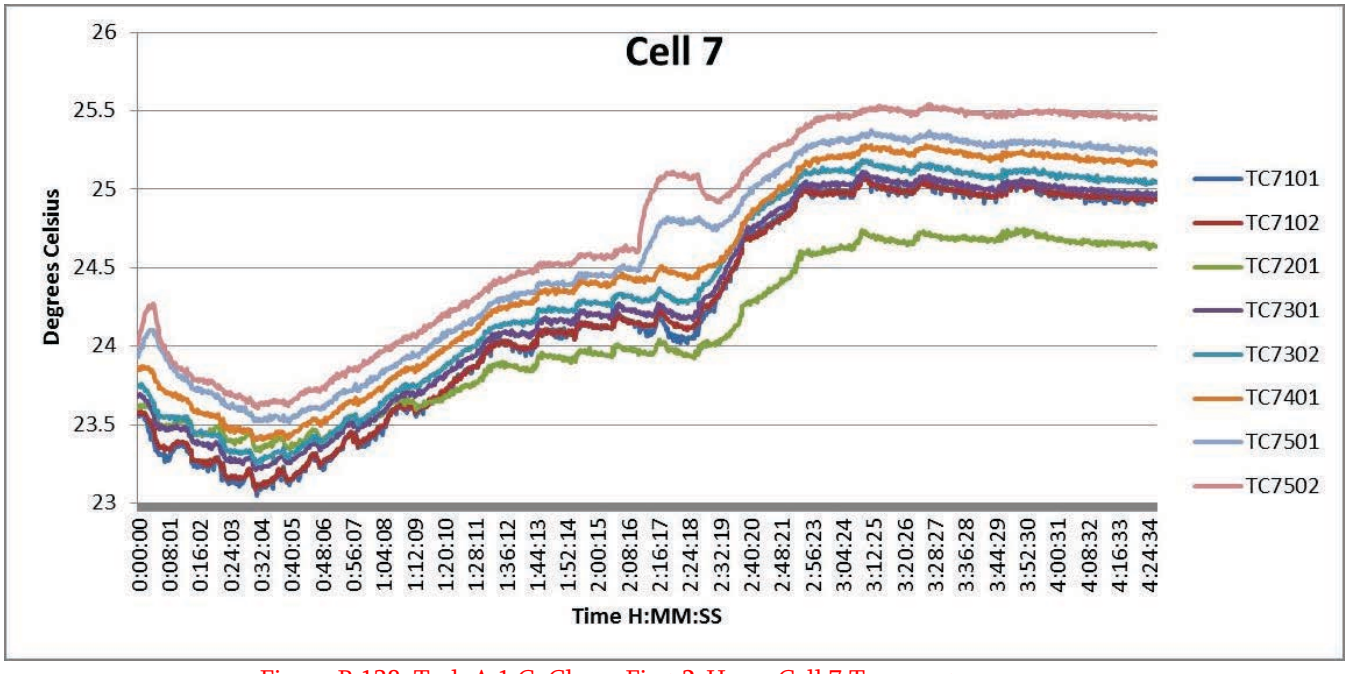

Figure B.138: Task A.1.C, Clean, First 2-Hour, Cell 7 Temperatures

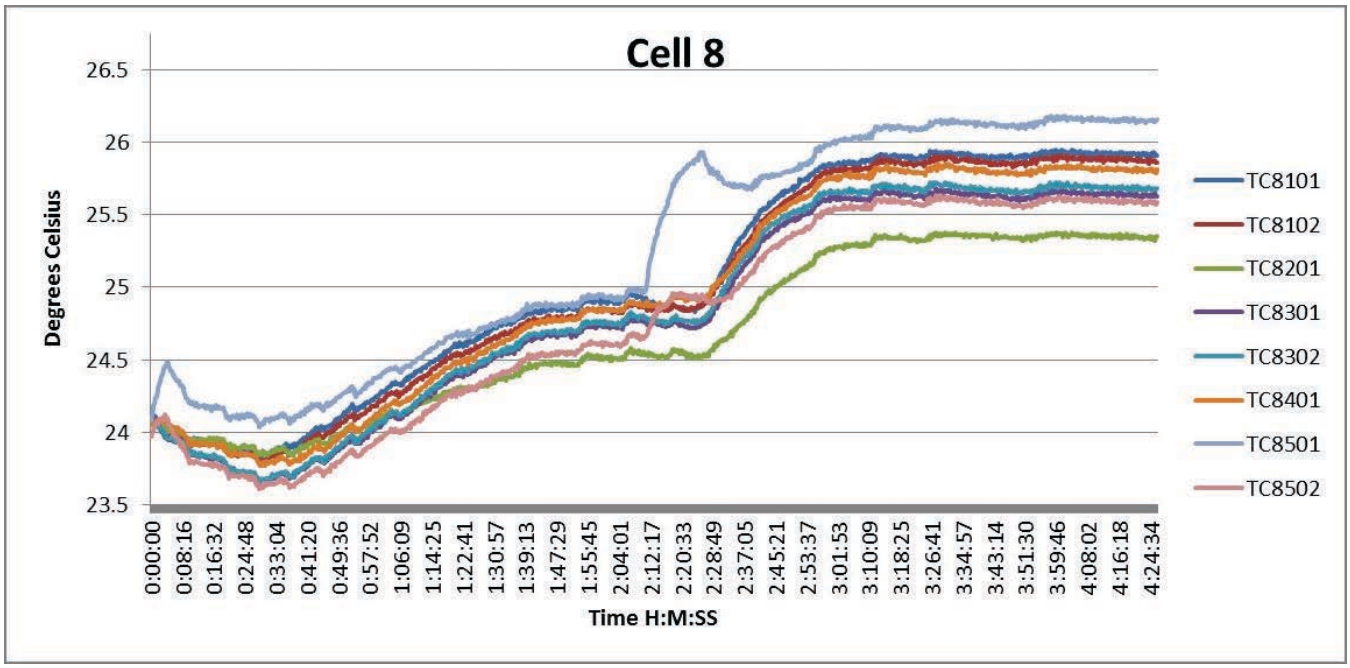

Figure B.139: Task A.1.C, Clean, First 2-Hour, Cell 8 Temperatures

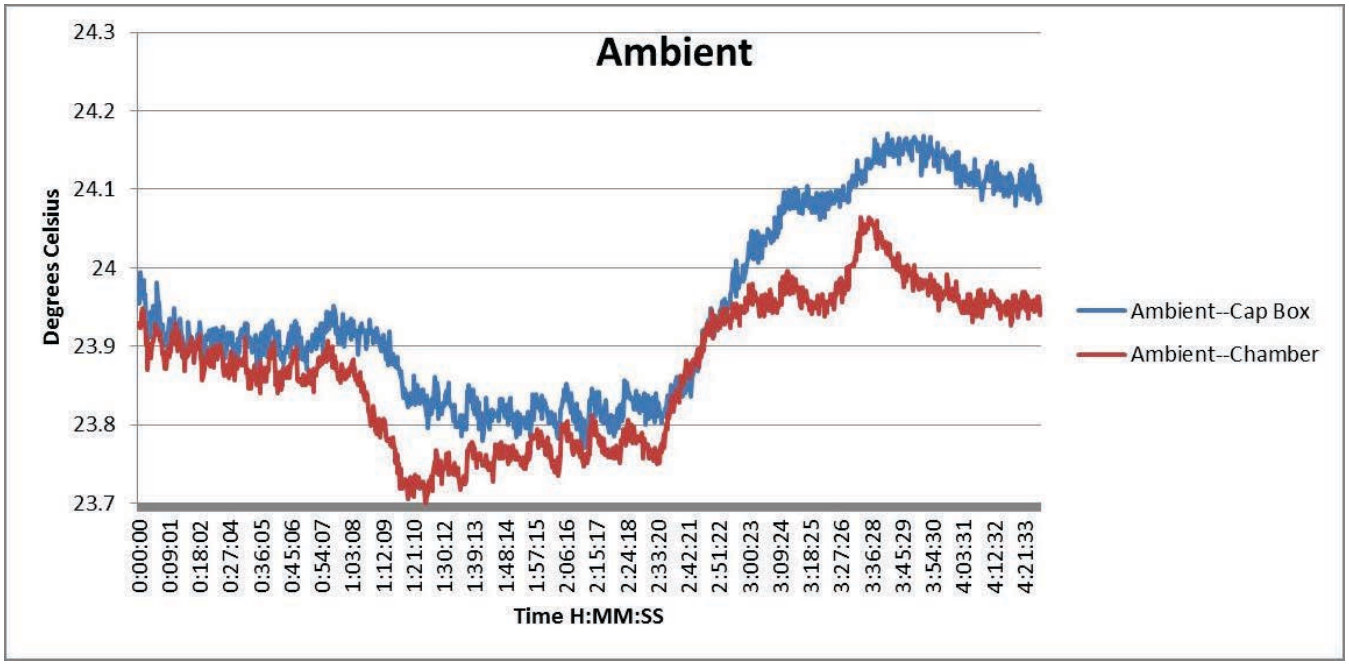

Figure B.140: Task A.1.C, Clean, First 2-Hour, Ambient Temperatures

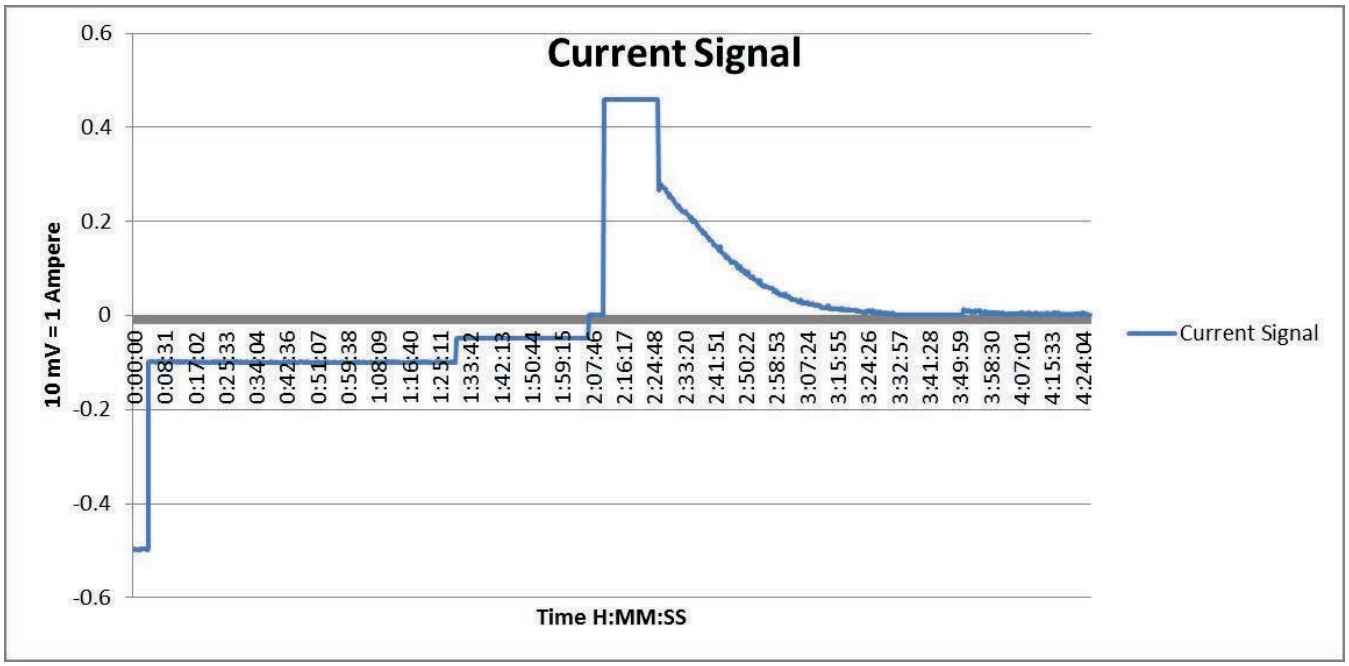

Figure B.141: Task A.1.C, Clean, First 2-Hour, Current Signal from BMU HECS

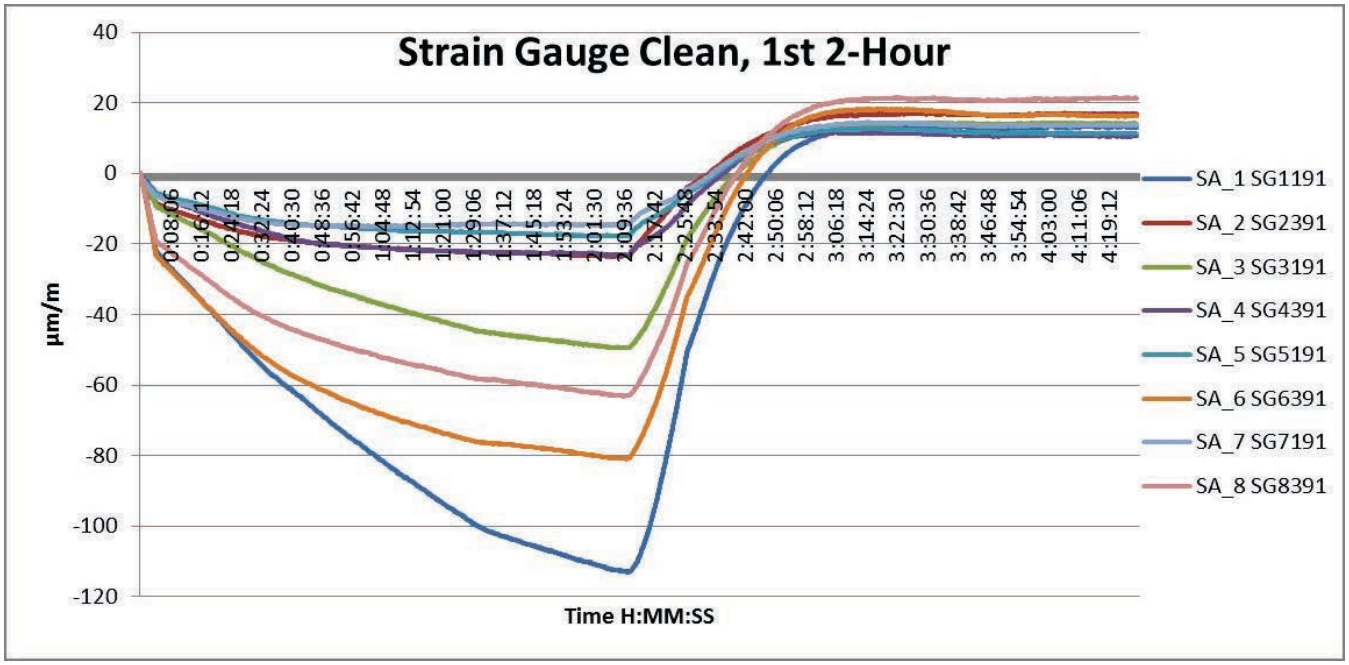

Figure B.142: Task A.1.C, Clean, First 2-Hour, Strain Gauges

Task A.1.C – Clean, Second 2-Hour

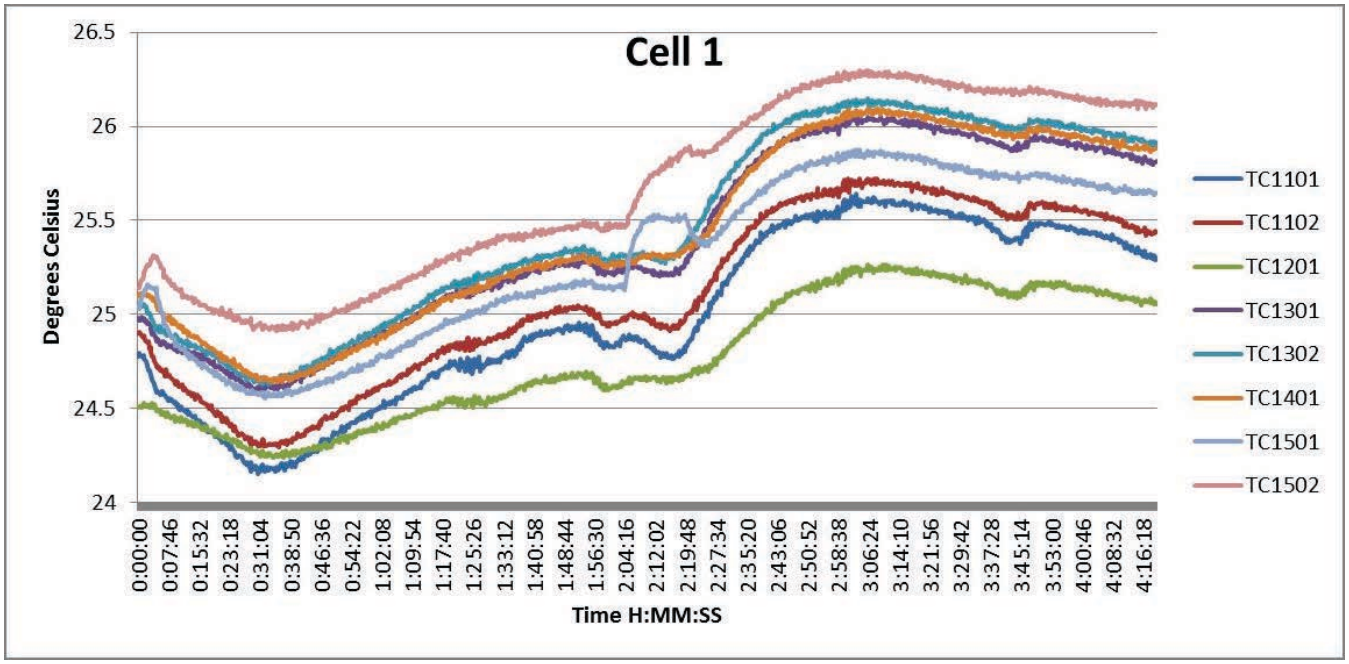

Figure B.143: Task A.1.C, Clean, Second 2-Hour, Cell 1 Temperatures

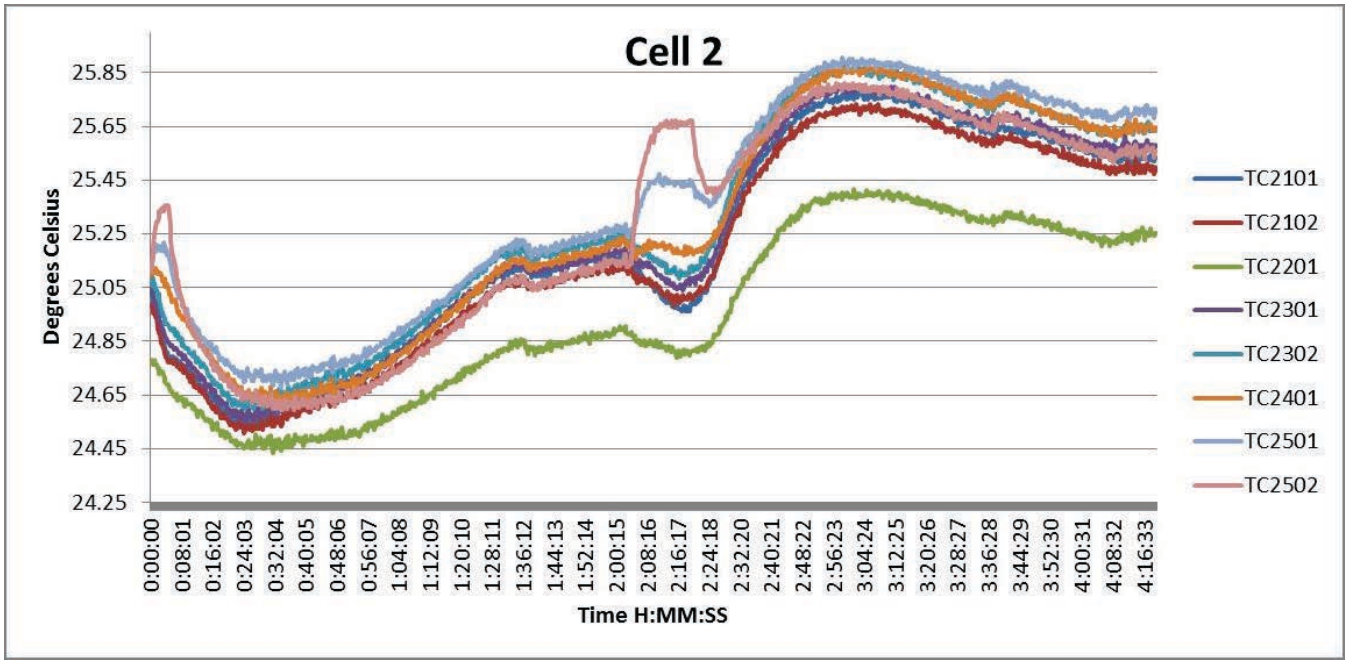

Figure B.144: Task A.1.C, Clean, Second 2-Hour, Cell 2 Temperatures

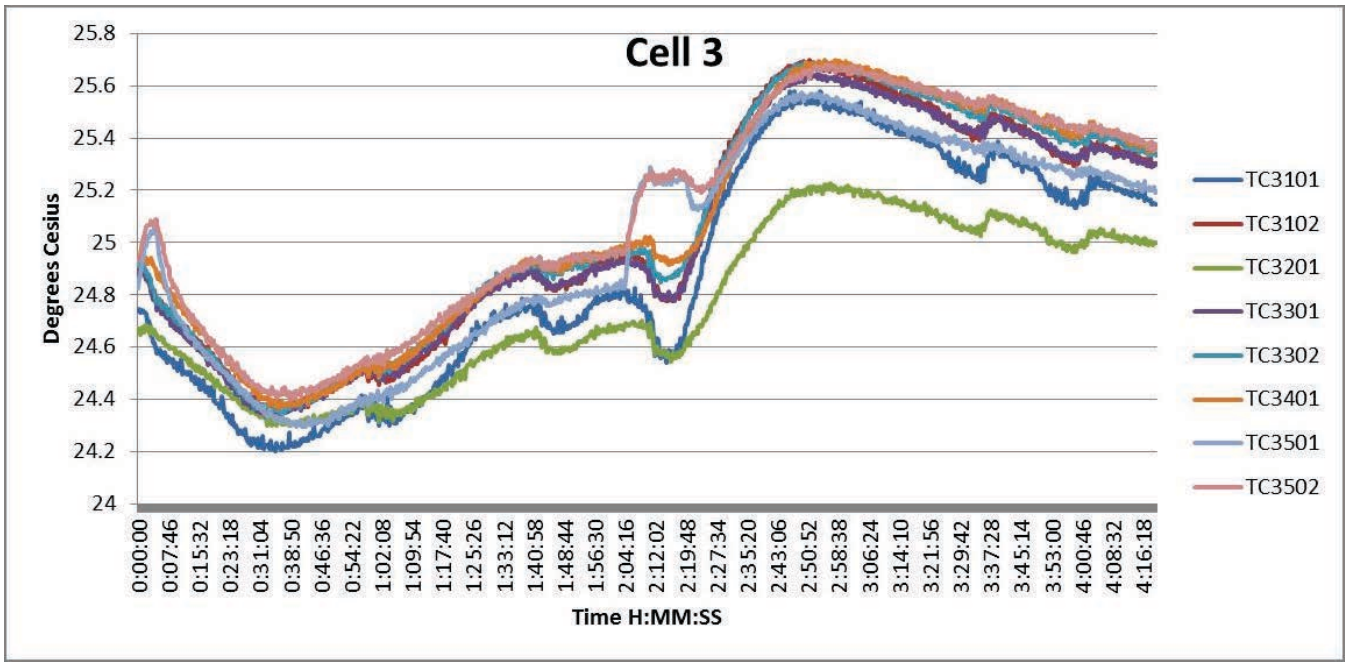

Figure B.145: Task A.1.C, Clean, Second 2-Hour, Cell 3 Temperatures

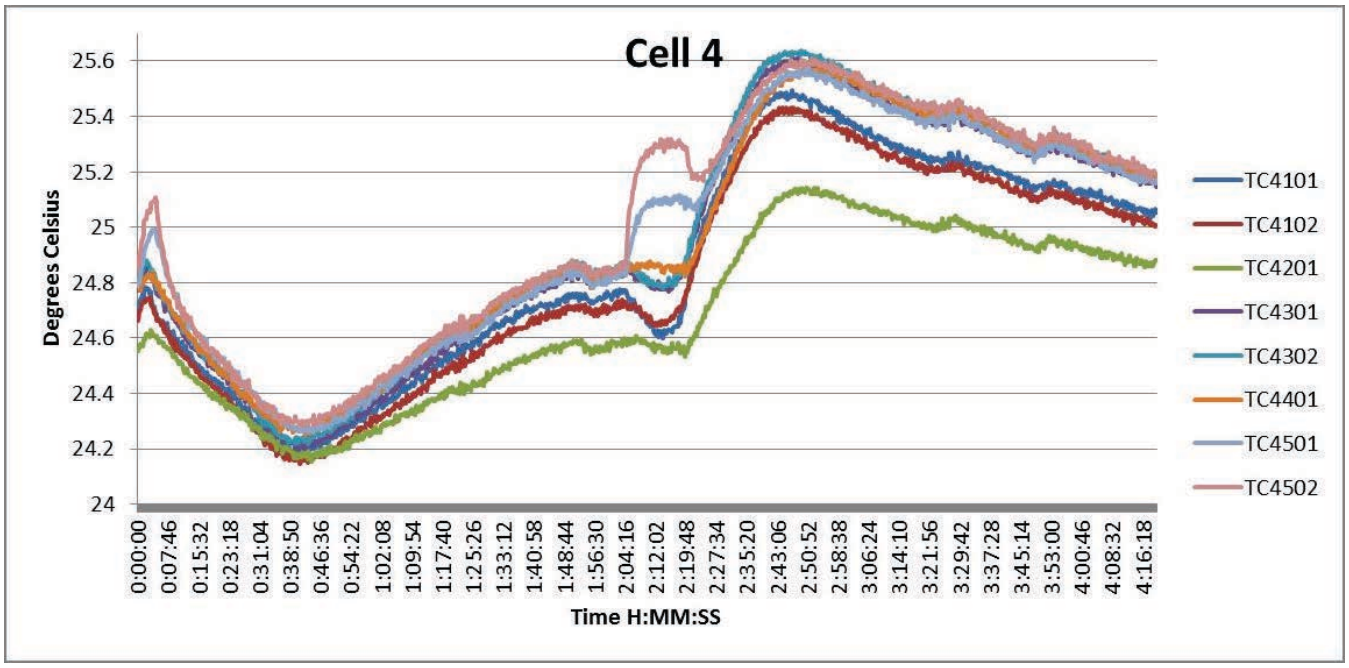

Figure B.146: Task A.1.C, Clean, Second 2-Hour, Cell 4 Temperatures

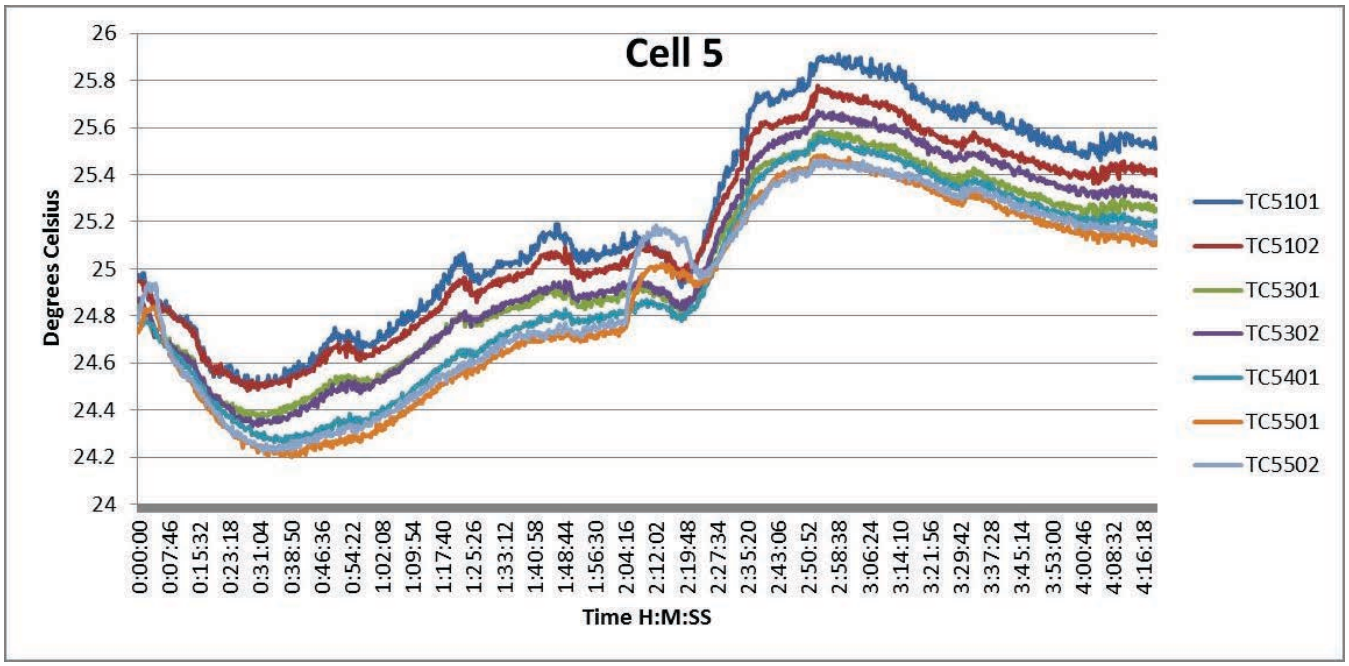

Figure B.147: Task A.1.C, Clean, Second 2-Hour, Cell 5 Temperatures

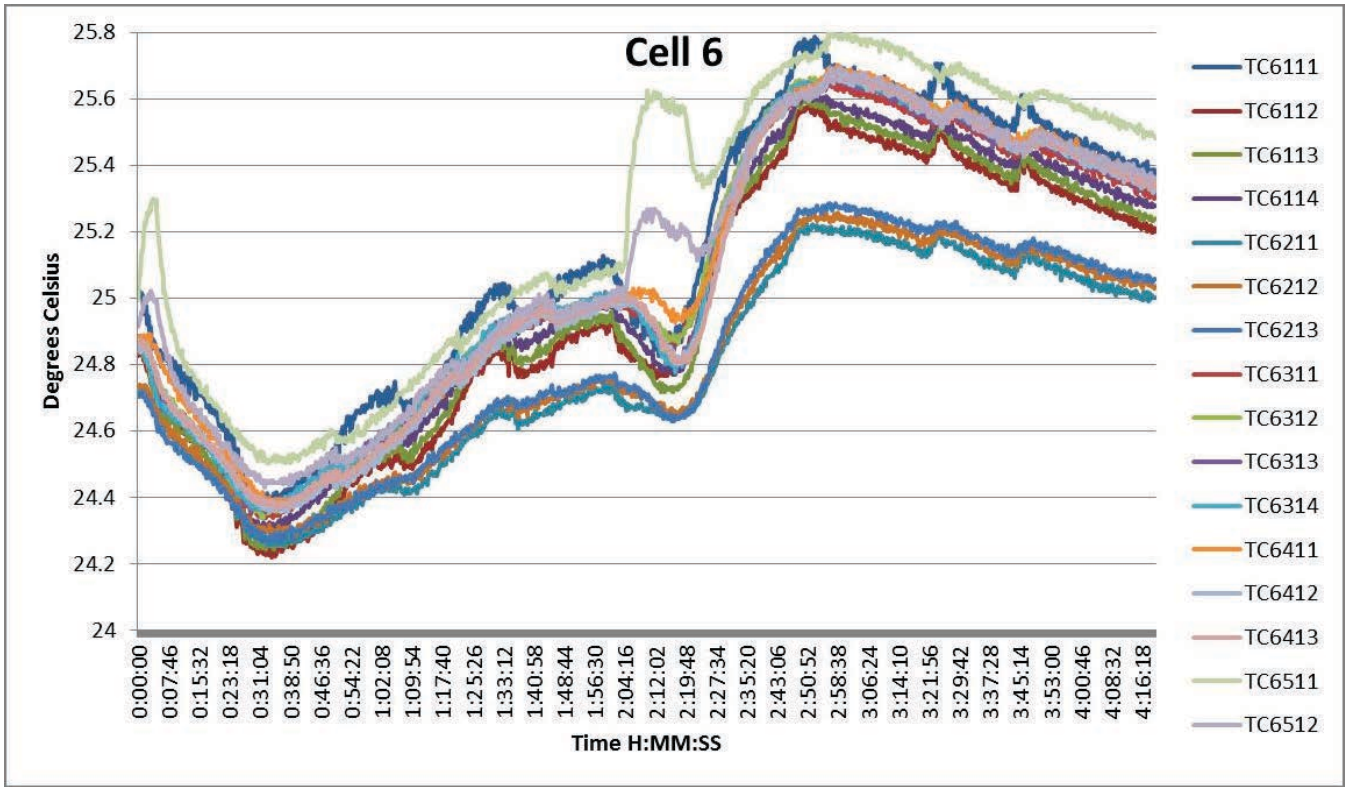

Figure B.148: Task A.1.C, Clean, Second 2-Hour, Cell 6 Temperatures

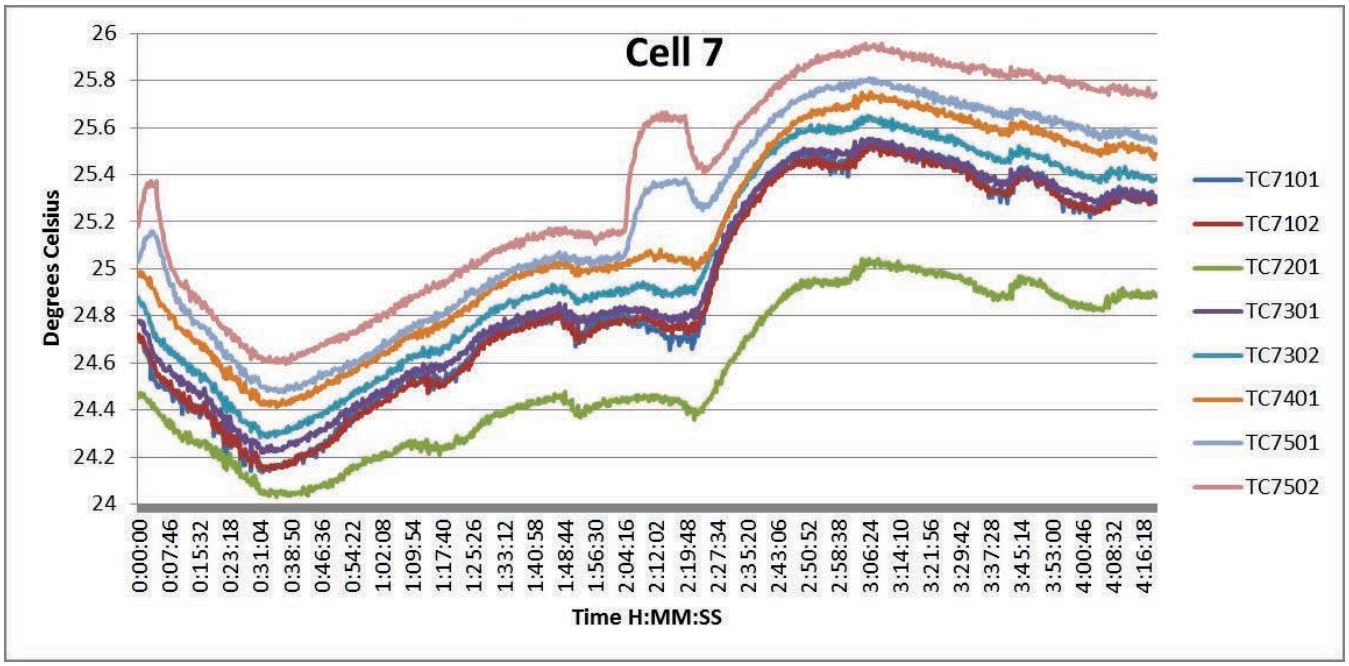

Figure B.149: Task A.1.C, Clean, Second 2-Hour, Cell 7 Temperatures

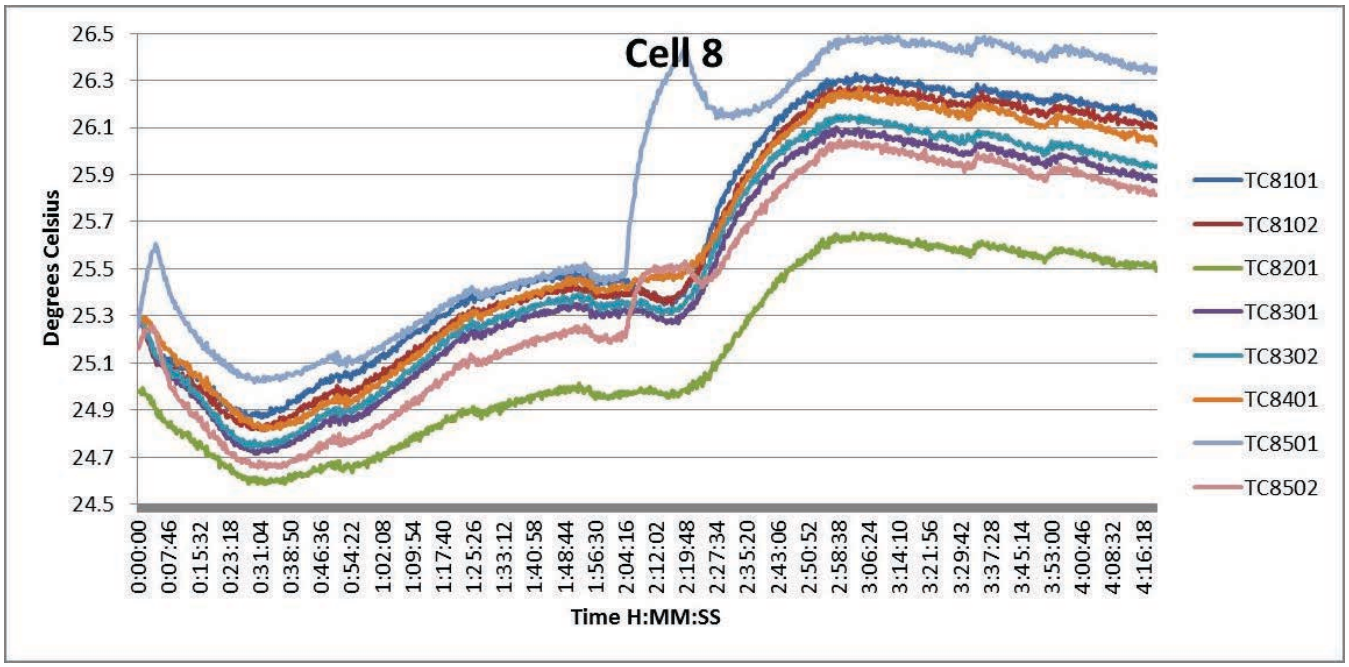

Figure B.150: Task A.1.C, Clean, Second 2-Hour, Cell 8 Temperatures

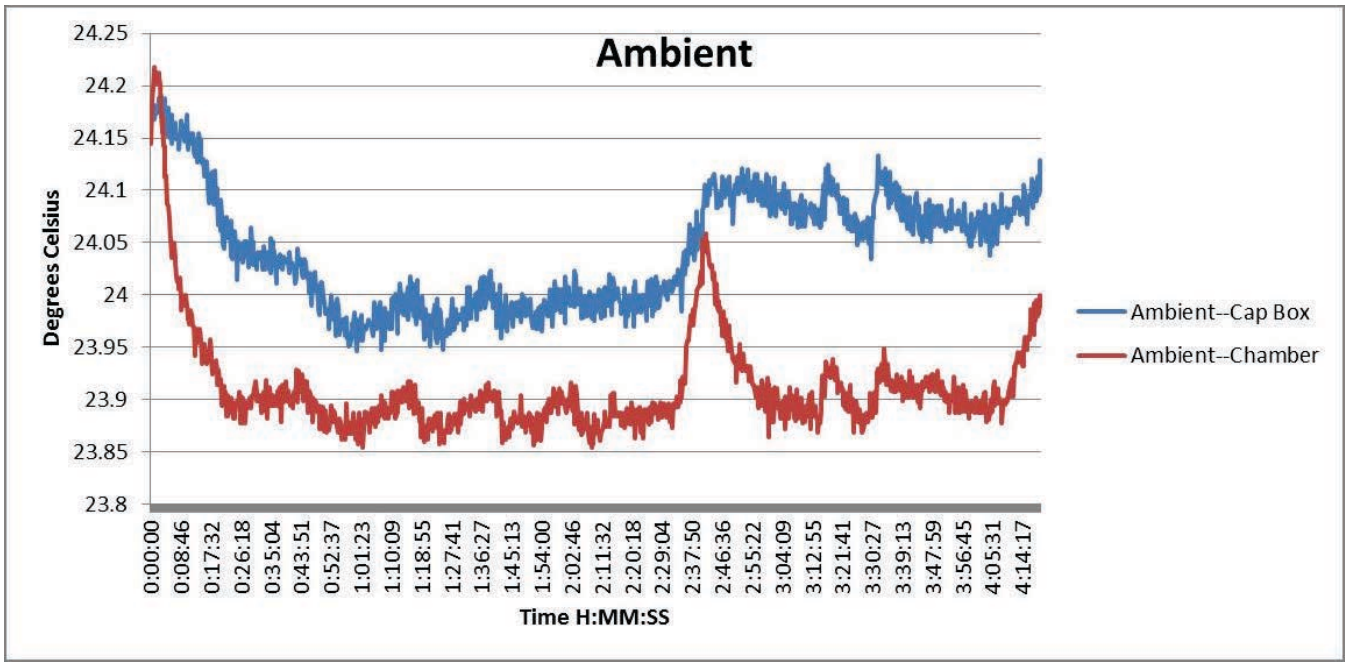

Figure B.151: Task A.1.C, Clean, Second 2-Hour, Ambient Temperatures

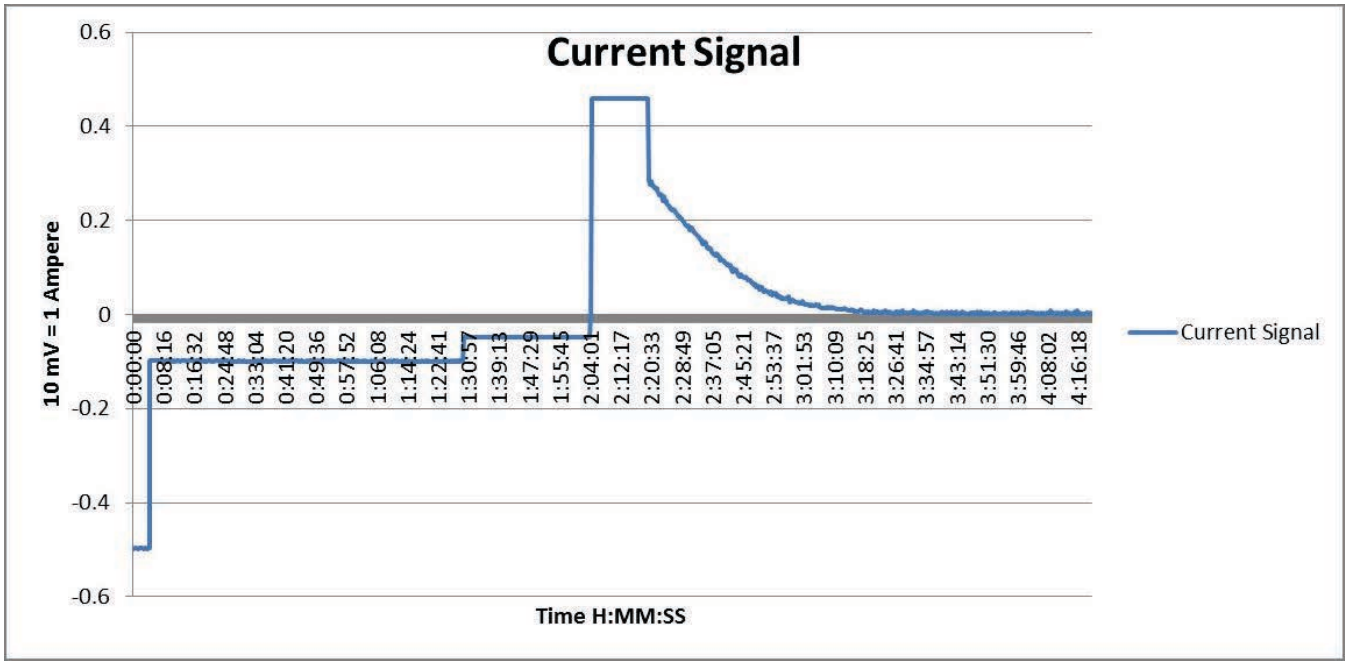

Figure B.152: Task A.1.C, Clean, Second 2-Hour, Current Signal from BMU HECS

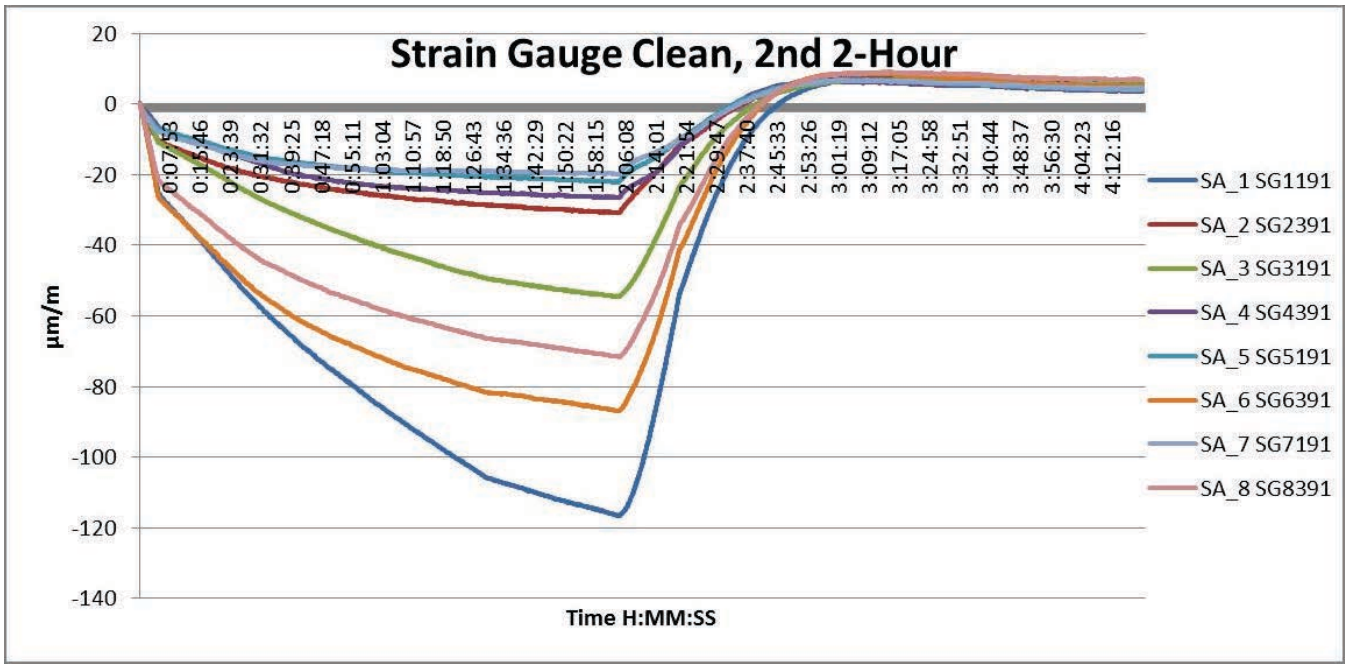

Figure B.153: Task A.1.C, Clean, Second 2-Hour, Strain Gauges

Task A.1.C – Noisy, 8-Hour

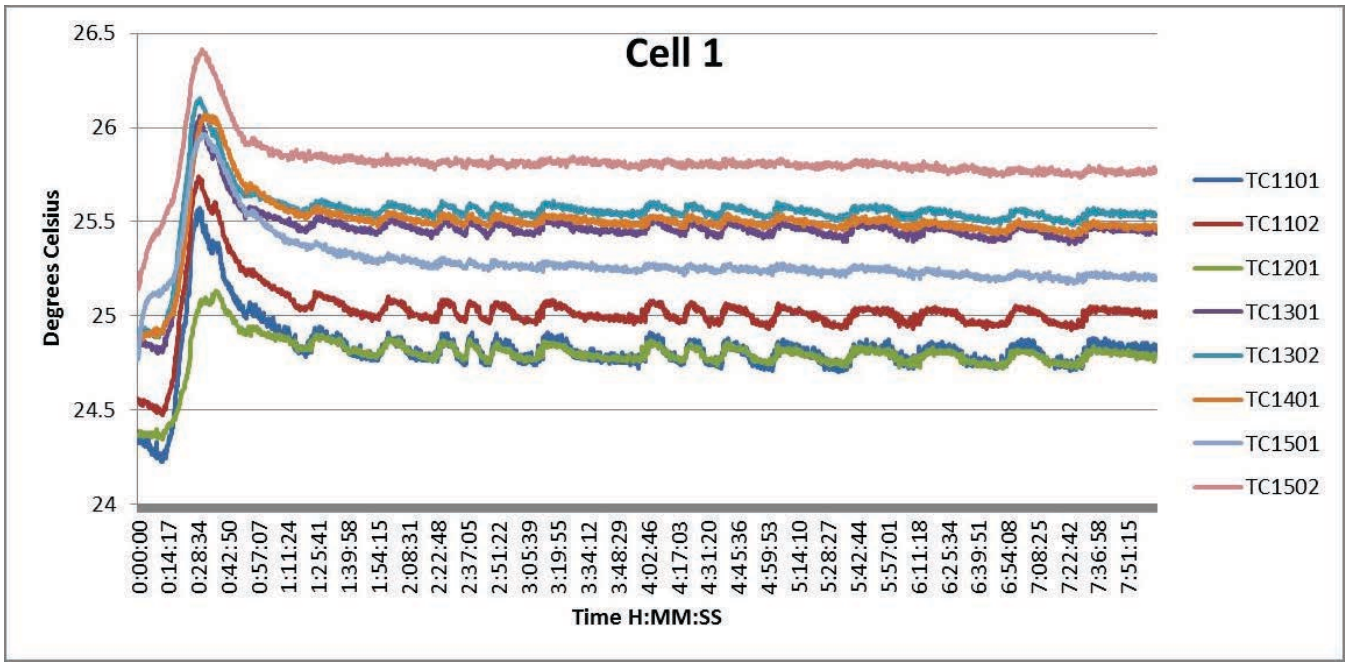

Figure B.154: Task A.1.C, Noisy, 8-Hour, Cell 1 Temperatures

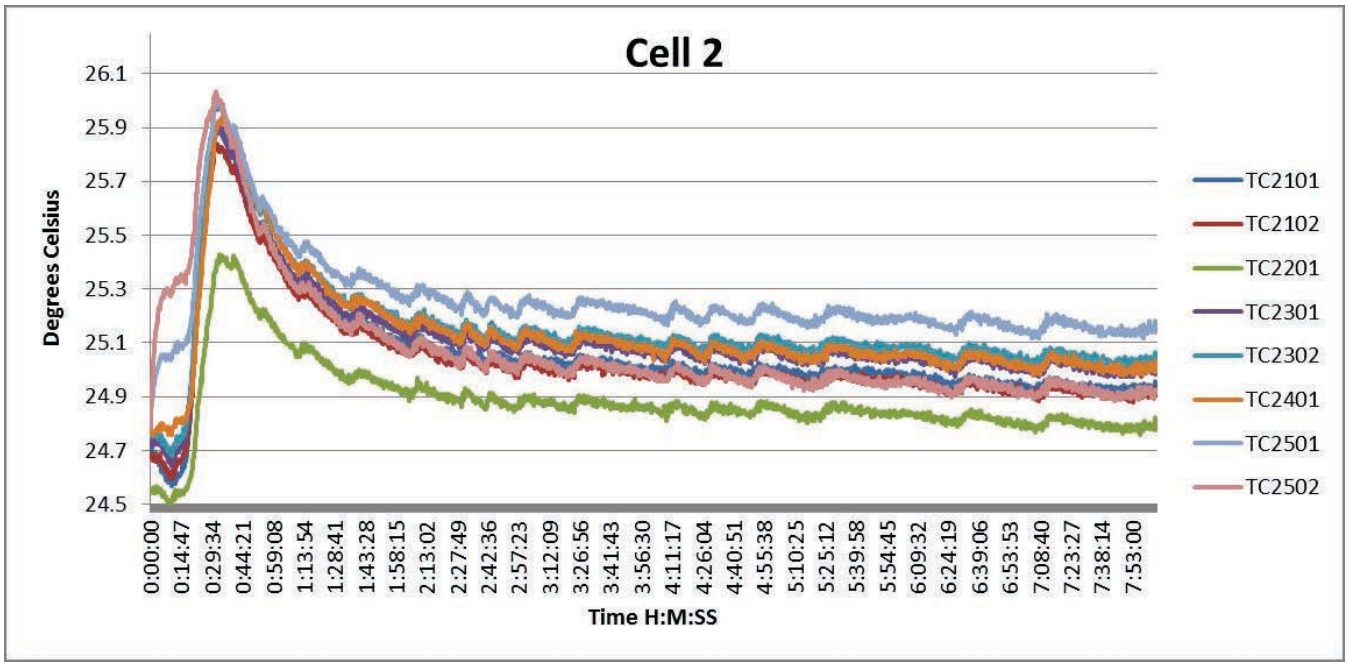

Figure B.155: Task A.1.C, Noisy, 8-Hour, Cell 2 Temperatures

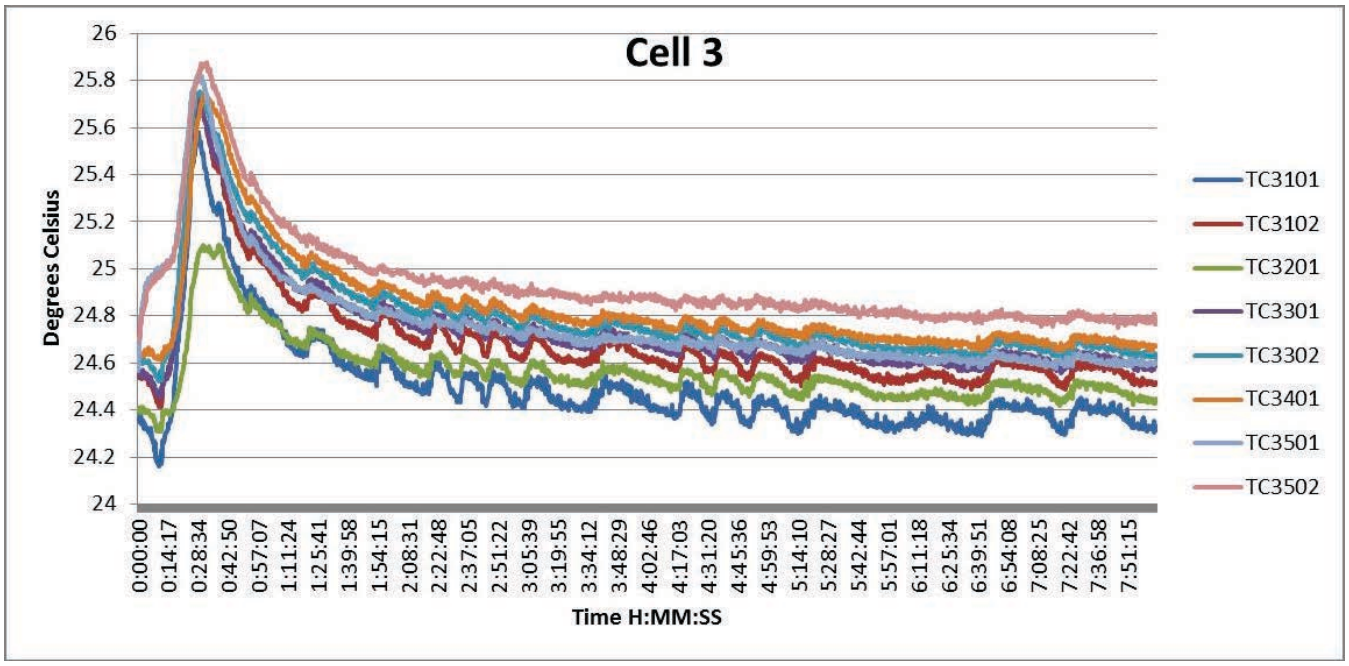

Figure B.156: Task A.1.C, Noisy, 8-Hour, Cell 3 Temperatures

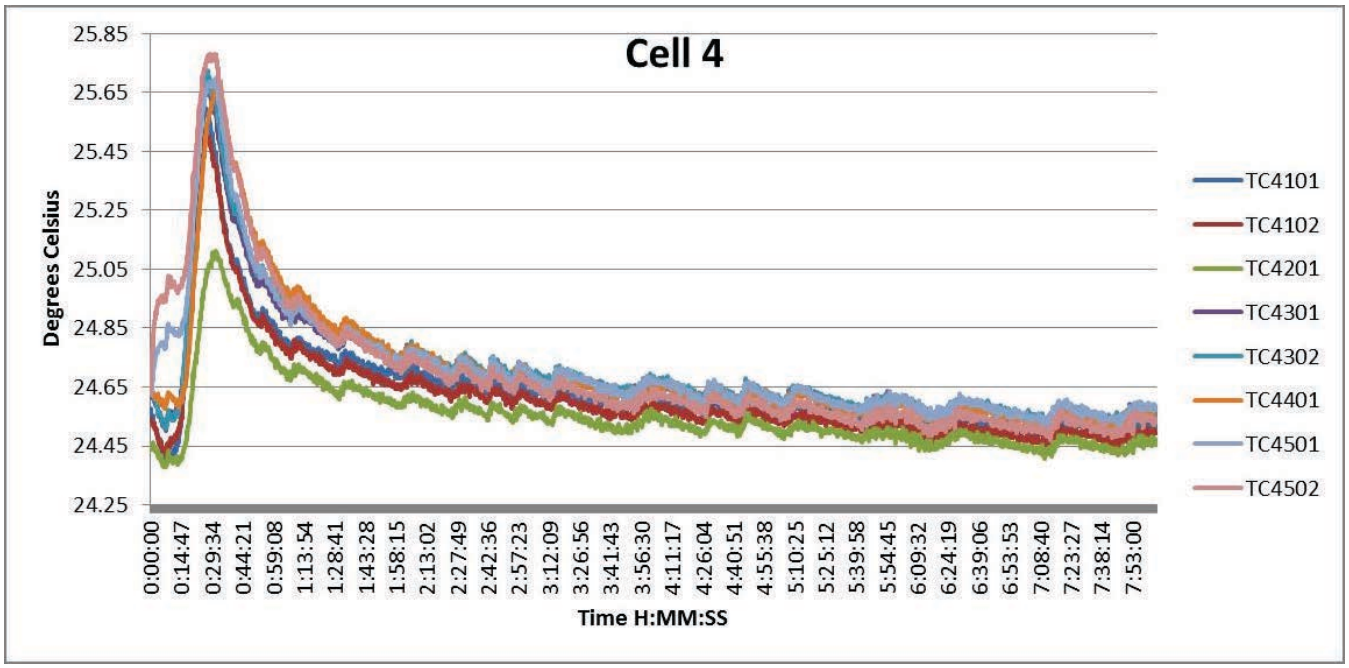

Figure B.157: Task A.1.C, Noisy, 8-Hour, Cell 4 Temperatures

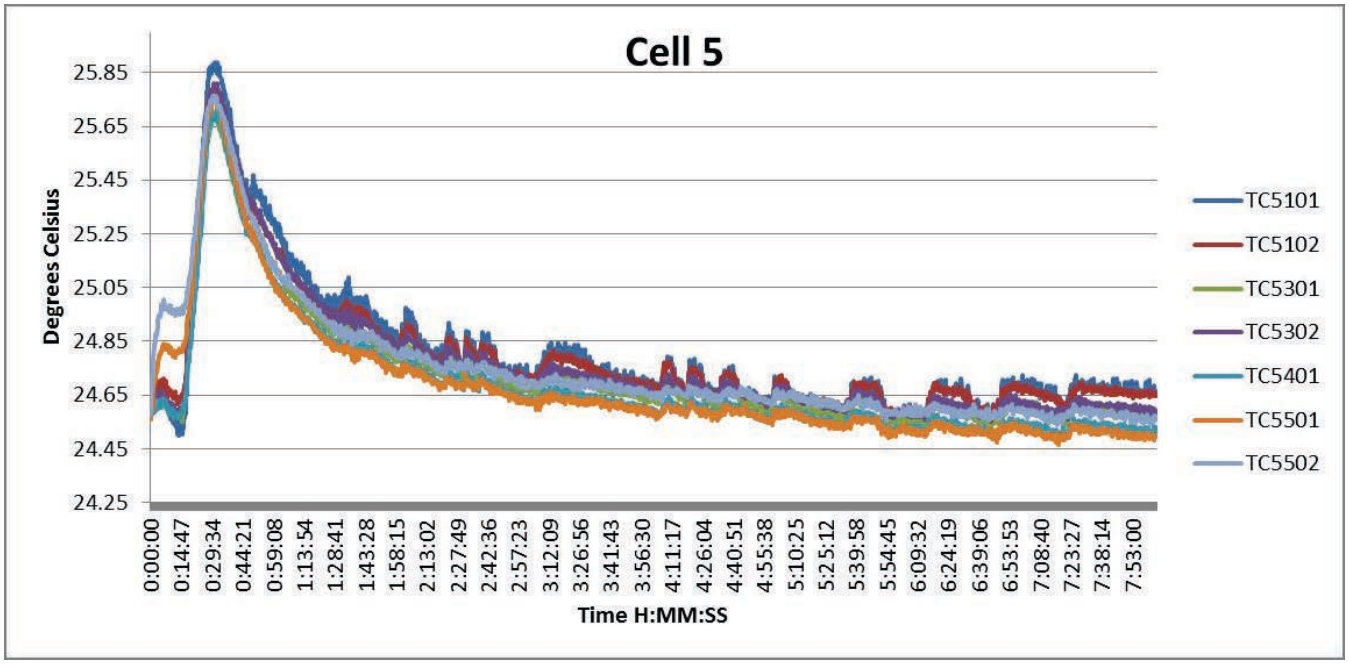

Figure B.158: Task A.1.C, Noisy, 8-Hour, Cell 5 Temperatures

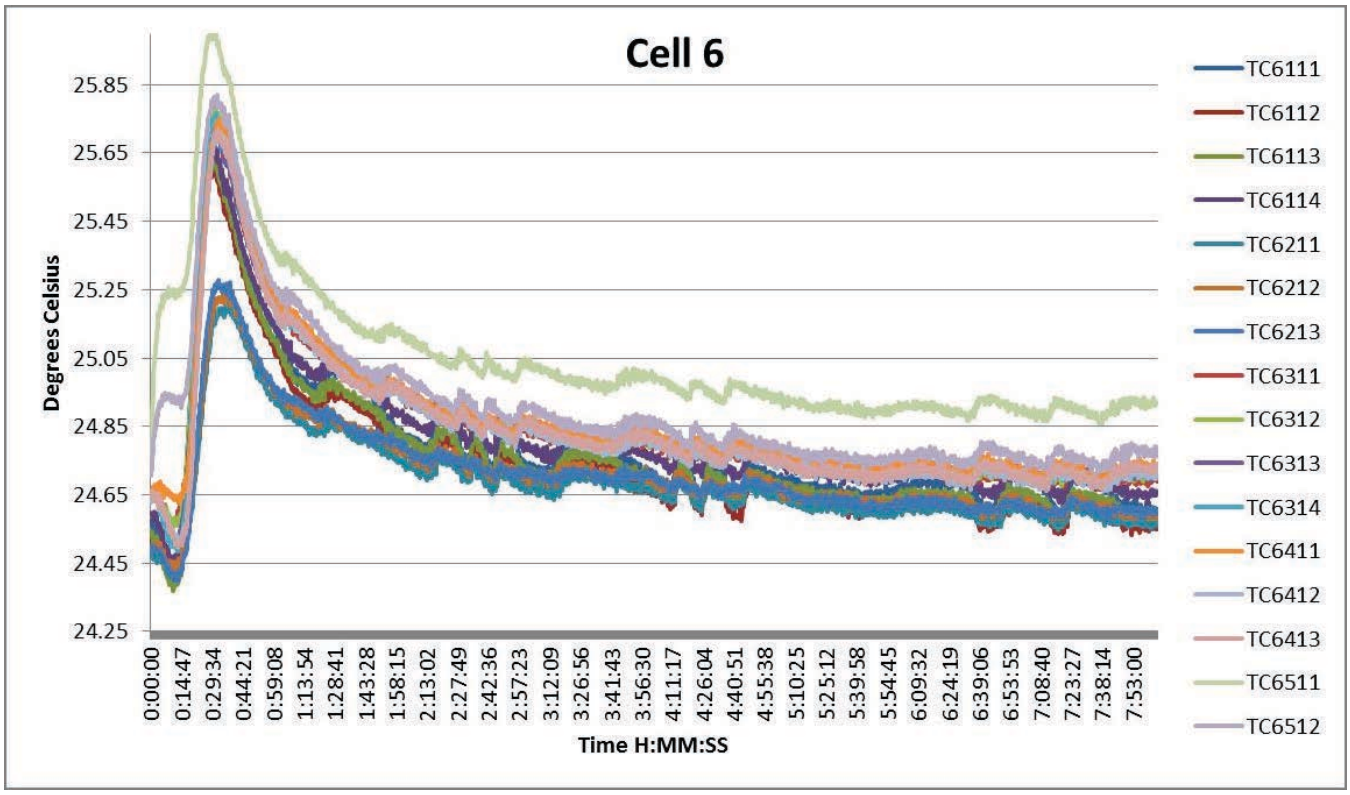

Figure B.159: Task A.1.C, Noisy, 8-Hour, Cell 6 Temperatures

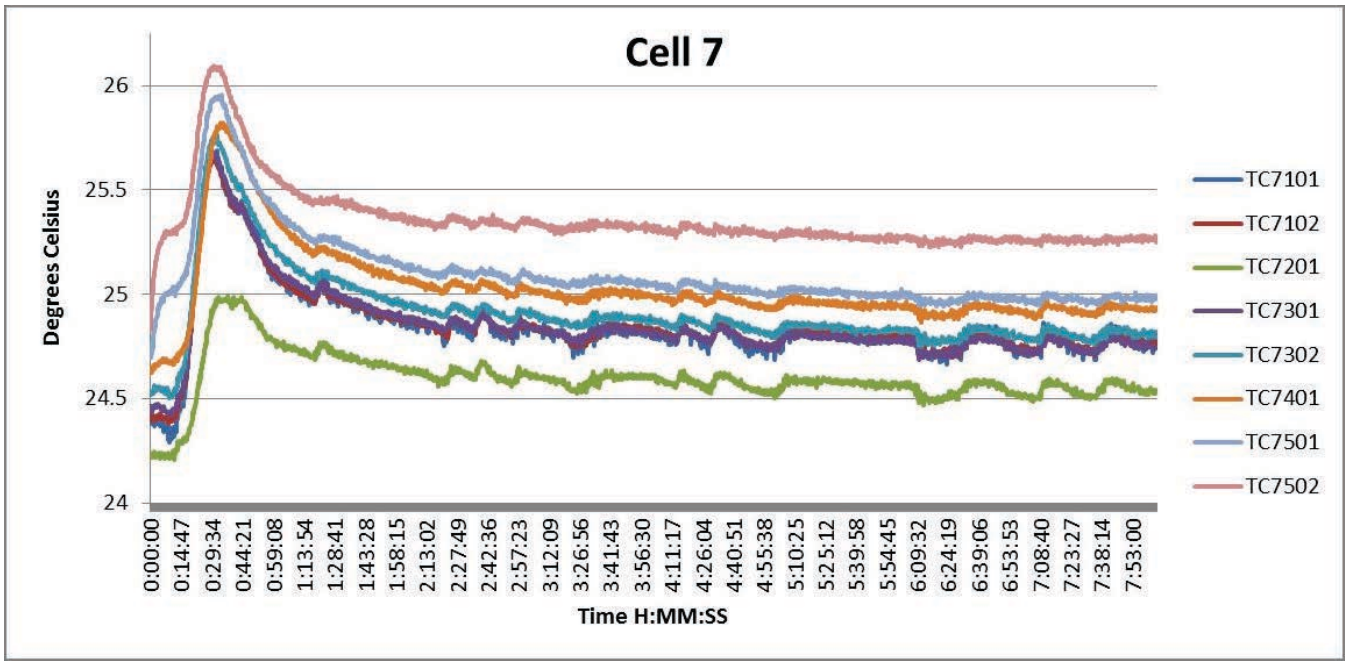

Figure B.160: Task A.1.C, Noisy, 8-Hour, Cell 7 Temperatures

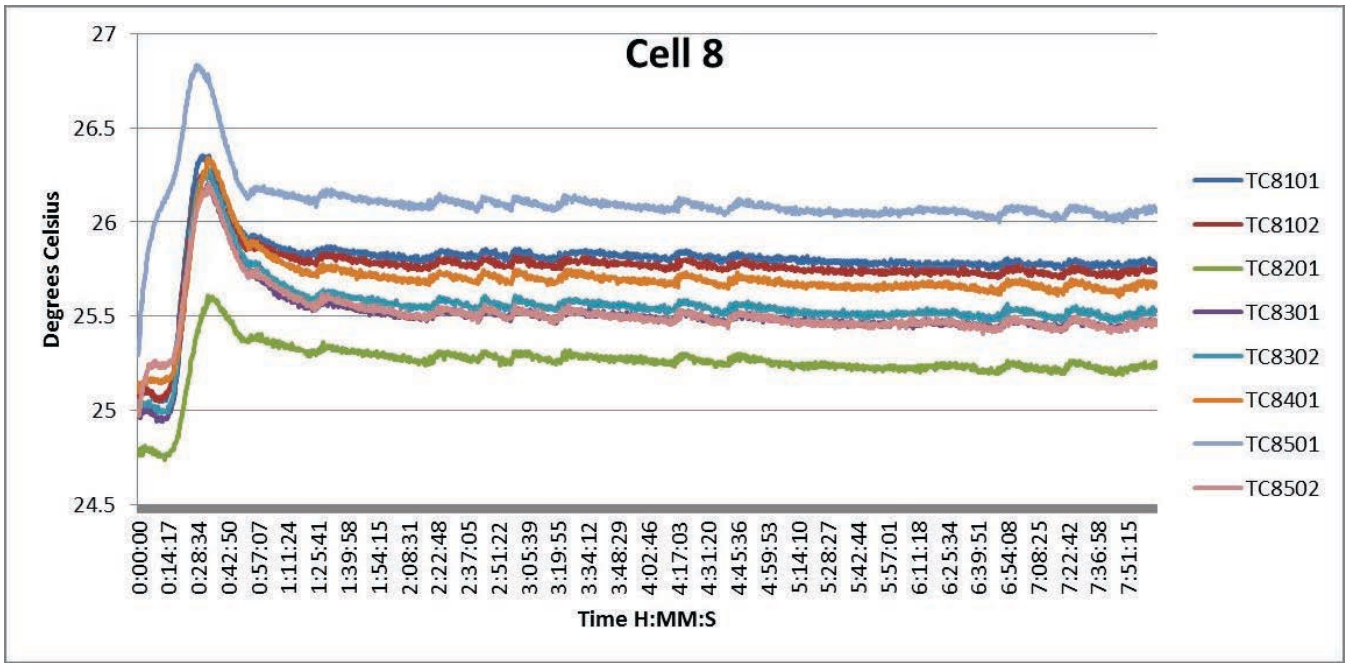

Figure B.161: Task A.1.C, Noisy, 8-Hour, Cell 8 Temperatures

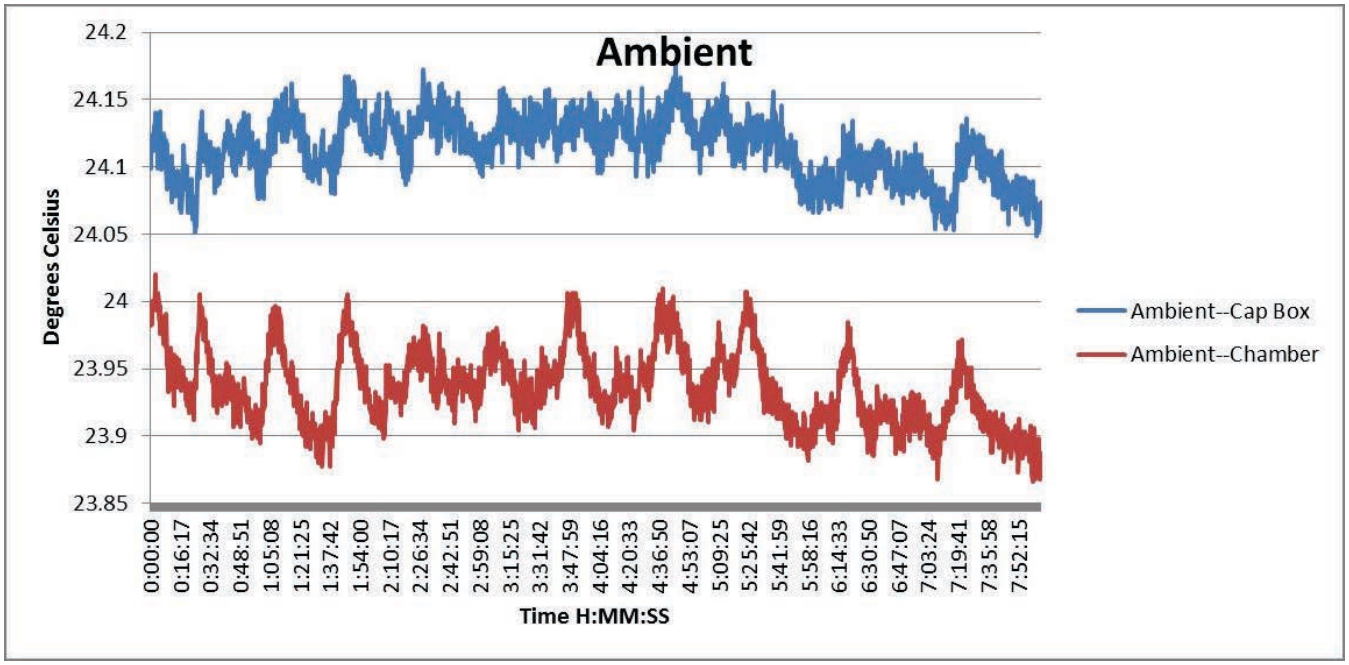

Figure B.162: Task A.1.C, Noisy, 8-Hour, Ambient Temperatures

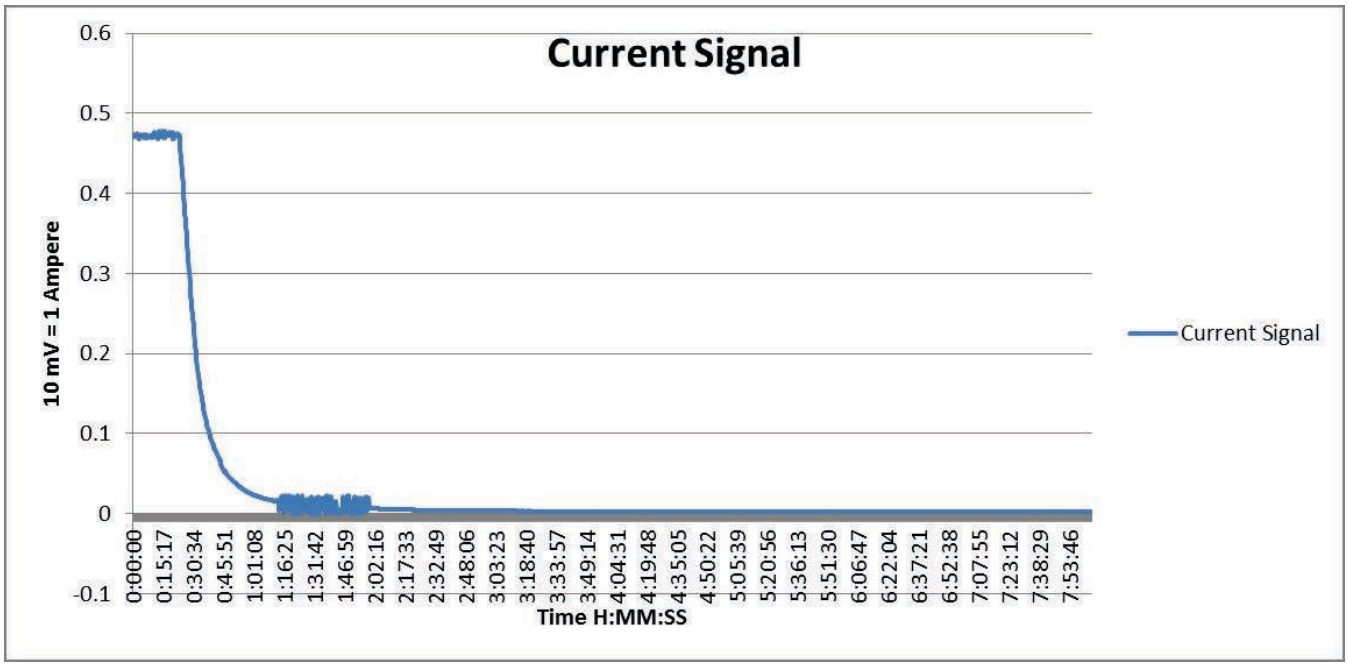

Figure B.163: Task A.1.C, Noisy, 8-Hour, Current Signal from BMU HECS

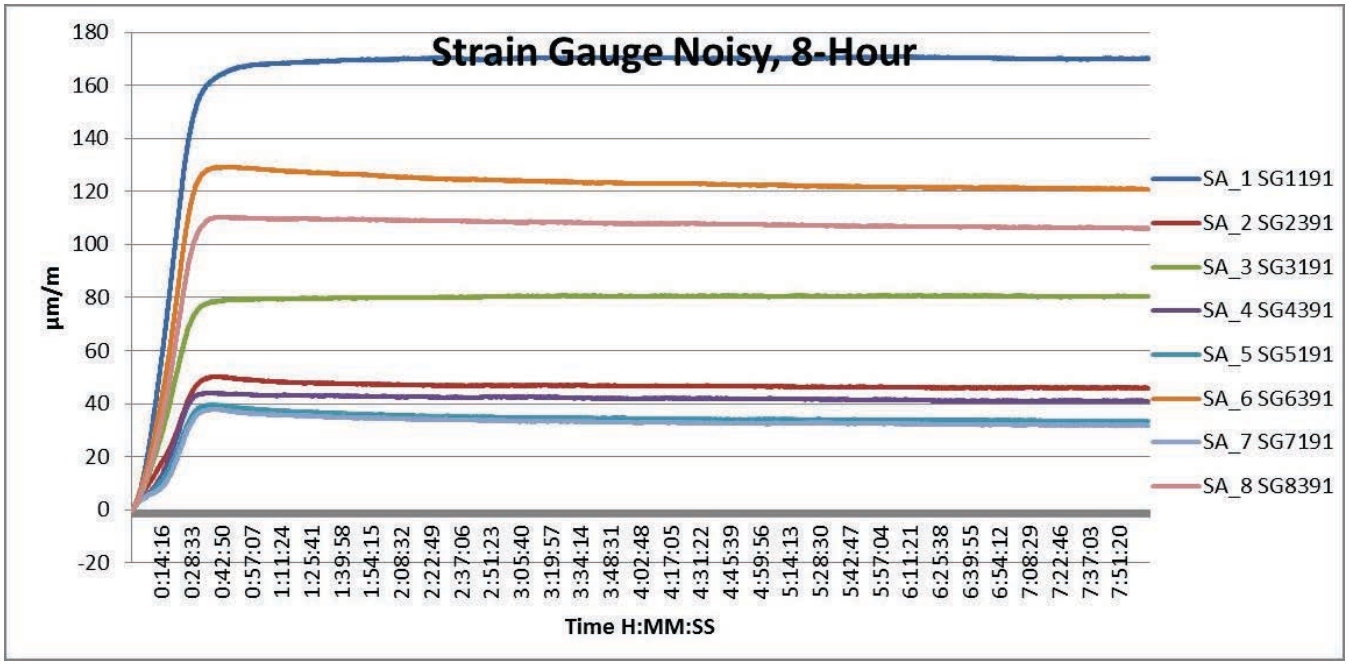

Figure B.164: Task A.1.C, Noisy, 8-Hour, Strain Gauge

Task A.1.C – Noisy, First 2-Hour

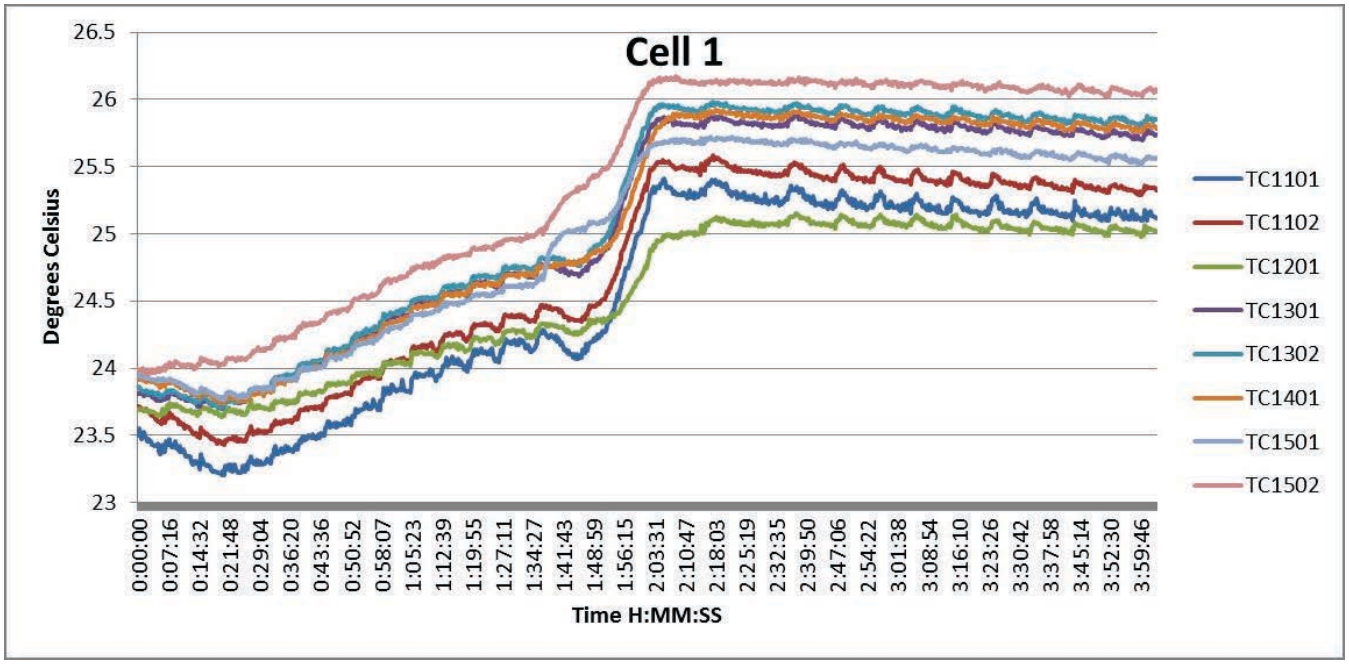

Figure B.165: Task A.1.C, Noisy, First 2-Hour, Cell 1 Temperatures

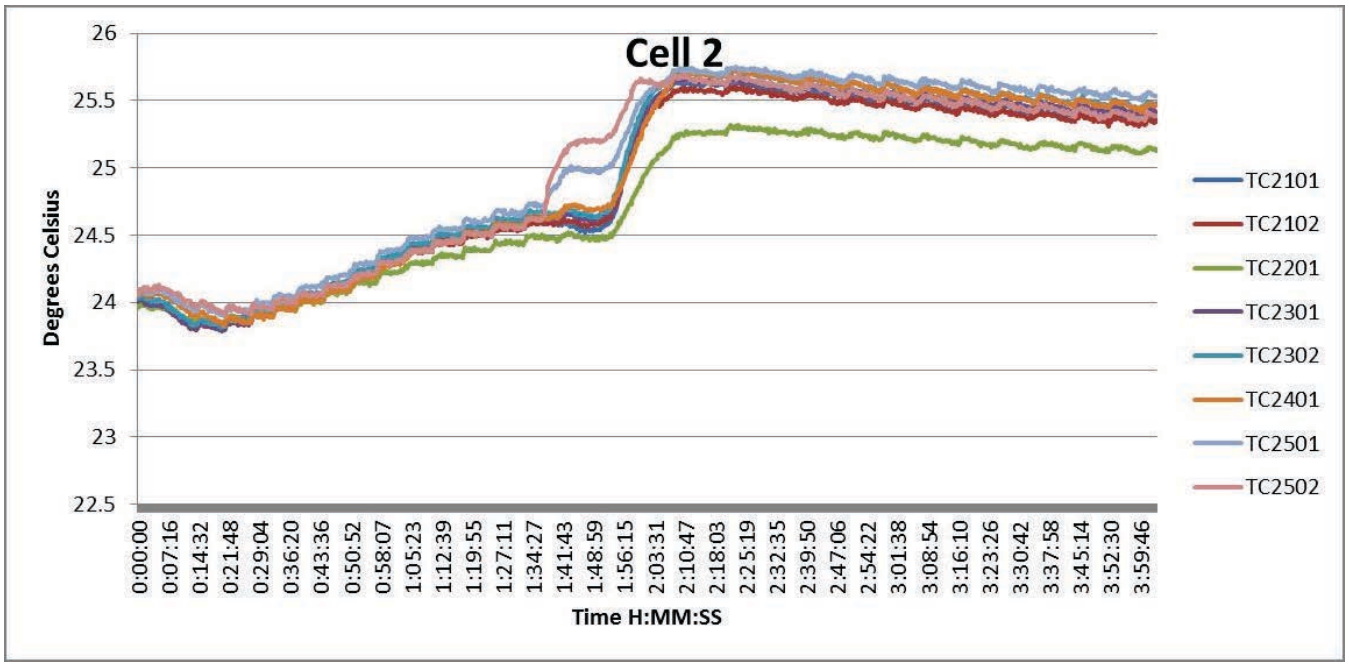

Figure B.166: Task A.1.C, Noisy, First 2-Hour, Cell 2 Temperatures

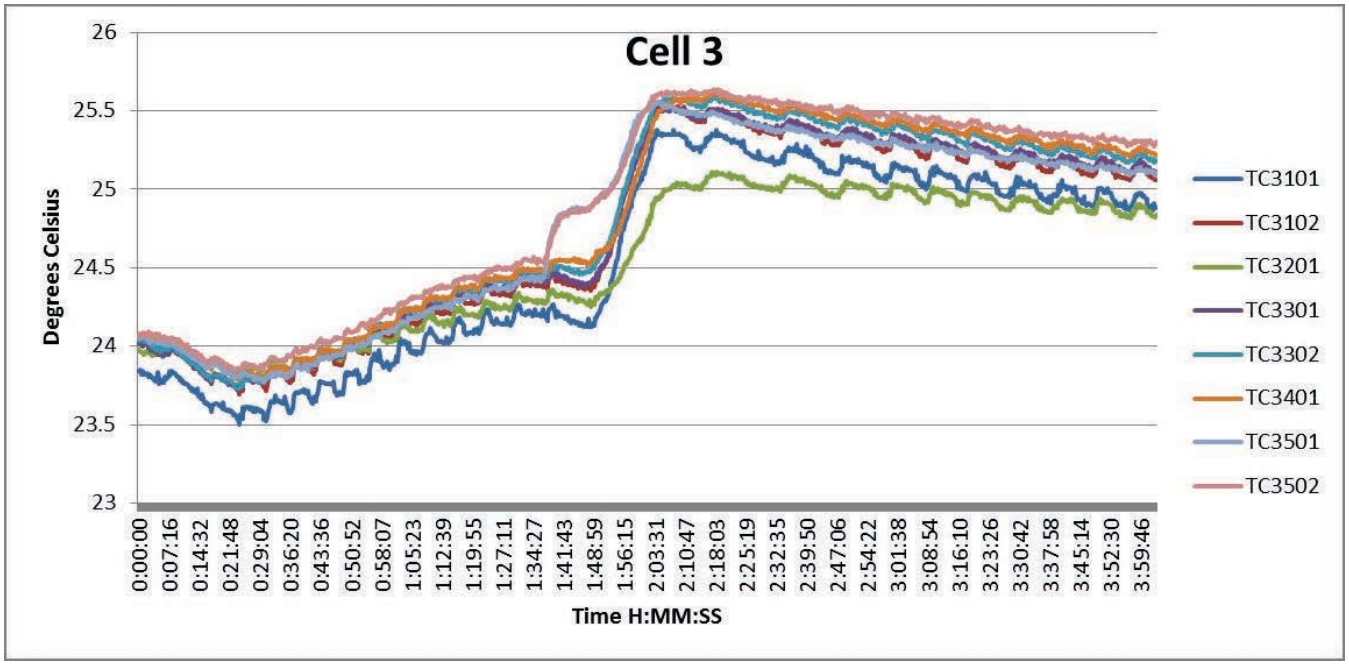

Figure B.167: Task A.1.C, Noisy, First 2-Hour, Cell 3 Temperatures

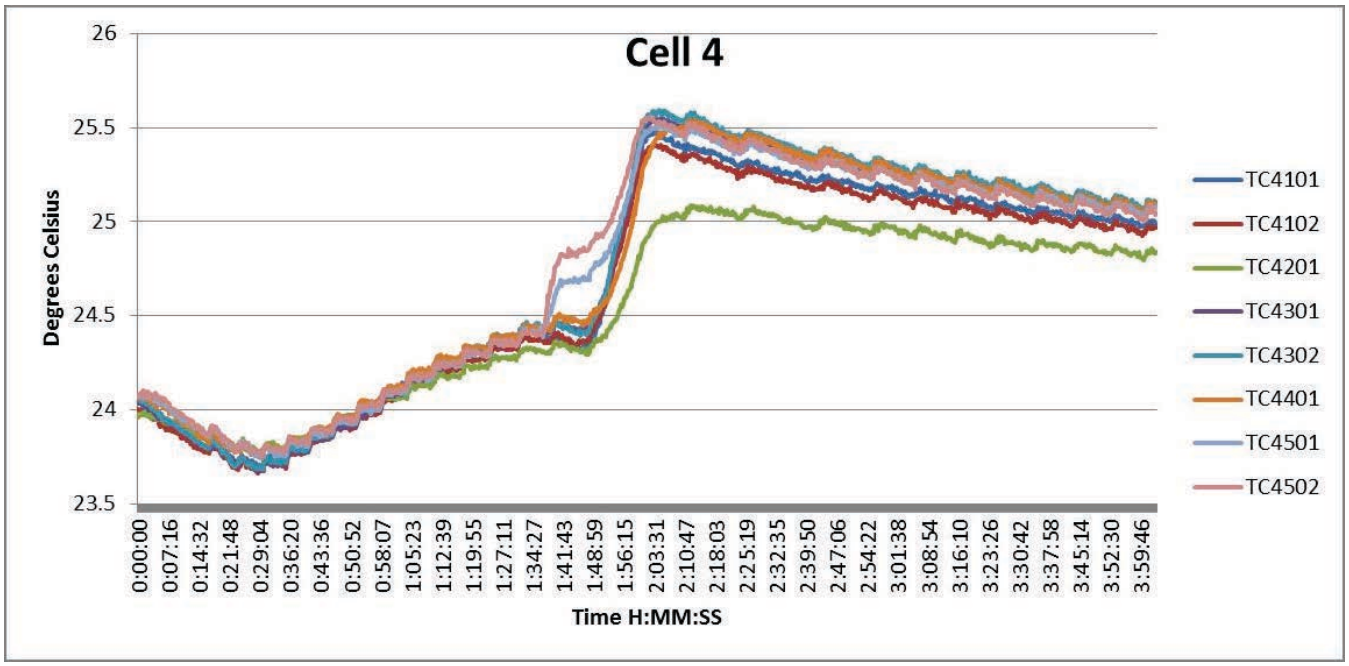

Figure B.168: Task A.1.C, Noisy, First 2-Hour, Cell 4 Temperatures

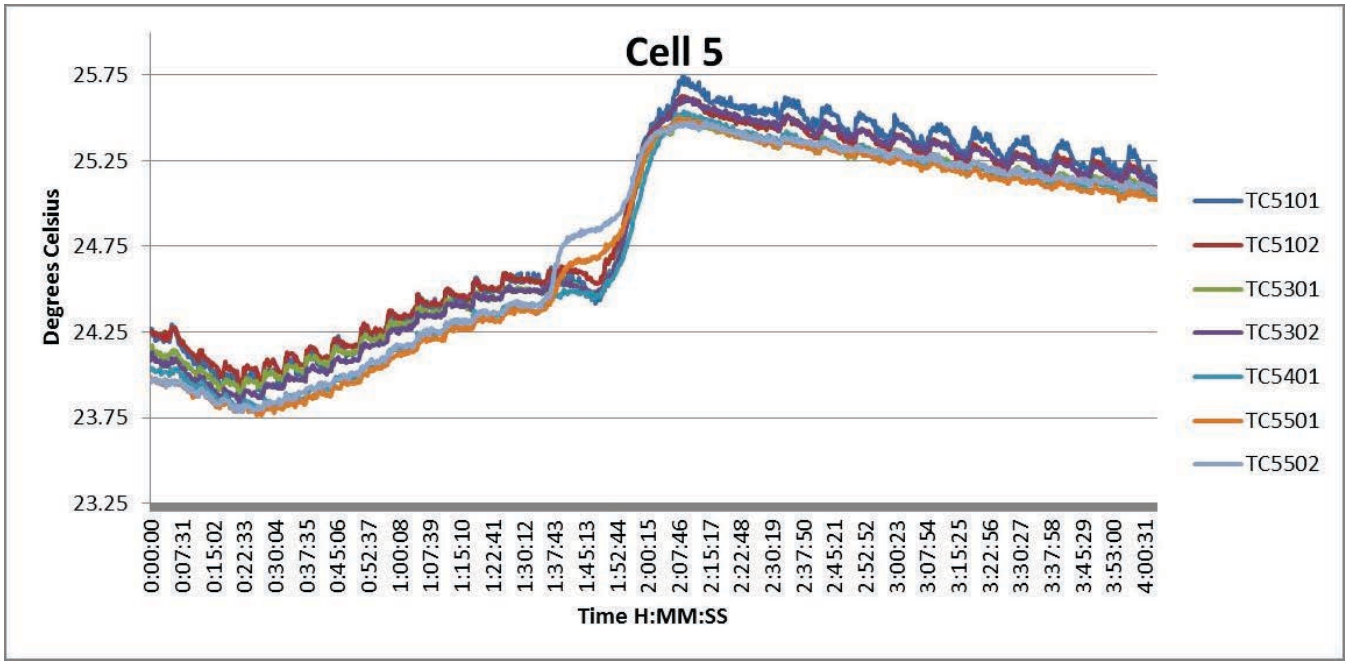

Figure B.169: Task A.1.C, Noisy, First 2-Hour, Cell 5 Temperatures

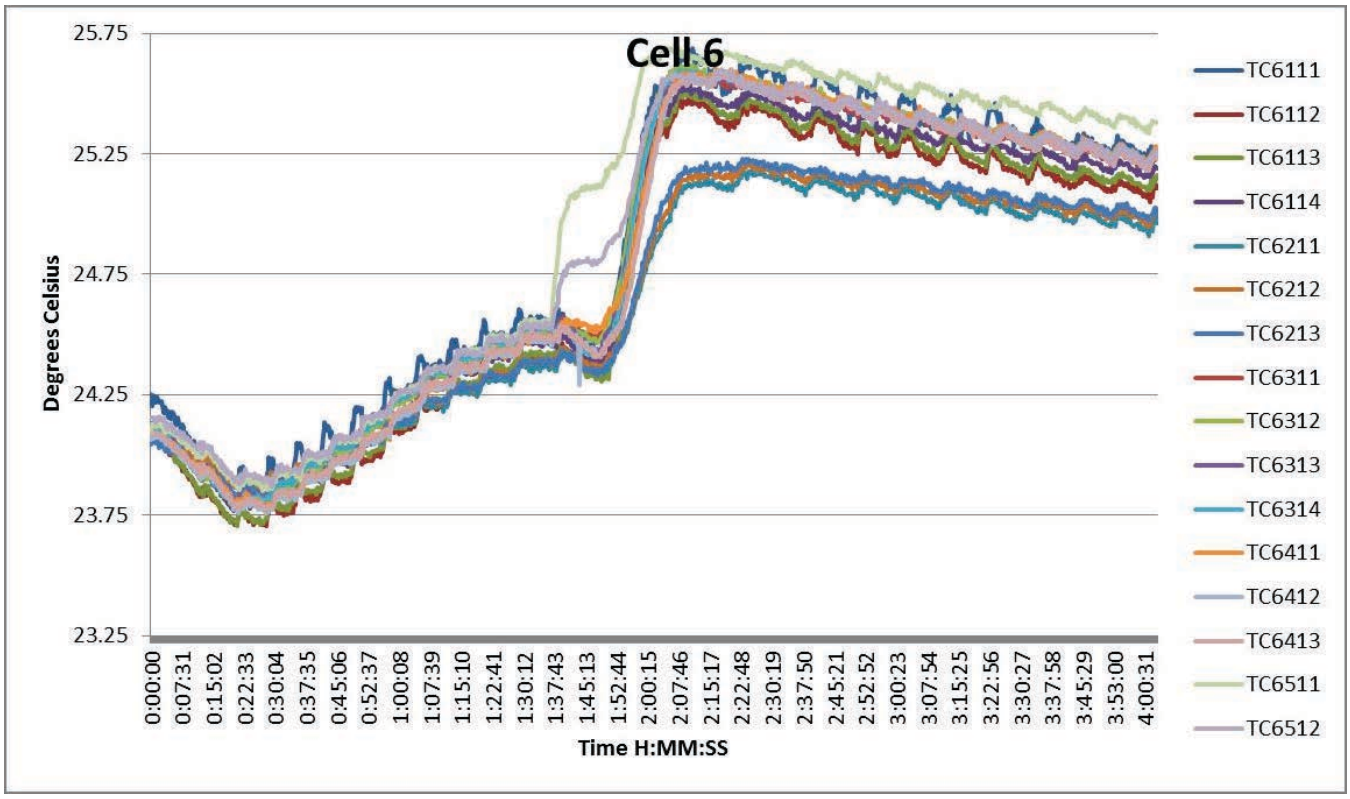

Figure B.170: Task A.1.C, Noisy, First 2-Hour, Cell 6 Temperatures

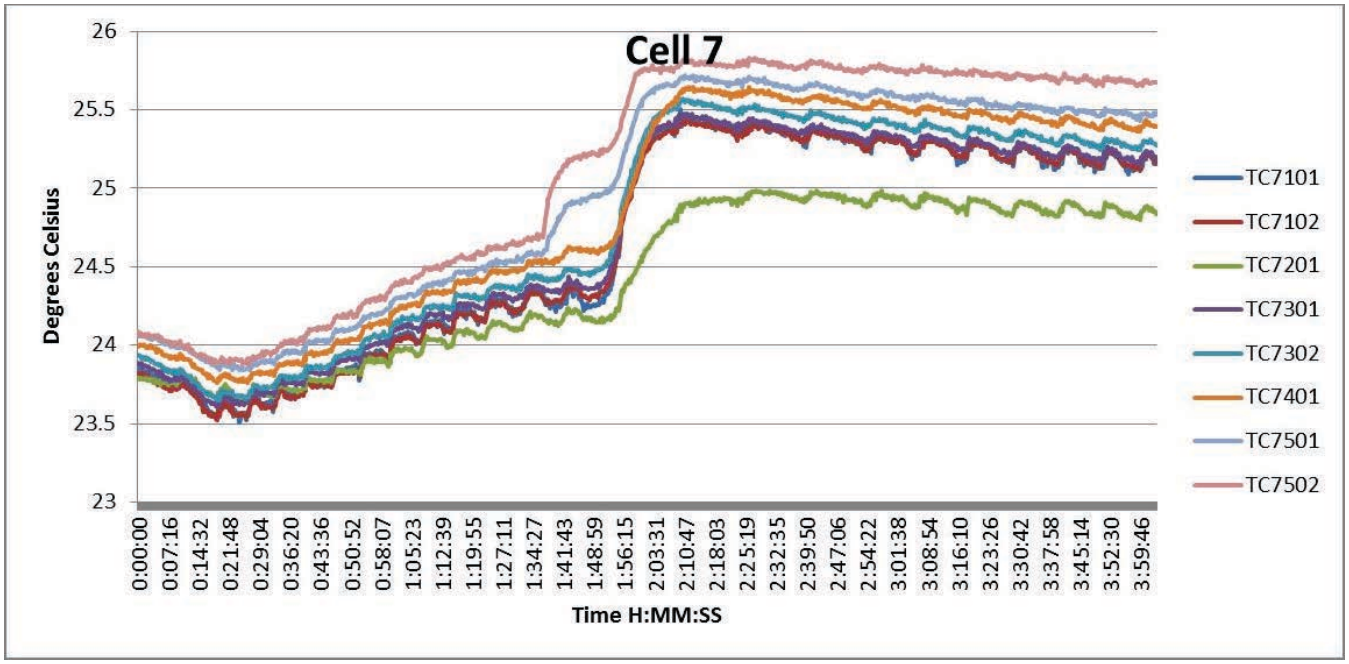

Figure B.171: Task A.1.C, Noisy, First 2-Hour, Cell 7 Temperatures

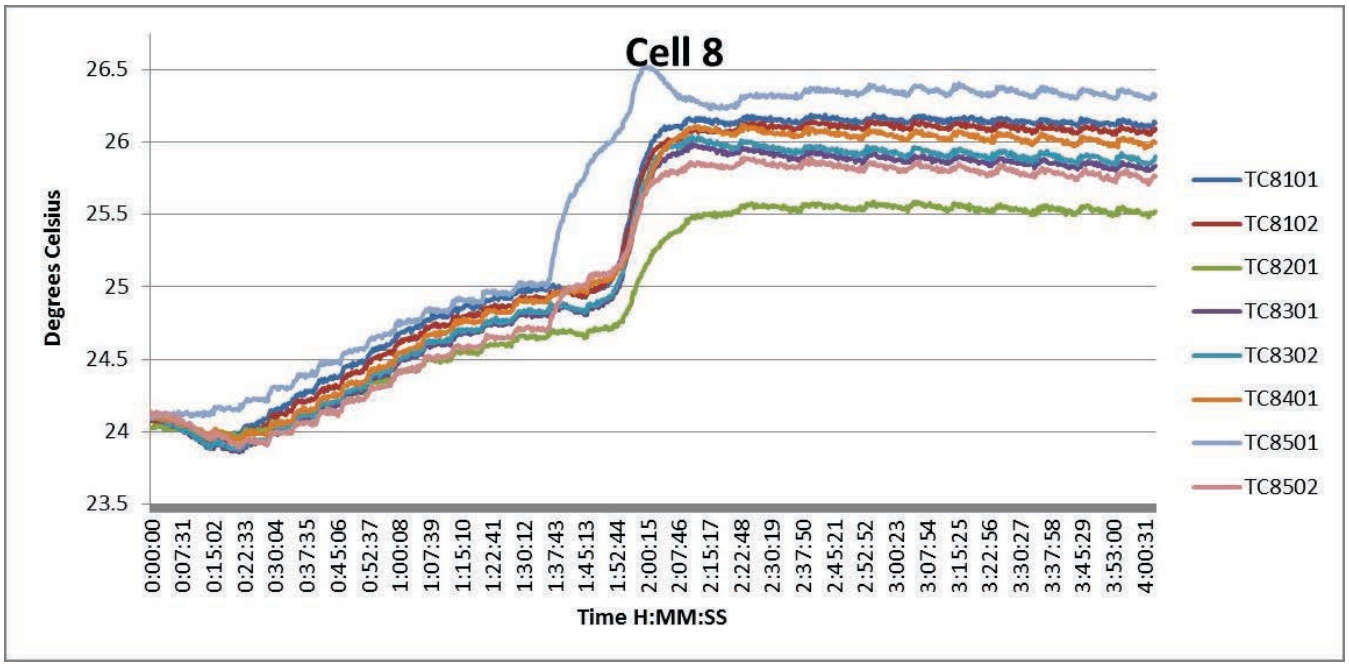

Figure B.172: Task A.1.C, Noisy, First 2-Hour, Cell 8 Temperatures

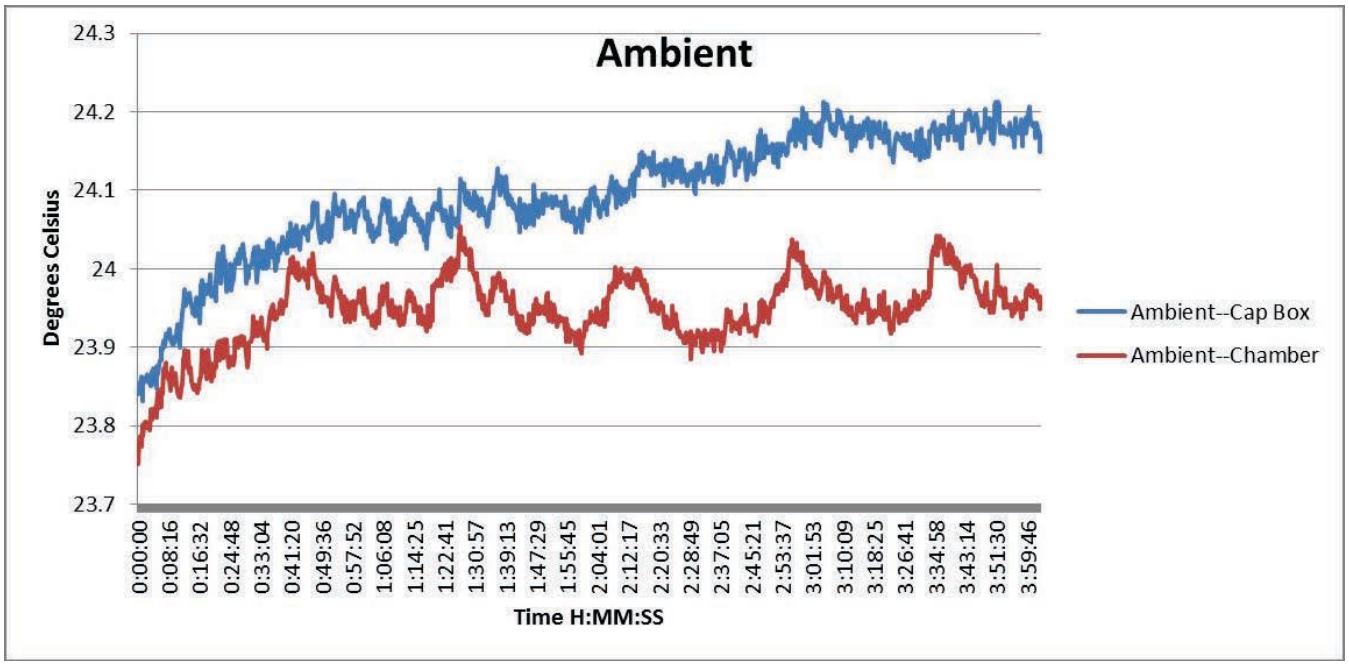

Figure B.173: Task A.1.C, Noisy, First 2-Hour, Ambient Temperatures

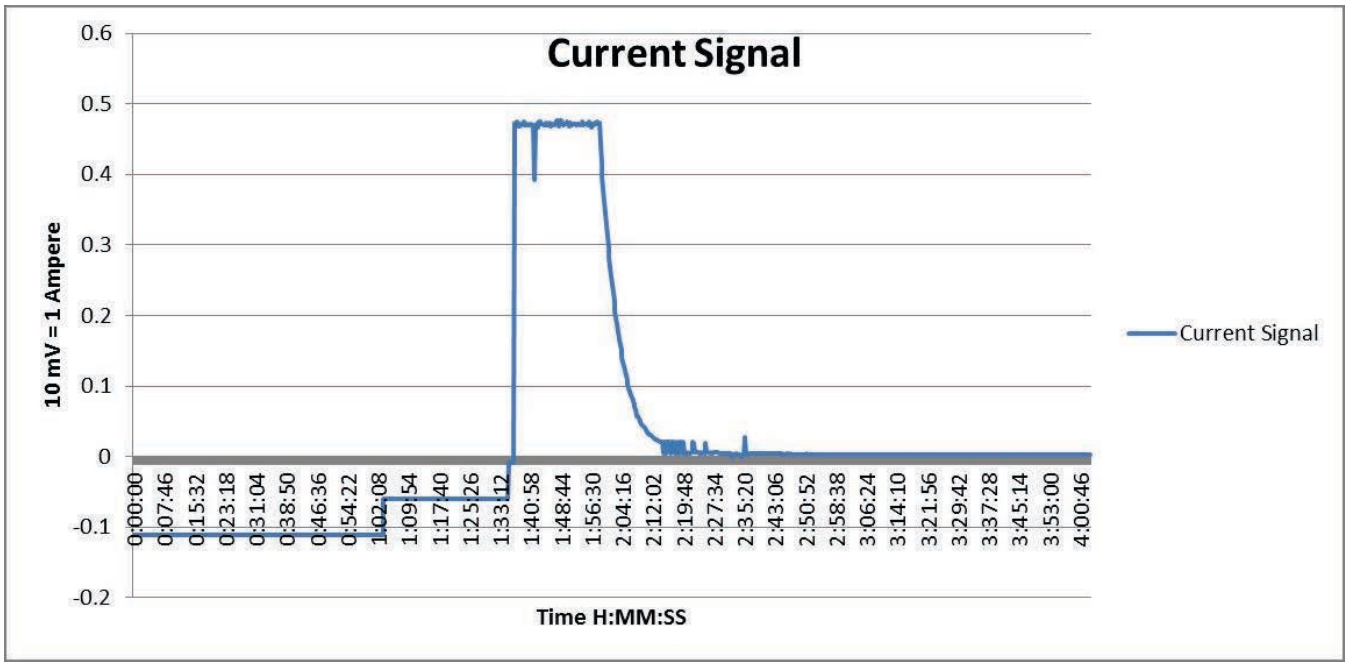

Figure B.174: Task A.1.C, Noisy, First 2-Hour, Current Signal from BMU HECS

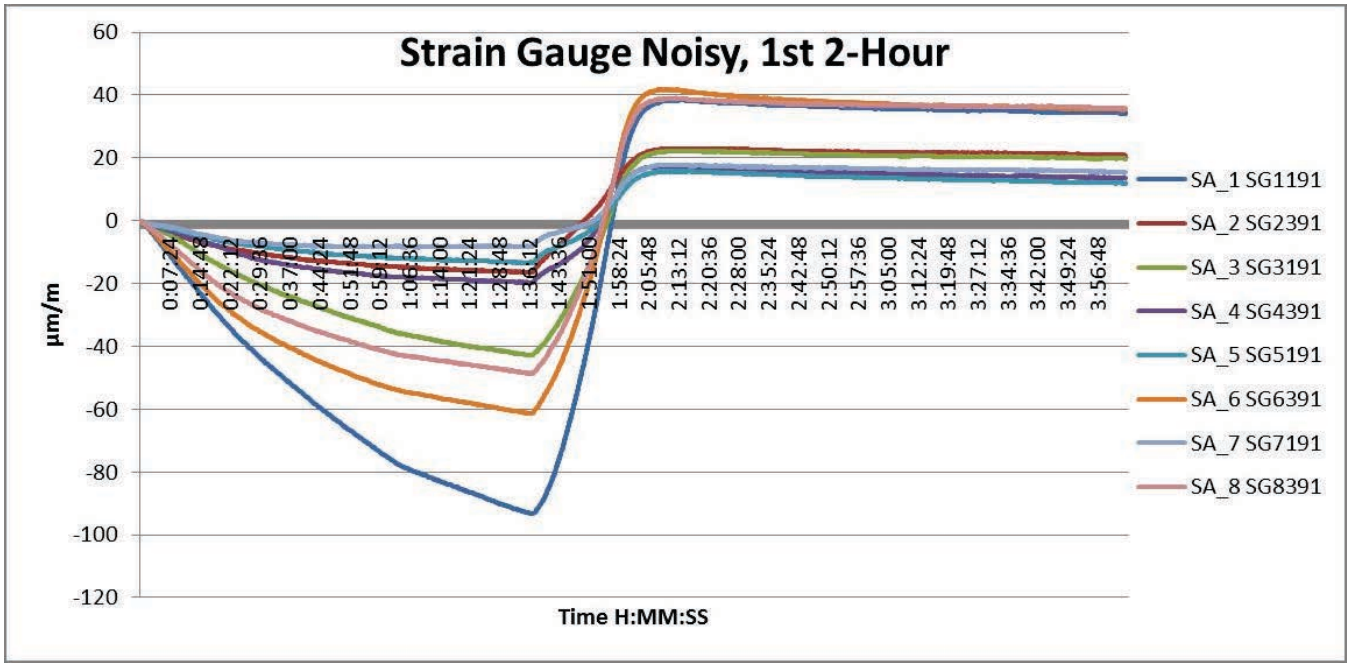

Figure B.175: Task A.1.C, Noisy, First 2-Hour, Strain Gauges

Task A.1.C – Noisy, Second 2-Hour

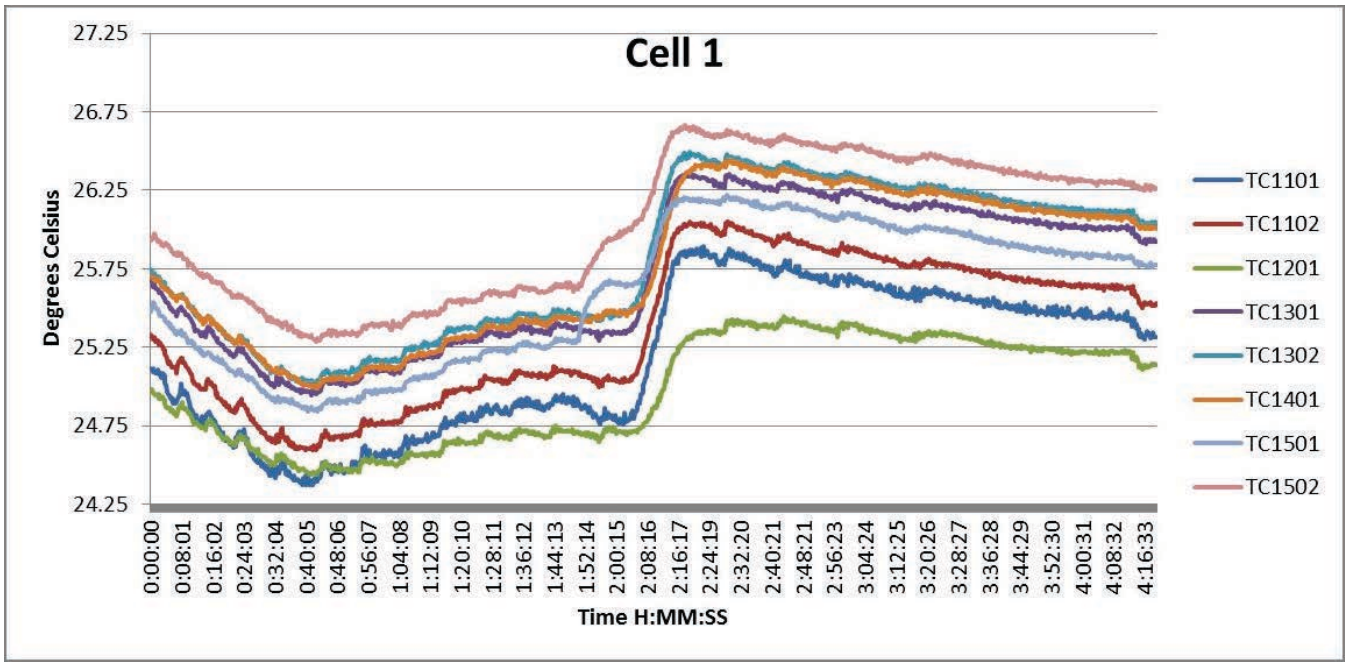

Figure B.176: Task A.1.C, Noisy, Second 2-Hour, Cell 1 Temperatures

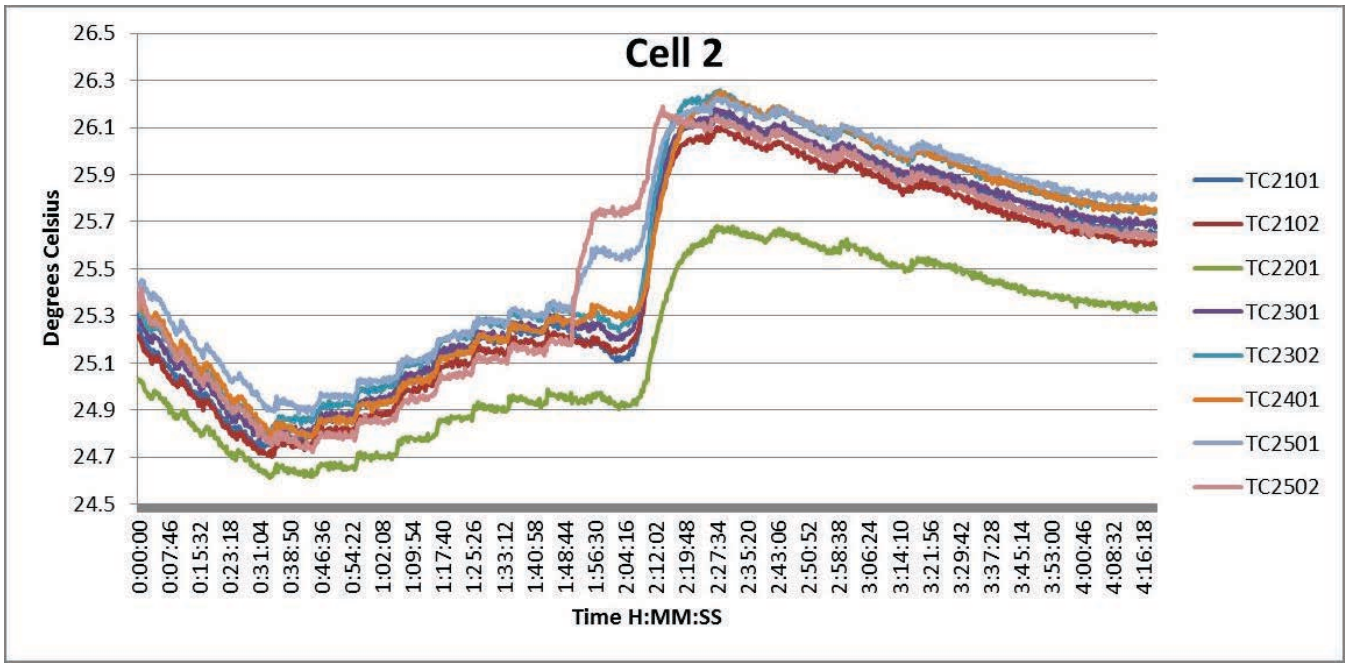

Figure B.177: Task A.1.C, Noisy, Second 2-Hour, Cell 2 Temperatures

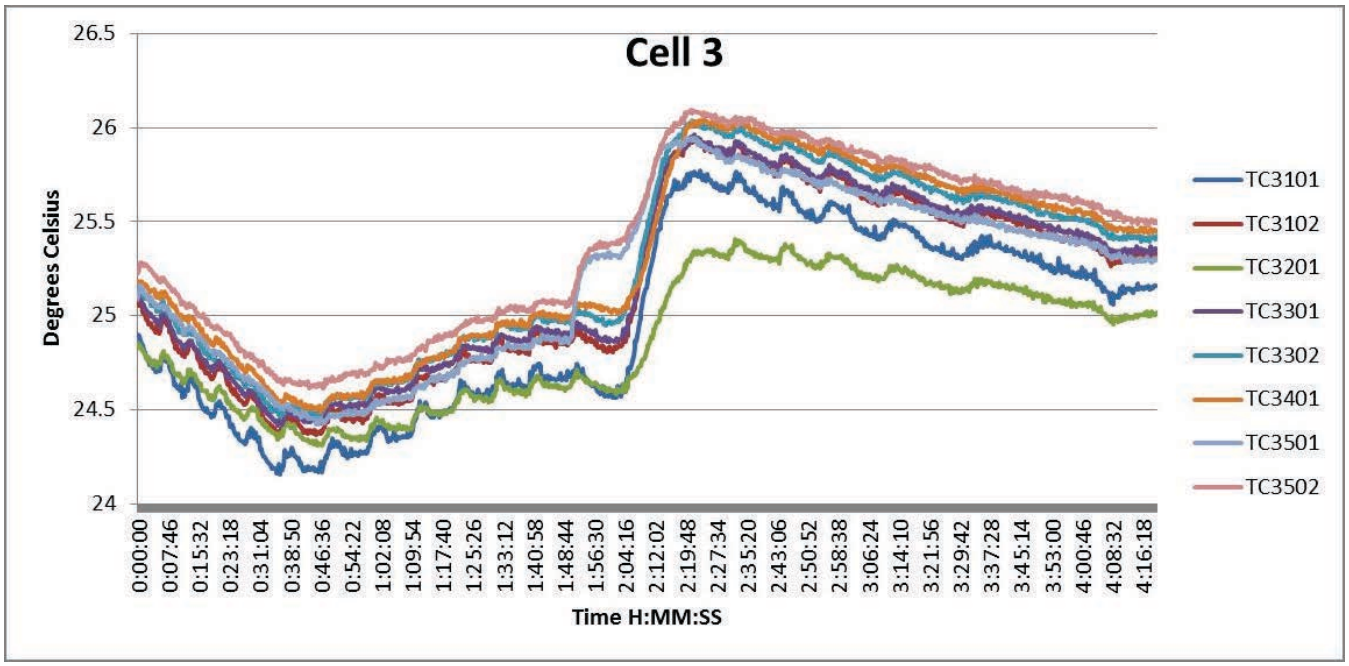

Figure B.178: Task A.1.C, Noisy, Second 2-Hour, Cell 3 Temperatures

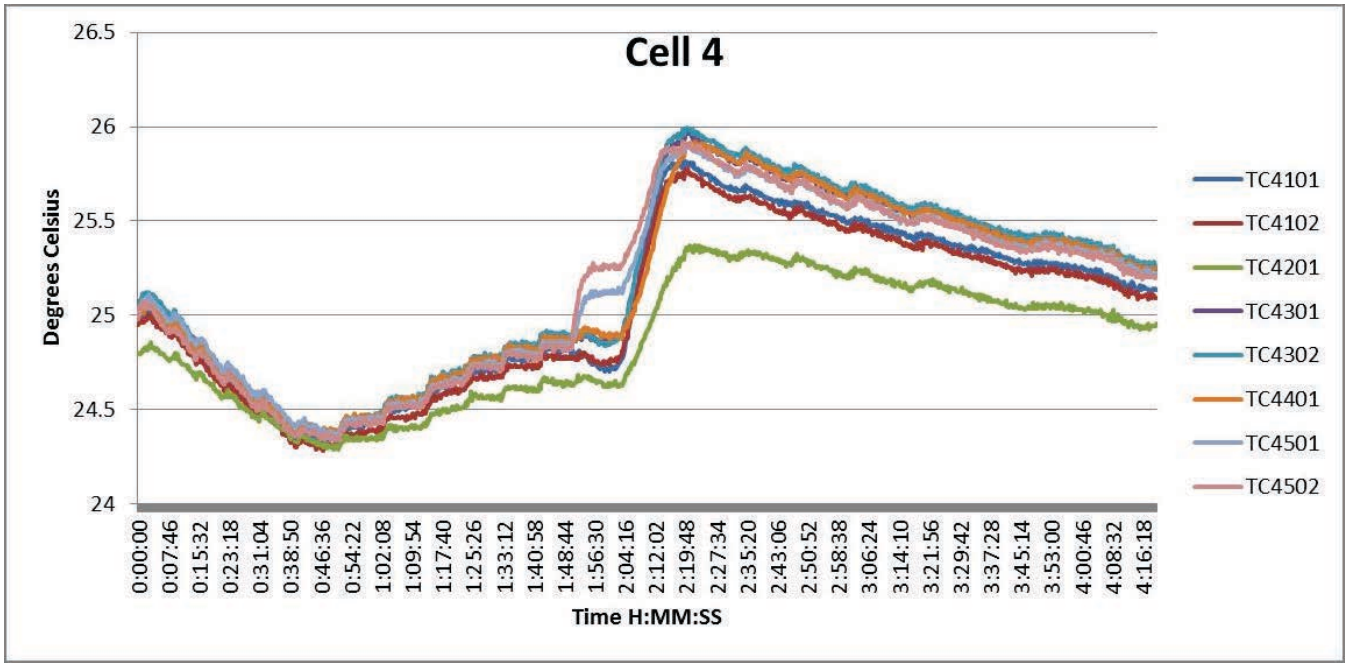

Figure B.179: Task A.1.C, Noisy, Second 2-Hour, Cell 4 Temperatures

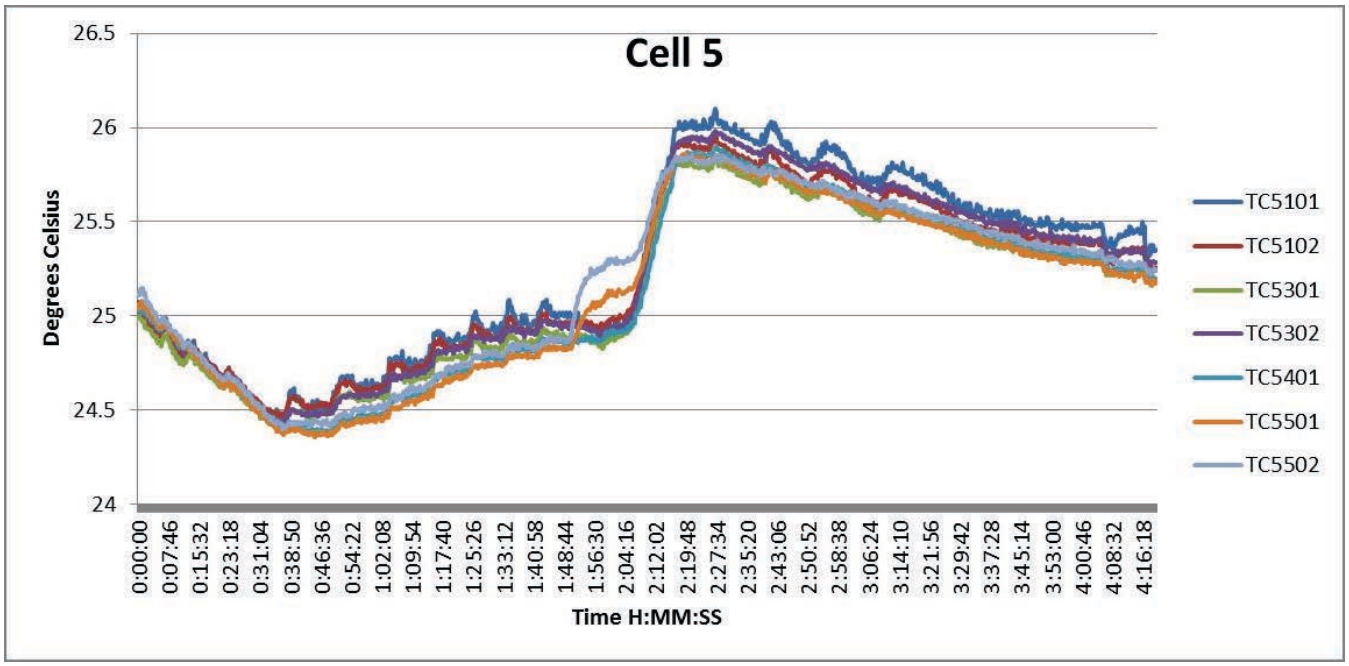

Figure B.180: Task A.1.C, Noisy, Second 2-Hour, Cell 5 Temperatures

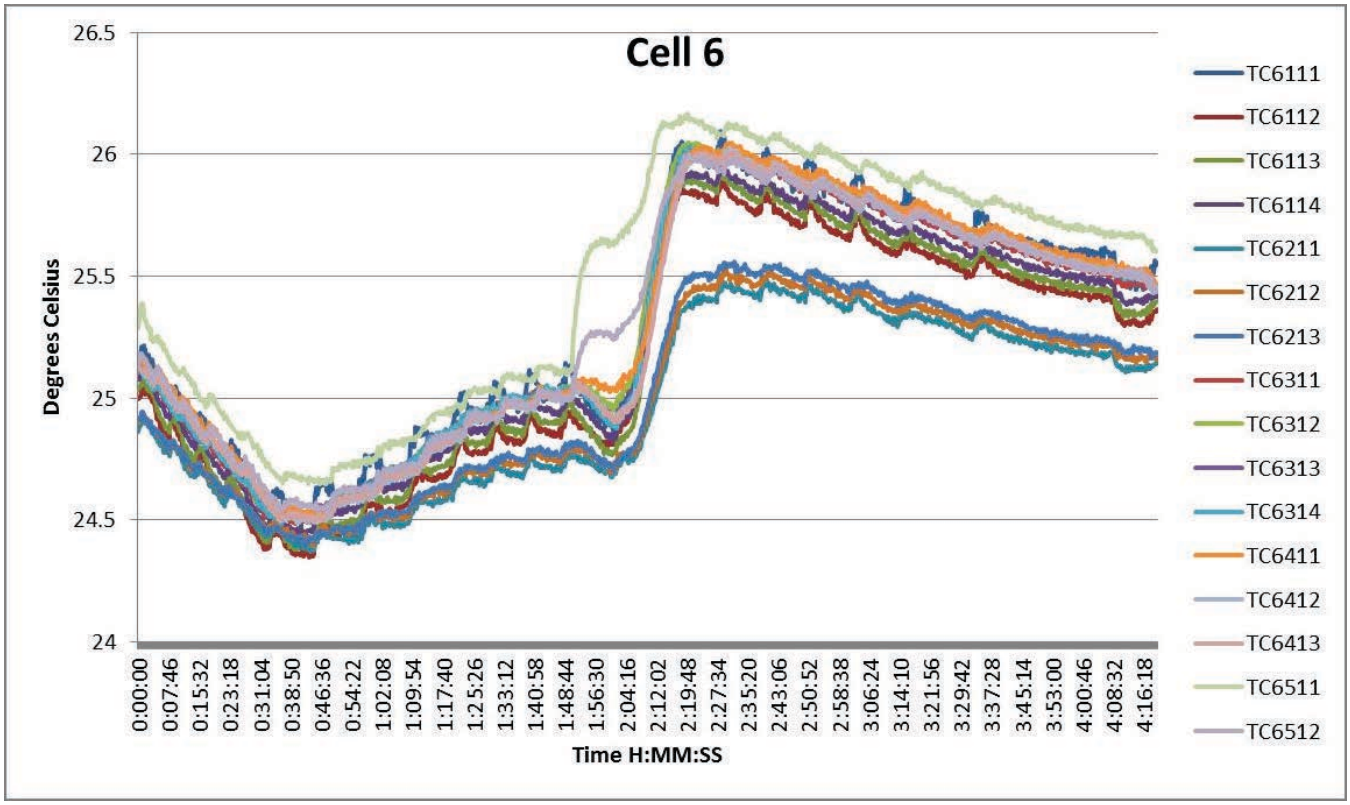

Figure B.181: Task A.1.C, Noisy, Second 2-Hour, Cell 6 Temperatures

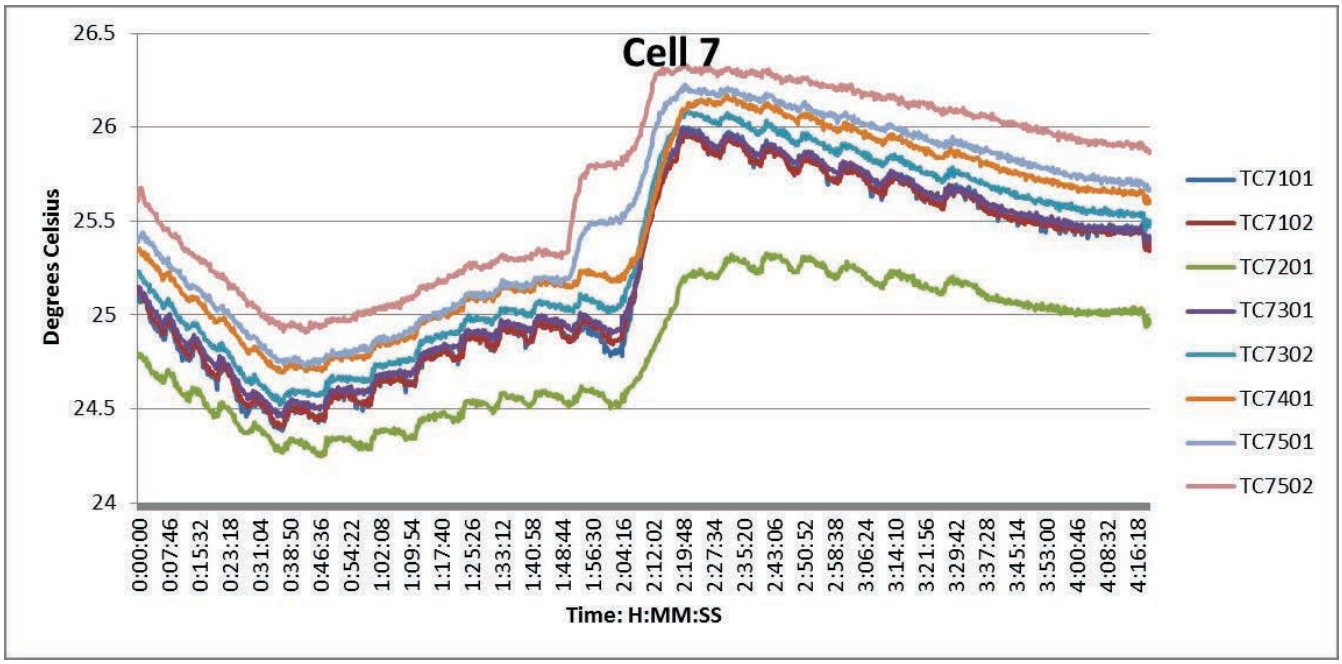

Figure B.182: Task A.1.C, Noisy, Second 2-Hour, Cell 7 Temperatures

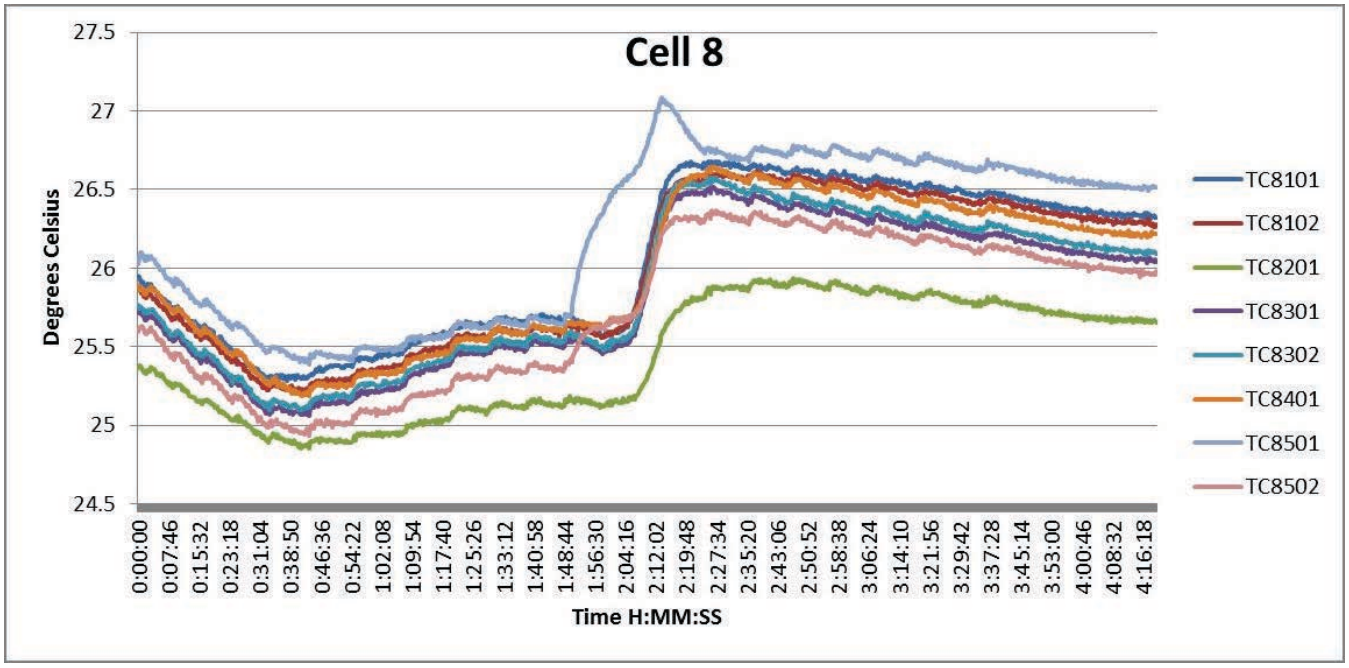

Figure B.183: Task A.1.C, Noisy, Second 2-Hour, Cell 8 Temperatures

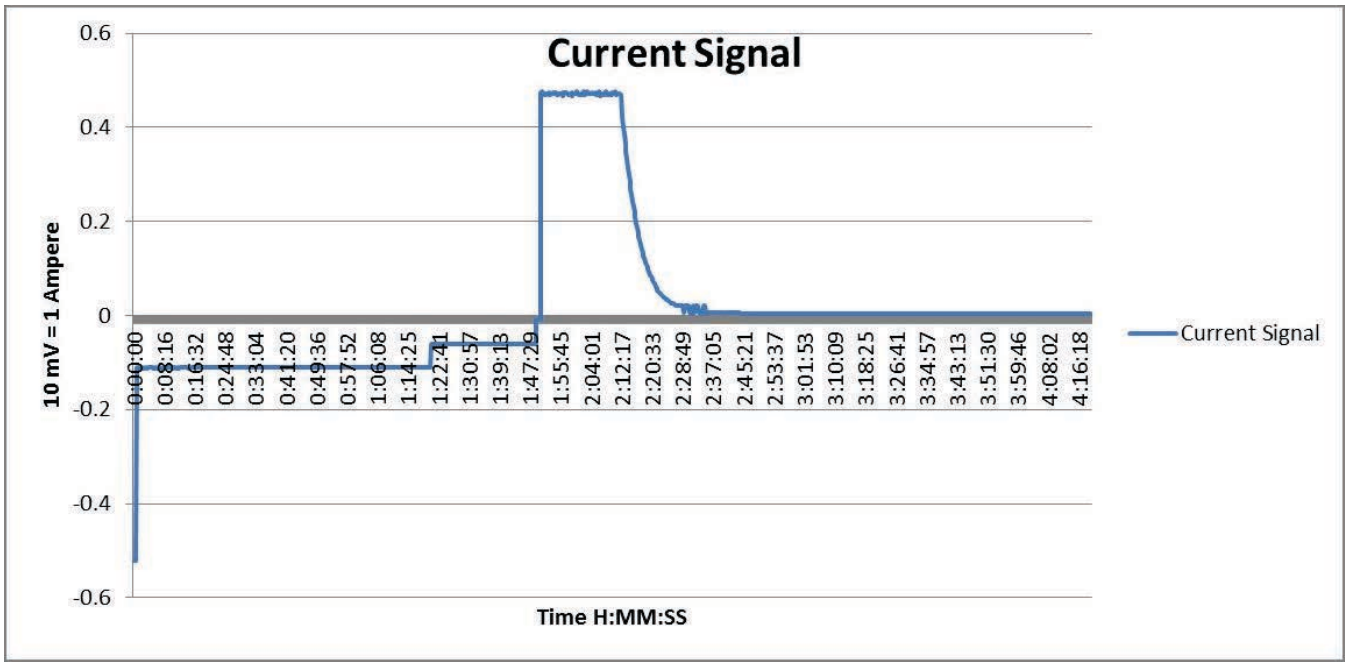

Figure B.184: Task A.1.C, Noisy, Second 2-Hour, Current Signal from BMU HECS

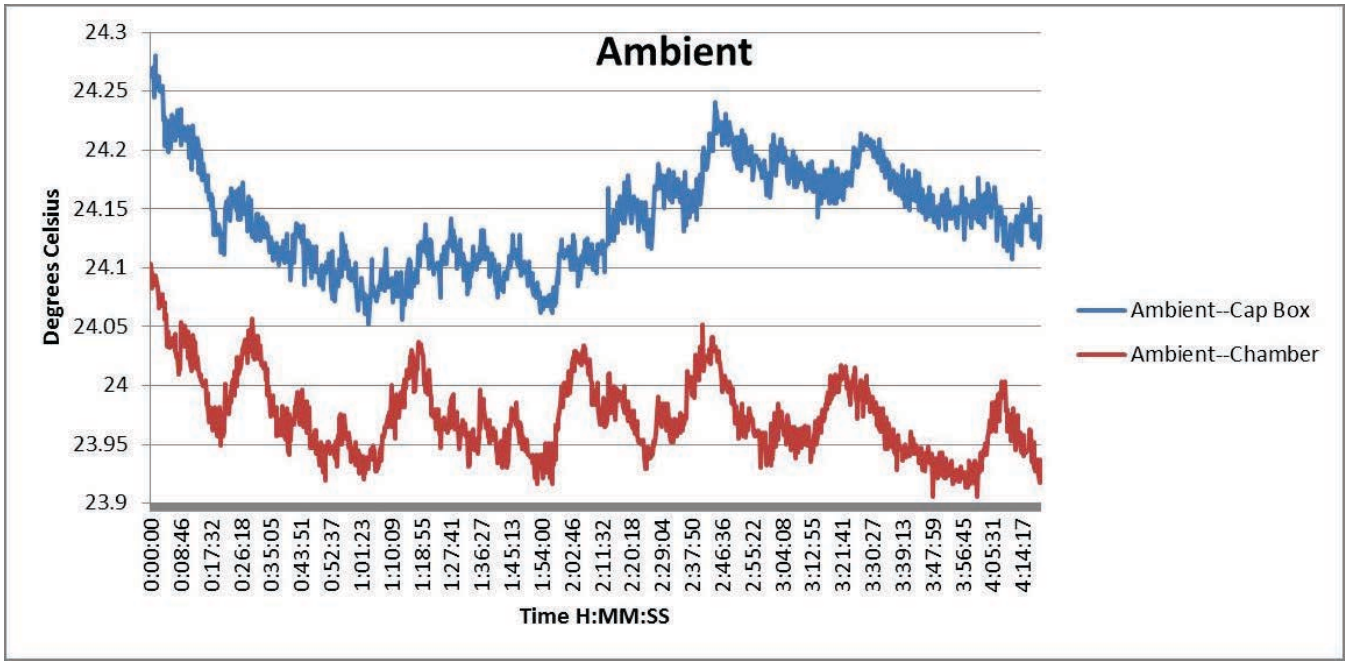

Figure B.185: Task A.1.C, Noisy, Second 2-Hour, Ambient Temperatures

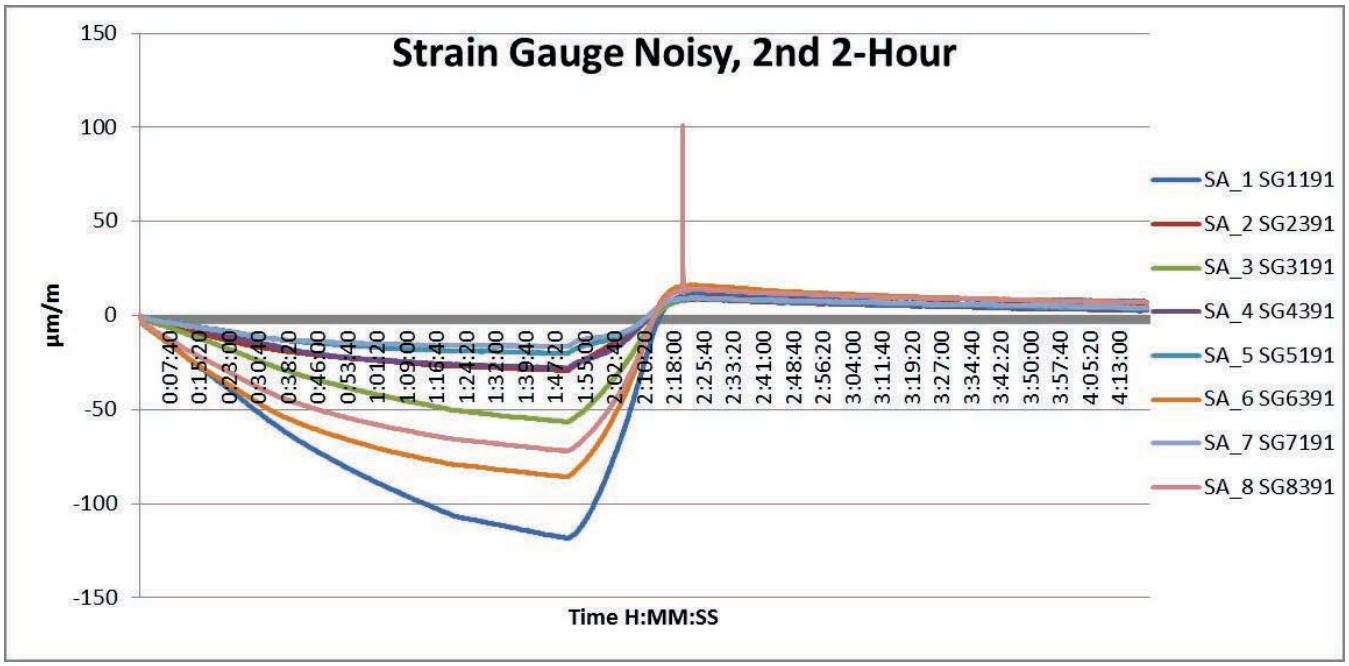

Figure B.186: Task A.1.C, Noisy, Second 2-Hour, Strain Gauges